

# **Charm at HERA I and HERA II with the ZEUS experiment.**

John Harry Loizides

London

2005



PhD thesis

Thesis submitted to University College London  
in accordance with the requirements of the degree of  
Doctor of Philosophy in the Faculty of Science

UMI Number: U592257

All rights reserved

INFORMATION TO ALL USERS

The quality of this reproduction is dependent upon the quality of the copy submitted.

In the unlikely event that the author did not send a complete manuscript and there are missing pages, these will be noted. Also, if material had to be removed, a note will indicate the deletion.



UMI U592257

Published by ProQuest LLC 2013. Copyright in the Dissertation held by the Author.  
Microform Edition © ProQuest LLC.

All rights reserved. This work is protected against  
unauthorized copying under Title 17, United States Code.



ProQuest LLC  
789 East Eisenhower Parkway  
P.O. Box 1346  
Ann Arbor, MI 48106-1346





## Abstract

Inclusive jet cross sections in photoproduction for events containing a  $D^*$  meson have been measured with the ZEUS detector at HERA using an integrated luminosity of  $78.6 \text{ pb}^{-1}$ . The events were required to have a virtuality of the incoming photon,  $Q^2$ , of less than  $1 \text{ GeV}^2$ , and a photon-proton centre-of-mass energy in the range  $130 < W_{\gamma p} < 280 \text{ GeV}$ . The measurements are compared with next-to-leading-order (NLO) QCD calculations. Good agreement is found with the NLO calculations over most of the measured kinematic region. Requiring a second jet in the event allowed a more detailed comparison with QCD calculations. The measured dijet cross sections are also compared to Monte Carlo (MC) predictions which incorporate leading-order matrix elements, followed by parton showers and hadronisation. The NLO QCD predictions are in general agreement with the data although differences have been isolated to regions where extra parton radiation is present. The MC models give a better description of the shape of the measured cross sections. This thesis ends with a look at the first HERA II data. The decay of  $D^\pm$  mesons were studied and for the first time the newly installed micro vertex detector (MVD) was used to tag charm mesons using secondary vertices arising from the decay of ( $c \rightarrow D^\pm$  or  $b \rightarrow c \rightarrow D^\pm$ ). This shows that the MVD will be a powerful tool in the future analyses of heavy quark production at ZEUS.

To my parents and brother

‘As the young lady said when shovelling manure-with all this shit there must be a pony in here somewhere.’

Malcolm Derrick

---

## Acknowledgments

---

I will start by thanking my parents and bother, who helped me through this with their love and support; without which I may have never finished - of course there was the nagging at times on the phone from my mum saying 'when are you going to finish', which spurred me on. To all my friends back in the UK specially Dishang, Diksha, Sahil, Mitesh, Joe (Anastasi), Sabrina and Farah I know they all can't believe I'm a Dr of physics - neither can I!

Alexandra Hachmeister for teaching me German in my first year in Hamburg, the people in DESY who kept day-to-day life at work fun and fresh in the past and present Steve Robins, Steve Hanlon, Joanna Hamilton, Joe Cole, Matt Lightwood, Chris Targett-Adams, Ben West, Mike Rigby, Mari Bell, Ingo Bloch, Oliver Gutsche, Claire Gwenlan, Mark Sutton, Chris Youngman, Alessandro Polini, Cathy Farrow, Billy Dunne, Cathrine Fry, Manuel Zambrana, Stuart Boogert, Philip Allfrey, Alex Tapper. The H1 posse of Dave South, Paul 'in the jungle' Laycock, Matthew Beckingham, Nick Maldon times have been fun meeting you lot out on the town usually late at night in some bar.

Of course a shout goes out to the DESY footy team who took their time to warm to me but turned out to be a great set of lads. Our adventures playing the many teams throughout Hamburg has been fun, I don't think any of us could believe we got promoted last year. Damir Lelas thanks for being a good friend and introducing me to the team. Steve Aplin, Tom Danielson, Jerome Whyte and my old friend Umer Noor - thanks for making DESY fun and going out to play Baseball and American Football whenever the slightest glimpse of sunlight was visible. Jerome (Yerome) you have been a good friend, hope all goes well for you in the future.

Thanks to Argonne in particular Jose Repond, Rik Yoshida, Malcolm Derrick and Steve

Magill for giving the chance to do this PhD.

Antonio Pellegrino and Danny Krakaur thanks for taking me under your wings and teaching me the ways of the CFLTp. It lead to many sleepless nights and panic situations but helped me understand the inner working of the experiment in ways that I would never have been able to alone. Also thanks to Antonio for being a great friend I wish you the best!

Many thanks go to Richard Hall-Wilton, Takanori Kohno, Erik Maddox, Matthew Wing and Jon Butterworth for working with me throughout the years teaching me physics along the way and being good friends. Thanks to Gudrun Heinrich for doing theoretical calculations for my work. A special thanks goes to Tegid Wyn Jones, who guided me to the end of my thesis telling me jokes and many story's along the way.

Dustin, Yee and Leo I started things of with you all. We were an unlikely set of people to start PhD's but we have all done it, you were all great guys.

To my office mates Silvia Miglioranzi and Sergei Chekanov thanks for putting up with me for 3 years, I sure you are glad I'm not in the office anymore telling you random stories.

The bbc football web-site also have to be mentioned, it is great! I visit it everyday without this I think I would have missed the Premier League football although I have now grown to appreciate German football, but there is only one Arsenal!

Cafe Lisboa on the corner of Grosse Brunnenstrasse, Carla, Rui and Betty thanks for making coffee in the mornings and getting my day of to a happy one.

Susan Ketels many thanks for making life easier to understand in Germany, sorting out bills, problems with landlords, moving etc.. the list is endless.

James and Jenny Ferrando, we will see each other till the end of the experiment thanks for being really nice people. James your great to work with very relaxed sometime a little too relaxed but in only the way James can be. Avraam you came to DESY and made things funny and slightly difficult at times but are a unique person; thanks for all the fun times. Amita you have taught me much about the U.S, we had fun traveling through China even if I nearly through you off a sand dune, I also think at that point neither of us could imagine finishing our PhD's, thanks for the fun times.

Tim Namssoo, Julia, Vito and Einstein what can I say expect everyday life living above a house with a Dog and a Cat is great fun! Tim man thanks for the support and coffees in the morning and being a good friend. I am now no longer scared of cats, anyone who as met Vito

will understand - he is maybe the biggest cat in the world! DESY, CCLRC, UCL and Argonne  
thanks for the support and employing me.

---

# Contents

---

<b>Acknowledgments</b>	<b>6</b>
<b>List of Figures</b>	<b>17</b>
<b>List of Tables</b>	<b>40</b>
<b>1 Introduction</b>	<b>41</b>
<b>2 Overview of <math>ep</math> scattering and previous results on heavy quark production in colliders</b>	<b>44</b>
2.1 Kinematics of $ep$ scattering . . . . .	44
2.2 QCD and $ep$ interactions . . . . .	45
2.2.1 The quark parton model . . . . .	47
2.2.2 The improved quark parton model . . . . .	48
2.3 Jets . . . . .	51
2.4 Photoproduction of heavy quarks . . . . .	51
2.4.1 NLO Photoproduction calculations (FMNR) ‘massive’ scheme . . . . .	52
2.4.2 NLO Photoproduction calculations ‘massless’ scheme . . . . .	53
2.4.3 Fixed order next-to-leading logarithmic calculations (FONLL) . . . . .	54
2.4.4 Heavy quark fragmentation functions . . . . .	54
2.5 QCD evolution and event generators . . . . .	56
2.5.1 Monte Carlo models . . . . .	56
2.5.2 Hadronisation . . . . .	57
2.5.3 The parton shower and fragmentation . . . . .	57



2.5.4	HERWIG . . . . .	57
2.5.5	PYTHIA . . . . .	58
2.6	Measurements of heavy quark production in $ep, ee, \gamma\gamma, pp$ collisions . . . . .	58
2.6.1	Inclusive $D^*$ cross sections in photoproduction . . . . .	58
2.6.2	Charm jet cross sections in photoproduction . . . . .	59
2.6.3	D meson cross sections at LEP . . . . .	60
2.6.4	D meson cross sections at the Tevatron . . . . .	61
2.6.5	Dijet correlations $ep, ee, \gamma\gamma, pp$ collisions . . . . .	63
2.7	Summary of charm production . . . . .	68
<b>3</b>	<b>The HERA collider and the ZEUS detector</b>	<b>75</b>
3.1	The HERA collider . . . . .	75
3.2	The ZEUS detector . . . . .	77
3.3	The Central Tracking Detector . . . . .	80
3.4	The Uranium–Scintillator Calorimeter . . . . .	80
3.5	The luminosity measurement . . . . .	83
3.6	The ZEUS trigger system . . . . .	84
3.6.1	The First Level Trigger (FLT) . . . . .	85
3.6.2	The Second Level Trigger (SLT) . . . . .	86
3.6.3	The Third Level Trigger (TLT) . . . . .	86
<b>4</b>	<b>Event reconstruction and selection</b>	<b>87</b>
4.1	Overview . . . . .	87
4.2	Reconstruction of the kinematic variables . . . . .	88
4.2.1	The $y_{JB}$ correction . . . . .	89
4.2.2	Removal of DIS events by electron identification . . . . .	92
4.3	Reconstruction of the hadronic final state . . . . .	93
4.3.1	Energy Flow Objects (EFOs) . . . . .	93
4.4	Jet reconstruction . . . . .	94
4.4.1	The $k_T$ clustering algorithm . . . . .	95
4.4.2	Jet energy correction . . . . .	96
4.4.3	Trigger selection . . . . .	100

## Contents

4.4.4	FLT . . . . .	100
4.4.5	SLT . . . . .	101
4.4.6	TLT . . . . .	102
4.4.7	Offline selections . . . . .	103
4.4.8	Selecting photoproduction events . . . . .	103
4.4.9	Selecting charm events . . . . .	104
4.4.10	Reconstruction of the $D^{*\pm}$ meson . . . . .	104
4.4.11	$D^*$ meson signal extraction . . . . .	105
4.4.12	$D^{*\pm}$ meson & jet matching . . . . .	108
4.4.13	Reconstruction of $x_\gamma^{obs}(D^*, \text{untagged jet})$ . . . . .	110
4.5	Extending the $p_T^{D^*}$ range . . . . .	111
4.6	$D^{*+}$ & $D^{*-}$ signals . . . . .	113
4.7	Dijet Variables $x_\gamma^{obs}$ , $\Delta\phi^{jj}$ , $p_T^{jj}$ and $m^{jj}$ . . . . .	114
4.8	Summary of the offline selection cuts . . . . .	116
<b>5</b>	<b>Characteristics of charm jet events</b>	<b>117</b>
5.0.1	Decay of charmed hadrons . . . . .	117
5.1	Signal and background Monte Carlo samples . . . . .	118
5.1.1	Charm Sample . . . . .	118
5.1.2	Beauty Sample . . . . .	119
5.2	Comparison between data and Monte Carlo simulation . . . . .	119
5.2.1	Reconstruction of $\cos\theta^*$ and $m^{jj}$ . . . . .	119
5.2.2	Jet energy balance . . . . .	121
5.2.3	Event variable modeling . . . . .	122
5.2.4	The separation power of direct-enriched and resolved-enriched events using $x_\gamma^{obs}(D^*, \text{untagged jet})$ and $x_\gamma^{obs}$ . . . . .	123
5.2.5	Parton and hadron level comparison . . . . .	125
5.2.6	Hadronisation corrections for NLO calculations . . . . .	125
<b>6</b>	<b>Data correction and systematic uncertainties</b>	<b>130</b>
6.1	Trigger efficiency . . . . .	130
6.2	Efficiency, Purity & Acceptance . . . . .	130

6.3	Systematic uncertainties . . . . .	131
6.3.1	$D^0$ mass width systematic . . . . .	133
6.3.2	Uncertainties in the jet selection . . . . .	139
6.3.3	Uncertainties of the statistical signal extraction . . . . .	139
6.3.4	Uncertainty of the luminosity measurement . . . . .	139
6.4	Summary of the systematic uncertainties . . . . .	139
<b>7</b>	<b>Inclusive charm &amp; jets</b>	<b>142</b>
7.1	Definition of the cross sections . . . . .	142
7.2	The unfolding method . . . . .	143
7.3	Measurement of $d\sigma/dE_T^{\text{jet}}$ . . . . .	143
7.4	Measurement of $d\sigma/d\eta^{\text{jet}}$ . . . . .	143
7.5	Measurement of $d\sigma/dE_T^{\text{jet}}$ and $d\sigma/d\eta^{\text{jet}}$ in regions of $p_T^{D^*}$ . . . . .	147
7.6	Measurement of $d\sigma/dx_\gamma^{\text{obs}}(D^*, \text{untagged jet})$ . . . . .	147
<b>8</b>	<b>Charm &amp; dijets</b>	<b>151</b>
8.1	Definition of the cross sections . . . . .	151
8.2	Measurement of $d\sigma/dx_\gamma$ , $d\sigma/dm^{jj}$ , $d\sigma/dp_T^{jj}$ and $d\sigma/dp_T^{2jj}$ , and $d\sigma/d\Delta\phi^{jj}$ . . . .	152
8.3	Measurement of $d\sigma/dm^{jj}$ , for $x_\gamma > 0.75$ (direct-enriched) and $x_\gamma < 0.75$ (resolved-enriched) . . . . .	152
8.4	Measurement of $d\sigma/dp_T^{2jj}$ and $d\sigma/d\Delta\phi^{jj}$ , for $x_\gamma > 0.75$ (direct-enriched) and $x_\gamma < 0.75$ (resolved-enriched) . . . . .	155
<b>9</b>	<b>Results &amp; discussions</b>	<b>159</b>
<b>10</b>	<b>The upgrade of HERA II</b>	<b>160</b>
10.1	The HERA collider upgrade . . . . .	160
10.1.1	The HERA luminosity upgrade . . . . .	161
10.1.2	The major problems encountered in the ZEUS interaction region . . . .	161
10.1.3	e-gas & p-gas background . . . . .	163
10.2	The detector components upgrade in ZEUS . . . . .	164
10.3	The ZEUS Micro Vertex Detector (MVD) . . . . .	165
10.3.1	Detector specifications . . . . .	165

<b>11 HERA II and tagging of heavy meson decays</b>	<b>168</b>
11.1 Triggering on D mesons after the upgrade . . . . .	168
11.1.1 Selecting $D^\pm$ events . . . . .	168
11.1.2 Reconstruction and tagging of the $D^\pm$ meson . . . . .	170
11.2 Upgrade potential summary . . . . .	179
<b>12 Summary &amp; Outlook</b>	<b>180</b>
<b>13 Appendix A : Inclusive jet cross section mass peaks</b>	<b>181</b>
13.0.1 $d\sigma/dE_T^{jet}$ Mass Peaks, $-1.5 < \eta^{jet} < 2.4$ . . . . .	182
13.0.2 $d\sigma/dE_T^{jet}$ Mass Peaks, $-1.5 < \eta^{jet} < -0.5$ . . . . .	183
13.0.3 $d\sigma/dE_T^{jet}$ Mass Peaks, $-0.5 < \eta^{jet} < 0.5$ . . . . .	184
13.0.4 $d\sigma/dE_T^{jet}$ Mass Peaks, $0.5 < \eta^{jet} < 1.5$ . . . . .	185
13.0.5 $d\sigma/dE_T^{jet}$ Mass Peaks, $1.5 < \eta^{jet} < 2.4$ . . . . .	186
13.0.6 $d\sigma/d\eta^{jet}$ Mass Peaks, $E_T^{jet} > 6$ GeV . . . . .	187
13.0.7 $d\sigma/d\eta^{jet}$ Mass Peaks, $6 < E_T^{jet} < 9$ GeV . . . . .	189
13.0.8 $d\sigma/d\eta^{jet}$ Mass Peaks, $E_T^{jet} > 9$ GeV . . . . .	191
13.0.9 $d\sigma/dE_T^{jet}$ Mass Peaks, $-1.5 < \eta^{jet} < 2.4$ tagged $D^*$ jets . . . . .	193
13.0.10 $d\sigma/d\eta^{jet}$ Mass Peaks, $E_T^{jet} > 6$ GeV tagged $D^*$ jets . . . . .	194
13.0.11 $d\sigma/d\eta^{jet}$ Mass Peaks, $6 < E_T^{jet} < 9$ GeV tagged $D^*$ jets . . . . .	196
13.0.12 $d\sigma/d\eta^{jet}$ Mass Peaks, $E_T^{jet} > 9$ GeV tagged $D^*$ jets . . . . .	198
13.0.13 $d\sigma/dE_T^{jet}$ Mass Peaks, $-1.5 < \eta^{jet} < 2.4$ untagged $D^*$ jets . . . . .	200
13.0.14 $d\sigma/d\eta^{jet}$ Mass Peaks, $E_T^{jet} > 6$ GeV untagged $D^*$ jets . . . . .	201
13.0.15 $d\sigma/d\eta^{jet}$ Mass Peaks, $6 < E_T^{jet} < 9$ GeV untagged $D^*$ jets . . . . .	203
13.0.16 $d\sigma/d\eta^{jet}$ Mass Peaks, $E_T^{jet} > 9$ GeV untagged $D^*$ jets . . . . .	205
13.0.17 $d\sigma/dE_T^{jet}$ Mass Peaks, $3.0 < p_T^{D^*} < 5.0$ GeV . . . . .	207
13.0.18 $d\sigma/d\eta^{jet}$ Mass Peaks, $3.0 < p_T^{D^*} < 5.0$ GeV . . . . .	208
13.0.19 $d\sigma/dE_T^{jet}$ Mass Peaks, $5.0 < p_T^{D^*} < 8.0$ GeV . . . . .	210
13.0.20 $d\sigma/d\eta^{jet}$ Mass Peaks, $5.0 < p_T^{D^*} < 8.0$ GeV . . . . .	211
13.0.21 $d\sigma/dE_T^{jet}$ Mass Peaks, $8.0 < p_T^{D^*} < 20.0$ GeV . . . . .	213
13.0.22 $d\sigma/d\eta^{jet}$ Mass Peaks, $8.0 < p_T^{D^*} < 20.0$ GeV . . . . .	214
13.0.23 $d\sigma/dx_\gamma^{obs}(D^*, \text{untagged jet})$ Mass Peaks . . . . .	216

<b>14 Appendix B : Dijet cross section mass peaks</b>	<b>218</b>
14.1 $d\sigma/dx_\gamma^{\text{obs}}$ mass peaks . . . . .	219
14.10 $d\sigma/dp_T^{\text{jj}}$ mass peaks, resolved-enriched $x_\gamma^{\text{obs}} < 0.75$ . . . . .	221
14.2 $d\sigma/dp_T^{\text{jj}}$ mass peaks . . . . .	222
14.3 $d\sigma/d\Delta\phi^{\text{jj}}$ mass peaks . . . . .	224
14.4 $d\sigma/dm^{\text{jj}}$ mass peaks . . . . .	226
14.5 $d\sigma/dp_T^{2\text{jj}}$ mass peaks . . . . .	228
14.6 $d\sigma/dp_T^{\text{jj}}$ mass peaks, direct-enriched $x_\gamma^{\text{obs}} > 0.75$ . . . . .	230
14.7 $d\sigma/d\Delta\phi^{\text{jj}}$ mass peaks, direct-enriched $x_\gamma^{\text{obs}} > 0.75$ . . . . .	232
14.8 $d\sigma/dm^{\text{jj}}$ mass peaks, direct-enriched $x_\gamma^{\text{obs}} > 0.75$ . . . . .	234
14.9 $d\sigma/dp_T^{2\text{jj}}$ mass peaks, direct-enriched $x_\gamma^{\text{obs}} > 0.75$ . . . . .	236
14.11 $d\sigma/d\Delta\phi^{\text{jj}}$ mass peaks, resolved-enriched $x_\gamma^{\text{obs}} < 0.75$ . . . . .	239
14.12 $d\sigma/dm^{\text{jj}}$ mass peaks, resolved-enriched $x_\gamma^{\text{obs}} < 0.75$ . . . . .	241
14.13 $d\sigma/dp_T^{2\text{jj}}$ mass peaks, resolved-enriched $x_\gamma^{\text{obs}} < 0.75$ . . . . .	243
<b>15 Appendix C : Inclusive Jet Purity/Efficiency/Acceptance/Hadronisation Corrections</b>	<b>245</b>
15.1 Purity/efficiency/acceptance/hadronisation corrections for $d\sigma/dE_T^{\text{jet}}$ & $d\sigma/d\eta^{\text{jet}}$ for $3.0 < P_T^{D^*} < 5.0$ GeV . . . . .	246
15.2 Purity/efficiency/acceptance/hadronisation corrections for $d\sigma/dE_T^{\text{jet}}$ and $d\sigma/d\eta^{\text{jet}}$ for $5.0 < p_T^{D^*} < 8.0$ GeV . . . . .	248
15.3 Purity/efficiency/acceptance/hadronisation corrections for $d\sigma/dE_T^{\text{jet}}$ and $d\sigma/d\eta^{\text{jet}}$ for $8.0 < p_T^{D^*} < 20.0$ GeV . . . . .	250
<b>16 Appendix D : Dijet purity/efficiency/acceptance/hadronisation corrections</b>	<b>252</b>
16.1 $d\sigma/dx_\gamma^{\text{obs}}$ , purity/efficiency/acceptance/hadronisation corrections . . . . .	253
16.2 $d\sigma/dm^{\text{jj}}$ , purity/efficiency/acceptance/hadronisation corrections . . . . .	254
16.3 $d\sigma/dp_T^{\text{jj}}$ , purity/efficiency/acceptance/hadronisation corrections . . . . .	255
16.4 $d\sigma/d\Delta\phi^{\text{jj}}$ , purity/efficiency/acceptance/hadronisation corrections . . . . .	257
16.5 $d\sigma/dp_T^{2\text{jj}}$ , purity/efficiency/acceptance/hadronisation corrections . . . . .	258
<b>17 Appendix E :Systematics</b>	<b>260</b>
17.0.1 $d\sigma/dE_T^{\text{jet}}$ Systematics, $-1.5 < \eta^{\text{jet}} < 2.4$ . . . . .	261
17.0.2 $d\sigma/dE_T^{\text{jet}}$ systematics, $-1.5 < \eta^{\text{jet}} < -0.5$ . . . . .	262

17.0.3 $d\sigma/dE_T^{jet}$ systematics, $-0.5 < \eta^{jet} < 0.5$ . . . . .	263
17.0.4 $d\sigma/dE_T^{jet}$ systematics, $0.5 < \eta^{jet} < 1.5$ . . . . .	264
17.0.5 $d\sigma/dE_T^{jet}$ systematics, $1.5 < \eta^{jet} < 2.4$ . . . . .	265
17.0.6 $d\sigma/d\eta^{jet}$ systematics, $E_T^{jet} > 6$ GeV . . . . .	266
17.0.7 $d\sigma/d\eta^{jet}$ systematics, $6 < E_T^{jet} < 9$ GeV . . . . .	267
17.0.8 $d\sigma/d\eta^{jet}$ systematics, $E_T^{jet} > 9$ GeV . . . . .	268
17.0.9 $d\sigma/dE_T^{jet}$ systematics, $-1.5 < \eta^{jet} < 2.4$ tagged $D^*$ jets . . . . .	269
17.0.10 $d\sigma/d\eta^{jet}$ systematics, $E_T^{jet} > 6$ GeV untagged $D^*$ jets . . . . .	270
17.0.11 $d\sigma/d\eta^{jet}$ systematics, $6 < E_T^{jet} < 9$ GeV tagged $D^*$ jets . . . . .	271
17.0.12 $d\sigma/d\eta^{jet}$ systematics, $E_T^{jet} > 9$ GeV tagged $D^*$ jets . . . . .	272
17.0.13 $d\sigma/dE_T^{jet}$ systematics, $-1.5 < \eta^{jet} < 2.4$ untagged $D^*$ jets . . . . .	273
17.0.14 $d\sigma/d\eta^{jet}$ systematics, $E_T^{jet} > 6$ GeV untagged $D^*$ jets . . . . .	274
17.0.15 $d\sigma/d\eta^{jet}$ systematics, $6 < E_T^{jet} < 9$ GeV untagged $D^*$ jets . . . . .	275
17.0.16 $d\sigma/d\eta^{jet}$ systematics, $E_T^{jet} > 9$ GeV untagged $D^*$ jets . . . . .	276
17.0.17 $d\sigma/dE_T^{jet}$ systematics, $3.0 < p_T^{D^*} < 5.0$ GeV . . . . .	277
17.0.18 $d\sigma/d\eta^{jet}$ systematics, $3.0 < p_T^{D^*} < 5.0$ GeV . . . . .	278
17.0.19 $d\sigma/dE_T^{jet}$ systematics, $5.0 < p_T^{D^*} < 8.0$ GeV . . . . .	279
17.0.20 $d\sigma/d\eta^{jet}$ systematics, $5.0 < p_T^{D^*} < 8.0$ GeV . . . . .	280
17.0.21 $d\sigma/dE_T^{jet}$ systematics, $8.0 < p_T^{D^*} < 20.0$ GeV . . . . .	281
17.0.22 $d\sigma/d\eta^{jet}$ systematics, $8.0 < p_T^{D^*} < 20.0$ GeV . . . . .	282
17.0.23 $d\sigma/dx_\gamma^{obs}(D^*, other\ jet)$ systematics . . . . .	283
17.0.24 $d\sigma/dx_\gamma^{obs}$ systematics . . . . .	284
17.0.25 $d\sigma/dp_T^{jj}$ systematics . . . . .	285
17.0.26 $d\sigma/d\Delta\phi^{jj}$ systematics . . . . .	286
17.0.27 $d\sigma/dm^{jj}$ systematics . . . . .	287
17.0.28 $d\sigma/dp_T^{2jj}$ systematics . . . . .	288
17.0.29 $d\sigma/dp_T^{jj}$ systematics, direct-enriched $x_\gamma^{obs} > 0.75$ . . . . .	289
17.0.30 $d\sigma/d\Delta\phi^{jj}$ systematics, direct-enriched $x_\gamma^{obs} > 0.75$ . . . . .	290
17.0.31 $d\sigma/dm^{jj}$ systematics, direct-enriched $x_\gamma^{obs} > 0.75$ . . . . .	291
17.0.32 $d\sigma/dp_T^{2jj}$ systematics, direct-enriched $x_\gamma^{obs} > 0.75$ . . . . .	292
17.0.33 $d\sigma/dp_T^{jj}$ systematics, resolved-enriched $x_\gamma^{obs} < 0.75$ . . . . .	293

## *Contents*

---

17.0.34 $d\sigma/d\Delta\phi^{jj}$ systematics, resolved-enriched $x_\gamma^{\text{obs}} < 0.75$ . . . . .	294
17.0.35 $d\sigma/dm^{jj}$ systematics, resolved-enriched $x_\gamma^{\text{obs}} < 0.75$ . . . . .	295
17.0.36 $d\sigma/dp_T^{2jj}$ systematics, resolved-enriched $x_\gamma^{\text{obs}} < 0.75$ . . . . .	296
<b>18 Appendix F : Resolutions</b>	<b>297</b>
<b>Bibliography</b>	<b>300</b>

---

## List of Figures

---

2.1	Diagrams of electron-proton scattering. (a) In a <i>neutral current</i> process a photon or a $Z^0$ is exchanged. (b) In a <i>charged current</i> process the exchanged boson is a charged $W^\pm$ . . . . .	44
2.2	The running coupling constant $\alpha_s$ as measured in DIS, $e^+e^-$ annihilation, hadronic collisions and heavy quarkonia. . . . .	47
2.3	$F_2$ vs. $Q^2$ for fixed $x$ . The fixed-target results are from NMC, BCDMS, E665 and ZEUS data. The results are compared to the ZEUS NLO QCD fit. . . . .	50
2.4	A few of the leading order processes in direct (a) boson-gluon fusion, (b) initial state radiation and (c) Compton scattering. Resolved processes (d) gluon-gluon fusion, (e and f) flavour excitation from the photon. . . . .	52
2.5	A few of the next-to-leading order processes, (a) and (b) are virtual corrections and (c) and (d) are real corrections calculated in the NLO programs. . . . .	53
2.6	Fragmentation functions $z = p_T(D^*)/E_T^{\text{jet}}(D^* \text{ matched jet})$ for the ARGUS data in the left plot, and for OPAL, ARGUS and ZEUS data in the right hand plot. . . . .	55
2.7	Overview of a leading order lepton-photon interaction. . . . .	56
2.8	Differential cross sections of $D^*$ photoproduction with respect to $\eta(D^*)$ measured by the ZEUS Collaboration. Measured cross sections (dots) are compared to the NLO calculation (solid histogram) with its uncertainty shown as the dashed histogram, and to the FONLL predictions (dotted curves and shaded bands). . . . .	59



2.9	Cross sections $d\sigma/d\eta^{\text{jet}}$ for $D^*$ matched jets and other jets in $E_T^{\text{jet}} > 6$ GeV and $E_T^{\text{jet}} > 8$ GeV ranges. The data (solid dots) is compared to ‘massive’ NLO pQCD predictions (FMNR) (solid and dashed lines). ZEUS 1996-1997 data were used. . . . .	61
2.10	Differential $D^*$ cross section in $p_T(D^*)$ for ALEPH, DELPHI, L3 and OPAL experiments (dots) compared to NLO pQCD ‘massive’ predictions. . . . .	62
2.11	Inclusive charm cross sections as a function of centre-of-mass energy in $\gamma\gamma$ collisions, for ALEPH, DELPHI, L3, OPAL, TASSO and JADE experiments compared to NLO pQCD predictions. . . . .	63
2.12	OPAL results for a) the cross-section $\sigma(e^+e^- \rightarrow e^+e^-c\bar{c}X)$ , with $5 < Q^2 < 100 \text{ GeV}^2$ and b) for the charm structure function of the photon divided by the fine structure constant, $F_{2,c}^\gamma(x, Q^2)/\alpha$ , at $Q^2 = 20 \text{ GeV}^2$ . The data points are the results obtained with the HERWIG Monte Carlo model. The outer error bar is the total error and the inner error bar the statistical error. The data points in b) are placed at those x values that correspond to the average predicted $F_{2,c}$ within a bin. The data are compared to the calculation performed in LO and NLO. The band for the NLO calculation indicates the theoretical error from uncertainties in the charm quark mass and the scale uncertainties in renormalisation and factorisation. In a) the cross-section prediction of the HERWIG Monte Carlo model is also given. b) also shows the prediction of the GRS-LO parametrisation for the structure function at $Q^2 = 20 \text{ GeV}^2$ and its point-like component separately. . . . .	64
2.13	D meson signals in the CDF data. . . . .	65
2.14	The differential cross section measurements for $ y  \leq 1$ . The inner bars represent the statistical uncertainties; the outer bars are the quadratic sums of the statistical and systematic uncertainties. The solid curves are the theoretical predictions from Cacciari and Nason [31], with the uncertainties indicated by the shaded bands. The dashed curve shown with the $D^{*+}$ cross section is the theoretical prediction from Kniehl [32]; the dotted lines indicate the uncertainty. No prediction is available yet for $D_s^+$ production. . . . .	66

2.15	The differential cross section $d\sigma/dx_\gamma^{\text{obs}}$ for dijet plus $D^*$ meson events. The shaded band represents the uncertainty from the calorimeter energy scale. In (a) the data are compared to the expectations of the HERWIG Monte Carlo simulations, normalised to the data. In (b) the data are compared to ‘massive’ NLO QCD predictions [35]. . . . .	69
2.16	Ratio of low to high $x_\gamma^{\text{obs}}$ for events with a $D^*$ compared to the predictions of the SaS1D [36] photon structure function (where the photon acts as a source of partons such that partons participate in the hard scatter) for the ratio without a $D^*$ tag. . . . .	70
2.17	Differential cross sections $d\sigma/d\cos\theta^*$ (dots) compared with: a-b) PYTHIA and HERWIG MC simulations (histograms); c-d) CASCADE (short-dashed lines) and NLO FO predictions after hadronisation correction (full lines) and at parton level (long-dashed lines). Results are given separately in a,c) for samples enriched in resolved photon events and in b,d) for samples enriched in direct photon events. The inner error bars show the statistical uncertainty, while the outer ones show the systematic uncertainties added in quadrature. The jet-energy-scale uncertainty is given by the two dashed-dotted lines. In a-b), each MC distribution is normalised to the data, as indicated in the brackets. Also shown as shaded areas in a) and b) are the contribution of the resolved photon process to the direct-enriched sample, respectively. The uncertainties of the NLO prediction after the hadronisation correction are shown as the shaded areas in c) and d). . . . .	71
2.18	The cross section for the production of dijets in association with a $D^{*\pm}$ meson versus the $D^{*\pm}$ meson production cross section measured by H1. The predictions of the RAPGAP, AROMA, and CASCADE are shown. . . . .	72
2.19	$D\bar{O} \Delta\phi^{\text{jj}}$ distributions in four regions based on the jet with the largest $p_T$ in an event ( $p_T^{\text{max}}$ ). Data and predictions with $p_T^{\text{max}} > 100$ GeV are scaled by successive factors of 20 for purposes of presentation. The solid (dashed) lines show the NLO (LO) pQCD predictions. . . . .	73

## List of Figures

---

2.20	DØ $\Delta\phi^{jj}$ distributions in different regions based on the jet with the largest $p_T$ in an event ( $p_T^{max}$ ). Results from HERWIG and PYTHIA are overlaid on the data. Data and predictions with $p_T^{max} > 100$ GeV are scaled by successive factors of 20 for purposes of presentation. . . . .	74
3.1	Layout of HERA and pre-accelerators. . . . .	76
3.2	$x - y$ view of the ZEUS detector . . . . .	78
3.3	The ZEUS detector . . . . .	79
3.4	$x-y$ view through the CTD and typical cell layout. . . . .	81
3.5	The ZEUS Calorimeter ( $y-z$ projection) and surroundings. . . . .	82
3.6	Diagram of a BCAL tower. . . . .	82
3.7	The layout of the ZEUS Luminosity Monitor. The nominal interaction point is located at (0,0). . . . .	83
3.8	The ZEUS gated luminosity. . . . .	84
3.9	Diagrammatic representation of data flow in the ZEUS trigger system. . . . .	85
4.1	Charm single jet event, $E_T^{jet} = 17.5$ GeV and $\eta^{jet} = 0.053$ . . . . .	87
4.2	Charm dijet event, the leading jet having $E_{T,1}^{jet} = 20.2$ GeV and $\eta_1^{jet} = -0.089$ and the second leading jet in $E_T^{jet}$ having $E_{T,2}^{jet} = 17.7$ GeV and $\eta_2^{jet} = 1.325$ . . . . .	88
4.3	Correlation between the measured $y_{JB}$ and $y_{true}$ . . . . .	89
4.4	Distribution of $y_{JB}$ for HERWIG Monte Carlo. The black line shows the total distribution for both DIS and photoproduction events. The shaded region shows events with a $Q^2 > 1$ GeV <sup>2</sup> and primary $ Z_{vtx}  < 50$ cm cut, and the dashed line shows the events selected with no electron found in the event and $ Z_{vtx}  < 50$ cm cut i.e. showing how the photoproduction distribution of $y_{JB}$ looks. The kinematic region selected corresponds to $130 < W < 280$ GeV. . . . .	91
4.5	$(y_{JB}^{rec} - y_{true})/y_{true}$ in bins of $y_{true}$ . Dotted histograms show the uncorrected $y_{JB}$ distributions, solid lines show $y_{JB}^{corr}$ , $y_{JB}$ after the correction is applied, with the mean width( $\sigma$ ) extracted from a Gaussian fit to $y_{JB}^{corr}$ . . . . .	92
4.6	A high $Q^2$ neutral current DIS event. . . . .	93
4.7	A schematic diagram showing how cell-islands are formed. . . . .	94

4.8	A figure illustrating the clustering into a cone-island (cell-islands 1,2 and 3 are merged) and the track-island matching. . . . .	95
4.9	Jet energy loss as a function of $\eta^{jet}$ . Solid points show the profile distribution for HERWIG Monte Carlo, open points show the profile distribution for PYTHIA Monte Carlo. . . . .	97
4.10	Jet energy correction profile plots in bins of $\eta^{jet}$ . Straight lines are fitted in each $\eta^{jet}$ bin in order to extract correction factors. . . . .	98
4.11	Jet resolutions for $\eta^{detjet} - \eta^{hadjet}$ , $\phi^{detjet} - \phi^{hadjet}$ and $(E_T^{detjet} - E_T^{hadjet})/E_T^{hadjet}$ , for both HERWIG and PYTHIA. The distributions were fitted with a Gaussian with the constant, mean and widths shown on the plots. . . . .	99
4.12	Cartoon of a $D^* \rightarrow (D^0 \rightarrow K, \pi), \pi_s$ decay as observed in the CTD. . . . .	105
4.13	$D^*$ right charge selection is shown (top histogram), and wrong charge distribution (bottom histogram), both separated into example signal regions 0.143 < $\Delta M$ < 0.148 GeV, and background normalisation regions 0.15 < $\Delta M$ < 0.17 GeV. . . . .	106
4.14	$m(K, \pi)$ distribution after all selection cuts, and a cut on 0.143 < $\Delta M$ < 0.148 GeV. The solid dots are the right charge combinations and histogram is the wrong charge distribution. The wrong charge is normalised to the right charge distribution in the region $2.0 < m(K, \pi) < 2.2$ GeV . . . . .	107
4.15	The distribution of the mass difference, $\Delta M = M(K\pi\pi_s) - M(K\pi)$ , for $D^{*\pm}$ candidates (solid dots). The histogram shows the $\Delta M$ distribution for wrong charge combinations. Only $D^{*\pm}$ candidates from the region 0.143 < $\Delta M$ < 0.148 GeV were used for the cross section measurement. . . . .	108
4.16	$\Delta R$ association between $D^*$ meson and jet. Points are the data, the filled area is the HERWIG Monte Carlo, and the PYTHIA Monte Carlo is the blue solid line. The dashed green line indicates where the cut is placed at $\Delta R = 0.6$ separating matched jets from unmatched jets. . . . .	109
4.17	$\Delta R$ association between $D^*$ meson and parton jet. The filled area is the HERWIG Monte Carlo, and the PYTHIA Monte Carlo is the blue dashed line. The arrow shows where the cut is placed at $\Delta R = 0.6$ separating matched jets from unmatched jets. . . . .	110

4.18	The distribution of the mass difference, $\Delta M = M(K\pi\pi_s) - M(K\pi)$ , for $D^{*\pm}$ candidates (solid dots). The histogram shows the $\Delta M$ distribution for wrong charge combinations. Only $D^{*\pm}$ candidates from the region $0.143 < \Delta M < 0.148$ GeV were used for the cross section measurement. $2 < p_T(D^*) < 3$ GeV. . . . .	111
4.19	The distribution of the mass difference, $\Delta M = M(K\pi\pi_s) - M(K\pi)$ , for $D^{*\pm}$ candidates (solid dots). The histogram shows the $\Delta M$ distribution for wrong charge combinations. Only $D^{*\pm}$ candidates from the region $0.143 < \Delta M < 0.148$ GeV were used for the cross section measurement. $p_T(D^*) > 2$ GeV. . . . .	112
4.20	The distribution of the mass difference, $\Delta M = M(K\pi\pi_s) - M(K\pi)$ , for $D^{*+}$ candidates (solid dots). The histogram shows the $\Delta M$ distribution for wrong charge combinations. Only $D^{*\pm}$ candidates from the region $0.143 < \Delta M < 0.148$ GeV were used for the cross section measurement. $p_T(D^*) > 3$ GeV. . . . .	113
4.21	The distribution of the mass difference, $\Delta M = M(K\pi\pi_s) - M(K\pi)$ , for $D^{*-}$ candidates (solid dots). The histogram shows the $\Delta M$ distribution for wrong charge combinations. Only $D^{*\pm}$ candidates from the region $0.143 < \Delta M < 0.148$ GeV were used for the cross-section measurement. $p_T(D^*) > 3$ GeV. . . . .	114
4.22	Event display showing an event with a small $\Delta\phi^{jj}$ . The Jets are shown by the arrowed lines. . . . .	115
5.1	The correlation of the $p_T^{D^*}$ and its decay products. The left plot shows the correlation between the $p_T^{D^*}$ and $p_T(\pi_s)$ , the right hand plot shows the correlation between the $p_T^{D^*}$ and $p_T(\pi, K)$ , with the dashed lines indicating the cuts on the transverse momenta. . . . .	117
5.2	The $m^{jj} - \cos\theta^*$ plane shown for HERWIG Monte Carlo (top plot) and data (bottom plot), the red line in both plots is the same and is a parameterisation which can be used to guide the eye. . . . .	120

5.3	Dijet distribution for $(E_T^{jet1} - E_T^{jet2})/(E_T^{jet1} + E_T^{jet2})$ , where for the top plot $E_T^{jet1}(E_T^{jet2})$ is the highest (second highest) transverse energy jets, and for the bottom plot the $E_T^{jet1}(E_T^{jet2})$ are the largest (second largest) $\eta^{jet}$ . . . . .	121
5.4	$z_{vtx}$ distribution wrong charge subtracted compared to HERWIG and PYTHIA area normalised to the data (solid dots) for dijet events containing a $D^*$ meson. . . . .	122
5.5	Distributions of $W_{jb}$ wrong charge subtracted compared to HERWIG and PYTHIA area normalised to the data (solid dots) for dijet events containing a $D^*$ meson. . . . .	123
5.6	Reconstructed distribution for $x_\gamma^{obs}(D^*, \text{untagged jet})$ wrong charge subtracted compared to HERWIG and PYTHIA area normalised to the data (solid dots) for inclusive jet events containing a $D^*$ meson. . . . .	124
5.7	Distributions of transverse momentum and pseudo-rapidity of the $D^*, K, \pi$ and $\pi_s$ , wrong charge subtracted compared to HERWIG and PYTHIA area normalised to the data (solid dots) for dijet events containing a $D^*$ meson. . . . .	124
5.8	Distributions of $p_T^{D^*}$ and $\eta^{D^*}$ wrong charge subtracted compared to HERWIG and PYTHIA area normalised to the data (solid dots) for dijet events containing a $D^*$ meson. . . . .	125
5.9	Distributions of $E_T^{jet}$ , $\eta^{jet}$ and $\phi^{jet}$ for the two highest transverse energy jets in the event for events containing a $D^*$ meson. . . . .	126
5.10	Reconstructed distributions for $x_\gamma^{obs}$ , $\Delta\phi^{jj}$ , $p_T^{jj}$ and $M^{jj}$ wrong charge subtracted compared to HERWIG and PYTHIA area normalised to the data (solid dots) for dijet events containing a $D^*$ meson. . . . .	127
5.11	Distributions for $x_\gamma^{obs}$ for direct events and resolved events, at reconstructed level distribution on the left plot, and at hadron level on the right hand plot. The vertical dashed line is at 0.75 indicating the separation used between direct and resolved events. . . . .	128
5.12	Distributions for $x_\gamma^{obs}(D^*, \text{untagged jet})$ for direct events and resolved events, at reconstructed level distribution on the left plot, and at hadron level on the right hand plot. The vertical dashed line is at 0.75 indicating the separation used between direct and resolved events. . . . .	128

## List of Figures

---

5.13	Hadron level compared to parton level HERWIG distributions for $x_\gamma^{\text{obs}}$ , $\Delta\phi^{\text{jj}}$ , $p_T^{\text{jj}}$ and $M^{\text{jj}}$ showing $(\frac{\text{hadron} - \text{parton}}{\text{parton}})$ for figures (a) - (d) and (hadron - parton) for figures (e) - (h). All histograms are fitted with a Gaussian. . . . .	129
6.1	Purity/efficiency/acceptance and hadronisation corrections for each bin of the dijet charm cross section $d\sigma/dx_\gamma$ for HERWIG 886 pb <sup>-1</sup> . . . . .	132
6.2	HERWIG $D^0$ mass peak . . . . .	134
6.3	PYTHIA $D^0$ mass peak . . . . .	134
6.4	98 - 00 data 78 pb <sup>-1</sup> , $D^0$ mass peak . . . . .	135
6.5	$\Delta M$ mass peaks for 98-00 data (top), HERWIG (middle) and PYTHIA (bottom) Monte Carlo's. Left column is for the mass range $1.80 < M(K\pi) < 1.92$ GeV, and the right column is for the mass range $1.76 < M(K\pi) < 1.92$ GeV. . . .	136
6.6	The $N(D^*)$ extracted from HERWIG and the data when changing the $D^0$ mass window as in (fig. 6.5). . . . .	136
6.7	The $N(D^*)$ extracted from PYTHIA and the data when changing the $D^0$ mass window as in (fig. 6.5). . . . .	137
6.8	$\Delta M$ mass peaks for 98-00 data (top), HERWIG (middle) and PYTHIA (bottom) Monte Carlo's. Left column is for the mass range $1.80 < M(K\pi) < 1.92$ GeV, and the right column is for the mass range $1.8 < M(K\pi) < 1.96$ GeV. . . .	137
6.9	The $N(D^*)$ extracted from HERWIG and the data when changing the $D^0$ mass window as in (fig. 6.8). . . . .	138
6.10	The $N(D^*)$ extracted from PYTHIA and the data when changing the $D^0$ mass window as in (fig. 6.8). . . . .	138
6.11	Systematics for each bin of the dijet charm cross section $d\sigma/dx_\gamma^{\text{obs}}$ for 1998-2000 data 78pb <sup>-1</sup> , 886pb <sup>-1</sup> of HERWIG MC and 350pb <sup>-1</sup> of PYTHIA MC . . . . .	141
7.1	Cross section $d\sigma/dE_T^{\text{jet}}$ for jets in events (dots) containing at least one $D^*$ meson for different regions in $\eta^{\text{jet}}$ . The comparison is made to massive QCD predictions with (solid line) and without (dotted line) hadronisation corrections applied. The theoretical uncertainties (hatched band) come from the simultaneous change in the scale and in the charm mass. The beauty component is also shown (lower histogram). . . . .	144

- 7.2 Cross section  $d\sigma/dE_T^{\text{jet}}$  for  $D^*$ -tagged jets and untagged jets (dots). The comparison is made to massive QCD predictions with (solid line) and without (dotted line) hadronisation corrections applied. The theoretical uncertainties (hatched band) come from the simultaneous change in the scale and in the charm mass. For the other jet distribution, the massless QCD predictions are shown with (solid line) and without (dotted line) hadronisation corrections applied. The uncertainties (hatched band) come from the changed renormalisation and factorisation scales. The beauty component is also shown (lower histogram). . . . 145
- 7.3 Cross section  $d\sigma/d\eta^{\text{jet}}$  for jets in events (dots) containing at least one  $D^*$  meson for different regions in  $E_T^{\text{jet}}$ . The comparison is made to massive QCD predictions with (solid line) and without (dotted line) hadronisation corrections applied. The theoretical uncertainties (hatched band) come from the simultaneous change in the scale and in the charm mass. The beauty component is also shown (lower histogram). . . . . 146
- 7.4 Cross section  $d\sigma/d\eta^{\text{jet}}$  for  $D^*$ -tagged jets and untagged jets (dots). The comparison is made to massive QCD predictions with (solid line) and without (dotted line) hadronisation corrections applied. The theoretical uncertainties (hatched band) come from the simultaneous change in the scale and in the charm mass. For the other jet distribution, the massless QCD predictions are shown with (solid line) and without (dotted line) hadronisation corrections applied. The uncertainties (hatched band) come from the change renormalisation and factorisation scales. The beauty component is also shown (lower histogram). . . . 148
- 7.5 Cross sections  $d\sigma/dE_T^{\text{jet}}$  and  $d\sigma/d\eta^{\text{jet}}$  in bins of  $p_T^{D^*}$ . The data (solid dots) are compared to the massive QCD predictions with (solid line) and without (dotted line) hadronisation corrections applied. The theoretical uncertainties (hatched band) come from the simultaneous change in the scale and in the charm mass. The beauty component is also shown (lower histogram). . . . . 149



- 7.6 Inclusive jet cross section  $d\sigma/dx_\gamma^{\text{obs}}(D^*, \text{untagged jet})$  for the events containing a  $D^*$  meson not associated with a jet. The data (solid dots) are compared to (a) the massive QCD predictions with (solid line) and without (dotted line) hadronisation corrections applied. The theoretical uncertainties (hatched band) come from the simultaneous change in the scale and in the charm mass. In (b) the data are compared to the massless QCD predictions shown with (solid line) and without (dotted line) hadronisation corrections applied. The uncertainties (hatched band) come from the change in the renormalisation and factorisation scales. The beauty component is also shown (lower histogram) details given in text. In (c) the data are compared to HERWIG (solid line) and PYTHIA (dashed line) MC predictions normalised to the data. The predicted HERWIG direct and resolved contributions are also shown. . . . . 150
- 8.1 Dijet cross sections (a)  $d\sigma/dx_\gamma^{\text{obs}}$ , (b)  $d\sigma/d\Delta\phi^{\text{jj}}$ , (c)  $d\sigma/d(p_T^{\text{jj}})^2$  and (d)  $d\sigma/dm^{\text{jj}}$  for the data (solid dots) compared to massive QCD predictions with (solid line) and without (dotted line) hadronisation corrections applied. The theoretical uncertainties (hatched band) come from the simultaneous change in the scale and in the charm mass. The beauty component is also shown (lower histogram). 153
- 8.2 Cross section for  $d\sigma/dM^{\text{jj}}$  separated into (a) and (c) direct enriched ( $x_\gamma^{\text{obs}} > 0.75$ ) and (b) and (d) resolved enriched ( $x_\gamma^{\text{obs}} < 0.75$ ). The data (solid dots) are compared (a) and (b) to the massive QCD prediction with (solid line) and without (dotted line) hadronisation corrections applied. The theoretical uncertainties (hatched band) come from the simultaneous change in the scale and in the charm mass. The beauty component is also shown (lower histogram). The data are also compared (c) and (d) with HERWIG (solid line) and PYTHIA (dashed line) MC predictions normalised to the data by a factor. . . . . 154

8.3	Cross section for $d\sigma/d(p_T^{jj})^2$ separated into (a) and (c) direct enriched ( $x_\gamma^{\text{obs}} > 0.75$ ) and (b) and (d) resolved enriched ( $x_\gamma^{\text{obs}} < 0.75$ ). The data (solid dots) are compared (a) and (b) to the massive QCD prediction with (solid line) and without (dotted line) hadronisation corrections applied. The theoretical uncertainties (hatched band) come from the simultaneous change in the scale and in the charm mass. The beauty component is also shown (lower histogram). The data are also compared (c) and (d) with HERWIG (solid line) and PYTHIA (dashed line) MC predictions normalised to the data by a factor. . . . .	156
8.4	Cross section for $d\sigma/d(p_T^{jj})$ separated into (a) and (c) direct enriched ( $x_\gamma^{\text{obs}} > 0.75$ ) and (b) and (d) resolved enriched ( $x_\gamma^{\text{obs}} < 0.75$ ). The data (solid dots) are compared (a) and (b) to the massive QCD prediction with (solid line) and without (dotted line) hadronisation corrections applied. The theoretical uncertainties (hatched band) come from the simultaneous change in the scale and in the charm mass. The beauty component is also shown (lower histogram). The data are also compared (c) and (d) with HERWIG (solid line) and PYTHIA (dashed line) MC predictions normalised to the data by a factor. . . . .	157
8.5	Cross section for $d\sigma/d\Delta\phi^{jj}$ separated into (a) and (c) direct enriched ( $x_\gamma^{\text{obs}} > 0.75$ ) and (b) and (d) resolved enriched ( $x_\gamma^{\text{obs}} < 0.75$ ). The data (solid dots) are compared (a) and (b) to the massive QCD prediction with (solid line) and without (dotted line) hadronisation corrections applied. The theoretical uncertainties (hatched band) come from the simultaneous change in the scale and in the charm mass. The beauty component is also shown (lower histogram). The data are also compared (c) and (d) with HERWIG (solid line) and PYTHIA (dashed line) MC predictions normalised to the data by a factor. . . . .	158
10.1	The delivered luminosity is shown in the left hand plot for the HERA II upgrade 02-05 data compared to HERA I 95-00 data. The right hand plot shows the gated luminosity at ZEUS for the 02-05 data set. . . . .	161
10.2	The ZEUS background parameterised as a function of positron current $I_e$ and current measured within the CTD. . . . .	162

10.3	The design of the positron orbit and its $10\sigma$ envelope, with the beam-pipe and collimators. The magnets closest to the ZEUS interaction point (IP) are also shown in their $z$ positions along the beam line. Note the highly exaggerated $y$ -axis scale. . . . .	163
10.4	An off-momentum positron as seen within the ZEUS detector. . . . .	164
10.5	The ZEUS detector, with the upgraded parts of the detector shown. . . . .	165
10.6	The layout of the MVD in the $xy$ plane on the top and the $zy$ plane on the bottom. . . . .	167
11.1	$J/\psi$ reconstructed from online tracks using the global tracking trigger. . . . .	169
11.2	The beam spots as a function of ZEUS run number, from 03-04, for $x, y$ , and $z$ vertex positions determined from the spread of primary vertices during a recorded run. . . . .	171
11.3	$M(K\pi\pi)$ invariant mass distribution without the decay length significance cut. The inclusive event sample is used (sample B, in the text). The data is fitted with a Gaussian for the signal and a first order polynomial for the background. No statistically significant signal is seen. . . . .	174
11.4	Significance $S_L = \frac{L}{\sigma_L}$ distribution for events within $1.845 < M(D^\pm) < 1.905$ GeV range. The inclusive event sample is used (sample B, in the text). The selection cut indicated the one used to extract the signal seen in (fig. 11.5). . . . .	175
11.5	$M(K\pi\pi)$ invariant mass distribution with decay length significance $L/\sigma_L > 7$ . The inclusive event sample is used (sample B, in the text). The data is fitted with a Gaussian for the signal and a first order polynomial for the background. . . . .	176
11.6	$M(K\pi\pi)$ invariant mass distribution with decay length significance $L/\sigma_L > 6$ . The DIS event sample is used (sample A, in the text). The data is fitted with a Gaussian for the signal and a first order polynomial for the background. The invariant mass distribution before the decay length significance cut is shown in the inserted plot. . . . .	177
11.7	Event display of a DIS $D^+$ candidate event. Three of the tracks combine to a secondary vertex $D^+$ candidate. Unfortunately also a fourth track fits to the secondary vertex. The large decay length means that this is almost certainly from a beauty decay. . . . .	178

13.1	Mass peaks for each bin of the inclusive charm jet cross section $d\sigma/dE_T^{jet}$ in the range $-1.5 < \eta^{jet} < 2.4$ for 1998-2000 data $78pb^{-1}$ . (a) goes from the lowest $E_T^{jet}$ bin to (d) the highest. . . . .	182
13.2	Mass peaks for each bin of the inclusive charm jet cross section $d\sigma/dE_T^{jet}$ in the range $-1.5 < \eta^{jet} < 2.4$ for $886pb^{-1}$ of HERWIG MC. (a) goes from the lowest $E_T^{jet}$ bin to (d) the highest. . . . .	182
13.3	Mass peaks for each bin of the inclusive charm jet cross section $d\sigma/dE_T^{jet}$ in the range $-1.5 < \eta^{jet} < -0.5$ for 1998-2000 data $78pb^{-1}$ . (a) goes from the lowest $E_T^{jet}$ bin to (d) the highest. . . . .	183
13.4	Mass peaks for each bin of the inclusive charm jet cross section $d\sigma/dE_T^{jet}$ in the range $-1.5 < \eta^{jet} < -0.5$ for $886pb^{-1}$ of HERWIG MC. (a) goes from the lowest $E_T^{jet}$ bin to (d) the highest. . . . .	183
13.5	Mass peaks for each bin of the inclusive charm jet cross section $d\sigma/dE_T^{jet}$ in the range $-0.5 < \eta^{jet} < 0.5$ for 1998-2000 data $78pb^{-1}$ . (a) goes from the lowest $E_T^{jet}$ bin to (d) the highest. . . . .	184
13.6	Mass peaks for each bin of the inclusive charm jet cross section $d\sigma/dE_T^{jet}$ in the range $-0.5 < \eta^{jet} < 0.5$ for $886pb^{-1}$ of HERWIG MC. (a) goes from the lowest $E_T^{jet}$ bin to (d) the highest. . . . .	184
13.7	Mass peaks for each bin of the inclusive charm jet cross section $d\sigma/dE_T^{jet}$ in the range $0.5 < \eta^{jet} < 1.5$ for 1998-2000 data $78pb^{-1}$ . (a) goes from the lowest $E_T^{jet}$ bin to (d) the highest. . . . .	185
13.8	Mass peaks for each bin of the inclusive charm jet cross section $d\sigma/dE_T^{jet}$ in the range $0.5 < \eta^{jet} < 1.5$ for $886pb^{-1}$ of HERWIG MC. (a) goes from the lowest $E_T^{jet}$ bin to (d) the highest. . . . .	185
13.9	Mass peaks for each bin of the inclusive charm jet cross section $d\sigma/dE_T^{jet}$ in the range $1.5 < \eta^{jet} < 2.4$ for 1998-2000 data $78pb^{-1}$ . (a) goes from the lowest $E_T^{jet}$ bin to (d) the highest. . . . .	186
13.10	Mass peaks for each bin of the inclusive charm jet cross section $d\sigma/dE_T^{jet}$ in the range $1.5 < \eta^{jet} < 2.4$ for $886pb^{-1}$ of HERWIG MC. (a) goes from the lowest $E_T^{jet}$ bin to (d) the highest. . . . .	186

13.11	Mass peaks for each bin of the inclusive charm jet cross section $d\sigma/d\eta^{jet}$ in the range $E_T^{jet} > 6$ GeV for 1998-2000 data $78pb^{-1}$ . (a) goes from the lowest $E_T^{jet}$ bin to (h) the highest. . . . .	187
13.12	Mass peaks for each bin of the inclusive charm jet cross section $d\sigma/d\eta^{jet}$ in the range $E_T^{jet} > 6$ GeV for $886pb^{-1}$ of HERWIG MC. (a) goes from the lowest $E_T^{jet}$ bin to (h) the highest. . . . .	188
13.13	Mass peaks for each bin of the inclusive charm jet cross section $d\sigma/d\eta^{jet}$ in the range $6 < E_T^{jet} < 9$ GeV for 1998-2000 data $78pb^{-1}$ . (a) goes from the lowest $E_T^{jet}$ bin to (h) the highest. . . . .	189
13.14	Mass peaks for each bin of the inclusive charm jet cross section $d\sigma/d\eta^{jet}$ in the range $6 < E_T^{jet} < 9$ GeV for $886pb^{-1}$ of HERWIG MC. (a) goes from the lowest $E_T^{jet}$ bin to (h) the highest. . . . .	190
13.15	Mass peaks for each bin of the inclusive charm jet cross section $d\sigma/d\eta^{jet}$ in the range $E_T^{jet} > 9$ GeV for 1998-2000 data $78pb^{-1}$ . (a) goes from the lowest $E_T^{jet}$ bin to (h) the highest. . . . .	191
13.16	Mass peaks for each bin of the inclusive charm jet cross section $d\sigma/d\eta^{jet}$ in the range $E_T^{jet} > 9$ GeV for $886pb^{-1}$ of HERWIG MC. (a) goes from the lowest $E_T^{jet}$ bin to (h) the highest. . . . .	192
13.17	Mass peaks for each bin of the tagged $D^*$ jet cross section $d\sigma/dE_T^{jet}$ in the range $-1.5 < \eta^{jet} < 2.4$ for 1998-2000 data $78pb^{-1}$ . (a) goes from the lowest $E_T^{jet}$ bin to (d) the highest. . . . .	193
13.18	Mass peaks for each bin of the tagged $D^*$ jet cross section $d\sigma/dE_T^{jet}$ in the range $-1.5 < \eta^{jet} < 2.4$ for $886pb^{-1}$ of HERWIG MC. (a) goes from the lowest $E_T^{jet}$ bin to (d) the highest. . . . .	193
13.19	Mass peaks for each bin of the untagged $D^*$ jet cross section $d\sigma/d\eta^{jet}$ in the range $E_T^{jet} > 6$ GeV for 1998-2000 data $78pb^{-1}$ . (a) goes from the lowest $\eta^{jet}$ bin to (h) the highest. . . . .	194
13.20	Mass peaks for each bin of the untagged $D^*$ jet cross section $d\sigma/d\eta^{jet}$ in the range $E_T^{jet} > 6$ GeV for $886pb^{-1}$ of HERWIG MC. (a) goes from the lowest $\eta^{jet}$ bin to (h) the highest. . . . .	195

13.21	Mass peaks for each bin of the untagged $D^*$ jet cross section $d\sigma/d\eta^{jet}$ in the range $6 < E_T^{jet} < 9$ GeV for 1998-2000 data $78pb^{-1}$ . (a) goes from the lowest $\eta^{jet}$ bin to (h) the highest. . . . .	196
13.22	Mass peaks for each bin of the untagged $D^*$ jet cross section $d\sigma/d\eta^{jet}$ in the range $6 < E_T^{jet} < 9$ GeV for $886pb^{-1}$ of HERWIG MC. (a) goes from the lowest $\eta^{jet}$ bin to (h) the highest. . . . .	197
13.23	Mass peaks for each bin of the untagged $D^*$ jet cross section $d\sigma/d\eta^{jet}$ in the range $E_T^{jet} > 9$ GeV for 1998-2000 data $78pb^{-1}$ . (a) goes from the lowest $\eta^{jet}$ bin to (h) the highest. . . . .	198
13.24	Mass peaks for each bin of the untagged $D^*$ jet cross section $d\sigma/d\eta^{jet}$ in the range $E_T^{jet} > 9$ GeV for $886pb^{-1}$ of HERWIG MC. (a) goes from the lowest $\eta^{jet}$ bin to (h) the highest. . . . .	199
13.25	Mass peaks for each bin of the untagged $D^*$ jet cross section $d\sigma/dE_T^{jet}$ in the range $-1.5 < \eta^{jet} < 2.4$ for 1998-2000 data $78pb^{-1}$ . (a) goes from the lowest $E_T^{jet}$ bin to (d) the highest. . . . .	200
13.26	Mass peaks for each bin of the untagged $D^*$ jet cross section $d\sigma/dE_T^{jet}$ in the range $-1.5 < \eta^{jet} < 2.4$ for $886pb^{-1}$ of HERWIG MC. (a) goes from the lowest $E_T^{jet}$ bin to (d) the highest. . . . .	200
13.27	Mass peaks for each bin of the tagged $D^*$ jet cross section $d\sigma/d\eta^{jet}$ in the range $E_T^{jet} > 6$ GeV for 1998-2000 data $78pb^{-1}$ . (a) goes from the lowest $\eta^{jet}$ bin to (h) the highest. . . . .	201
13.28	Mass peaks for each bin of the tagged $D^*$ jet cross section $d\sigma/d\eta^{jet}$ in the range $E_T^{jet} > 6$ GeV for $886pb^{-1}$ of HERWIG MC. (a) goes from the lowest $\eta^{jet}$ bin to (h) the highest. . . . .	202
13.29	Mass peaks for each bin of the tagged $D^*$ jet cross section $d\sigma/d\eta^{jet}$ in the range $6 < E_T^{jet} < 9$ GeV for 1998-2000 data $78pb^{-1}$ . (a) goes from the lowest $\eta^{jet}$ bin to (h) the highest. . . . .	203
13.30	Mass peaks for each bin of the tagged $D^*$ jet cross section $d\sigma/d\eta^{jet}$ in the range $6 < E_T^{jet} < 9$ GeV for $886pb^{-1}$ of HERWIG MC. (a) goes from the lowest $\eta^{jet}$ bin to (h) the highest. . . . .	204

## List of Figures

---

13.31	Mass peaks for each bin of the tagged $D^*$ jet cross section $d\sigma/d\eta^{jet}$ in the range $E_T^{jet} > 9$ GeV for 1998-2000 data $78pb^{-1}$ . (a) goes from the lowest $\eta^{jet}$ bin to (h) the highest. . . . .	205
13.32	Mass peaks for each bin of the tagged $D^*$ jet cross section $d\sigma/d\eta^{jet}$ in the range $E_T^{jet} > 9$ GeV for $886pb^{-1}$ of HERWIG MC. (a) goes from the lowest $\eta^{jet}$ bin to (h) the highest. . . . .	206
13.33	Mass peaks for each bin of the inclusive charm jet cross section $d\sigma/dE_T^{jet}$ in the range $3.0 < P_T^{D^*} < 5.0$ GeV for 1998-2000 data $78pb^{-1}$ . (a) goes from the lowest $E_T^{jet}$ bin to (d) the highest. . . . .	207
13.34	Mass peaks for each bin of the inclusive charm jet cross section $d\sigma/dE_T^{jet}$ in the range $3.0 < P_T^{D^*} < 5.0$ GeV for $886pb^{-1}$ of HERWIG MC. (a) goes from the lowest $E_T^{jet}$ bin to (d) the highest. . . . .	207
13.35	Mass peaks for each bin of the inclusive charm jet cross section $d\sigma/d\eta^{jet}$ in the range $3.0 < P_T^{D^*} < 5.0$ GeV for 1998-2000 data $78pb^{-1}$ . (a) goes from the lowest $\eta^{jet}$ bin to (h) the highest. . . . .	208
13.36	Mass peaks for each bin of the inclusive charm jet cross section $d\sigma/d\eta^{jet}$ in the range $3.0 < P_T^{D^*} < 5.0$ GeV for $886pb^{-1}$ of HERWIG MC. (a) goes from the lowest $\eta^{jet}$ bin to (h) the highest. . . . .	209
13.37	Mass peaks for each bin of the inclusive charm jet cross section $d\sigma/dE_T^{jet}$ in the range $5.0 < P_T^{D^*} < 8.0$ GeV for 1998-2000 data $78pb^{-1}$ . (a) goes from the lowest $E_T^{jet}$ bin to (d) the highest. . . . .	210
13.38	Mass peaks for each bin of the inclusive charm jet cross section $d\sigma/dE_T^{jet}$ in the range $5.0 < P_T^{D^*} < 8.0$ GeV for $886pb^{-1}$ of HERWIG MC. (a) goes from the lowest $E_T^{jet}$ bin to (d) the highest. . . . .	210
13.39	Mass peaks for each bin of the inclusive charm jet cross section $d\sigma/d\eta^{jet}$ in the range $5.0 < P_T^{D^*} < 8.0$ GeV for 1998-2000 data $78pb^{-1}$ . (a) goes from the lowest $\eta^{jet}$ bin to (h) the highest. . . . .	211
13.40	Mass peaks for each bin of the inclusive charm jet cross section $d\sigma/d\eta^{jet}$ in the range $5.0 < P_T^{D^*} < 8.0$ GeV for $886pb^{-1}$ of HERWIG MC. (a) goes from the lowest $\eta^{jet}$ bin to (h) the highest. . . . .	212

13.41	Mass peaks for each bin of the inclusive charm jet cross section $d\sigma/dE_T^{jet}$ in the range $8.0 < P_T^{D^*} < 20.0$ GeV for 1998-2000 data $78pb^{-1}$ . (a) goes from the lowest $E_T^{jet}$ bin to (d) the highest. . . . .	213
13.42	Mass peaks for each bin of the inclusive charm jet cross section $d\sigma/dE_T^{jet}$ in the range $8.0 < P_T^{D^*} < 20.0$ GeV for $886pb^{-1}$ of HERWIG MC. (a) goes from the lowest $E_T^{jet}$ bin to (d) the highest. . . . .	213
13.43	Mass peaks for each bin of the inclusive charm jet cross section $d\sigma/d\eta^{jet}$ in the range $8.0 < P_T^{D^*} < 20.0$ GeV for 1998-2000 data $78pb^{-1}$ . (a) goes from the lowest $\eta^{jet}$ bin to (h) the highest. . . . .	214
13.44	Mass peaks for each bin of the inclusive charm jet cross section $d\sigma/d\eta^{jet}$ in the range $8.0 < P_T^{D^*} < 20.0$ GeV for $886pb^{-1}$ of HERWIG MC. (a) goes from the lowest $\eta^{jet}$ bin to (h) the highest. . . . .	215
13.45	Mass peaks for each bin of the inclusive charm jet cross section $d\sigma/dx_\gamma^{obs}(D^*, \text{untagged jet})$ for 1998-2000 data $78pb^{-1}$ . (a) goes from the lowest $x_\gamma^{obs}(D^*, \text{untagged jet})$ bin to (g) the highest. . . . .	216
13.46	Mass peaks for each bin of the inclusive charm jet cross section $d\sigma/dx_\gamma^{obs}(D^*, \text{untagged jet})$ for $886pb^{-1}$ of HERWIG MC. (a) goes from the lowest $x_\gamma^{obs}(D^*, \text{untagged jet})$ bin to (g) the highest. . . . .	217
14.1	Mass peaks for each bin of the dijet charm cross section $d\sigma/dx_\gamma^{obs}$ for 1998-2000 data $78pb^{-1}$ . (a) goes from the lowest $x_\gamma^{obs}$ bin to (g) the highest. . . . .	219
14.2	Mass peaks for each bin of the dijet charm cross section $d\sigma/dx_\gamma^{obs}$ for $886pb^{-1}$ of HERWIG MC. (a) goes from the lowest $x_\gamma^{obs}$ bin to (g) the highest. . . . .	220
14.19	Mass peaks for each bin of the dijet charm cross section $d\sigma/dp_T^{jj}$ for 1998-2000 data $78pb^{-1}$ , with $x_\gamma^{obs} < 0.75$ . (a) goes from the lowest $p_T^{jj}$ bin to (g) the highest.	221
14.3	Mass peaks for each bin of the dijet charm cross section $d\sigma/dp_T^{jj}$ for 1998-2000 data $78pb^{-1}$ . (a) goes from the lowest $p_T^{jj}$ bin to (g) the highest. . . . .	222
14.4	Mass peaks for each bin of the dijet charm cross section $d\sigma/dp_T^{jj}$ for $886pb^{-1}$ of HERWIG MC. (a) goes from the lowest $p_T^{jj}$ bin to (g) the highest. . . . .	223
14.5	Mass peaks for each bin of the dijet charm cross section $d\sigma/d\Delta\phi^{jj}$ for 1998-2000 data $78pb^{-1}$ . (a) goes from the lowest $\Delta\phi^{jj}$ bin to (g) the highest. . . . .	224



## List of Figures

---

14.6	Mass peaks for each bin of the dijet charm cross section $d\sigma/d\Delta\phi^{jj}$ for $886pb^{-1}$ of HERWIG MC. (a) goes from the lowest $\Delta\phi^{jj}$ bin to (g) the highest. . . . .	225
14.7	Mass peaks for each bin of the dijet charm cross section $d\sigma/dm^{jj}$ for 1998-2000 data $78pb^{-1}$ . (a) goes from the lowest $m^{jj}$ bin to (g) the highest. . . . .	226
14.8	Mass peaks for each bin of the dijet charm cross section $d\sigma/dm^{jj}$ for $886pb^{-1}$ of HERWIG MC. (a) goes from the lowest $m^{jj}$ bin to (g) the highest. . . . .	227
14.9	Mass peaks for each bin of the dijet charm cross section $d\sigma/dp_T^{2jj}$ for 1998-2000 data $78pb^{-1}$ . (a) goes from the lowest $p_T^{2jj}$ bin to (g) the highest. . . . .	228
14.10	Mass peaks for each bin of the dijet charm cross section $d\sigma/dp_T^{2jj}$ for $886pb^{-1}$ of HERWIG MC. (a) goes from the lowest $p_T^{2jj}$ bin to (g) the highest. . . . .	229
14.11	Mass peaks for each bin of the dijet charm cross section $d\sigma/dp_T^{jj}$ for 1998-2000 data $78pb^{-1}$ , with $x_\gamma^{obs} > 0.75$ . (a) goes from the lowest $p_T^{jj}$ bin to (g) the highest.	230
14.12	Mass peaks for each bin of the dijet charm cross section $d\sigma/dp_T^{jj}$ for $886pb^{-1}$ of HERWIG MC, with $x_\gamma^{obs} > 0.75$ . (a) goes from the lowest $p_T^{jj}$ bin to (g) the highest. . . . .	231
14.13	Mass peaks for each bin of the dijet charm cross section $d\sigma/d\Delta\phi^{jj}$ for 1998-2000 data $78pb^{-1}$ , with $x_\gamma^{obs} > 0.75$ . (a) goes from the lowest $\Delta\phi^{jj}$ bin to (g) the highest. . . . .	232
14.14	Mass peaks for each bin of the dijet charm cross section $d\sigma/d\Delta\phi^{jj}$ for $886pb^{-1}$ of HERWIG MC, with $x_\gamma^{obs} > 0.75$ . (a) goes from the lowest $\Delta\phi^{jj}$ bin to (g) the highest. . . . .	233
14.15	Mass peaks for each bin of the dijet charm cross section $d\sigma/dm^{jj}$ for 1998-2000 data $78pb^{-1}$ , with $x_\gamma^{obs} > 0.75$ . (a) goes from the lowest $m^{jj}$ bin to (g) the highest.	234
14.16	Mass peaks for each bin of the dijet charm cross section $d\sigma/dm^{jj}$ for $886pb^{-1}$ of HERWIG MC, with $x_\gamma^{obs} > 0.75$ . (a) goes from the lowest $m^{jj}$ bin to (g) the highest. . . . .	235
14.17	Mass peaks for each bin of the dijet charm cross section $d\sigma/dp_T^{2jj}$ for 1998-2000 data $78pb^{-1}$ , with $x_\gamma^{obs} > 0.75$ . (a) goes from the lowest $p_T^{2jj}$ bin to (g) the highest.	236
14.18	Mass peaks for each bin of the dijet charm cross section $d\sigma/dp_T^{2jj}$ for $886pb^{-1}$ of HERWIG MC, with $x_\gamma^{obs} > 0.75$ . (a) goes from the lowest $p_T^{2jj}$ bin to (g) the highest. . . . .	237

## List of Figures

---

14.20	Mass peaks for each bin of the dijet charm cross section $d\sigma/dp_T^{jj}$ for $886pb^{-1}$ of HERWIG MC, with $x_\gamma^{obs} < 0.75$ . (a) goes from the lowest $p_T^{jj}$ bin to (g) the highest. . . . .	238
14.21	Mass peaks for each bin of the dijet charm cross section $d\sigma/d\Delta\phi^{jj}$ for 1998-2000 data $78pb^{-1}$ , with $x_\gamma^{obs} < 0.75$ . (a) goes from the lowest $\Delta\phi^{jj}$ bin to (g) the highest. . . . .	239
14.22	Mass peaks for each bin of the dijet charm cross section $d\sigma/d\Delta\phi^{jj}$ for $886pb^{-1}$ of HERWIG MC, with $x_\gamma^{obs} < 0.75$ . (a) goes from the lowest $\Delta\phi^{jj}$ bin to (g) the highest. . . . .	240
14.23	Mass peaks for each bin of the dijet charm cross section $d\sigma/dm^{jj}$ for 1998-2000 data $78pb^{-1}$ , with $x_\gamma^{obs} < 0.75$ . (a) goes from the lowest $m^{jj}$ bin to (g) the highest.	241
14.24	Mass peaks for each bin of the dijet charm cross section $d\sigma/dm^{jj}$ for $886pb^{-1}$ of HERWIG MC, with $x_\gamma^{obs} < 0.75$ . (a) goes from the lowest $m^{jj}$ bin to (g) the highest. . . . .	242
14.25	Mass peaks for each bin of the dijet charm cross section $d\sigma/dp_T^{2jj}$ for 1998-2000 data $78pb^{-1}$ , with $x_\gamma^{obs} < 0.75$ . (a) goes from the lowest $p_T^{2jj}$ bin to (g) the highest.	243
14.26	Mass peaks for each bin of the dijet charm cross section $d\sigma/dp_T^{2jj}$ for $886pb^{-1}$ of HERWIG MC, with $x_\gamma^{obs} < 0.75$ . (a) goes from the lowest $p_T^{2jj}$ bin to (g) the highest. . . . .	244
15.1	Purity/efficiency/acceptance and hadronisation corrections for each bin of the inclusive charm jet cross section $d\sigma/dE_T^{jet}$ in the range $3.0 < P_T^{D^*} < 5.0$ GeV.	246
15.2	Purity/efficiency/acceptance and hadronisation corrections for each bin of the inclusive charm jet cross section $d\sigma/d\eta^{jet}$ in the range $3.0 < P_T^{D^*} < 5.0$ GeV.	247
15.3	Purity/efficiency/acceptance and hadronisation corrections for each bin of the inclusive charm jet cross section $d\sigma/dE_T^{jet}$ in the range $5.0 < P_T^{D^*} < 8.0$ GeV.	248
15.4	Purity/efficiency/acceptance and hadronisation corrections for each bin of the inclusive charm jet cross section $d\sigma/d\eta^{jet}$ in the range $5.0 < P_T^{D^*} < 8.0$ GeV.	249
15.5	Purity/efficiency/acceptance and hadronisation corrections for each bin of the inclusive charm jet cross section $d\sigma/dE_T^{jet}$ in the range $8.0 < P_T^{D^*} < 20.0$ GeV.	250
15.6	Purity/efficiency/acceptance and hadronisation corrections for each bin of the inclusive charm jet cross section $d\sigma/d\eta^{jet}$ in the range $8.0 < P_T^{D^*} < 20.0$ GeV.	251

## List of Figures

---

16.1 Purity/efficiency/acceptance and hadronisation corrections for each bin of the dijet charm cross section $d\sigma/dx_\gamma$ for HERWIG 886 pb <sup>-1</sup> . . . . .	253
16.2 Purity/efficiency/acceptance and hadronisation corrections for each bin of the inclusive charm jet cross section $d\sigma/dm^{jj}$ for HERWIG 886 pb <sup>-1</sup> . . . . .	254
16.3 Purity/efficiency/acceptance and hadronisation corrections for each bin of the inclusive charm jet cross section $d\sigma/dm^{jj}$ , direct-enriched $x_\gamma^{\text{obs}} > 0.75$ for HERWIG 886 pb <sup>-1</sup> . . . . .	254
16.4 Purity/efficiency/acceptance and hadronisation corrections for each bin of the inclusive charm jet cross section $d\sigma/dm^{jj}$ , resolved-enriched $x_\gamma^{\text{obs}} < 0.75$ for HERWIG 886 pb <sup>-1</sup> . . . . .	255
16.5 Purity/efficiency/acceptance and hadronisation corrections for each bin of the inclusive charm jet cross section $d\sigma/dp_T^{jj}$ for HERWIG 886 pb <sup>-1</sup> . . . . .	255
16.6 Purity/efficiency/acceptance and hadronisation corrections for each bin of the inclusive charm jet cross section $d\sigma/dp_T^{jj}$ , direct-enriched $x_\gamma^{\text{obs}} > 0.75$ for HERWIG 886 pb <sup>-1</sup> . . . . .	256
16.7 Purity/efficiency/acceptance and hadronisation corrections for each bin of the inclusive charm jet cross section $d\sigma/dp_T^{jj}$ , resolved-enriched $x_\gamma^{\text{obs}} < 0.75$ for HERWIG 886 pb <sup>-1</sup> . . . . .	256
16.8 Purity/efficiency/acceptance and hadronisation corrections for each bin of the inclusive charm jet cross section $d\sigma/d\Delta\phi^{jj}$ , for HERWIG 886 pb <sup>-1</sup> . . . . .	257
16.9 Purity/efficiency/acceptance and hadronisation corrections for each bin of the inclusive charm jet cross section $d\sigma/d\Delta\phi^{jj}$ , direct-enriched $x_\gamma^{\text{obs}} > 0.75$ for HERWIG 886 pb <sup>-1</sup> . . . . .	257
16.10 Purity/efficiency/acceptance and hadronisation corrections for each bin of the inclusive charm jet cross section $d\sigma/d\Delta\phi^{jj}$ , resolved-enriched $x_\gamma^{\text{obs}} < 0.75$ for HERWIG 886 pb <sup>-1</sup> . . . . .	258
16.11 Purity/efficiency/acceptance and hadronisation corrections for each bin of the inclusive charm jet cross section $d\sigma/dp_T^{2jj}$ , for HERWIG 886 pb <sup>-1</sup> . . . . .	258
16.12 Purity/efficiency/acceptance and hadronisation corrections for each bin of the inclusive charm jet cross section $d\sigma/dp_T^{2jj}$ , direct-enriched $x_\gamma^{\text{obs}} > 0.75$ for HERWIG 886 pb <sup>-1</sup> . . . . .	259

16.13	Purity/efficiency/acceptance and hadronisation corrections for each bin of the inclusive charm jet cross section $d\sigma/dp_T^{2jj}$ , resolved-enriched $x_\gamma^{\text{obs}} < 0.75$ for HERWIG 886 pb <sup>-1</sup> . . . . .	259
17.1	Systematics for each bin of the inclusive charm jet cross section $d\sigma/dE_T^{\text{jet}}$ in the range $-1.5 < \eta^{\text{jet}} < 2.4$ for 1998-2000 data 78pb <sup>-1</sup> . . . . .	261
17.2	Systematics for each bin of the inclusive charm jet cross section $d\sigma/dE_T^{\text{jet}}$ in the range $-1.5 < \eta^{\text{jet}} < -0.5$ for 1998-2000 data 78pb <sup>-1</sup> . . . . .	262
17.3	Systematics for each bin of the inclusive charm jet cross section $d\sigma/dE_T^{\text{jet}}$ in the range $-0.5 < \eta^{\text{jet}} < 0.5$ for 1998-2000 data 78pb <sup>-1</sup> . . . . .	263
17.4	Systematics for each bin of the inclusive charm jet cross section $d\sigma/dE_T^{\text{jet}}$ in the range $0.5 < \eta^{\text{jet}} < 1.5$ for 1998-2000 data 78pb <sup>-1</sup> . . . . .	264
17.5	Systematics for each bin of the inclusive charm jet cross section $d\sigma/dE_T^{\text{jet}}$ in the range $1.5 < \eta^{\text{jet}} < 2.4$ for 1998-2000 data 78pb <sup>-1</sup> . . . . .	265
17.6	Systematics for each bin of the inclusive charm jet cross section $d\sigma/d\eta^{\text{jet}}$ in the range $E_T^{\text{jet}} > 6$ GeV for 1998-2000 data 78pb <sup>-1</sup> . . . . .	266
17.7	Systematics for each bin of the inclusive charm jet cross section $d\sigma/d\eta^{\text{jet}}$ in the range $6 < E_T^{\text{jet}} < 9$ GeV for 1998-2000 data 78pb <sup>-1</sup> . . . . .	267
17.8	Systematics for each bin of the inclusive charm jet cross section $d\sigma/d\eta^{\text{jet}}$ in the range $E_T^{\text{jet}} > 9$ GeV for 1998-2000 data 78pb <sup>-1</sup> . . . . .	268
17.9	Systematics for each bin of the tagged $D^*$ jet cross section $d\sigma/dE_T^{\text{jet}}$ in the range $-1.5 < \eta^{\text{jet}} < 2.4$ for 1998-2000 data 78pb <sup>-1</sup> . . . . .	269
17.10	Systematics for each bin of the untagged $D^*$ jet cross section $d\sigma/d\eta^{\text{jet}}$ in the range $E_T^{\text{jet}} > 6$ GeV for 1998-2000 data 78pb <sup>-1</sup> . . . . .	270
17.11	Systematics for each bin of the untagged $D^*$ jet cross section $d\sigma/d\eta^{\text{jet}}$ in the range $6 < E_T^{\text{jet}} < 9$ GeV for 1998-2000 data 78pb <sup>-1</sup> . . . . .	271
17.12	Systematics for each bin of the untagged $D^*$ jet cross section $d\sigma/d\eta^{\text{jet}}$ in the range $E_T^{\text{jet}} > 9$ GeV for 1998-2000 data 78pb <sup>-1</sup> . . . . .	272
17.13	Systematics for each bin of the untagged $D^*$ jet cross section $d\sigma/dE_T^{\text{jet}}$ in the range $-1.5 < \eta^{\text{jet}} < 2.4$ for 1998-2000 data 78pb <sup>-1</sup> . . . . .	273
17.14	Systematics for each bin of the untagged $D^*$ jet cross section $d\sigma/d\eta^{\text{jet}}$ in the range $E_T^{\text{jet}} > 6$ GeV for 1998-2000 data 78pb <sup>-1</sup> . . . . .	274

*List of Figures*

---

17.15	Systematics for each bin of the untagged $D^*$ jet cross section $d\sigma/d\eta^{jet}$ in the range $6 < E_T^{jet} < 9$ GeV for 1998-2000 data $78pb^{-1}$ . . . . .	275
17.16	Systematics for each bin of the tagged $D^*$ jet cross section $d\sigma/d\eta^{jet}$ in the range $E_T^{jet} > 9$ GeV for 1998-2000 data $78pb^{-1}$ . . . . .	276
17.17	Systematics for each bin of the inclusive charm jet cross section $d\sigma/dE_T^{jet}$ in the range $3.0 < P_T^{D^*} < 5.0$ GeV for 1998-2000 data $78pb^{-1}$ . . . . .	277
17.18	Systematics for each bin of the inclusive charm jet cross section $d\sigma/d\eta^{jet}$ in the range $3.0 < P_T^{D^*} < 5.0$ GeV for 1998-2000 data $78pb^{-1}$ . . . . .	278
17.19	Systematics for each bin of the inclusive charm jet cross section $d\sigma/dE_T^{jet}$ in the range $5.0 < P_T^{D^*} < 8.0$ GeV for 1998-2000 data $78pb^{-1}$ . . . . .	279
17.20	Systematics for each bin of the inclusive charm jet cross section $d\sigma/d\eta^{jet}$ in the range $5.0 < P_T^{D^*} < 8.0$ GeV for 1998-2000 data $78pb^{-1}$ . . . . .	280
17.21	Systematics for each bin of the inclusive charm jet cross section $d\sigma/dE_T^{jet}$ in the range $8.0 < P_T^{D^*} < 20.0$ GeV for 1998-2000 data $78pb^{-1}$ . . . . .	281
17.22	Systematics for each bin of the inclusive charm jet cross section $d\sigma/d\eta^{jet}$ in the range $8.0 < P_T^{D^*} < 20.0$ GeV for 1998-2000 data $78pb^{-1}$ . . . . .	282
17.23	Systematics for each bin of the inclusive charm jet cross section $d\sigma/dx_\gamma^{obs}(D^*, other\ jet)$ for 1998-2000 data $78pb^{-1}$ . . . . .	283
17.24	Systematics for each bin of the dijet charm cross section $d\sigma/dx_\gamma^{obs}$ for 1998-2000 data $78pb^{-1}$ . . . . .	284
17.25	Systematics for each bin of the dijet charm cross section $d\sigma/dp_T^{jj}$ for 1998-2000 data $78pb^{-1}$ . . . . .	285
17.26	Systematics for each bin of the dijet charm cross section $d\sigma/d\Delta\phi^{jj}$ for 1998-2000 data $78pb^{-1}$ . . . . .	286
17.27	Systematics for each bin of the dijet charm cross section $d\sigma/dm^{jj}$ for 1998-2000 data $78pb^{-1}$ . . . . .	287
17.28	Systematics for each bin of the dijet charm cross section $d\sigma/dp_T^{2jj}$ for 1998-2000 data $78pb^{-1}$ . . . . .	288
17.29	Systematics for each bin of the dijet charm cross section $d\sigma/dp_T^{jj}$ for 1998-2000 data $78pb^{-1}$ , with $x_\gamma^{obs} > 0.75$ . . . . .	289

## List of Figures

---

17.30	Systematics for each bin of the dijet charm cross section $d\sigma/d\Delta\phi^{\text{jj}}$ for 1998-2000 data $78\text{pb}^{-1}$ , with $x_{\gamma}^{\text{obs}} > 0.75$ . . . . .	290
17.31	Systematics for each bin of the dijet charm cross section $d\sigma/dm^{\text{jj}}$ for 1998-2000 data $78\text{pb}^{-1}$ , with $x_{\gamma}^{\text{obs}} > 0.75$ . . . . .	291
17.32	Systematics for each bin of the dijet charm cross section $d\sigma/dp_T^{2\text{jj}}$ for 1998-2000 data $78\text{pb}^{-1}$ , with $x_{\gamma}^{\text{obs}} > 0.75$ . . . . .	292
17.33	Systematics for each bin of the dijet charm cross section $d\sigma/dp_T^{\text{jj}}$ for 1998-2000 data $78\text{pb}^{-1}$ , with $x_{\gamma}^{\text{obs}} < 0.75$ . . . . .	293
17.34	Systematics for each bin of the dijet charm cross section $d\sigma/d\Delta\phi^{\text{jj}}$ for 1998-2000 data $78\text{pb}^{-1}$ , with $x_{\gamma}^{\text{obs}} < 0.75$ . . . . .	294
17.35	Systematics for each bin of the dijet charm cross section $d\sigma/dm^{\text{jj}}$ for 1998-2000 data $78\text{pb}^{-1}$ , with $x_{\gamma}^{\text{obs}} < 0.75$ . . . . .	295
17.36	Systematics for each bin of the dijet charm cross section $d\sigma/dp_T^{2\text{jj}}$ for 1998-2000 data $78\text{pb}^{-1}$ , with $x_{\gamma}^{\text{obs}} < 0.75$ . . . . .	296
18.1	The resolution of $x_{\gamma}^{\text{obs}}$ using $886\text{ pb}^{-1}$ of HERWIG Monte Carlo. The fits are Gaussian. . . . .	297
18.2	The resolution of $m^{\text{jj}}$ using $886\text{ pb}^{-1}$ of HERWIG Monte Carlo. The fits are Gaussian. . . . .	298
18.3	The resolution of $p_T^{\text{jj}}$ using $886\text{ pb}^{-1}$ of HERWIG Monte Carlo. The fits are Gaussian. . . . .	298
18.4	The resolution of $\Delta\phi^{\text{jj}}$ using $886\text{ pb}^{-1}$ of HERWIG Monte Carlo. The fits are Gaussian. . . . .	299

---

## List of Tables

---

2.1	Leptons, quarks, and bosons. . . . .	46
2.2	Parton level processes included in FMNR. . . . .	54
2.3	The measured fragmentation fractions from H1 and ZEUS for the mesons $D^+$ , $D^0$ , $D_s^+$ , $D^{*+}$ and $\Lambda_c^+$ compared to the world average $e^+e^-$ results. . . . .	60
3.1	HERA's design parameters for the 1998-2000 data taking period. . . . .	77
5.1	Decay modes generated in HERWIG and PYTHIA Monte Carlo samples. . . .	118
7.1	Inclusive charm and jet(s) cross section kinematic region. . . . .	142
8.1	Dijet jet cross section kinematic region. . . . .	152
10.1	HERA's design parameters for the upgrade data taking period. . . . .	160
10.2	MVD hit residual results for cosmic ray muon events. . . . .	166

---

# 1 Introduction

---

The aim of particle physics is to discover fundamental particles and to understand their interactions. Together with other branches of physics, particle physics tries to find a consistent description of our world, and tries to explain all known phenomena. The range over which the universe is to be understood is enormous, the visible universe extends across  $10^{26}$  meters, whereas the smallest particles are believed to be on the Planck scale  $\sim 10^{-35}$  meters. There have been 14 billion years of evolution in the universe's structure but the initial processes which occurred within the first  $10^{-43}$  seconds are those which have shaped and made our universe the way it is. Our constant thirst for knowledge and understanding of the universe drives us to explore and understand why things are the way they are.

Our current understanding of the fundamental particles in this world are quarks and leptons. There are three quark doublets : up (u) and down (d), strange (s) and charm (c) and bottom (b) and top (t) from the lightest to the heaviest respectively. These quarks also have their respective anti-particles. They are never observed alone/directly due to confinement but are observed via bound states of quarks and anti-quarks called mesons and baryons (three quark states) and possibly more recently discovered pentaquarks (five quark states). Leptons are particles which do not interact via the strong force (see below), and replicate the generation pattern of the quarks. Each lepton pair consists of a charged lepton and a neutrino, the neutrino masses being small.

In addition the fundamental particles interact via fundamental forces. In the 19<sup>th</sup> century the electromagnetic force was known and in the 20<sup>th</sup> century two new types of elementary forces were discovered namely; the weak force, which is responsible for radioactive decay and necessary for the process of solar energy; and the strong force, which holds together the protons and neutrons within the nuclei of atoms. Interactions are mediated by particles - the



massless photon mediates the electromagnetic interaction, the massive  $W^\pm$ ,  $Z^0$  particles the weak interaction and the massless gluon mediates the colour force between the quarks. The fourth fundamental force of nature, gravity dictates the structure of the universe, the way stars form and move. Although we have been aware of gravity for centuries it has been the most mystifying of all four fundamental forces.

Since the middle of the 20<sup>th</sup> century particle physics has been revealing the fundamental laws of nature. It has succeeded in revealing the structure of known matter, and also explaining the interactions, and fundamental forces between these interactions. The present state of this knowledge is known as the Standard Model of particle physics. This model incorporates the lepton and quark families, as well as the electromagnetic, weak, and strong interactions.

The Standard Model is based on gauge theories, which are theories based on the idea that symmetry transformations can be performed globally as well as locally. When the transformations are identically performed at every space-time point they have global symmetries. Gauge theory extends this idea by requiring that the Lagrangians (which define the particle fields, from which the equations of motion of a dynamical system can be derived) must possess local symmetries as well it should be possible to perform these symmetry transformations in a particular region of space-time without affecting what happens in another region. This requirement is a generalised version of the equivalence principle of general relativity. The importance of gauge theories for physics stems from the tremendous success of the mathematical formalism in providing a unified framework to describe the quantum field theories of electromagnetism, the weak force and the strong force. Modern theories like string theory, as well as some formulations of general relativity, are in one way or another, gauge theories. The Standard Model unifies the description of electromagnetism, weak interactions and strong interactions in the language of gauge theory.

Experimental results have confirmed the Standard Model with accuracies of the per mil range or better for these theories. There are still many un-answered questions; What is the origin of mass? Are the different forces derived from a common ‘universal force’? Does space-time consist of more than four dimensions? From cosmological observations it seems that the standard model only accounts for some 4% of the universe - what is the nature of the dark matter and energy which constitutes the rest of the universe?

To explore matter’s tiniest particle structure requires the construction of machines in which

individual particles are accelerated to very large energies and are then brought together in an interaction point in which the resulting collision fragments are detected in huge detectors. From these pieces of information the initial interaction can be found by working backwards from the final state to the initial state. The higher the energy to which individual particles can be accelerated the smaller the distances that can be investigated. Particle physics operates at the forefront of technology, developing bigger and better particle accelerators pushing the frontiers of science forward.

HERA, an electron-proton storage ring facility at the DESY research centre in Hamburg is used as a ‘microscope’ for exploring the innermost structure of the proton. In fact, HERA’s resolution can be so high that details as small as one-thousandth of a proton’s diameter can be examined. The research described in this thesis is carried out at the ZEUS experiment at HERA.

In this thesis new areas of heavy-flavour physics at HERA are used to test perturbative quantum chromodynamics (pQCD), and hence test an integral part of the standard model. Charm quark production at HERA is discussed. In addition, new methods and techniques to tag and trigger on these charmed particles in the recent running phase of HERA II are also described.

---

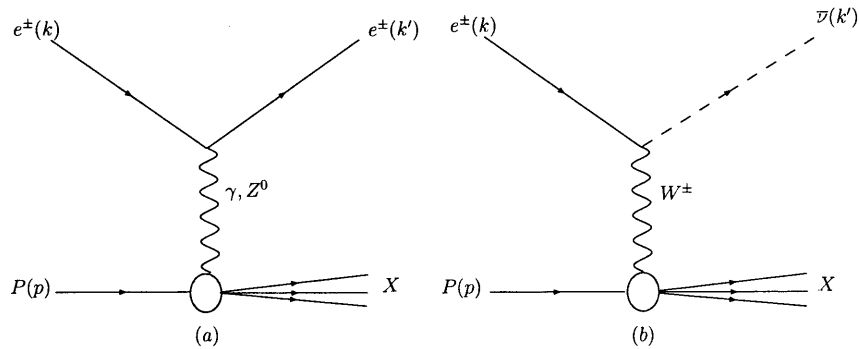
## 2 Overview of $ep$ scattering and previous results on heavy quark production in colliders

---

Before discussing heavy quarks in photoproduction, the main topic of this thesis, it is necessary to describe  $ep$  kinematics, and thereby introduce some concepts in QCD.

### 2.1 Kinematics of $ep$ scattering

In the Standard Model the interaction between an electron/positron and a proton is realised through the exchange of a vector boson. If the boson is a photon ( $\gamma$ ) or a  $Z^0$  the process is called *neutral current* scattering (NC, fig. 2.1-a). Additionally, a charged  $W^\pm$  boson can be exchanged, which is called *charged current* scattering (CC, fig. 2.1-b).



**Figure 2.1** Diagrams of electron-proton scattering. (a) In a *neutral current* process a photon or a  $Z^0$  is exchanged. (b) In a *charged current* process the exchanged boson is a charged  $W^\pm$ .

In the above Feynman diagrams,  $k$ ,  $k'$  and  $P$  are the four-momenta of the incoming electron, the scattered electron and proton, respectively. The four-momentum  $q$  of the boson exchanged

between the electron and the proton is given by

$$q = k - k'. \quad (2.1)$$

The scattering process is characterized by the following Lorentz scalars:

$$Q^2 = -q^2 = -(k - k')^2, \quad (2.2)$$

$$s = (k + P)^2 \simeq 2k \cdot P, \quad (2.3)$$

$$y = \frac{P \cdot q}{P \cdot k} \simeq \frac{2P \cdot q}{s} \quad \text{and} \quad (2.4)$$

$$x = \frac{Q^2}{2P \cdot q} \quad (2.5)$$

where  $s$  is the square of the total center-of-mass energy,  $y$  and  $x$  are the *Bjorken scaling variables*. The variable  $y$  measures the energy fraction from the electron transferred to the interaction in the proton rest frame,  $x$  is the fraction of the proton momentum carried by the struck quark, and  $Q^2$  is the virtuality of the exchanged boson and corresponds to the resolution of the probe. A structure in the proton is resolved if its dimension is of the order of the probe wavelength  $\lambda \simeq \hbar/\sqrt{Q^2} \simeq 0.197/\sqrt{Q^2}$  fm. The variables  $x$ ,  $y$  and  $Q^2$  are related by the square of the centre of mass energy

$$Q^2 = sxy. \quad (2.6)$$

The variable

$$W^2 = (q + P)^2 = q^2 + P^2 + 2q \cdot P \simeq -Q^2 + ys, \quad (2.7)$$

which is the invariant mass squared of the system recoiling against the scattered lepton, can be interpreted as the square of the centre of mass energy of the virtual boson-proton system.

## 2.2 QCD and $ep$ interactions

Quantum Chromodynamics (QCD) is a non-abelian gauge theory, based on the SU(3) colour symmetry group, describing the interactions of quarks and gluons.

The quarks come in three colour charges, interacting by the exchange of a gluon with the properties shown in Table.2.1. Quarks interact strongly the further they are apart, which as a consequence they cannot be seen individually, a phenomenon known as ‘colour confinement’. The strength of the interaction between two coloured objects decreases the closer they are together. This is known as asymptotic freedom. At the scales in which QCD processes occur,

## 2.2 QCD and ep interactions

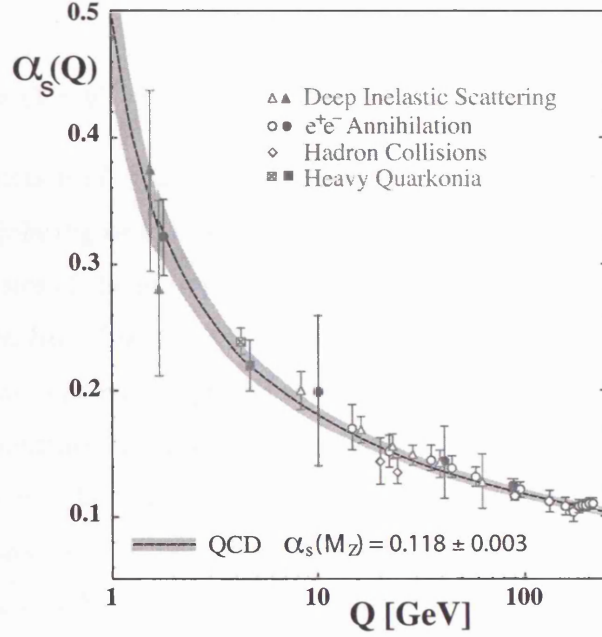
	Particle	Charge (e)	Mass (MeV)
Leptons	electron	-1	0.511
	electron neutrino ( $\nu_e$ )	0	< 1 eV
	muon	-1	106
	muon neutrino ( $\nu_\mu$ )	0	< 0.19
	tau	-1	1777
	tau neutrino ( $\nu_\tau$ )	0	< 18.2
Quarks	up	+2/3	1.5-5
	down	-1/3	3-9
	charm	+2/3	$\sim 1200-1700$
	strange	-1/3	60-170
	top	+2/3	174000
	bottom	-1/3	$\sim 4200$
Bosons	photon ( $\gamma$ )	0	0
	$Z^0$	0	91187
	$W^\pm$	$\pm 1$	80410
	8 gluons ( $g$ )	0	0

**Table 2.1** Leptons, quarks, and bosons.

this coupling ( $\alpha_s$ ) between the quarks and gluons is dependent on  $Q^2$ . As  $Q^2$  varies across many orders of magnitude  $\alpha_s$  also changes significantly (see fig.2.2). As  $Q^2$  rises, smaller and smaller distances can be probed within the proton.

In (eq. 2.8) the formula for  $\alpha_s$  is given, where  $\mu_r$  is the renormalisation scale. In DIS  $\mu_r^2$  can be replaced with  $Q^2$  but in photoproduction  $Q^2 \sim 0$  and the scale is determined by the kinematics of the second vertex (see fig. 2.4).  $N_f$  is the number of active quark flavours in the interaction, and  $\Lambda_{QCD}$  is a parameter which is determined experimentally, and is of  $\mathcal{O}(100\text{MeV})$ .

$$\alpha_s(\mu_r^2) = \ln\left(\frac{12\pi}{(33 - 2N_f)\ln(\frac{\mu_r^2}{\Lambda_{QCD}^2})}\right), \quad (2.8)$$



**Figure 2.2** The running coupling constant  $\alpha_s$  as measured in DIS,  $e^+e^-$  annihilation, hadronic collisions and heavy quarkonia.

As  $\mu_r^2$  increases when  $\mu_r^2 \gg \Lambda_{QCD}^2$ , then  $\alpha_s \ll 1$ , which is a manifestation of asymptotic freedom ( $\alpha_s \rightarrow 0$  as  $\mu_r^2 \rightarrow \infty$ ). For these cases perturbative models can be applied to QCD calculations. In the case where  $\mu_r^2 \rightarrow \Lambda_{QCD}^2$ ,  $\alpha_s \sim \mathcal{O}(1)$ , higher order terms in a perturbative expansion may not necessarily converge. This is where pQCD cannot be used, and non-perturbative techniques are necessary, such as phenomenological models based on experimental results. HERA provides an excellent environment for such tests of QCD and pQCD.

### 2.2.1 The quark parton model

The neutral current (NC) cross section, (eq. 2.9), can be described in terms of ‘structure functions’,  $F_i$ , which parameterise the structure of the proton target as seen by the virtual boson.

$$\frac{d^2\sigma^{ep}}{dx dQ^2} = \frac{4\pi\alpha^2}{xQ^4} \left[ \frac{y^2}{2} 2xF_1(x, Q^2) + (1-y)F_2(x, Q^2) \mp \left(y - \frac{y^2}{2}\right)x F_3 \right] \quad (2.9)$$

where  $F_L = F_2 - 2xF_1$  which then yields,

$$\frac{d^2\sigma^{ep}}{dx dQ^2} = \frac{2\pi\alpha^2}{xQ^4} [(1 + (1-y)^2)F_2(x, Q^2) \mp (1 - (1-y)^2)x F_3(x, Q^2) - y^2 F_L(x, Q^2)]. \quad (2.10)$$

$F_2$  is the structure function of  $\gamma$  and  $Z^0$  exchange,  $F_L$  is the longitudinal structure function, and  $F_3$  is the parity violating term arising from  $Z^0$  exchange.

All the detailed physics of the proton are contained within the structure functions, from the relation  $\nu = P \cdot q$  taken from (fig. 2.1). It was predicted [1][2] that structure functions should ‘scale’, i.e. become functions not of  $Q^2$  and  $\nu$  independently but on their ratio  $Q^2/\nu$ . Indeed this prediction was confirmed in SLAC at  $Q^2 \approx 4 \text{ GeV}^2$  [3]. This led to the model that the proton was made of point-like objects, called partons. If the partons are quarks, this has the implication that partons are massless spin 1/2, non-interacting particles resulting in  $F_L$  being zero. Bjorken’s scaling variable,  $x$  (eq. 2.5) was interpreted as the momentum fraction carried by the struck parton in the hard scatter. The parton model structure functions were then given by:

$$F_1(x) = \frac{1}{2} \sum_i e_i^2 f_i(x) \text{ and} \quad (2.11)$$

$$F_2(x) = \sum_i e_i^2 x f_i(x), \quad (2.12)$$

where  $e_i$  are the charges of the partons,  $f_i(x)$  are the density functions, i.e. the probability of finding a parton  $i$  with momentum fraction  $x$  in the proton.  $F_1$  and  $F_2$  are connected by the Callan-Gross relation

$$2xF_1(x) = F_2(x). \quad (2.13)$$

This model was then modified when experimental data at higher  $Q^2$  did not match the simple theory and ‘scaling violation’ was discovered (see section 2.2.2).

### 2.2.2 The improved quark parton model

Summing up all of the momenta of the quarks within the proton should equal the momentum of the proton, i.e. the momentum fractions should sum to unity,

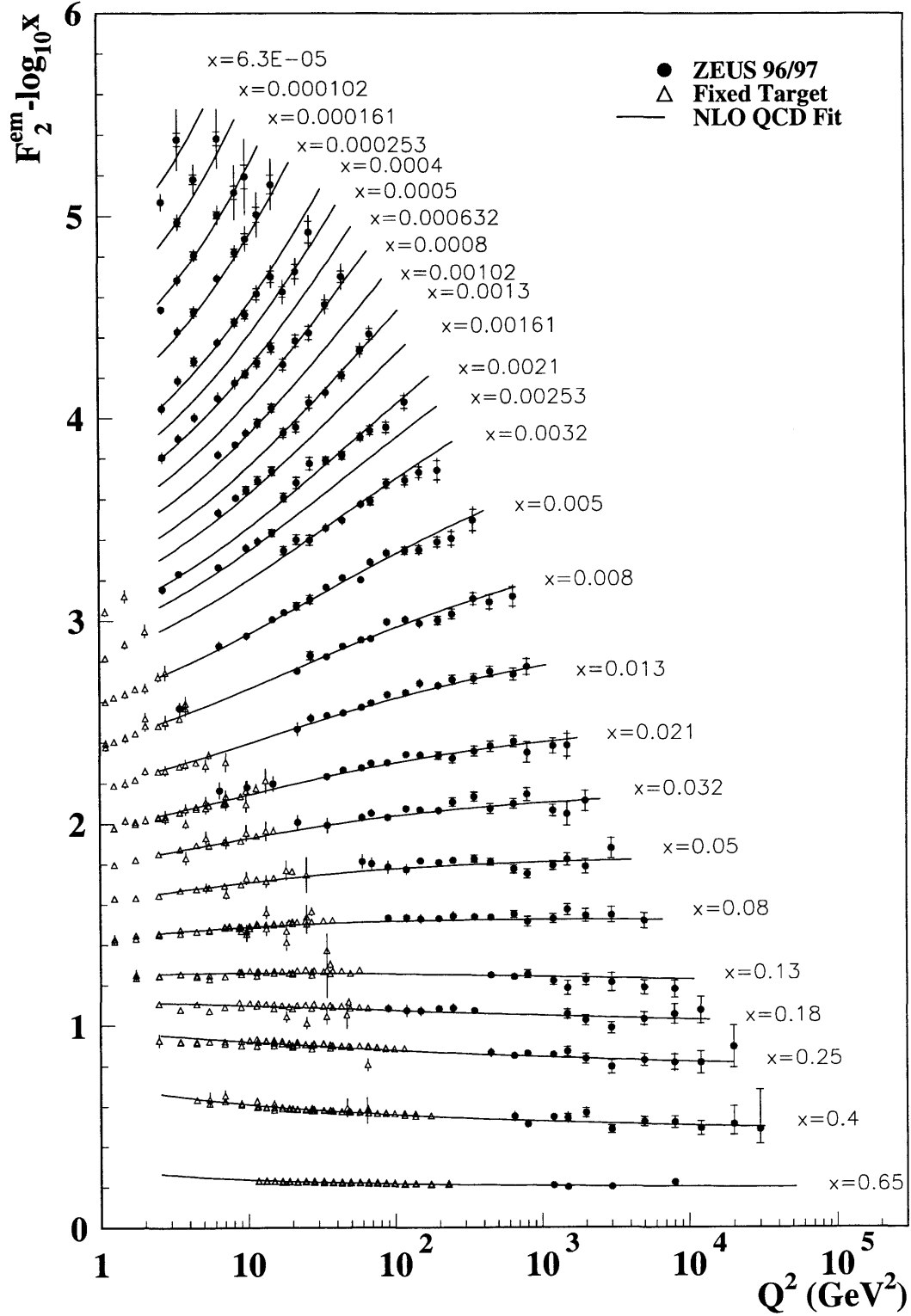
$$\sum_i \int_0^1 dx f_i(x) x = 1 . \quad (2.14)$$

Experimentally this was found not to be the case, instead the value found was  $\sim 0.5$  [4]. Therefore there had to be 50% of momentum carried by neutral particles within the proton. These particles are known as gluons, direct evidence for these being the observation of 3-jet events in  $e^+e^-$  annihilation at DESY in 1979 at the TASSO and JADE experiments [5].

Because gluons can be emitted or absorbed partons can acquire transverse momentum. These interactions are described in quantum chromodynamics (QCD), by the exchange of gluons, radiation of gluons by quarks and the splitting of gluons into quark anti-quark pairs. The proton then becomes a dynamical system of quarks and gluons interacting with one another, the total number of partons which can be seen now depends on the ‘scale’  $\mu_r^2$  at which the proton is probed. At high values of  $x$ , valence quarks dominate,  $F_2$  falls with increasing  $Q^2$ , but at low  $x$  the number of ‘sea’ quarks and gluons rises and  $F_2$  rises with  $Q^2$  (see Fig. 2.3) - the structure functions exhibit scaling violations.



## ZEUS



**Figure 2.3**  $F_2$  vs.  $Q^2$  for fixed  $x$ . The fixed-target results are from NMC, BCDMS, E665 and ZEUS data. The results are compared to the ZEUS NLO QCD fit.

## 2.3 Jets

These are the collimated cluster of hadrons in the final state emerging in the direction of each original parton. They occur due to colour confinement (section 2.2). Local Parton Hadron Duality (LPHD) [6], states that the distribution of hadrons reflects that of the partons involved in creating the subprocess, therefore the study of jet properties allows for the understanding of the underlying dynamics of the interaction. All jets in the measurements in this thesis are constructed in the lab frame with the  $k_T$ -algorithm in massless mode using the Snowmass convention [7], with the jet having an  $E_T^{\text{jet}} > 6$  GeV and  $-1.5 < \eta^{\text{jet}} < 2.4$  for the single jet case. When dijets are required the conditions are  $E_T^{\text{jet1}} > 7$  GeV,  $-1.5 < \eta^{\text{jet1}} < 2.4$  and  $E_T^{\text{jet2}} > 6$  GeV and  $-1.5 < \eta^{\text{jet2}} < 2.4$ .

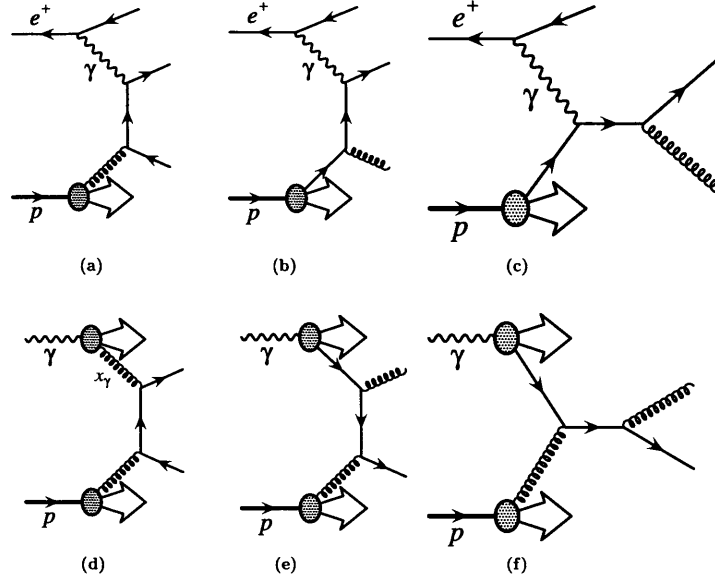
## 2.4 Photoproduction of heavy quarks

Photoproduction processes with high transverse energy( $E_T$ ) jets are calculable in pQCD as described in (section 2.2). Heavy quarks( $c$  or  $b$ ) produced in these collision provide an additional energy scale due to their large mass,  $m_c \sim 1.5$  GeV or  $m_b \sim 5$  GeV. Theoretically the calculation for these processes can be done in the massive scheme [8, 9] where the masses of the heavy quarks are considered and the massless scheme [10] in which the  $c$ -quark or  $b$ -quark is taken from the parton density functions and are considered massless like light quarks ( $u, d$  and  $s$ ). Figure 2.4 shows some of the leading order processes in these calculations, and (fig. 2.5) shows some NLO order diagrams involved in the NLO calculations for both virtual and real corrections.

In the massive scheme light quarks are considered as massless active flavours in the proton and photon, and the charm quark mass is non-zero in the matrix element calculation. Charm is therefore only produced in the final state. Boson-gluon fusion (BGF)  $\gamma g \rightarrow c\bar{c}$  is the dominant process contributing to charm production in direct processes where the photon is point like. At low  $p_T$  the massive approach is expected to provide reliable calculations since contributions from the parton density function are small. Large terms can arise from the collinear emission of a gluon from the charm quark, due to the mass of the charm quark being small relative

---

<sup>1</sup>The pseudorapidity is defined as  $\eta = -\ln\left(\tan\frac{\theta}{2}\right)$ , where the polar angle,  $\theta$ , is measured with respect to the proton beam direction.



**Figure 2.4** A few of the leading order processes in direct (a) boson-gluon fusion, (b) initial state radiation and (c) Compton scattering. Resolved processes (d) gluon-gluon fusion, (e and f) flavour excitation from the photon.

to the  $p_T$ . The perturbative calculation is expected to become unreliable when  $p_T \gg m_c$ , causing problems in the perturbative calculation. Both these difficulties arise from  $\ln(p_T^2/m_c^2)$  terms.

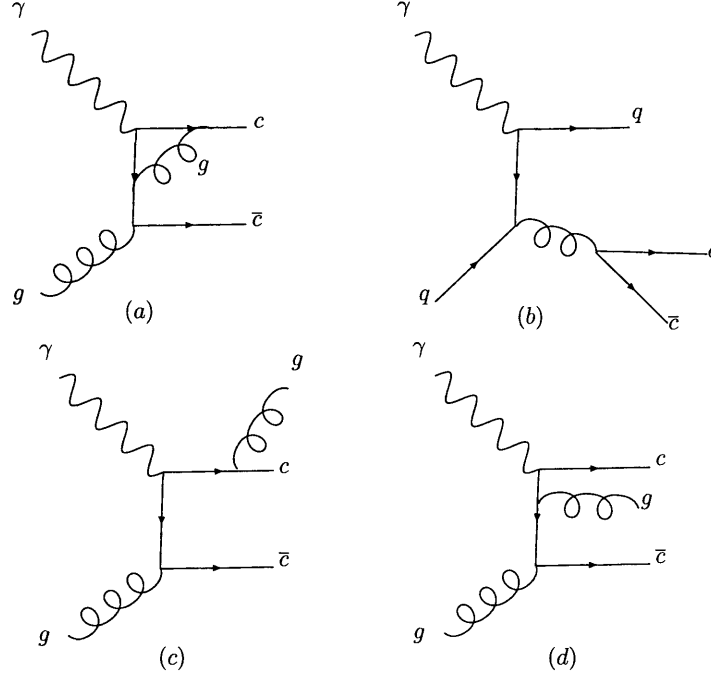
In the massless scheme charm is used in addition to  $u$ ,  $d$  and  $s$  as an active flavour in the hadrons. The calculation is expected to be valid when  $p_T \gg m_c$ , where the mass of the charm has less importance and light flavours and charm can be considered like for like.

The predicted cross sections are not wildly different in each method, although the contributions from direct and resolved processes differ in the two different approaches.

### 2.4.1 NLO Photoproduction calculations (FMNR) ‘massive’ scheme

The calculations of charm photoproduction in the ‘massive’ scheme used in this thesis were developed by Frixione et al [8, 9]. The processes calculated in this program are summarised in table. 2.2.

Charm quarks are not active flavours in the PDF’s, therefore charm excitation appears at



**Figure 2.5** A few of the next-to-leading order processes, (a) and (b) are virtual corrections and (c) and (d) are real corrections calculated in the NLO programs.

NLO in the massive calculation, whereas in the massless calculation it is LO. The calculation is used as a ‘parton’ event generator, with the the jet finder used on the partons to select the same kinematic region as can be measured in the data.

### 2.4.2 NLO Photoproduction calculations ‘massless’ scheme

In the ‘massless’ scheme [10] the quark is treated as massless and appears as an active parton in the incoming hadron or photon, having a non-perturbative parton density function (PDF). The energy scale characteristic  $\mu$  has to be in a range where  $\mu \gg m_Q$  i.e. where the  $D^*$  meson transverse momenta are  $p_T(D^*) \gg m_Q$ . At NLO, real and virtual partons can be radiated in the hard interaction, which can cause soft and collinear singularities, due to the partons being treated as massless. The soft singularities cancel between real and virtual corrections, while the collinear ones are absorbed into the PDF’s or fragmentation functions.

direct process		
LO	NLO	
$\gamma g \rightarrow c\bar{c}$	virtual correction	$\gamma g \rightarrow c\bar{c}$
	real correction	$\gamma g \rightarrow c\bar{c}g$ $\gamma g \rightarrow c\bar{c}q$
resolved process		
LO	NLO	
$gg \rightarrow c\bar{c}$	virtual correction	$gg \rightarrow c\bar{c}$
$q\bar{q} \rightarrow c\bar{c}$		$q\bar{q} \rightarrow c\bar{c}$
	real correction	$gg \rightarrow c\bar{c}g$
		$q\bar{q} \rightarrow c\bar{c}q$
		$qg \rightarrow c\bar{c}q$
		$\bar{q}g \rightarrow c\bar{c}q$

Table 2.2 Parton level processes included in FMNR.

### 2.4.3 Fixed order next-to-leading logarithmic calculations (FONLL)

The conceptually most promising approach to calculate heavy quark cross sections is to combine the benefits of the ‘massive’ and the ‘massless’ scheme. In the FONLL [11, 12] approach the calculation at low momenta  $p_T \approx m_c$  is effectively performed in the massive scheme and at high momenta in the ‘massless’ scheme. A transition is defined to avoid double counting of common terms. A further *merged* approach compared to  $D^*$  photoproduction at HERA can be found in [13]. At present the FONLL calculation cannot be used to calculate the final states required in the analyses within this thesis, but will hopefully be available soon.

### 2.4.4 Heavy quark fragmentation functions

Due to colour confinement partons are not directly observed, whereas the cross sections are theoretically calculated from the production of partons. Fragmentation and hadronisation processes are applied to these partons which then can produce colourless hadrons.

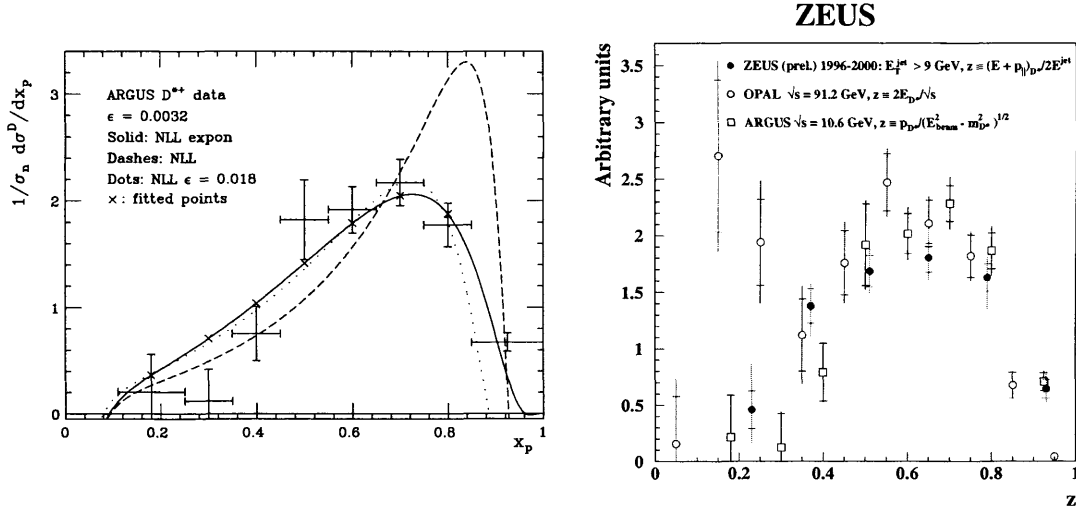
A large fraction of the momentum carried by a meson initiated from heavy quarks comes

from the corresponding heavy quark. The momentum distribution of a  $c$  or  $b$  quark is a phenomenological function known as the fragmentation function, which is obtained by a fit to experimental data of the fractional momentum carried by the hadron with respect to the parent quark.

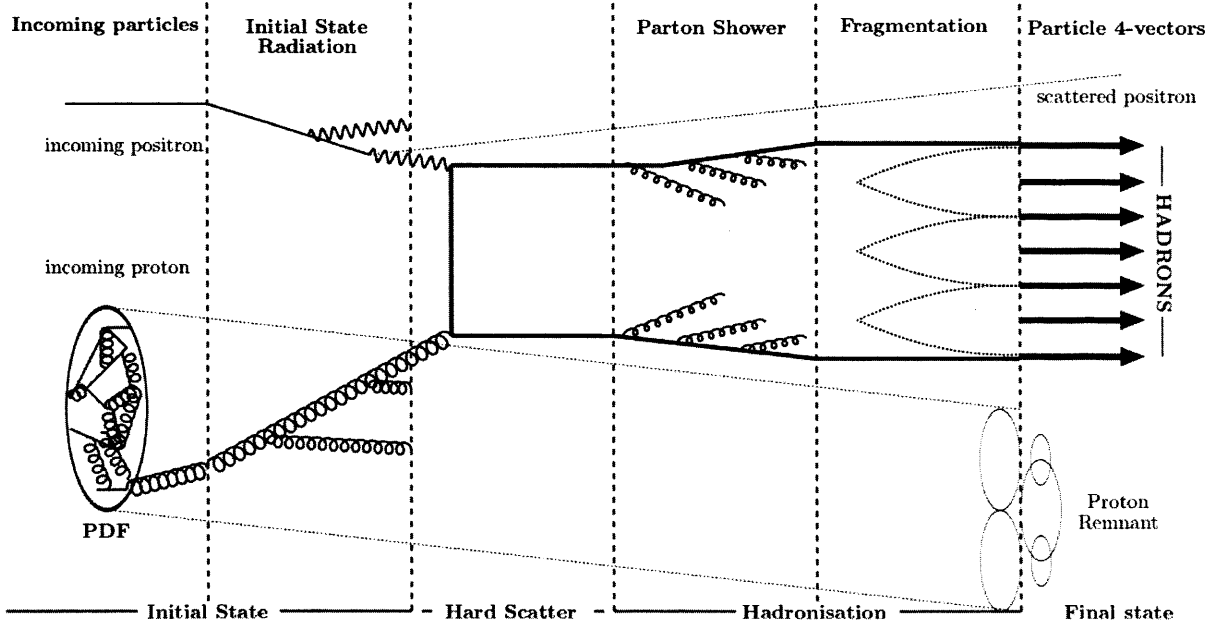
The Peterson function [18] is used in both NLO schemes and is given by:

$$f(z) = \frac{1}{z(1 - \frac{1}{z} - \frac{\epsilon}{1-z})^2}. \quad (2.15)$$

The momentum fraction of the parent quark is  $z$ , and the parameter  $\epsilon$  is determined by fitting the Peterson function to the fragmentation function measured by experiments. For the calculation used to compare the measured cross sections in this analysis the value  $\epsilon = 0.035$  was used, which was obtained by an NLO fit to ARGUS data [19].



**Figure 2.6** Fragmentation functions  $z = p_T(D^*)/E_T^{\text{jet}}$  ( $D^*$  matched jet) for the ARGUS data in the left plot, and for OPAL, ARGUS and ZEUS data in the right hand plot.



**Figure 2.7** Overview of a leading order lepton-photon interaction.

## 2.5 QCD evolution and event generators

### 2.5.1 Monte Carlo models

The LO+PS MC generators used in this thesis are Herwig 6.301 [20, 21] and Pythia 6.16 [25]. They use on-shell LO matrix elements for charm photoproduction processes, higher order QCD effects are simulated in the leading-logarithmic approximation with the initial-state and final-state radiation obeying Dokshitzer-Gribov-Lipatov-Altarelli-Parisi (DGLAP) evolution equations[22, 23, 24], which describe the way in which the quark and gluon momentum distributions in a hadron evolve with the scale of the interaction. Direct and resolved LO photon processes were generated proportionally to their predicted MC cross sections, using c-quark and b-quark masses of  $m_C = 1.5$  GeV and  $m_b = 4.75$  GeV, respectively. The main parts of the generators are:

**Initial-state radiation** Each of the two incoming partons go through splittings like  $q \rightarrow qg$ , governed by the DGLAP evolution equations .

**Hard scatter** At leading order (LO)  $2 \rightarrow 2$  body scattering the matrix elements are exactly calculable in pQCD. However parton showers have to be added to account for higher order

effects. These parton shower models are tuned in the Monte Carlo to data. Initial- and final-state radiation is set by the  $Q^2$  of the interaction.

The Monte Carlo models described above generally underestimate the cross section by a factor between 1.5 and 2.5, which reflects the NLO contributions that have not been calculated. The massive and massless scheme described in (section 2.4.1) and (section 2.4.2) attempt to calculate the NLO contributions.

### 2.5.2 Hadronisation

Hadronisation is the process in which colourless hadrons are formed starting from coloured partons. This is non-perturbative and not fully understood, therefore phenomenological models are used to simulate this phenomenon. There are two parts to the hadronisation stage, parton shower and fragmentation which are described in (section 2.5.3). Figure 2.7 shows pictorially how the hadronisation develops after the hard scatter.

### 2.5.3 The parton shower and fragmentation

The two MC used in this thesis use different approaches and models for hadronisation of the partons produced in the initial interaction.

### 2.5.4 HERWIG

Herwig considers three types of non-perturbative contributions namely incoming partons as constituents of the incoming particles, outgoing partons turning into hadrons, and spectator partons in the final state. Quarks are combined to their nearest neighbour to form colour singlet clusters, whose mass distribution is peaked at small values and falls rapidly for large masses. The clusters are then fragmented into hadrons in the following ways:

If the cluster is too light to decay into two hadrons, it is taken to represent the lightest single hadron of its flavour, and its mass is determined by the exchange of momentum with a neighbouring cluster.

Clusters which are massive enough to decay into pairs of hadrons are allowed to do so isotropically according to rules which leave an unbiased selection of decay products conserving flavour.



The rest of the particles which have a very large mass decay isotropically into pairs of hadrons then these are fragmented using a fission model, until they are below a certain fission threshold and can then be treated in the ways described above.

### 2.5.5 PYTHIA

Pythia fragmentation is performed by the JETSET program, which implements the Lund string fragmentation model [25]. The model uses colour flux tubes with transverse dimensions of 1 fm, the typical hadronic size which are stretched between  $q$  and  $\bar{q}$  pairs created on a common production vertex. The tube is uniform along its length. As the  $q$  and  $\bar{q}$  move apart the potential energy stored in the string increases, the string is allowed to break and form a new  $q'$  and  $\bar{q}'$  pair. If the invariant mass is large enough further breaking can occur until only on-mass-shell hadrons remain.

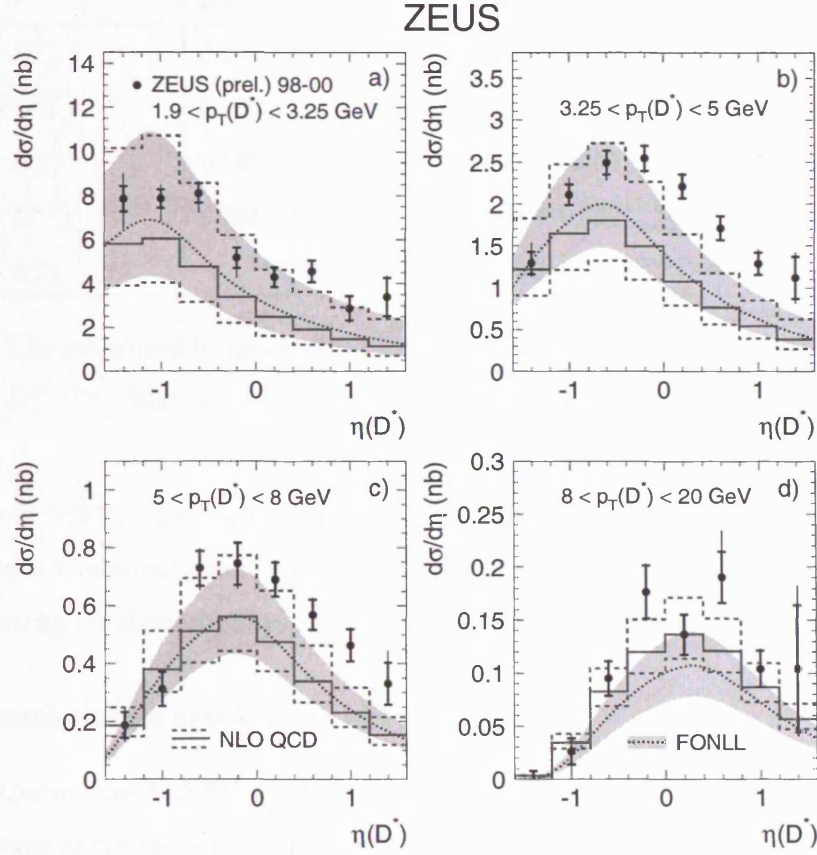
The  $p_T$  of a hadron is made up of the  $p_T$  of the quark and anti-quark forming it, since the string has no  $p_T$ . Quantum mechanical tunneling is used in the generation of quark anti-quark pairs, which suppresses heavy quark production so that charm and heavier quarks are not expected to be produced in soft fragmentation. Heavy quark production only results from perturbative parton showers  $g \rightarrow q\bar{q}$ .

## 2.6 Measurements of heavy quark production in $ep, ee, \gamma\gamma, pp$ collisions

### 2.6.1 Inclusive $D^*$ cross sections in photoproduction

Differential cross sections of a  $D^*$  meson in the photoproduction regime have been measured by ZEUS [26]. The measurement was performed in the kinematic range of  $Q^2 < 1 \text{ GeV}^2$  and  $130 < W < 300 \text{ GeV}$  with the  $D^*$  selected in  $|\eta(D^*)| < 1.6$  and  $p_T(D^*) > 1.9 \text{ GeV}$ , and compared to the ‘massive’ fixed order next-to-leading-log (FONLL) calculation. Measurements were made as a function of the pseudo-rapidity of the  $D^*$ ,  $\eta(D^*)$  in bins of  $p_T(D^*)$  shown in (fig. 2.8), where positive  $\eta$  is the direction of the proton.

Ratios of the total production rates are used to test the isospin invariance of the fragmentation process and to extract the strangeness suppression factor  $\gamma_s$  and the fraction  $P_V$  of D-mesons produced in a vector state. The results are compared with values measured



**Figure 2.8** Differential cross sections of  $D^*$  photoproduction with respect to  $\eta(D^*)$  measured by the ZEUS Collaboration. Measured cross sections (dots) are compared to the NLO calculation (solid histogram) with its uncertainty shown as the dashed histogram, and to the FONLL predictions (dotted curves and shaded bands).

e.g. at  $e^+e^-$  colliders and allow tests of the assumed universality of the charm fragmentation process[27, 28]. Table 2.3 shows the results for the mesons  $D^+$ ,  $D^0$ ,  $D_s^+$ ,  $D^{*+}$  and  $\Lambda_c^+$ . The values at the different colliders are in good agreement, so the assumption that charm fragmentation fractions are universal is confirmed.

### 2.6.2 Charm jet cross sections in photoproduction

Charm jet cross sections were measured previously at ZEUS [29], (fig. 2.9) shows  $d\sigma/d\eta^{\text{jet}}$  cross sections for both  $D^*$  matched jets and other jets. These results are compared with NLO pQCD predictions and show discrepancies between data and theory specially in the forward

	H1	ZEUS(prel.)	$e^+e^-$
$f(c \rightarrow D^+)$	$0.203 \pm 0.026$	$0.249 \pm 0.014^{+0.004}_{-0.008}$	$0.232 \pm 0.018$
$f(c \rightarrow D^0)$	$0.560 \pm 0.046$	$0.557 \pm 0.019^{+0.005}_{-0.013}$	$0.549 \pm 0.026$
$f(c \rightarrow D_s^+)$	$0.151 \pm 0.055$	$0.107 \pm 0.009^{+0.005}_{-0.005}$	$0.101 \pm 0.027$
$f(c \rightarrow D^{*+})$	$0.263 \pm 0.032$	$0.223 \pm 0.009^{+0.003}_{-0.005}$	$0.235 \pm 0.010$
$f(c \rightarrow \Lambda_c^+)$		$0.076 \pm 0.020^{+0.017}_{-0.001}$	$0.076 \pm 0.007$

**Table 2.3** The measured fragmentation fractions from H1 and ZEUS for the mesons  $D^+$ ,  $D^0$ ,  $D_s^+$ ,  $D^{*+}$  and  $\Lambda_c^+$  compared to the world average  $e^+e^-$  results.

region i.e.  $\eta^{\text{jet}} > 1.0$ . The disagreement is more visible for  $D^*$  matched jets then for other jets. This also leads to similar conclusions as in the inclusive  $D^*$  production cross sections, and this thesis follows up on these findings in order to pin down why and where these differences arise.

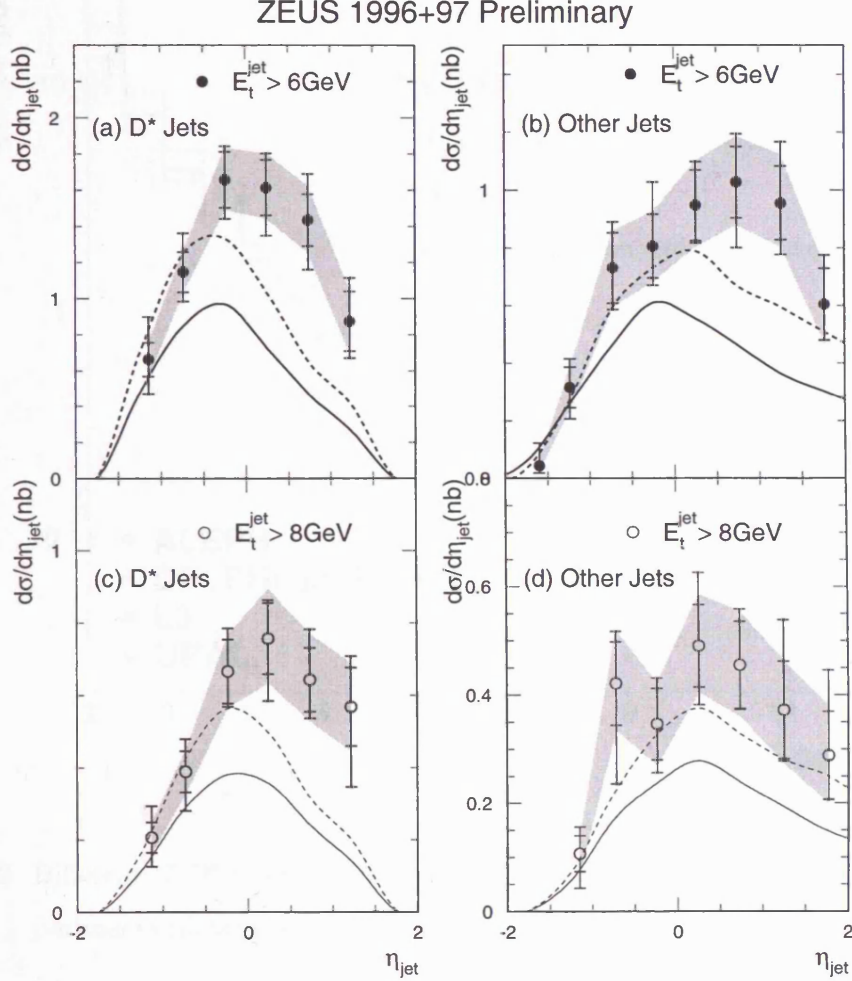
### 2.6.3 D meson cross sections at LEP

The LEP experiments ALEPH, DELPHI, L3 and OPAL measured the cross section of  $d\sigma/dp_T(D^*)$  in  $\gamma\gamma$  collisions and compared their measurements to NLO pQCD ‘massive’ predictions.

All experimental measurements are compatible with one another over the whole  $p_T(D^*)$  range and follow the upper most bound of the NLO pQCD prediction favouring a lower charm mass and change in renormalisation scale.

Figure 2.11 shows the inclusive charm cross sections as a function of centre-of-mass energy for the ALEPH, DELPHI, L3, OPAL, TASSO and JADE experiments, these results are compared to NLO pQCD prediction. These data lie within the theoretical uncertainty and are compatible with one another, with all experimental errors dwarfed by theoretical uncertainties.

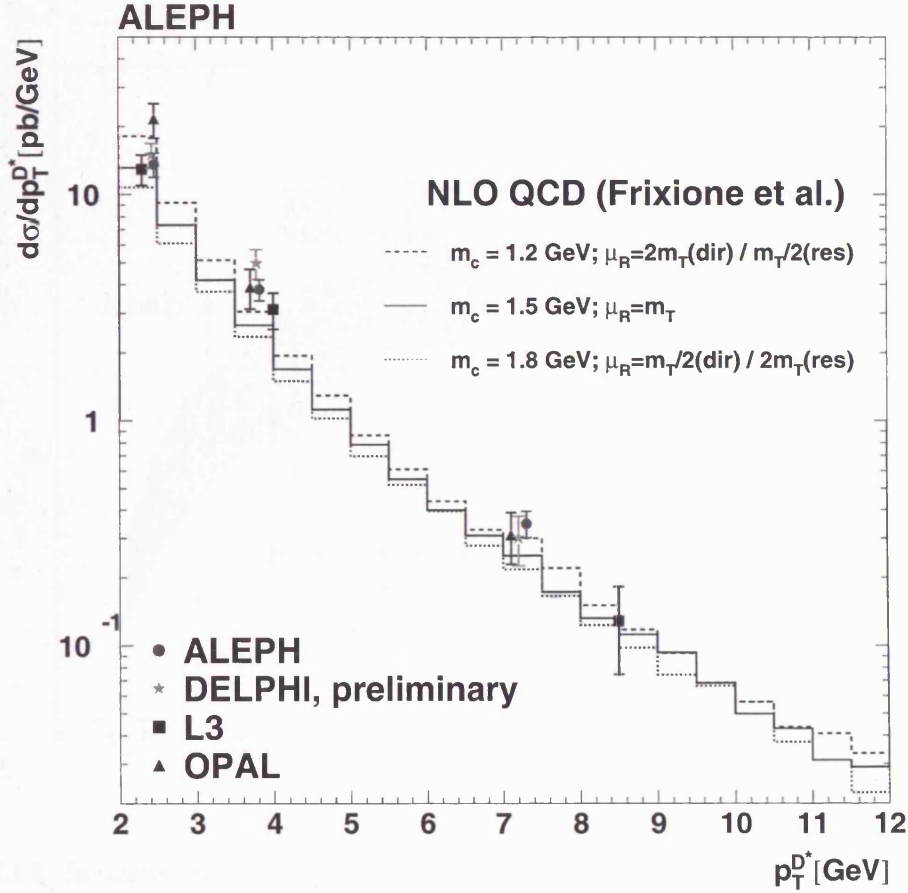
The charm structure function  $F_{2,c}^\gamma(x, Q^2)/\alpha$  of the photon was measured at LEP (fig. 2.12) at a  $Q^2 = 20 \text{ GeV}^2$ . The  $x$  values are calculated for the full  $F_{2,c}^\gamma(x, Q^2)$  and for the point-like component alone. For  $x > 0.1$  the difference is invisible and for  $x < 0.1$  the hadron-like contribution to  $F_{2,c}^\gamma(x, Q^2)/\alpha$  amounts to  $0.154 \pm 0.059 \pm 0.029$ . The NLO prediction is  $0.026^{+0.007}_{-0.005}$  therefore the prediction lies below the data.



**Figure 2.9** Cross sections  $d\sigma/d\eta^{\text{jet}}$  for  $D^*$  matched jets and other jets in  $E_T^{\text{jet}} > 6 \text{ GeV}$  and  $E_T^{\text{jet}} > 8 \text{ GeV}$  ranges. The data (solid dots) is compared to ‘massive’ NLO pQCD predictions (FMNR) (solid and dashed lines). ZEUS 1996-1997 data were used.

#### 2.6.4 D meson cross sections at the Tevatron

Figure 2.13 shows recent data amounting to  $5.8 \pm 0.3 \text{ pb}^{-1}$  from the CDF experiment at the Tevatron [30]. The charm mesons were reconstructed in the following channels,  $D^0 \rightarrow K^-\pi^+$ ,  $D^{*+} \rightarrow D^0\pi^+$  with  $D^0 \rightarrow K^-\pi^+$ ,  $D^+ \rightarrow K^-\pi^+\pi^+$ ,  $D_s^+ \rightarrow \phi\pi^+$  with  $\phi \rightarrow K^+K^-$  and their charge conjugates. All the signals are summed over all  $p_T$  bins, with the number of candidates

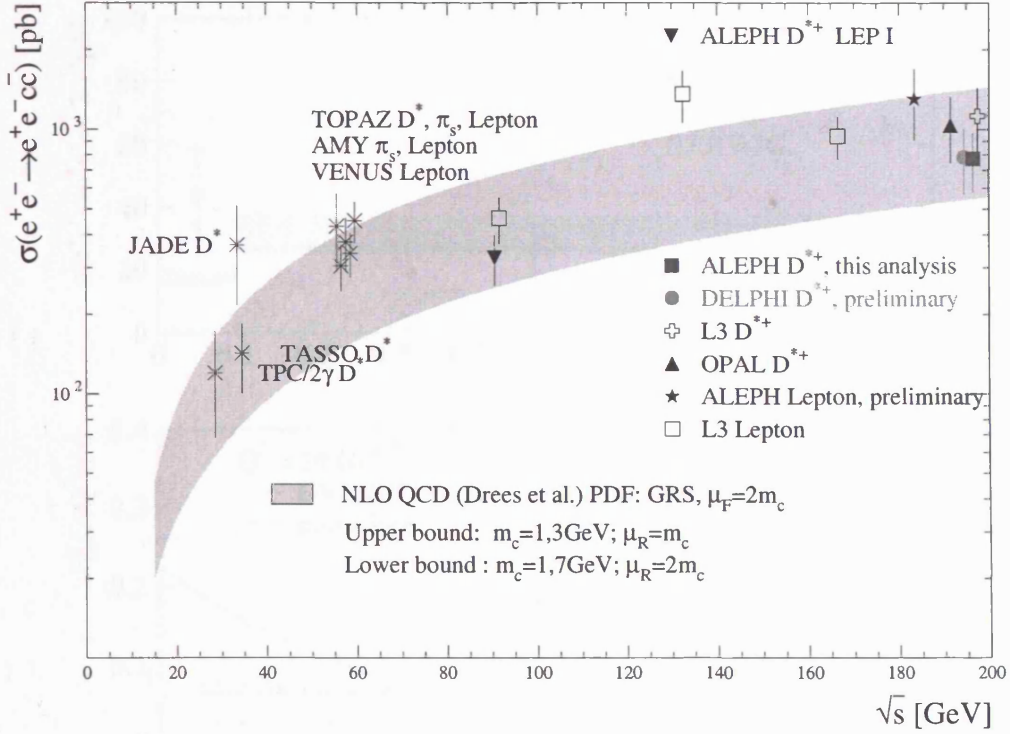


**Figure 2.10** Differential  $D^*$  cross section in  $p_T(D^*)$  for ALEPH, DELPHI, L3 and OPAL experiments (dots) compared to NLO pQCD ‘massive’ predictions.

corresponding to  $36804 \pm 409$  for the  $D^0$ ,  $5515 \pm 85$  for the  $D^{*+}$ ,  $28361 \pm 294$  for the  $D^+$  and  $851 \pm 43$  for the  $D_s^+$ .

The prompt charm ( $p\bar{p}$  interactions) can be separated from  $B$  decay (secondary charm) using the impact parameter of the net momentum vector of the charm candidate to the beamline. Prompt charm mesons point back to the beamline. Differential cross sections (fig. 2.14) measured by CDF are compared to two NLO QCD theoretical predictions in the ‘massive’ and ‘massless’ cases. The uncertainties from the the NLO QCD come from varying independently the renormalization and factorisation scales between 0.5 and 2 times the default value. Contributions to the uncertainty from the value of the strong coupling constant and the fragmentation functions, were small and were not taken into account. The measured differential





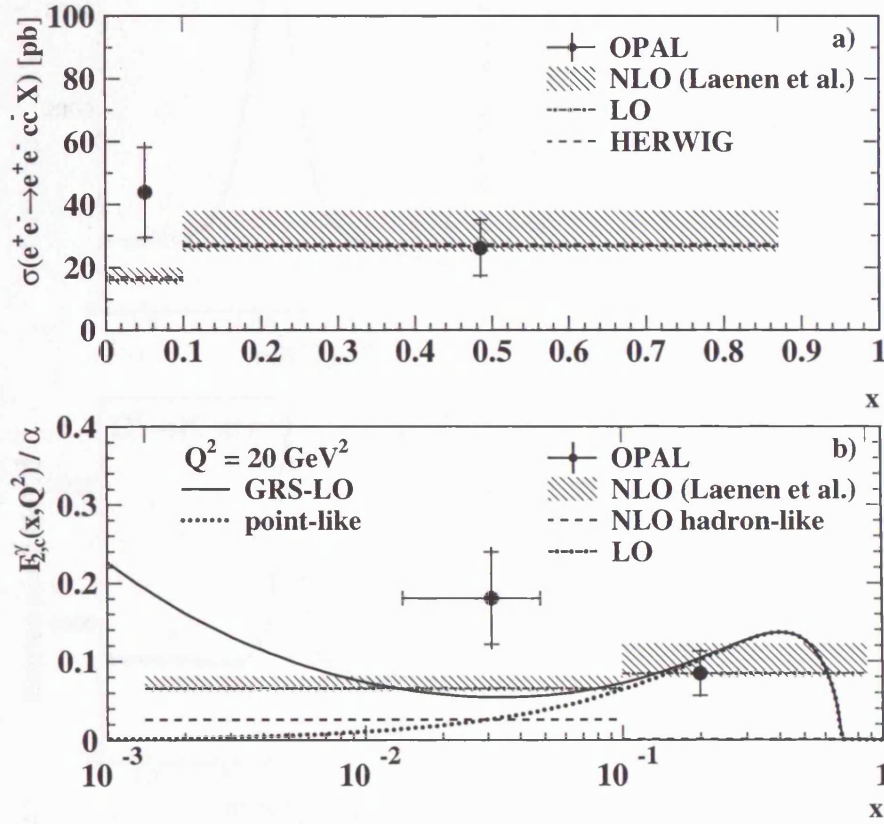
**Figure 2.11** Inclusive charm cross sections as a function of centre-of-mass energy in  $\gamma\gamma$  collisions, for ALEPH, DELPHI, L3, OPAL, TASSO and JADE experiments compared to NLO pQCD predictions.

cross sections are higher than the theoretical predictions by about 100% at low  $p_T$  and 50% at high  $p_T$ , however they are compatible within uncertainties. The same models also underestimate the  $B$  meson production by similar factors.

### 2.6.5 Dijet correlations $ep, ee, \gamma\gamma, pp$ collisions

The  $x_\gamma^{\text{obs}}$  variable, is defined in terms of the two highest transverse energy jets in the event. This is an estimator for the fraction of the photon's momentum participating in the hard scatter.

$$x_\gamma^{\text{obs}} = \frac{E_T^{\text{jet1}} e^{-\eta^{\text{jet1}}} + E_T^{\text{jet2}} e^{-\eta^{\text{jet2}}}}{2yE_e}. \quad (2.16)$$



**Figure 2.12** OPAL results for a) the cross-section  $\sigma(e^+e^- \rightarrow e^+e^-c\bar{c}X)$ , with  $5 < Q^2 < 100 \text{ GeV}^2$  and b) for the charm structure function of the photon divided by the fine structure constant,  $F_{2,c}^\gamma(x, Q^2)/\alpha$ , at  $Q^2 = 20 \text{ GeV}^2$ . The data points are the results obtained with the HERWIG Monte Carlo model. The outer error bar is the total error and the inner error bar the statistical error. The data points in b) are placed at those  $x$  values that correspond to the average predicted  $F_{2,c}$  within a bin. The data are compared to the calculation performed in LO and NLO. The band for the NLO calculation indicates the theoretical error from uncertainties in the charm quark mass and the scale uncertainties in renormalisation and factorisation. In a) the cross-section prediction of the HERWIG Monte Carlo model is also given. b) also shows the prediction of the GRS-LO parametrisation for the structure function at  $Q^2 = 20 \text{ GeV}^2$  and its point-like component separately.

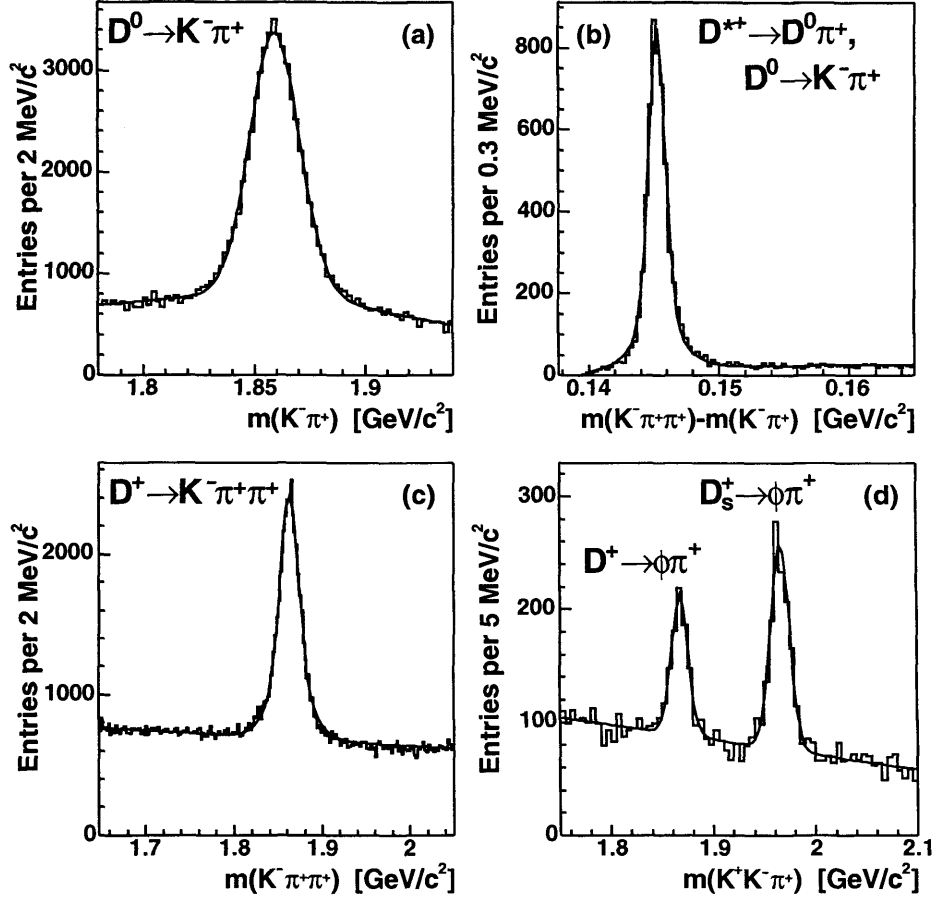
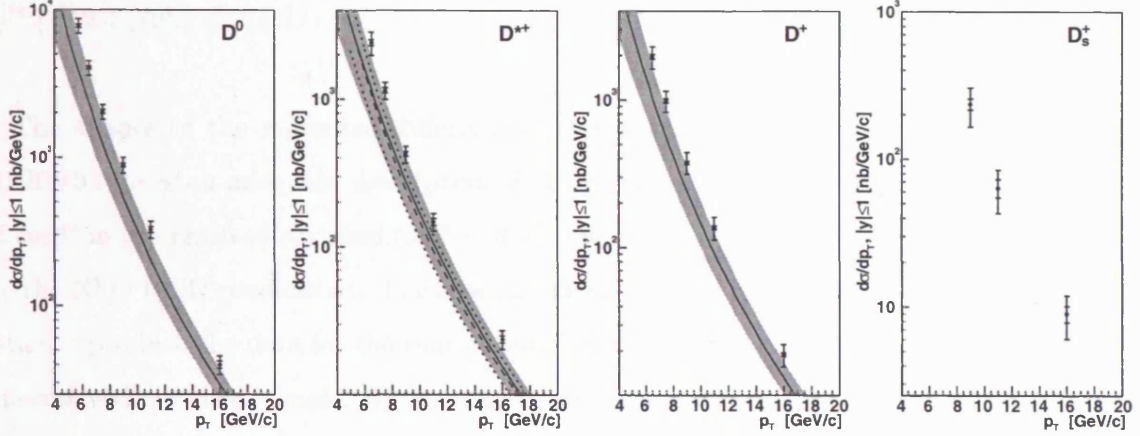


Figure 2.13 D meson signals in the CDF data.

An experimental separation of direct and resolved processes can be done using a cut on  $x_\gamma^{\text{obs}}$ : direct(resolved) which are defined as  $x_\gamma^{\text{obs}} > 0.75$  ( $x_\gamma^{\text{obs}} < 0.75$ ).

Figure 2.15 shows the differential cross section  $d\sigma/dx_\gamma^{\text{obs}}$  calculated in the photoproduction regime for  $Q^2 < 1 \text{ GeV}^2$ ,  $130 < W < 280 \text{ GeV}$ , requiring two jets with  $E_T^{\text{jet1}} > 7 \text{ GeV}$ ,  $E_T^{\text{jet2}} > 6 \text{ GeV}$ , and at least one  $D^*$  with  $p_T^{D^*} > 3 \text{ GeV}$  in the angular range  $-1.5 < \eta^{D^*} < 1.5$ . These measurements are compared to LO+PS HERWIG MC in (fig. 2.15) (a) which is separated into its direct and resolved components, with the data being reproduced reasonably well in shape by HERWIG. Figure 2.15 (b) shows the comparison of this measurement to NLO QCD predictions. The NLO cannot describe the data in the low  $x_\gamma^{\text{obs}}$  region even with extreme choices of parameters which are shown in the graph. There are no hadronisation corrections





**Figure 2.14** The differential cross section measurements for  $|y| \leq 1$ . The inner bars represent the statistical uncertainties; the outer bars are the quadratic sums of the statistical and systematic uncertainties. The solid curves are the theoretical predictions from Cacciari and Nason [31], with the uncertainties indicated by the shaded bands. The dashed curve shown with the  $D^{*+}$  cross section is the theoretical prediction from Kniehl [32]; the dotted lines indicate the uncertainty. No prediction is available yet for  $D_s^+$  production.

applied to the NLO QCD predictions or beauty contributions added which are present in the data, which could explain the difference. In this thesis these points are addressed.

The cross section ratio  $R = \sigma(x_\gamma^{\text{obs}} < 0.75) / \sigma(x_\gamma^{\text{obs}} > 0.75)$  as a function of  $Q^2$  in (fig. 2.16) for the case of dijet events containing a  $D^{\pm}$  in the kinematic range  $Q^2 < 5 \cdot 10^3 \text{ GeV}^2$  [34, 33]. The result is extrapolated to the full kinematic region using the HERWIG MC. The result is shown requiring charm and the “no charm required” case. These results show that the ratio of the low  $x_\gamma^{\text{obs}}$  cross section to the high  $x_\gamma^{\text{obs}}$  contribution falls off much slower in the presence of charm than it does when charm is not required. This shows for the first time that the observed suppression of the low  $x_\gamma^{\text{obs}}$  cross section due to non-zero photon virtuality and due to charm are not independent.

Differential cross sections (fig. 2.17) as a function of  $\cos\theta^*$  (eq. 5.1), the dijet centre of mass scattering angle,  $\theta^*$ , for charm dijet photoproduction events have been measured in the kinematic range  $130 < W < 280 \text{ GeV}$ ,  $Q^2 < 1 \text{ GeV}^2$ ,  $p_T^{D^*} > 3 \text{ GeV}$ ,  $|\eta^{D^*}| < 1.5$ ,  $E_T^{\text{jet}} > 5 \text{ GeV}$  and

$$|\eta^{jet}| < 2.4 \text{ [70]}.$$

The shapes of the measured differential cross sections are well reproduced by PYTHIA, HERWIG gives an adequate description of these shapes but does not describe the low values of  $\cos\theta^*$  in the resolved enriched ( $x_\gamma^{\text{obs}} < 0.75$ ) region. The approximate shapes are reproduced by the NLO QCD predictions. The absolute cross sections predicted by the NLO QCD calculation reproduce the data for the sample enriched in direct photons but are below the data for the resolved-enriched sample. By associating the  $D^*$  meson with one of the jets allows the sign of  $\cos\theta^*$  to be defined. In all cases, the  $\cos\theta^*$  distributions show a mild rise towards  $|\cos\theta^*| = 1$ , as expected from quark exchange, except for the resolved-enriched sample in which the cross section rises steeply in the photon direction ( $\cos\theta^* = -1$ ), as expected from gluon exchange. This observation then indicates that most of the resolved photon contribution in LO QCD charm production is due to charm originating from the photon, rather than to the competing resolved photon process  $gg \rightarrow c\bar{c}$ . This leads to the result that charm originating from the photon is the dominant component in the resolved photoproduction of dijet events with charm.

Figure 2.18 shows the cross sections for the production of dijets in association with a  $D^{*\pm}$  meson versus the  $D^{*\pm}$  meson production cross section [27] measured at H1. The MC's RAPGAP [14], AROMA [15], CASCADE [16] all reproduce the inclusive cross section but do not well describe the cross section of dijets in association with a  $D^{*\pm}$  meson.

DØ have measured the dijet azimuthal decorrelation (fig. 2.19) and (fig. 2.20) [17] in different ranges of leading jet  $p_T$  and observe an increased decorrelation towards smaller  $p_T$ . NLO pQCD describes the data except for values of  $\Delta\phi^{jj}$  close to  $\pi$  where the calculation is not predictive.

This shows particular sensitivity to higher orders and within ZEUS this measurement can be performed across the whole  $\Delta\phi^{jj}$  range. In this thesis this angular distribution is measured and compared to ‘massive’ NLO QCD predictions with charm dijets.

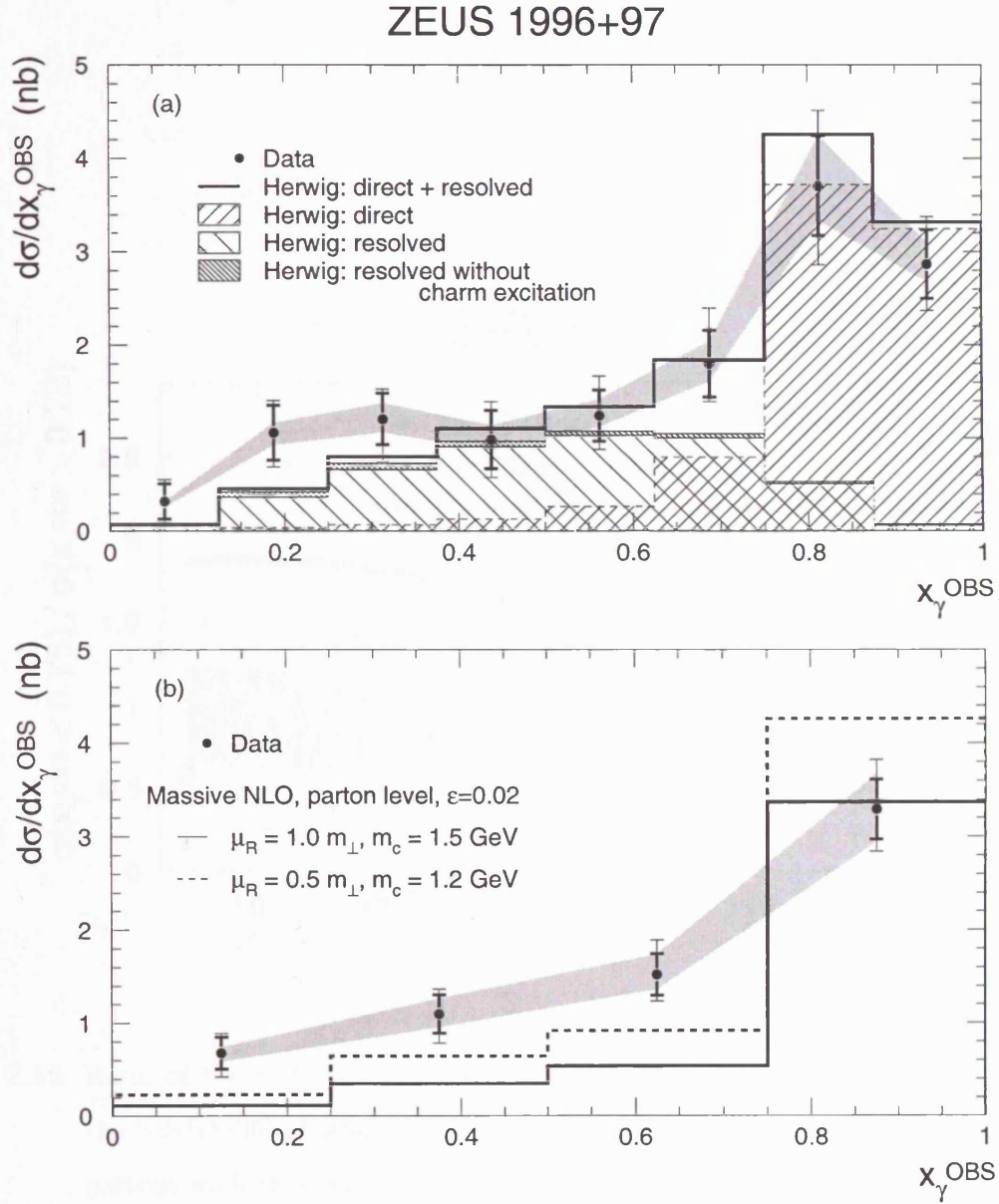
## 2.7 Summary of charm production

Charm fragmentation ratios and fractions generally support the hypothesis that fragmentation proceeds independently of the hard sub-process in  $ep$  and  $e^+e^-$  collisions. This test of charm universality is confirmed by the measured D meson ground states at H1, ZEUS and LEP.

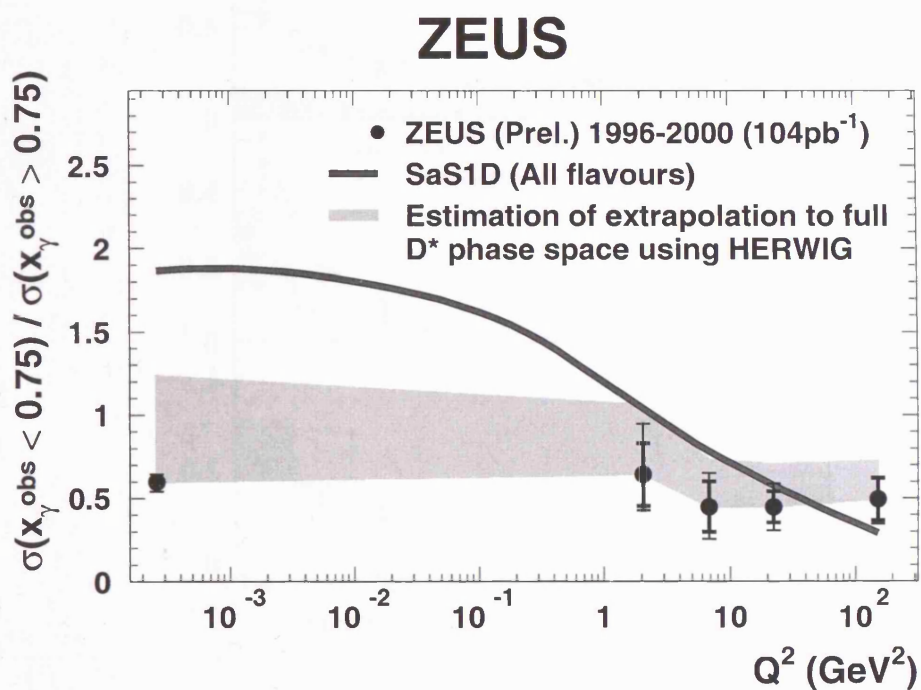
Many aspects of inclusive charm and dijets with charm have been measured and compared to NLO QCD calculations. There is a trend in the ZEUS data that the data lie on the upper most bound of the theoretical uncertainties, also that there is sensitivity to higher orders in dijet angular variables. Divergences between data and theory are still visible which could be due to contributions from B hadrons, hadronisation effects and due to additional higher orders missing in calculations having big effects in some kinematic regions. The Tevatron also observes such divergences and has large uncertainties in its theoretical predictions. Charm production still needs to be understood in order to have confidence in understanding all the underlying subprocesses contributing to charm and the relevant scales applicable to NLO QCD calculations.

HERA has an advantage over higher energy experiments as jets can be selected at relatively low energies i.e.  $E_T^{\text{jet}} > 6$  GeV, with the  $p_T^{D^*} > 3$  GeV allowing the boundary of the two calculation scheme ‘massive’ and ‘massless’ to be compared. This ‘massive’ scheme is expected to work well in regions where the transverse momentum of the outgoing  $c$ -quark is of similar magnitude to the quark mass. At higher transverse momenta or high photon virtualities the ‘massless’ scheme[10] should be applicable, in which charm and beauty are regarded as active flavours (massless partons) in the proton and in the photon and are fragmented only after the hard process into massive quarks.

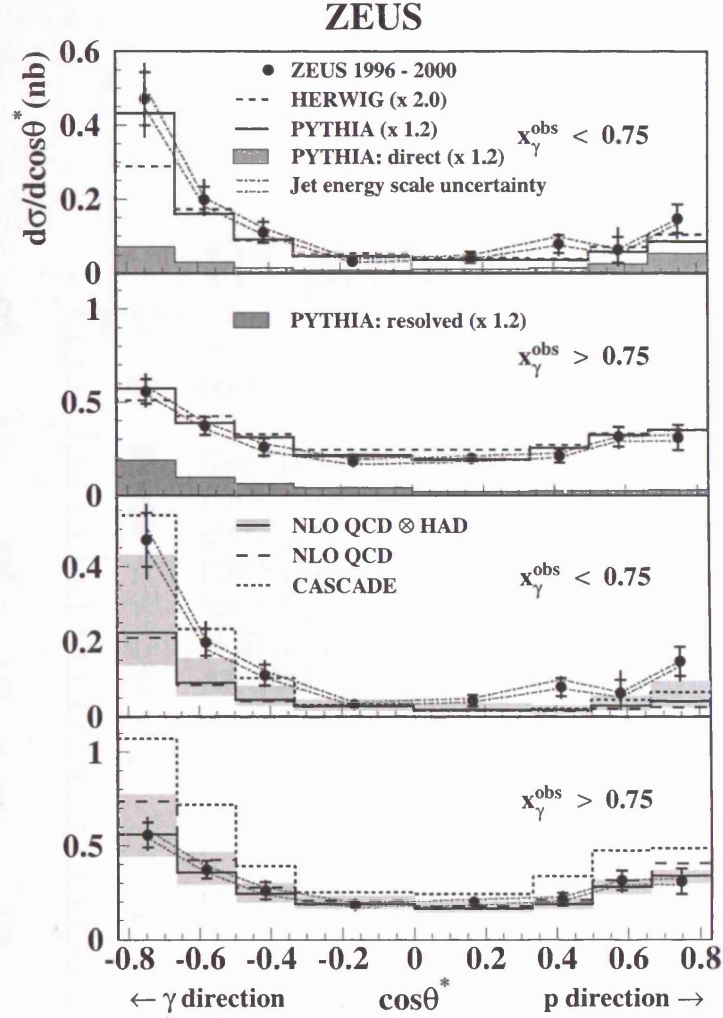
These remaining questions will be addressed within this thesis concentrating on charm jet and dijet production.



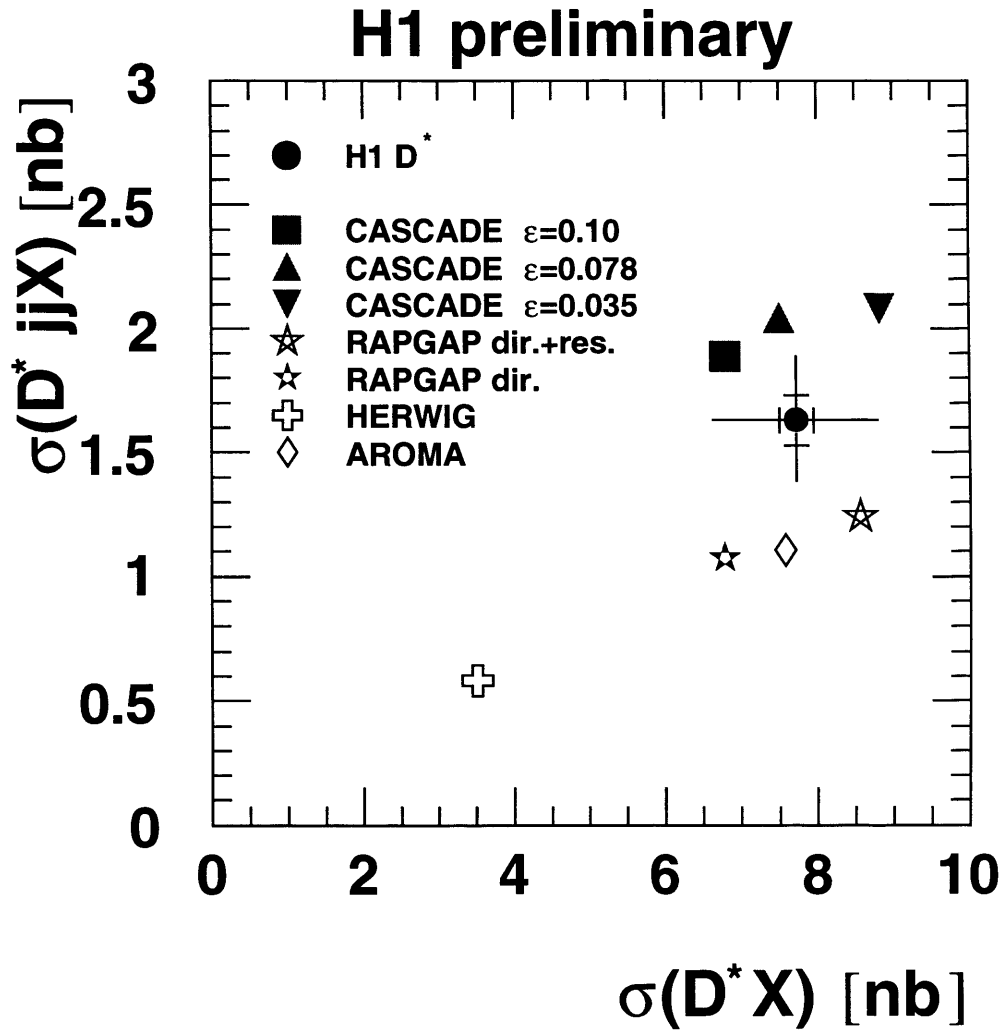
**Figure 2.15** The differential cross section  $d\sigma/dx_{\gamma}^{\text{obs}}$  for dijet plus  $D^*$  meson events. The shaded band represents the uncertainty from the calorimeter energy scale. In (a) the data are compared to the expectations of the HERWIG Monte Carlo simulations, normalised to the data. In (b) the data are compared to ‘massive’ NLO QCD predictions [35].



**Figure 2.16** Ratio of low to high  $x_{\gamma}^{\text{obs}}$  for events with a  $D^*$  compared to the predictions of the SaS1D [36] photon structure function (where the photon acts as a source of partons such that partons participate in the hard scatter) for the ratio without a  $D^*$  tag.

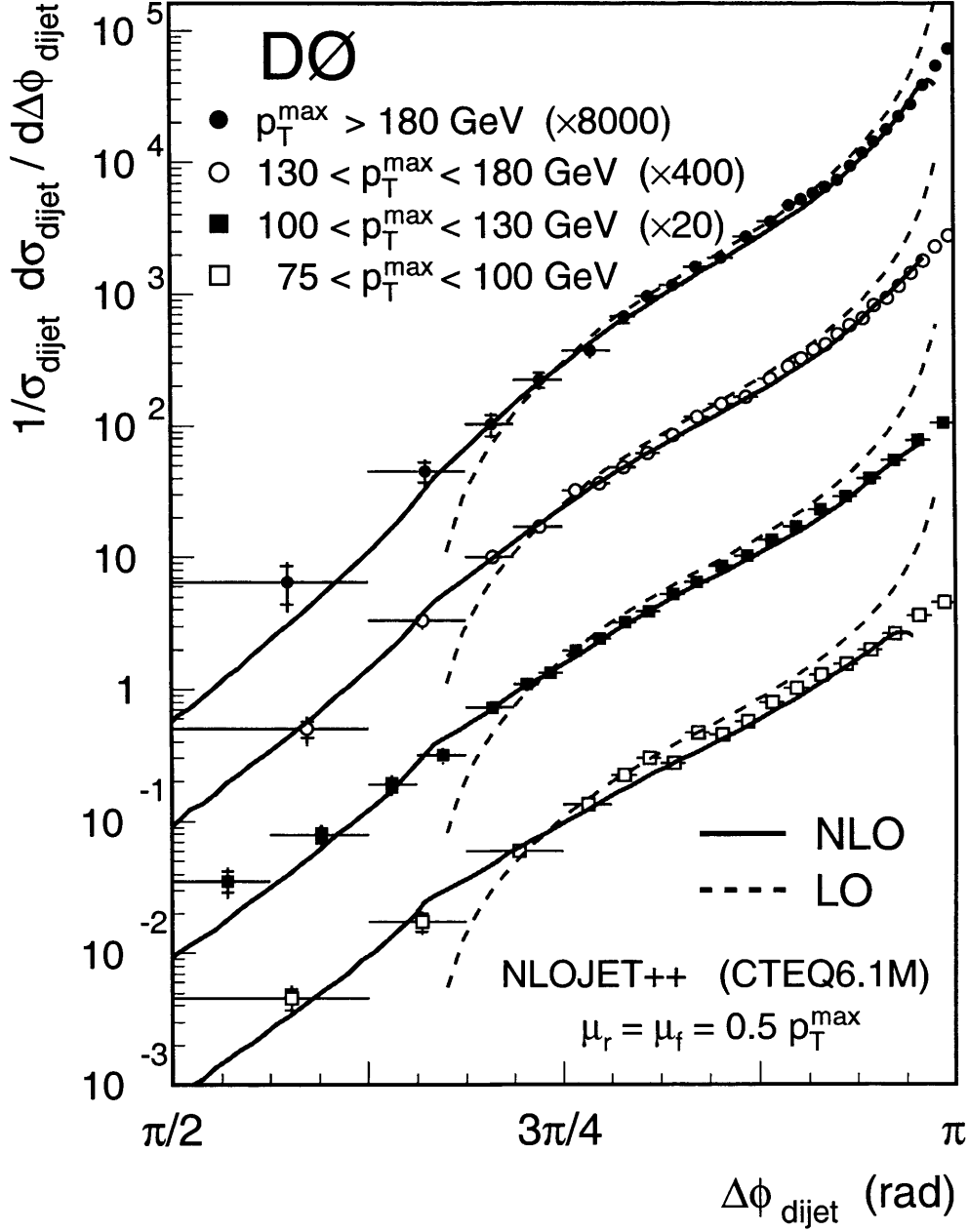


**Figure 2.17** Differential cross sections  $d\sigma/d\cos\theta^*$  (dots) compared with: a-b) PYTHIA and HERWIG MC simulations (histograms); c-d) CASCADE (short-dashed lines) and NLO FO predictions after hadronisation correction (full lines) and at parton level (long-dashed lines). Results are given separately in a,c) for samples enriched in resolved photon events and in b,d) for samples enriched in direct photon events. The inner error bars show the statistical uncertainty, while the outer ones show the systematic uncertainties added in quadrature. The jet-energy-scale uncertainty is given by the two dashed-dotted lines. In a-b), each MC distribution is normalised to the data, as indicated in the brackets. Also shown as shaded areas in a) and b) are the contribution of the resolved photon process to the direct-enriched sample, respectively. The uncertainties of the NLO prediction after the hadronisation correction are shown as the shaded areas in c) and d).



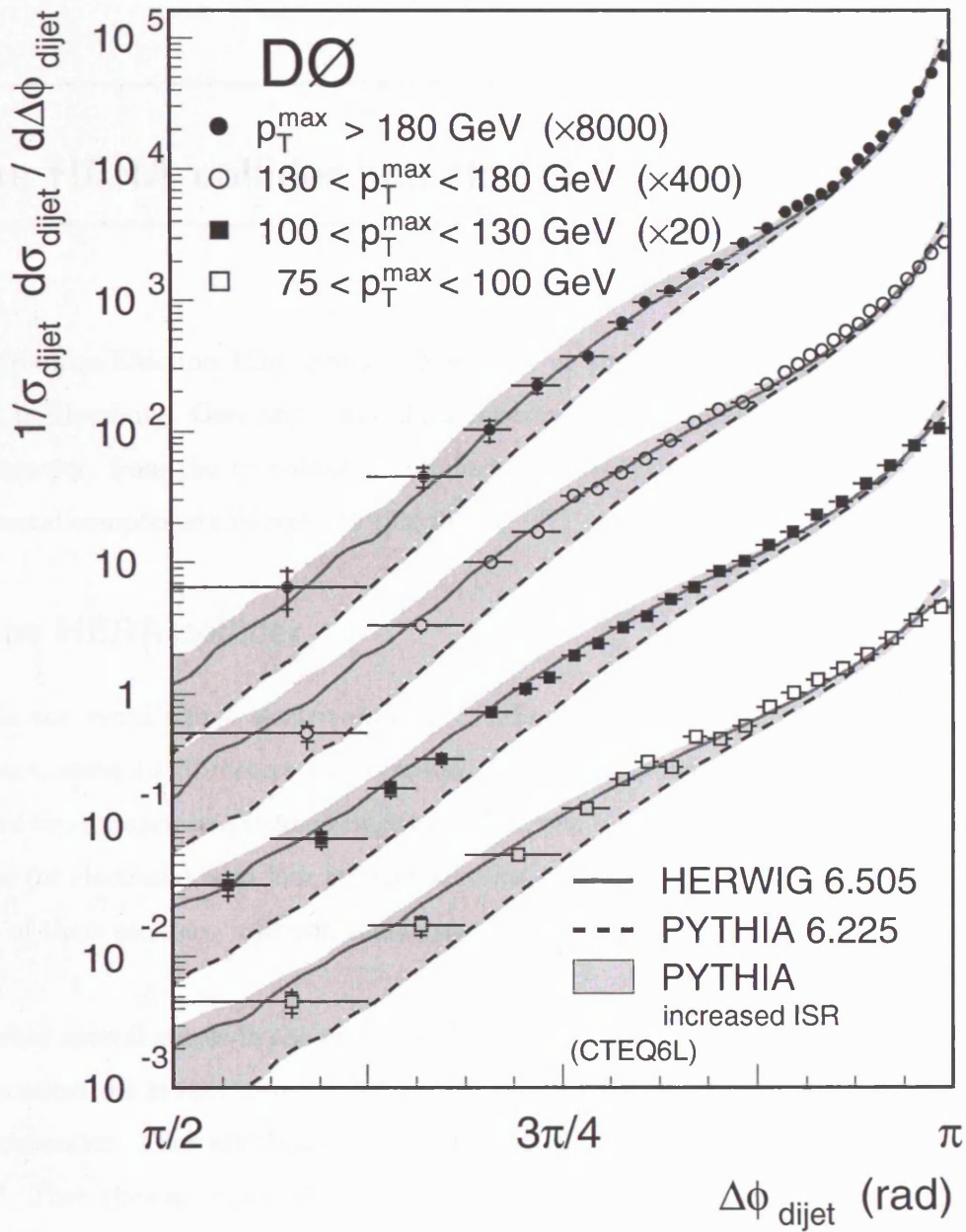
**Figure 2.18** The cross section for the production of dijets in association with a  $D^{*\pm}$  meson versus the  $D^{*\pm}$  meson production cross section measured by H1. The predictions of the RAPGAP, AROMA, and CASCADE are shown.





**Figure 2.19** DØ  $\Delta\phi^{jj}$  distributions in four regions based on the jet with the largest  $p_T$  in an event ( $p_T^{\max}$ ). Data and predictions with  $p_T^{\max} > 100$  GeV are scaled by successive factors of 20 for purposes of presentation. The solid (dashed) lines show the NLO (LO) pQCD predictions.





**Figure 2.20** DØ  $\Delta\phi^{jj}$  distributions in different regions based on the jet with the largest  $p_T$  in an event ( $p_T^{max}$ ). Results from HERWIG and PYTHIA are overlaid on the data. Data and predictions with  $p_T^{max} > 100$  GeV are scaled by successive factors of 20 for purposes of presentation.

---

## 3 The HERA collider and the ZEUS detector

---

HERA (Hadron-Elektron Ring Anlage) is located at the Deutsches Elektronen Synchrotron (DESY) in Hamburg, Germany. The data reported in this thesis were collected with the ZEUS detector, from the  $ep$  collisions supplied by HERA ring. This chapter highlights the experimental components relevant to this thesis.

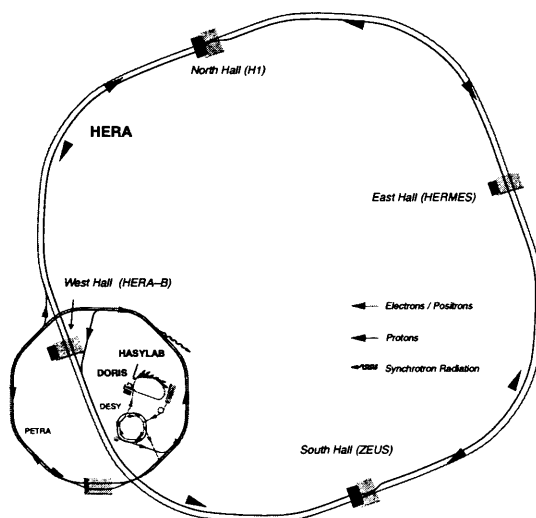
### 3.1 The HERA collider

HERA is the world's first electron-proton colliding beam accelerator. It is 6.3 km in circumference, some 10-20 meters underground. Regular data-taking commenced in May 1992. There are two independent storage rings in HERA, one for protons (or deuterons), and one for positrons (or electrons), and four straight sections each 360 m long. Interaction regions occur in three of these sections, injection taking place in the fourth.

There are several stages in the injection of electrons and protons. The layout of HERA and its pre-accelerators is shown in (fig. 3.1). Electrons are first accelerated up to 200 MeV in the linear accelerator. They are then transferred to the DESY II synchrotron and accelerated up to 7.5 GeV. Then they are injected into the PETRA ring where they are ramped up to 14 GeV ready for injection into HERA. Once in HERA the electrons are accelerated to 27.5 GeV.

$H^-$  ions are accelerated to 50 MeV in the proton LINAC. They are transferred to DESY III and accelerated to 7.5 GeV, after which the electrons are stripped off. The protons are then accelerated up to 40 GeV in PETRA II at which point they are ready for injection into HERA, and then accelerated up to 920 GeV.

### 3.1 The HERA collider



**Figure 3.1** Layout of HERA and pre-accelerators.

Superconducting dipole and quadrupole magnets guide the protons round the ring, and they are accelerated up to 920 GeV using conventional (non-superconducting) radio frequency cavities.

The electron ring uses warm (non-superconducting) magnets and superconducting radio frequency cavities to accelerate the electrons up to 27.5 GeV.

When the protons and electrons traverse the interaction region they are put into the same orbit in order to collide at zero crossing angle. The guiding magnets deflect the protons until they run in the same vacuum pipe as the electrons, and are brought back into the proton ring after passing the interaction region.

The electrons and protons travel in ‘bunches’ in each beam. Each ‘bunch’ has a separation of 29 m and HERA has capacity for 220 bunches. The time between bunch crossings is 96 ns. Table 10.1 has the design parameters for the 1998-2000 data taking period.

### 3.2 The ZEUS detector

	electron ring	proton ring
circumference	6336 m	
nominal energy	30 GeV	920 GeV
c.m. energy	314 GeV	
circulating current	60 mA	160 mA
number of particles/beam	$0.8 \times 10^{13}$	$2.1 \times 10^{13}$
number of bunch packets	220	220
number of bunches	210	210
current/bunch	0.3 mA	0.8 mA
time between beam crossings	96 ns	
beam size at interaction point ( $\sigma_x$ )	0.286 mm	0.28 mm
beam size at interaction point ( $\sigma_y$ )	0.060 mm	0.058 mm
beam size at interaction point ( $\sigma_z$ )	0.85 cm	19 cm
luminosity	$1.5 \times 10^{31} \text{ cm}^{-2}\text{s}^{-1}$	
specific luminosity	$3.3 \times 10^{29} \text{ cm}^{-2}\text{s}^{-1}\text{mA}^{-2}$	
polarization time at $E_e = 30 \text{ GeV}$	25 min	

**Table 3.1** HERA's design parameters for the 1998-2000 data taking period.

## 3.2 The ZEUS detector

The ZEUS detector [37] is a multipurpose particle detector to measure final state particles in  $ep$  collisions. It covers nearly all of the possible  $4\pi$  solid angle around the interaction point. Figure 3.2 and (fig. 3.3) show different views of the ZEUS detector.

The main components from the inside of the detector out are the Central Tracking Detector (CTD) [39, 41], the Uranium Calorimeter (UCAL) and then the MUON chambers. Between the CTD and the UCAL there is a solenoid which provides a 1.43 T magnetic field, and the iron yoke outside the UCAL is used as the return path of the magnetic field. In order to get rid of background from p-gas, e-gas and secondary collisions there are several detectors to veto such events. The Veto Wall (VETO) and the C5 counter (C5) (fig. 10.3 shows the location of

### 3.2 The ZEUS detector

the C5 counter) are two of these detectors which are used to reject this type of background. The Luminosity monitor (LUMI) is located 104 m away from the detector.

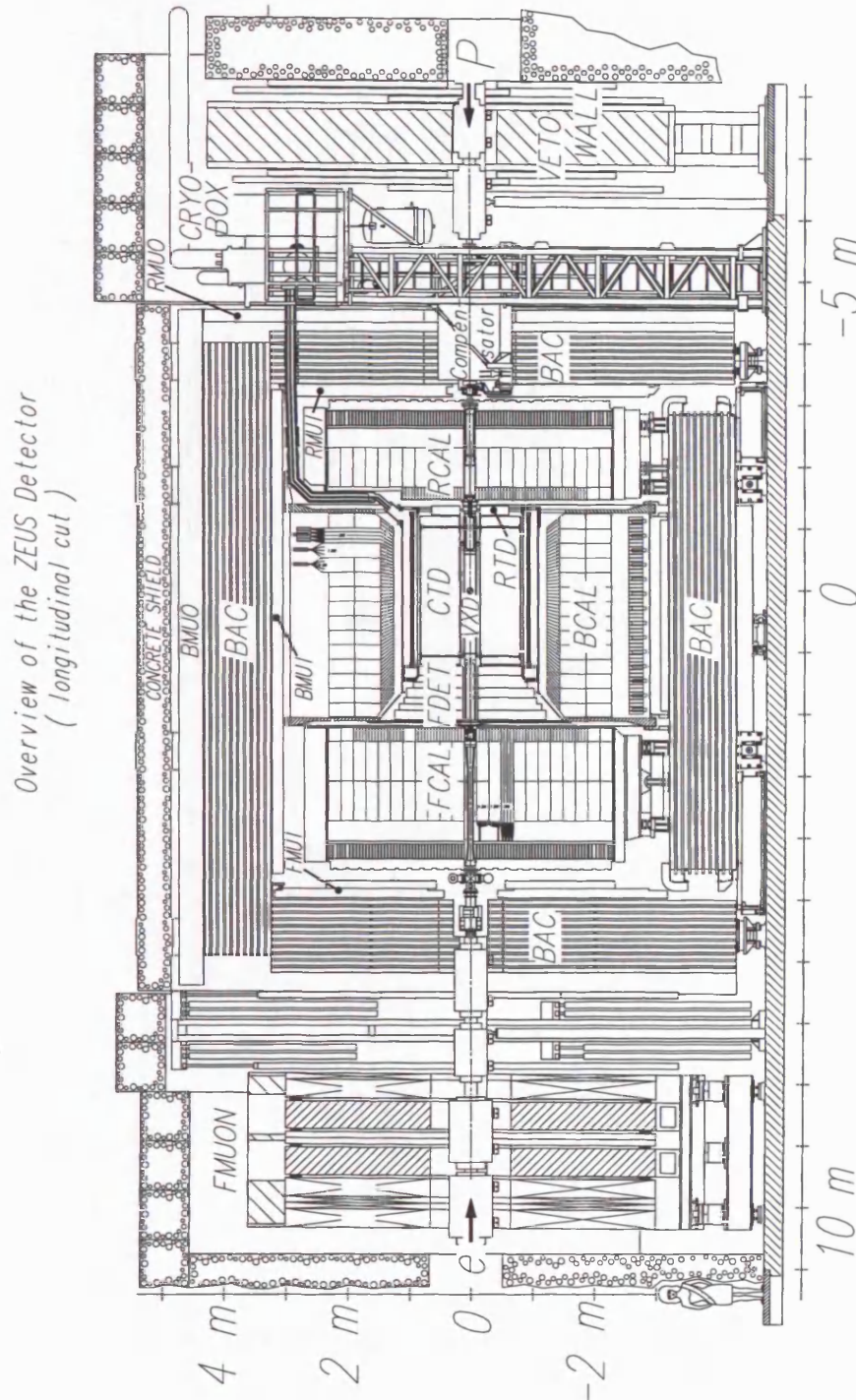


Figure 3.2  $x - y$  view of the ZEUS detector



### 3.2 The ZEUS detector

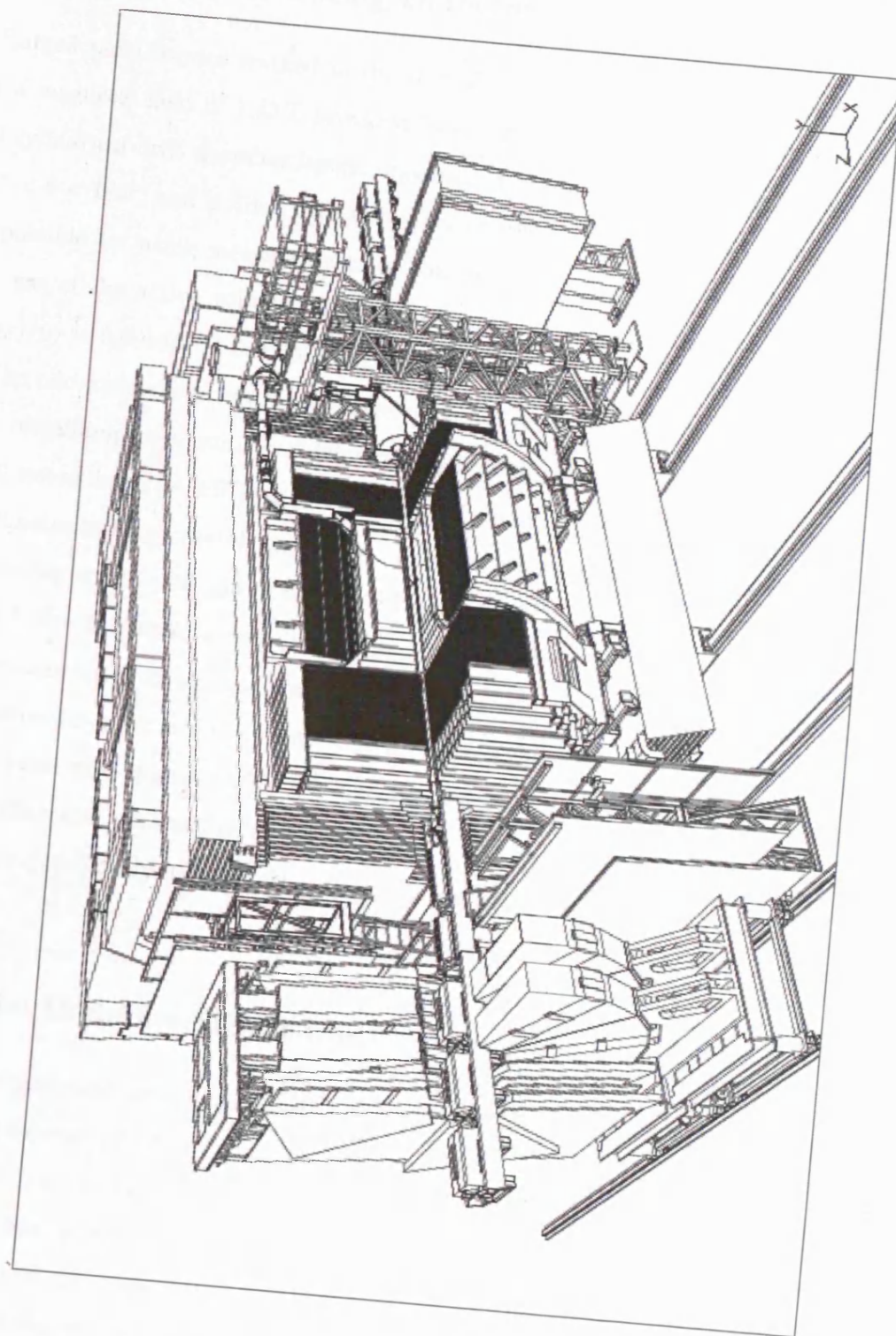


Figure 3.3 The ZEUS detector

### 3.3 The Central Tracking Detector

Charged particles are tracked in the central tracking detector (CTD) [39, 41] which operates in a magnetic field of 1.43 T provided by a thin superconducting coil. The CTD consists of 72 cylindrical drift chamber layers, organized in 9 superlayers covering the polar-angle region  $15^\circ < \theta < 164^\circ$ , and is filled with a mixture of argon, CO<sub>2</sub>, and ethane. Particle identification is possible by using measurements of the mean energy loss  $dE/dx$  of charged particles in the gas of the active volume. The transverse-momentum resolution for full-length tracks is  $\sigma(p_T)/p_T = 0.0058p_T \oplus 0.0065 \oplus 0.0014/p_T$  ( $p_T$  in GeV).

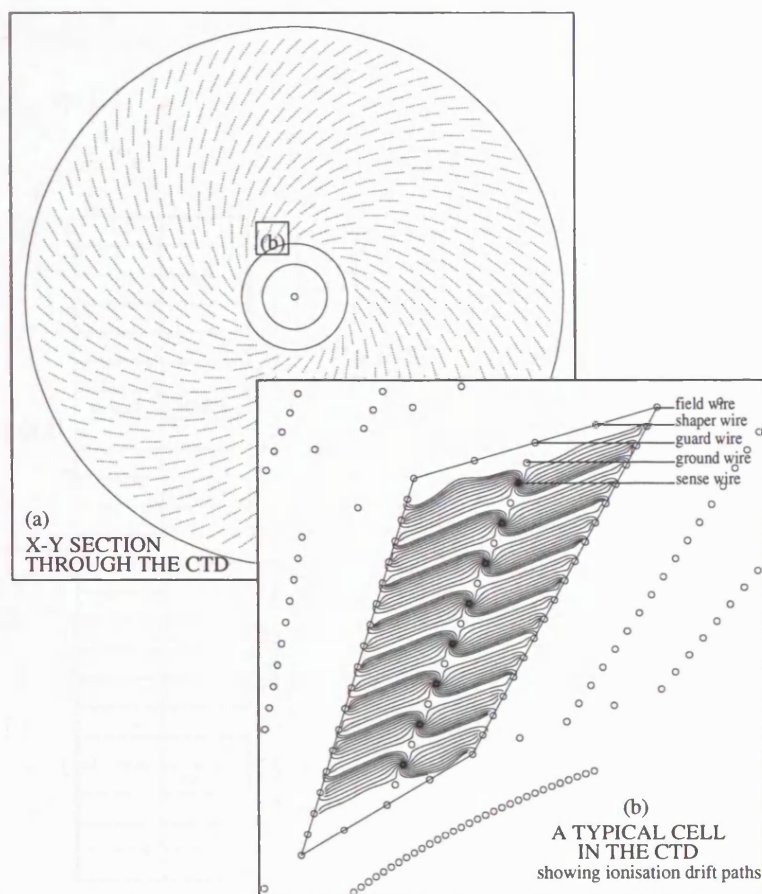
The odd-numbered (axial) superlayers contain drift wires which run parallel to the  $z$ -axis. The remaining even numbered (stereo) superlayers contain wires which are orientated at a small stereo angle ( $\sim \pm 5^\circ$ ) with respect to the  $z$ -axis. This arrangement allows both  $r\phi$  and  $z$  coordinates to be accurately measured. The normal resolution for a track which has traversed all superlayers is  $\sim 180 \mu\text{m}$  in  $r\phi$  and  $\sim 2 \text{ mm}$  in  $z$ . The measured event vertex is accurate to about 1 mm in  $xy$  and 4 mm in  $z$ .

The inner three axial superlayers of the CTD are instrumented with a  $z$ -by-timing system. This estimates the  $z$ -position of a hit by measuring the difference in arrival time of the pulses on the same wire at each end of the detector. This has a resolution of  $\sim 4 \text{ cm}$  which is much cruder than that obtained using the full axial and stereo wire information. It is relatively fast and is predominantly used for triggering purposes and seed-finding.

### 3.4 The Uranium–Scintillator Calorimeter

The high-resolution uranium–scintillator calorimeter (CAL) [42, 43, 44, 45] consists of three parts: the forward (FCAL), the barrel (BCAL) and the rear (RCAL) calorimeters. Each part is subdivided transversely into towers, and longitudinally into an electromagnetic section (EMC) and either one (in RCAL) or two (in BCAL and FCAL) hadronic sections (HAC). The smallest subdivision of the calorimeter is called a cell. The CAL energy resolutions, as measured under test-beam conditions, are  $\sigma(E)/E = 0.18/\sqrt{E}$  for electrons and  $\sigma(E)/E = 0.35/\sqrt{E}$  for hadrons ( $E$  in GeV).

Figure 3.5 shows the ZEUS calorimeter [46, 47, 38]. Holes of 20x20cm in the forward region



**Figure 3.4** *x-y* view through the CTD and typical cell layout.

and 20x8cm in the rear region accommodate the HERA beam pipe. The layout of a BCAL tower is shown in (fig. 3.6). The front surface dimensions are 20x20cm. In the FCAL and RCAL the towers are rectangular, while in the BCAL towers are wedge shaped and projective in  $\phi$ . The HAC section consists of one cell, and an EMC section consists of four cells with dimensions 5x20cm in FCAL/BCAL and two cells with dimensions 10x20cm in the RCAL. Each cell consists of alternating plates of absorber 3.3 mm thick depleted uranium (absorber) and 2.6 mm thick plastic scintillator (active material). As the particles shower the light generated in this active material is collected by light guides and wavelength shifters on both the left and right sides of the towers, which is then fed into photo-multiplier tubes located behind these modules. Position information is obtained from the imbalance between these two signals. The EMC sections have a depth of 25 radiation lengths and one interaction length. For the combined HAC sections the depths are of 6, 4 and 3 interaction lengths in FCAL, BCAL, and RCAL respectively.



### 3.5 The ZEUS Calorimeter

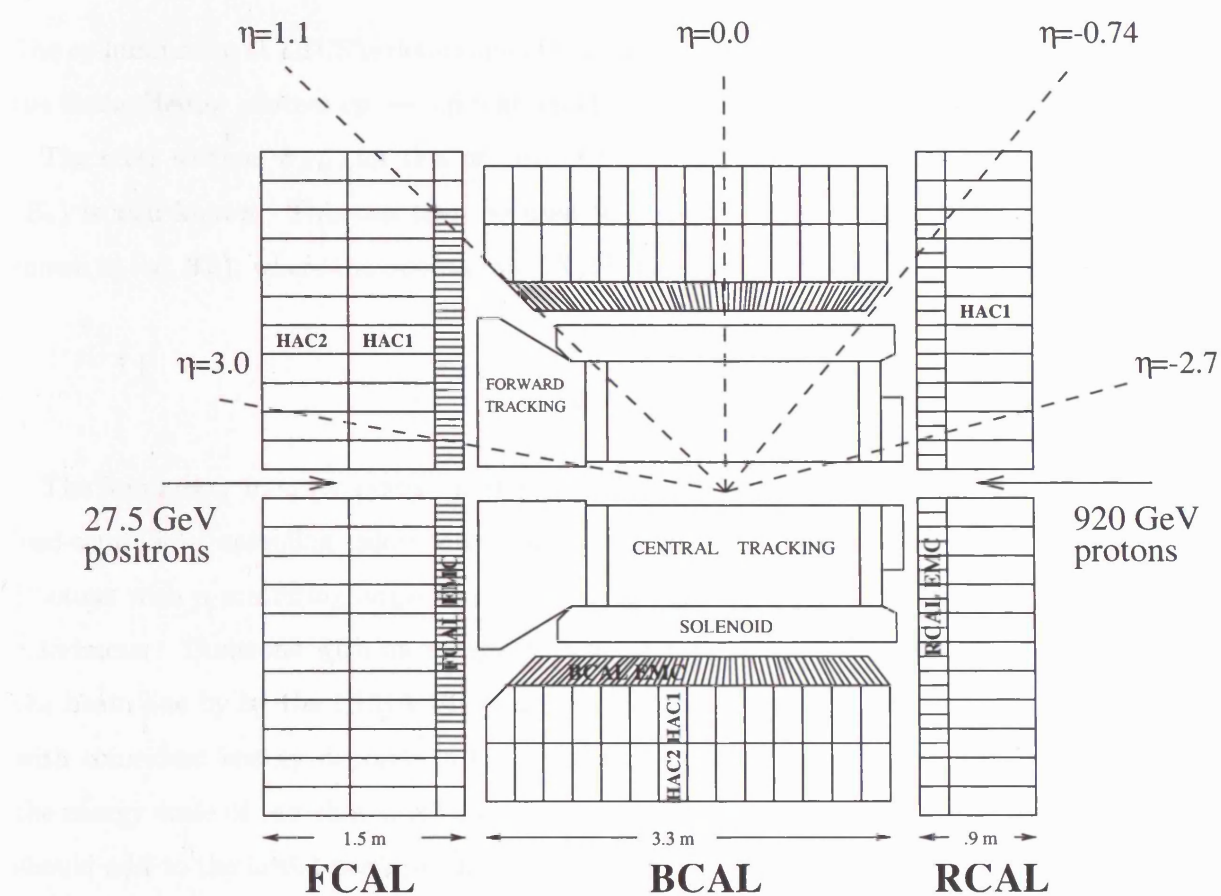


Figure 3.5 The ZEUS Calorimeter ( $y$ - $z$  projection) and surroundings.

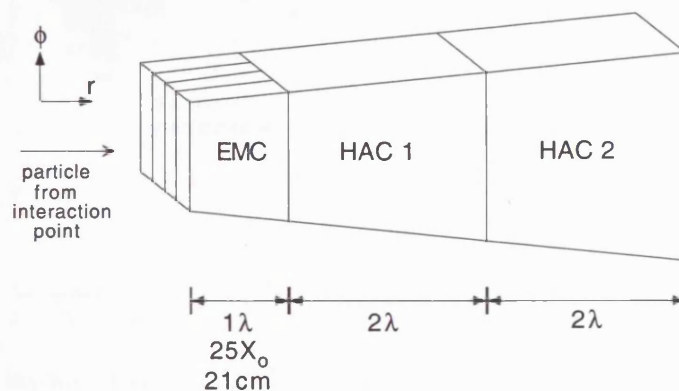


Figure 3.6 Diagram of a BCAL tower.

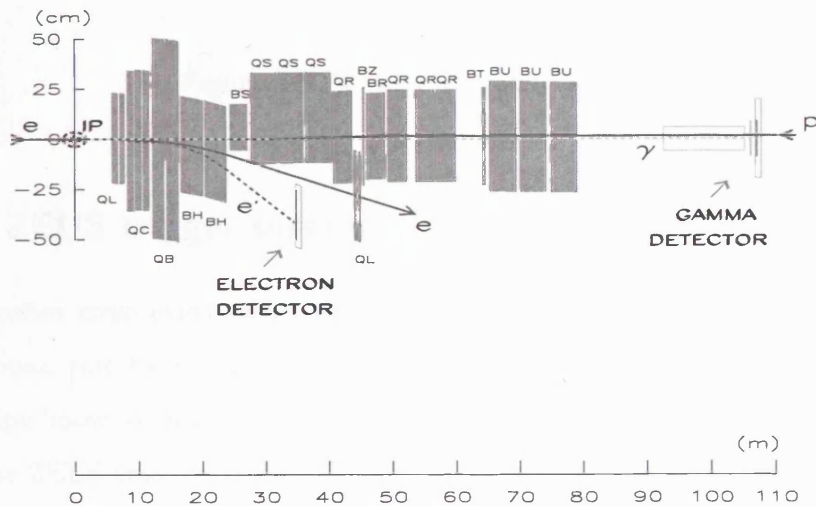
### 3.5 The luminosity measurement

The  $ep$  luminosity at ZEUS is determined by measuring the rate of photons which emerge from the Bethe-Heitler process  $ep \rightarrow ep\gamma$  at small angles.

The cross section,  $\sigma_{BH}$ , for this process at fixed photon scattering angle ( $\theta_\gamma$ ), and energy ( $E_\gamma$ ) is well known. This can then be used to determine the luminosity using the relation shown in (eq. 3.1), where the photon rate ( $N_\gamma$ ) is measured by the luminosity monitor system.

$$\mathcal{L} = N_\gamma / \sigma_{BH} \quad (3.1)$$

The luminosity monitor system is shown in (fig. 3.7), it consists of a positron and photon lead-scintillator sampling calorimeter placed at  $z = -35$  m and  $z = -107$  m respectively. Photons with a scattering angle  $\theta_\gamma < 0.5$  mrad exit the beam pipe and strike the photon calorimeter. Positrons with an energy between  $0.2 E_e$  and  $0.8 E_e$  are deflected away from the beam line by the HERA BH magnet (fig. 3.7), and hit the positron detector. Events with coincident energy deposits in the photon and positron detectors are used to calibrate the energy scale of the photon calorimeter since the sum of the photon and positron energies should add to the initial positron energy.



**Figure 3.7** The layout of the ZEUS Luminosity Monitor. The nominal interaction point is located at (0,0).

Figure 3.8 shows the amount of luminosity delivered by HERA and gated by ZEUS from 1993 until the year 2000. The complete sample corresponds to an integrated luminosity of  $140 \text{ pb}^{-1}$ .

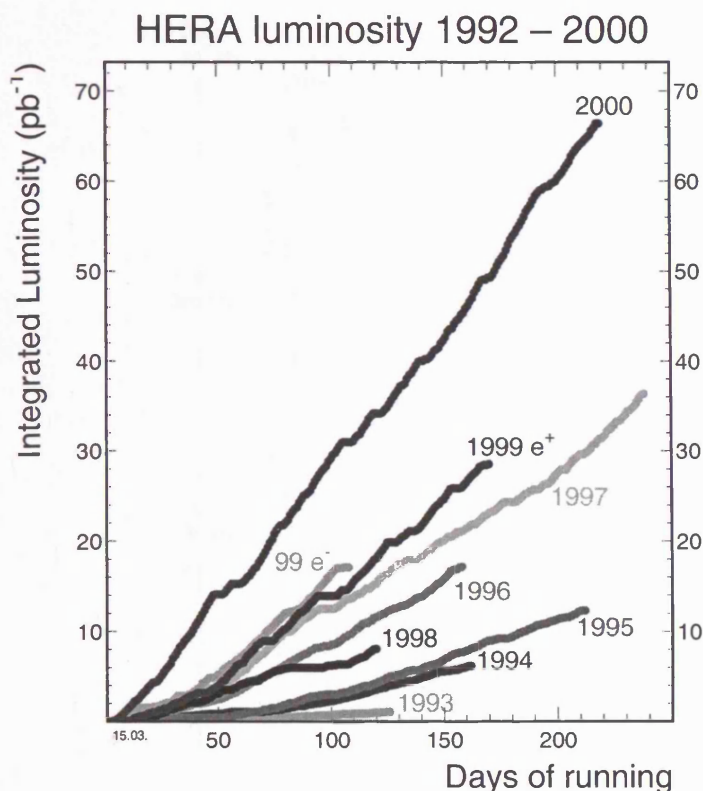
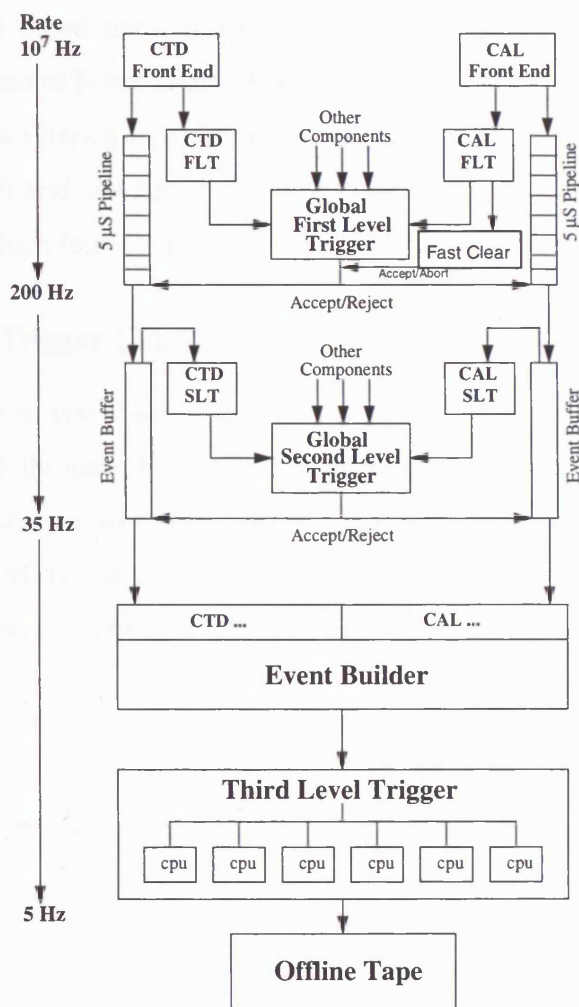


Figure 3.8 The ZEUS gated luminosity.

### 3.6 The ZEUS trigger system

HERA's bunches cross every 96 ns which corresponds to a bunch crossing rate of 10 MHz. The background rate from non  $ep$  collisions (i.e. particles in the beam colliding with gas in the beam pipe known as beam gas) is about 10 kHz, which is brought down to 10 – 200 Hz online by the ZEUS trigger system with the number of interesting  $e^\pm p$  interactions being at about 5 Hz. As the input rates for each trigger stage decrease, the complexity of algorithms and time each stage has to perform them increases; ZEUS has adopted a three level trigger system as shown diagrammatically in (fig. 3.9).

All three trigger levels were required for the analysis within this thesis, the requirements of these triggers are shown in more detail for the FLT in (section 4.4.4), for the SLT in (section 4.4.5) and for the TLT in (section 4.4.6).



**Figure 3.9** Diagrammatic representation of data flow in the ZEUS trigger system.

### 3.6.1 The First Level Trigger (FLT)

The trigger [37, 48] cannot make decisions within the 96 ns bunch crossing time, so the information is stored in 5 μs long pipelines. A coarse set of information is computed by the respective component FLT's which send these calculations to the Global First Level Trigger (GFLT). The GFLT then selects on the combined information from these components to reject

or to keep events to be passed onto the second level.

#### 3.6.2 The Second Level Trigger (SLT)

The SLT's of each component receive almost all the complete data from each component. The component SLT's are based upon transputers and send processed information to the transputer-based Global Second Level Trigger GSLT. The algorithms are more complex at the GSLT and includes physics filters for particular types and topologies of events. The typical accept rates are between 30 and 100 Hz. The complete event information is then passed onto the event builder (EVB) which formats the data before transferring it to the third level trigger.

#### 3.6.3 The Third Level Trigger (TLT)

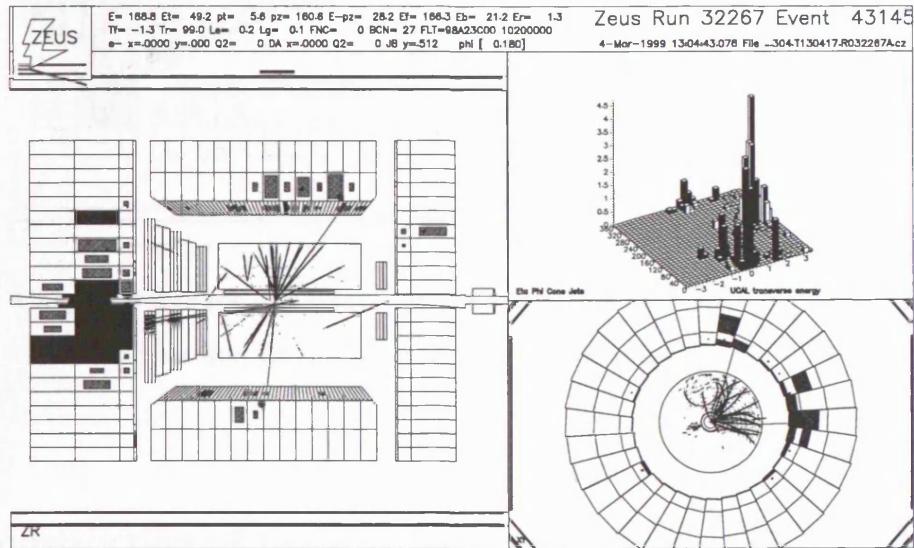
The full event information is available for the TLT, and 'offline' like algorithms are used to reconstruct the the event fully using information from several components. These events are then categorized into physics groups filters and the accepted events which have a typical rate of 5 – 10Hz are written to mass storage tape for re-processing with complete calibrations and the full reconstruction software. The total time between a bunch crossing and a TLT accept is around 0.3s.

## 4 Event reconstruction and selection

### 4.1 Overview

There are three stages in the event selection of photoproduced charm with a jet:

- the selection of photoproduction events,
- reconstruction of the  $D^*$  meson and
- jet finding.

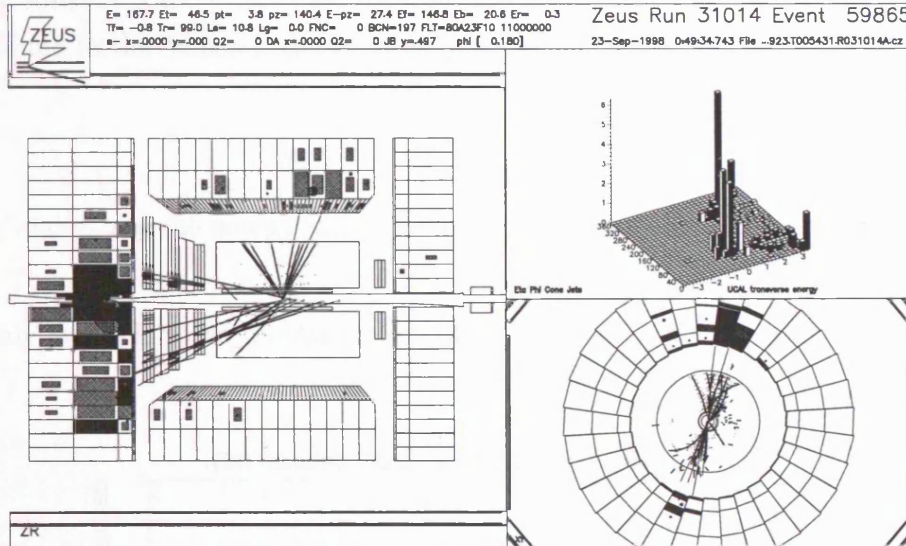


**Figure 4.1** Charm single jet event,  $E_T^{jet} = 17.5$  GeV and  $\eta^{jet} = 0.053$ .

Figure 4.1 shows a typical charm jet event containing only one reconstructed jet above the  $E_T^{jet}$  and  $\eta^{jet}$  thresholds. Figure 4.2 shows a dijet event where both jets are reconstructed as



well as the  $D^*$  meson. The jets can clearly be seen in the lego plot in the top right of both figures where there is a collimation of particles in one region of  $\eta\phi$  space within the detector. The  $D^*$  meson is the particle reconstructed from the tracks within the CTD by forming the invariant mass. No electron is seen in these events as it escapes down the beam pipe. If there were an electron within the acceptance of the CTD, it would look like a single isolated high energy deposit in the electromagnetic section of the calorimeter as demonstrated in (fig. 4.6), and a high  $p_T$  track pointing to the isolated energy deposit. As expected these events have a lot of hadronic activity. This chapter explains how the kinematic variables are calculated from the hadronic final state with the use of jet and energy flow objects, as well as explaining how to reconstruct  $D^*$  mesons.



**Figure 4.2** Charm dijet event, the leading jet having  $E_{T,1}^{jet} = 20.2$  GeV and  $\eta_1^{jet} = -0.089$  and the second leading jet in  $E_T^{jet}$  having  $E_{T,2}^{jet} = 17.7$  GeV and  $\eta_2^{jet} = 1.325$ .

## 4.2 Reconstruction of the kinematic variables

The kinematic variables in photoproduction must be calculated from the hadronic final state. This is because the electron/positron escapes down the beam pipe and therefore is not detected in ZEUS.

### 4.2.1 The $y_{JB}$ correction

The *Jacquet-Blondel* method [49] is used to calculate the kinematic variables  $y$  and  $W$ ;  $W$  and  $y$  are calculated from energy flow objects (EFO's see section 4.3.1) where  $i$  in (eq. 4.1) runs over these objects giving the total  $E - P_z$  in the event and are defined below.

$$y_{JB} = \frac{\sum_{i=1}^n E_i - P_{i,z}}{2E_e} \text{ and} \quad (4.1)$$

$$W_{JB} = \sqrt{s \cdot y_{JB}}. \quad (4.2)$$

$E_e$  is the initial electron energy,  $s$  in (eq. 4.2) is the total centre of mass energy squared in the collision which is equivalent to  $s = 4 \times 920 \times 27.5 = 1.01 \times 10^5 \text{ GeV}^2$ . If the scattered electron is found in the detector, the variable  $y$  can be calculated as:

$$y_{el} = 1 - \frac{E'_e(1 - \cos\theta_e)}{2E_e} \quad (4.3)$$

where  $E'_e$  and  $\theta_e$  are the energy and angle of the scattered electron and can be compared with  $y_{JB}$ . This comparison is not possible in photoproduction ( $Q^2 < 1$ ), as the hadronic system is only available to do the calculation of  $y$ .

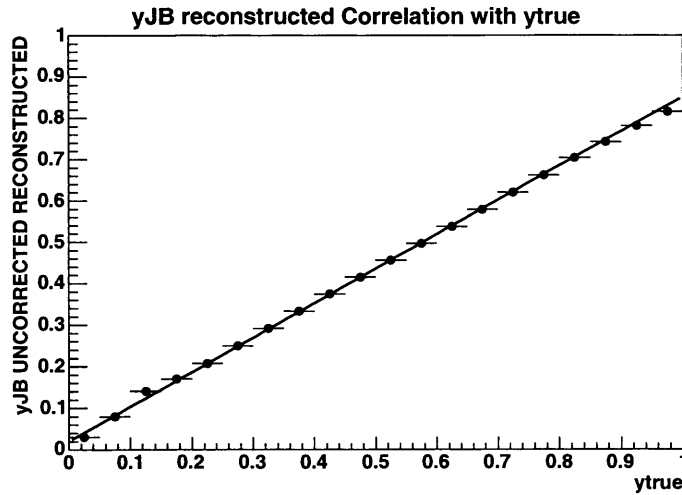


Figure 4.3 Correlation between the measured  $y_{JB}$  and  $y_{true}$ .



Figure 4.3 shows the correlation between the uncorrected reconstructed  $y_{JB}$  and the  $y_{true}$  as given from HERWIG Monte Carlo for events with  $Q^2 \leq 1\text{GeV}^2$ . The correlation is in excellent agreement with the fit:

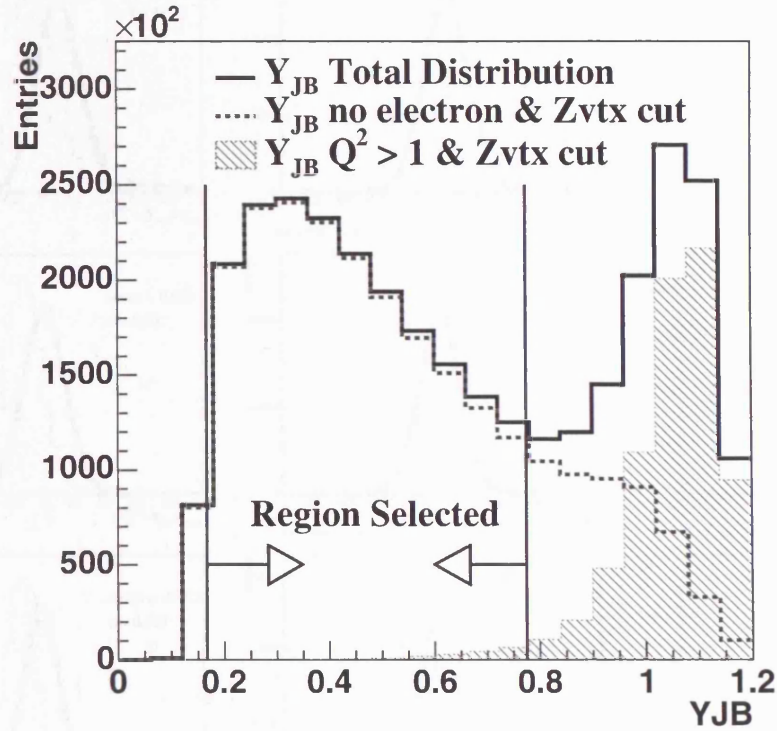
$$y_{JB}^{corr} = \frac{y_{JB} - 0.02}{0.86} \quad (4.4)$$

Equation 4.4 is the result of a first order polynomial fit to (fig. 4.3) used to correct the value of  $y_{JB}$ , and  $y_{JB}^{corr}$  is used to calculate  $W_{JB}$ .

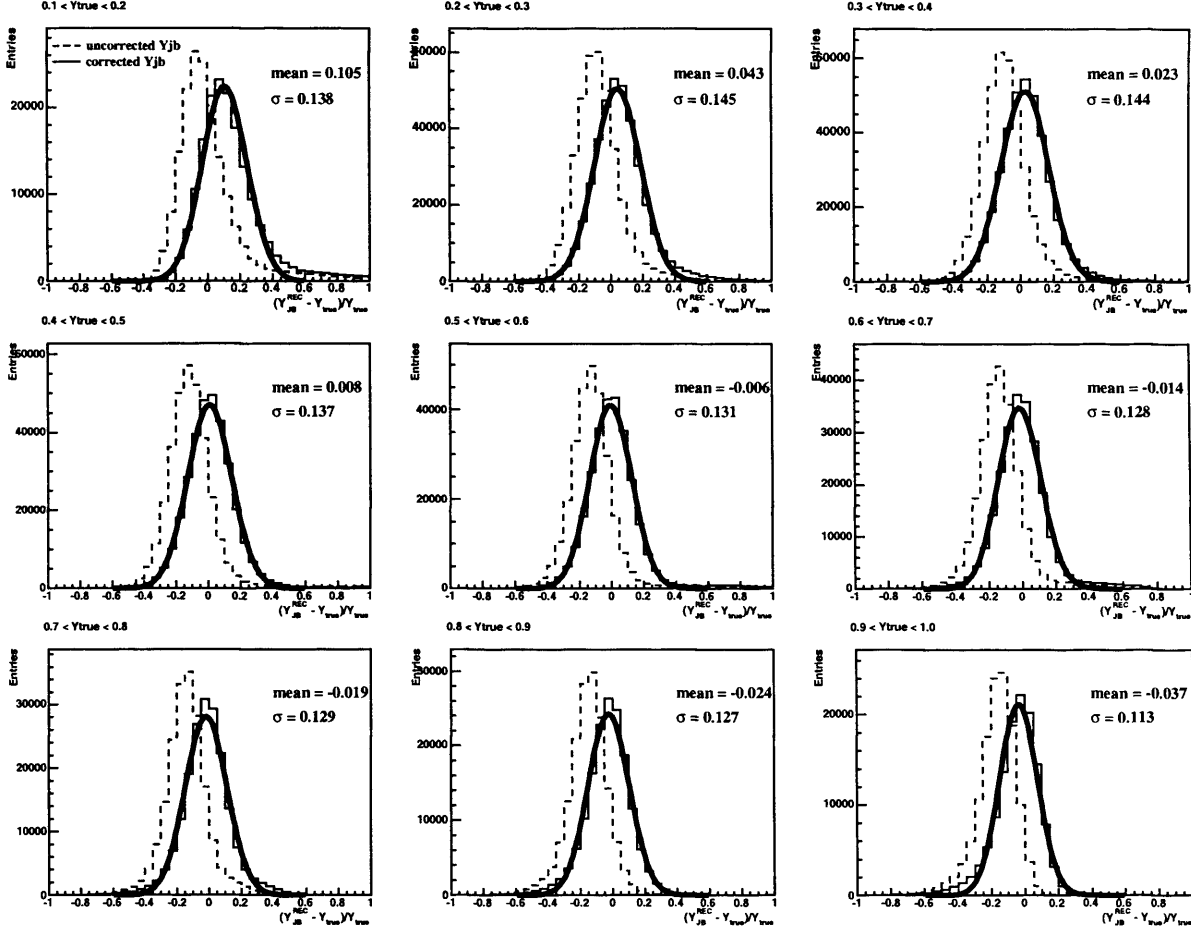
Figure 4.5 shows the distributions for  $(y_{JB} - y_{true})/y_{true}$  in different ranges of  $y_{true}$ . The distributions peak at zero after corrections and have a small dependence on the  $y_{true}$  value, and the resolution of the  $y_{JB}$  measurement is around 11 - 14%.

The distribution of  $y_{JB}$  for HERWIG Monte Carlo is shown in (fig. 4.4). For the kinematic region selected  $130 < W_{JB} < 280\text{GeV}$ , the contamination from DIS events is small.

## YJB Reconstruction



**Figure 4.4** Distribution of  $y_{JB}$  for HERWIG Monte Carlo. The black line shows the total distribution for both DIS and photoproduction events. The shaded region shows events with a  $Q^2 > 1 \text{ GeV}^2$  and primary  $|Z_{vtx}| < 50 \text{ cm}$  cut, and the dashed line shows the events selected with no electron found in the event and  $|Z_{vtx}| < 50 \text{ cm}$  cut i.e. showing how the photoproduction distribution of  $y_{JB}$  looks. The kinematic region selected corresponds to  $130 < W < 280 \text{ GeV}$ .



**Figure 4.5**  $(y_{JB}^{rec} - y_{true})/y_{true}$  in bins of  $y_{true}$ . Dotted histograms show the uncorrected  $y_{JB}$  distributions, solid lines show  $y_{JB}^{corr}$ ,  $y_{JB}$  after the correction is applied, with the mean width( $\sigma$ ) extracted from a Gaussian fit to  $y_{JB}^{corr}$ .

#### 4.2.2 Removal of DIS events by electron identification

Figure 4.6 shows how a neutral current DIS event looks in the ZEUS detector. Electrons are identified with a neural-net algorithm trained on Monte Carlo events [50, 51]. The calorimeter is not uniform because of gaps and dead material. This therefore makes the signature of the electron change from region to region. The electron finder is used on the calorimeter cells which have not had energy correction or the removal of noisy channels applied at the third level trigger system, in order to separate these events from background. From  $\sim 8 - 10\text{GeV}$  upwards the electron finding efficiency is  $\geq 90\%$ , and is used to remove DIS events.

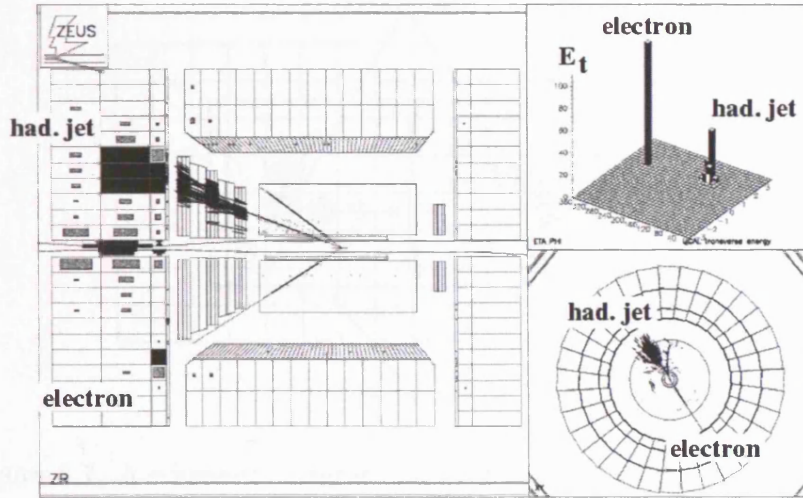


Figure 4.6 A high  $Q^2$  neutral current DIS event.

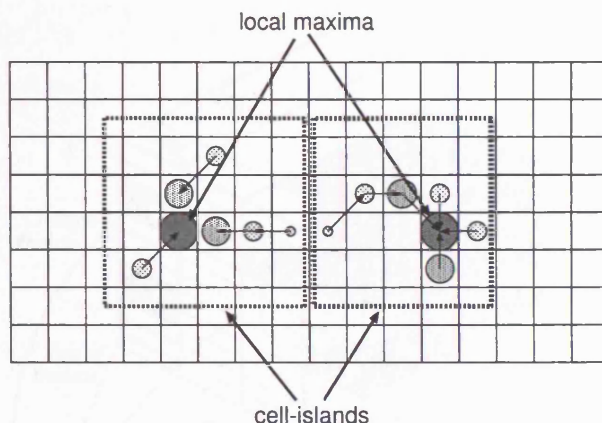
### 4.3 Reconstruction of the hadronic final state

The hadronic final state can be reconstructed by combining information from the calorimeter and the CTD. Low momentum charged particles are better measured in the CTD than in the calorimeter. An algorithm [52, 53, 54] has been written to make best use of these two pieces of information, and to output energy momentum four vectors known as Energy Flow Objects (EFOs see next section 4.3.1).

#### 4.3.1 Energy Flow Objects (EFOs)

EFOs can consist of both neutral and charged particles measured from the CAL and CTD. There is a three stage reconstruction procedure to form these EFO objects.

1. **Clustering** is initiated by combining adjacent cells in the EMC, HAC1 and HAC2 regions separately as shown in (fig. 4.7). A three dimensional 'cone-island' is formed from the CAL information, using the angular separation of the cell islands.
2. **Matching** of the cone islands begins by extrapolating all charged tracks in the CTD to the CAL surface. Matched tracks must pass through 4 superlayers of the CTD with a transverse momentum in the range  $0.1 < p_T < 20$  GeV, with the upper limit being increased to 25 GeV for tracks passing through more than 7 superlayers. Tracks are



**Figure 4.7** A schematic diagram showing how cell-islands are formed.

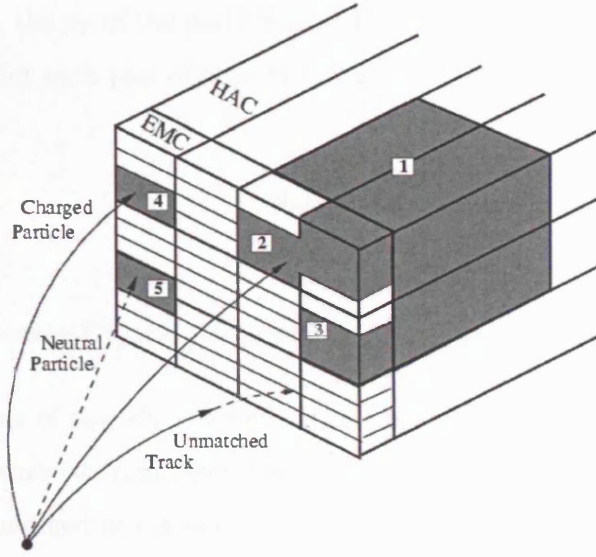
excluded if they cannot be fitted to a primary vertex. If the track passes within 20cm of a cone island it is matched.

3. **The final decision** of how CTD and CAL information are combined is only made for tracks which are matched to islands. The momentum resolution for each CTD track and the energy resolution of the matching cone island in the CAL is calculated. Where the CTD has a better resolution then the CTD tracks are taken. Charged tracks which leave no energy deposit are all assumed to be low energy pions. Unmatched energy deposits are all assumed to come from neutral particles and CAL information must be used here as there is no other choice. The CAL information is then used to determine the energy of the hadronic islands with more than three matched tracks and no use is made of CTD information.

## 4.4 Jet reconstruction

To determine the dynamics of the subprocess in a hadronic interaction, particles in the final state are grouped into jets of collimated particles. Jets correspond closely to the kinematics of the partons produced in the hard subprocess. The jet finding algorithm has to be infrared safe, i.e. the outcome of the algorithm is not sensitive to the emission of soft collinear partons.

In this analysis the  $k_T$  clustering algorithm [7, 55] is used on EFO objects in the experiment, and hadrons from the Monte Carlo programs, to produce a set of objects in the final state.



**Figure 4.8** A figure illustrating the clustering into a cone-island (cell-islands 1,2 and 3 are merged) and the track-island matching.

Jet properties are calculated with the relations.

$$E_T^{jet} = \sum_i^n E_{T,i}^{EFO}, \quad (4.5)$$

$$\eta^{jet} = \frac{\sum_i^n \eta_i^{EFO} E_{T,i}^{EFO}}{\sum_i^n E_{T,i}^{EFO}} \quad \text{and} \quad (4.6)$$

$$\phi^{jet} = \frac{\sum_i^n \phi_i^{EFO} E_{T,i}^{EFO}}{\sum_i^n E_{T,i}^{EFO}}. \quad (4.7)$$

where the sum runs over all EFO objects  $i$  assigned to a jet.

#### 4.4.1 The $k_T$ clustering algorithm

The longitudinal invariant  $k_T$  clustering algorithm [7, 55] was used in inclusive mode and the procedure to reconstruct the jets is as follows.

- The momentum of all objects is scaled so that it equals the energy of the object, so all objects are considered massless. All the massless objects in this list are then input into the jet finder

- The variable  $d_{kB}$ , the  $p_T$  of the particle from the proton beam, is calculated and for each object  $k$  and  $d_{ij}$  for each pair of objects  $i$  and  $j$ , given by,

$$d_{kB} = E_T^2, \quad (4.8)$$

$$d_{ij} = \min(E_{T,i}^2, E_{T,j}^2) R_{ij}^2 \quad \text{where} \quad R_{ij}^2 = (\eta_i - \eta_j)^2 + (\phi_i - \phi_j)^2, \quad (4.9)$$

- The smallest value of  $d_{kB}, d_{ij}$  is found. If  $d_{kB}$  is smallest then the object  $k$  is taken to be a jet and is removed from the list of objects. If  $d_{ij}$  is found to be the smallest, the objects  $(i,j)$  are merged into a new object, given by,

$$E_T = E_{T,i} + E_{T,j} \quad (4.10)$$

$$\eta = \frac{E_{T,i} \cdot \eta_i + E_{T,j} \cdot \eta_j}{E_T} \quad (4.11)$$

$$\phi = \frac{E_{T,i} \cdot \phi_i + E_{T,j} \cdot \phi_j}{E_T} \quad (4.12)$$

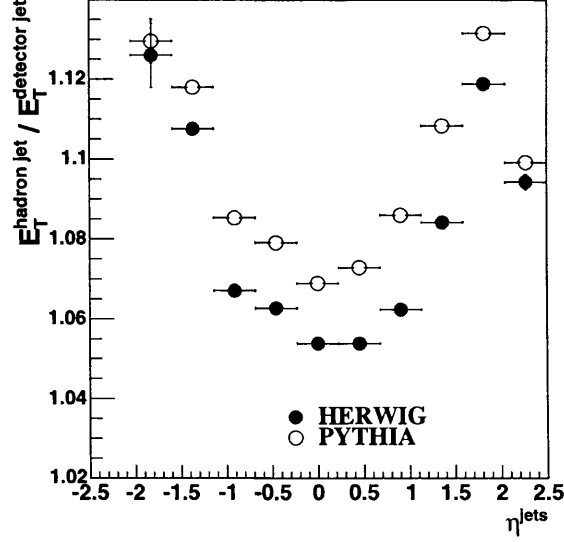
- This procedure is continued until there are no more entries in the list.

#### 4.4.2 Jet energy correction

Energy loss occurs because of dead material, and gaps in the detector which can be investigated using the Monte Carlo (see fig. 4.9). The correction is applied to the jets in the laboratory frame as the detector effects causing this energy loss can be easily be seen and isolated. This correction is more dependent on position of the jet in the calorimeter rather than the kinematics of the event.

The correction procedure was performed on HERWIG Monte Carlo events. The jets were split into eleven different  $\eta^{jet}$  bins as shown in (fig. 4.10). The correlation of the  $E_T^{jet}$  made out of the EFO objects and matched hadronic simulated jets was plotted in these ranges. The hadronic and EFO jets were matched using the criteria  $\Delta R = \sqrt{(\Phi_{jet}^{efo} - \Phi_{jet}^{had})^2 + (\eta_{jet}^{efo} - \eta_{jet}^{had})^2}$ ,





**Figure 4.9** Jet energy loss as a function of  $\eta^{jet}$ . Solid points show the profile distribution for HERWIG Monte Carlo, open points show the profile distribution for PYTHIA Monte Carlo.

$\Delta R < 1$ . Least square fitting within each  $\eta^{jet}$  bin enables the following correction function to be determined.

$$E_{T,EFO,i}^{jet} = m(E_{T,i}^{jet}, \eta_i^{jet}) \cdot E_{T,had,i}^{jet} + c(E_{T,i}^{jet}, \eta_i^{jet}), \quad (4.13)$$

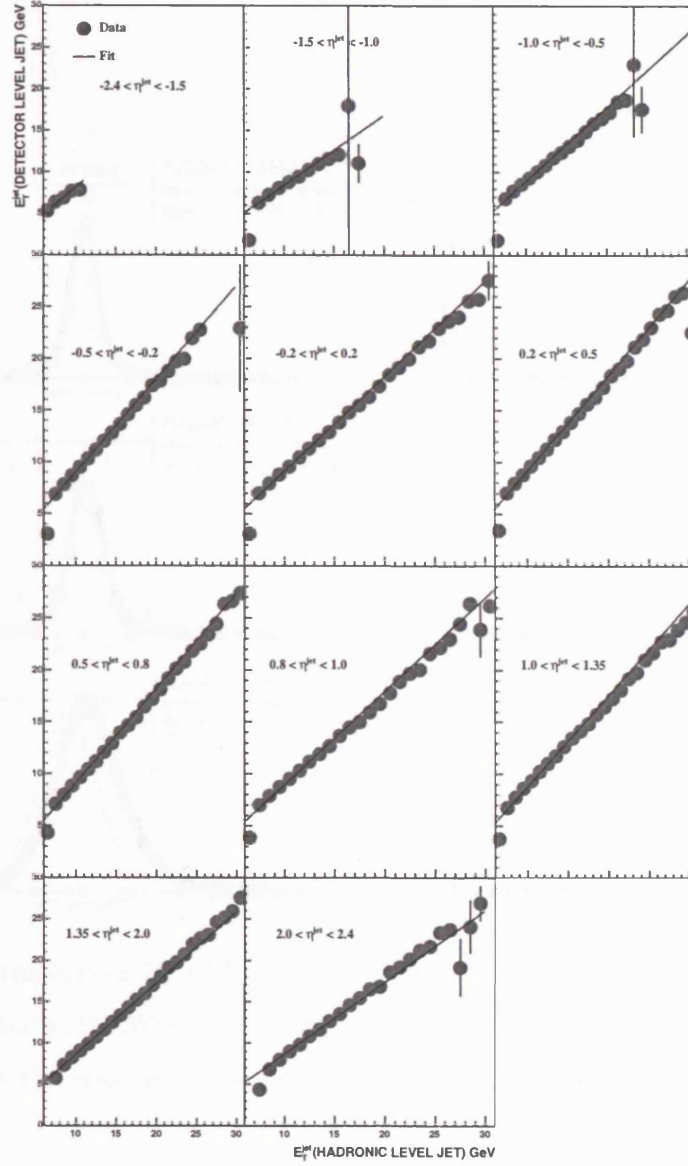
where  $m$  is the slope and  $c$  is the intercept as a function of the transverse energy and the pseudorapidity for that bin. The corrected value for the  $E_{T,corr}^{jet}$  is calculated by:

$$E_{T,corr}^{jet} = \frac{E_{T,efo}^{jet} - c}{m}. \quad (4.14)$$

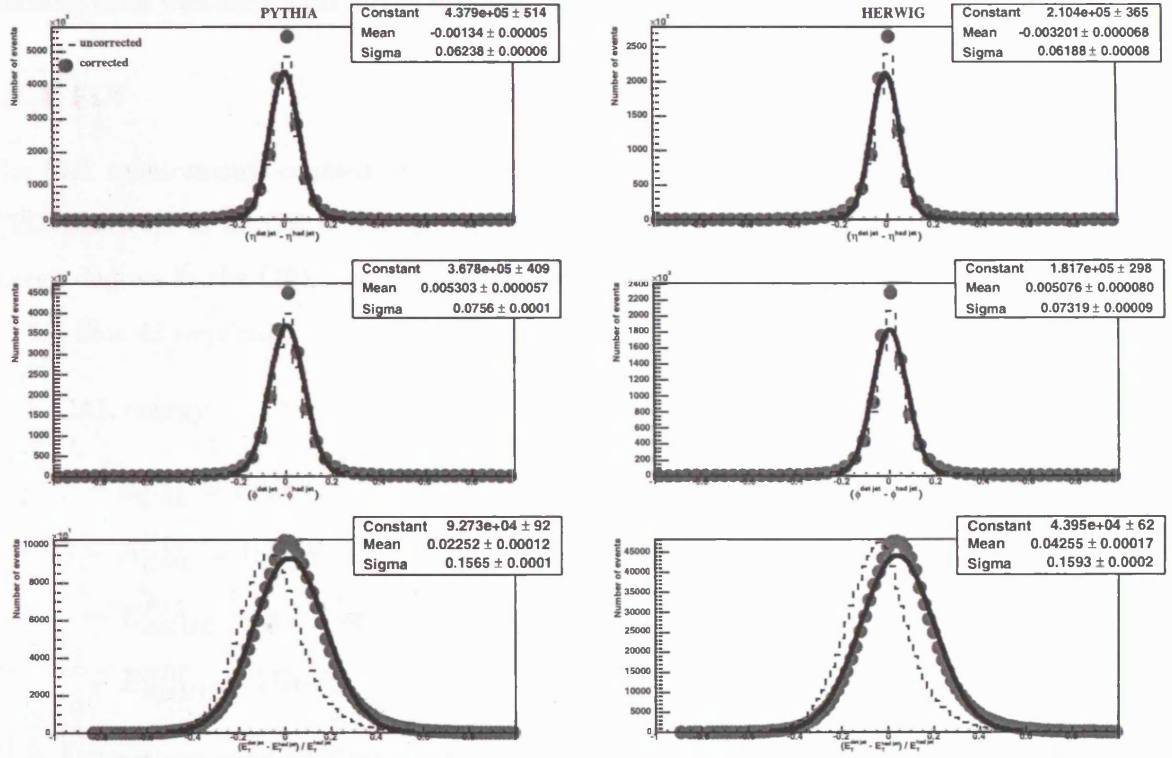
These parameters are then applied to the data jets in exactly the same way, and the corrected values  $E_{T,corr}^{jet}$ ,  $\phi_{corr}^{jet}$  and  $\eta_{corr}^{jet}$  are obtained for jets with an  $E_{T,corr}^{jet} > 6\text{GeV}$ .

Figure 4.11 shows the jets resolutions after applying the jet energy corrections.





**Figure 4.10** Jet energy correction profile plots in bins of  $\eta^{jet}$ . Straight lines are fitted in each  $\eta^{jet}$  bin in order to extract correction factors.



**Figure 4.11** Jet resolutions for  $\eta^{\text{detjet}} - \eta^{\text{hadjet}}$ ,  $\phi^{\text{detjet}} - \phi^{\text{hadjet}}$  and  $(E_T^{\text{detjet}} - E_T^{\text{hadjet}})/E_T^{\text{hadjet}}$ , for both HERWIG and PYTHIA. The distributions were fitted with a Gaussian with the constant, mean and widths shown on the plots.

### 4.4.3 Trigger selection

The triggers selected were designed in order to pickup hard photoproduction events, which two high- $E_T$  jets are created after the collision. In this case at least one jet above a threshold of  $E_T^{jet} > 6$  GeV, with the electron lost down the beam pipe  $Q^2 < 1$ . The FLT requires large energy deposits in the CAL and good FLT tracks. At the SLT, events with a higher  $E_T$  and good vertex tracks were needed to trigger the event, and at the TLT a modified version of the tracking code was used with loose selection cuts on the  $D^*$  meson to select the events.

### 4.4.4 FLT

The FLT requirements concentrate on summed calorimeter quantities and good tracks in the CTD. The FLT is an OR of two GFLT slots; 42 and 59. Both of these slots require a large energy deposit in the CAL and a good track from the CTD FLT.

FLT Slot 42 requires:

- CAL energy
  - $E_{CAL}^{FLT} > 15\text{GeV}$ ,
  - $E_{EMC}^{FLT} > 10\text{GeV}$  or
  - $E_{BEMC}^{FLT} > 2\text{GeV}$  or
  - $E_{REMC}^{FLT} > 2\text{GeV}$ .
- At least one good FLT track which comes close to the nominal interaction point ( $-50 < z < 80\text{cm}$ ).
- Timing information measured by the VETO, C5 counter and small angle rear tracking detector (SRTD) are not consistent with the beam-gas timing of  $ep$  interactions.

FLT Slot 59 requires:

- CAL energy
  - $E_{CAL}^{FLT} > 2\text{GeV}$  and ( $E_{REMC}^{FLT} > 0.5\text{GeV}$  or  $E_{BEMC}^{FLT} > 2\text{GeV}$ ) or
  - $E_{CAL}^{FLT} > 8\text{GeV}$  and  $E_{FCAL}^{FLT}/E_{CAL}^{FLT} < 0.65$ .

- At least 9 FLT tracks found and the fraction of the number of good FLT tracks to the total number of FLT tracks is greater than 50%.
- Timing information measured by the VETO, C5 counter and SRTD are not consistent with the beam-gas timing.

### 4.4.5 SLT

At the SLT, events are vetoed using the timing ( $t$ ) obtained from the FCAL( $t_{FCAL}$ ), RCAL( $t_{RCAL}$ ), top half of the BCAL( $t_{BCAL}^{top}$ ) and bottom half of the BCAL( $t_{BCAL}^{bottom}$ ). If one of the relations below is satisfied the event is vetoed.

1.  $|t_{RCAL}| > 8\text{ns}$  or
2.  $t_{FCAL} - t_{RCAL} > 8\text{ns}$  or
3.  $t_{BCAL}^{top} - t_{BCAL}^{bottom} < -10\text{ns}$ .

Timings are calibrated such that  $t = 0$  ns corresponds to physics events colliding at the nominal interaction point (0,0,0)<sup>1</sup>. The first two vetos above remove backgrounds from proton beam gas events, the third removes cosmic ray events.

A cut on  $\sum_{cells,i}^n E_i^{cells} - P_{z,i}^{cells} < 75\text{GeV}$  is also required in order to further remove background and reduce the rate.

In order to select  $D^*$  meson photoproduction events, the following conditions must be all satisfied.

- $-60 < z_{vtx} < 60\text{cm}$  or no CTD information and
- $\sum_{cells,i}^n E_i^{cells} - P_{z,i}^{cells} > 7\text{GeV}$  and
- $\sum_{cells,i}^n E_{T,i}^{cells}$  (excluding the FCAL inner ring)  $> 6\text{GeV}$  and
- $\sum_{cells,i}^n P_{z,i}^{cells} / \sum_{cells,i}^n E_i^{cells} < 0.96$  and

---

<sup>1</sup>The ZEUS coordinate system is a right-handed Cartesian system, with the  $z$  axis pointing in the proton beam direction, referred to as the ‘forward’ direction, and the  $x$  axis pointing left towards the centre of HERA. The coordinate origin is at the nominal interaction point ( $x,y,z$ ) (0,0,0)

- ( $N_{foundtracks} \geq 5$  and  $N_{vertextracks} \geq 3$ ) or
- $N_{foundtracks} \geq 16$  or  $\sum_{1,2} P_T > 1.2\text{GeV}$ .

where  $\sum_{1,2} P_T$  is the scalar sum of the transverse momenta of the two highest  $p_T$  tracks. The lower  $E - P_z$  cut is applied to remove beam gas events, since these events are boosted towards positive  $z$  direction, which can result  $E \sim P_z$ . Requiring large- $E_T$  and removing the region where  $P_z \sim E$  removes large amounts of proton beam gas events, as proton beam gas is boosted in the forward direction and characterised by  $P_z \sim E$ . This ensures there is a large energy deposit in the central part of the detector. The number of track requirements ensure  $D^*$  meson reconstruction is possible. This SLT slot also requires that FLT 42 or 59 have been fired.

#### 4.4.6 TLT

The following global veto logic is applied at the TLT, if one of these requirements below is satisfied the event is vetoed,

- $|t_{RCAL}| > 6\text{ns}$ ,
- $|t_{FCAL}| > 8\text{ns}$ ,
- $t_{FCAL} - t_{RCAL} > 8\text{ns}$  and
- $|t_{GLOBAL}| > 8\text{ns}$

where  $t_{GLOBAL}$  is the timing obtained from all CAL cells. These cuts remove non- $ep$  background further.

At the TLT, almost full tracking information is available and a stripped down version of the offline tracking code is run in order to achieve a high performance.  $D^*$  mesons are then reconstructed as described in (section 4.4.10), but with wider mass windows namely

- $1.40 < m(D^0) < 2.2 \text{ GeV}$  and
- $\Delta m < 0.17 \text{ GeV}$ .

#### 4.4.7 Offline selections

The events obtained with the online trigger selection still contain some contamination from non- $ep$  physics interactions, as well as from non-photoproduction interactions which still have to be removed. Before cuts on calorimeter quantities are made corrections for noise, originating from the electronics and the radioactive decay of the uranium, are applied. Also a complete set of fully calibration constants are provided by the detector components before the full reconstruction is run over the data forming a new data structure with the final track and calorimetry information available.

#### 4.4.8 Selecting photoproduction events

Photoproduction in  $ep$  collisions is characterised by the interaction of quasi-real photons (photon virtuality  $Q^2 < 1$ ). The absence of the scattered electron within the ZEUS detector is a signal of photoproduction events, as the electron is lost down the beam pipe. The following cuts were used to select photoproduction events.

- $-50 < z_{vtx} < 50$  cm

This rejects background from proton beam gas and cosmic ray events.

- $y_{el} < 0.7$

Events are rejected if there is an electron in the event with  $y_{el} < 0.7$ . Neutral particles such as  $\pi^0$  fake electron signatures in the detector with lower energies than the scattered electrons in DIS events. The value for  $y_{el}$  will be therefore larger for fake electron than for DIS events.

- $130 < W_{\gamma p} < 280$  GeV

The lower cut rejects contributions from proton beam gas interactions, which are boosted to the positive  $z$  direction. The upper cut is required to reduce the contribution from DIS events where the electron finder could not identify the scattered electron.

#### 4.4.9 Selecting charm events

Charm is identified by tagging charmed mesons in the final state. The  $D^*$  meson is selected in this analysis by the decay mode:

$$D^{*\pm} \rightarrow (D^0 \rightarrow K^\mp, \pi^\pm), \pi_s^\pm \quad (4.15)$$

where  $\pi_s^\pm$  is the ‘slow’ pion.

The branching ratios from the PDG [56] of these decay channels are.

$$Br(D^{*\pm} \rightarrow D^0, \pi_s^\pm) = 67.7 \pm 0.5\% \quad \text{and} \quad (4.16)$$

$$Br(D^0 \rightarrow K^\mp, \pi^\pm) = 3.80 \pm 0.09\% . \quad (4.17)$$

The combined branching ratio for this decay chain is thus 2.57%, and fragmentation probability  $f(c \rightarrow D^{*+})$  is 23.5% [57]. Although the conversion of a c-quark into the detected final state is small ( $0.0257 * 0.23 = 0.59\%$ ) the decay products are all charged particles and are well measured within the acceptance of the CTD and the invariant masses can be well determined. There are two mass constraints, the mass of the  $D^0$  and the mass difference between the  $D^*$  and the  $D^0$ , known as  $\Delta m$  (eq. 4.18).

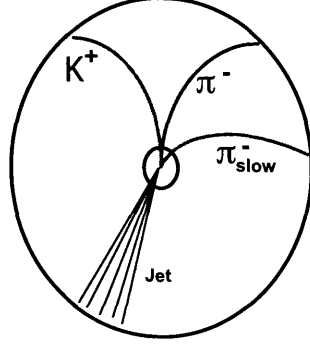
$$\Delta m = m(K\pi\pi_s) - m(K\pi) \quad (4.18)$$

The  $\pi_s$  allows for an accurate momentum measurement and since this is the only particle different between the  $D^0$  and  $D^*$  decay it determines the resolution in which the  $D^*$  can be measured. Since the signal is near threshold the background is low and can be well estimated using wrong track charge combinations (see section 4.4.10). Other particle identification methods are available within ZEUS such as  $dE/dx$  from the CTD and particle identification within the calorimeter, but are found not to be very effective at background reduction within the kinematic range of this measurement.

#### 4.4.10 Reconstruction of the $D^{*\pm}$ meson

Figure 4.12 shows a  $D^{*\pm}$  meson decaying into a kaon, pion and slow pion. It is not possible to distinguish kaon tracks from pion tracks, therefore all sets of tracks are alternately assigned to

the kaon or pion mass. All the combinations of tracks with opposite charge  $P_T(K, \pi) > 0.4$  GeV and  $|\eta(K, \pi)| < 1.75$  are combined to form the  $D^0$  candidates.  $D^0$  candidates are kept if their mass was in the range  $1.8 < m(D^0) < 1.92$  GeV (fig. 4.14).



**Figure 4.12** Cartoon of a  $D^* \rightarrow (D^0 \rightarrow K, \pi), \pi_s$  decay as observed in the CTD.

The  $D^0$  candidates are then combined with another track of opposite charge to that of the kaon, which is the slow pion candidate track. This combination of three tracks then forms the  $D^*$  candidates which are accepted if  $P_T(D^*) > 3.0$  GeV and  $|\eta(D^*)| < 1.5$ . The pseudorapidity cut ensures that the tracks are within a well understood region of the CTD. The  $p_T$  cut also reduces the combinatorial background, which is much higher at lower  $p_T$  since the background is predominantly from low  $p_T$  tracks. The tracks selection criteria are,

- $p_T(K, \pi) > 0.4$  GeV ,
- $p_T(\pi_s) > 0.12$  GeV and
- $|\eta(K, \pi, \pi_s)| < 1.75$  .

#### 4.4.11 $D^*$ meson signal extraction

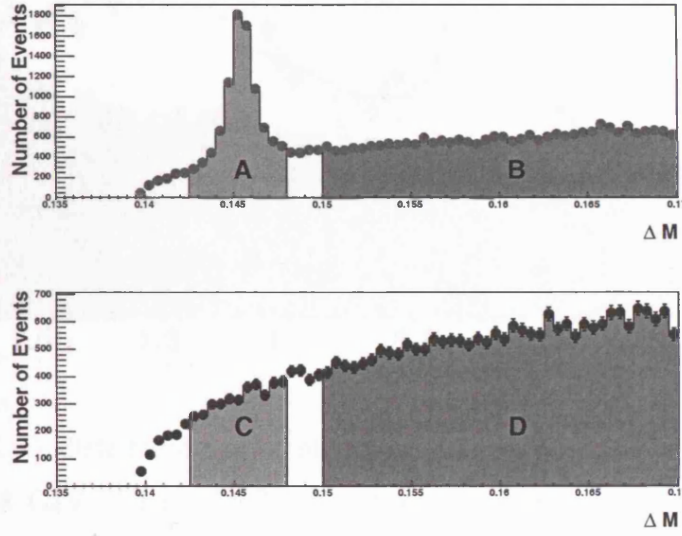
Wrong charge combinations are used in order to estimate the combinatorial backgrounds to the  $D^*$  decay. Figure 4.13 shows the signal and background distributions for  $D^*$  meson reconstruction separated into sample signal region  $0.143 < \Delta M < 0.148$  GeV, and background normalisation region  $0.15 < \Delta M < 0.17$  GeV. To extract the  $D^*$  signal the background wrong charge distribution has to be normalised to the right charge signal distribution. The number of events in the signal region in the right charge distribution is A and the number in the wrong



charge is C. If B is the number in the right charge normalisation region and D is for the wrong charge normalisation region, then  $N(D^*)$  the number of  $D^*$  mesons and the error are given by:

$$N(D^*) = A - \left[ \frac{B}{D} \right] \cdot C , \quad (4.19)$$

$$\delta N(D^*) = \sqrt{A + \left[ (C \cdot B) \cdot \left[ \frac{C + B + C \cdot \frac{B}{D}}{D^2} \right] \right]} . \quad (4.20)$$

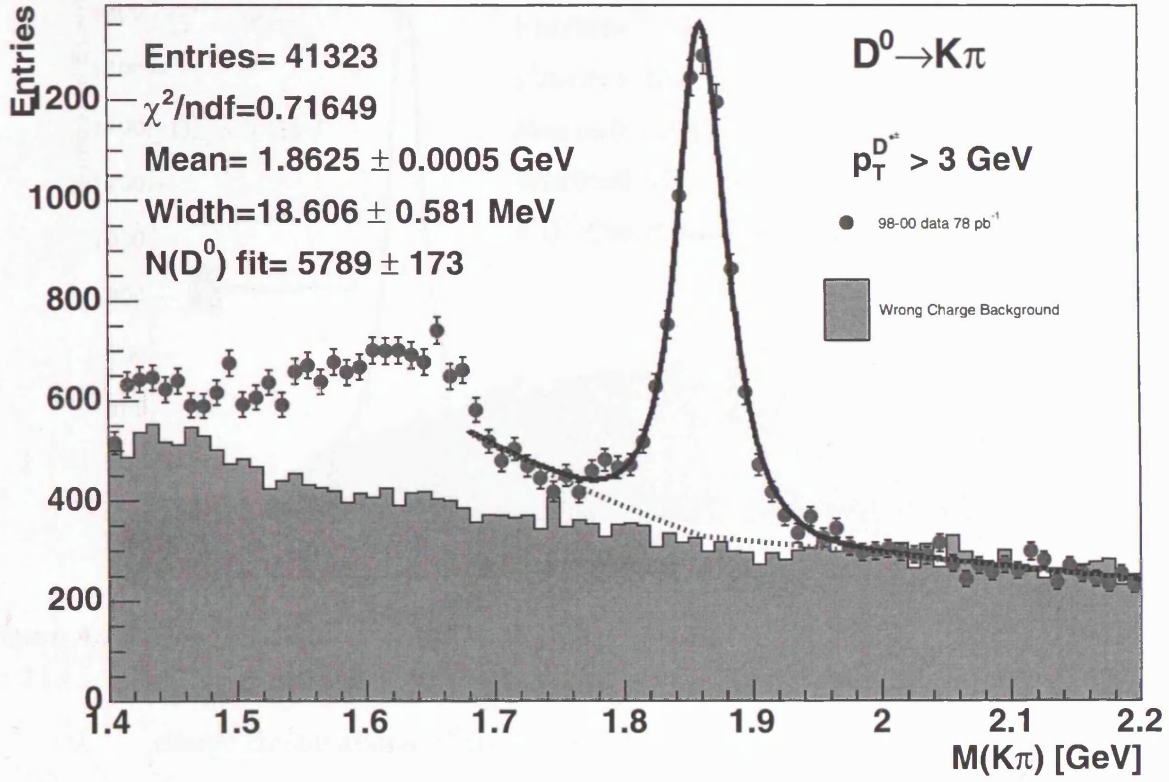


**Figure 4.13**  $D^*$  right charge selection is shown (top histogram), and wrong charge distribution (bottom histogram), both separated into example signal regions  $0.143 < \Delta M < 0.148$  GeV, and background normalisation regions  $0.15 < \Delta M < 0.17$  GeV.

A fitting procedure is also used to extract a signal from the distributions. Figure 4.15 shows the mass distribution fitted to a modified Gaussian [28] (eq. 4.21) plus a background threshold function (eq. 4.23) which is approximately exponential.

$$G_{mod}(x; d, p_1, p_2, p_3) = \frac{d \cdot p_1}{\sqrt{2\pi} \cdot p_3} \exp\left(-\frac{1}{2} T^{1+\frac{1}{1+0.5T}}\right) , \quad (4.21)$$

$$T = \left| \frac{x - p_2}{p_3} \right| , \quad (4.22)$$



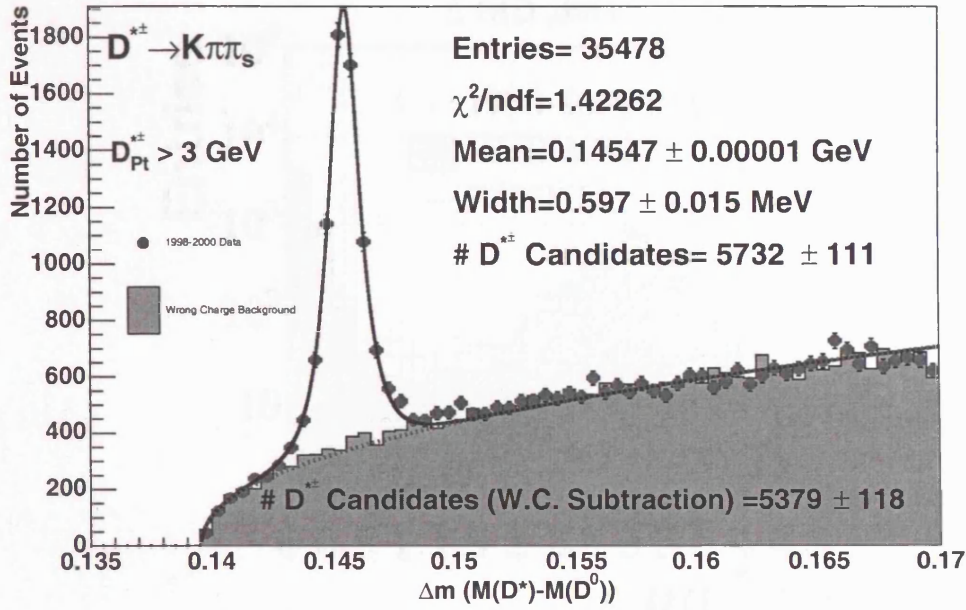
**Figure 4.14**  $m(K,\pi)$  distribution after all selection cuts, and a cut on  $0.143 < \Delta M < 0.148$  GeV. The solid dots are the right charge combinations and histogram is the wrong charge distribution. The wrong charge is normalised to the right charge distribution in the region  $2.0 < m(K,\pi) < 2.2$  GeV

$$background_{func} = p_4(x - m_\pi)^{p_5}, \quad (4.23)$$

where  $m_\pi$  is the pion mass,  $d$  is the bin width,  $p_1 \dots p_5$  are the free parameters and  $x = \Delta m$ . The number of candidates is then  $N(D^*) = p_1 \times G_0$ , where  $G_0$  is the normalisation factor, which is one for a pure Gaussian. For this new functional form the normalisation has to be worked out numerically (eq. 4.24).

$$\int_{-\infty}^{\infty} dx \ G_{mod}(x; d, p_1, p_2, p_3) = 1.218. \quad (4.24)$$

In summary, the signal region definitions and kinematic cuts on the  $D^*$  meson are:



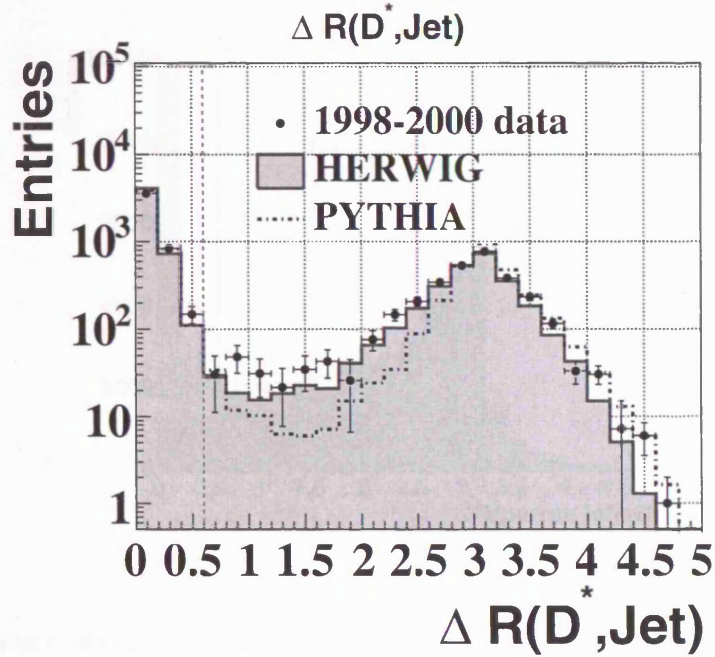
**Figure 4.15** The distribution of the mass difference,  $\Delta M = M(K\pi\pi_s) - M(K\pi)$ , for  $D^{*\pm}$  candidates (solid dots). The histogram shows the  $\Delta M$  distribution for wrong charge combinations. Only  $D^{*\pm}$  candidates from the region  $0.143 < \Delta M < 0.148$  GeV were used for the cross section measurement.

- Signal region:
  - $1.80 < m(D^0) < 1.92$  GeV and
  - $0.143 < \Delta m < 0.148$  GeV .
- Kinematic region:
  - $P_T(D^*) > 3.0$  GeV and
  - $|\eta(D^*)| < 1.5$  .

#### 4.4.12 $D^{*\pm}$ meson & jet matching

The  $D^*$  meson and jet matching is done via the  $\Delta R$  cone association between the  $D^*$  and the jet shown in (eq.4.25) in  $\eta - \phi$  space.

$$\Delta R = \sqrt{(\Phi_{jet} - \Phi_{D^*})^2 + (\eta_{jet} - \eta_{D^*})^2} . \quad (4.25)$$



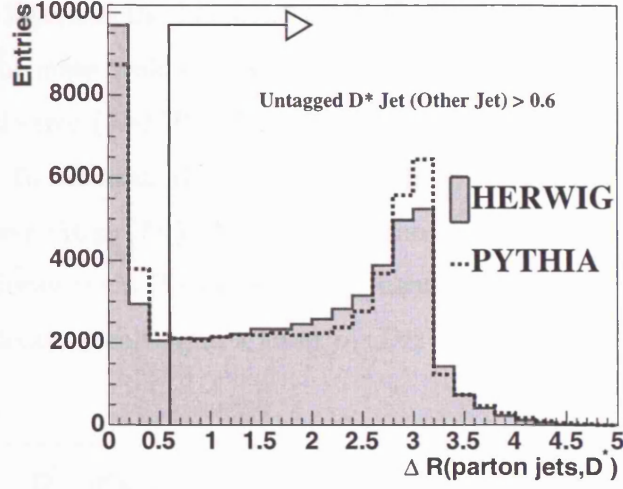
**Figure 4.16**  $\Delta R$  association between  $D^*$  meson and jet. Points are the data, the filled area is the HERWIG Monte Carlo, and the PYTHIA Monte Carlo is the blue solid line. The dashed green line indicates where the cut is placed at  $\Delta R = 0.6$  separating matched jets from unmatched jets.

If  $\Delta R < 0.6$  the  $D^*$  is matched to a jet. Figure 4.16 shows the  $\Delta R$  data distribution compared to HERWIG and PYTHIA Monte Carlos. The main association comes at a value smaller than 0.6 and the second peak seen at 3.14 is due to the  $D^*$  being in opposite hemispheres in the detector i.e. back to back with the jet. These effects appear to be well reproduced in the Monte Carlo.

$D^*$  mesons are clustered into the jet finder with the removal of the final state kaon, pion and slow pion from the list of particles given to the jet finder, allowing for the jet containing the  $D^*$  meson to be identified unambiguously at hadron level.

At parton level the jets are matched in the same way as detector level using the  $\Delta R$  method, (fig. 4.17) shows this for both HERWIG and PYTHIA Monte Carlo. Again  $\Delta R < 0.6$  selects matched jets, and  $\Delta R > 0.6$  for unmatched jets to  $D^*$  mesons.



Parton Jet  $\Delta R$  to  $D^*$  association

**Figure 4.17**  $\Delta R$  association between  $D^*$  meson and parton jet. The filled area is the HERWIG Monte Carlo, and the PYTHIA Monte Carlo is the blue dashed line. The arrow shows where the cut is placed at  $\Delta R = 0.6$  separating matched jets from unmatched jets.

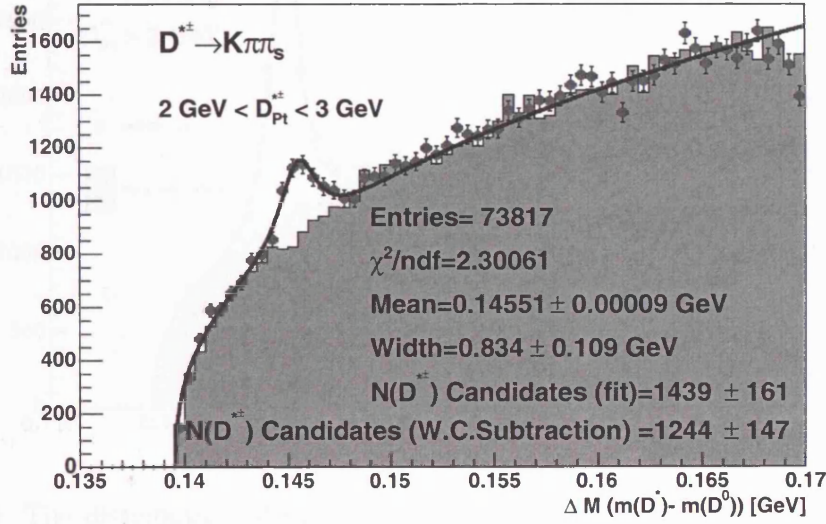
#### 4.4.13 Reconstruction of $x_\gamma^{obs}(D^*, \text{untagged jet})$

In order to be sensitive to higher order effects, and to distinguish between direct and resolved enhanced regions,  $x_\gamma^{obs}(D^*, \text{untagged jet})$  can be constructed [10], which is ‘analogous’ to the traditional  $x_\gamma^{obs}$  but has the advantage of being able to go to lower  $p_T$  by exchanging one of the jets for a  $D^*$  meson and calculating the quantity  $x_\gamma^{obs}(D^*, \text{untagged jet})$  using (eq. 7.1). The highest  $E_T^{jet}$  not associated to the  $D^*$  meson is selected using  $\Delta R > 0.6$ .

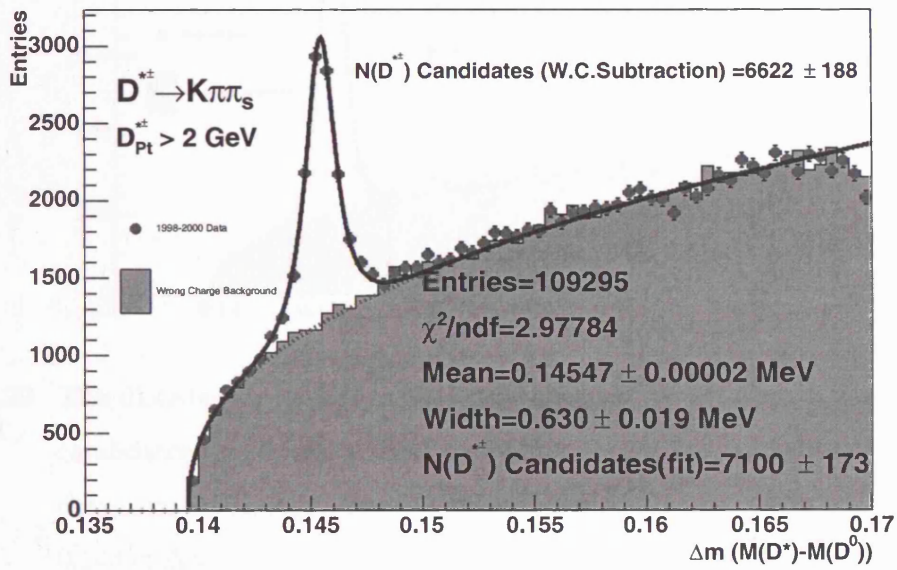
$$x_\gamma^{obs}(D^*, \text{untagged jet}) = \frac{P_T(D^*)e^{-\eta(D^*)} + E_T^{\text{untagged jet}}e^{-\eta^{\text{untagged jet}}}}{2yE_e} \quad (4.26)$$

## 4.5 Extending the $p_T^{D^*}$ range

Going to lower  $p_T(D^*)$  increases the statistics. Figure 4.19 shows the mass peak for  $p_T(D^*) > 2$  GeV and (fig. 4.18) shows the mass peak for  $2 < p_T(D^*) < 3$  GeV. The statistics are increased by 20% but the fractional error ( $\delta N(D^*)/N(D^*)$ ) is increased from 2.3% to 3.0% because background has increased. To minimise the error propagated to the cross sections measurements it was decided not to lower the  $p_T(D^*)$ . Also at low values of  $p_T(D^*)$  the beauty contamination increases, due to the decay chain ( $b \rightarrow c \rightarrow D^*$ ) momentum transfer to the  $D^*$  is lost through this large number of decays resulting in a lower  $p_T(D^*)$  which originates from b quarks.



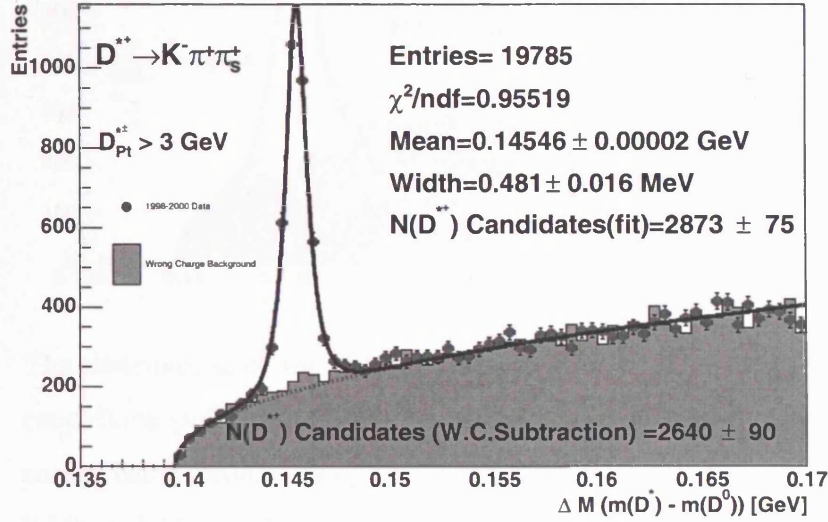
**Figure 4.18** The distribution of the mass difference,  $\Delta M = M(K\pi\pi_s) - M(K\pi)$ , for  $D^{*\pm}$  candidates (solid dots). The histogram shows the  $\Delta M$  distribution for wrong charge combinations. Only  $D^{*\pm}$  candidates from the region  $0.143 < \Delta M < 0.148$  GeV were used for the cross section measurement.  $2 < p_T(D^*) < 3$  GeV.



**Figure 4.19** The distribution of the mass difference,  $\Delta M = M(K\pi\pi_s) - M(K\pi)$ , for  $D^{*\pm}$  candidates (solid dots). The histogram shows the  $\Delta M$  distribution for wrong charge combinations. Only  $D^{*\pm}$  candidates from the region  $0.143 < \Delta M < 0.148 \text{ GeV}$  were used for the cross section measurement.  $p_T(D^*) > 2 \text{ GeV}$ .

## 4.6 $D^{*+}$ & $D^{*-}$ signals

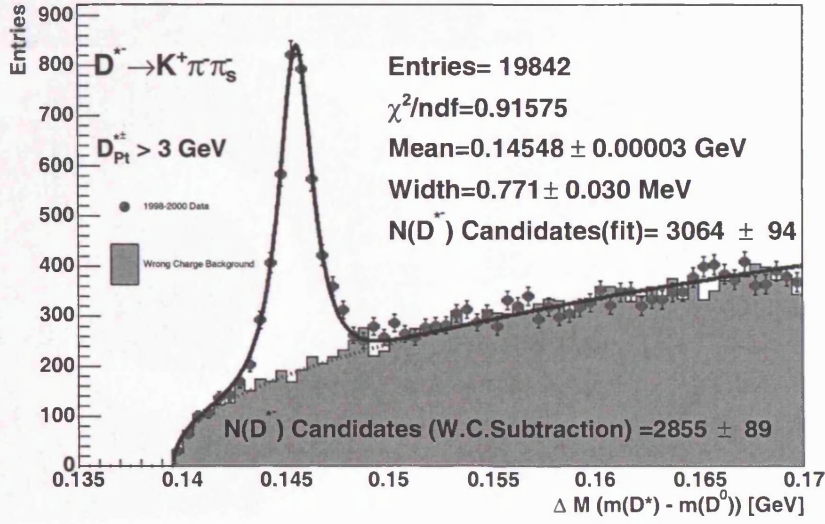
There is a different response in the CTD for positive and negative tracks which is shown in the widths of the  $\Delta M$  peaks of (fig. 4.20) and (fig. 4.21).



**Figure 4.20** The distribution of the mass difference,  $\Delta M = M(K\pi\pi_s) - M(K\pi)$ , for  $D^{*+}$  candidates (solid dots). The histogram shows the  $\Delta M$  distribution for wrong charge combinations. Only  $D^{*\pm}$  candidates from the region  $0.143 < \Delta M < 0.148 \text{ GeV}$  were used for the cross section measurement.  $p_T(D^*) > 3 \text{ GeV}$ .

As the negative tracks have a worse resolution due to the geometrical arrangement of the wires in the CTD the width of the  $D^{*-}$  meson is measured to be  $0.757 \pm 0.032 \text{ MeV}$ , and  $0.493 \pm 0.018 \text{ MeV}$  for  $D^{*+}$  mesons, the number of candidate  $D^*$  mesons is the same within errors.





**Figure 4.21** The distribution of the mass difference,  $\Delta M = M(K\pi\pi_s) - M(K\pi)$ , for  $D^{*\pm}$  candidates (solid dots). The histogram shows the  $\Delta M$  distribution for wrong charge combinations. Only  $D^{*\pm}$  candidates from the region  $0.143 < \Delta M < 0.148$  GeV were used for the cross-section measurement.  $p_T(D^*) > 3$  GeV.

## 4.7 Dijet Variables $x_\gamma^{obs}$ , $\Delta\phi^{jj}$ , $p_T^{jj}$ and $m^{jj}$

In this section the dijet variables  $x_\gamma^{obs}$ ,  $\Delta\phi^{jj}$ ,  $p_T^{jj}$  and  $m^{jj}$  are defined.

$x_\gamma^{obs}$  [35] is the fractional momentum of the photon participating in the production of the two highest  $E_T^{jet}$  jets.

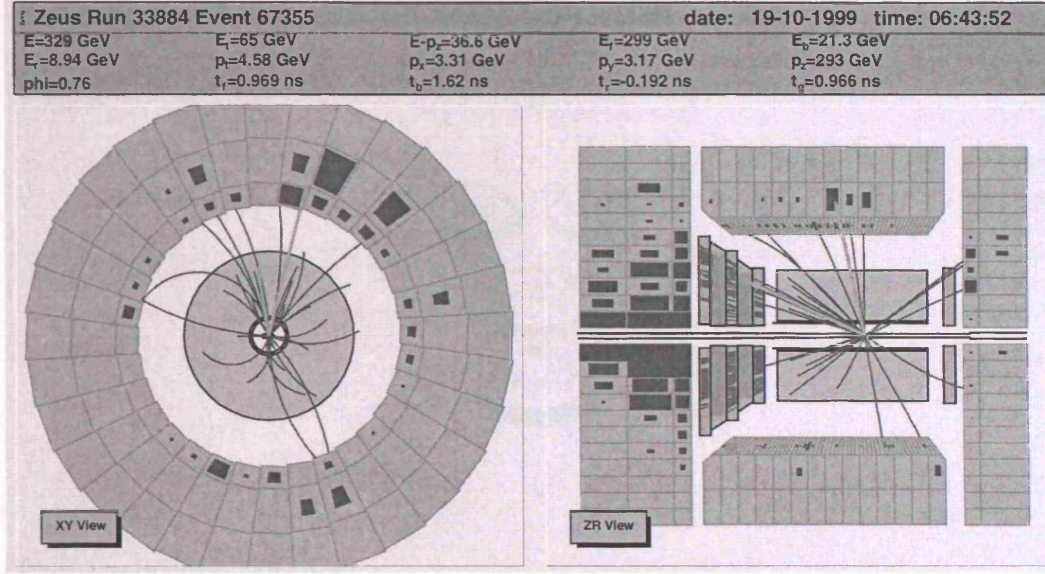
$$x_\gamma^{obs} = \frac{E_T^{jet1} e^{-\eta^{jet1}} + E_T^{jet2} e^{-\eta^{jet2}}}{2yE_e} . \quad (4.27)$$

This is in the leading order massless approach and under the assumption that partons in the photon are collinear with the photon, i.e. in the infinite momentum limit,  $x_\gamma^{obs}$  is equivalent to Bjorken  $x$  of the parton in the photon.

$\Delta\phi^{jj}$  is the difference in  $\phi$  from the highest  $E_T^{jet}$  jet to the second highest  $E_T^{jet}$  jet (eq. 4.28)

$$\Delta\Phi^{JJ} = \phi^{jet1} - \phi^{jet2} . \quad (4.28)$$

Figure 4.22 is an event display showing an event with a small  $\Delta\phi^{jj}$ .



**Figure 4.22** Event display showing an event with a small  $\Delta\phi^{jj}$ . The Jets are shown by the arrowed lines.

$p_T^{jj}$  is the vector sum of the transverse momenta of the two highest  $E_T^{jet}$  jets,

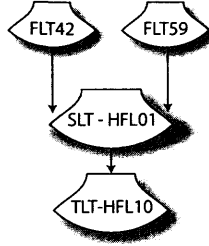
$$p_T^{jj} = \sqrt{(p_{x,1}^{jet} + p_{x,2}^{jet})^2 + (p_{y,1}^{jet} + p_{y,2}^{jet})^2} . \quad (4.29)$$

$m^{jj}$  is the Mass of the dijet system,

$$M^{jj} = \sqrt{2E_T^{jet1} E_T^{jet2} [\cosh(\eta^{jet1} - \eta^{jet2}) - \cos(\phi^{jet1} - \phi^{jet2})]} . \quad (4.30)$$

## 4.8 Summary of the offline selection cuts

- Trigger:



- Photoproduction selection:

- No electron candidate (Sinistra electron finder probability  $> 0.9$  &  $y_{el} < 0.7$ ),
- $|z_{vtx}| < 50$  cm,  $130 < W_{\gamma p} < 280$  GeV

- $D^{*\pm}$  selection:

- $p_T^{\pi_s} > 0.12$  GeV,  $p_T^{\pi, K} > 0.4$  GeV,  $|\eta^{track}| < 1.75$
- $p_T^{D^*} > 3.0$  GeV,  $|\eta^{D^*}| < 1.5$
- $1.80 < m(D^0) < 1.92$  GeV
- $0.143 < \Delta M (m(D^*) - m(D^0)) < 0.148$  GeV

- Jet Selection; one or more jets with:

- $E_T^{jet} > 6$  GeV,  $-1.5 < \eta^{jet} < 2.4$

- Luminosity used: 1998-2000 Data  $\rightarrow 78 pb^{-1}$

For Dijets the same except

- Jet Selection; two or more jets with:

- $E_T^{jet1} > 7$  GeV,  $-1.5 < \eta^{jet1} < 2.4$
- $E_T^{jet2} > 6$  GeV,  $-1.5 < \eta^{jet2} < 2.4$

---

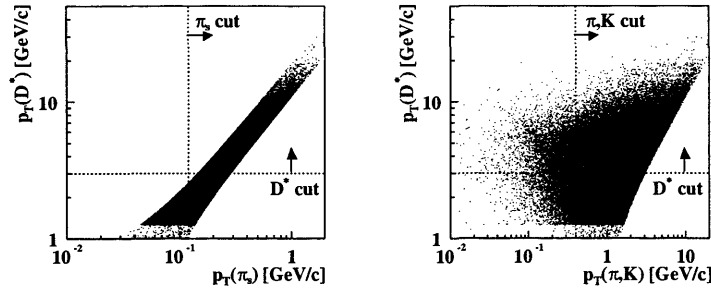
## 5 Characteristics of charm jet events

---

In this chapter the event properties of charm with one or more jet(s) is discussed. More information on distributions of the underlying event and inclusive charm jet properties can be found in [58, 59, 60, 61]. Here the focus is mainly on charm and dijet events.

### 5.0.1 Decay of charmed hadrons

Figure 5.1 shows the correlation of the  $p_T^{D^*}$ ,  $p_T(\pi_s)$  and  $p_T(\pi, K)$  from HERWIG at hadron level. There is a strong correlation between  $p_T^{D^*}$  and  $p_T(\pi_s)$ . It can be seen that once the cut is applied to the  $p_T^{D^*}$ , indicated by the dashed line, no further events are removed at hadron level by the  $p_T(\pi_s)$  cut. However this distribution is smeared across the boundaries of these cuts by the finite resolution of the detector. There is no strong correlation between the  $p_T^{D^*}$  and  $p_T(\pi, K)$ .



**Figure 5.1** The correlation of the  $p_T^{D^*}$  and its decay products. The left plot shows the correlation between the  $p_T^{D^*}$  and  $p_T(\pi_s)$ , the right hand plot shows the correlation between the  $p_T^{D^*}$  and  $p_T(\pi, K)$ , with the dashed lines indicating the cuts on the transverse momenta.

## 5.1 Signal and background Monte Carlo samples

The MC programs HERWIG 6.301 [20, 21] and PYTHIA 6.156 [25], which implement leading-order matrix elements, followed by parton showers and hadronisation, were used to model the final state. See (section 2.5.1) for more details. Direct and resolved events were generated separately and in proportion to the cross sections predicted by the MC programs. The relative fraction of charm and beauty events was also generated in proportion to the cross sections predicted by the MC programs. Events were generated using CTEQ5L [62] and GRV-G LO [63] parton density functions (PDF) for the proton and the photon, respectively.

### 5.1.1 Charm Sample

Charm quarks were generated and required to fragment into a  $D^{*\pm}$  meson in both HERWIG and PYTHIA, and eight decay modes of ( $c \rightarrow D$ ) were chosen in order to study charm decay (see table 5.1). The  $p_T$  cuts were placed on these decay modes to generate Monte Carlo efficiently in the kinematic region required to make the measurement. The  $c$ -quark mass was set to  $m_c = 1.5$  GeV.

Decay Modes	$p_T$ cut [GeV]
$D^{*+} \rightarrow D^0 \pi_s^+ \rightarrow K^- \pi^+ \pi_s^+$	1.25
$D^{*+} \rightarrow D^0 \pi_s^+ \rightarrow K_0^S \pi^+ \pi^- \pi_s^+$	1.35
$D^{*+} \rightarrow D^0 \pi_s^+ \rightarrow K^- \pi^+ \pi^+ \pi^- \pi_s^+$	2.3
$D^0 \rightarrow K^- \pi^+$	2.6
$D_s^+ \rightarrow K^+ K^- \pi^+$	1.7
$D^+ \rightarrow K^+ K^- \pi^+$	1.7
$D^+ \rightarrow K^- \pi^+ \pi^+$	2.8
$\Lambda_c^+ \rightarrow p K^- \pi^+$	2.8

**Table 5.1** Decay modes generated in HERWIG and PYTHIA Monte Carlo samples.

### 5.1.2 Beauty Sample

A  $D^*$  meson can also be produced from the decay of B-mesons. The contribution from  $b$ -quark production is estimated by the Monte Carlo. The  $b$  fraction is about 3% at low  $E_T^{\text{jet}}$  and increases as  $E_T^{\text{jet}}$  becomes larger and as  $p_T^{D^*}$  becomes smaller. The contribution is smaller than the statistical uncertainty in most bins. Due to the large theoretical uncertainty in  $b$ -quark production the contribution from  $b$ -quarks has to be handled in a consistent way when added to the NLO ‘massive’ charm prediction as described below.

An NLO prediction of  $D^*$  production for beauty is not available so this contribution was estimated using a combination of the  $B$  hadron cross section at NLO and  $B$  decays in PYTHIA. The  $p_T$  distributions of the two stable  $B$  hadrons produced in the PYTHIA MC programme were re-weighted to the distribution in the NLO calculation. In the NLO calculation, the  $b$ -quark mass,  $m_b$  was set to 4.75 GeV,  $\mu = m_T = \sqrt{\langle p_T^b \rangle^2 + m_b^2}$  and  $\epsilon = 0.0035$  [64]. The upper (lower) bound of the NLO QCD prediction was estimated by setting  $\mu_R = m_T/2$  and  $m_b = 4.5$  GeV ( $\mu_R = 2m_T$  and  $m_b = 5.0$  GeV). The contribution from beauty production for the inclusive jet distribution, as predicted by NLO+PYTHIA, is about 3% at low  $E_T^{\text{jet}}$  and increases to 12% at high  $E_T^{\text{jet}}$ . For each cross section, this beauty contribution was added linearly to the massive  $D^*$  prediction from charm quarks. The gluon splitting contribution, using MC predictions, was found to be negligible even at the highest  $E_T^{\text{jet}}$  measured.

## 5.2 Comparison between data and Monte Carlo simulation

After generating the final state partons using the Monte Carlo generators they are input into the detector simulation. The simulation is performed by the MOZART program which is based on GEANT3.13 package [65]. The MOZART program simulates the way in which the particles interact with the different types of material within the detector, simulating the response of the detector including the magnetic fields as well as this trigger simulations. The same event reconstruction as in the data is used to fully reconstruct what is seen in the detector.

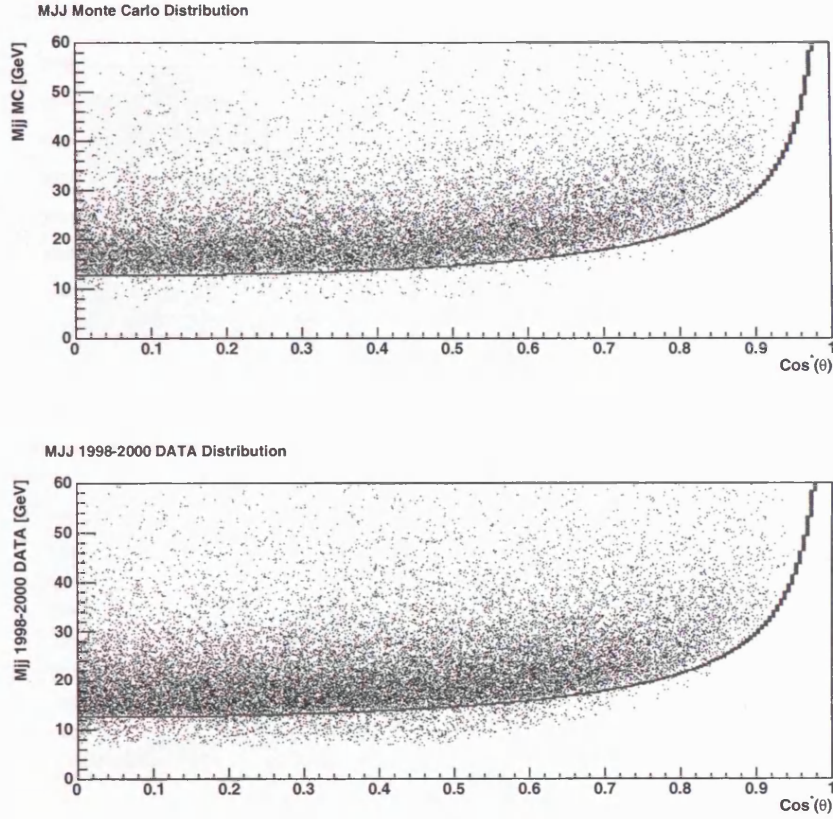
### 5.2.1 Reconstruction of $\cos\theta^*$ and $m^{jj}$

The invariant mass of the two jets with the highest  $E_T^{\text{jet}}$  in the event has been reconstructed using the corrected jet transverse energies and jet angular variables according to the formula 4.30

and

$$\cos\theta^* = \tanh\left(\frac{\eta^{\text{jet}1} - \eta^{\text{jet}2}}{2}\right). \quad (5.1)$$

The effect of the  $E_T^{\text{jet}}$  and  $\eta^{\text{jet}}$  cuts on the  $(m^{jj} - \cos\theta^*)$  plane is shown in (fig. 5.2), with the solid line being the same in both top and bottom plots to guide the eye, showing that this phase space effect is well modeled in the Monte Carlo. Due to the resolution of these variables some points are smeared and lie outside the plane.

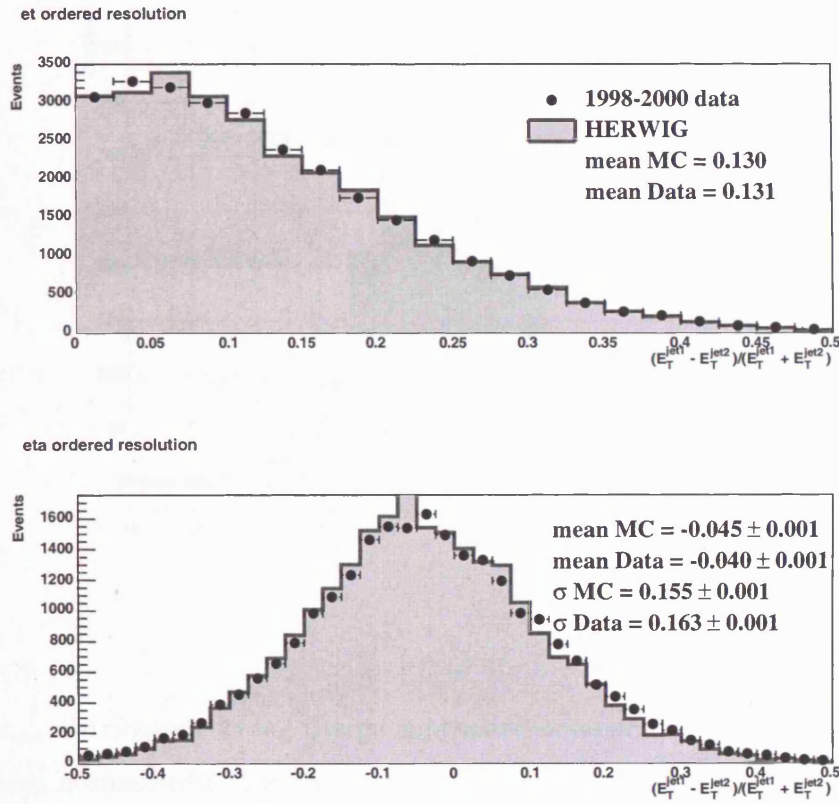


**Figure 5.2** The  $m^{jj} - \cos\theta^*$  plane shown for HERWIG Monte Carlo (top plot) and data (bottom plot), the red line in both plots is the same and is a parameterisation which can be used to guide the eye.



## 5.2.2 Jet energy balance

Figure 5.3 (not wrong charge subtracted) shows the distributions  $(E_T^{jet1} - E_T^{jet2})/(E_T^{jet1} + E_T^{jet2})$  where  $E_T^{jet1}(E_T^{jet2})$  is the highest (second highest) transverse energy jet. This check shows that the Monte Carlo well reproduces the energy balance of the two highest transverse energy jets. The second distribution  $(E_T^{jet1} - E_T^{jet2})/(E_T^{jet1} + E_T^{jet2})$  is plotted for data and Monte Carlo where  $E_T^{jet1}(E_T^{jet2})$  are the largest (second largest)  $\eta^{jet}$ . This also shows that the dijet systems are well modeled by the Monte Carlo.

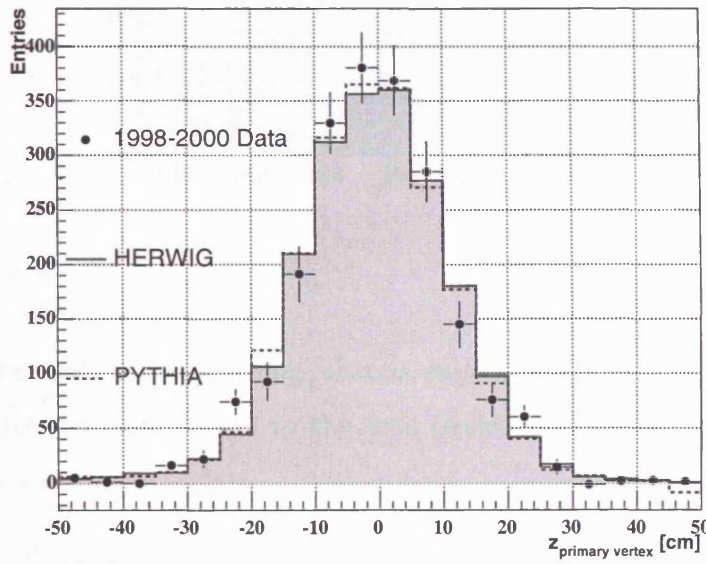


**Figure 5.3** Dijet distribution for  $(E_T^{jet1} - E_T^{jet2})/(E_T^{jet1} + E_T^{jet2})$ , where for the top plot  $E_T^{jet1}(E_T^{jet2})$  is the highest (second highest) transverse energy jets, and for the bottom plot the  $E_T^{jet1}(E_T^{jet2})$  are the largest (second largest)  $\eta^{jet}$ .



### 5.2.3 Event variable modeling

In order to have confidence in unfolding cross sections the kinematics of the event variables used to select the final sample of events must be modeled well. Figure 5.4 shows the event  $z_{vtx}$  as modeled by HERWIG and PYTHIA area normalised to the data distribution (shown as solid dots). There is also a good description of the photon proton center of mass  $W_{JB}$  as shown in (fig. 5.5).

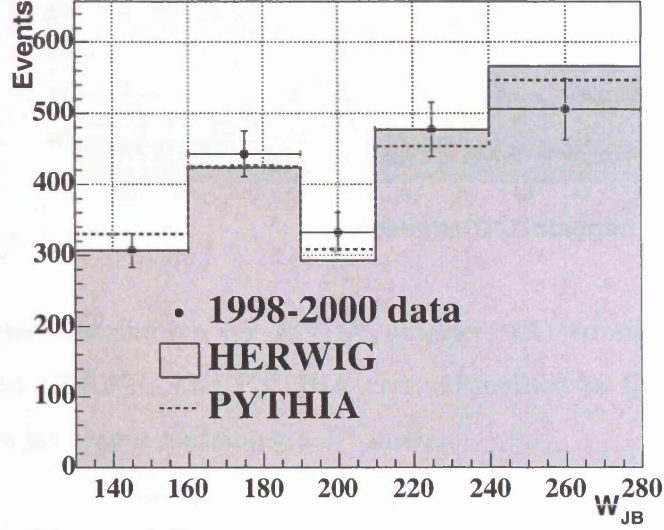


**Figure 5.4**  $z_{vtx}$  distribution wrong charge subtracted compared to HERWIG and PYTHIA area normalised to the data (solid dots) for dijet events containing a  $D^*$  meson.

The comparison plot for  $x_\gamma^{\text{obs}}(D^*, \text{untagged jet})$  (section 4.4.13) between HERWIG and PYTHIA is shown in (fig. 5.6), and the shape is well described by the Monte Carlo.

Figure 5.7 shows the transverse momentum distributions for  $\pi, K$  and  $\pi_s$  compared to HERWIG and PYTHIA. These are background subtracted using the wrong charge method [66]. All distributions agree well although HERWIG reproduces the shape of the data in  $\eta$  distributions slightly better. Figure 5.8 shows the distributions for  $p_T^{D^*}$  and  $\eta^{D^*}$  compared in the same way; again there is reasonable agreement between the data and Monte Carlo models.

The jet quantities  $E_T^{\text{jet}}$ ,  $\eta^{\text{jet}}$  and  $\phi^{\text{jet}}$  were also checked and are shown to agree well in shape

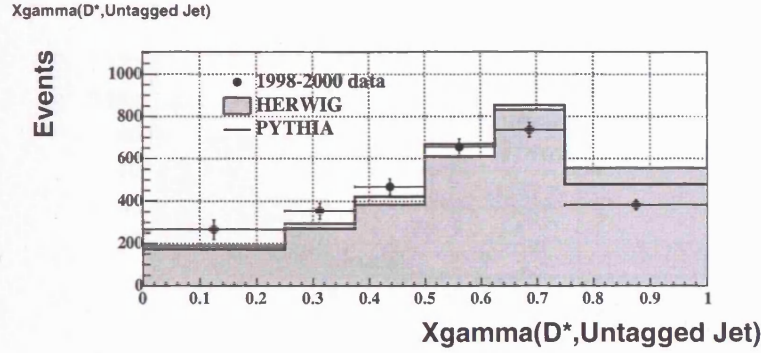


**Figure 5.5** Distributions of  $W_{jb}$  wrong charge subtracted compared to HERWIG and PYTHIA area normalised to the data (solid dots) for dijet events containing a  $D^*$  meson.

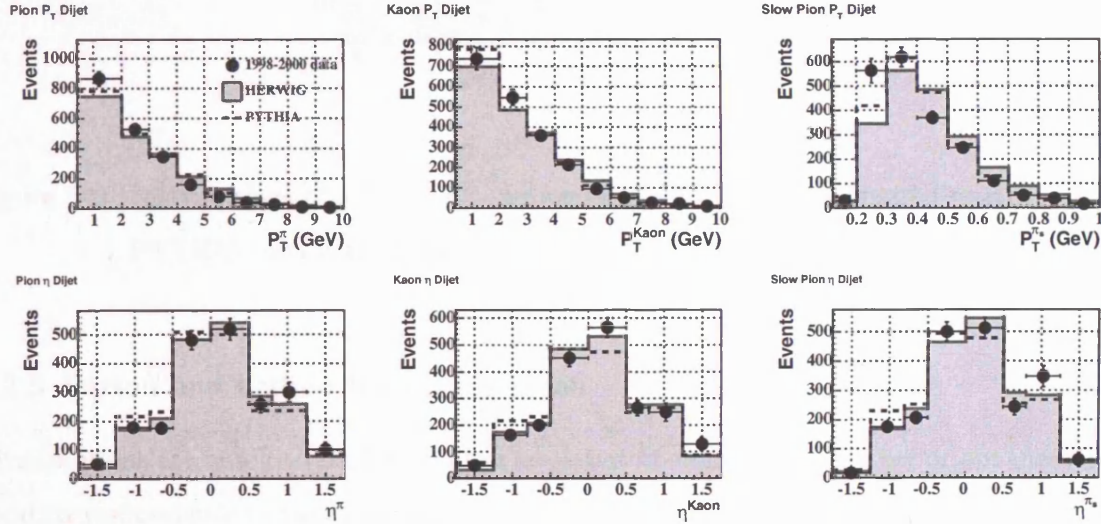
for both the Monte Carlo's compared to the data, (see fig. 5.9 for the dijet sample). Also the dijet variables to be measured (fig. 5.10) show good agreement with HERWIG having a much better description of  $\Delta\phi^{jj}$  and  $p_T^{jj}$  of the dijet system than PYTHIA.

#### 5.2.4 The separation power of direct-enriched and resolved-enriched events using $x_\gamma^{\text{obs}}(D^*, \text{untagged jet})$ and $x_\gamma^{\text{obs}}$

The separation between direct and resolved events can be seen for the 'traditional'  $x_\gamma^{\text{obs}}$  in (fig. 5.11) and for  $x_\gamma^{\text{obs}}(D^*, \text{untagged jet})$  in (fig. 5.12). There is a clear separation of direct events from resolved events in both variables, with  $x_\gamma^{\text{obs}}$  separation being at 0.75 which is the cut used in this analysis also shown in the (fig. 5.11) and (fig. 5.12) by the vertical green dashed line. The separation power for  $x_\gamma^{\text{obs}}(D^*, \text{untagged jet})$  can also clearly be seen but is at lower values of  $x_\gamma^{\text{obs}}(D^*, \text{untagged jet})$  than for  $x_\gamma^{\text{obs}}$ , at around 0.6. By taking the  $D^*$  alone any energy in an associated jet is not used in the calculation. The advantage of this variable is that



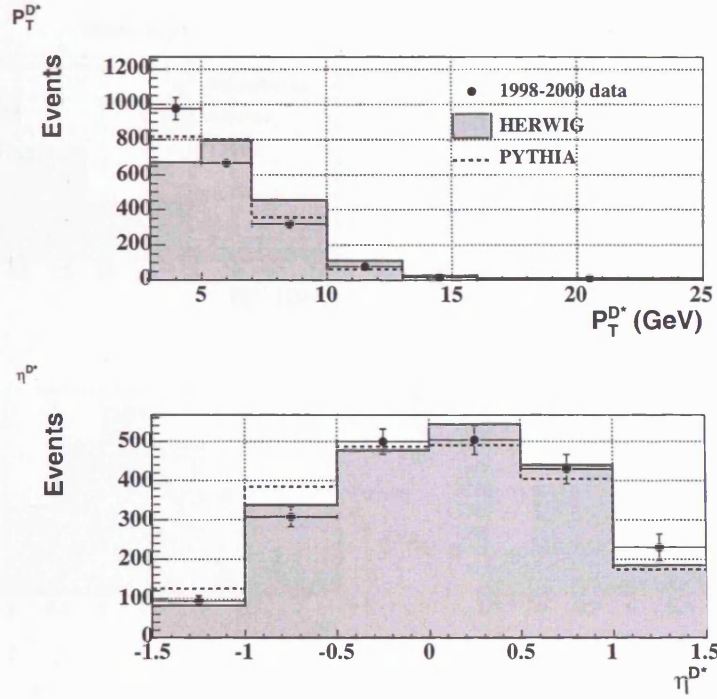
**Figure 5.6** Reconstructed distribution for  $x_{\gamma}^{\text{obs}}(D^*, \text{untagged jet})$  wrong charge subtracted compared to HERWIG and PYTHIA area normalised to the data (solid dots) for inclusive jet events containing a  $D^*$  meson.



**Figure 5.7** Distributions of transverse momentum and pseudo-rapidity of the  $D^*, K, \pi$  and  $\pi_s$ , wrong charge subtracted compared to HERWIG and PYTHIA area normalised to the data (solid dots) for dijet events containing a  $D^*$  meson.

the transverse energy that a  $D^*$  meson can be reconstructed to is much lower than that for jets, therefore yielding a large increase in statistics. This then allows for parton dynamics of charm production to be studied in more detail such as angular correlations between the  $D^*$  and jets. The separation power between direct events and resolved events is approximately the same, giving a similar insight into the production diagrams of photoproduction as in 'traditional'  $x_{\gamma}^{\text{obs}}$ .





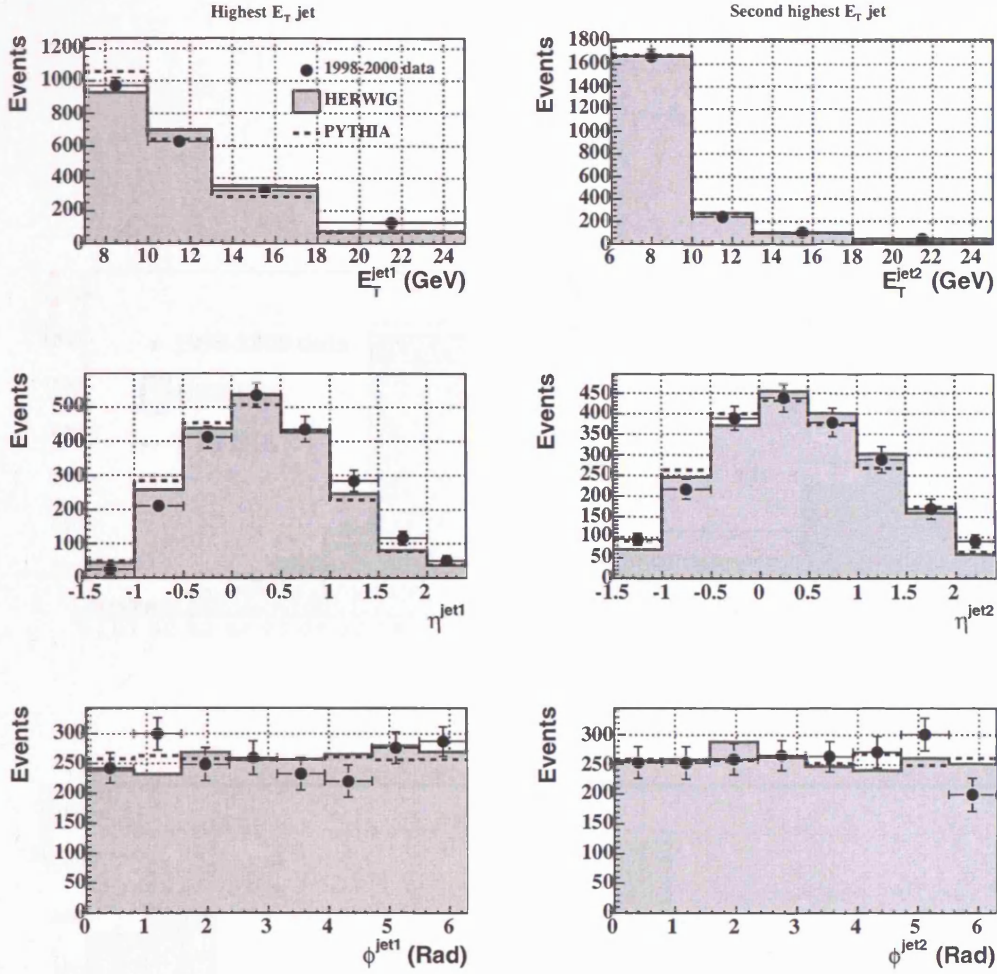
**Figure 5.8** Distributions of  $p_T^{D^*}$  and  $\eta^{D^*}$  wrong charge subtracted compared to HERWIG and PYTHIA area normalised to the data (solid dots) for dijet events containing a  $D^*$  meson.

### 5.2.5 Parton and hadron level comparison

Cross sections are unfolded back to hadron level, but in order to see whether or not these have a good correspondence to the original partons generated the resolutions are shown in (fig. 5.13). There are very good agreements for  $x_\gamma^{\text{obs}}$ ,  $\Delta\phi^{\text{jj}}$ ,  $p_T^{\text{jj}}$  and  $M^{\text{jj}}$  of the dijet system between parton and hadron levels. This then gives confidence that the cross sections unfolded back to hadron level give a good representation of the parton dynamics in the initial interactions.

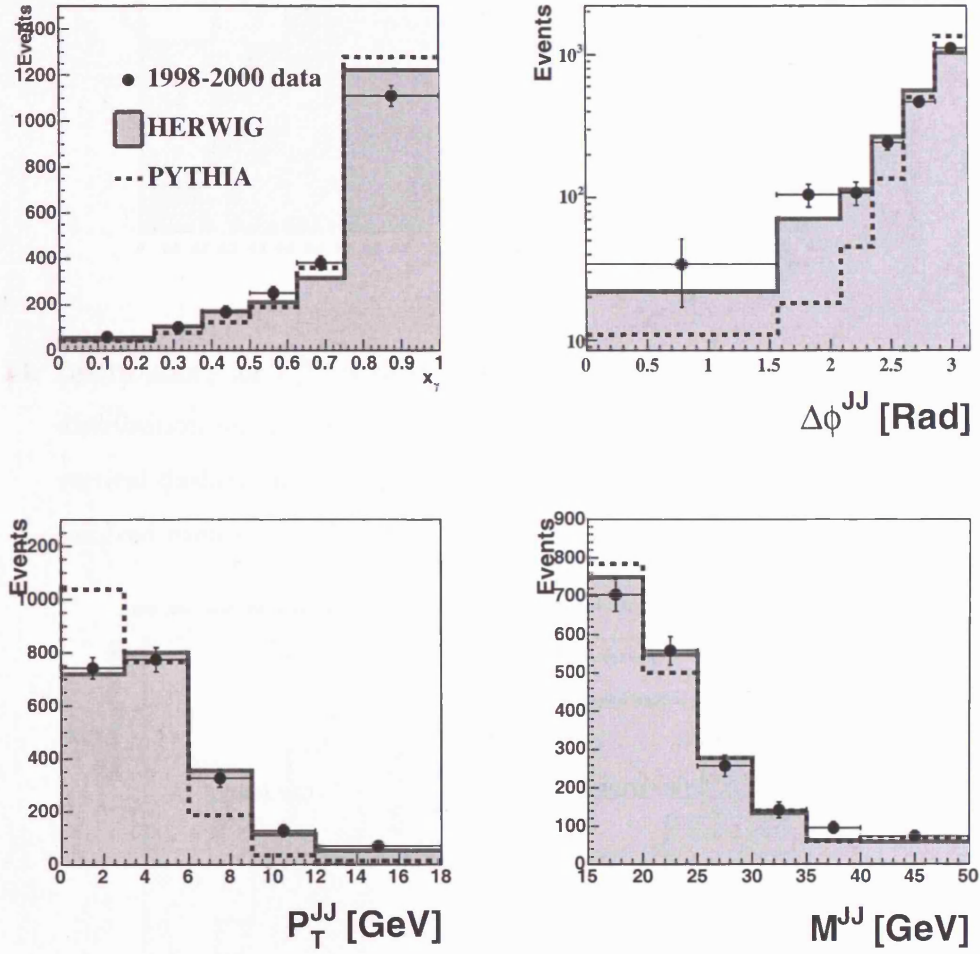
### 5.2.6 Hadronisation corrections for NLO calculations

As the NLO calculations produce final state partons, the effects of hadronisation are considered when comparing the predictions with the data. The NLO QCD predictions were corrected using a bin-by-bin procedure according to  $d\sigma = d\sigma^{\text{NLO}} \cdot C_{\text{had}}$ , where  $d\sigma^{\text{NLO}}$  is the cross section for parton jets in the final state of the NLO calculation. The hadronisation correction factor was defined as the ratio of the jet cross sections after and before the hadronisation process,



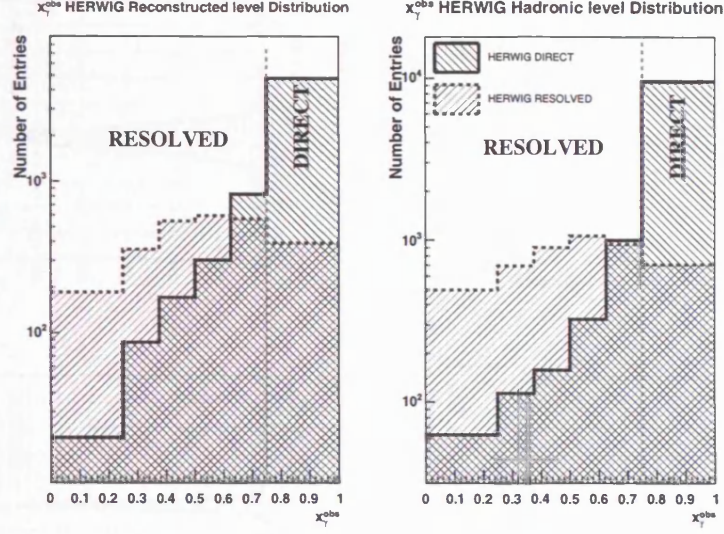
**Figure 5.9** Distributions of  $E_T^{\text{jet}}$ ,  $\eta^{\text{jet}}$  and  $\phi^{\text{jet}}$  for the two highest transverse energy jets in the event for events containing a  $D^*$  meson.

$C_{\text{had}} = d\sigma_{\text{MC}}^{\text{hadrons}}/d\sigma_{\text{MC}}^{\text{partons}}$ . Here, parton-level cross sections were obtained using partons after the initial- and final-state showering of the MC simulations described in (section 5.1). Distributions at the parton level in the MC programs were checked to be similar to those calculated using the NLO program, assuring the validity of using a bin-by-bin correction. The value of  $C_{\text{had}}$  was taken as the mean of the ratios obtained using the HERWIG and PYTHIA predictions. The uncertainty on this value was estimated as half the difference between the values obtained using the two models. These uncertainties were added in quadrature to the other uncertainties of the NLO calculations.

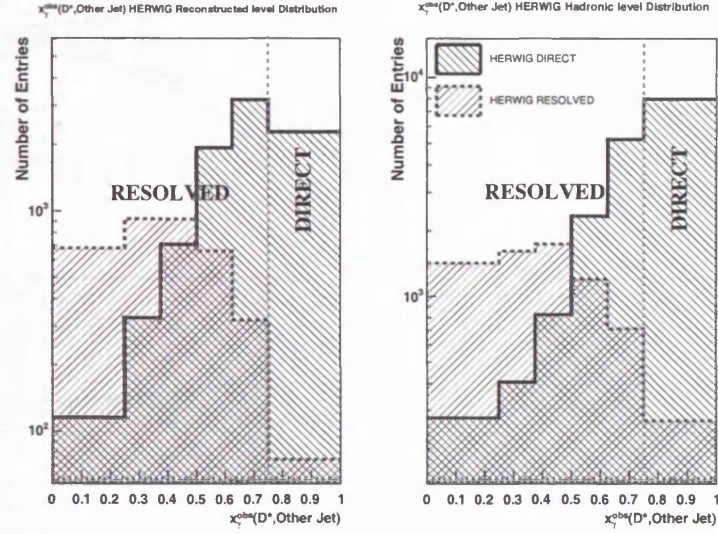


**Figure 5.10** Reconstructed distributions for  $x_\gamma^{\text{obs}}$ ,  $\Delta\phi^{\text{jj}}$ ,  $p_T^{\text{jj}}$  and  $M^{\text{jj}}$  wrong charge subtracted compared to HERWIG and PYTHIA area normalised to the data (solid dots) for dijet events containing a  $D^*$  meson.

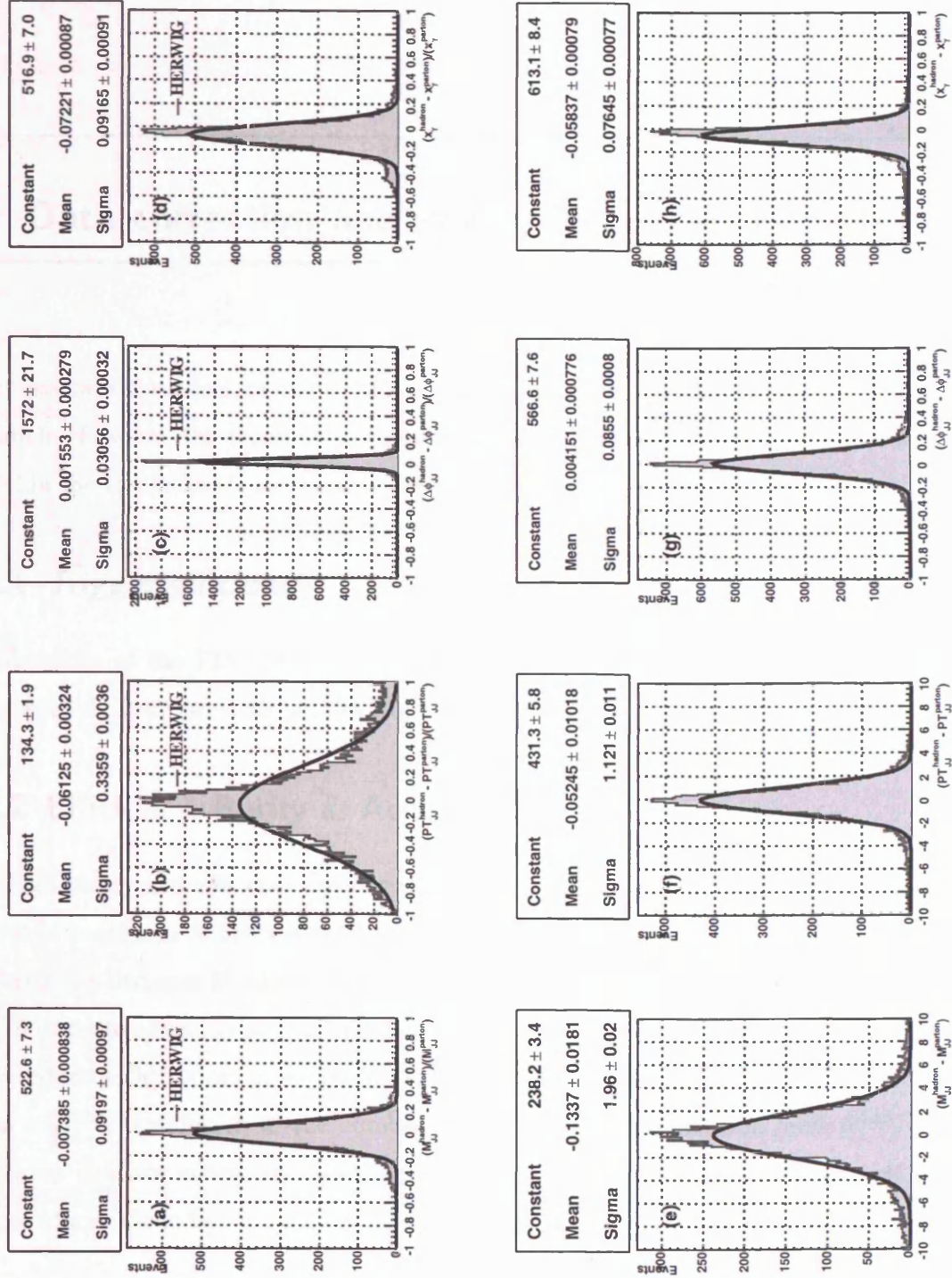




**Figure 5.11** Distributions for  $x_\gamma^{\text{obs}}$  for direct events and resolved events, at reconstructed level distribution on the left plot, and at hadron level on the right hand plot. The vertical dashed line is at 0.75 indicating the separation used between direct and resolved events.



**Figure 5.12** Distributions for  $x_\gamma^{\text{obs}}(D^*, \text{untagged jet})$  for direct events and resolved events, at reconstructed level distribution on the left plot, and at hadron level on the right hand plot. The vertical dashed line is at 0.75 indicating the separation used between direct and resolved events.



**Figure 5.13** Hadron level compared to parton level HERWIG distributions for  $x_{\gamma}^{\text{obs}}$ ,  $\Delta\phi_{JJ}^{\text{jj}}$ ,  $p_T^{\text{jj}}$  and  $M_{JJ}^{\text{jj}}$  showing  $(\frac{\text{hadron} - \text{parton}}{\text{parton}})$  for figures (a) - (d) and  $(\text{hadron} - \text{parton})$  for figures (e) - (h). All histograms are fitted with a Gaussian.



---

## 6 Data correction and systematic uncertainties

---

To estimate the effect of the resolution of the measured quantities used to select the final sample of events, the thresholds of these various cuts were moved positively and negatively, within the resolution of the variables shown in appendix F (section 18), [60].

### 6.1 Trigger efficiency

Efficiencies of the FLT, SLT and the TLT were found to be  $\sim 88\%$ ,  $\sim 97\%$  and  $\sim 100\%$  respectively from previous studies [60].

### 6.2 Efficiency, Purity & Acceptance

A high purity and efficiency ensures that the variable in question can be measured to a high level of precision. When the model does not describe the data, the correction for bin-to-bin migrations becomes Monte Carlo model dependent.

In order to obtain cross sections from detector level distributions by a bin-by-bin unfolding procedure with respect to a variable  $Y$  for example, the number of jets observed in a certain bin  $i$ ,  $N_i^{\text{obs}}$ , is unfolded to the number of jets in that bin at hadron level  $N_i^{\text{had}}$ , taking into account detector effects and selection efficiencies. The acceptance correction  $A_i$  is obtained from Monte Carlo by

$$A_i = \frac{N_i^{\text{obs}}}{N_i^{\text{had}}} . \quad (6.1)$$

HERWIG is used as the central Monte Carlo and PYTHIA is used as a cross check with the model dependence included in the systematic errors. The unfolding method of differential cross sections can be found in (section 7.2).

The efficiency,  $\mathcal{E}_i$ , and purity,  $\mathcal{P}_i$  are defined as

$$\mathcal{E}_i = \frac{N_i^{\text{had}\cap\text{obs}}}{N_i^{\text{had}}} \text{ and} \quad (6.2)$$

$$\mathcal{P}_i = \frac{N_i^{\text{had}\cap\text{obs}}}{N_i^{\text{obs}}} \quad (6.3)$$

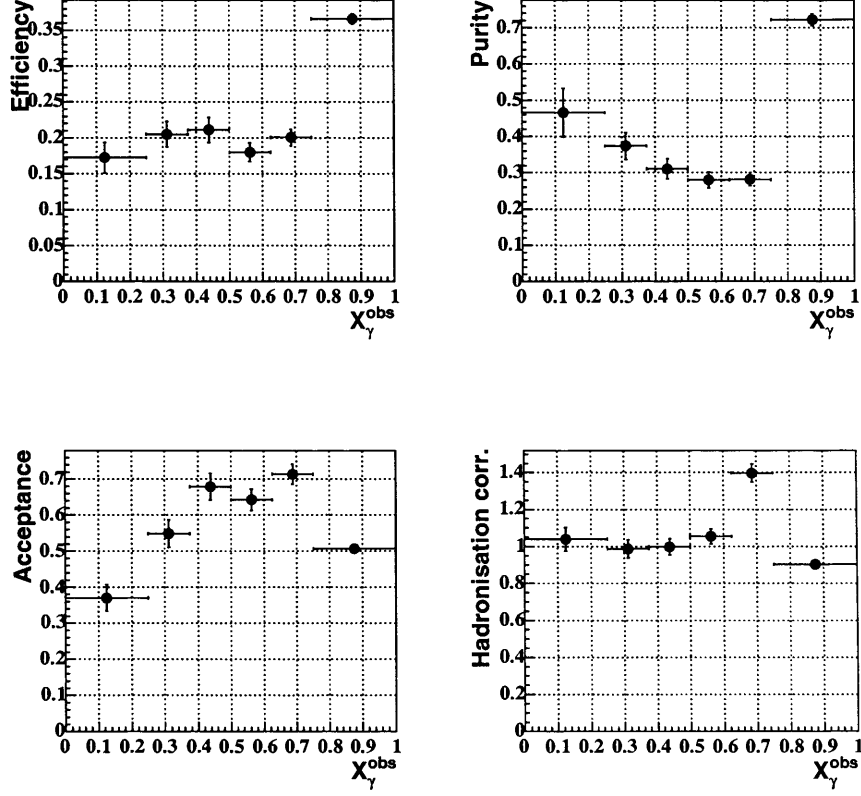
where  $N_i^{\text{had}\cap\text{obs}}$  is the number of events reconstructed in that bin and generated in that same bin of a given variable. The efficiency is the probability to reconstruct a jet in the same bin as the bin it was generated in. Purity represents the fraction of jets which were generated in that bin with respect to the number of reconstructed jets in that bin.

An example of an efficiency, purity and acceptance is show in (fig. 6.1) for the cross section  $d\sigma/dx_\gamma$ . All efficiencies, purities, and acceptance corrections can be seen in appendix C (section 15) for inclusive jets and appendix D (section 16) for dijets. For inclusive(dijets) jets the purity is typically 70%-80%(30%-40%) and the efficiency is 50%(25%) giving an acceptance of 40%-70% for both inclusive jets and dijets with charm.

### 6.3 Systematic uncertainties

The thresholds of these various cuts below were changed in both data and Monte Carlo, in order to determine the best estimate of systematic error calculable, some large errors reflect statistical effects, which could be taken into account in a more accurate estimation of the systematic error.

- $z_{vtx} \rightarrow \pm 5 \text{ cm}$
- $p_T^{\pi_s} \rightarrow \pm 0.02 \text{ GeV}$
- $p_T^\pi \rightarrow \pm 0.1 \text{ GeV}$
- $p_T^K \rightarrow \pm 0.1 \text{ GeV}$
- $\eta(\text{track}) \rightarrow \pm 0.05$
- $p_T^{D^{*\pm}} \rightarrow \pm 0.07 \text{ GeV}$
- $\eta^{D^*} \rightarrow \pm 0.05$



**Figure 6.1** Purity/efficiency/acceptance and hadronisation corrections for each bin of the dijet charm cross section  $d\sigma/dx_\gamma$  for HERWIG 886  $\text{pb}^{-1}$ .

- $E_T^{\text{jet}} \rightarrow \pm 1 \text{ GeV}$
- $\eta^{\text{jet}} \rightarrow \pm 0.07$
- $W_{JB} \rightarrow \pm 10 \text{ GeV}$

All of the errors from these sources were negligible.

The systematic uncertainties calculated are compared to the nominal cross sections ( $\sigma_0$ ) with all the nominal cuts described in the previous chapters. Once the cuts are changed in the Monte Carlo and data simultaneously a new cross section value is obtained ( $\sigma'_0$ ). For each of the systematic sources  $i$ , upper and lower systematical errors are calculated by

$$\Delta_i^+ = \begin{cases} \delta_i & (if \delta_i > 0) \\ 0 & (if \delta_i < 0) \end{cases} \quad (6.4)$$

$$\Delta_i^- = \begin{cases} 0 & (if \delta_i > 0) \\ \delta_i & (if \delta_i < 0) \end{cases} \quad (6.5)$$

where  $\delta_i$  is the deviation from the nominal cross section given by

$$\delta_i = \sigma'_0 - \sigma_0. \quad (6.6)$$

All the errors except for the  $E_T^{\text{jet}}$  correction, and jet energy scale, are then summed in quadrature giving the total systematic errors per bin of

$$\Delta^+ = \sqrt{\sum_i (\Delta_i^+)^2} \text{ and} \quad (6.7)$$

$$\Delta^- = -\sqrt{\sum_i (\Delta_i^-)^2}. \quad (6.8)$$

### 6.3.1 $D^0$ mass width systematic

Since HERWIG (the central MC) does not have all the decay modes for the  $D^0$  included in this Monte Carlo sample used, the systematic error arising from changing the width of the  $D^0$  is not well simulated. Figure 6.2 shows the  $D^0$  mass peak from HERWIG.

Figure 6.3 shows the  $M(K\pi)$  spectrum for the PYTHIA sample of  $350 \text{ pb}^{-1}$  and (fig. 6.4) shows the data. The main difference between the simulations arises because the decay mode  $D^0 \rightarrow K^\pm, \pi^\mp, \pi^0$  is not simulated by HERWIG which contributes to the signal of  $D^0 \rightarrow K^\pm, \pi^\mp$  in the data.

Figure 6.5 shows what happens to the  $\Delta M$  peak for HERWIG, PYTHIA and the data when lowering the cut on the left of the  $D^0$  peak from  $1.80 < M(K\pi) < 1.92 \text{ GeV}$  to  $1.76 < M(K\pi) < 1.92 \text{ GeV}$ .

This effect is summarised in (fig. 6.6) and (fig. 6.7), which shows how the number of  $D^*$  extracted from data and the Monte Carlo behave when moving this lower mass  $M(K\pi)$  cut, in increments of  $0.0025 \text{ GeV}$  with the first bin being the original distribution at  $1.8 < M(K\pi) < 1.92 \text{ GeV}$

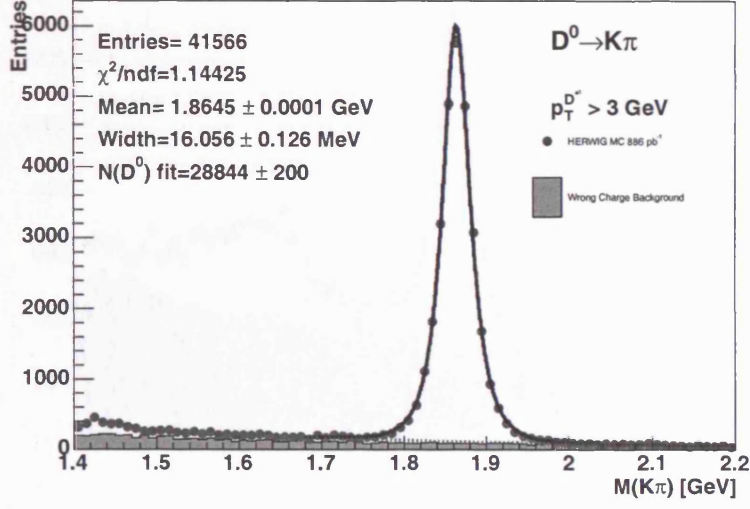


Figure 6.2 HERWIG  $D^0$  mass peak

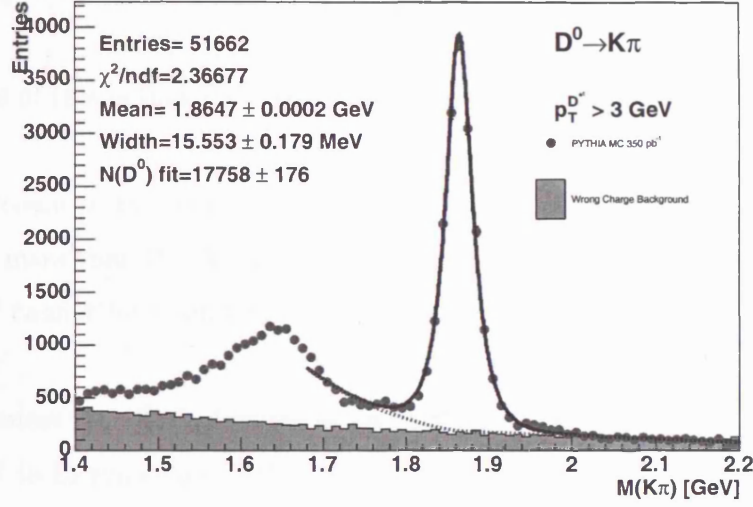
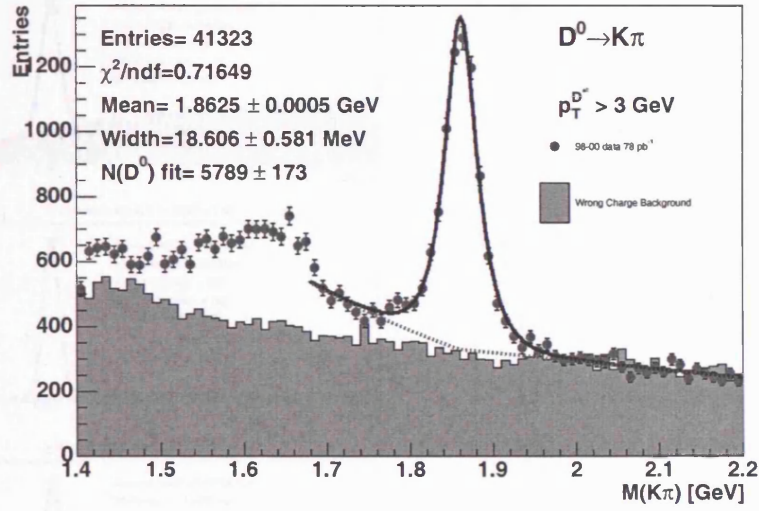


Figure 6.3 PYTHIA  $D^0$  mass peak

until the second last bin in the range from  $1.78 < M(K\pi) < 1.92$  GeV, with the final bin being in the range  $1.76 < M(K\pi) < 1.92$  GeV.

There is hardly any change in the number of  $D^*$  from this change in HERWIG where in the data there is an increase as this cut is lowered. A rise is also observed in PYTHIA, showing



**Figure 6.4** 98 – 00 data 78 pb<sup>-1</sup>,  $D^0$  mass peak

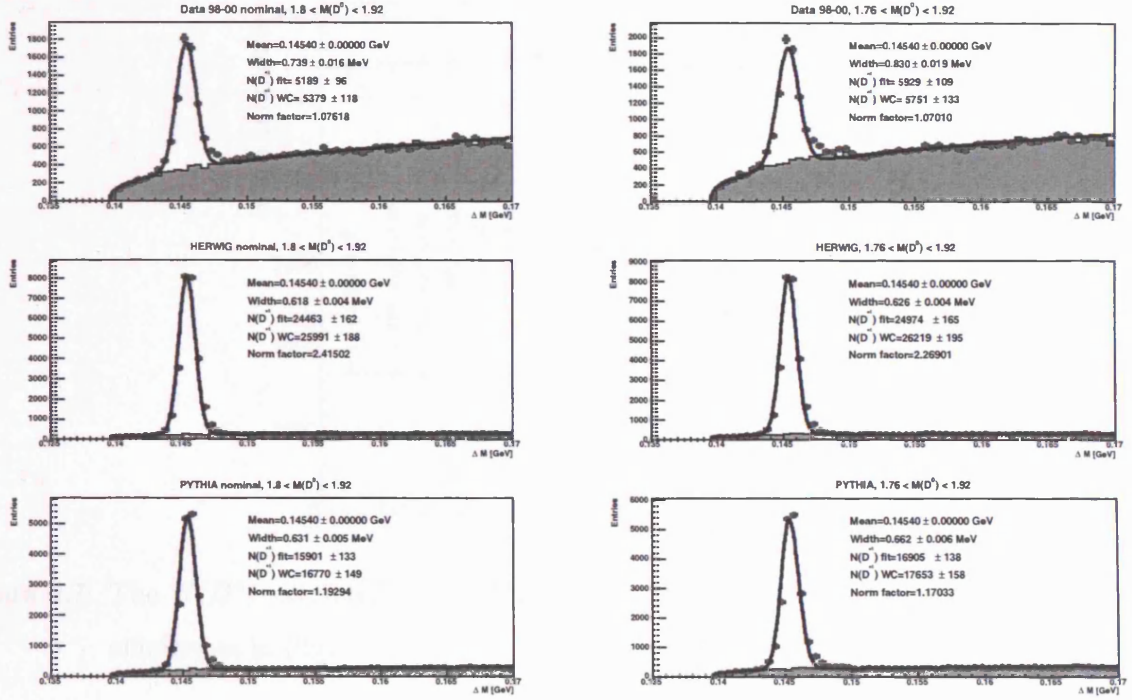
better modeling of the background and peak positions.

The outcome of this is that PYTHIA is used for the  $D^0$  mass window systematic.

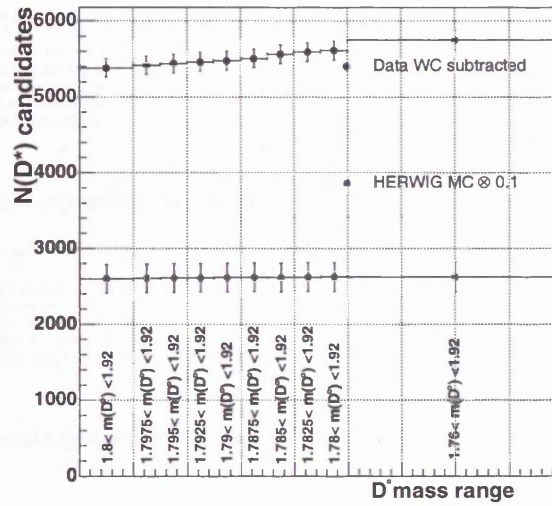
Another outcome of this study is that from (fig. 6.5) the secondary peak emerging at a slightly higher mass than the  $\Delta M$  peak can be attributed to the decay of  $D^0 \rightarrow K^\pm, \pi^\mp, \pi^0$  because the  $\pi^0$  cannot be reconstructed within the ZEUS detector.

For completeness the effect of widening the  $1.80 < M(K\pi) < 1.92$  GeV cut on the right from 1.92 GeV in increments of 0.0025 GeV, this is summarised in (fig. 6.9) and (fig. 6.10) with the first bin being the number of  $D^*$  extracted from data and the Monte Carlo in the original distribution at  $1.8 < M(K\pi) < 1.92$  GeV until the second last bin in the range from  $1.8 < M(K\pi) < 1.94$  GeV, with the final bin being in the range  $1.8 < M(K\pi) < 1.96$  GeV. The  $\Delta M$  distributions (fig. 6.8) are show for the data, HERWIG and PYTHIA in the mass ranges  $1.80 < M(K\pi) < 1.92$  GeV and  $1.8 < M(K\pi) < 1.96$  GeV.

### 6.3 Systematic uncertainties

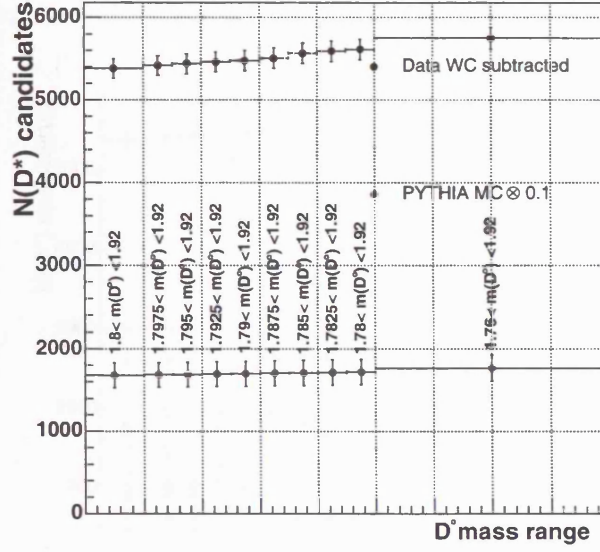


**Figure 6.5**  $\Delta M$  mass peaks for 98-00 data (top), HERWIG (middle) and PYTHIA (bottom) Monte Carlo's. Left column is for the mass range  $1.80 < M(K\pi) < 1.92$  GeV, and the right column is for the mass range  $1.76 < M(K\pi) < 1.92$  GeV.

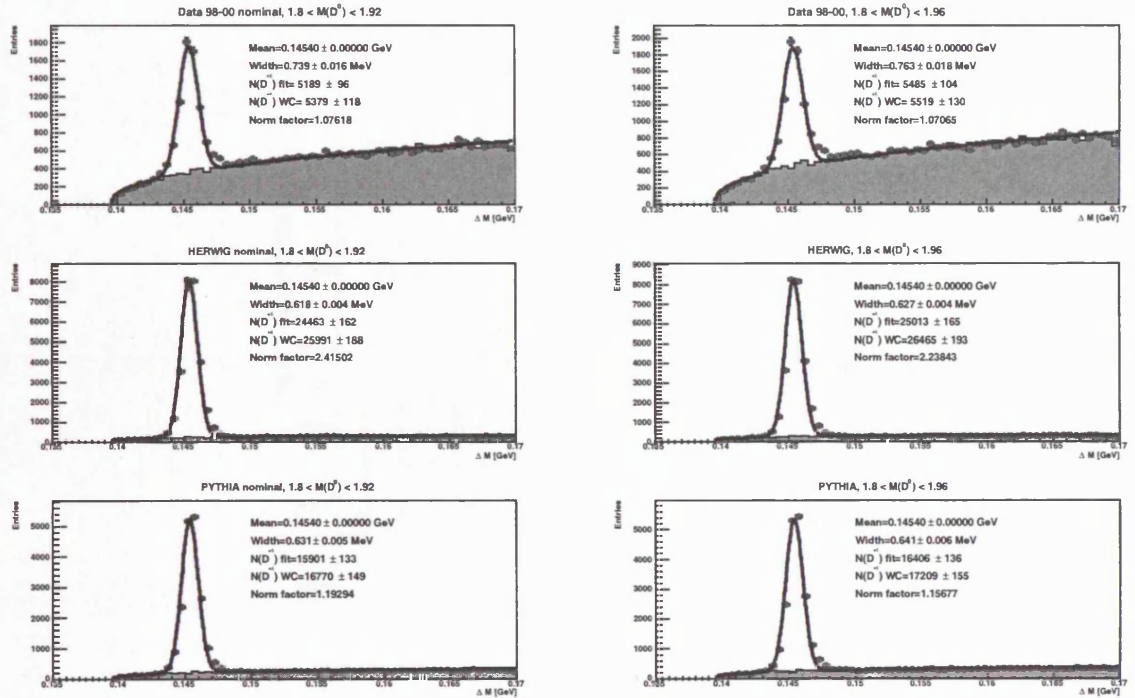


**Figure 6.6** The  $N(D^*)$  extracted from HERWIG and the data when changing the  $D^0$  mass window as in (fig. 6.5).



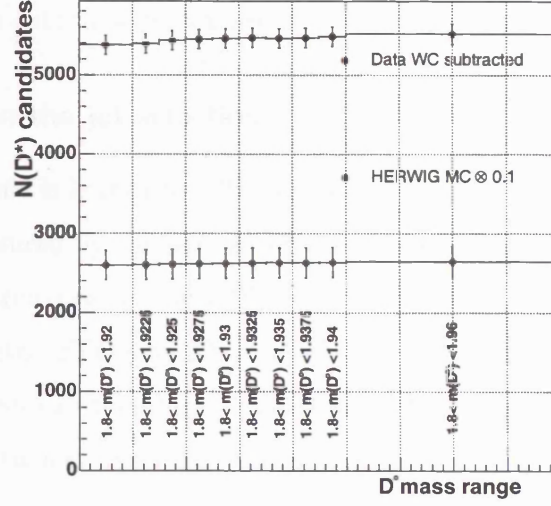


**Figure 6.7** The  $N(D^*)$  extracted from PYTHIA and the data when changing the  $D^0$  mass window as in (fig. 6.5).

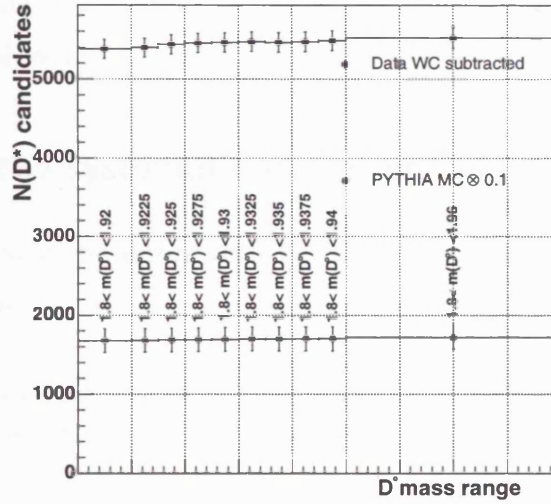


**Figure 6.8**  $\Delta M$  mass peaks for 98-00 data (top), HERWIG (middle) and PYTHIA (bottom) Monte Carlo's. Left column is for the mass range  $1.80 < M(K\pi) < 1.92$  GeV, and the right column is for the mass range  $1.8 < M(K\pi) < 1.96$  GeV.





**Figure 6.9** The  $N(D^*)$  extracted from HERWIG and the data when changing the  $D^0$  mass window as in (fig. 6.8).



**Figure 6.10** The  $N(D^*)$  extracted from PYTHIA and the data when changing the  $D^0$  mass window as in (fig. 6.8).

Figure 6.11 shows an example of the systematic checks performed on  $d\sigma/dx_\gamma^{\text{obs}}$ , the check performed is labeled within each figure, the open dots being a shift down to narrower cuts and solid points opening the cuts to wider values.

### 6.3.2 Uncertainties in the jet selection

The hadronic energy scale is known to  $\pm 2\%$  over an  $E_T$  of 10 GeV and to  $\pm 3\%$  below an  $E_T$  of 10 GeV. This is measured by comparing the transverse energy of the jet(hadronic system) with the scattered electron/positron in DIS events. This effect is evaluated by changing the energy scale of calorimetric EFO's by 3% in the MC. The measured  $E_T$  in the data can also be changed and this effect can then be estimated from the data, but due to small statistics in the high  $E_T^{\text{jet}}$  region statistical uncertainty contributes.

### 6.3.3 Uncertainties of the statistical signal extraction

The signal extraction was changed from wrong charge subtraction to the fit comprising of a Gaussian and threshold function in order to fit the signal and background simultaneously.

### 6.3.4 Uncertainty of the luminosity measurement

The luminosity measurement is accurate to 2%. This is not included in the quoted systematic uncertainty, and is not shown in any cross sections.

## 6.4 Summary of the systematic uncertainties

The main sources of systematic errors with the resulting uncertainty on the cross sections given in parentheses, are

- varying the values of the selection cuts by the experimental resolutions in the corresponding quantity ( $+2.7\%$ );
- varying the efficiencies of the CAL first-level trigger (4.1%).
- the acceptance was recalculated by re-weighting the prediction from the HERWIG MC simulation in  $p_T^{D^*}/E_T^{\text{jet}}$  to reproduce the distribution of this variable in the data (5.0%);

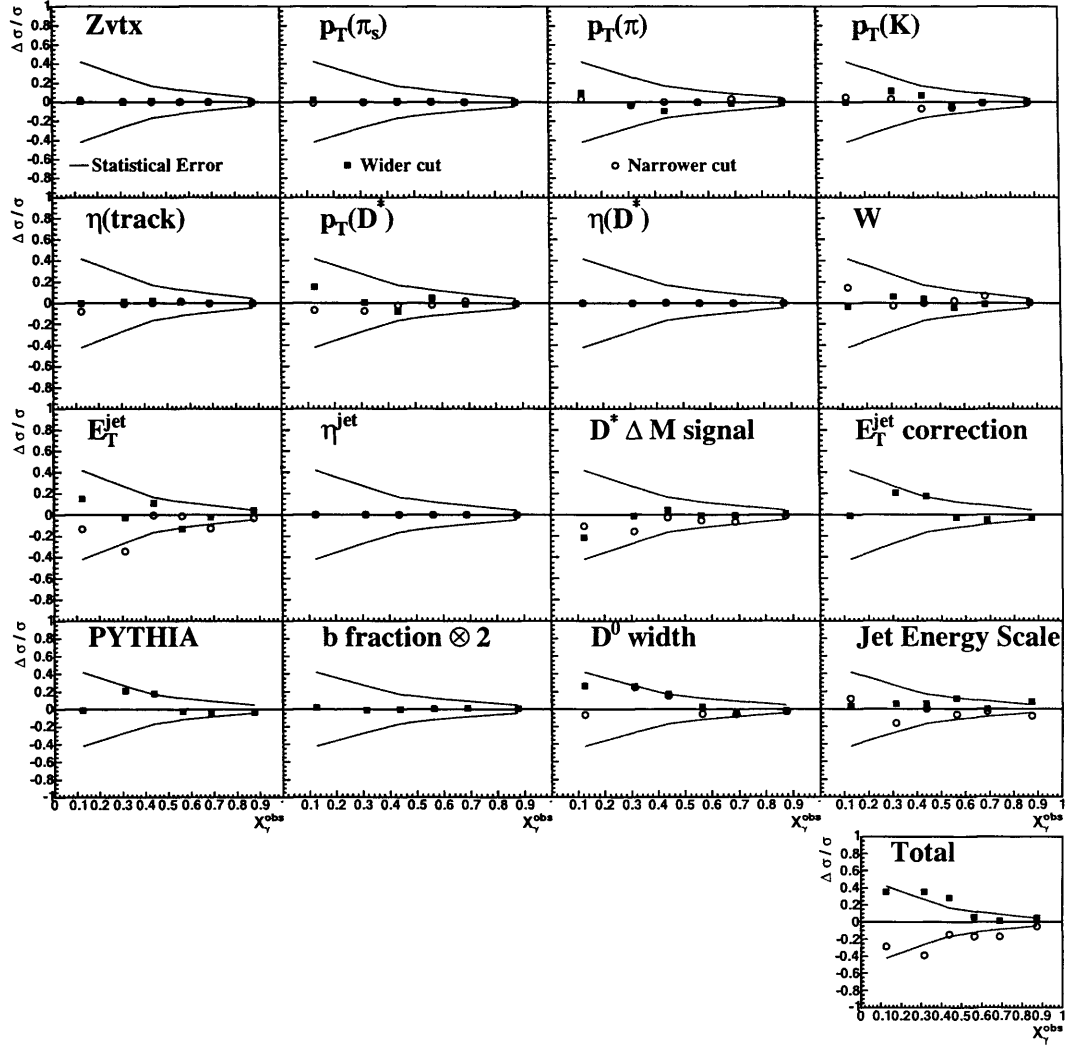
#### 6.4 Summary of the systematic uncertainties

---

- the uncertainty from the modeling of the hadronisation process was estimated by using PYTHIA instead of HERWIG (0.4%);
- the effect of the uncertainty of the beauty cross section on the acceptance correction was taken into account by increasing the beauty contribution by a factor two ( $< \pm 1\%$ );
- varying the the procedure to extract the  $D^*$  signal ( $^{+1.3}_{-2.9}\%$ );
- the uncertainty scale of the jet energy scale in the CAL is known to be within 3%. Therefore the CAL EFOs input to the jet finder were varied by  $\pm 3\%$  leaving the EFOs which are tracks the same ( $^{+2.7}_{-2.5}\%$ ).

The jet energy scale uncertainty is shown separately in all figures and is not added in quadrature because of the large correlation between bins.

The other systematic uncertainties were added in quadrature to obtain the total systematic uncertainty. In most bins of the differential cross sections, the total systematic uncertainty is comparable to the statistical errors.



**Figure 6.11** Systematics for each bin of the dijet charm cross section  $d\sigma/dx_\gamma^{\text{obs}}$  for 1998-2000 data  $78\text{pb}^{-1}$ ,  $886\text{pb}^{-1}$  of HERWIG MC and  $350\text{pb}^{-1}$  of PYTHIA MC

---

## 7 Inclusive charm & jets

---

In this chapter the cross section measurements of events containing charm and one or more jets (the inclusive charm and jet(s) sample) are analysed and compared to NLO QCD predictions. The method to unfold the cross sections from the detector level distributions is described below. More details on these measurements can be found here [59, 58, 60, 61].

### 7.1 Definition of the cross sections

Inclusive cross sections with a  $D^*$  meson in the final state are measured as a function of  $E_T^{\text{jet}}$ ,  $\eta^{\text{jet}}$  and the pseudo  $x_\gamma^{\text{obs}}(D^*, \text{untagged jet})$ . The cross sections measured are  $d\sigma/dE_T^{\text{jet}}$ ,  $d\sigma/d\eta^{\text{jet}}$  and  $d\sigma/dx_\gamma^{\text{obs}}(D^*, \text{untagged jet})$  all within the kinematic region summarised in the Table. 7.1.

$Q^2 < 1 \text{ GeV}^2$
$130 < W_{\gamma p} < 280 \text{ GeV}$
$p_T^{D^*} > 3 \text{ GeV}$
$ \eta^{D^*}  < 1.5$
$E_T^{\text{jet}} > 6 \text{ GeV}$
$-1.5 < \eta^{\text{jet}} < 2.4$
a $D^*$ -jet match is required only where explicitly stated.

**Table 7.1** Inclusive charm and jet(s) cross section kinematic region.

At the hadron level, the  $D^*$  meson is used as input into the jet finder therefore allowing a  $D^*$ -tagged jet to be identified unambiguously. The definition of the cross section includes events with a  $D^*$  from both  $c$ -quark and  $b$ -quark decays.

## 7.2 The unfolding method

The data were initially compared to the MC simulation in shape and found to generally agree well for the all kinematic quantities. The is higher in the data than the MC due to not all the background processes being simulated in the MC. Since HERWIG gives a better overall description of the data than PYTHIA, it was chosen as the primary MC generator to correct the data. The cross sections for a given observable  $Y$  were determined using

$$\frac{d\sigma}{dY} = \frac{N}{A \cdot \mathcal{L} \cdot B \cdot \Delta Y},$$

where  $N$  is the number of  $D^*$  events in a bin of size  $\Delta Y$ ,  $A$  is the acceptance (which takes into account migrations and efficiencies for that bin) and  $\mathcal{L}$  is the integrated luminosity. The product,  $B$ , of the appropriate branching fractions for the  $D^*$  and  $D^0$  was set to  $(2.57 \pm 0.06)\%$  [67]. The same unfolding method was used for both inclusive jet and dijet analyses (see section 8).

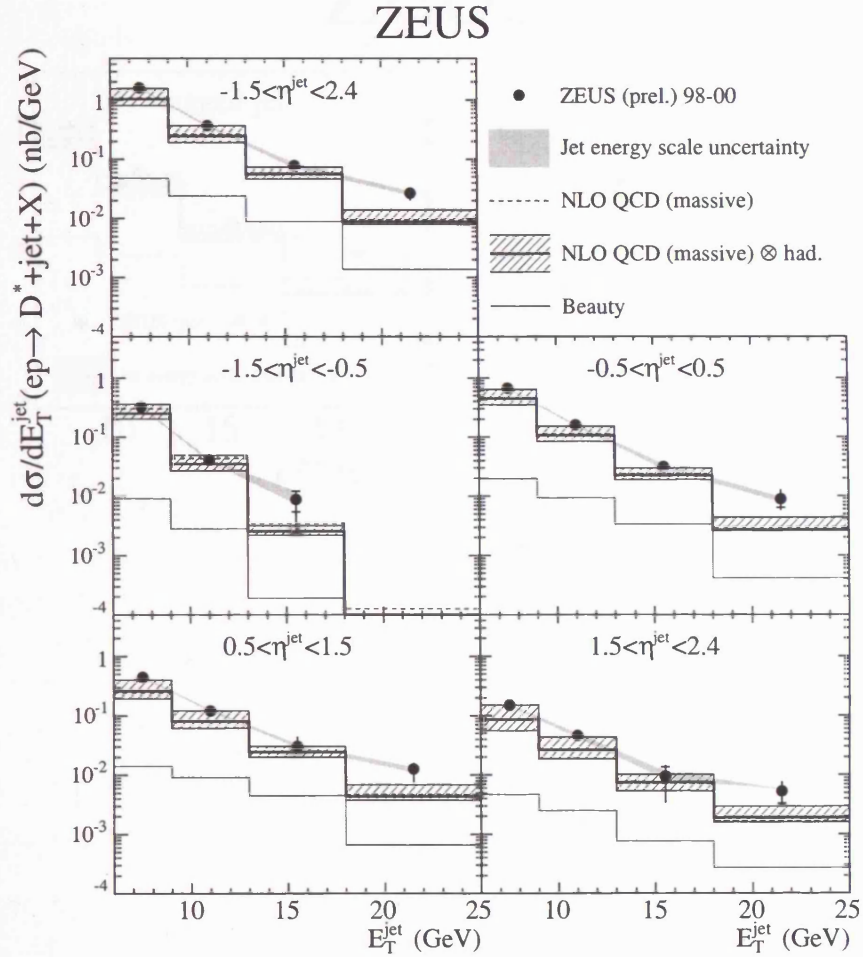
## 7.3 Measurement of $d\sigma/dE_T^{\text{jet}}$

The mass peaks for the data and HERWIG MC are shown in appendix A (section 17), for  $d\sigma/dE_T^{\text{jet}}$ .

The cross sections  $d\sigma/dE_T^{\text{jet}}$  in different regions of  $\eta^{\text{jet}}$  are shown in (fig. 7.1) for all jets and in (fig. 7.2) for  $D^*$ -tagged and untagged jets. The measurements have a harder spectrum as  $\eta^{\text{jet}}$  increases.

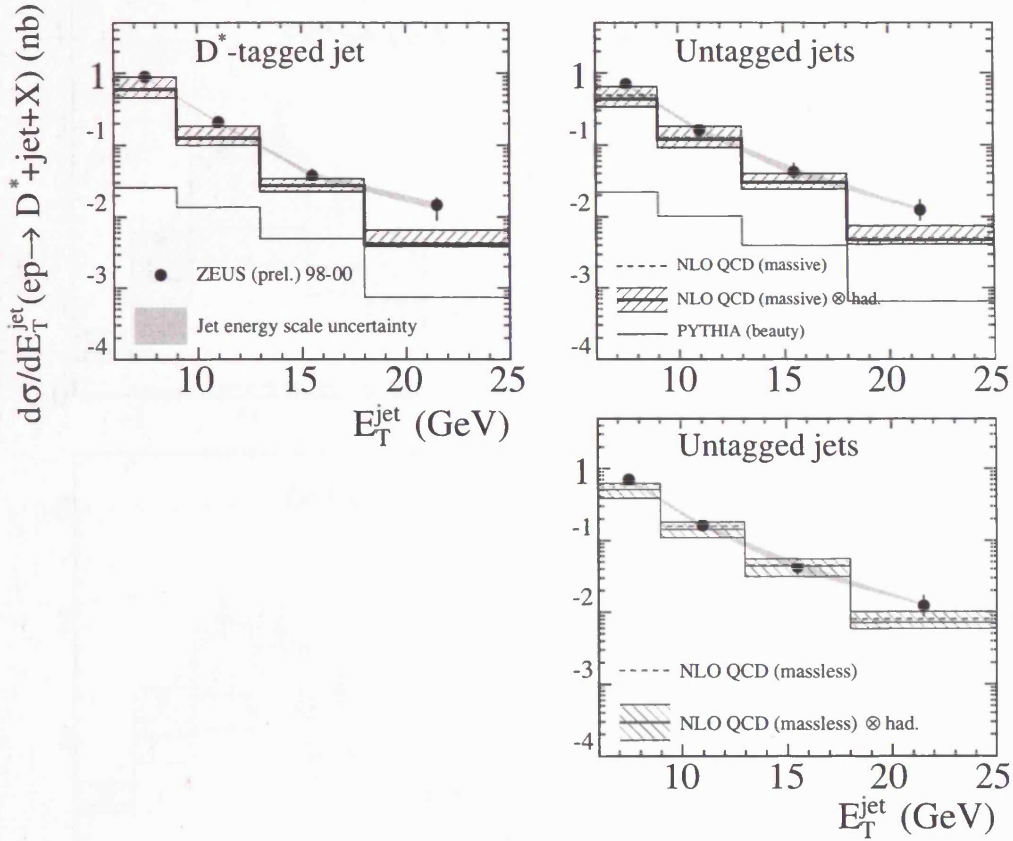
## 7.4 Measurement of $d\sigma/d\eta^{\text{jet}}$

The cross sections  $d\sigma/d\eta^{\text{jet}}$  in different regions of  $E_T^{\text{jet}}$  are shown in (fig. 7.3) for all jets and in (fig. 7.4) for  $D^*$ -tagged and untagged jets. Due to the requirement  $|\eta^{D^*}| < 1.5$ , the  $D^*$ -tagged jet is centered around 0 and falls off rapidly at large  $\eta^{\text{jet}}$ . The advantage of reconstructing jets is observed in the untagged-jet distribution where a significant cross section is measured up to  $\eta^{\text{jet}} = 2.4$ .



**Figure 7.1** Cross section  $d\sigma/dE_T^{\text{jet}}$  for jets in events (dots) containing at least one  $D^*$  meson for different regions in  $\eta^{\text{jet}}$ . The comparison is made to massive QCD predictions with (solid line) and without (dotted line) hadronisation corrections applied. The theoretical uncertainties (hatched band) come from the simultaneous change in the scale and in the charm mass. The beauty component is also shown (lower histogram).

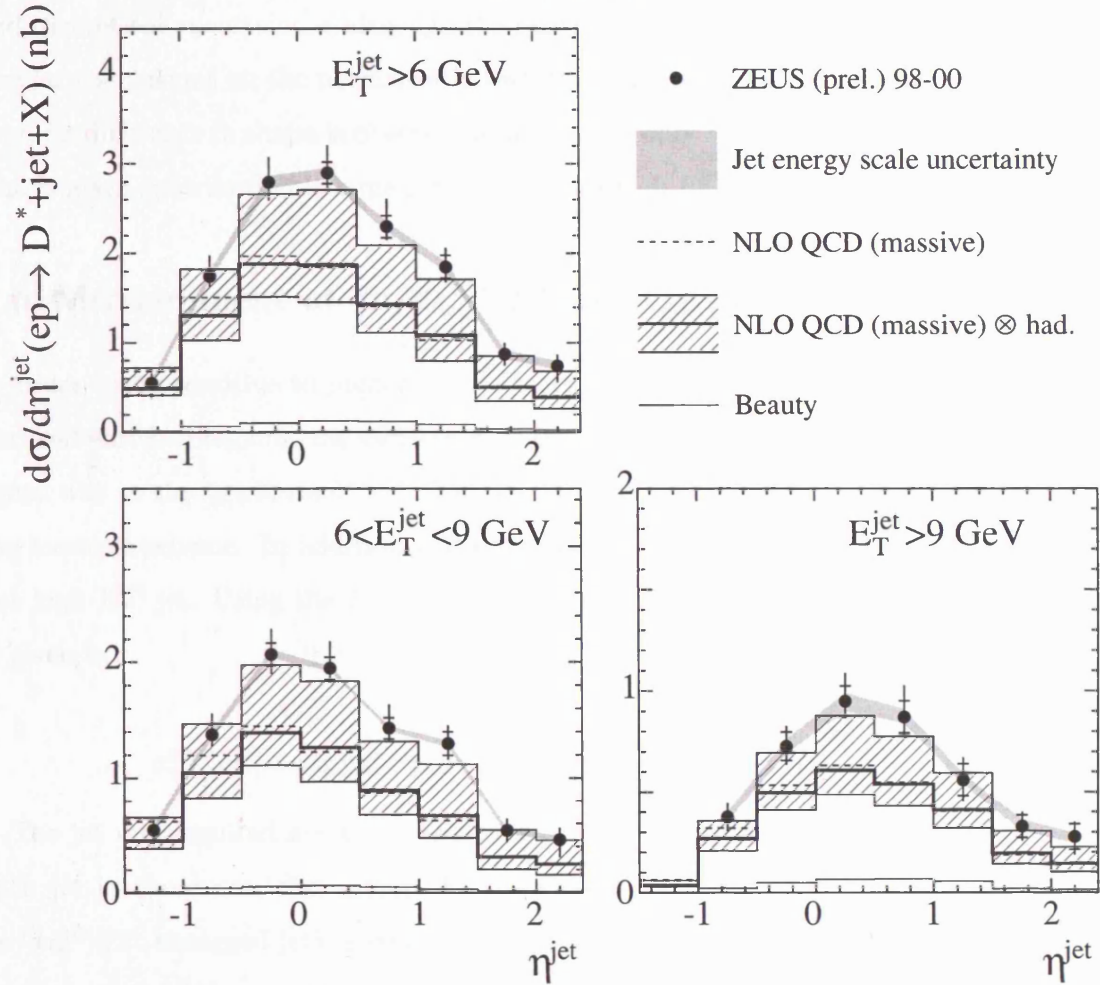
## ZEUS



**Figure 7.2** Cross section  $d\sigma/dE_T^{\text{jet}}$  for  $D^*$ -tagged jets and untagged jets (dots). The comparison is made to massive QCD predictions with (solid line) and without (dotted line) hadronisation corrections applied. The theoretical uncertainties (hatched band) come from the simultaneous change in the scale and in the charm mass. For the other jet distribution, the massless QCD predictions are shown with (solid line) and without (dotted line) hadronisation corrections applied. The uncertainties (hatched band) come from the changed renormalisation and factorisation scales. The beauty component is also shown (lower histogram).



## ZEUS



**Figure 7.3** Cross section  $d\sigma/d\eta^{\text{jet}}$  for jets in events (dots) containing at least one  $D^*$  meson for different regions in  $E_T^{\text{jet}}$ . The comparison is made to massive QCD predictions with (solid line) and without (dotted line) hadronisation corrections applied. The theoretical uncertainties (hatched band) come from the simultaneous change in the scale and in the charm mass. The beauty component is also shown (lower histogram).

## 7.5 Measurement of $d\sigma/dE_T^{\text{jet}}$ and $d\sigma/d\eta^{\text{jet}}$ in regions of $p_T^{D^*}$

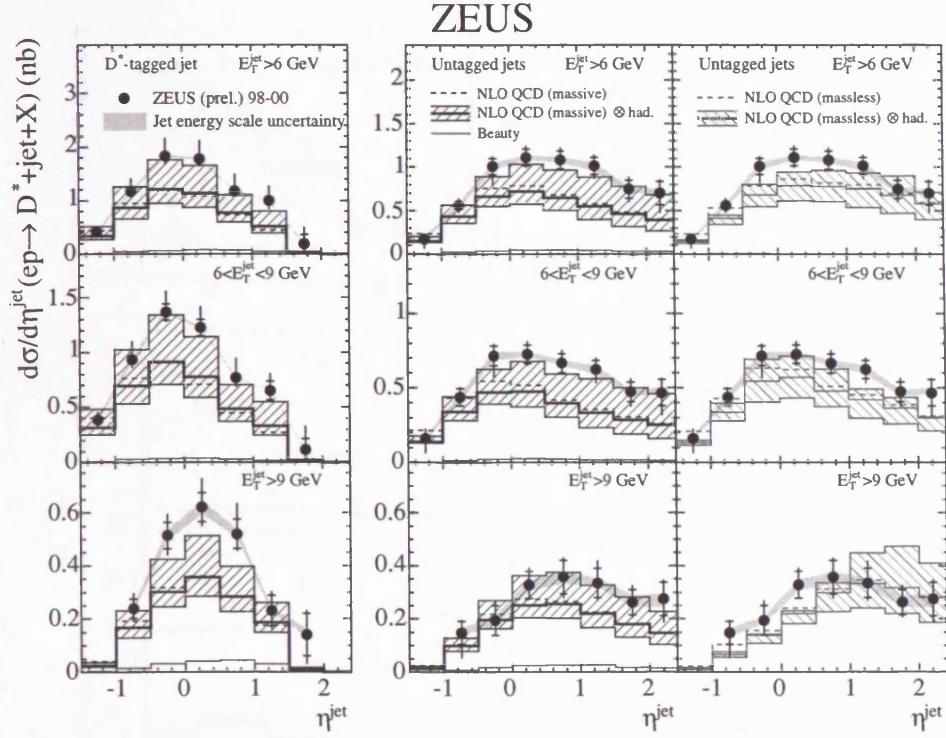
Measurements of  $d\sigma/dE_T^{\text{jet}}$  and  $d\sigma/d\eta^{\text{jet}}$  in regions of  $p_T^{D^*}$  are shown in (fig. 7.5) compared to the massive NLO prediction. The data and NLO are compatible within the experimental and theoretical uncertainties although the relative normalisation of the two changes with  $p_T^{D^*}$ . Similar conclusions on the normalisation were seen for inclusive  $D^*$  measurements [26]. However, no difference in shape is observed as a function of  $\eta^{\text{jet}}$  as was observed as a function  $\eta^{D^*}$ . The  $b$ -quark contribution is large for low  $p_T^{D^*}$  and high  $E_T^{\text{jet}}$ .

## 7.6 Measurement of $d\sigma/dx_\gamma^{\text{obs}}(D^*, \text{untagged jet})$

In order to be sensitive to higher-order effects, and distinguish between direct-enriched and resolved-enriched regions, the variable  $x_\gamma^{\text{obs}}(D^*, \text{untagged jet})$  was constructed [10], in an analogous way to the ‘traditional’  $x_\gamma^{\text{obs}}$  [35]. The variable has the advantage of being calculable in the massless scheme. In addition it takes advantage of increased statistics by requiring only one high  $E_T^{\text{jet}}$  jet. Using the  $D^*$  meson and untagged jet, the quantity  $x_\gamma^{\text{obs}}(D^*, \text{untagged jet})$  is given by:

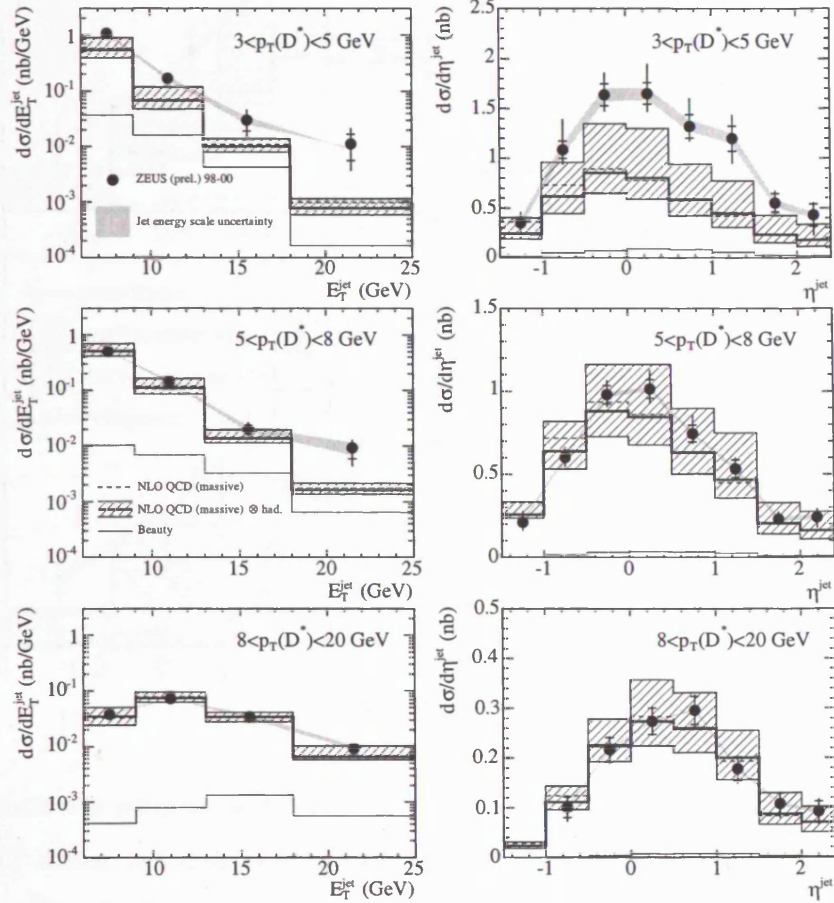
$$x_\gamma^{\text{obs}}(D^*, \text{untagged jet}) = \frac{p_T^{D^*} e^{-\eta^{D^*}} + E_T^{(\text{untagged jet})} e^{-\eta^{(\text{untagged jet})}}}{2yE_e} . \quad (7.1)$$

The jet was required not to be associated to the  $D^*$  meson. If there were more than one such jet in the event, the highest  $E_T^{\text{jet}}$  was used. In (fig. 7.6) the measured cross section  $d\sigma/dx_\gamma^{\text{obs}}(D^*, \text{untagged jet})$  is compared to both the massless and massive predictions. The upper bound of the massive prediction gives a good description of the data; the massless prediction is somewhat poorer. The MC models describe the shape well but do not provide the correct normalisation.

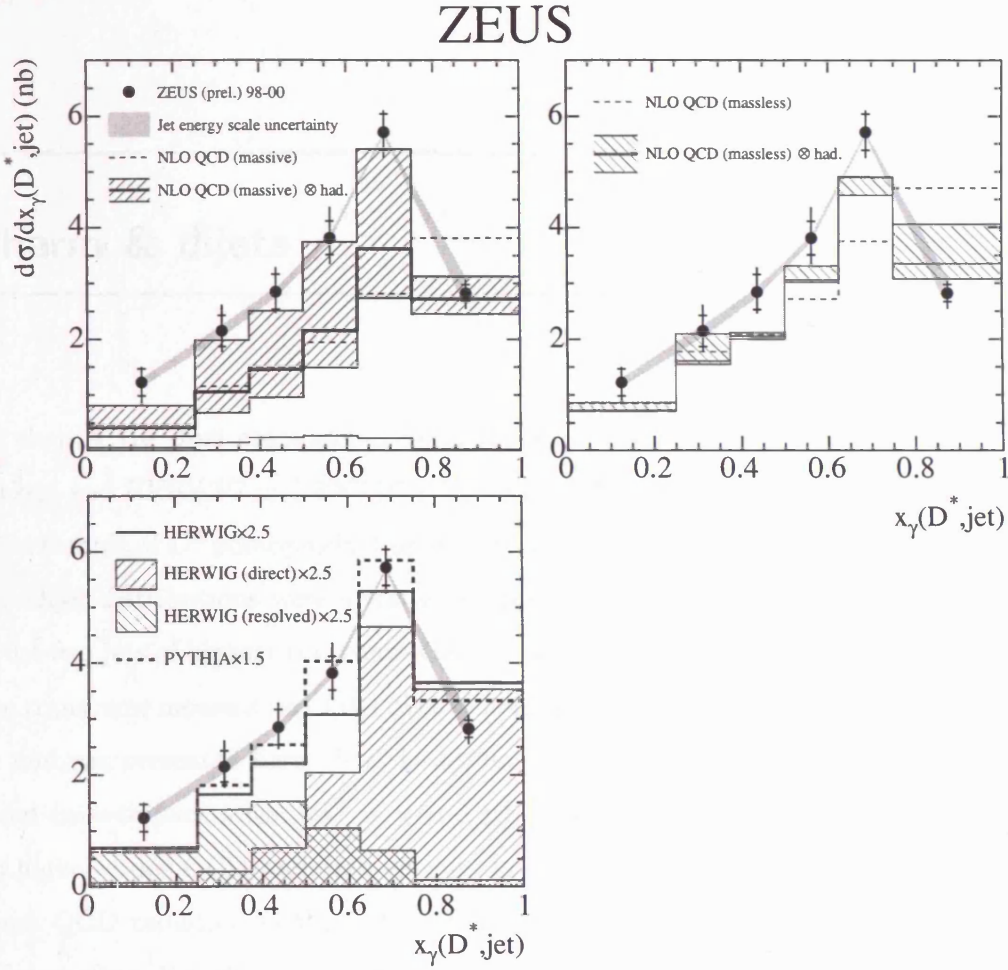


**Figure 7.4** Cross section  $d\sigma/d\eta^{\text{jet}}$  for  $D^*$ -tagged jets and untagged jets (dots). The comparison is made to massive QCD predictions with (solid line) and without (dotted line) hadronisation corrections applied. The theoretical uncertainties (hatched band) come from the simultaneous change in the scale and in the charm mass. For the other jet distribution, the massless QCD predictions are shown with (solid line) and without (dotted line) hadronisation corrections applied. The uncertainties (hatched band) come from the change renormalisation and factorisation scales. The beauty component is also shown (lower histogram).

## ZEUS



**Figure 7.5** Cross sections  $d\sigma/dE_T^{\text{jet}}$  and  $d\sigma/d\eta^{\text{jet}}$  in bins of  $p_T^{D^*}$ . The data (solid dots) are compared to the massive QCD predictions with (solid line) and without (dotted line) hadronisation corrections applied. The theoretical uncertainties (hatched band) come from the simultaneous change in the scale and in the charm mass. The beauty component is also shown (lower histogram).



**Figure 7.6** Inclusive jet cross section  $d\sigma/dx_\gamma^{\text{obs}}(D^*, \text{untagged jet})$  for the events containing a  $D^*$  meson not associated with a jet. The data (solid dots) are compared to (a) the massive QCD predictions with (solid line) and without (dotted line) hadronisation corrections applied. The theoretical uncertainties (hatched band) come from the simultaneous change in the scale and in the charm mass. In (b) the data are compared to the massless QCD predictions shown with (solid line) and without (dotted line) hadronisation corrections applied. The uncertainties (hatched band) come from the change in the renormalisation and factorisation scales. The beauty component is also shown (lower histogram) details given in text. In (c) the data are compared to HERWIG (solid line) and PYTHIA (dashed line) MC predictions normalised to the data. The predicted HERWIG direct and resolved contributions are also shown.



---

## 8 Charm & dijets

---

In this chapter the dijet cross section measurements are shown and compared to NLO QCD predictions and HERWIG and PYTHIA LO+PS models.

A dijet sample of  $D^*$  photoproduction may also be used to study higher-order QCD radiation effects. Dijet distributions were investigated previously [26, 70]. Additional correlations between the two jets of highest transverse energy, namely the difference in azimuthal angle,  $\Delta\phi^{jj}$ , and the transverse momentum of the dijet system,  $p_T^{jj}$ , are particularly sensitive to higher-order effects and are presented here. For the leading order (LO)  $2 \rightarrow 2$  process, the two jets are produced back-to-back with  $\Delta\phi^{jj} = \pi$  and  $p_T^{jj} = 0$ . Large deviations from these values are due to higher-order QCD radiation effects. In charm photoproduction, the resolved process has more QCD radiation in the initial state than for the direct process, this is due to the photon interacting directly with the parton in the proton in direct processes, while in resolved processes, the photon acts as a source of partons such that partons from both photon and proton participate in the hard scatter. Hence measurement of these correlations for direct- and resolved-enriched samples provides a test of higher-order effects.

### 8.1 Definition of the cross sections

Dijet cross sections with a  $D^*$  meson in the final state are measured as a function of  $d\sigma/dx_\gamma$ ,  $d\sigma/dm^{jj}$ ,  $d\sigma/dp_T^{jj}$ ,  $d\sigma/dp_T^{2jj}$ , and  $d\sigma/d\Delta\phi^{jj}$ , in both direct-enriched ( $x_\gamma > 0.75$ ) and resolved-enriched ( $x_\gamma < 0.75$ ) all within the kinematic region summarised in the Table. 8.1.

$Q^2 < 1 \text{ GeV}^2$
$130 < W_{\gamma p} < 280 \text{ GeV}$
$p_T^{D^*} > 3 \text{ GeV}$
$ \eta^{D^*}  < 1.5$
$E_T^{\text{jet1}} > 7 \text{ GeV} \ \& \ E_T^{\text{jet2}} > 6 \text{ GeV}$
$-1.5 < \eta^{\text{jet1,jet2}} < 2.4$

**Table 8.1** Dijet jet cross section kinematic region.

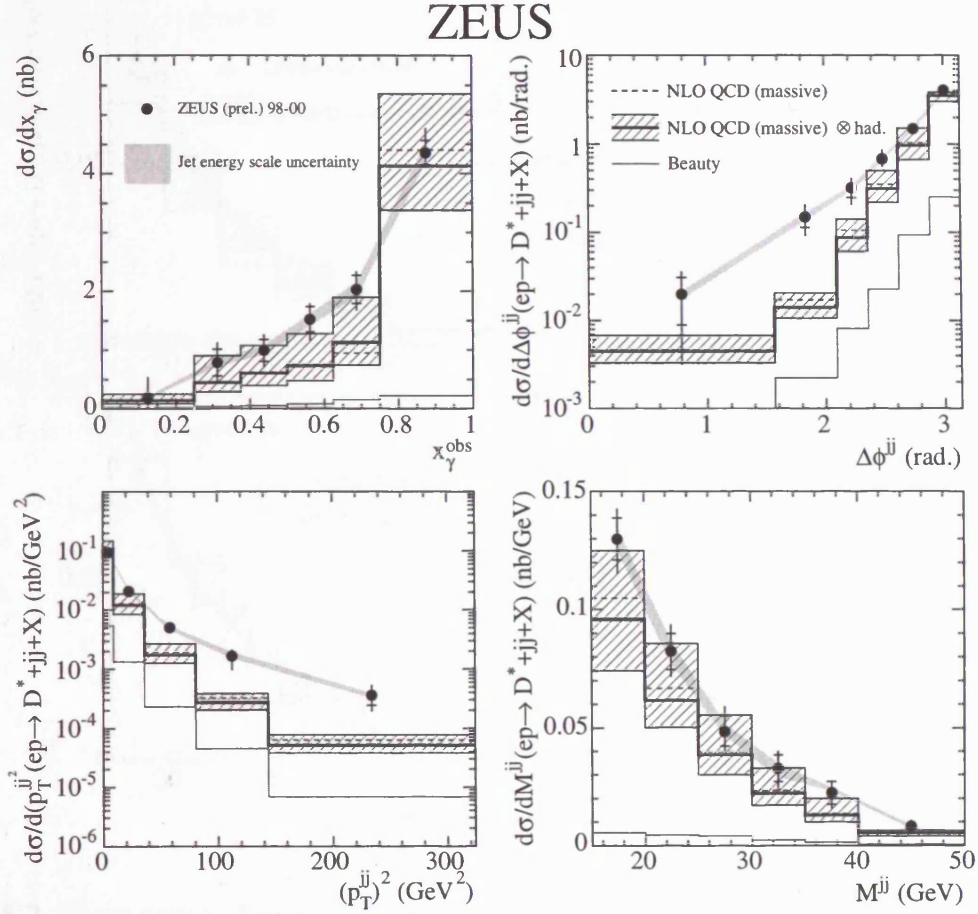
## 8.2 Measurement of $d\sigma/dx_\gamma$ , $d\sigma/dm^{jj}$ , $d\sigma/dp_T^{jj}$ and $d\sigma/dp_T^{2jj}$ , and $d\sigma/d\Delta\phi^{jj}$

Figure 8.1a shows the dijet cross section as a function of  $x_\gamma^{\text{obs}}$ . The massive prediction gives a good description for  $x_\gamma^{\text{obs}} > 0.75$  by its central value, while underestimating the measurement for  $x_\gamma^{\text{obs}} < 0.75$ . In (fig. 8.1), the cross sections as a function of  $\Delta\phi^{jj}$ ,  $p_T^{2jj}$  and  $M^{jj}$  are also shown. For  $\Delta\phi^{jj}$  there is agreement between data and the NLO prediction at large angular separation, but at smaller  $\Delta\phi^{jj}$  values the NLO prediction underestimates the data. This is correlated with the agreement and disagreement at low and high  $p_T^{2jj}$  values, respectively. The distribution in dijet invariant mass is described well by the upper NLO prediction as was the case for the inclusive jet cross sections.

## 8.3 Measurement of $d\sigma/dm^{jj}$ , for $x_\gamma > 0.75$ (direct-enriched) and $x_\gamma < 0.75$ (resolved-enriched)

The cross section  $d\sigma/dM^{jj}$  in (fig. 8.2) is described well by the upper bound of the NLO prediction and both MC models, HERWIG and PYTHIA, for both regions in  $x_\gamma^{\text{obs}}$ .

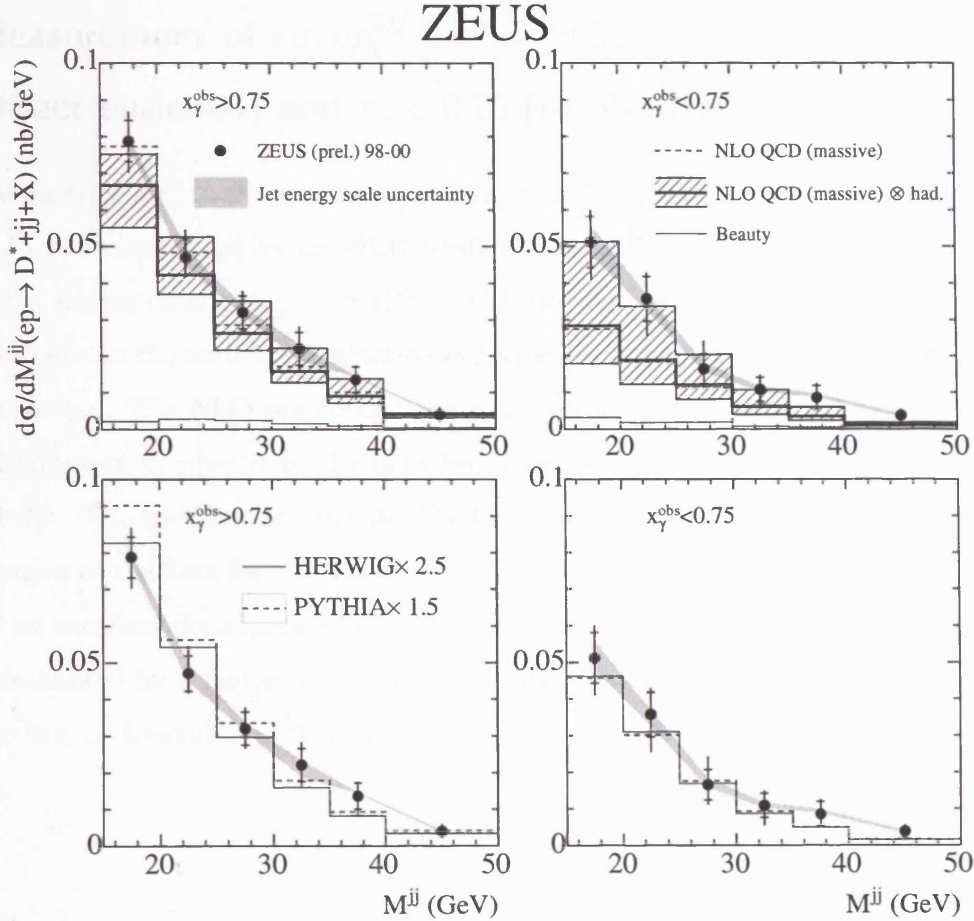
8.3 Measurement of  $d\sigma/dm^{jj}$ , for  $x_\gamma > 0.75$  (direct-enriched) and  $x_\gamma < 0.75$  (resolved-enriched)



**Figure 8.1** Dijet cross sections (a)  $d\sigma/dx_\gamma^{\text{obs}}$ , (b)  $d\sigma/d\Delta\phi^{jj}$ , (c)  $d\sigma/d(p_T^{jj})^2$  and (d)  $d\sigma/dm^{jj}$  for the data (solid dots) compared to massive QCD predictions with (solid line) and without (dotted line) hadronisation corrections applied. The theoretical uncertainties (hatched band) come from the simultaneous change in the scale and in the charm mass. The beauty component is also shown (lower histogram).



8.3 Measurement of  $d\sigma/dm^{jj}$ , for  $x_\gamma > 0.75$  (direct-enriched) and  $x_\gamma < 0.75$  (resolved-enriched)

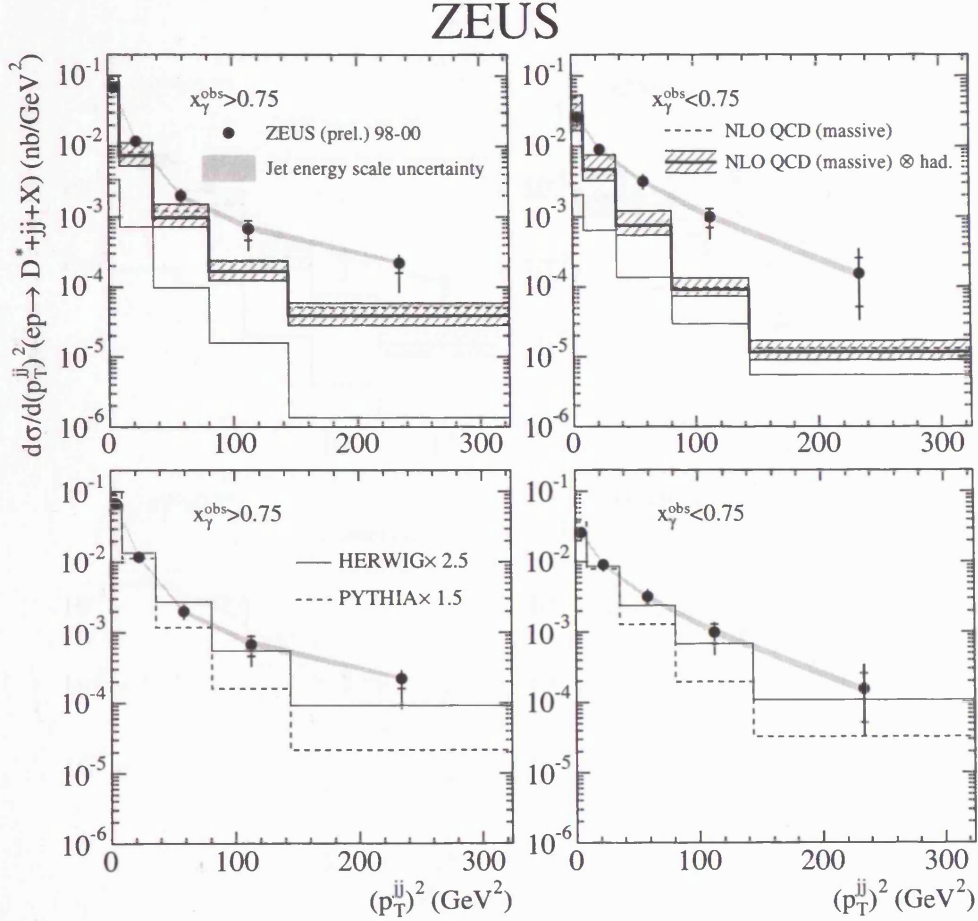


**Figure 8.2** Cross section for  $d\sigma/dM^{jj}$  separated into (a) and (c) direct enriched ( $x_\gamma^{\text{obs}} > 0.75$ ) and (b) and (d) resolved enriched ( $x_\gamma^{\text{obs}} < 0.75$ ). The data (solid dots) are compared (a) and (b) to the massive QCD prediction with (solid line) and without (dotted line) hadronisation corrections applied. The theoretical uncertainties (hatched band) come from the simultaneous change in the scale and in the charm mass. The beauty component is also shown (lower histogram). The data are also compared (c) and (d) with HERWIG (solid line) and PYTHIA (dashed line) MC predictions normalised to the data by a factor.

## 8.4 Measurement of $d\sigma/dp_T^{2jj}$ and $d\sigma/d\Delta\phi^{jj}$ , for $x_\gamma > 0.75$ (direct-enriched) and $x_\gamma < 0.75$ (resolved-enriched)

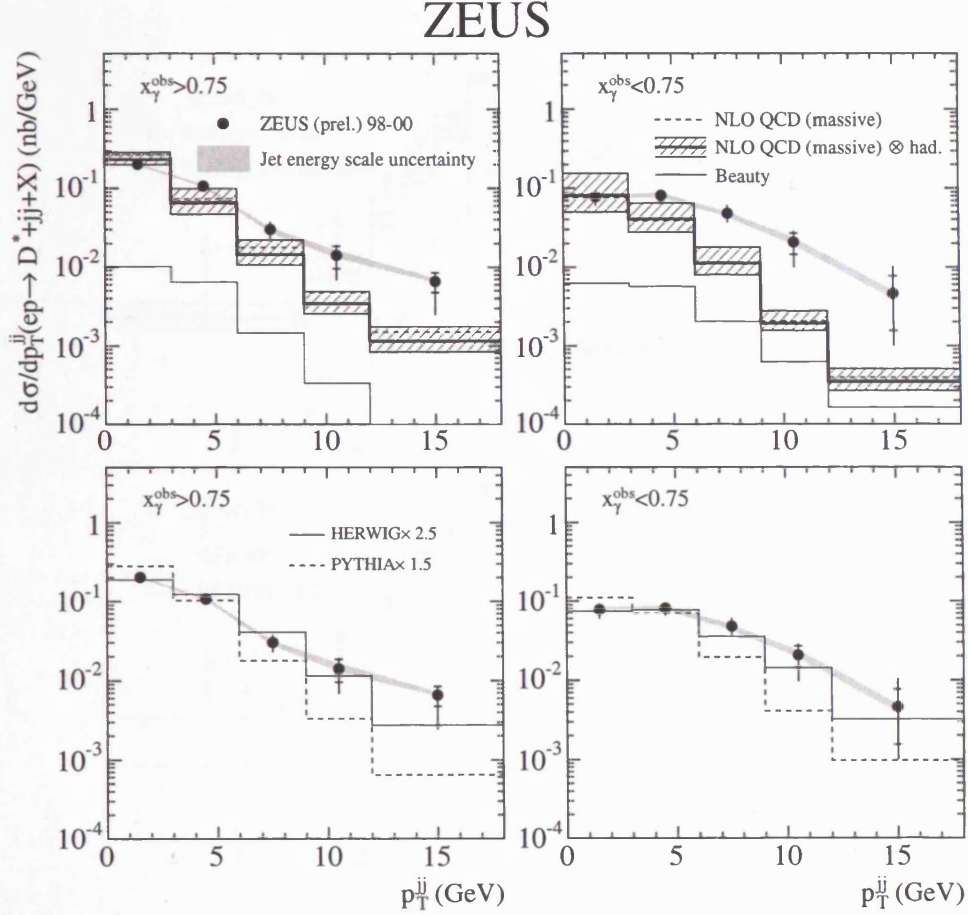
The cross sections  $d\sigma/d\Delta\phi^{jj}$  (see fig. 8.5),  $d\sigma/dp_T^{2jj}$  and  $d\sigma/dp_T^{jj}$  (see fig. 8.3) and (fig. 8.4) are reasonably well reproduced by the NLO prediction for  $x_\gamma^{\text{obs}} > 0.75$  although the data exhibit a somewhat harder distribution. For  $x_\gamma^{\text{obs}} < 0.75$ , the data exhibit a harder spectrum than for  $x_\gamma^{\text{obs}} > 0.75$  due to the additional radiation expected from the photon remnant in the resolved-enriched sample. The NLO prediction does not reproduce this effect and has a significantly softer distribution compared to the data for the cross sections both as a function of  $\Delta\phi^{jj}$ ,  $p_T^{2jj}$  and  $p_T^{jj}$ . The predictions from the PYTHIA MC reproduce neither the shape nor the normalisation of the data for low and high  $x_\gamma^{\text{obs}}$ . However, the predictions from the HERWIG MC give an excellent description of the shapes of all distributions, although the normalisation is underestimated by a factor of 2.5. This indicates that the NLO QCD calculation requires higher orders, or a simulation thereof, such as in the MC@NLO program [68, 69], to describe the data.

8.4 Measurement of  $d\sigma/dp_T^{2jj}$  and  $d\sigma/d\Delta\phi^{jj}$ , for  $x_\gamma > 0.75$  (direct-enriched) and  $x_\gamma < 0.75$  (resolved-enriched)



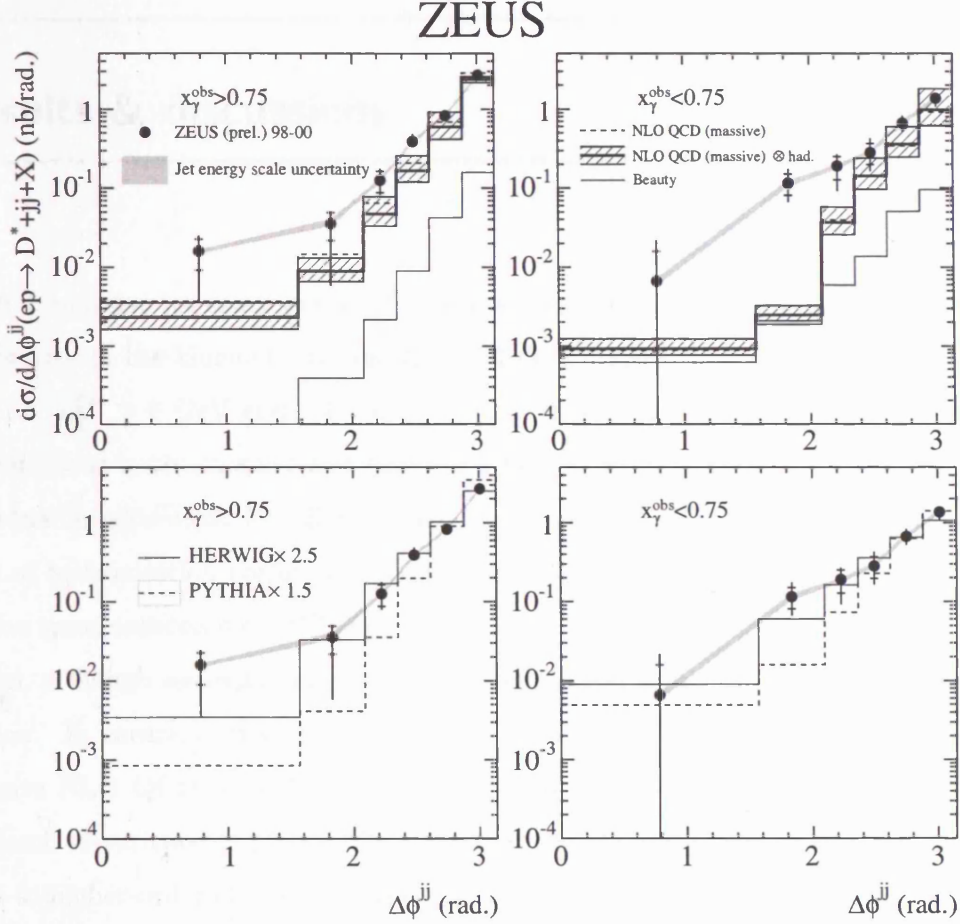
**Figure 8.3** Cross section for  $d\sigma/d(p_T^{jj})^2$  separated into (a) and (c) direct enriched ( $x_\gamma^{\text{obs}} > 0.75$ ) and (b) and (d) resolved enriched ( $x_\gamma^{\text{obs}} < 0.75$ ). The data (solid dots) are compared (a) and (b) to the massive QCD prediction with (solid line) and without (dotted line) hadronisation corrections applied. The theoretical uncertainties (hatched band) come from the simultaneous change in the scale and in the charm mass. The beauty component is also shown (lower histogram). The data are also compared (c) and (d) with HERWIG (solid line) and PYTHIA (dashed line) MC predictions normalised to the data by a factor.

8.4 Measurement of  $d\sigma/dp_T^{jj}$  and  $d\sigma/d\Delta\phi^{jj}$ , for  $x_\gamma > 0.75$  (direct-enriched) and  $x_\gamma < 0.75$  (resolved-enriched)



**Figure 8.4** Cross section for  $d\sigma/d(p_T^{jj})$  separated into (a) and (c) direct enriched ( $x_\gamma^{\text{obs}} > 0.75$ ) and (b) and (d) resolved enriched ( $x_\gamma^{\text{obs}} < 0.75$ ). The data (solid dots) are compared (a) and (b) to the massive QCD prediction with (solid line) and without (dotted line) hadronisation corrections applied. The theoretical uncertainties (hatched band) come from the simultaneous change in the scale and in the charm mass. The beauty component is also shown (lower histogram). The data are also compared (c) and (d) with HERWIG (solid line) and PYTHIA (dashed line) MC predictions normalised to the data by a factor.

8.4 Measurement of  $d\sigma/dp_T^{2jj}$  and  $d\sigma/d\Delta\phi^{jj}$ , for  $x_\gamma > 0.75$  (direct-enriched) and  $x_\gamma < 0.75$  (resolved-enriched)



**Figure 8.5** Cross section for  $d\sigma/d\Delta\phi^{jj}$  separated into (a) and (c) direct enriched ( $x_\gamma^{\text{obs}} > 0.75$ ) and (b) and (d) resolved enriched ( $x_\gamma^{\text{obs}} < 0.75$ ). The data (solid dots) are compared (a) and (b) to the massive QCD prediction with (solid line) and without (dotted line) hadronisation corrections applied. The theoretical uncertainties (hatched band) come from the simultaneous change in the scale and in the charm mass. The beauty component is also shown (lower histogram). The data are also compared (c) and (d) with HERWIG (solid line) and PYTHIA (dashed line) MC predictions normalised to the data by a factor.

---

## 9 Results & discussions

---

Differential inclusive jet cross sections for events containing  $D^*$  have been measured with the ZEUS detector in the kinematic region;  $Q^2 < 1 \text{ GeV}^2$ ,  $130 < W_{\gamma p} < 280 \text{ GeV}$ ,  $p_T^{D^*} > 3 \text{ GeV}$ ,  $|\eta^{D^*}| < 1.5$ ,  $E_T^{\text{jet}} > 6 \text{ GeV}$  and  $-1.5 < \eta^{\text{jet}} < 2.4$ . The measurements are compared to NLO QCD predictions in the massive and massless schemes. Both calculations show similar trends and reasonable agreement for all measured cross sections. This is achieved only with the addition of hadronisation corrections to the upper limit of the theoretical predictions. Dijet correlation cross sections  $d\sigma/dM^{\text{jj}}$  and  $d\sigma/dx_{\gamma}^{\text{obs}}$  are described well by the massive NLO QCD prediction, although again the data tends to agree better with the upper bound of the NLO calculation. In contrast, cross sections  $d\sigma/d\Delta\phi_{\text{jj}}$  and  $d\sigma/dp_T^{\text{jj}}$  show a large deviation from the massive NLO QCD prediction at low  $\Delta\phi_{\text{jj}}$  and high  $p_T^{\text{jj}}$ . This discrepancy is enhanced for the resolved-enriched ( $x_{\gamma}^{\text{obs}} < 0.75$ ) sample. These regions are expected to be particularly sensitive to higher-order effects, due to the photon behaving as a source of partons and from higher-order radiative processes that dominate the resolved-enriched region. The HERWIG MC model which incorporates leading-order matrix elements, followed by parton showers and hadronisation describes the shape of the measurements well. This indicates that for the precise description of charm dijet photoproduction, higher-order calculations or the implementation of additional parton showers in current NLO calculations are needed.

---

## 10 The upgrade of HERA II

---

### 10.1 The HERA collider upgrade

Table 10.1 shows the design parameters for HERA I compared to HERA II. The main difference is the increase in luminosity from the year 2000 by a factor of 5, as well as the particle beam sizes being reduced in order to attain this luminosity goal.

	Design	2000	Upgrade
Center of mass energy [GeV]	300	318	318
Luminosity [ $\text{cm}^{-2}\text{sec}^{-1}$ ]	$1.6 \cdot 10^{31}$	$1.5 \cdot 10^{31}$	$7.0 \cdot 10^{31}$
Max. number of bunches (both for leptons and protons)	210	210	180
$I_e$ (mA)	60	60	60
$I_p$ (mA)	160	160	140
Particles per lepton bunch	$3.65 \cdot 10^{10}$	$3.65 \cdot 10^{10}$	$4.18 \cdot 10^{10}$
Particles per proton bunch	$10^{11}$	$10^{11}$	$10^{11}$
Lepton beam width ( $\sigma_x$ mm)	0.286	0.286	0.118
Proton beam width ( $\sigma_x$ mm)	0.280	0.280	0.118
Lepton beam height ( $\sigma_y$ mm)	0.060	0.060	0.032
Proton beam height ( $\sigma_y$ mm)	0.058	0.058	0.032

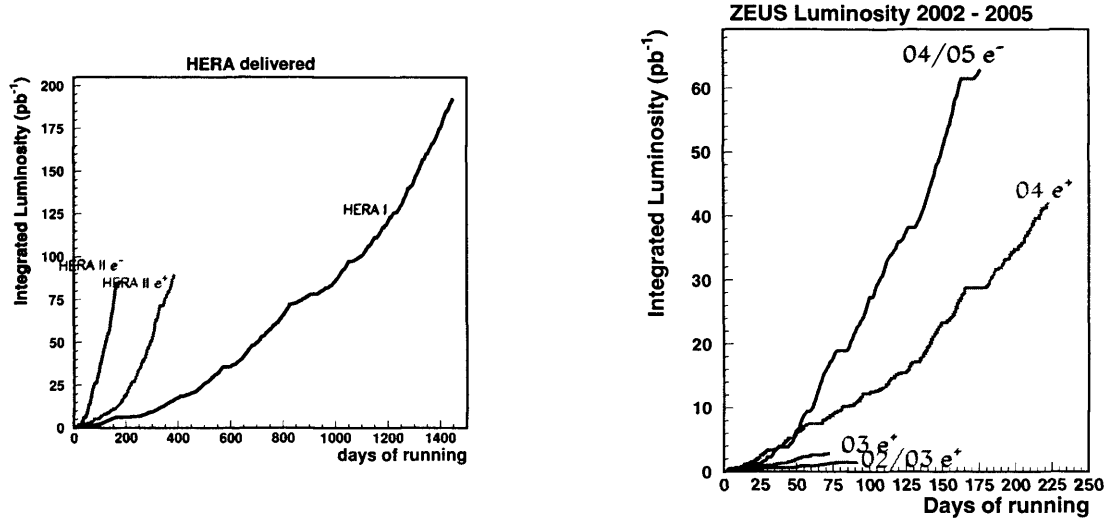
**Table 10.1** HERA's design parameters for the upgrade data taking period.



### 10.1.1 The HERA luminosity upgrade

The main goal of the HERA II project was to maximise luminosity with a goal of achieving  $1 \text{ fb}^{-1}$  by 2005. In order to do this many systems in HERA had to be upgraded as well as the interaction regions at ZEUS and H1. This was a major task, and took 2 years to complete. Unfortunately there were unforeseen problems after HERA was turned back on leading to extra simulation, understanding and isolation of these problems in order to be able to run the HERA machine and detectors. Some of these problems are discussed in (section 10.1.2).

Figure 10.1 shows the delivered/gated luminosity for HERA II and the comparison for the HERA I period of data taking. One goal which has already been achieved is that there are more electron-proton interactions recorded in HERA II than in HERA I.



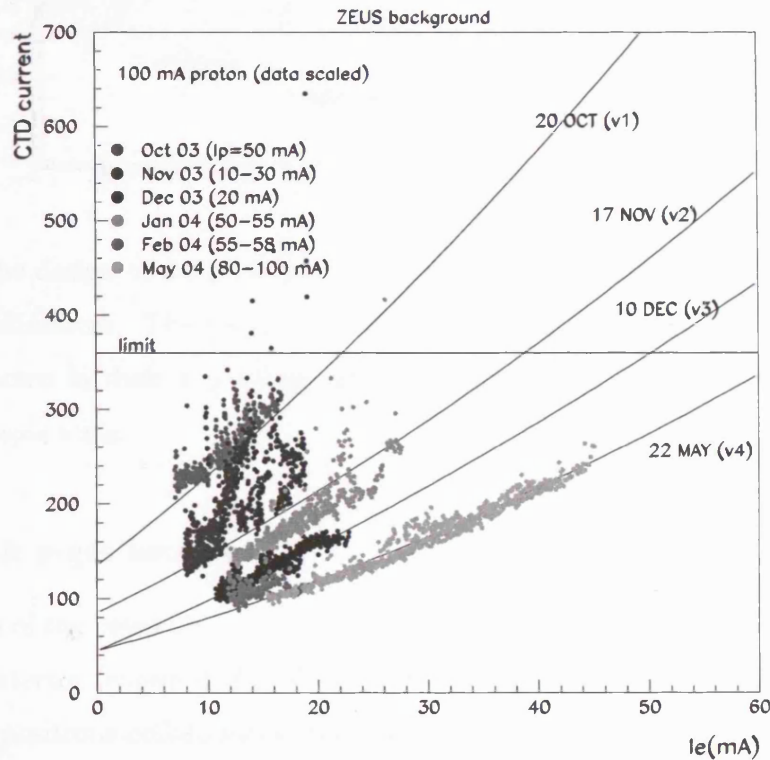
**Figure 10.1** The delivered luminosity is shown in the left hand plot for the HERA II upgrade 02-05 data compared to HERA I 95-00 data. The right hand plot shows the gated luminosity at ZEUS for the 02-05 data set.

### 10.1.2 The major problems encountered in the ZEUS interaction region

The main sources of trouble within the ZEUS interaction region were from off-momentum positrons and synchrotron radiation from the positron beam. Problems encountered from the proton beam were mainly due to the bad vacuum conditions which over time would improve. Figure 10.2 shows the ZEUS background as measured by the current in the CTD, as a function of time and the positron current ( $I_e$ ). The CTD currents shown in (fig. 10.2) are intergrated

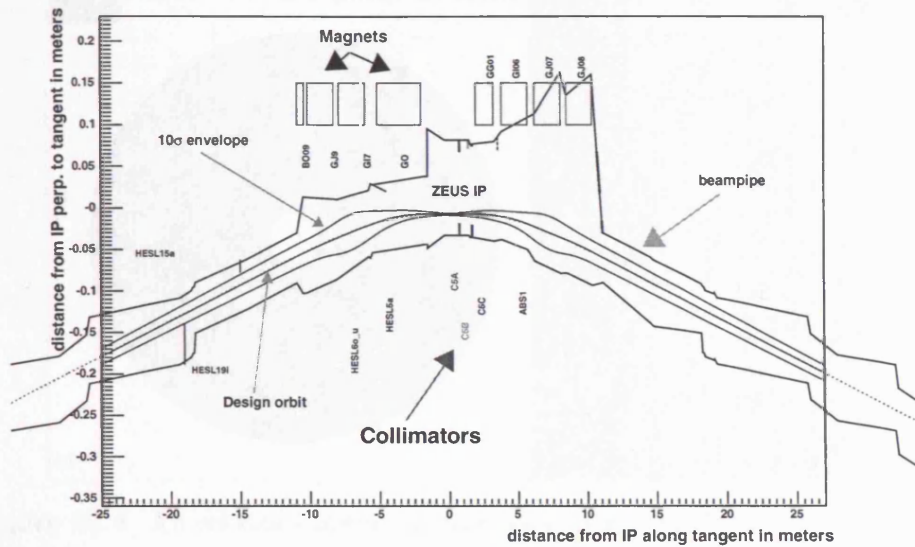


over all the sense wires in each superlayer of each quadrant, and is measured in  $0.1\mu\text{A}$ . This is dependent upon the gain it is not a universal quantity. Superlayer one currents for all four quadrants are shown in (fig. 10.2). In order for smooth running conditions at ZEUS, the CTD current had to be kept below a certain threshold above which the CTD would trip and stop the data taking [71]. The present running conditions are approximately the same as those shown in (fig. 10.2) shown for May 22<sup>nd</sup>, allowing for full currents in the machine without the CTD reaching trip threshold.



**Figure 10.2** The ZEUS background parameterised as a function of positron current  $I_e$  and current measured within the CTD.

Another important part of the re-design was improvement of the collimators, in which there was a major source of secondary scatters, causing large multiplicities within the CTD and raising the standing current in the chamber. Figure 10.3 shows the location of the magnets and collimators around the ZEUS interaction point (IP).

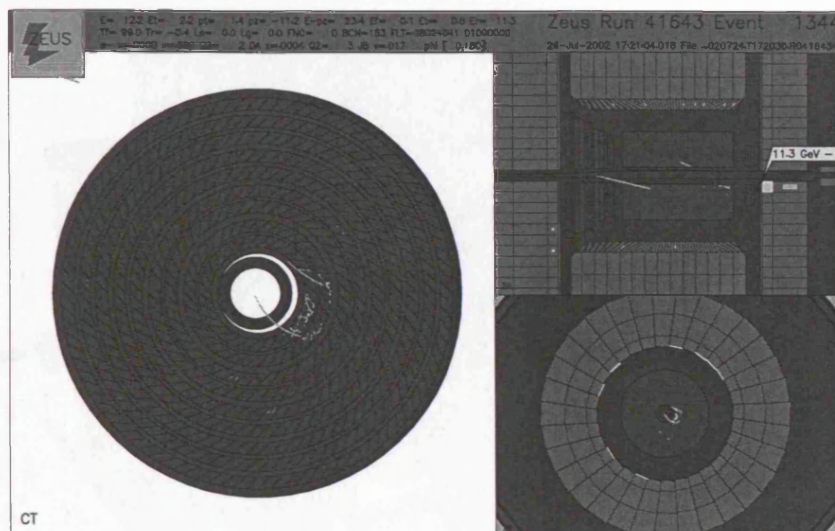


**Figure 10.3** The design of the positron orbit and its  $10\sigma$  envelope, with the beam-pipe and collimators. The magnets closest to the ZEUS interaction point (IP) are also shown in their  $z$  positions along the beam line. Note the highly exaggerated  $y$ -axis scale.

### 10.1.3 e-gas & p-gas background

Bremsstrahlung of the beam off the residual gas is the source of off-momentum positrons being bent into the detector (shown in fig. 10.4) by the final focusing and bending magnets. These off-momentum positrons collide inside the detector and generate a background in the CTD. This background can be reduced by decreasing the amount of material close to the beam and improving the vacuum pressure. At small positron currents the contribution from off-momentum positrons to the positron-beam backgrounds in the CTD current was estimated to be 15 to 20%. Studies were carried out to see what kind of improvement was needed in order to run the CTD without reaching CTD current trip threshold. It was found that a factor of 10 improvement was necessary in the positron-beam background, due to synchrotron radiation and off-momentum positrons [72].

Proton-beam gas interactions occurring upstream of the ZEUS detector was the main source of background. Again like the positron-beam gas a solution would be to reduce the amount of material close to the beam. The effect of reducing the thickness of collimators was studied and



**Figure 10.4** An off-momentum positron as seen within the ZEUS detector.

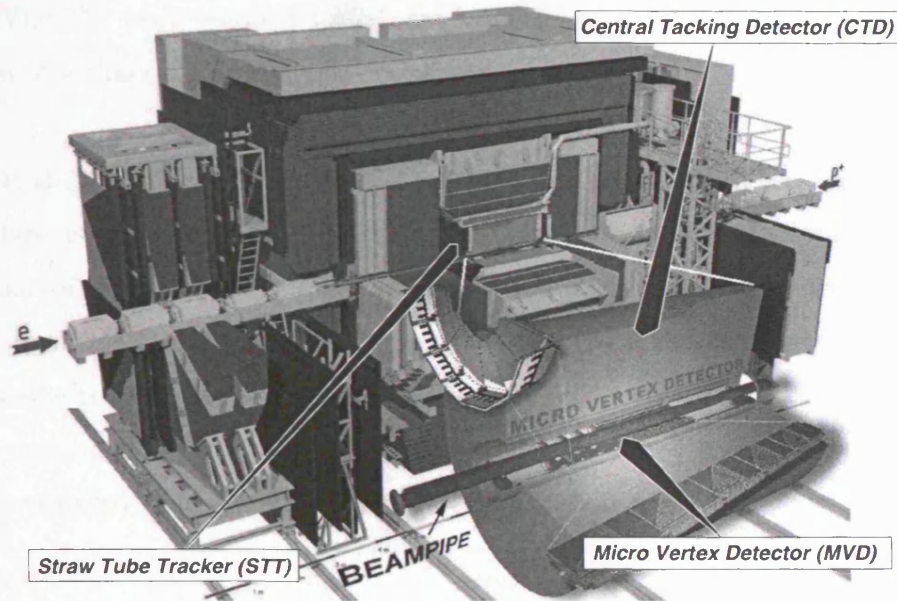
found to only have a small contribution to the CTD current from the proton-beam background. Most of the improvement was due to the bad vacuum conditions which changed *dynamically* from the IP. The improvement factor for the proton-beam was estimated at a factor of 20 so as to be able to run at full currents without the CTD reaching its current trip threshold. The only action available was to run the machine with steadily increasing current in the positron-beam in order to condition the vacuum, as well as a redesign of the collimator systems near to ZEUS to reduce the particle background.

## 10.2 The detector components upgrade in ZEUS

Figure 10.5 shows the ZEUS detector with an exploded view of the detector components installed in the upgrade phase. The straw tube tracker (STT) was one of these components designed to significantly improve the track finding efficiency in the forward region of the detector. The STT will cover a polar angle range of  $5^\circ - 25^\circ$ , consisting of straw drift tube layers grouped into wedge shaped sectors. There are four superlayers with a sector containing 194 or 266 straws. The precision of an individual straw is accurate to within  $200\ \mu\text{m}$  giving a resolution of distance of closest approach to a wire of  $180 - 220\ \mu\text{m}$ .

The micro vertex detector (MVD) is described in more detail in (section 10.3) and (section 10.3.1).





**Figure 10.5** The ZEUS detector, with the upgraded parts of the detector shown.

### 10.3 The ZEUS Micro Vertex Detector (MVD)

The MVD, installed in 2001 during the upgrade shutdown is designed to improve tracking capabilities allowing for secondary vertex tagging of long lived particles and a better vertex resolution. The MVD has the design characteristics of covering a polar angular coverage between  $10^\circ$  and  $150^\circ$ , at least  $20\ \mu\text{m}$  hit resolution for normal incident tracks, a two track separation resolution of  $200\ \mu\text{m}$ , a single hit efficiency of 99%. When including dead regions and geometry, the effective efficiency is better than 95% with noise occupancy better than  $10^{-3}$ .

#### 10.3.1 Detector specifications

The MVD is split mechanically into the barrel region (BMVD) and forward region (FMVD). Figure 10.6

The MVD supports 712 single sided silicon strip detectors (sensors). In the barrel MVD (BMVD) 600 silicon sensors (with size  $6.4\text{ cm} \times 6.4\text{ cm} \times 300\mu\text{m}$ ) are mounted in three layers around the beam pipe. The closest position measurement to the interaction point has been reduced from 18 cm (most inner layer central tracking detector (CTD)) to 4 cm. In the forward

MVD (FMVD) 112 wedge shaped sensors are mounted on 4 disks. Each sensor can measure the position of a charged particle with a precision of  $20\mu m$  in the direction perpendicular to the strips.

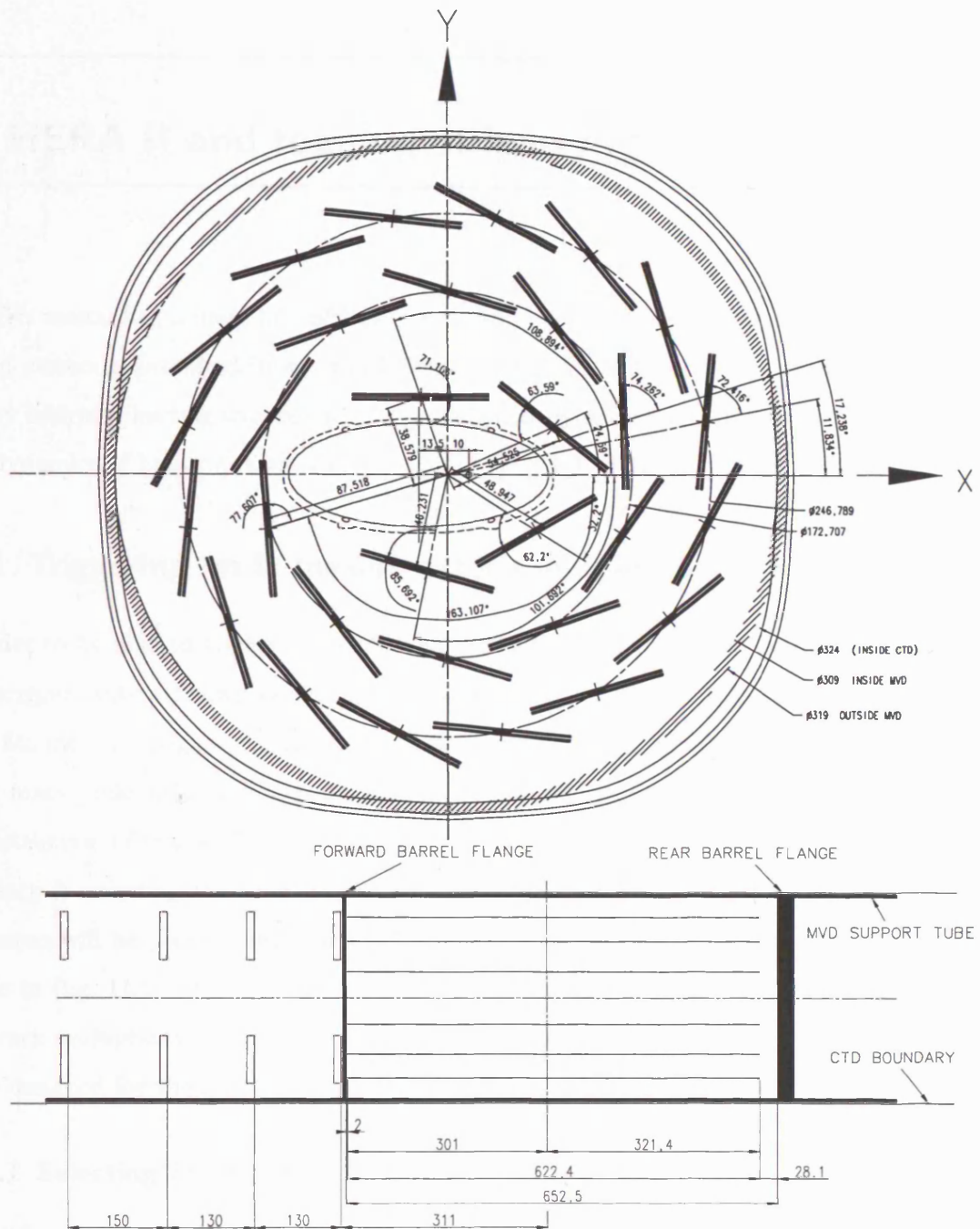
In order to align the MVD cosmic ray muon events were taken, which pass through the ZEUS detector. Low multiplicity high momentum tracks are reconstructed allowing for a precise determination of the detector. In order to gain improvement in the alignment the number of cosmic ray muon events taken has to be increased, or the selection of high momentum low multiplicity events can be used during physics running to increase statistics. The analysis in chapter 11 uses the first set of alignment parameters determined from approximately 100k of cosmic ray events giving the MVD hit residuals as shown in table 10.2 [73].

	mean [ $\mu m$ ]	$\sigma$ [ $\mu m$ ]
$z$ hits	1	34
$r\phi$ hits	7	53
forward wheel hits	-40	63

**Table 10.2** MVD hit residual results for cosmic ray muon events.

The current alignment also gives a resolution on the beam spot of  $\sigma_x \sim 150 \mu m$  and  $\sigma_y \sim 140 \mu m$ , which was determined by distribution of all primary vertices during a run, (fig. 11.2) shows the distribution of the beam spots during the 03-04 running phase for all physics runs taken at ZEUS.

### 10.3 The ZEUS Micro Vertex Detector (MVD)



**Figure 10.6** The layout of the MVD in the  $xy$  plane on the top and the  $zy$  plane on the bottom.

---

## 11 HERA II and tagging of heavy meson decays

---

The  $D^\pm$  meson has a mass of 1.869 GeV and the lifetime is relatively long:  $c\tau = 315\mu m$  [56].

The methods described below will be extended in the future to tag many other charm or beauty hadrons, leading to more data on, and hopefully more understanding of, the production and dynamics of heavy quarks from the ZEUS HERA-II data.

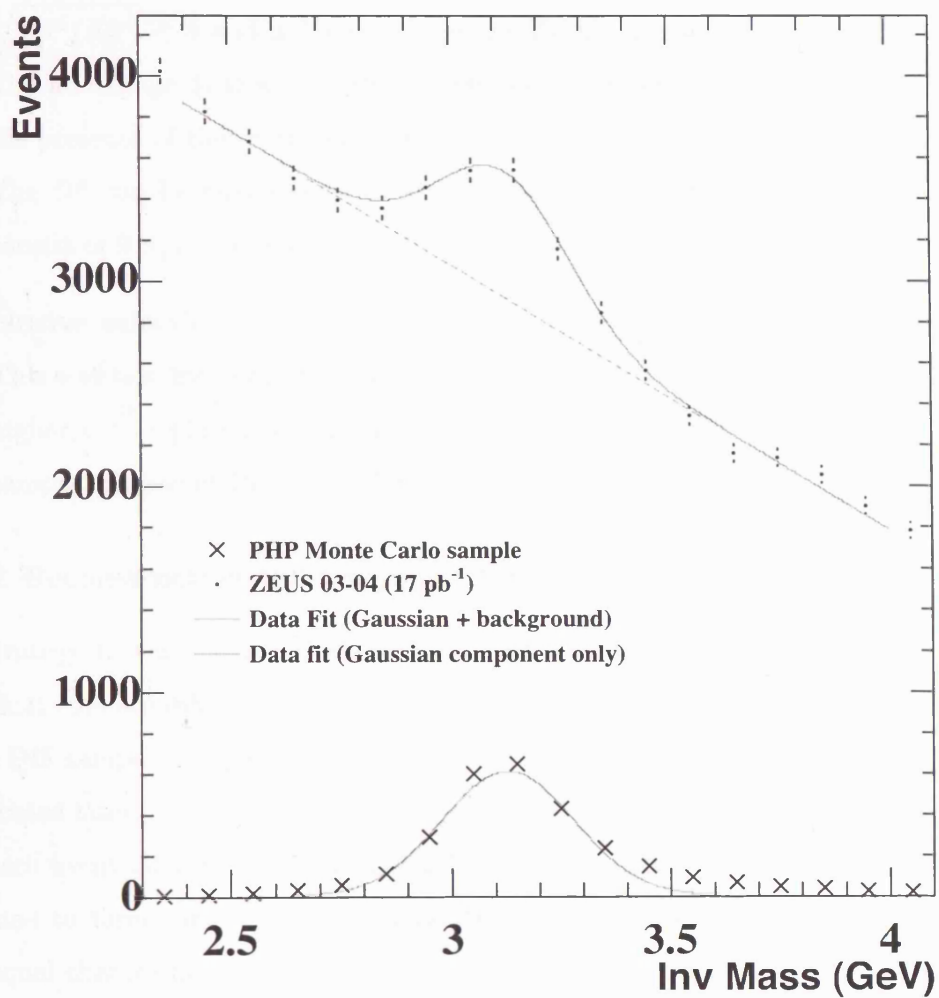
### 11.1 Triggering on D mesons after the upgrade

In order to be able to trigger more efficiently on D mesons and other heavy flavour decays a new trigger system known as the global tracking trigger (GTT) [74, 75, 76, 77] was set up. This fits into the trigger system at the second level. It has the ability to combine tracks, to make mass peaks using a fast track reconstruction, and can use the MVD information in the reconstruction of tracks. Logic similar to existing triggers was used in order to maintain high efficiency in selecting D meson events while keeping the rate low. In the future the tagging of D mesons will be possible using the GTT. An example of tagging particles using the GTT is shown in (fig. 11.1) where the  $J/\psi$  meson is reconstructed online. This is a simple case with low track multiplicity allowing for tracking studies to be performed and optimised algorithms to be designed for the more complicated D meson decays.

#### 11.1.1 Selecting $D^\pm$ events

The  $D^\pm$  decay to three charged particles was studied:  $D^\pm \rightarrow K^\mp, \pi^\pm, \pi^\pm$ .

The selection of events for the reconstruction of  $D^\pm$  is described in this section. Two samples were chosen, sample (A) which is the selection of DIS events only [73] and sample (B) a mixture of both DIS and photoproduction events.



**Figure 11.1**  $J/\psi$  reconstructed from online tracks using the global tracking trigger.



### A. DIS selection

The deep inelastic scattering selection is based by the identification of a clearly measured scattered positron in the CAL. The selection follows a similar strategy to that used in the inclusive neutral current analysis of the HERA-I data [78]. Events are selected and backgrounds are reduced if  $E_e > 8 \text{ GeV}$ ,  $38 < E - P_z < 65 \text{ GeV}$ ,  $P_T^{CAL}/E_T^{cal} < 0.7$ ,  $\sqrt{P_T^{cal}/E_T^{cal}} < 3$  and a “box-cut” on the RCAL face of  $|x| > 13 \text{ cm}$  and  $|y| > 10 \text{ cm}$ . The advantage of this selection is that the events are triggered during data taking on the presence of the scattered positron. Hence, no selection has to be done on the tracks. The  $D^\pm$  can be reconstructed to much lower transverse momentum ( $p_T$ ). This sample consist of  $9.8 \text{ pb}^{-1}$  of data.

### B. Inclusive selection

This selection includes all events on tape. Due to the large photoproduction rate a much higher cut is placed on the transverse momentum of the tracks in the trigger. This sample consists of  $15 \text{ pb}^{-1}$  of data.

#### 11.1.2 Reconstruction and tagging of the $D^\pm$ meson

The strategy to tag the  $D^\pm$  is the same for both event selections, except that some of the individual cuts are different.

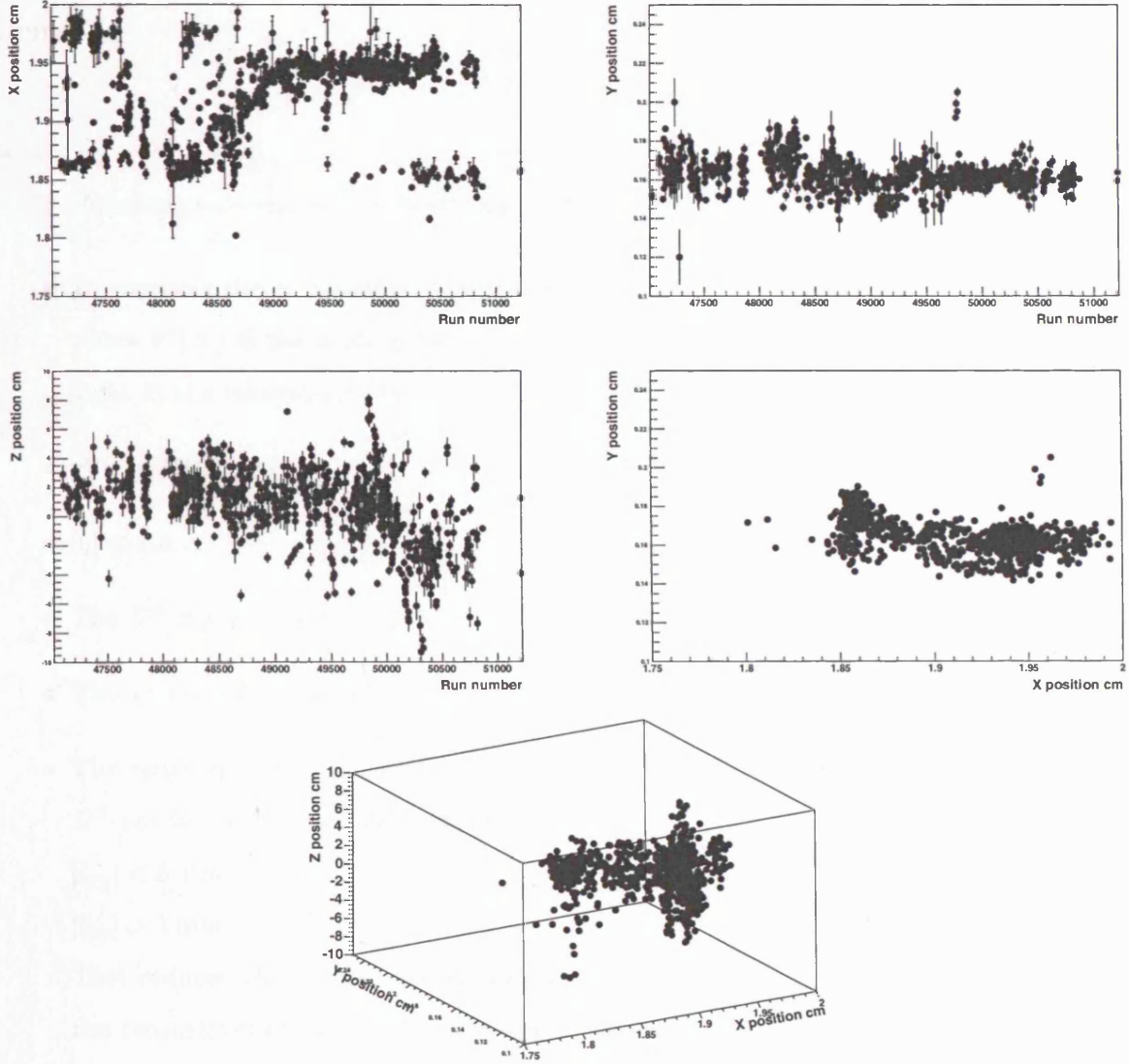
The DIS sample (sample A) is discussed with the differences between sample A and sample B indicated later.

In each event all track pairs with equal charge and a third track with opposite charge are combined to form the  $D^\pm$  meson candidates. The pion mass is assigned to the two tracks with equal charges and the kaon mass is assigned to the third track. Subsequently, the  $D^\pm$  candidate invariant mass,  $M(K\pi\pi)$  is calculated. Only the tracks with transverse momentum larger than  $0.4 \text{ GeV}$  were selected.

Candidates with  $p_T^{D^\pm} > 1.5 \text{ GeV}$  and in the invariant mass region between  $1.6 \text{ GeV}$  to  $2.2 \text{ GeV}$  were re-vertexed. The  $D^\pm$  vertex position is recalculated using only the three tracks from the decay of the  $D^\pm$ . The vertex re-fitted tracks are used to determine the  $D^\pm$  invariant mass. The remaining tracks were input to the primary vertex algorithm with the beam spot as initial estimate. Figure 11.2 shows the variation of the beam position from late 2003 until middle of 2004, the error is the  $\sigma$  coming from a Gaussian fit to the vertex position run by run. The

### 11.1 Triggering on $D$ mesons after the upgrade

result is a new re-fitted primary vertex position. The distance between the  $D^\pm$  vertex and the new primary vertex is used to tag  $D^\pm$  decays.



**Figure 11.2** The beam spots as a function of ZEUS run number, from 03-04, for  $x$ ,  $y$ , and  $z$  vertex positions determined from the spread of primary vertices during a recorded run.

The signed decay length  $l$  is defined as:

$$l = |\vec{l}| \text{sign}(\vec{l} \cdot \vec{p}_{D^\pm}), \quad (11.1)$$

with  $\vec{l} = \vec{s} - \vec{p}$ ,  $\vec{p}$  is the position vector of the primary vertex,  $\vec{s}$  that of the secondary and  $\vec{p}_{D^\pm}$  is the re-fitted momentum vector of the  $D^\pm$ . In the case  $l$  is positive (negative) the decay is in

front (behind the vertex). The uncertainty in the primary vertex and  $D^\pm$  candidate position are both described by a covariance matrix. The errors ( $\sigma_{\text{vtx}}$  and  $\sigma_{D^\pm}$ ) were calculated by projecting both covariance matrices on to the decay vector. The decay length significance is defined as:

$$S_L = L/\sigma_L, \quad (11.2)$$

where  $\sigma_L^2 = \sigma_{\text{vtx}}^2 + \sigma_{D^\pm}^2$ .

The following selection was done to select good  $D^\pm$  and to reduce combinatorial background.

- To suppress the combinatorial background, a cut of  $\cos \theta^*(K) > -0.75$  was imposed, where  $\theta^*(K)$  is the angle between the kaon in the  $K\pi\pi$  rest frame and the  $K\pi\pi$  line of flight in the laboratory. Furthermore for the  $D^\pm$  was required that:
- $p_T^{D^\pm} > 2.0 \text{ GeV}$ ,
- $|\eta| < 1.5$ ,
- The  $D^\pm$  decay length error  $\sigma_{D^\pm} < 0.5 \text{ mm}$ ,
- The  $\chi^2$  probability  $P(\chi^2) > 0.05$  and
- The radial decay length was defined as  $l_{xy} = l \sin(\theta)$ , where  $\theta$  is the polar angle of the  $D^\pm$  candidate. Candidates were selected if:
  - $|l_{xy}| < 5 \text{ mm}$ ,
  - $|l_{xy}| > 1 \text{ mm}$ .

This reduces the combinatorial background from primary vertex tracks [73]. Due to the reconstruction of the decay distance being smeared due to the resolution of vertex finding, which is in the region of  $200 - 500 \mu\text{m}$ , a cut of  $|l_{xy}| > 1 \text{ mm}$  was therefore applied to select a well understood region of reconstruction. Effectively this results in a selection of beauty enriched  $D^\pm$  mesons.

The next step was to study the significance  $S_L$  for the signal region  $1.82 < M(K\pi\pi) < 1.92$  and select decays which are separated from the primary vertex. To decide on the cut value one can compare with a side band sample or with the mirror image of the negative side of the decay length significance. In contrast to the signal band sample, these samples are not expected to contain  $D^\pm$  candidates. For this sample (A) the best signal was observed for  $S_L > 6$ .

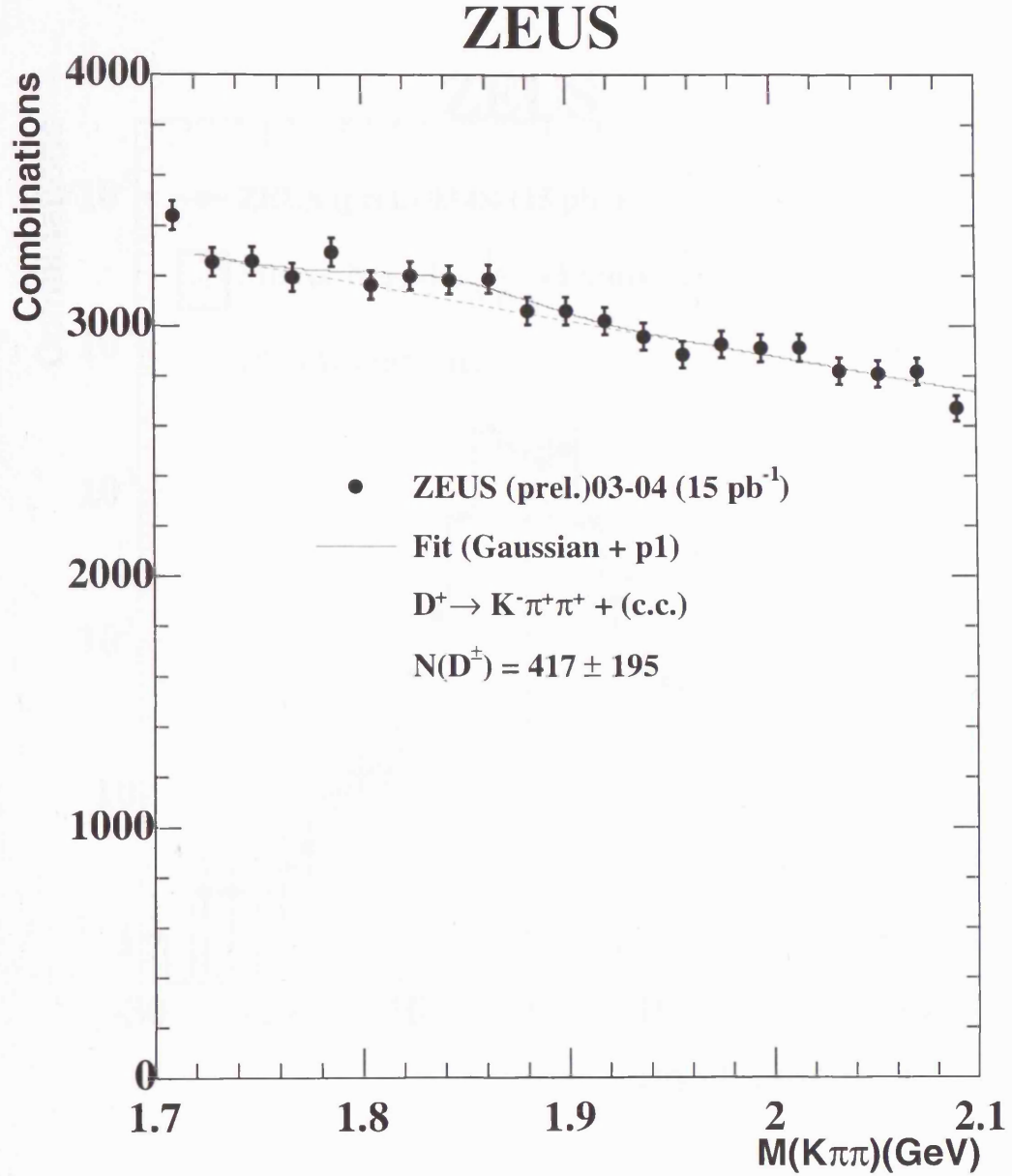
### 11.1 Triggering on $D$ mesons after the upgrade

---

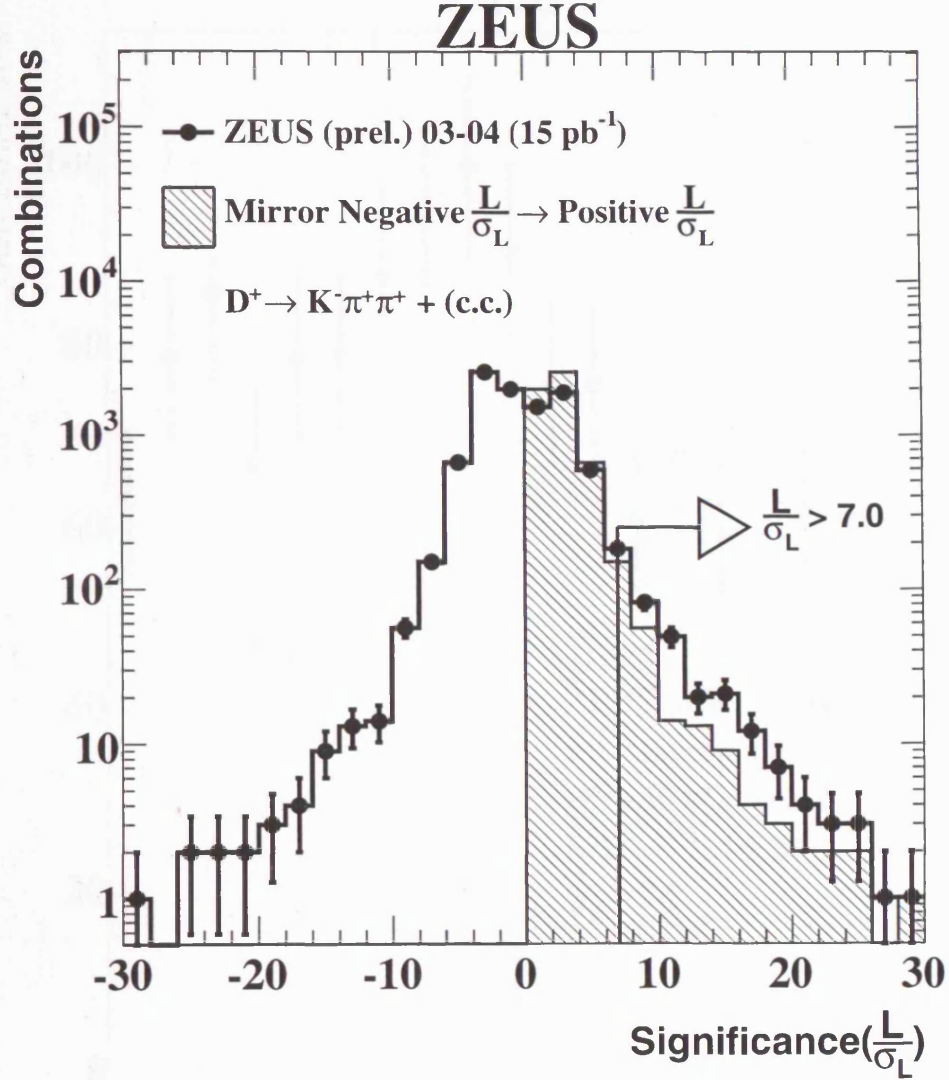
For the inclusive sample (sample B) the following selections were made:

- Tracks were selected with  $p_T > 0.8 \text{ GeV}$  ,
- at least 4 MVD hits on each track ,
- Candidates were re-vertexed if  $|\eta| < 1.75$  ,  $p_T(D^\pm) > 3.7 \text{ GeV}$  and  $1.7 < M(K\pi\pi) < 2.1 \text{ GeV}$  and
- $\sigma_L < 0.6 \text{ mm}$  .

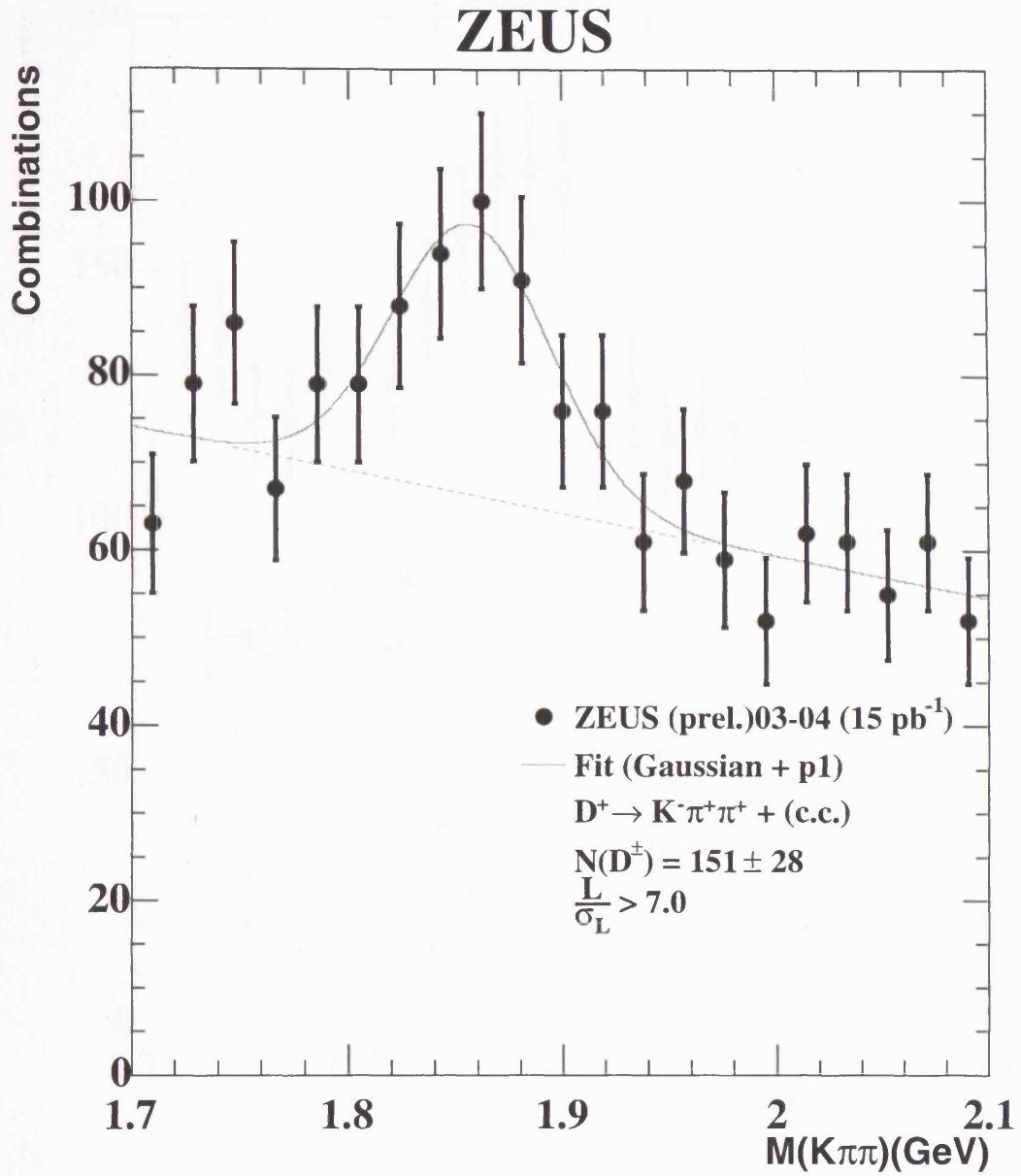
The significance calculated by taking track combinations around the region where the signal is expected,  $1.845 < M(D^\pm) < 1.905 \text{ GeV}$ . The optimal decay length significance cut turned out to be  $S_L = 7$  .



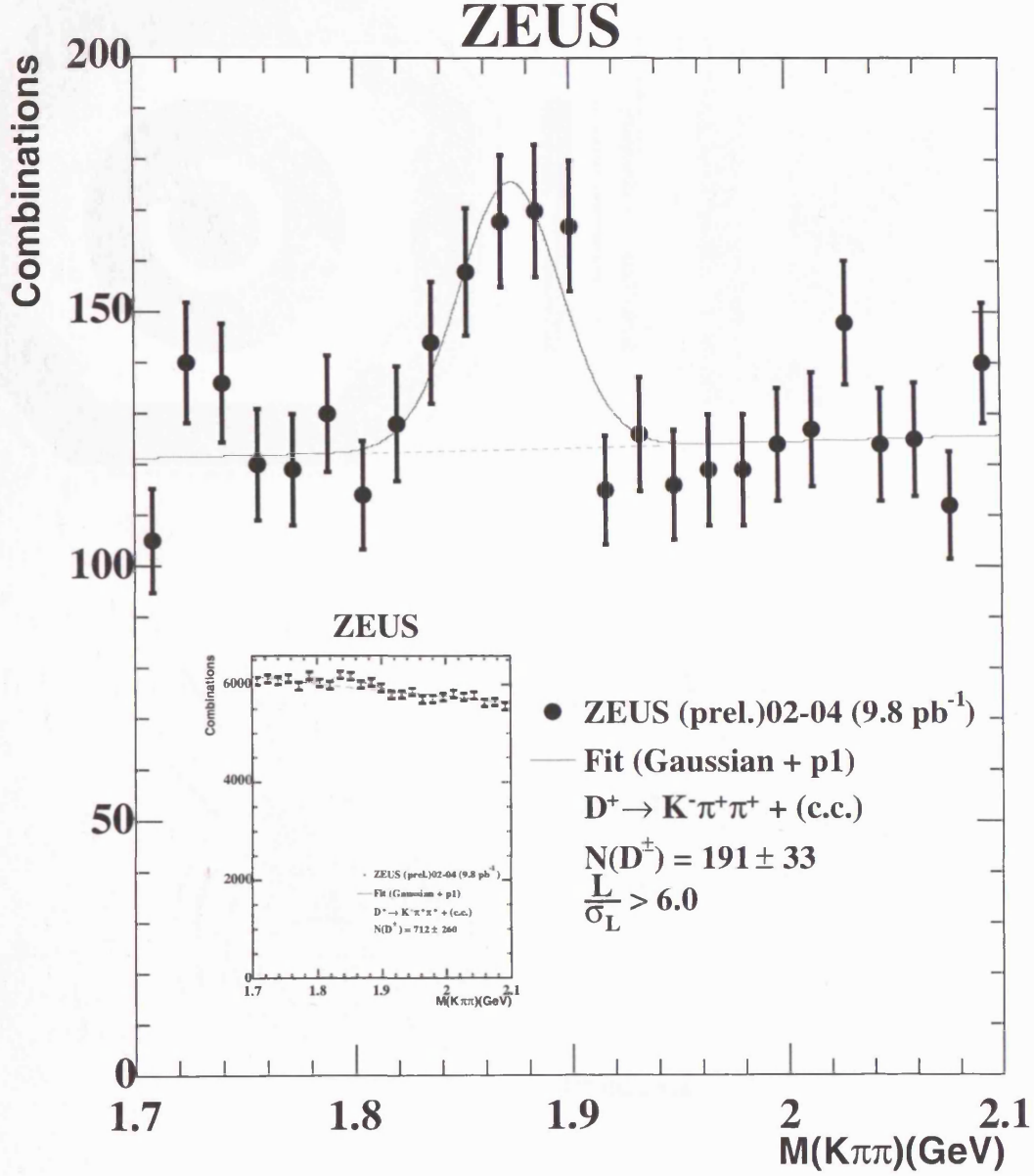
**Figure 11.3**  $M(K\pi\pi)$  invariant mass distribution without the decay length significance cut. The inclusive event sample is used (sample B, in the text). The data is fitted with a Gaussian for the signal and a first order polynomial for the background. No statistically significant signal is seen.



**Figure 11.4** Significance  $S_L = \frac{L}{\sigma_L}$  distribution for events within  $1.845 < M(D^\pm) < 1.905 \text{ GeV}$  range. The inclusive event sample is used (sample B, in the text). The selection cut indicated the one used to extract the signal seen in (fig. 11.5).

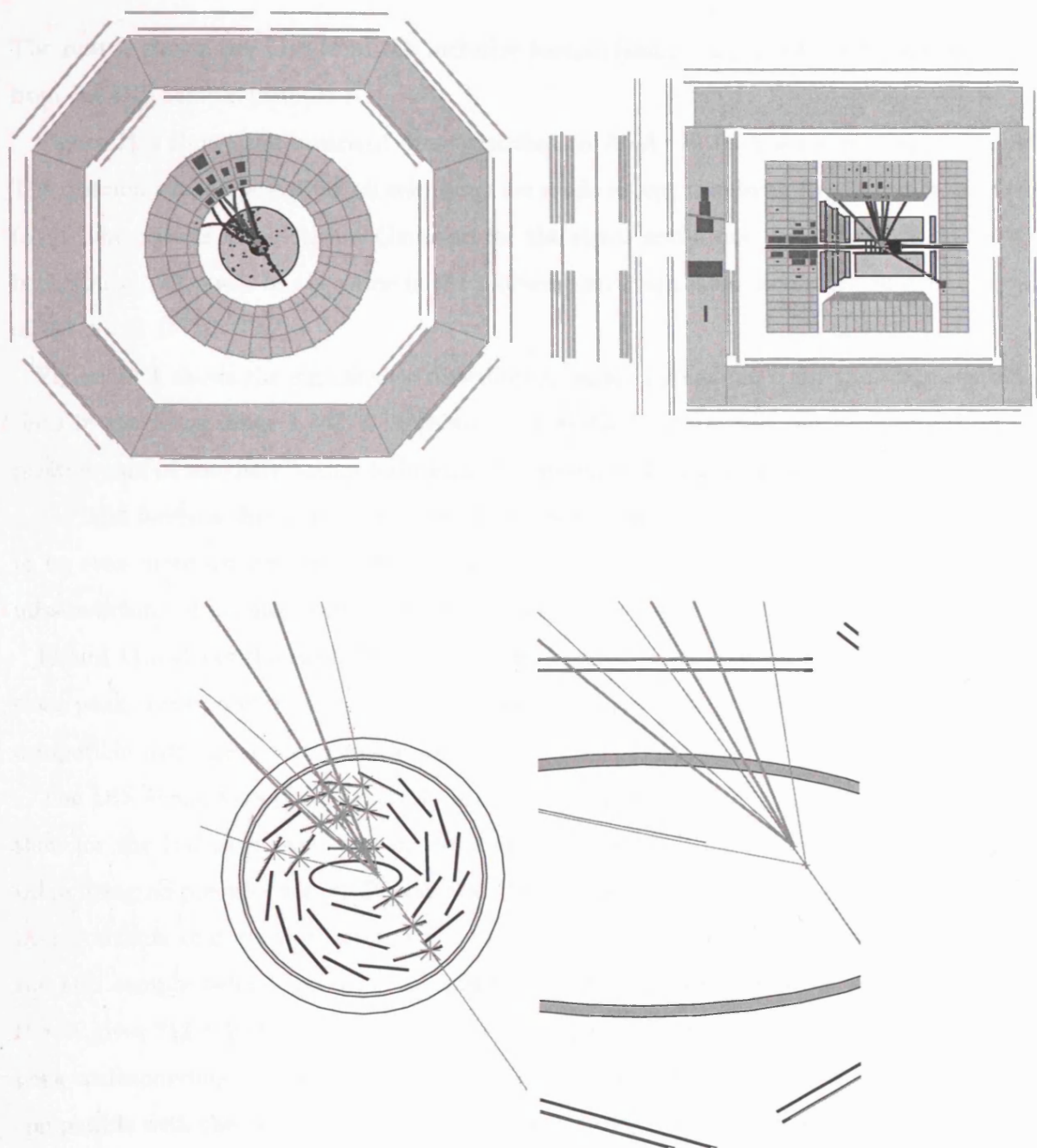


**Figure 11.5**  $M(K\pi\pi)$  invariant mass distribution with decay length significance  $L/\sigma_L > 7$ . The inclusive event sample is used (sample B, in the text). The data is fitted with a Gaussian for the signal and a first order polynomial for the background.



**Figure 11.6**  $M(K\pi\pi)$  invariant mass distribution with decay length significance  $L/\sigma_L > 6$ . The DIS event sample is used (sample A, in the text). The data is fitted with a Gaussian for the signal and a first order polynomial for the background. The invariant mass distribution before the decay length significance cut is shown in the inserted plot.





**Figure 11.7** Event display of a DIS  $D^+$  candidate event. Three of the tracks combine to a secondary vertex  $D^+$  candidate. Unfortunately also a fourth track fits to the secondary vertex. The large decay length means that this is almost certainly from a beauty decay.

## 11.2 Upgrade potential summary

The results shown are first from the inclusive sample (sample B) and then a result is shown from the DIS sample (sample A).

Figure 11.3 shows the invariant mass distribution  $M(K\pi\pi)$  for the inclusive data sample. The distribution is made after all selections are made except the decay length significance cut ( $S_L$ ). The data is fitted with a Gaussian for the signal and a first order polynomial for the background. This will be the same in the following invariant mass plots. The fit gave a signal of  $417 \pm 195$   $D^\pm$ 's.

Figure 11.4 shows the significance distribution (again for sample B) for the track combinations in the mass range  $1.845 < M(K\pi\pi) < 1.905$  GeV. An excess can be observed on the positive side of the distribution indicating the presence of long-lived decays.

For light flavours this distribution is expected to be symmetric, and for beauty it is expected to be even more asymmetric. The feature at low values of significance can be attributed to miss matching of primary and secondary vertices.

Figure 11.5 shows the mass distribution after the significance cut of  $S_L > 7.0$  is applied. A clear peak corresponding to  $151 \pm 28$   $D^\pm$  mesons is observed at the  $D^\pm$  mass with a width compatible with the detector resolution.

The DIS signal selection (fig. 11.6) has the advantage of having a looser signal selection than for the inclusive case, due to the lower average track multiplicity in DIS events and there being no pre-selection of  $D^\pm$  mesons. The inclusive selection is predominantly triggered by algorithms that reconstruct the  $D^\pm$  mesons online. Figure 11.6 shows the results from the DIS sample before and after a significance cut is applied. Without a significance cut, the fit gives  $712 \pm 260$   $D^\pm$  candidates. After a significance cut of 6 is applied, again a clear peak corresponding to  $191 \pm 33$   $D^\pm$  mesons is observed at the correct mass and with a width compatible with the detector resolution. This cut reduces the combinatorial background by a factor of 45, while reducing the signal by a factor of 2.7.

Figure 11.7 shows an example DIS event from the  $D^\pm$  candidate sample. The scattered positron is separated from the other tracks. The three tracks that fit to the secondary vertex combine to make the  $D^+$  candidate with  $p_T^{D^\pm} = 5.1$  GeV.

This is the first time that  $D^\pm$  mesons have been tagged within the ZEUS micro vertex detector, showing the possibility to identifying long lived decays.

---

## 12 Summary & Outlook

---

Inclusive jet cross sections in photoproduction for events containing a  $D^*$  meson have been measured with the ZEUS detector at HERA using an integrated luminosity of  $78.6 \text{ pb}^{-1}$ . The events were required to have a virtuality of the incoming photon,  $Q^2$ , of less than  $1 \text{ GeV}^2$ , and a photon-proton centre-of-mass energy in the range  $130 < W_{\gamma p} < 280 \text{ GeV}$ . The measurements are compared with next-to-leading-order (NLO) QCD calculations. Good agreement is found with the NLO calculations over most of the measured kinematic region. Requiring a second jet in the event allowed a more detailed comparison with QCD calculations. The measured dijet cross sections are also compared to Monte Carlo (MC) predictions which incorporate leading-order matrix elements, followed by parton showers and hadronisation. The NLO QCD predictions are in general agreement with the data although differences have been isolated to regions where extra parton radiation is present. The MC models give a better description of the shape of the measured cross sections.

$D^\pm$  mesons in the three body decay  $D^\pm \rightarrow K^\mp, \pi^\pm, \pi^\pm$  have been tagged in the ZEUS microvertex detector for the first time, establishing that these new techniques can be used to select samples of such mesons in order pin down the production dynamics and to make direct measurements of these particles at HERA.

---

## 13 Appendix A : Inclusive jet cross section mass peaks

---

In this appendix the mass peaks are shown for the inclusive cross sections  $d\sigma/dE_T^{jet}$  fig. 17.1(13.2), and in subregions of  $\eta^{jet}$ :

$-1.5 < \eta^{jet} < -0.5$  fig.17.2(13.4),

$-0.5 < \eta^{jet} < 0.5$  fig.17.3(13.6),

$0.5 < \eta^{jet} < 1.5$  fig.17.4(13.8),  $1.5 < \eta^{jet} < 2.4$  fig.17.5(13.10) for data(HERWIG MC).

Mass peaks are shown for tagged(untagged) inclusive cross sections  $d\sigma/dE_T^{jet}$  fig. 17.9(17.13), fig.13.18(13.26) and for the cross sections  $d\sigma/d\eta^{jet}$  in regions of  $E_T^{jet}$ :

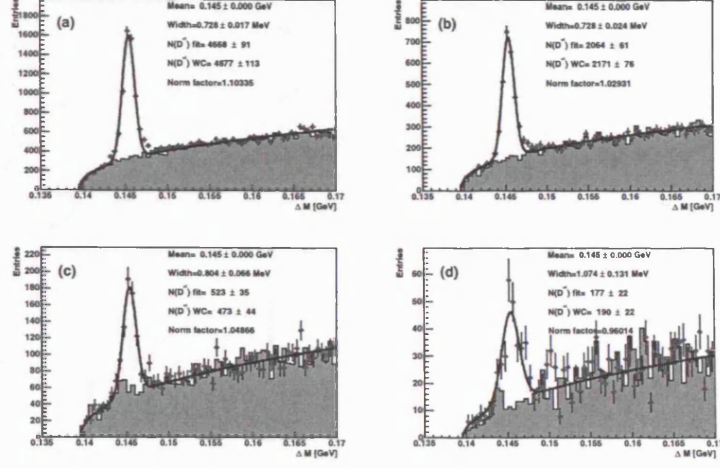
$E_T^{jet} > 6$  GeV fig. 17.10(17.14),fig.13.20(13.28),

$6 < E_T^{jet} < 9$  GeV fig. 17.11(17.15),fig.13.22(13.30),

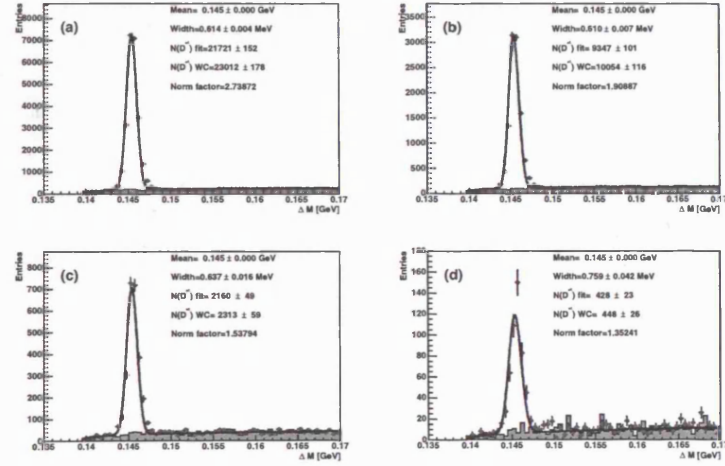
$E_T^{jet} > 9$  GeV fig. 17.12(17.16),fig.13.24(17.16).

The mass peaks for the inclusive cross sections  $d\sigma/d\eta^{jet}$  are show in fig. 17.6(13.12),fig.17.7(13.14), fig.17.8(13.16)

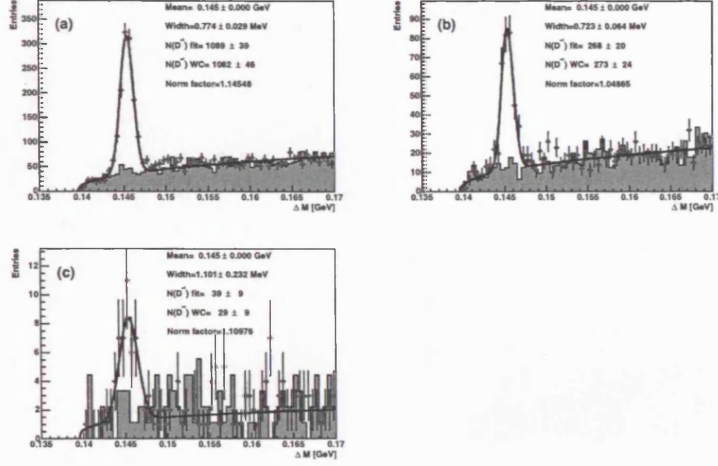
The mass peaks for the inclusive cross sections  $d\sigma/d\eta^{jet}$  are show in fig. 17.6(13.12), fig.17.7(13.14),fig.17.8(13.16).

13.0.1  $d\sigma/dE_T^{jet}$  Mass Peaks,  $-1.5 < \eta^{jet} < 2.4$ 


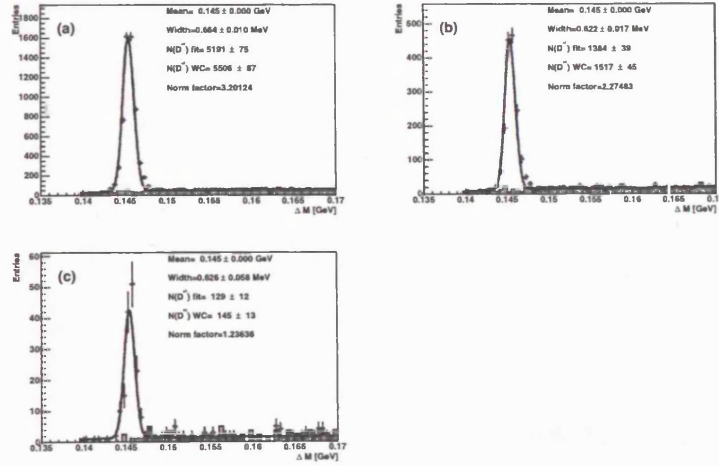
**Figure 13.1** Mass peaks for each bin of the inclusive charm jet cross section  $d\sigma/dE_T^{jet}$  in the range  $-1.5 < \eta^{jet} < 2.4$  for 1998-2000 data  $78pb^{-1}$ . (a) goes from the lowest  $E_T^{jet}$  bin to (d) the highest.



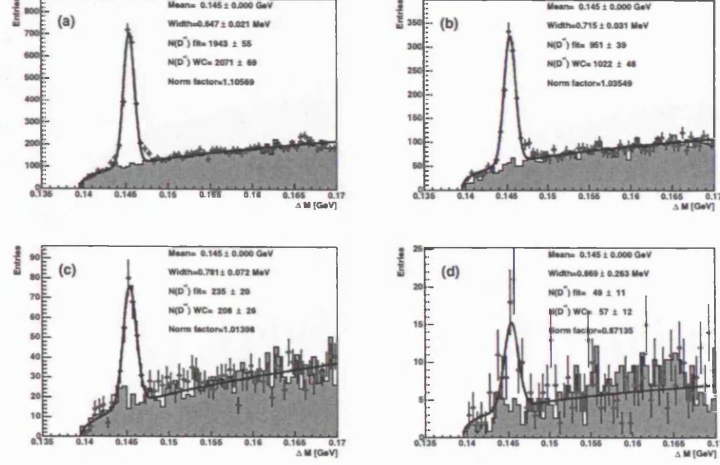
**Figure 13.2** Mass peaks for each bin of the inclusive charm jet cross section  $d\sigma/dE_T^{jet}$  in the range  $-1.5 < \eta^{jet} < 2.4$  for  $886pb^{-1}$  of HERWIG MC. (a) goes from the lowest  $E_T^{jet}$  bin to (d) the highest.

13.0.2  $d\sigma/dE_T^{jet}$  Mass Peaks,  $-1.5 < \eta^{jet} < -0.5$ 


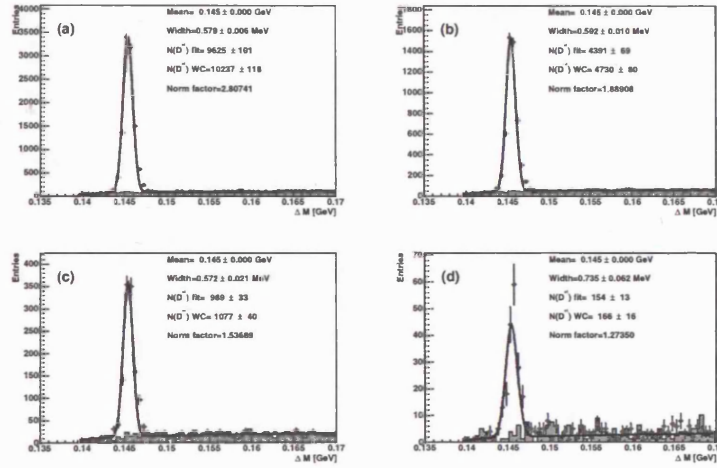
**Figure 13.3** Mass peaks for each bin of the inclusive charm jet cross section  $d\sigma/dE_T^{jet}$  in the range  $-1.5 < \eta^{jet} < -0.5$  for 1998-2000 data  $78pb^{-1}$ . (a) goes from the lowest  $E_T^{jet}$  bin to (d) the highest.



**Figure 13.4** Mass peaks for each bin of the inclusive charm jet cross section  $d\sigma/dE_T^{jet}$  in the range  $-1.5 < \eta^{jet} < -0.5$  for  $886pb^{-1}$  of HERWIG MC. (a) goes from the lowest  $E_T^{jet}$  bin to (d) the highest.

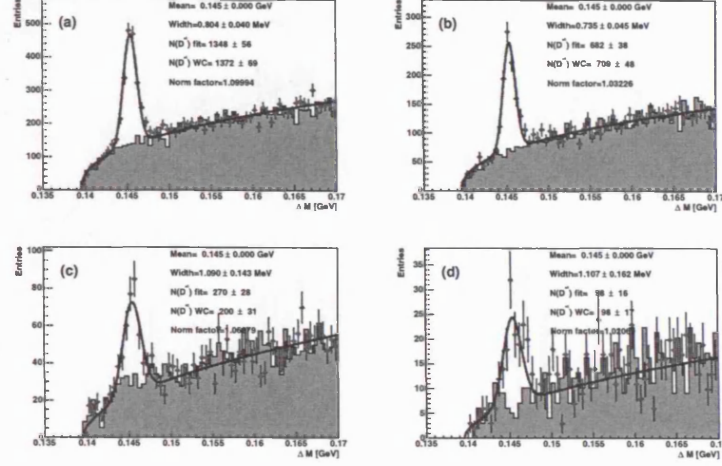
13.0.3  $d\sigma/dE_T^{jet}$  Mass Peaks,  $-0.5 < \eta^{jet} < 0.5$ 

**Figure 13.5** Mass peaks for each bin of the inclusive charm jet cross section  $d\sigma/dE_T^{jet}$  in the range  $-0.5 < \eta^{jet} < 0.5$  for 1998-2000 data  $78pb^{-1}$ . (a) goes from the lowest  $E_T^{jet}$  bin to (d) the highest.

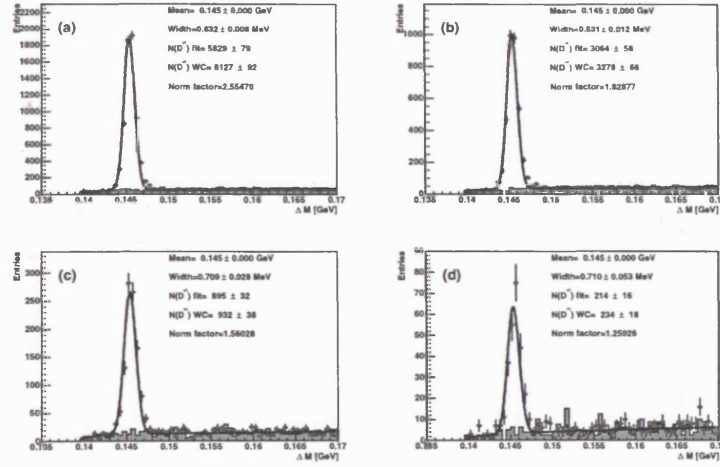


**Figure 13.6** Mass peaks for each bin of the inclusive charm jet cross section  $d\sigma/dE_T^{jet}$  in the range  $-0.5 < \eta^{jet} < 0.5$  for  $886pb^{-1}$  of HERWIG MC. (a) goes from the lowest  $E_T^{jet}$  bin to (d) the highest.



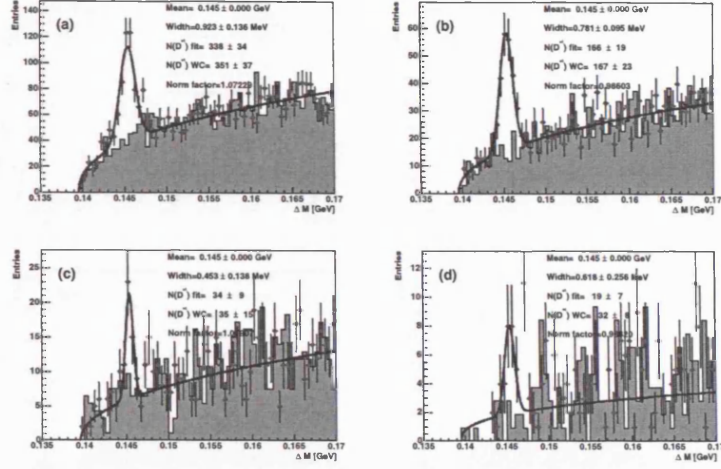
13.0.4  $d\sigma/dE_T^{jet}$  Mass Peaks,  $0.5 < \eta^{jet} < 1.5$ 

**Figure 13.7** Mass peaks for each bin of the inclusive charm jet cross section  $d\sigma/dE_T^{jet}$  in the range  $0.5 < \eta^{jet} < 1.5$  for 1998-2000 data  $78pb^{-1}$ . (a) goes from the lowest  $E_T^{jet}$  bin to (d) the highest.

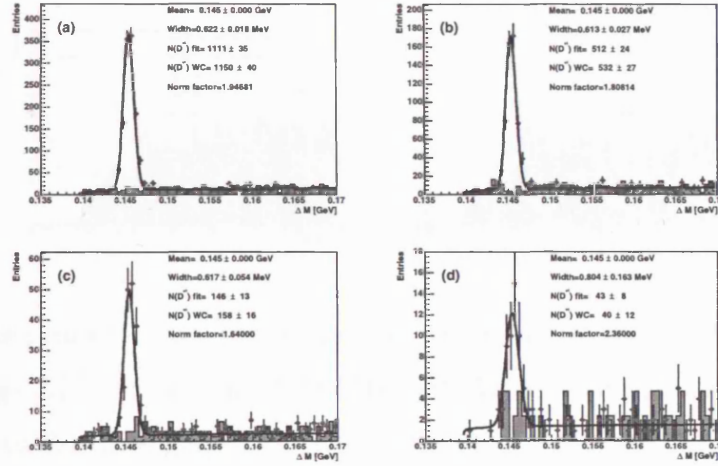


**Figure 13.8** Mass peaks for each bin of the inclusive charm jet cross section  $d\sigma/dE_T^{jet}$  in the range  $0.5 < \eta^{jet} < 1.5$  for  $886pb^{-1}$  of HERWIG MC. (a) goes from the lowest  $E_T^{jet}$  bin to (d) the highest.

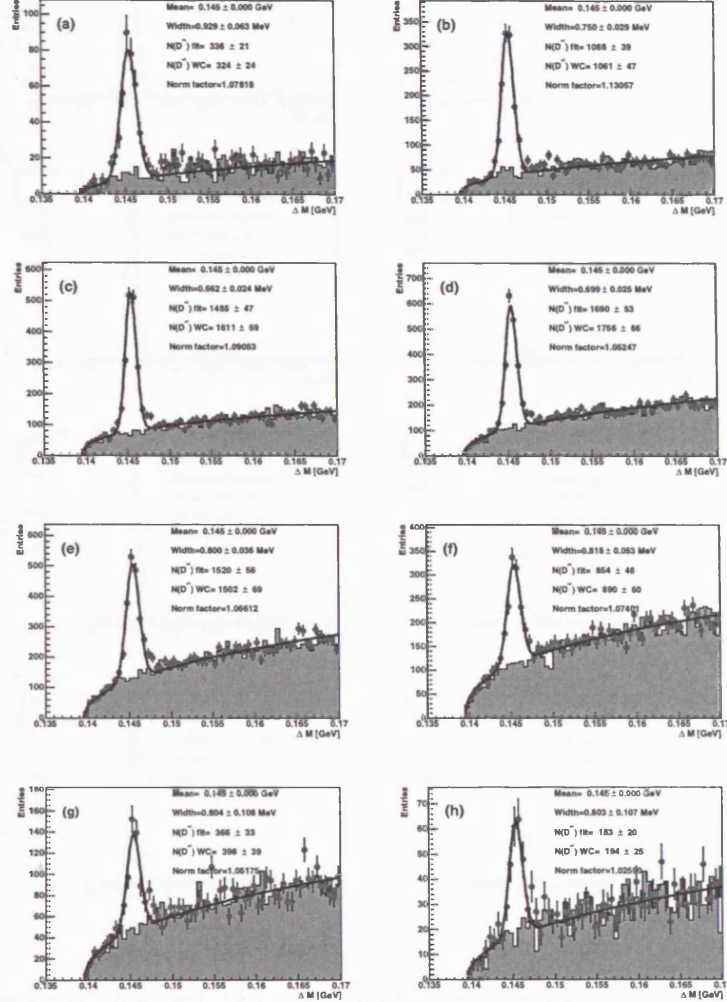


13.0.5  $d\sigma/dE_T^{jet}$  Mass Peaks,  $1.5 < \eta^{jet} < 2.4$ 


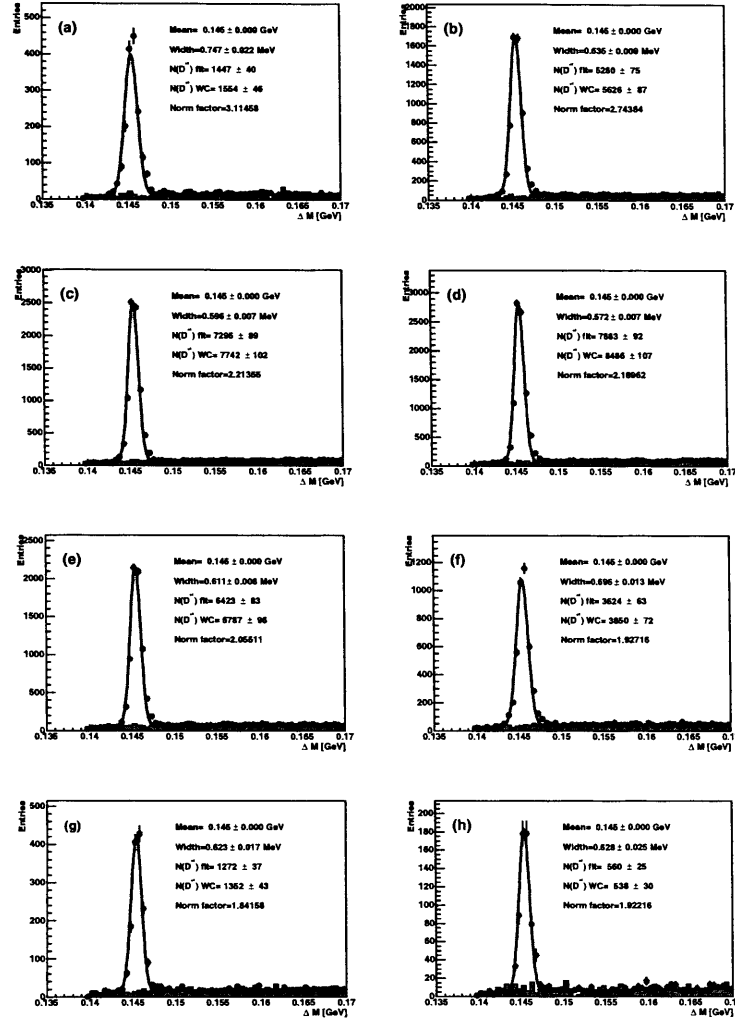
**Figure 13.9** Mass peaks for each bin of the inclusive charm jet cross section  $d\sigma/dE_T^{jet}$  in the range  $1.5 < \eta^{jet} < 2.4$  for 1998-2000 data  $78pb^{-1}$ . (a) goes from the lowest  $E_T^{jet}$  bin to (d) the highest.



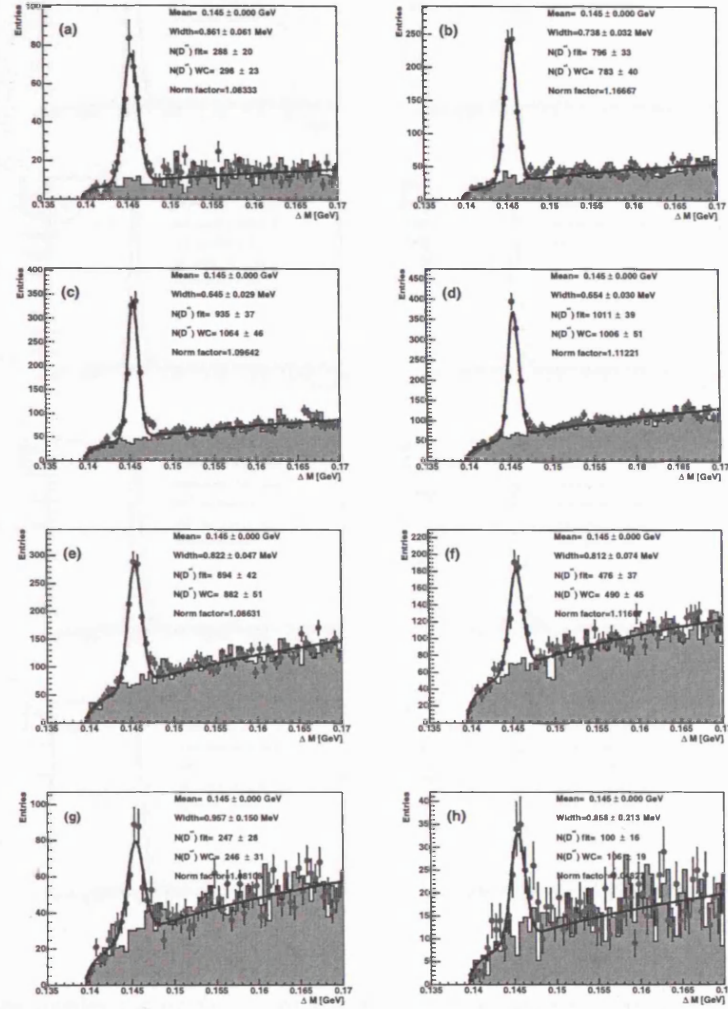
**Figure 13.10** Mass peaks for each bin of the inclusive charm jet cross section  $d\sigma/dE_T^{jet}$  in the range  $1.5 < \eta^{jet} < 2.4$  for 886 $pb^{-1}$  of HERWIG MC. (a) goes from the lowest  $E_T^{jet}$  bin to (d) the highest.

13.0.6  $d\sigma/d\eta^{jet}$  Mass Peaks,  $E_T^{jet} > 6$  GeV

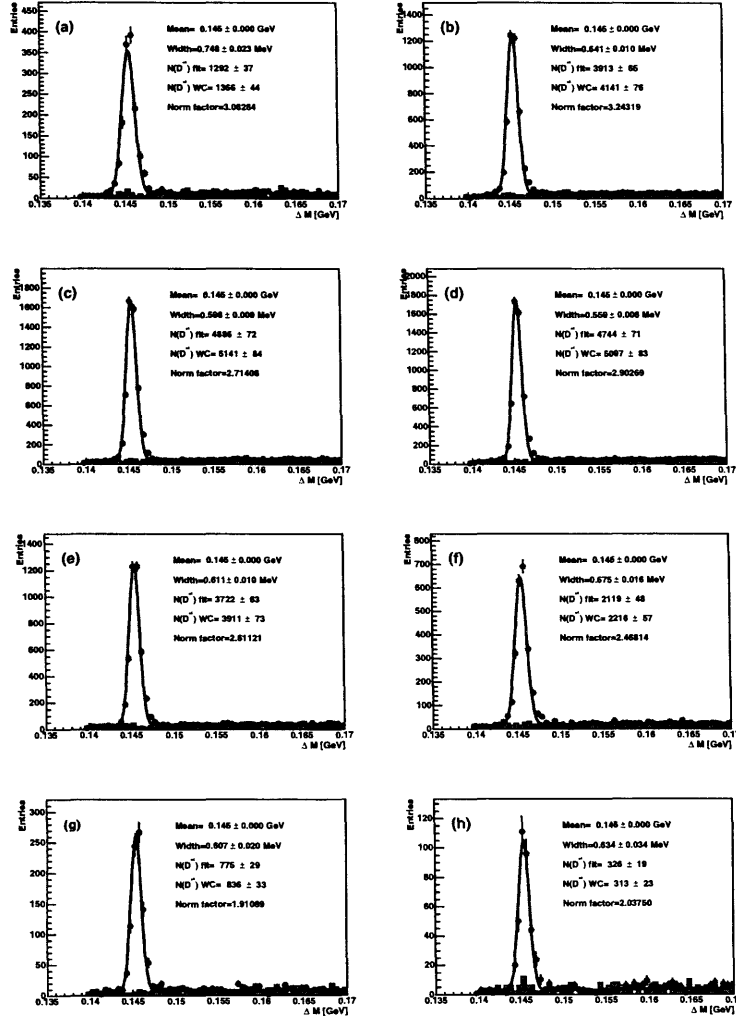
**Figure 13.11** Mass peaks for each bin of the inclusive charm jet cross section  $d\sigma/d\eta^{jet}$  in the range  $E_T^{jet} > 6$  GeV for 1998-2000 data  $78pb^{-1}$ . (a) goes from the lowest  $E_T^{jet}$  bin to (h) the highest.



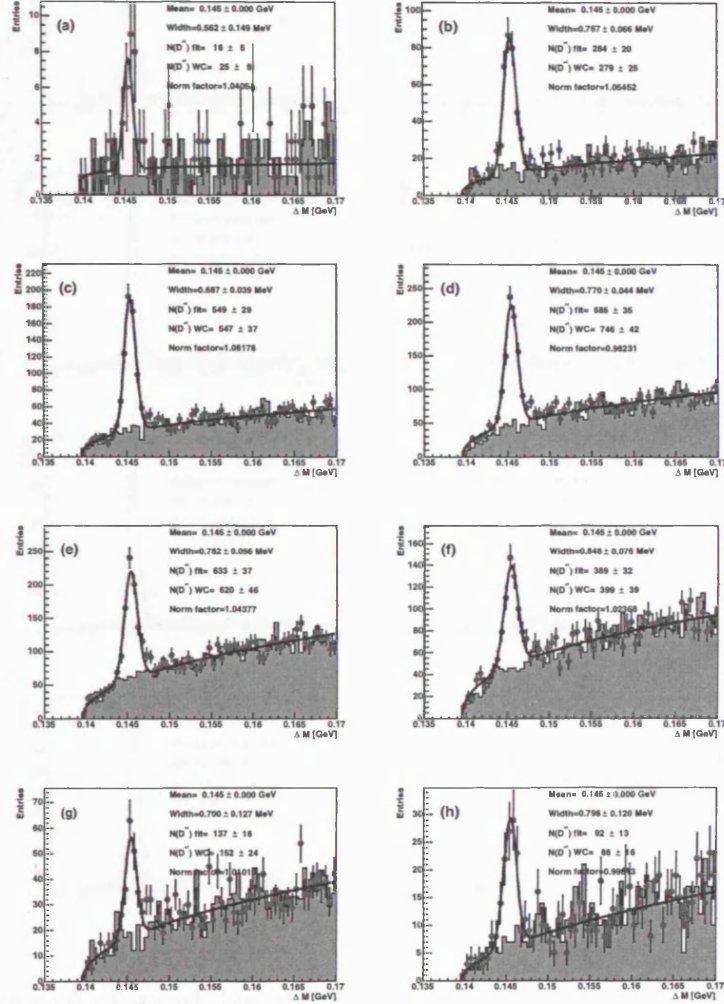
**Figure 13.12** Mass peaks for each bin of the inclusive charm jet cross section  $d\sigma/d\tau^{jet}$  in the range  $E_T^{jet} > 6$  GeV for  $886pb^{-1}$  of HERWIG MC. (a) goes from the lowest  $E_T^{jet}$  bin to (h) the highest.

13.0.7  $d\sigma/d\eta^{jet}$  Mass Peaks,  $6 < E_T^{jet} < 9$  GeV

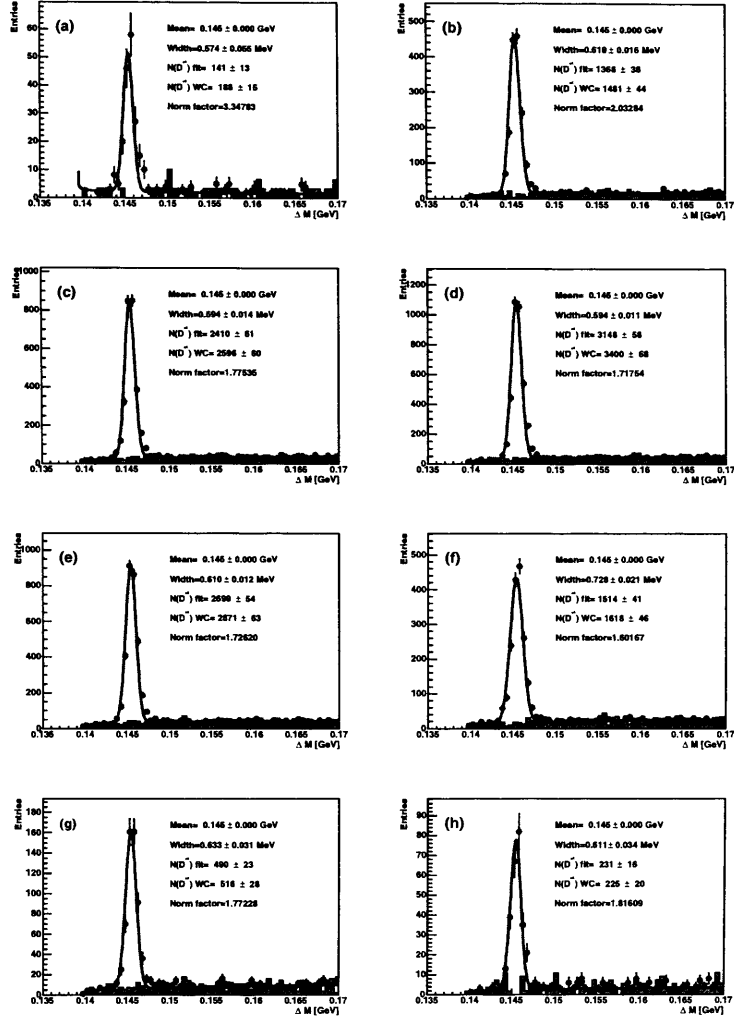
**Figure 13.13** Mass peaks for each bin of the inclusive charm jet cross section  $d\sigma/d\eta^{jet}$  in the range  $6 < E_T^{jet} < 9$  GeV for 1998-2000 data  $78pb^{-1}$ . (a) goes from the lowest  $E_T^{jet}$  bin to (h) the highest.



**Figure 13.14** Mass peaks for each bin of the inclusive charm jet cross section  $d\sigma/d\eta^{jet}$  in the range  $6 < E_T^{jet} < 9$  GeV for  $886 pb^{-1}$  of HERWIG MC. (a) goes from the lowest  $E_T^{jet}$  bin to (h) the highest.

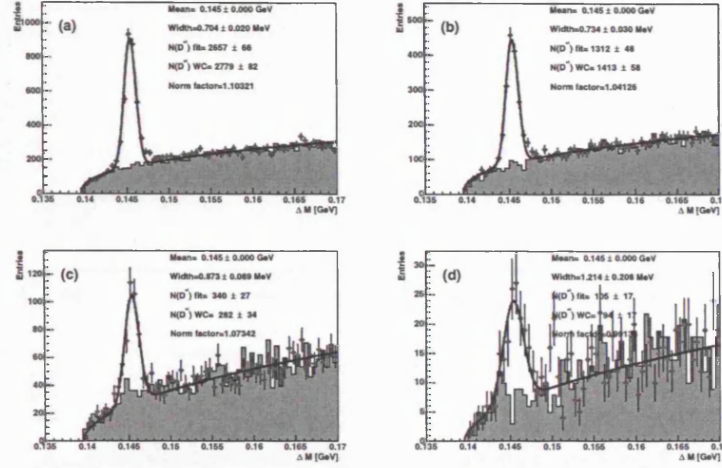
13.0.8  $d\sigma/d\eta^{jet}$  Mass Peaks,  $E_T^{jet} > 9$  GeV

**Figure 13.15** Mass peaks for each bin of the inclusive charm jet cross section  $d\sigma/d\eta^{jet}$  in the range  $E_T^{jet} > 9$  GeV for 1998-2000 data  $78pb^{-1}$ . (a) goes from the lowest  $E_T^{jet}$  bin to (h) the highest.

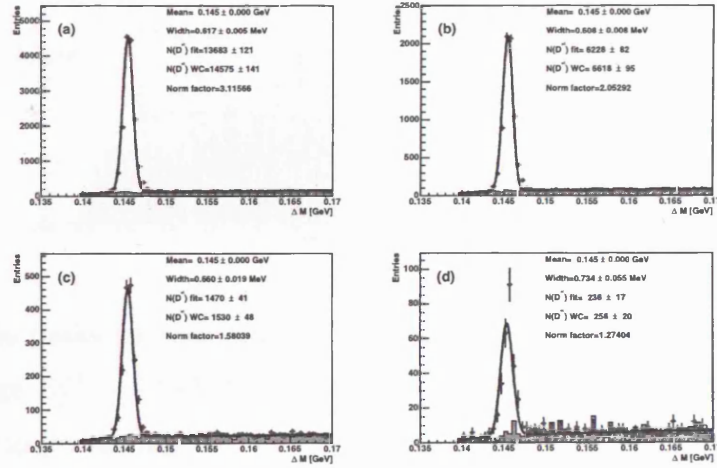


**Figure 13.16** Mass peaks for each bin of the inclusive charm jet cross section  $d\sigma/d\eta^{jet}$  in the range  $E_T^{jet} > 9$  GeV for  $886pb^{-1}$  of HERWIG MC. (a) goes from the lowest  $E_T^{jet}$  bin to (h) the highest.



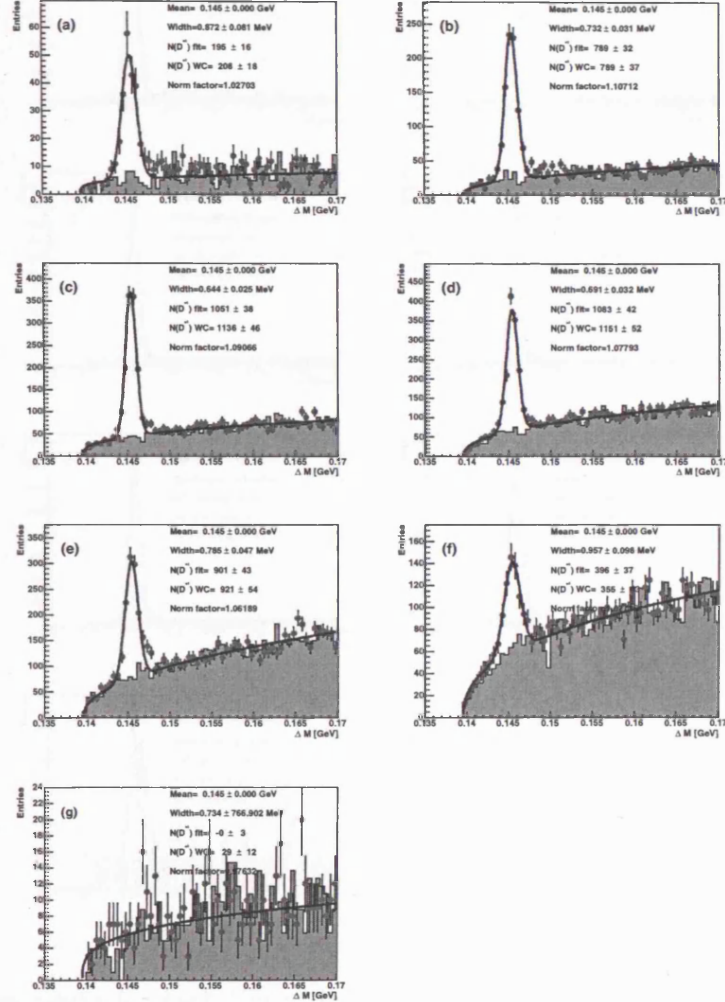
13.0.9  $d\sigma/dE_T^{jet}$  Mass Peaks,  $-1.5 < \eta^{jet} < 2.4$  tagged  $D^*$  jets

**Figure 13.17** Mass peaks for each bin of the tagged  $D^*$  jet cross section  $d\sigma/dE_T^{jet}$  in the range  $-1.5 < \eta^{jet} < 2.4$  for 1998-2000 data  $78pb^{-1}$ . (a) goes from the lowest  $E_T^{jet}$  bin to (d) the highest.

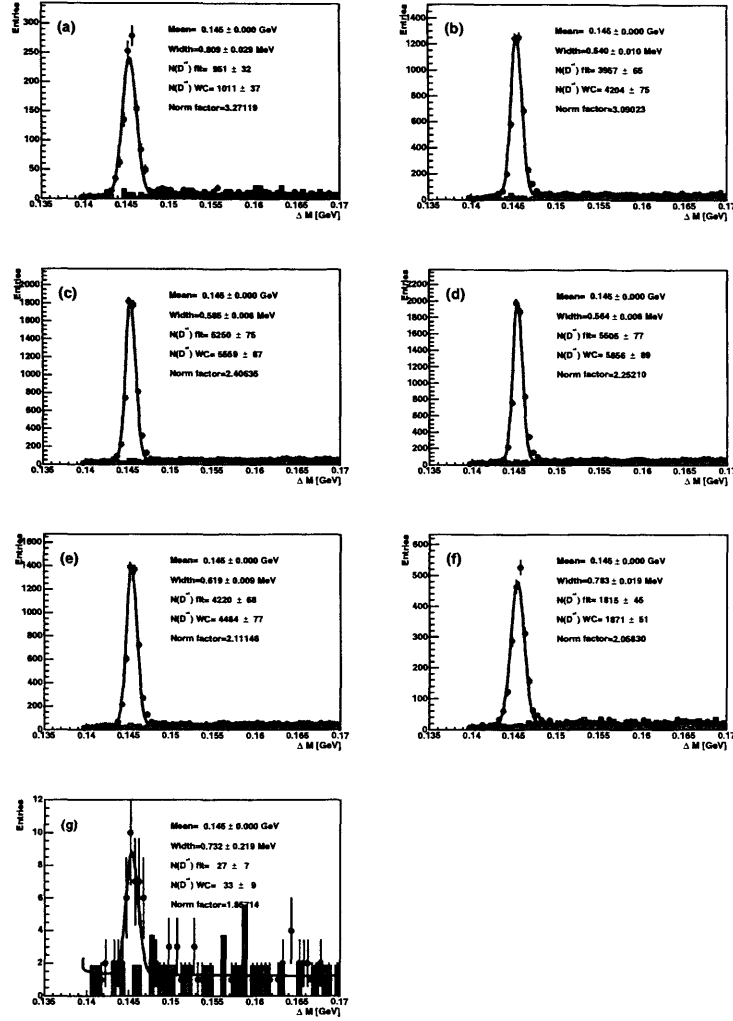


**Figure 13.18** Mass peaks for each bin of the tagged  $D^*$  jet cross section  $d\sigma/dE_T^{jet}$  in the range  $-1.5 < \eta^{jet} < 2.4$  for  $886pb^{-1}$  of HERWIG MC. (a) goes from the lowest  $E_T^{jet}$  bin to (d) the highest.

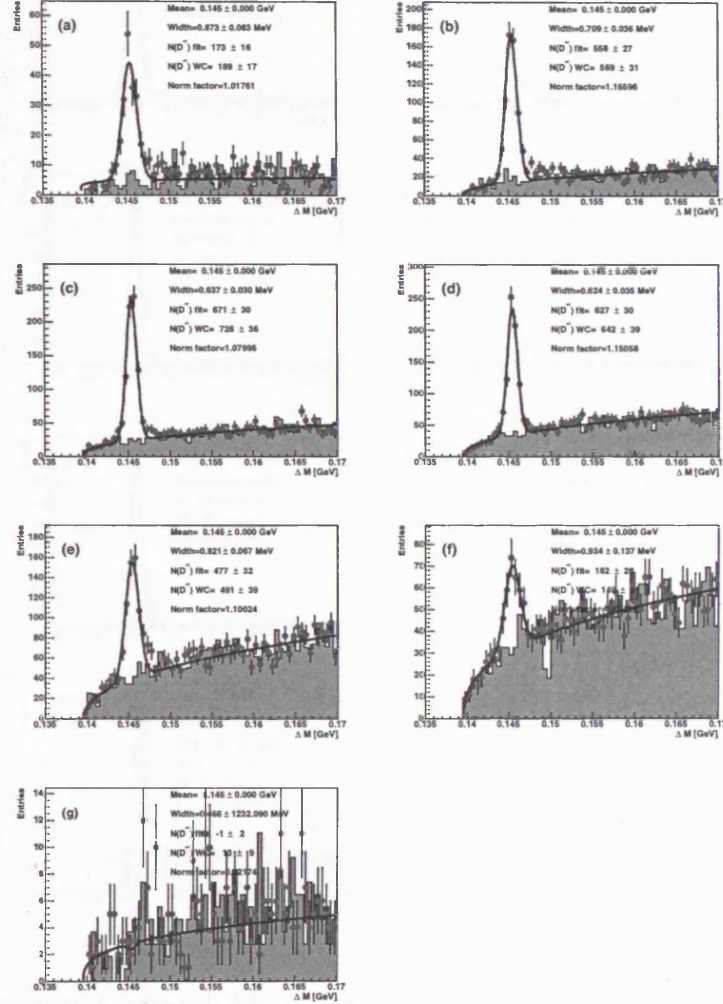


13.0.10  $d\sigma/d\eta^{jet}$  Mass Peaks,  $E_T^{jet} > 6$  GeV tagged  $D^*$  jets

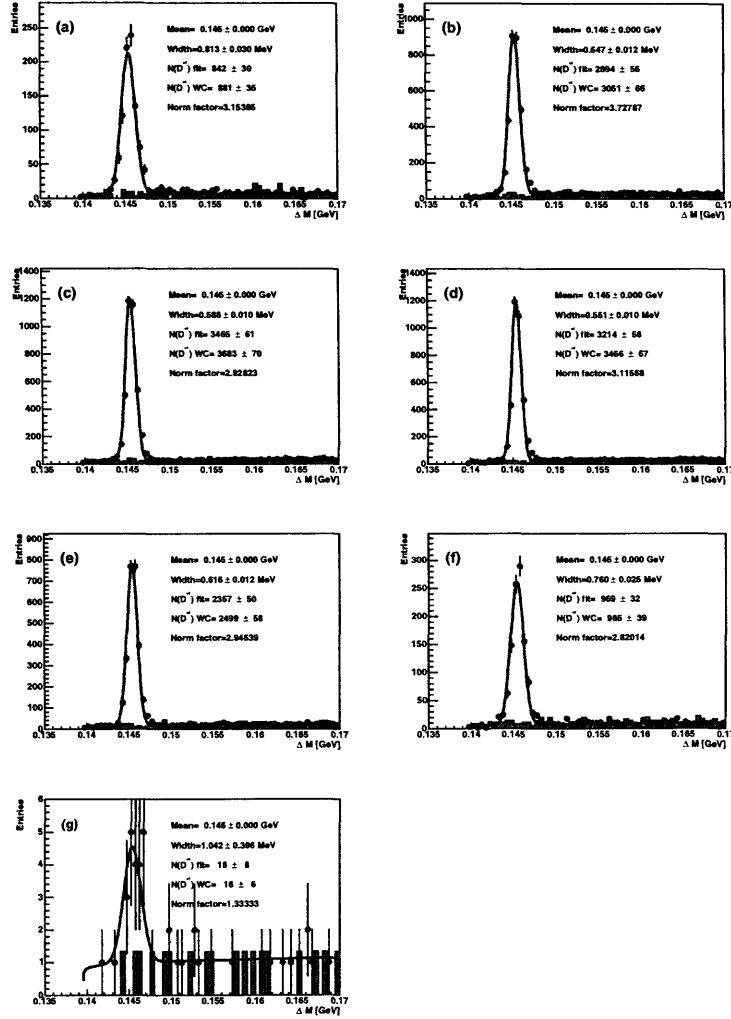
**Figure 13.19** Mass peaks for each bin of the untagged  $D^*$  jet cross section  $d\sigma/d\eta^{jet}$  in the range  $E_T^{jet} > 6$  GeV for 1998-2000 data  $78pb^{-1}$ . (a) goes from the lowest  $\eta^{jet}$  bin to (h) the highest.



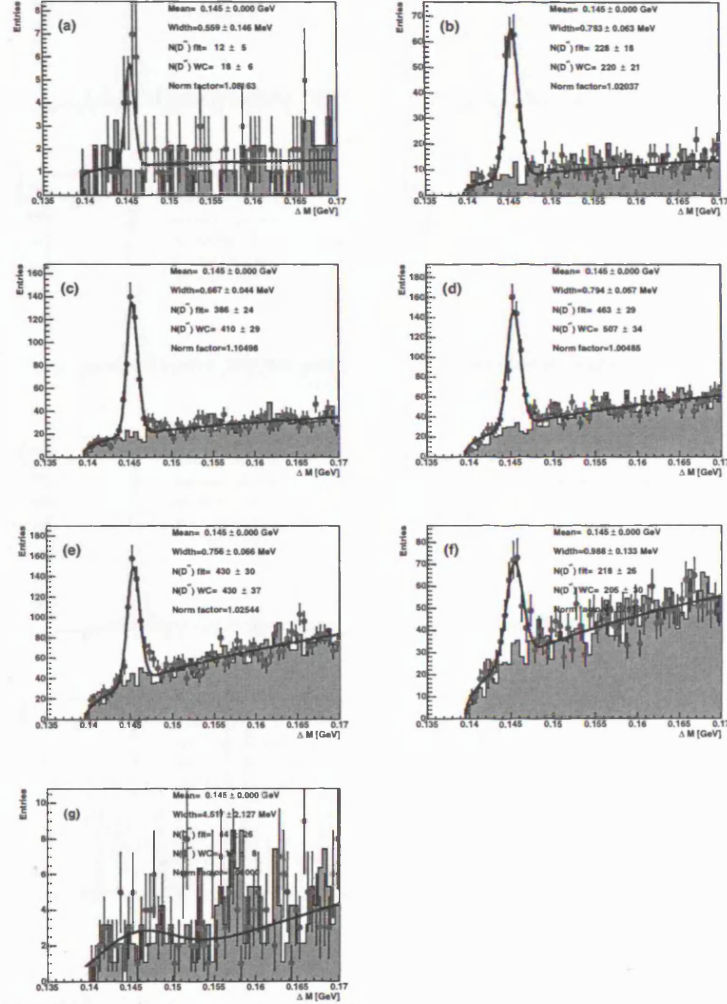
**Figure 13.20** Mass peaks for each bin of the untagged  $D^*$  jet cross section  $d\sigma/d\eta^{jet}$  in the range  $E_T^{jet} > 6$  GeV for  $886pb^{-1}$  of HERWIG MC. (a) goes from the lowest  $\eta^{jet}$  bin to (h) the highest.

13.0.11  $d\sigma/d\eta^{jet}$  Mass Peaks,  $6 < E_T^{jet} < 9$  GeV tagged  $D^*$  jets

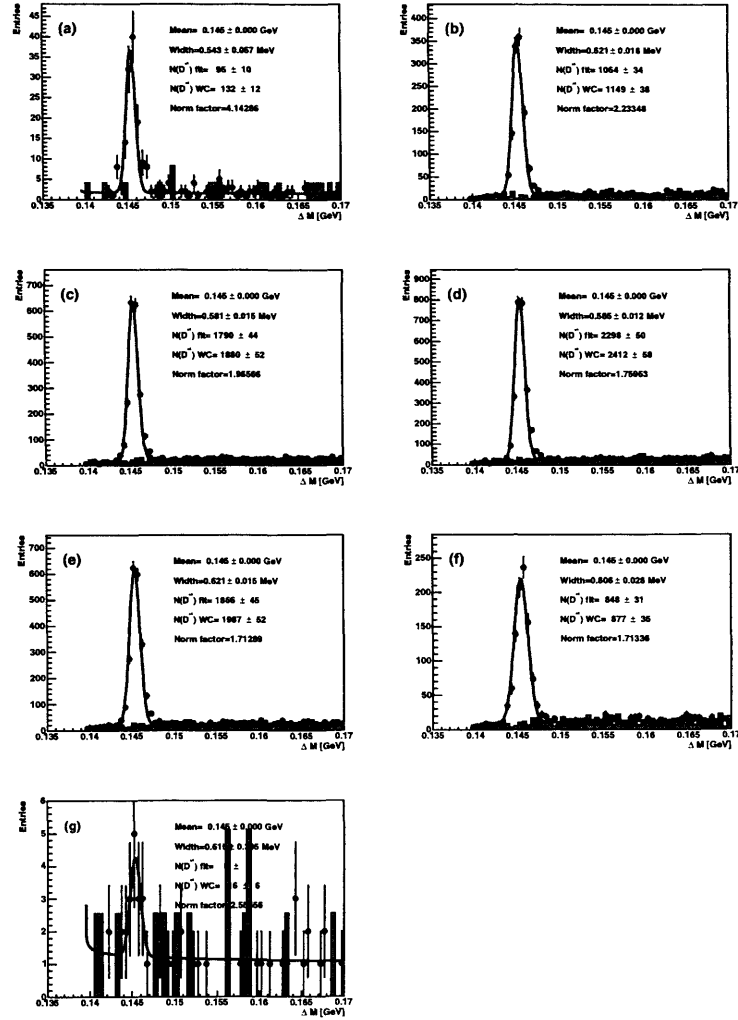
**Figure 13.21** Mass peaks for each bin of the untagged  $D^*$  jet cross section  $d\sigma/d\eta^{jet}$  in the range  $6 < E_T^{jet} < 9$  GeV for 1998-2000 data  $78pb^{-1}$ . (a) goes from the lowest  $\eta^{jet}$  bin to (h) the highest.



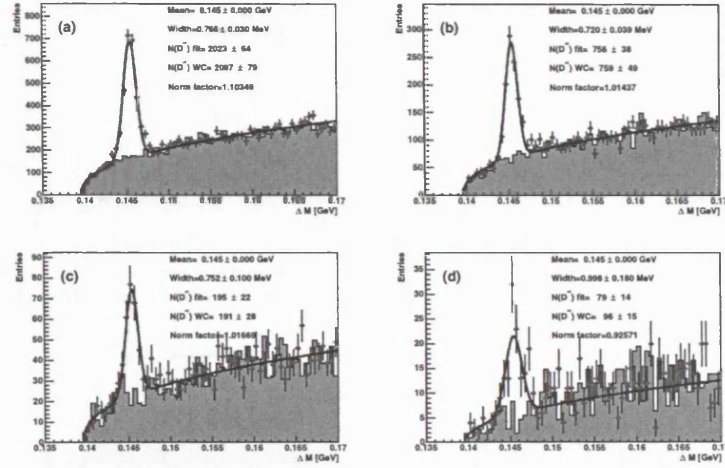
**Figure 13.22** Mass peaks for each bin of the untagged  $D^*$  jet cross section  $d\sigma/d\eta^{jet}$  in the range  $6 < E_T^{jet} < 9$  GeV for  $886 pb^{-1}$  of HERWIG MC. (a) goes from the lowest  $\eta^{jet}$  bin to (h) the highest.

13.0.12  $d\sigma/d\eta^{jet}$  Mass Peaks,  $E_T^{jet} > 9$  GeV tagged  $D^*$  jets

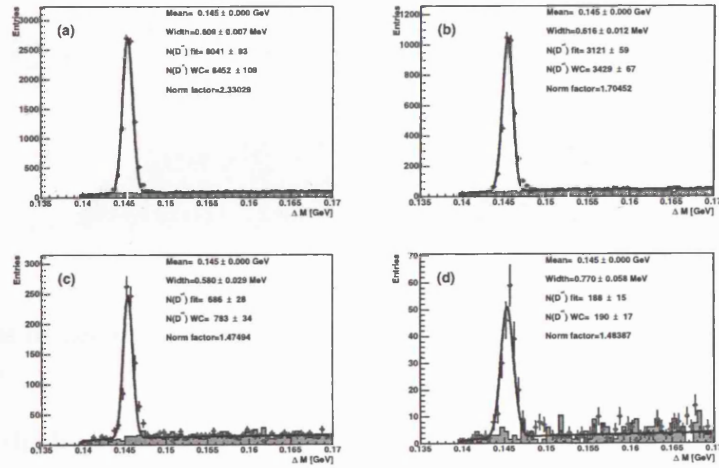
**Figure 13.23** Mass peaks for each bin of the untagged  $D^*$  jet cross section  $d\sigma/d\eta^{jet}$  in the range  $E_T^{jet} > 9$  GeV for 1998-2000 data  $78pb^{-1}$ . (a) goes from the lowest  $\eta^{jet}$  bin to (h) the highest.



**Figure 13.24** Mass peaks for each bin of the untagged  $D^*$  jet cross section  $d\sigma/d\eta^{jet}$  in the range  $E_T^{jet} > 9$  GeV for  $886pb^{-1}$  of HERWIG MC. (a) goes from the lowest  $\eta^{jet}$  bin to (h) the highest.

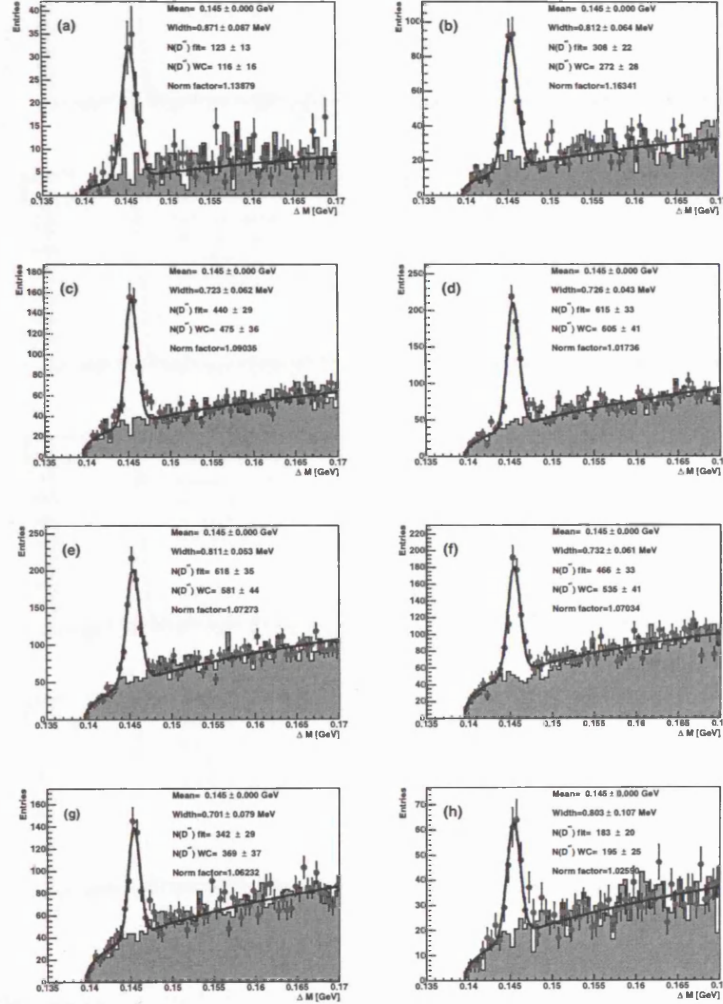
13.0.13  $d\sigma/dE_T^{jet}$  Mass Peaks,  $-1.5 < \eta^{jet} < 2.4$  untagged  $D^*$  jets

**Figure 13.25** Mass peaks for each bin of the untagged  $D^*$  jet cross section  $d\sigma/dE_T^{jet}$  in the range  $-1.5 < \eta^{jet} < 2.4$  for 1998-2000 data  $78pb^{-1}$ . (a) goes from the lowest  $E_T^{jet}$  bin to (d) the highest.



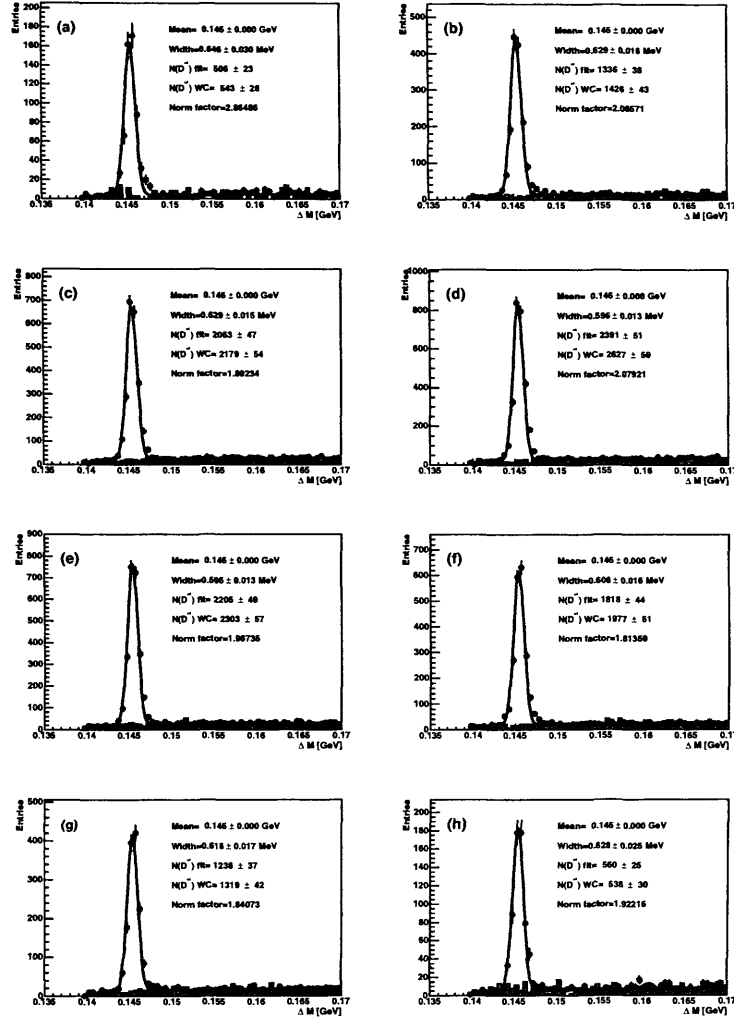
**Figure 13.26** Mass peaks for each bin of the untagged  $D^*$  jet cross section  $d\sigma/dE_T^{jet}$  in the range  $-1.5 < \eta^{jet} < 2.4$  for  $886pb^{-1}$  of HERWIG MC. (a) goes from the lowest  $E_T^{jet}$  bin to (d) the highest.



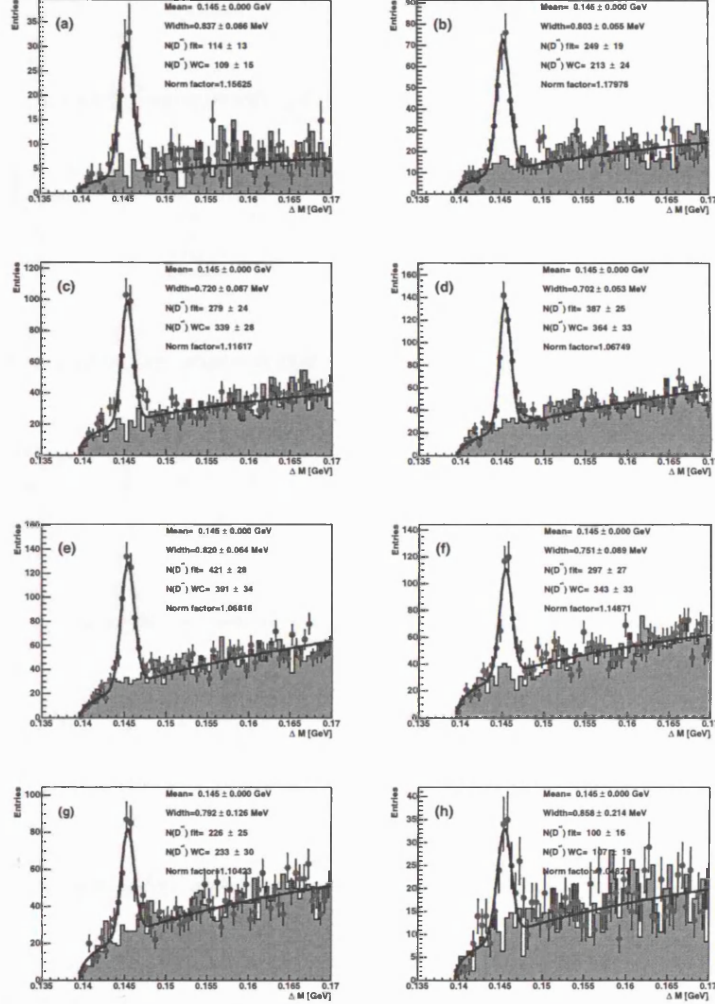
13.0.14  $d\sigma/d\eta^{jet}$  Mass Peaks,  $E_T^{jet} > 6$  GeV untagged  $D^*$  jets

**Figure 13.27** Mass peaks for each bin of the tagged  $D^*$  jet cross section  $d\sigma/d\eta^{jet}$  in the range  $E_T^{jet} > 6$  GeV for 1998-2000 data  $78pb^{-1}$ . (a) goes from the lowest  $\eta^{jet}$  bin to (h) the highest.

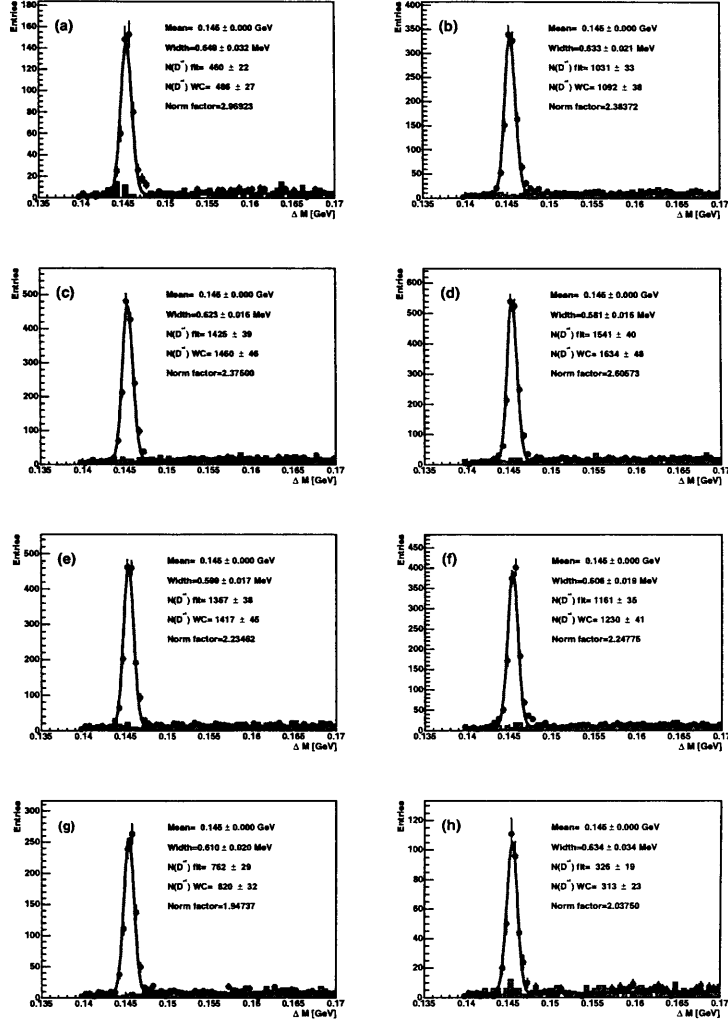




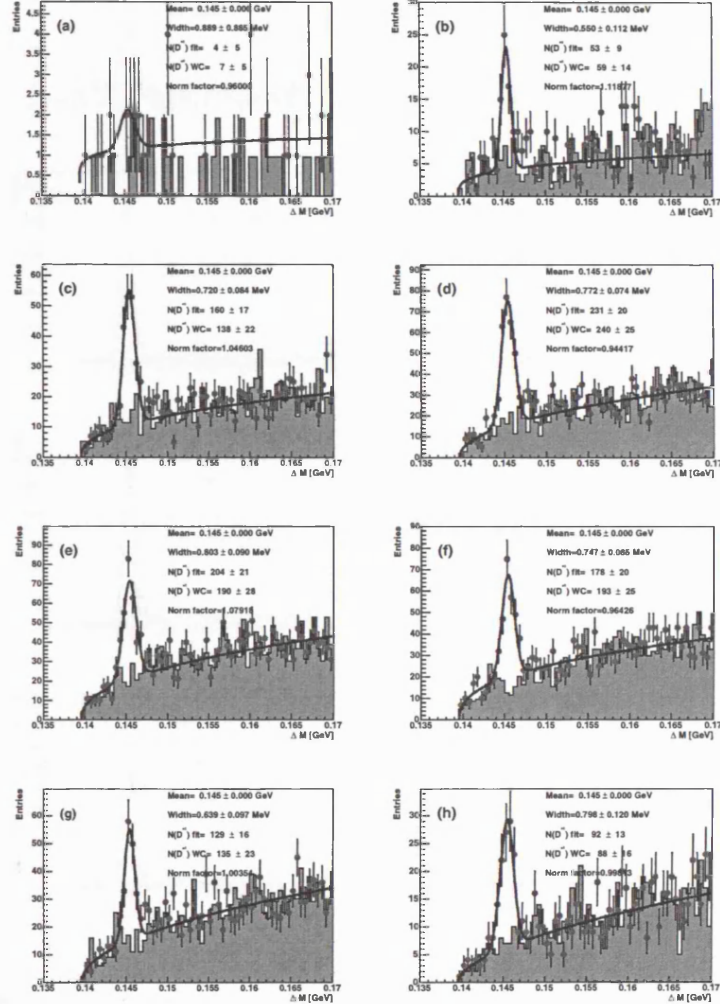
**Figure 13.28** Mass peaks for each bin of the tagged  $D^*$  jet cross section  $d\sigma/d\eta^{jet}$  in the range  $E_T^{jet} > 6$  GeV for 886 pb<sup>-1</sup> of HERWIG MC. (a) goes from the lowest  $\eta^{jet}$  bin to (h) the highest.

13.0.15  $d\sigma/d\eta^{jet}$  Mass Peaks,  $6 < E_T^{jet} < 9$  GeV untagged  $D^*$  jets

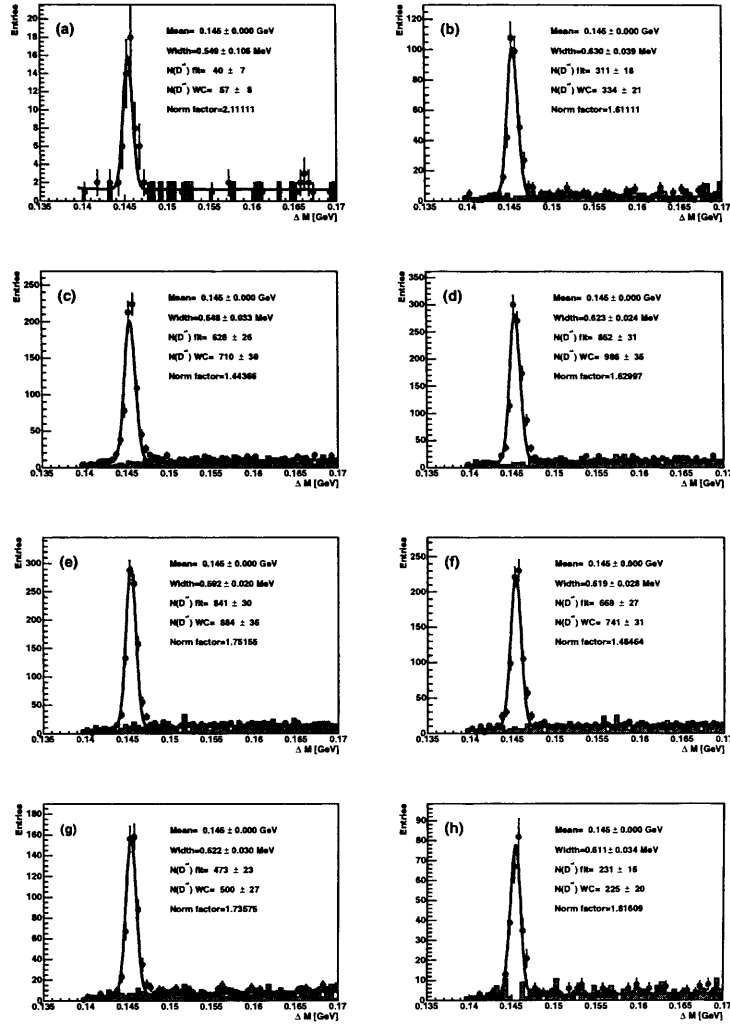
**Figure 13.29** Mass peaks for each bin of the tagged  $D^*$  jet cross section  $d\sigma/d\eta^{jet}$  in the range  $6 < E_T^{jet} < 9$  GeV for 1998-2000 data  $78pb^{-1}$ . (a) goes from the lowest  $\eta^{jet}$  bin to (h) the highest.



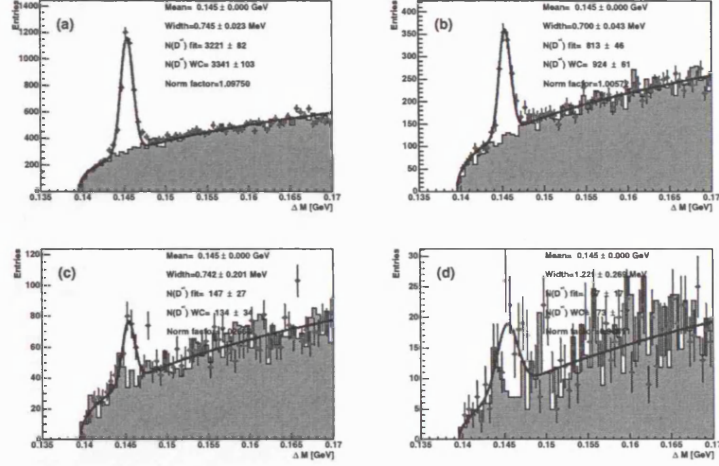
**Figure 13.30** Mass peaks for each bin of the tagged  $D^*$  jet cross section  $d\sigma/d\eta^{jet}$  in the range  $6 < E_T^{jet} < 9$  GeV for  $886 pb^{-1}$  of HERWIG MC. (a) goes from the lowest  $\eta^{jet}$  bin to (h) the highest.

13.0.16  $d\sigma/d\eta^{jet}$  Mass Peaks,  $E_T^{jet} > 9$  GeV untagged  $D^*$  jets

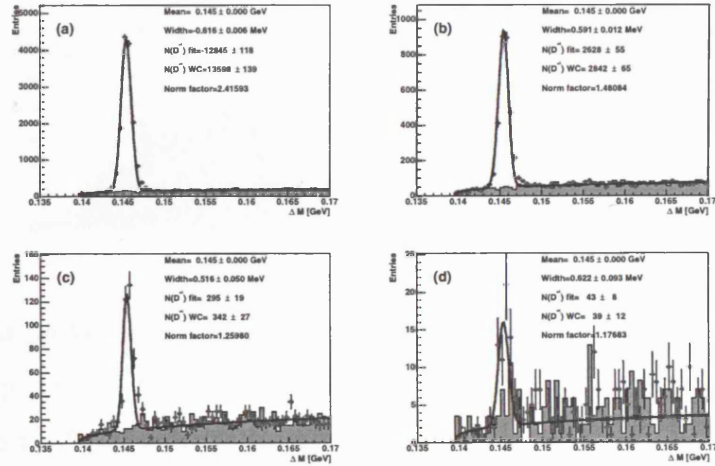
**Figure 13.31** Mass peaks for each bin of the tagged  $D^*$  jet cross section  $d\sigma/d\eta^{jet}$  in the range  $E_T^{jet} > 9$  GeV for 1998-2000 data  $78pb^{-1}$ . (a) goes from the lowest  $\eta^{jet}$  bin to (h) the highest.



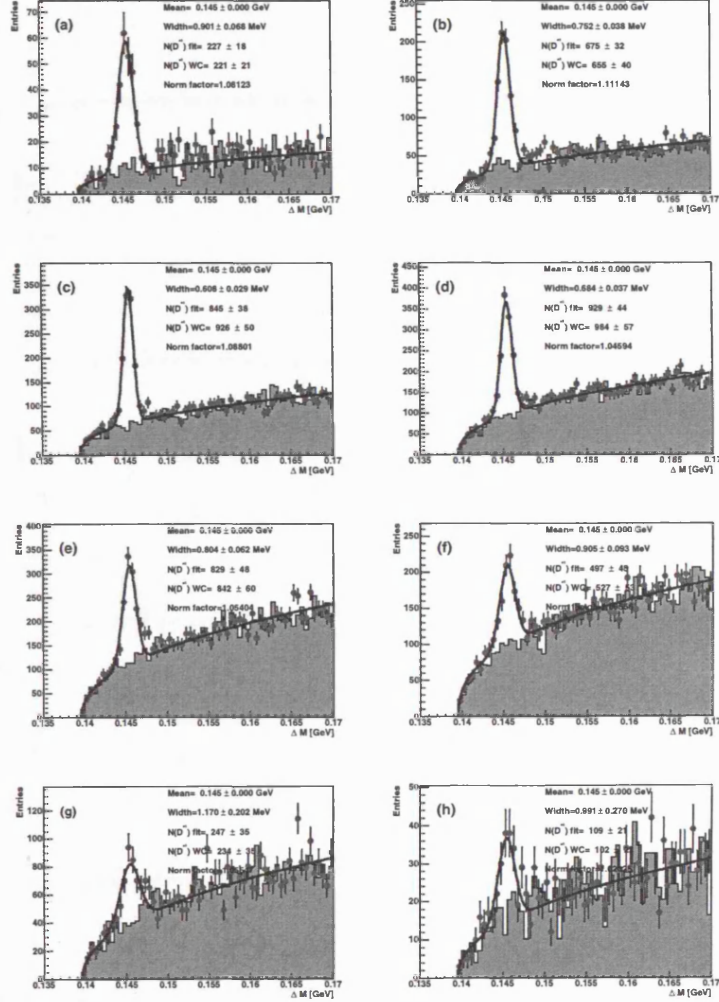
**Figure 13.32** Mass peaks for each bin of the tagged  $D^*$  jet cross section  $d\sigma/d\eta^{jet}$  in the range  $E_T^{jet} > 9$  GeV for 886 pb<sup>-1</sup> of HERWIG MC. (a) goes from the lowest  $\eta^{jet}$  bin to (h) the highest.

13.0.17  $d\sigma/dE_T^{jet}$  Mass Peaks,  $3.0 < p_T^{D^*} < 5.0$  GeV

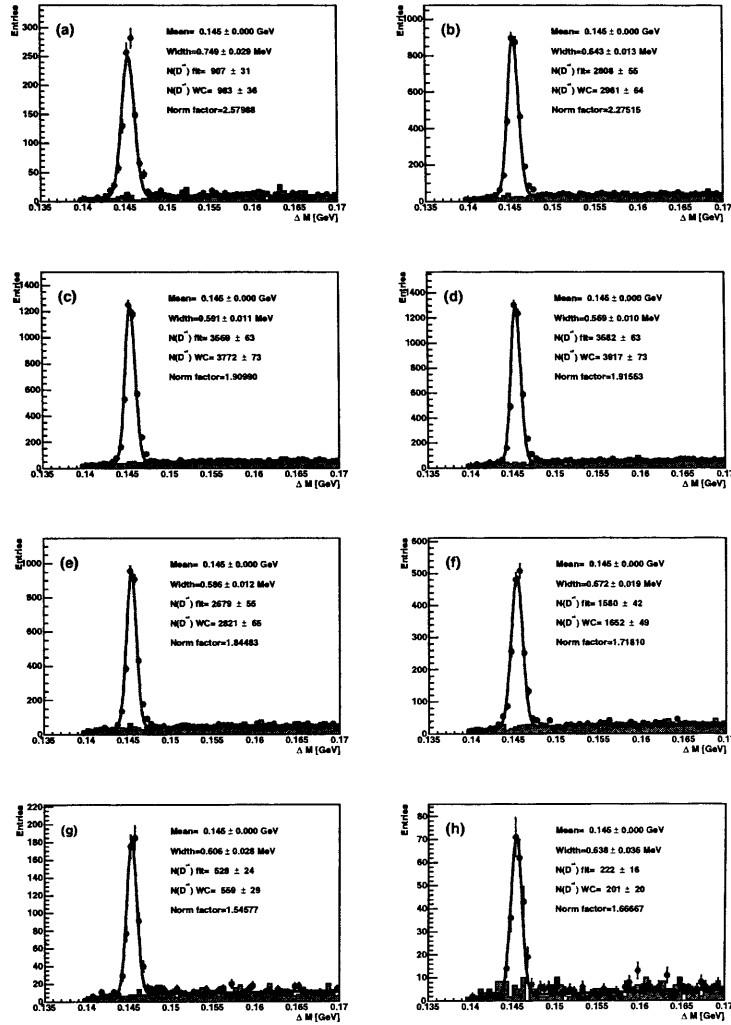
**Figure 13.33** Mass peaks for each bin of the inclusive charm jet cross section  $d\sigma/dE_T^{jet}$  in the range  $3.0 < P_T^{D^*} < 5.0$  GeV for 1998-2000 data  $78pb^{-1}$ . (a) goes from the lowest  $E_T^{jet}$  bin to (d) the highest.



**Figure 13.34** Mass peaks for each bin of the inclusive charm jet cross section  $d\sigma/dE_T^{jet}$  in the range  $3.0 < P_T^{D^*} < 5.0$  GeV for  $886pb^{-1}$  of HERWIG MC. (a) goes from the lowest  $E_T^{jet}$  bin to (d) the highest.

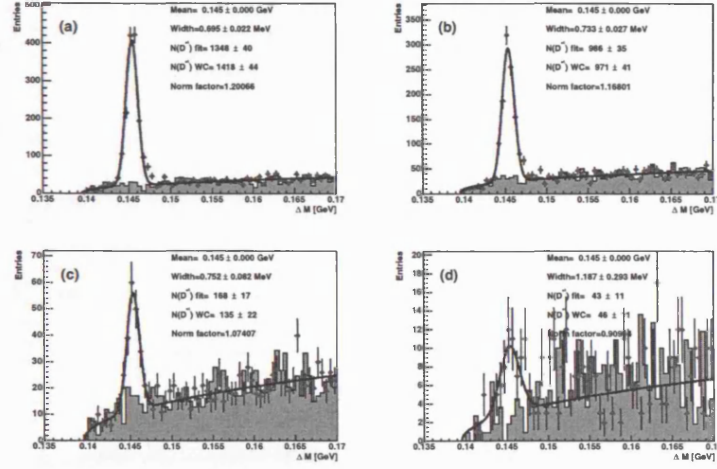
13.0.18  $d\sigma/d\eta^{jet}$  Mass Peaks,  $3.0 < p_T^{D^*} < 5.0$  GeV

**Figure 13.35** Mass peaks for each bin of the inclusive charm jet cross section  $d\sigma/d\eta^{jet}$  in the range  $3.0 < P_T^{D^*} < 5.0$  GeV for 1998-2000 data  $78pb^{-1}$ . (a) goes from the lowest  $\eta^{jet}$  bin to (h) the highest.

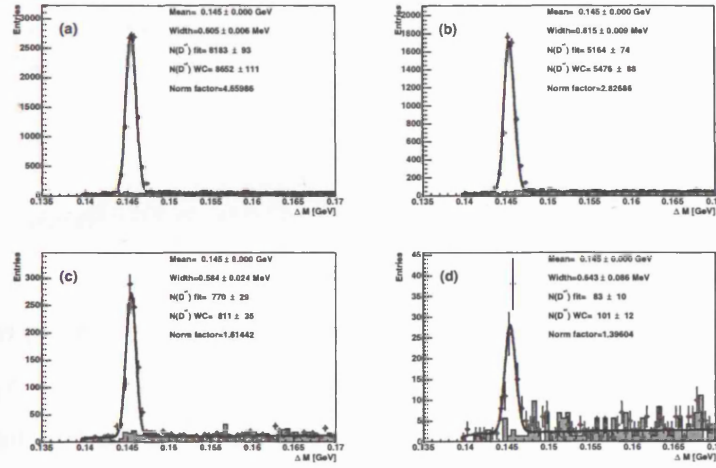


**Figure 13.36** Mass peaks for each bin of the inclusive charm jet cross section  $d\sigma/d\eta^{jet}$  in the range  $3.0 < P_T^{D^*} < 5.0$  GeV for  $886 pb^{-1}$  of HERWIG MC. (a) goes from the lowest  $\eta^{jet}$  bin to (h) the highest.

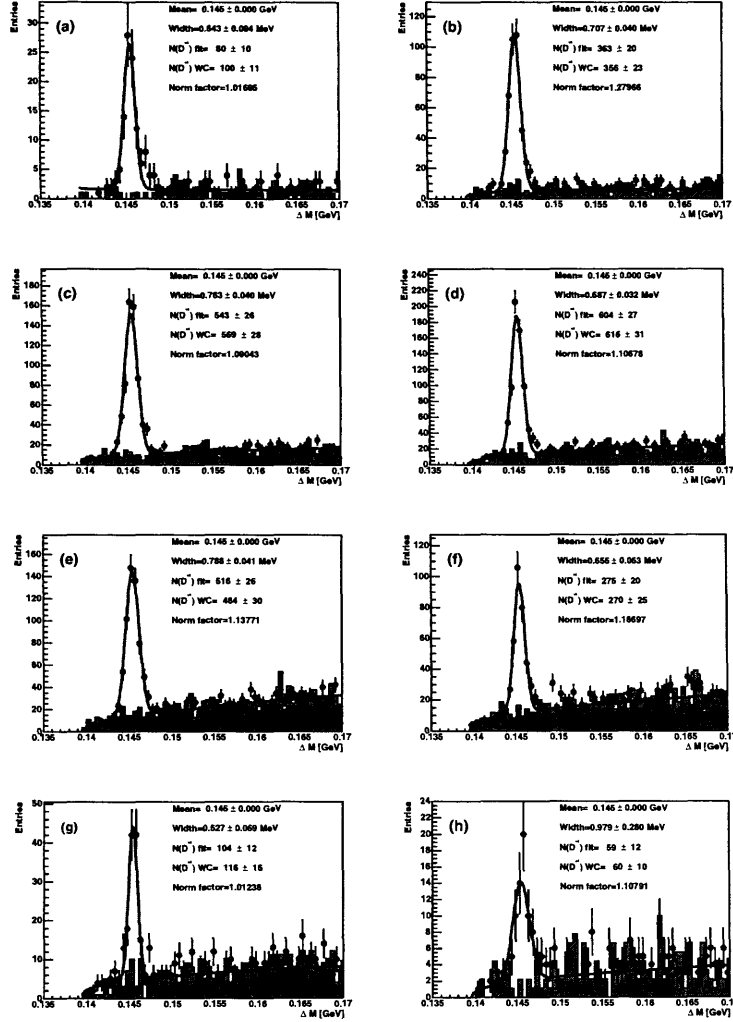


13.0.19  $d\sigma/dE_T^{jet}$  Mass Peaks,  $5.0 < p_T^{D^*} < 8.0$  GeV

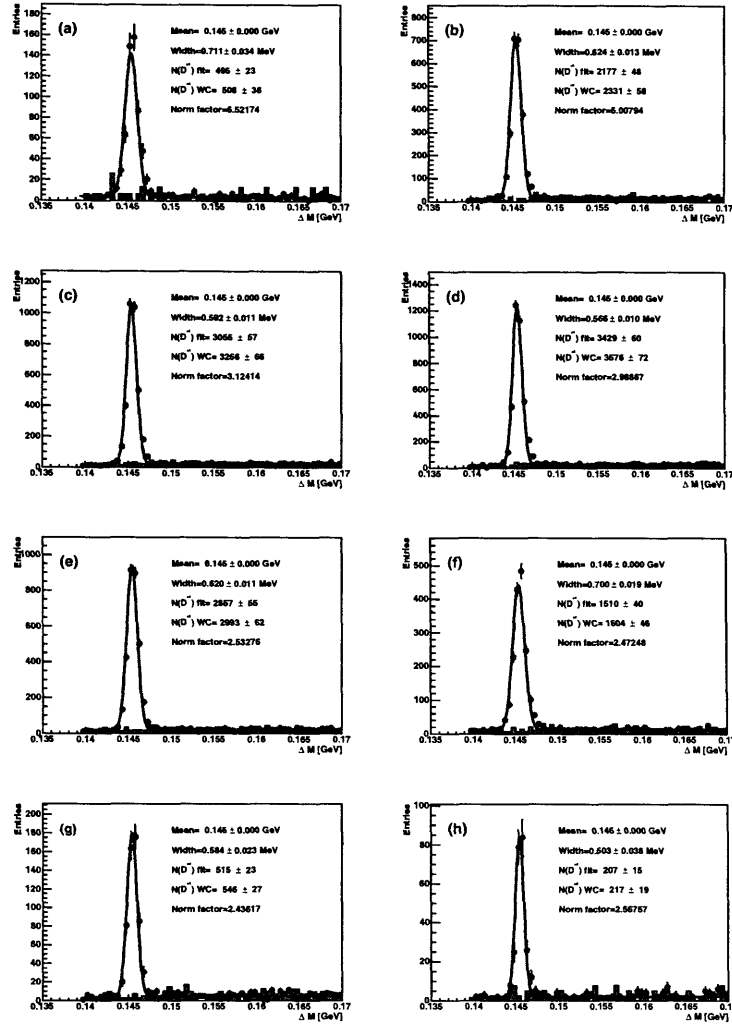
**Figure 13.37** Mass peaks for each bin of the inclusive charm jet cross section  $d\sigma/dE_T^{jet}$  in the range  $5.0 < P_T^{D^*} < 8.0$  GeV for 1998-2000 data  $78pb^{-1}$ . (a) goes from the lowest  $E_T^{jet}$  bin to (d) the highest.



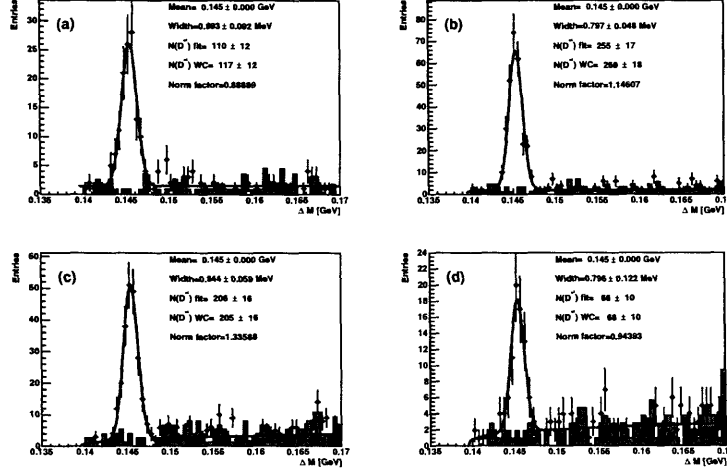
**Figure 13.38** Mass peaks for each bin of the inclusive charm jet cross section  $d\sigma/dE_T^{jet}$  in the range  $5.0 < P_T^{D^*} < 8.0$  GeV for  $886pb^{-1}$  of HERWIG MC. (a) goes from the lowest  $E_T^{jet}$  bin to (d) the highest.

13.0.20  $d\sigma/d\eta^{jet}$  Mass Peaks,  $5.0 < p_T^{D^*} < 8.0$  GeV


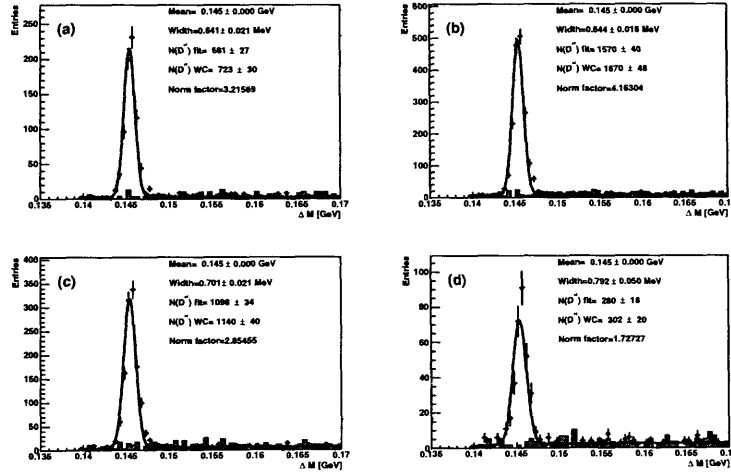
**Figure 13.39** Mass peaks for each bin of the inclusive charm jet cross section  $d\sigma/d\eta^{jet}$  in the range  $5.0 < p_T^{D^*} < 8.0$  GeV for 1998-2000 data  $78pb^{-1}$ . (a) goes from the lowest  $\eta^{jet}$  bin to (h) the highest.



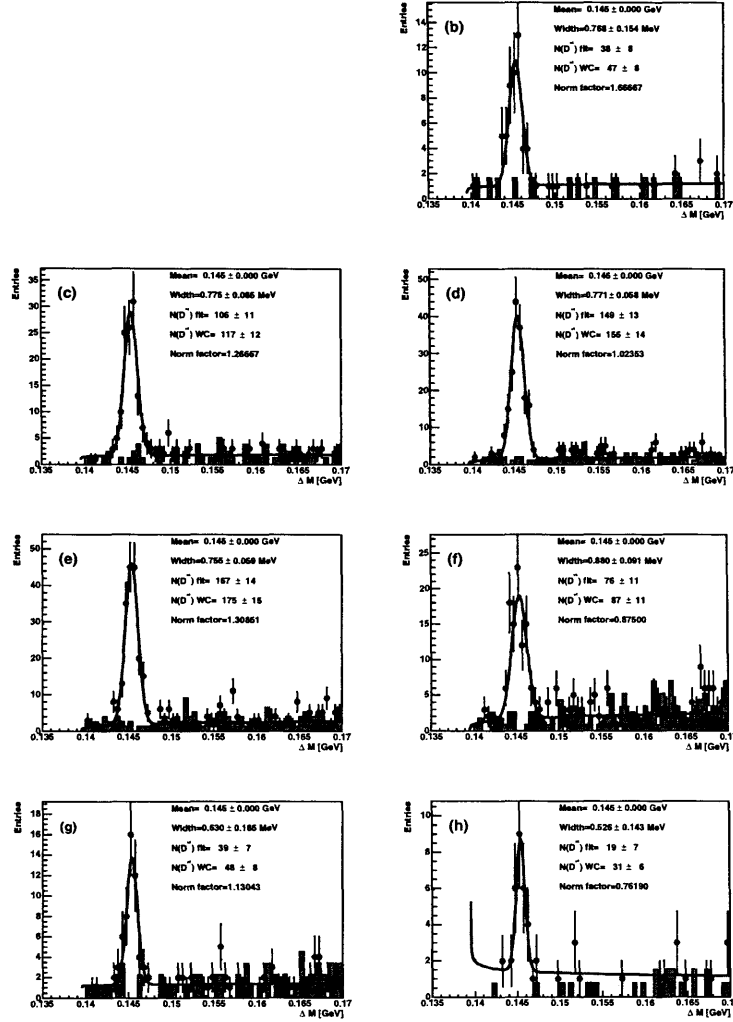
**Figure 13.40** Mass peaks for each bin of the inclusive charm jet cross section  $d\sigma/d\eta^{jet}$  in the range  $5.0 < P_T^{D^*} < 8.0$  GeV for 886 pb<sup>-1</sup> of HERWIG MC. (a) goes from the lowest  $\eta^{jet}$  bin to (h) the highest.

13.0.21  $d\sigma/dE_T^{jet}$  Mass Peaks,  $8.0 < p_T^{D^*} < 20.0$  GeV


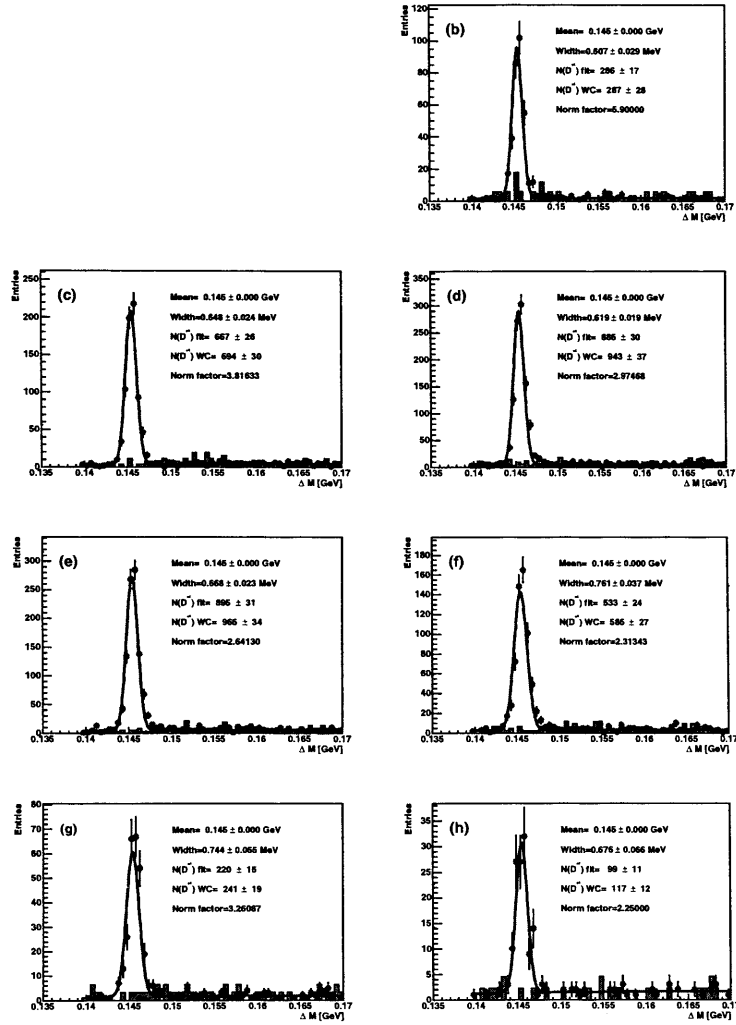
**Figure 13.41** Mass peaks for each bin of the inclusive charm jet cross section  $d\sigma/dE_T^{jet}$  in the range  $8.0 < P_T^{D^*} < 20.0$  GeV for 1998-2000 data  $78pb^{-1}$ . (a) goes from the lowest  $E_T^{jet}$  bin to (d) the highest.



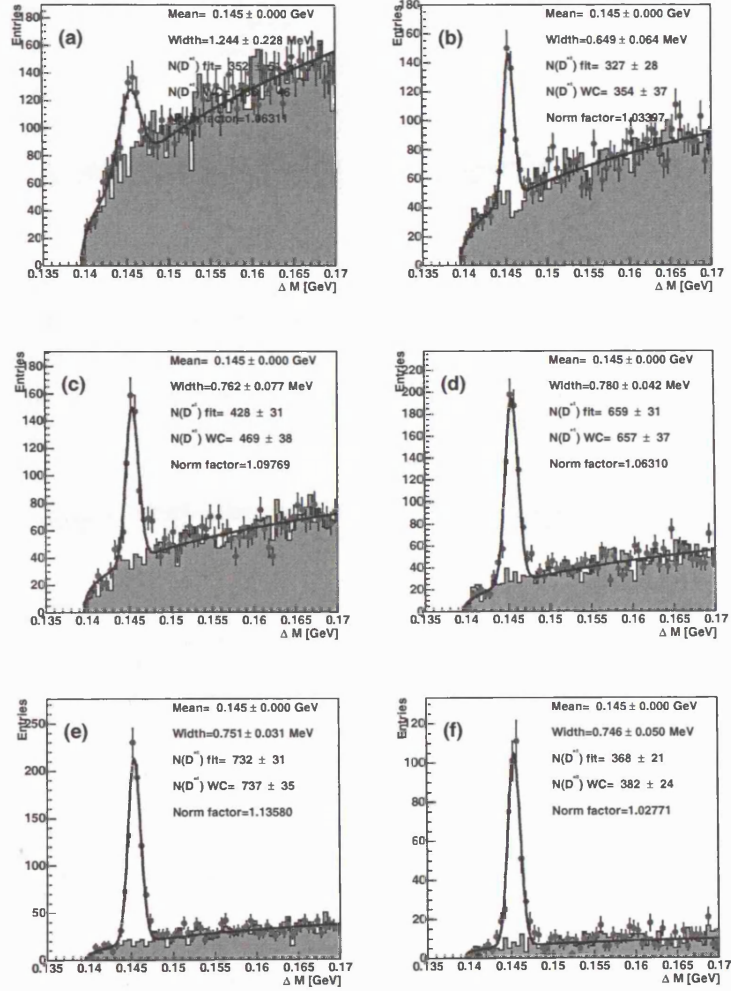
**Figure 13.42** Mass peaks for each bin of the inclusive charm jet cross section  $d\sigma/dE_T^{jet}$  in the range  $8.0 < P_T^{D^*} < 20.0$  GeV for  $886pb^{-1}$  of HERWIG MC. (a) goes from the lowest  $E_T^{jet}$  bin to (d) the highest.

13.0.22  $d\sigma/d\eta^{jet}$  Mass Peaks,  $8.0 < p_T^{D^*} < 20.0$  GeV


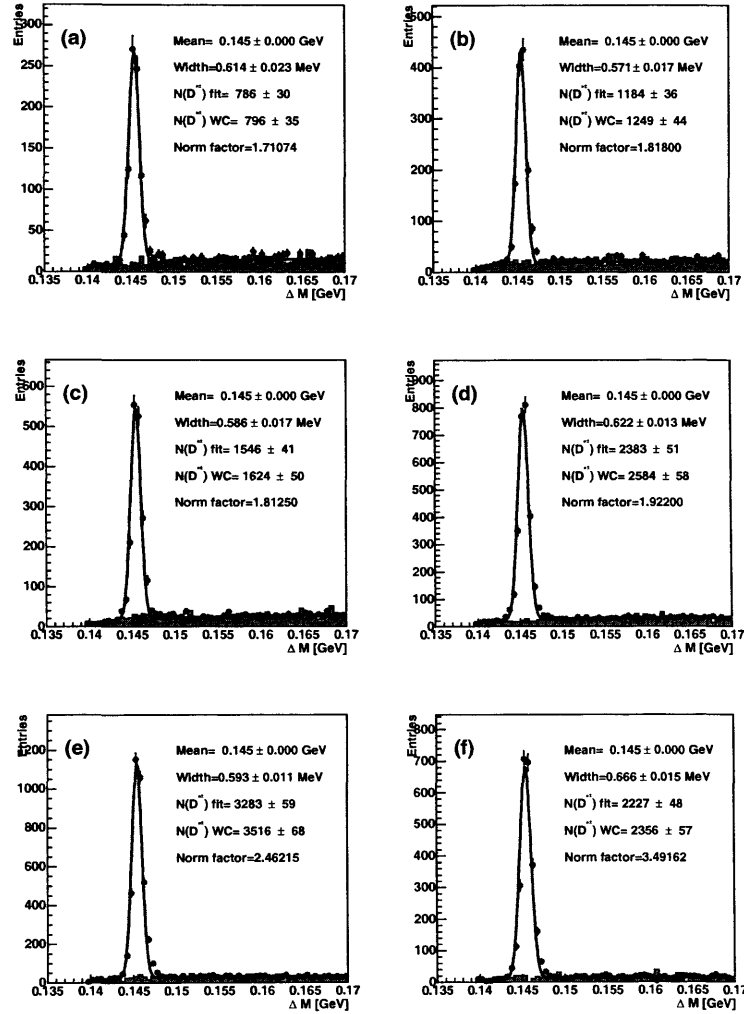
**Figure 13.43** Mass peaks for each bin of the inclusive charm jet cross section  $d\sigma/d\eta^{jet}$  in the range  $8.0 < P_T^{D^*} < 20.0$  GeV for 1998-2000 data  $78pb^{-1}$ . (a) goes from the lowest  $\eta^{jet}$  bin to (h) the highest.



**Figure 13.44** Mass peaks for each bin of the inclusive charm jet cross section  $d\sigma/d\eta^{jet}$  in the range  $8.0 < P_T^{D^*} < 20.0$  GeV for  $886pb^{-1}$  of HERWIG MC. (a) goes from the lowest  $\eta^{jet}$  bin to (h) the highest.

13.0.23  $d\sigma/dx_\gamma^{\text{obs}}(D^*, \text{untagged jet})$  Mass Peaks

**Figure 13.45** Mass peaks for each bin of the inclusive charm jet cross section  $d\sigma/dx_\gamma^{\text{obs}}(D^*, \text{untagged jet})$  for 1998-2000 data  $78\text{pb}^{-1}$ . (a) goes from the lowest  $x_\gamma^{\text{obs}}(D^*, \text{untagged jet})$  bin to (g) the highest.



**Figure 13.46** Mass peaks for each bin of the inclusive charm jet cross section  $d\sigma/dx_\gamma^{\text{obs}}(D^*, \text{untagged jet})$  for  $886\text{pb}^{-1}$  of HERWIG MC. (a) goes from the lowest  $x_\gamma^{\text{obs}}(D^*, \text{untagged jet})$  bin to (g) the highest.



---

## 14 Appendix B : Dijet cross section mass peaks

---

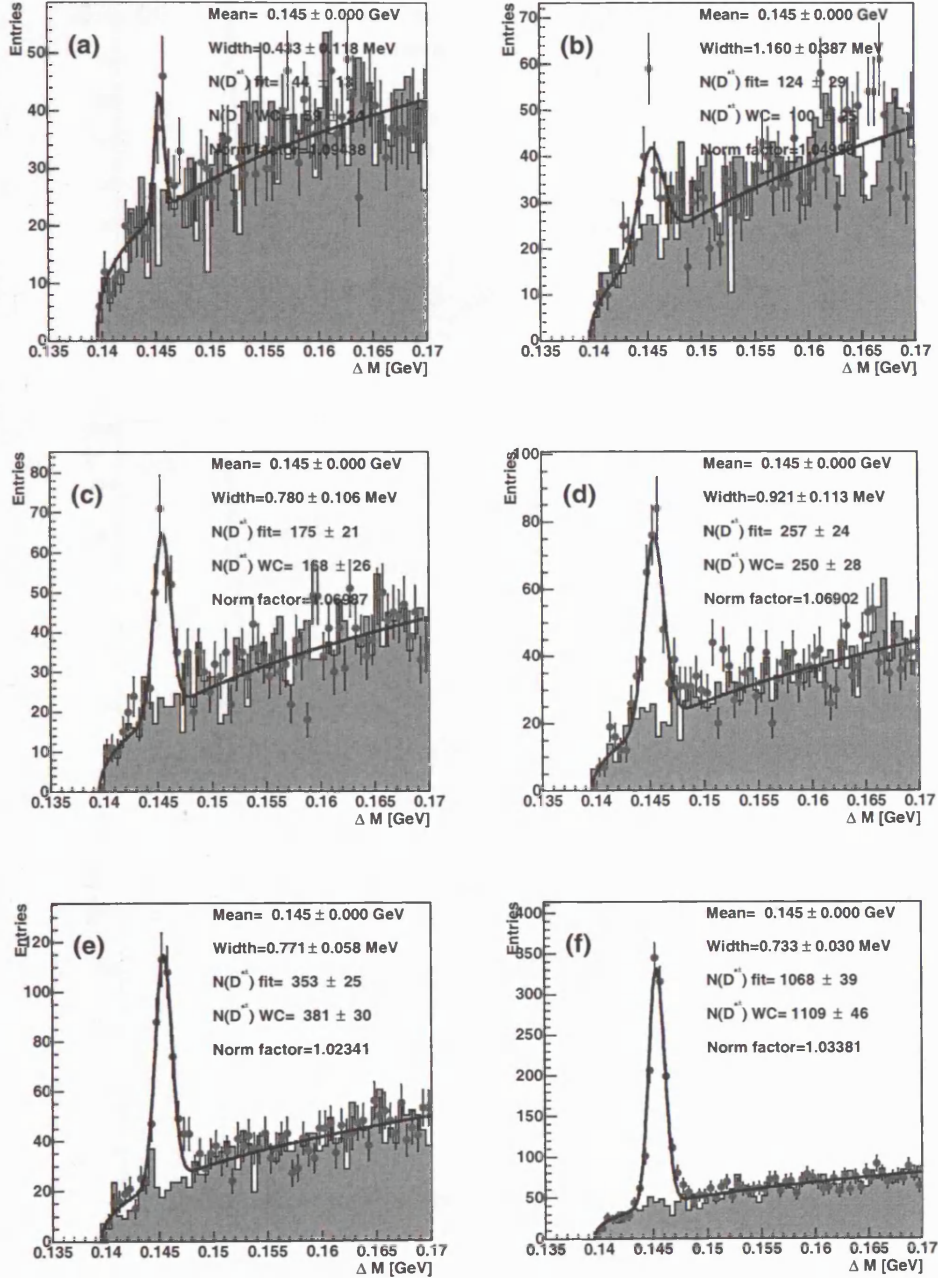
This chapter contains the mass peaks for both the (98-00) data( $886pb^{-1}$  HERWIG MC) for  $d\sigma/dx_{\gamma}^{\text{obs}}$  fig. 17.24(fig. 14.2),  $d\sigma/p_T^{jj}$  fig. 17.25(fig. 14.4),  $d\sigma/\Delta\phi^{jj}$  fig. 17.26(fig. 14.6),  $d\sigma/m^{jj}$  fig. 17.27(fig. 14.8),  $d\sigma/p_T^{2jj}$  fig. 17.28(fig. 14.10).

$d\sigma/p_T^{jj}$  direct-enriched fig. 17.29(fig. 14.12) and resolved-enriched fig. 17.33(fig. 14.20).

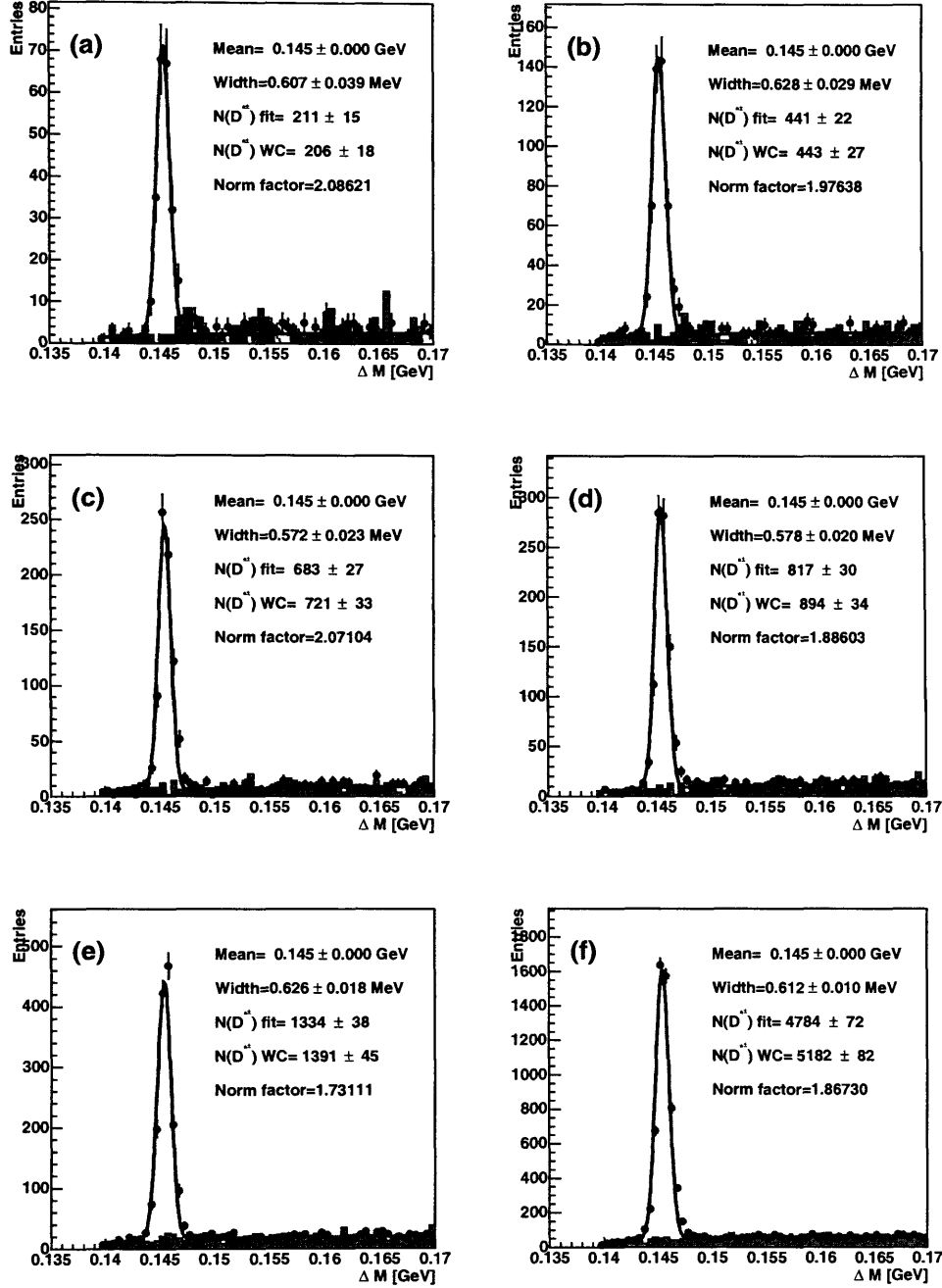
$d\sigma/\Delta\phi^{jj}$  direct-enriched fig. 17.30(fig. 14.14) and resolved-enriched fig. 17.34(fig. 14.22).

$d\sigma/m^{jj}$  direct-enriched fig. 17.31(fig. 14.16) and resolved-enriched fig. 17.35(fig. 14.24).

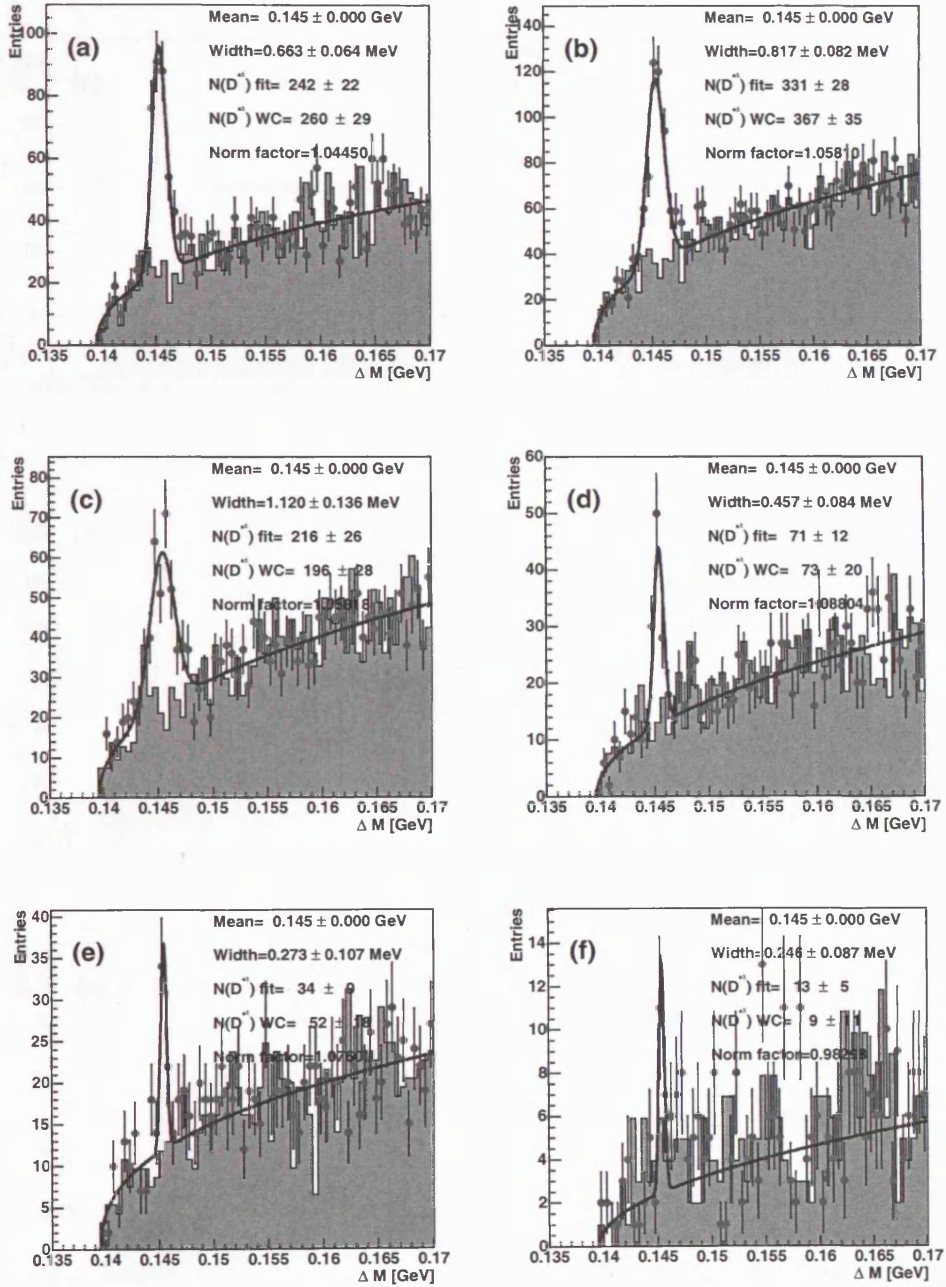
$d\sigma/p_T^{2jj}$  direct-enriched fig. 17.32(fig. 14.18) and resolved-enriched fig. 17.36(fig. 14.26).

14.1  $d\sigma/dx_\gamma^{\text{obs}}$  mass peaks

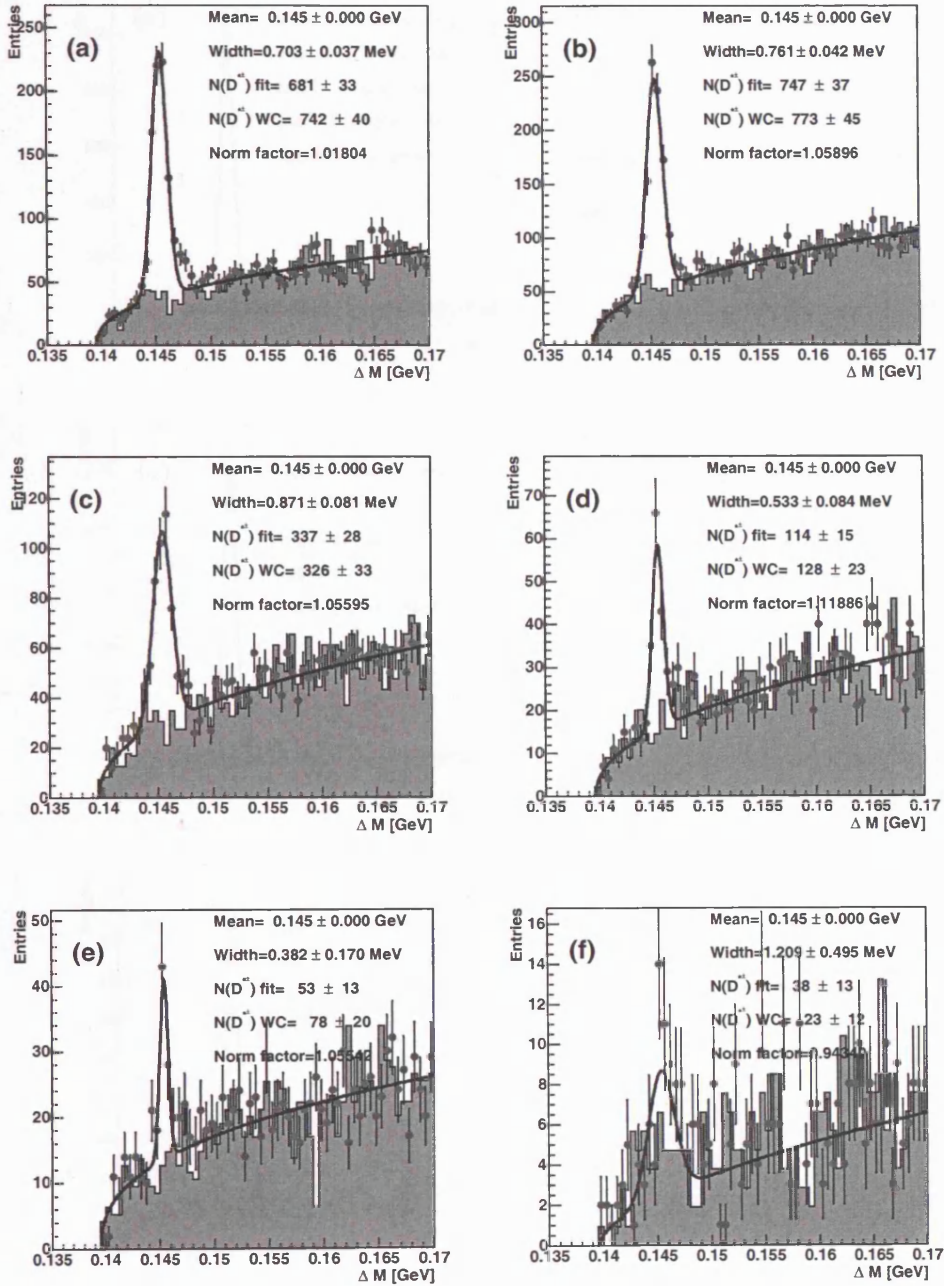
**Figure 14.1** Mass peaks for each bin of the dijet charm cross section  $d\sigma/dx_\gamma^{\text{obs}}$  for 1998-2000 data  $78\text{pb}^{-1}$ . (a) goes from the lowest  $x_\gamma^{\text{obs}}$  bin to (g) the highest.



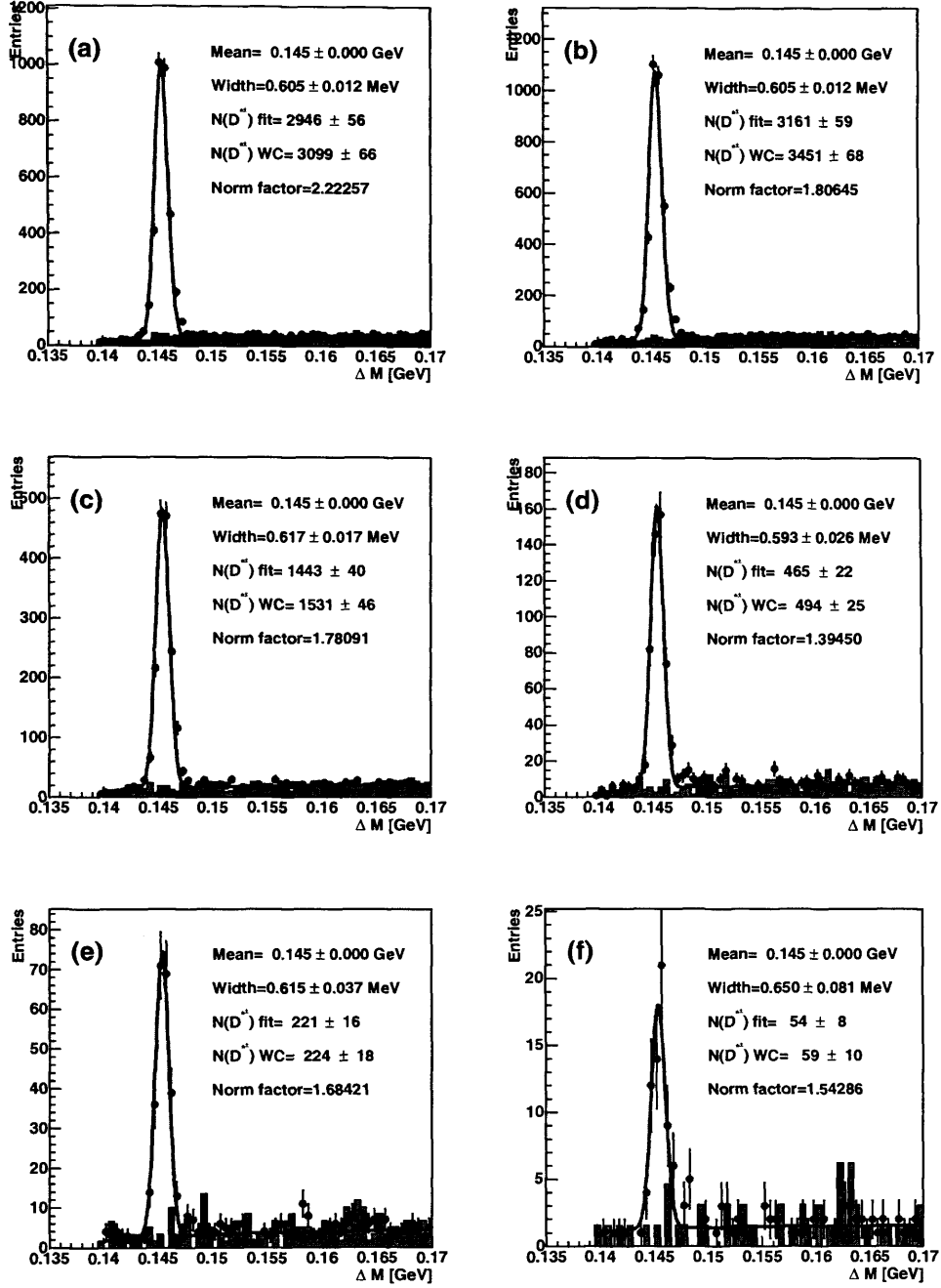
**Figure 14.2** Mass peaks for each bin of the dijet charm cross section  $d\sigma/dx_\gamma^{\text{obs}}$  for  $886\text{pb}^{-1}$  of HERWIG MC. (a) goes from the lowest  $x_\gamma^{\text{obs}}$  bin to (g) the highest.

14.10  $d\sigma/dp_T^{jj}$  mass peaks, resolved-enriched  $x_\gamma^{\text{obs}} < 0.75$ 

**Figure 14.19** Mass peaks for each bin of the dijet charm cross section  $d\sigma/dp_T^{jj}$  for 1998-2000 data  $78\text{pb}^{-1}$ , with  $x_\gamma^{\text{obs}} < 0.75$ . (a) goes from the lowest  $p_T^{jj}$  bin to (g) the highest.

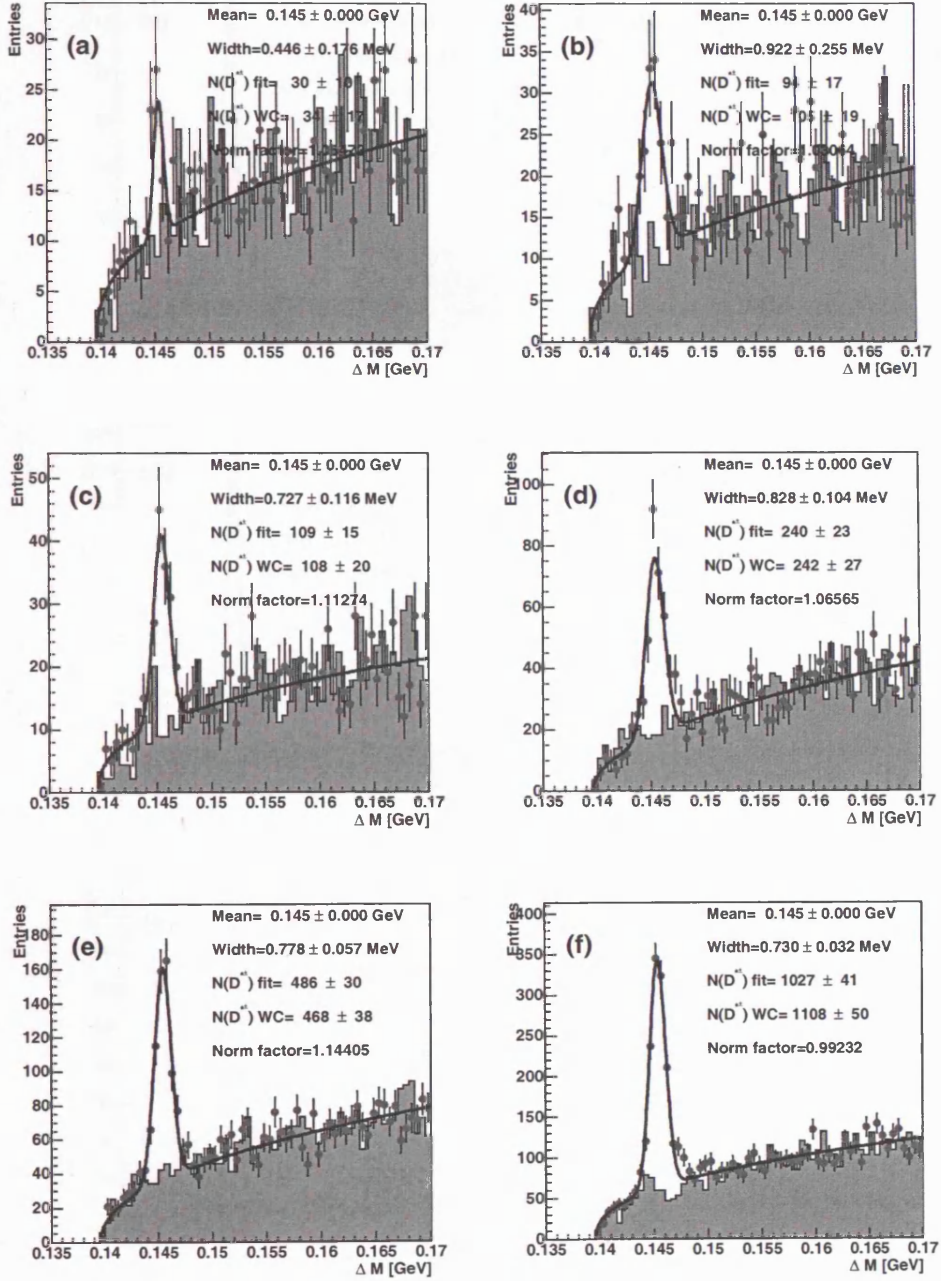
14.2  $d\sigma/dp_T^{jj}$  mass peaks

**Figure 14.3** Mass peaks for each bin of the dijet charm cross section  $d\sigma/dp_T^{jj}$  for 1998-2000 data  $78pb^{-1}$ . (a) goes from the lowest  $p_T^{jj}$  bin to (g) the highest.

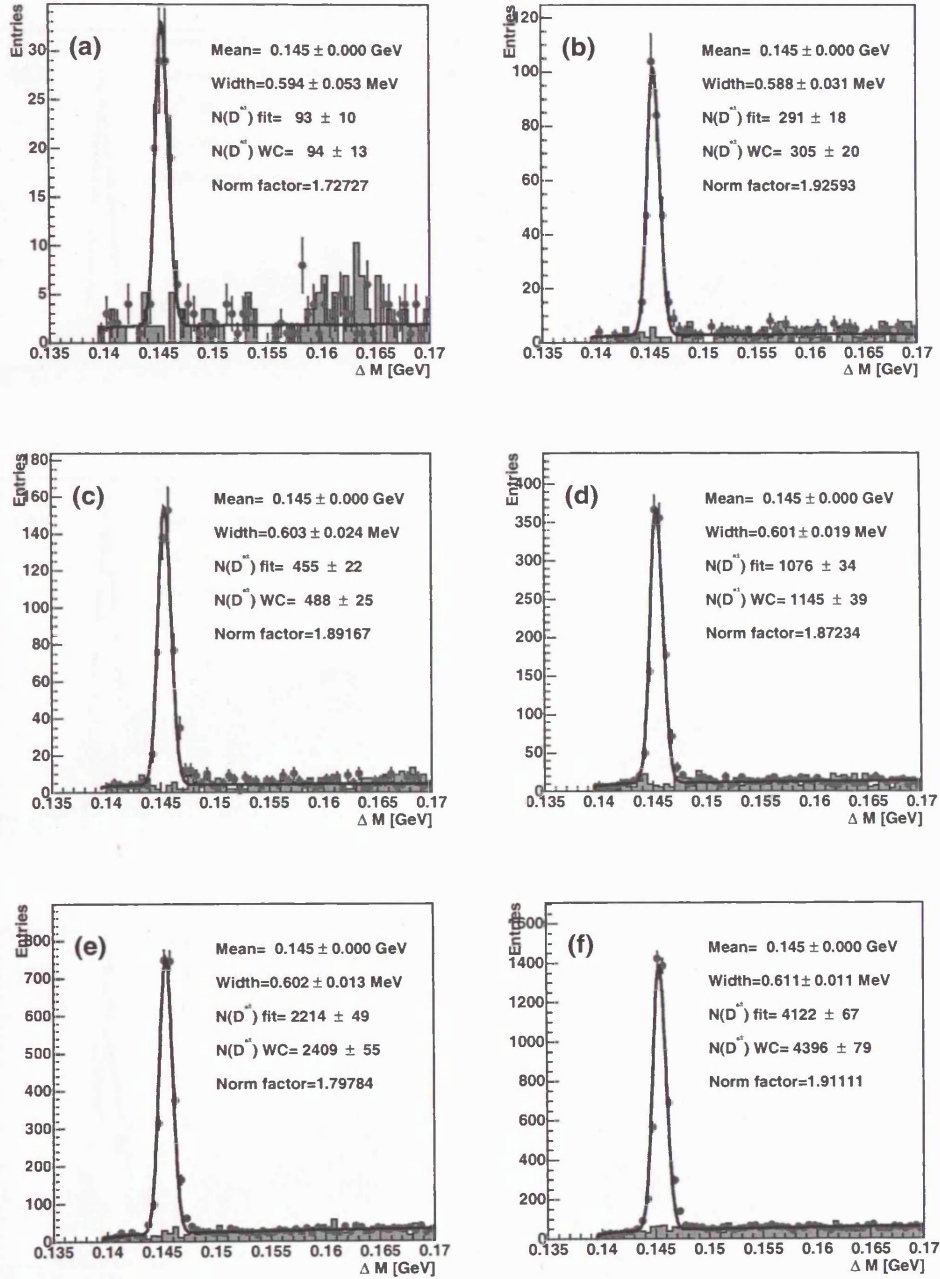


**Figure 14.4** Mass peaks for each bin of the dijet charm cross section  $d\sigma/dp_T^{jj}$  for  $886pb^{-1}$  of HERWIG MC. (a) goes from the lowest  $p_T^{jj}$  bin to (g) the highest.



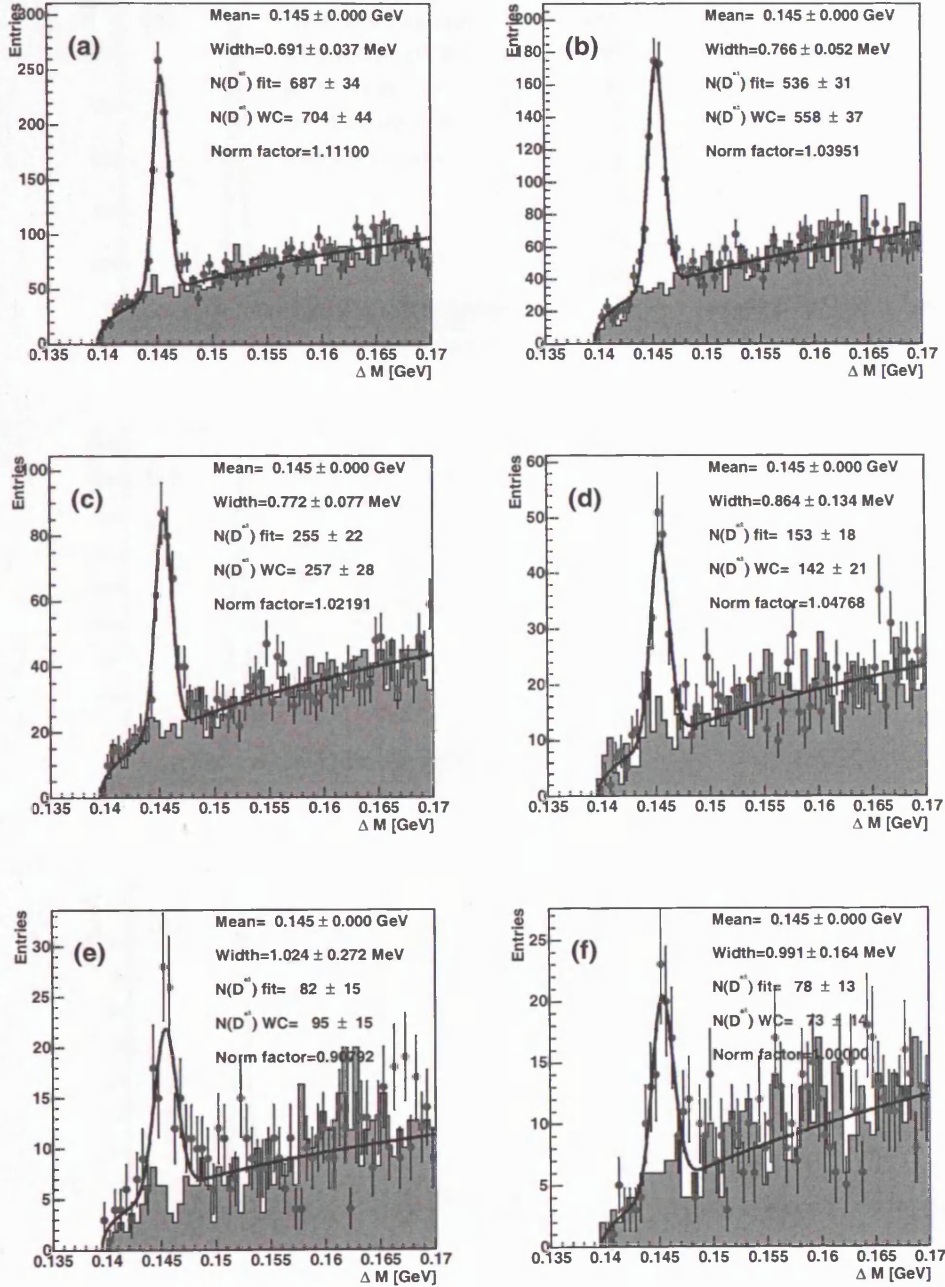
14.3  $d\sigma/d\Delta\phi^{jj}$  mass peaks

**Figure 14.5** Mass peaks for each bin of the dijet charm cross section  $d\sigma/d\Delta\phi^{jj}$  for 1998-2000 data  $78pb^{-1}$ . (a) goes from the lowest  $\Delta\phi^{jj}$  bin to (g) the highest.

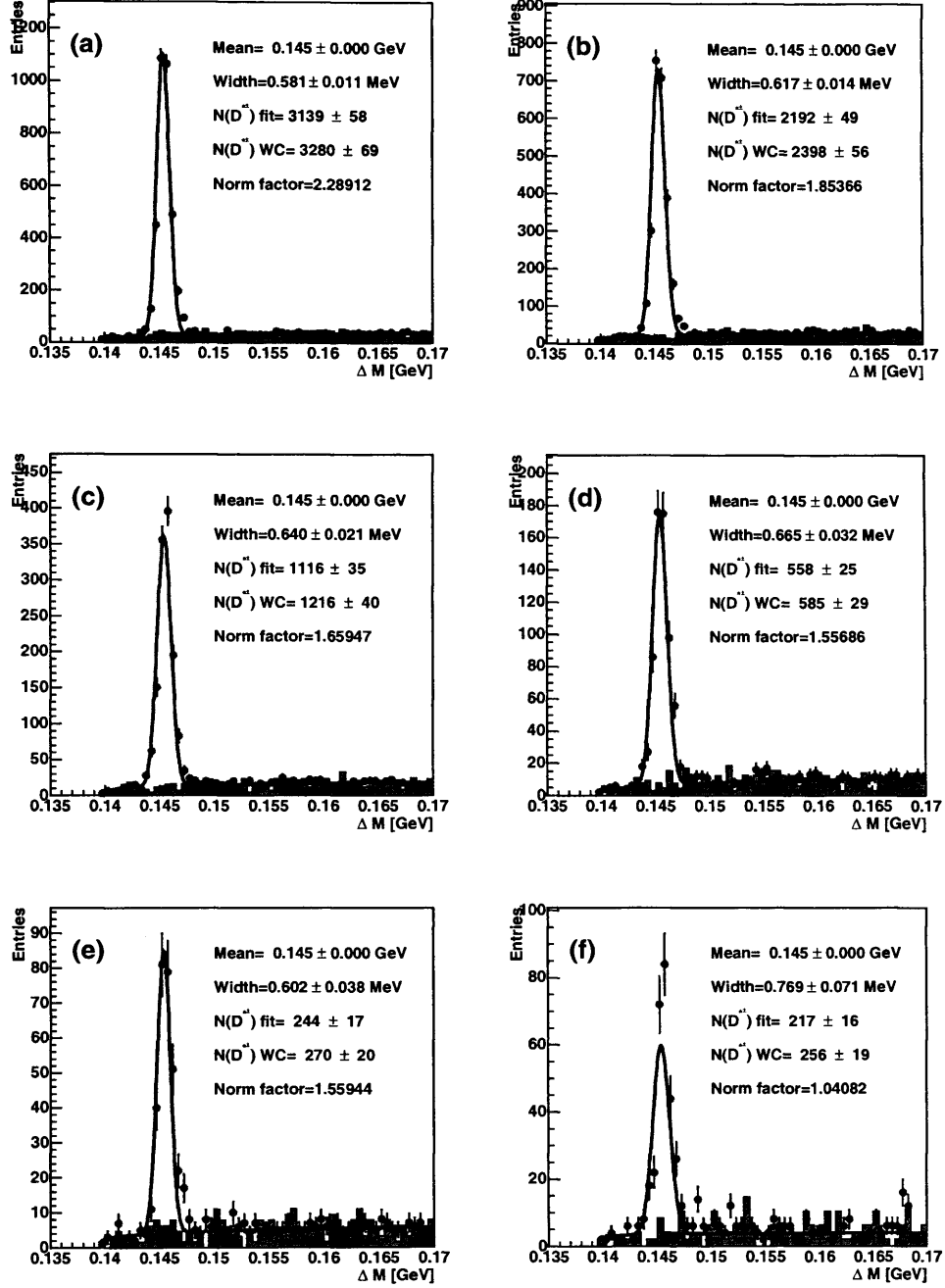


**Figure 14.6** Mass peaks for each bin of the dijet charm cross section  $d\sigma/d\Delta\phi^{jj}$  for  $886\text{pb}^{-1}$  of HERWIG MC. (a) goes from the lowest  $\Delta\phi^{jj}$  bin to (g) the highest.

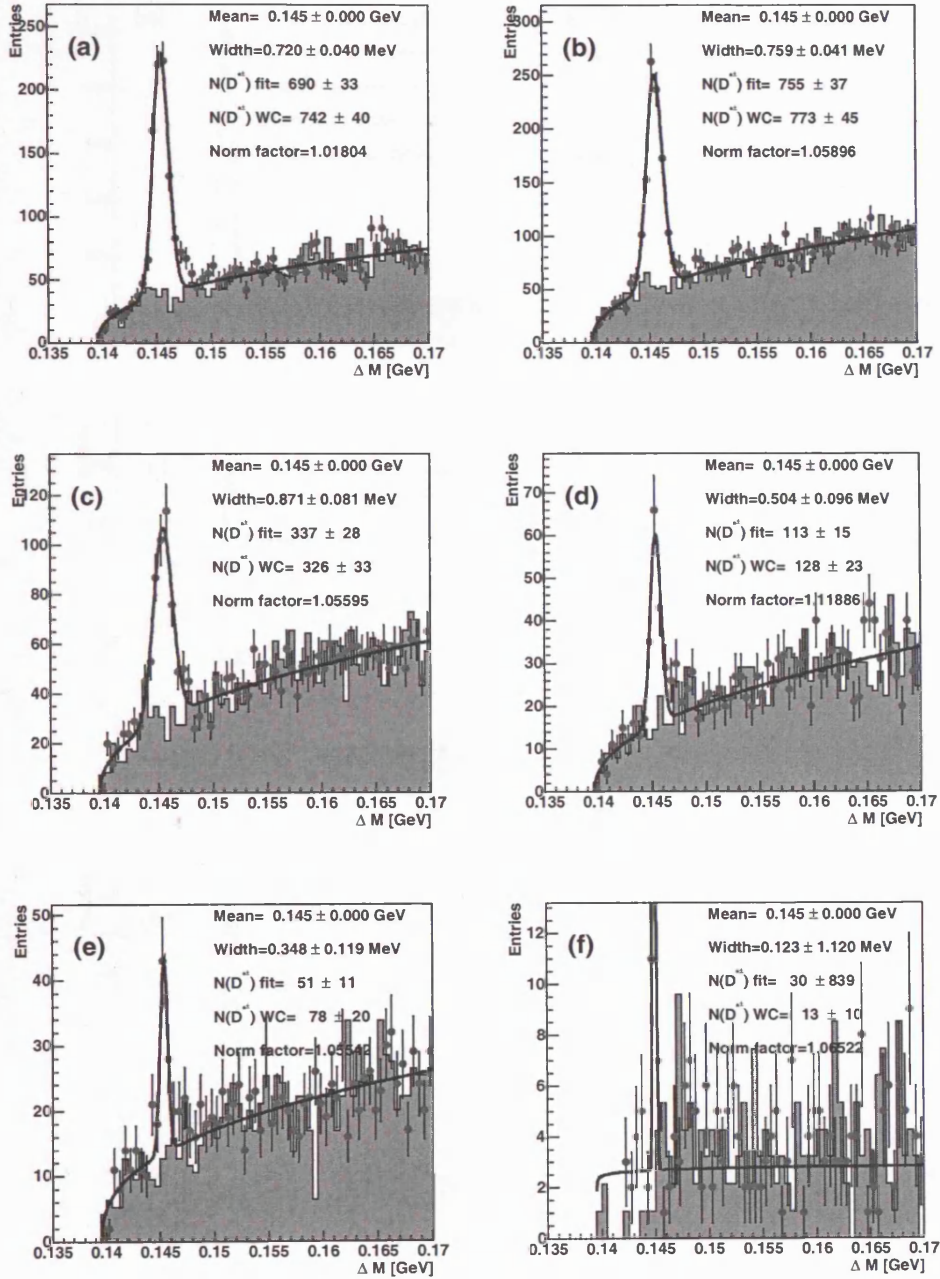


14.4  $d\sigma/dm^{jj}$  mass peaks

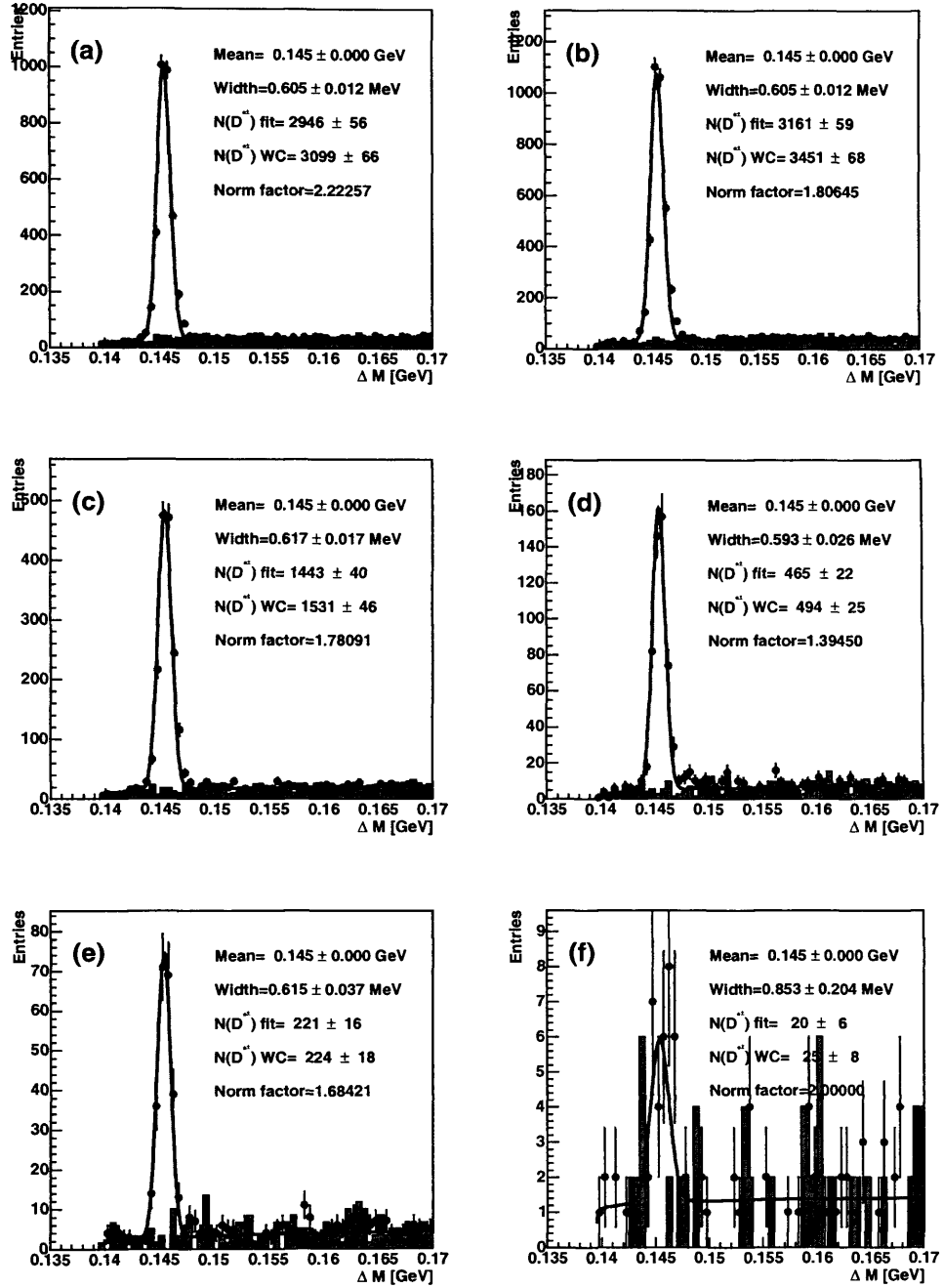
**Figure 14.7** Mass peaks for each bin of the dijet charm cross section  $d\sigma/dm^{jj}$  for 1998-2000 data  $78pb^{-1}$ . (a) goes from the lowest  $m^{jj}$  bin to (g) the highest.



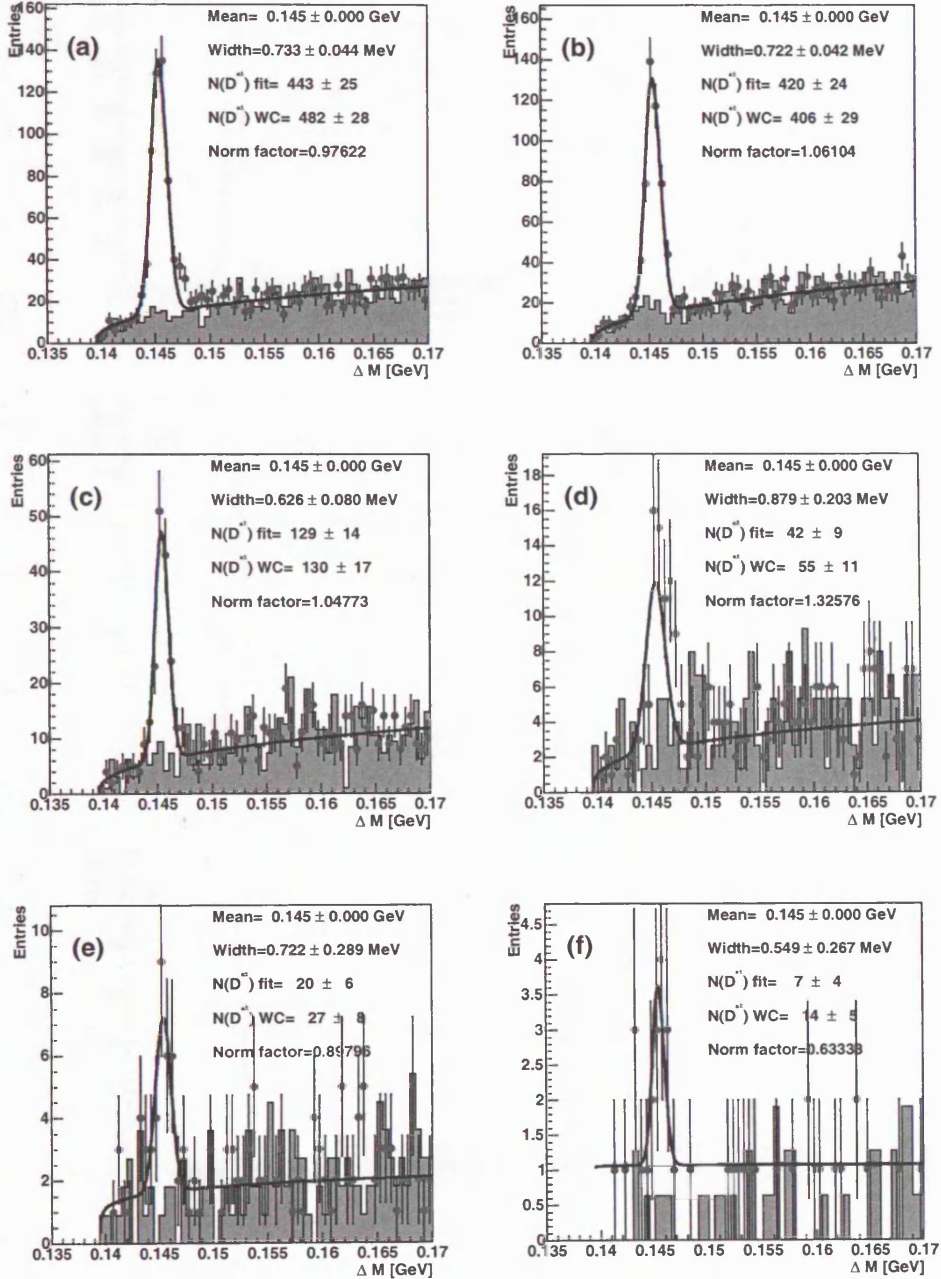
**Figure 14.8** Mass peaks for each bin of the dijet charm cross section  $d\sigma/dm^{jj}$  for  $886pb^{-1}$  of HERWIG MC. (a) goes from the lowest  $m^{jj}$  bin to (g) the highest.

14.5  $d\sigma/dp_T^{2jj}$  mass peaks

**Figure 14.9** Mass peaks for each bin of the dijet charm cross section  $d\sigma/dp_T^{2jj}$  for 1998-2000 data  $78pb^{-1}$ . (a) goes from the lowest  $p_T^{2jj}$  bin to (g) the highest.

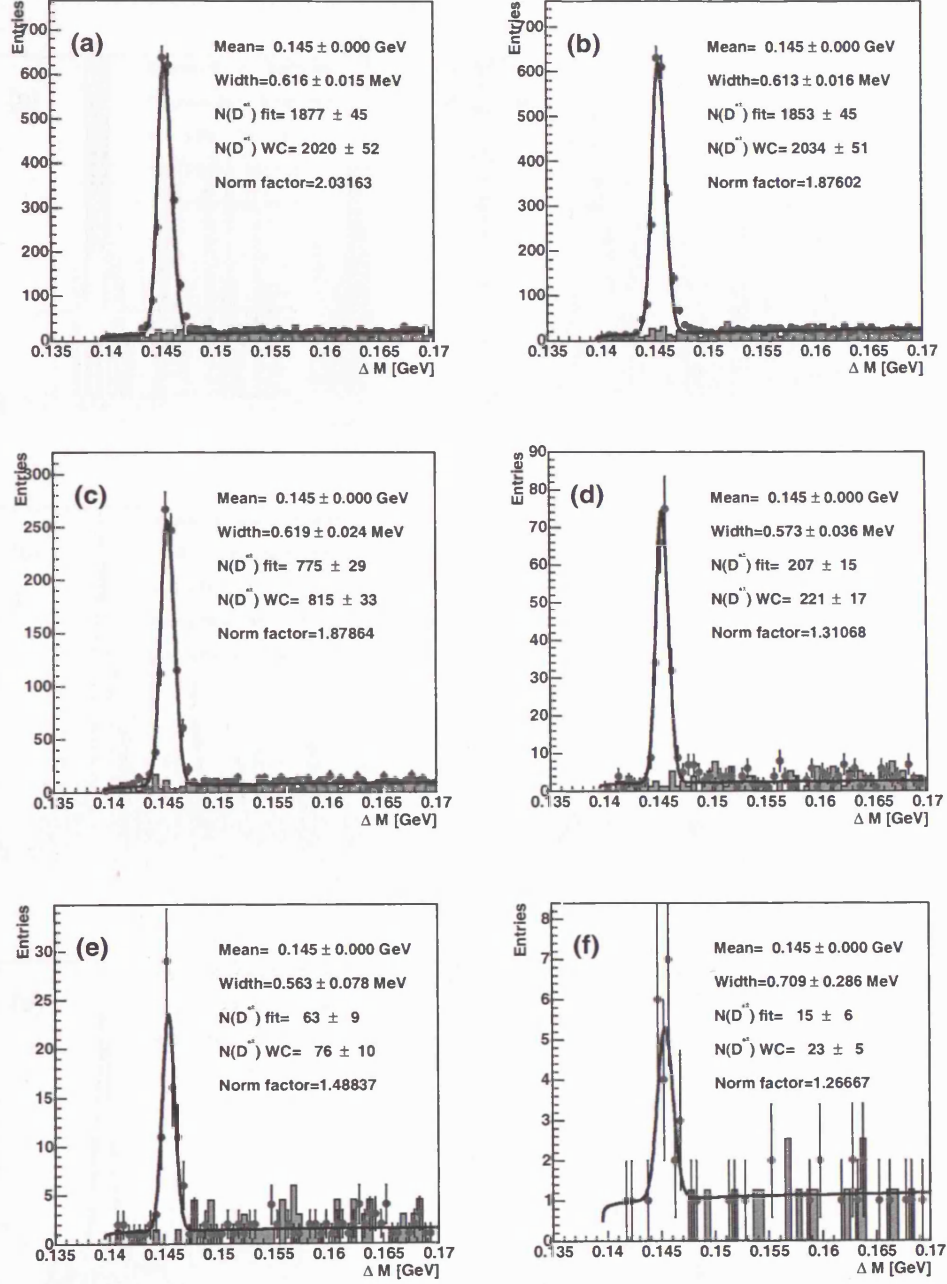


**Figure 14.10** Mass peaks for each bin of the dijet charm cross section  $d\sigma/dp_T^{2jj}$  for  $886 pb^{-1}$  of HERWIG MC. (a) goes from the lowest  $p_T^{2jj}$  bin to (g) the highest.

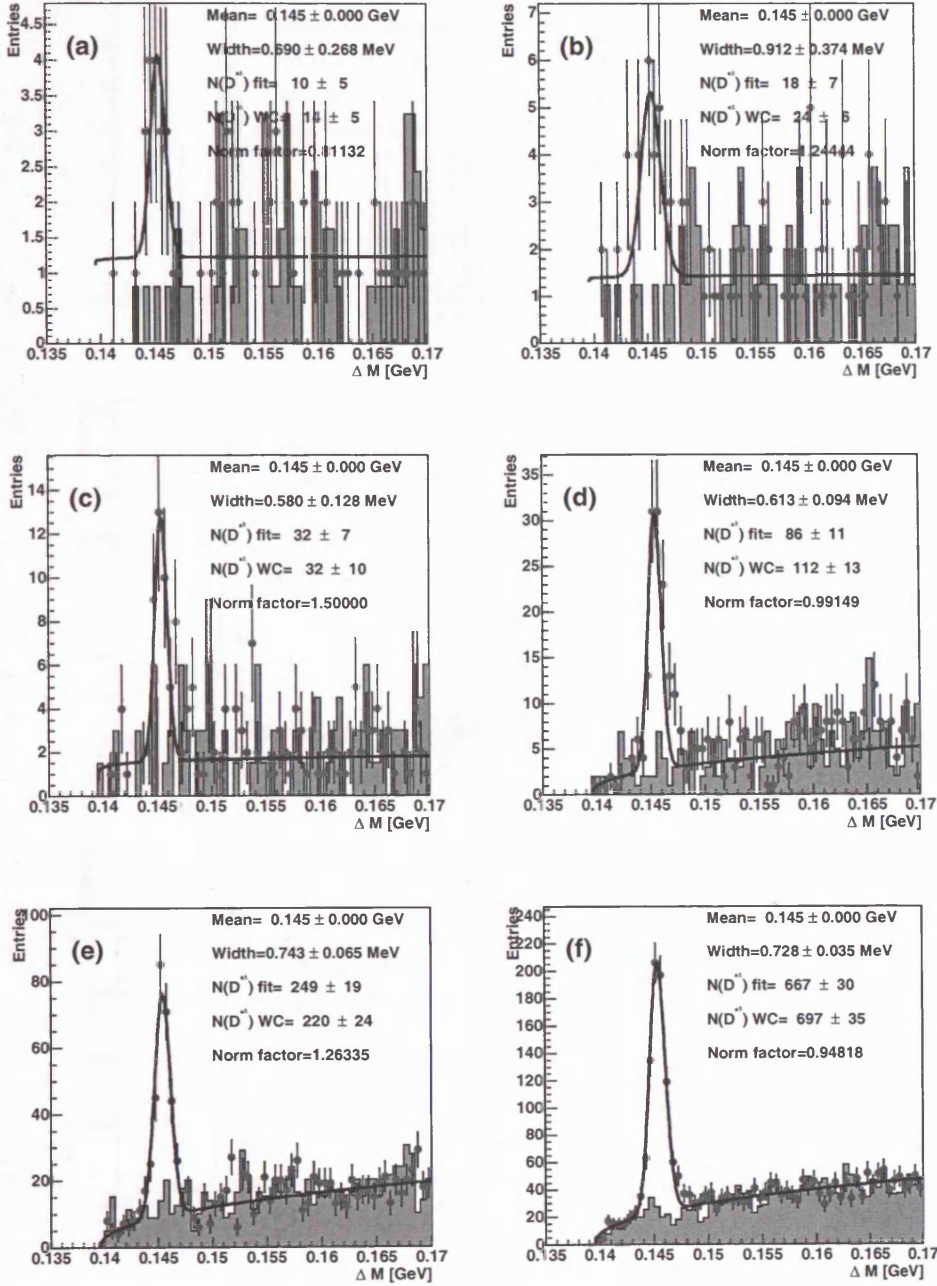
14.6  $d\sigma/dp_T^{jj}$  mass peaks, direct-enriched  $x_\gamma^{\text{obs}} > 0.75$ 

**Figure 14.11** Mass peaks for each bin of the dijet charm cross section  $d\sigma/dp_T^{jj}$  for 1998-2000 data  $78pb^{-1}$ , with  $x_\gamma^{\text{obs}} > 0.75$ . (a) goes from the lowest  $p_T^{jj}$  bin to (g) the highest.

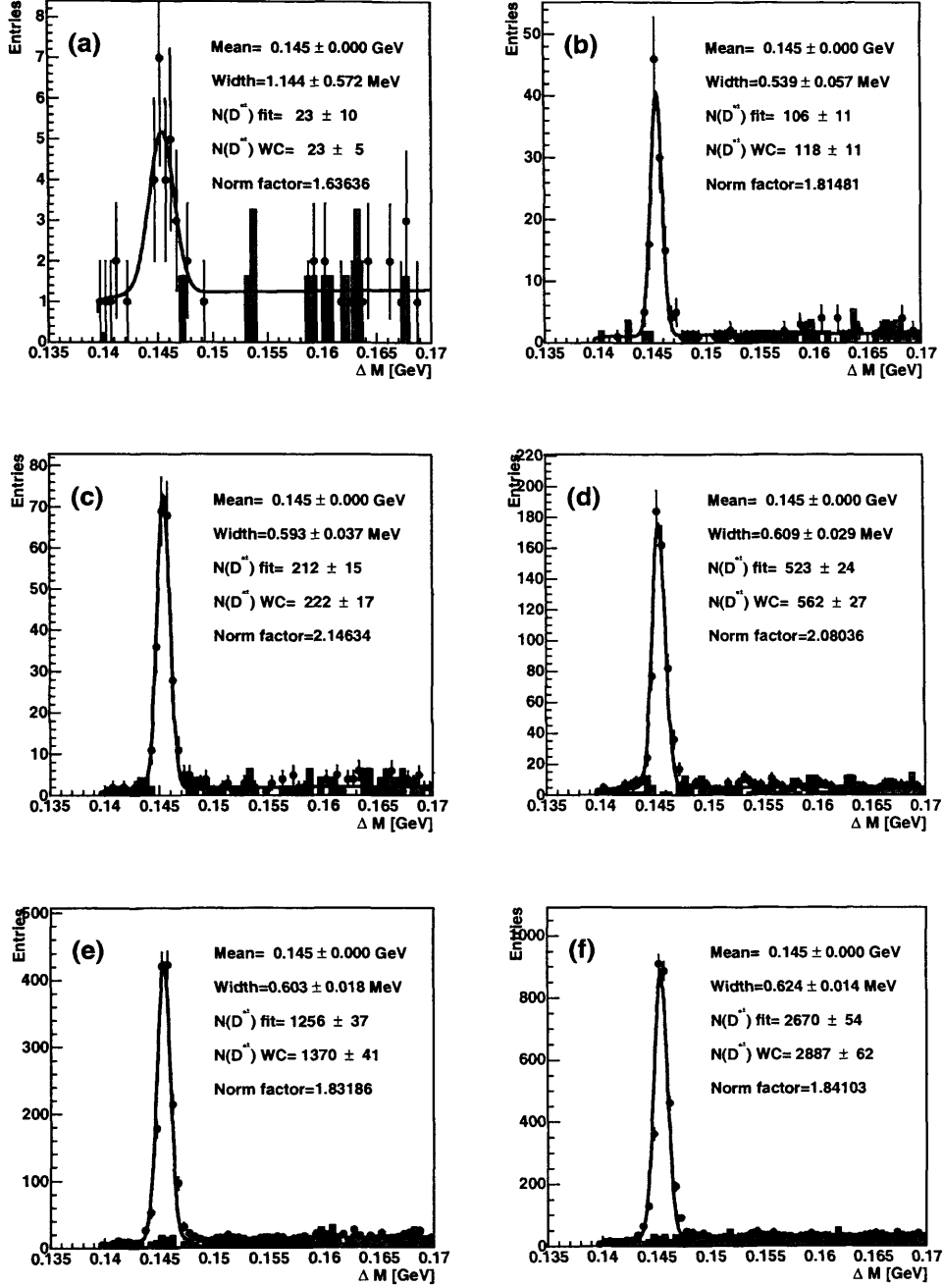




**Figure 14.12** Mass peaks for each bin of the dijet charm cross section  $d\sigma/dp_T^{jj}$  for  $886pb^{-1}$  of HERWIG MC, with  $x_{\gamma}^{obs} > 0.75$ . (a) goes from the lowest  $p_T^{jj}$  bin to (g) the highest.

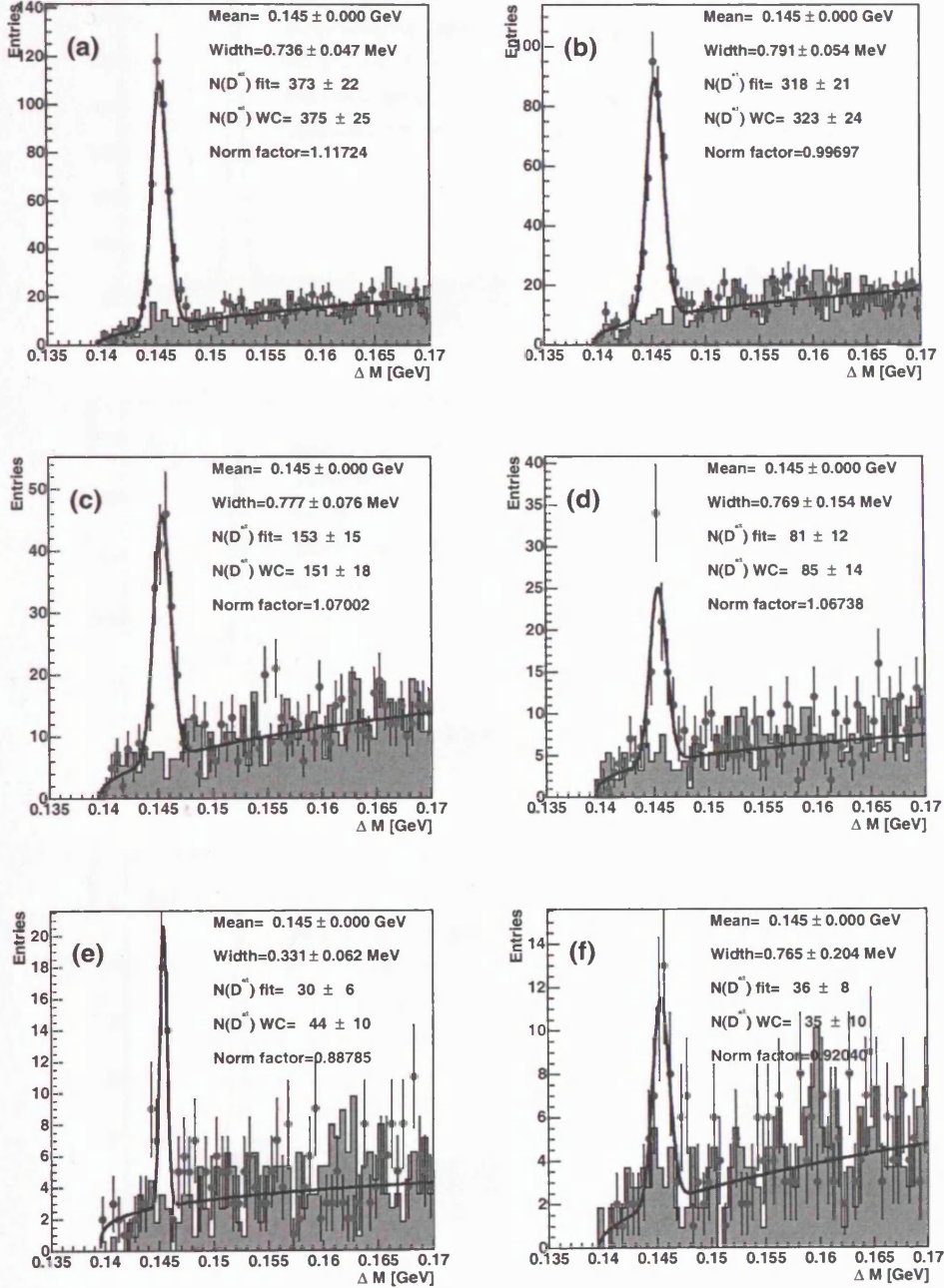
14.7  $d\sigma/d\Delta\phi^{jj}$  mass peaks, direct-enriched  $x_\gamma^{\text{obs}} > 0.75$ 

**Figure 14.13** Mass peaks for each bin of the dijet charm cross section  $d\sigma/d\Delta\phi^{jj}$  for 1998-2000 data  $78\text{pb}^{-1}$ , with  $x_\gamma^{\text{obs}} > 0.75$ . (a) goes from the lowest  $\Delta\phi^{jj}$  bin to (g) the highest.

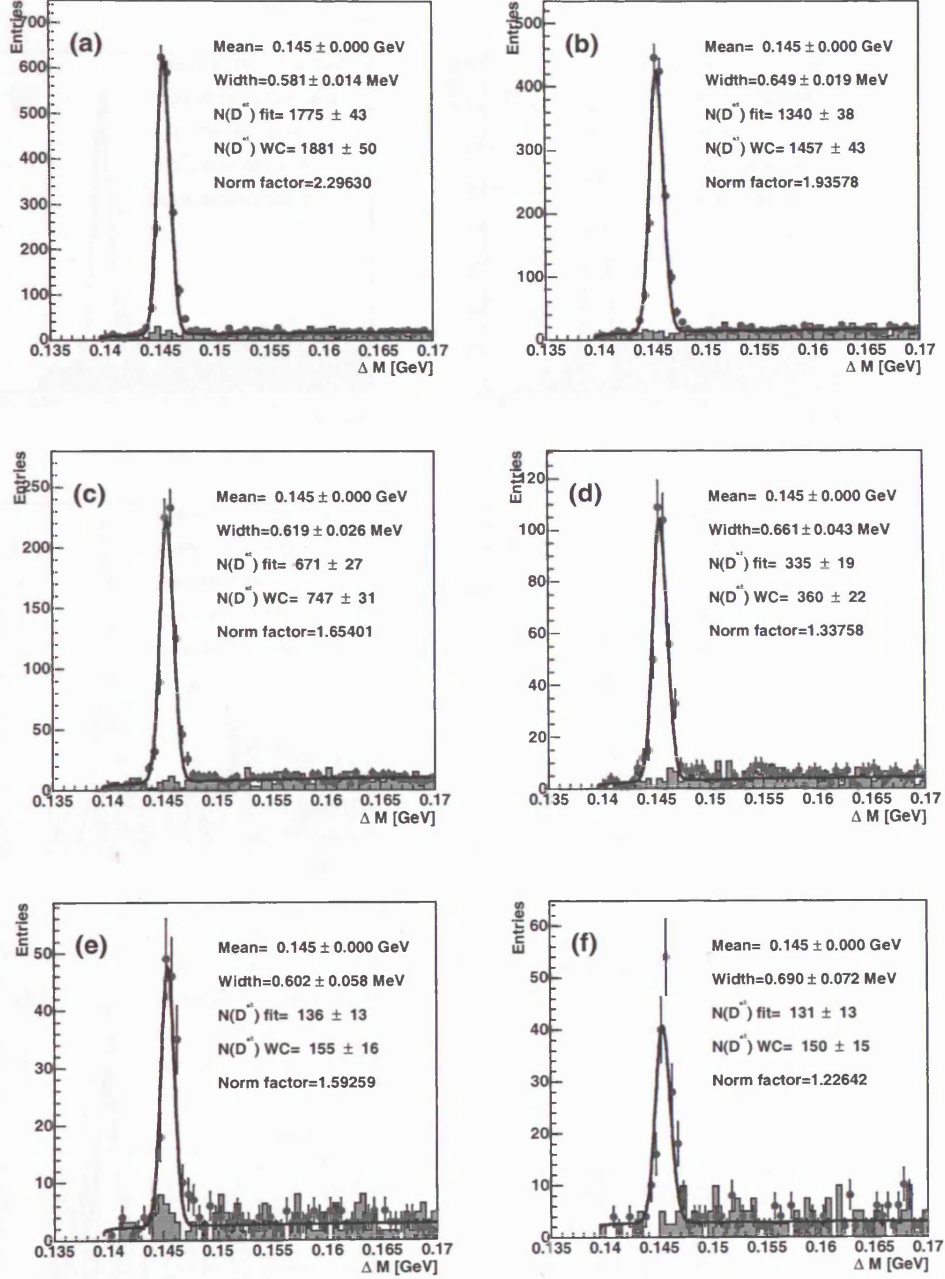


**Figure 14.14** Mass peaks for each bin of the dijet charm cross section  $d\sigma/d\Delta\phi^{jj}$  for  $886pb^{-1}$  of HERWIG MC, with  $x_\gamma^{obs} > 0.75$ . (a) goes from the lowest  $\Delta\phi^{jj}$  bin to (g) the highest.

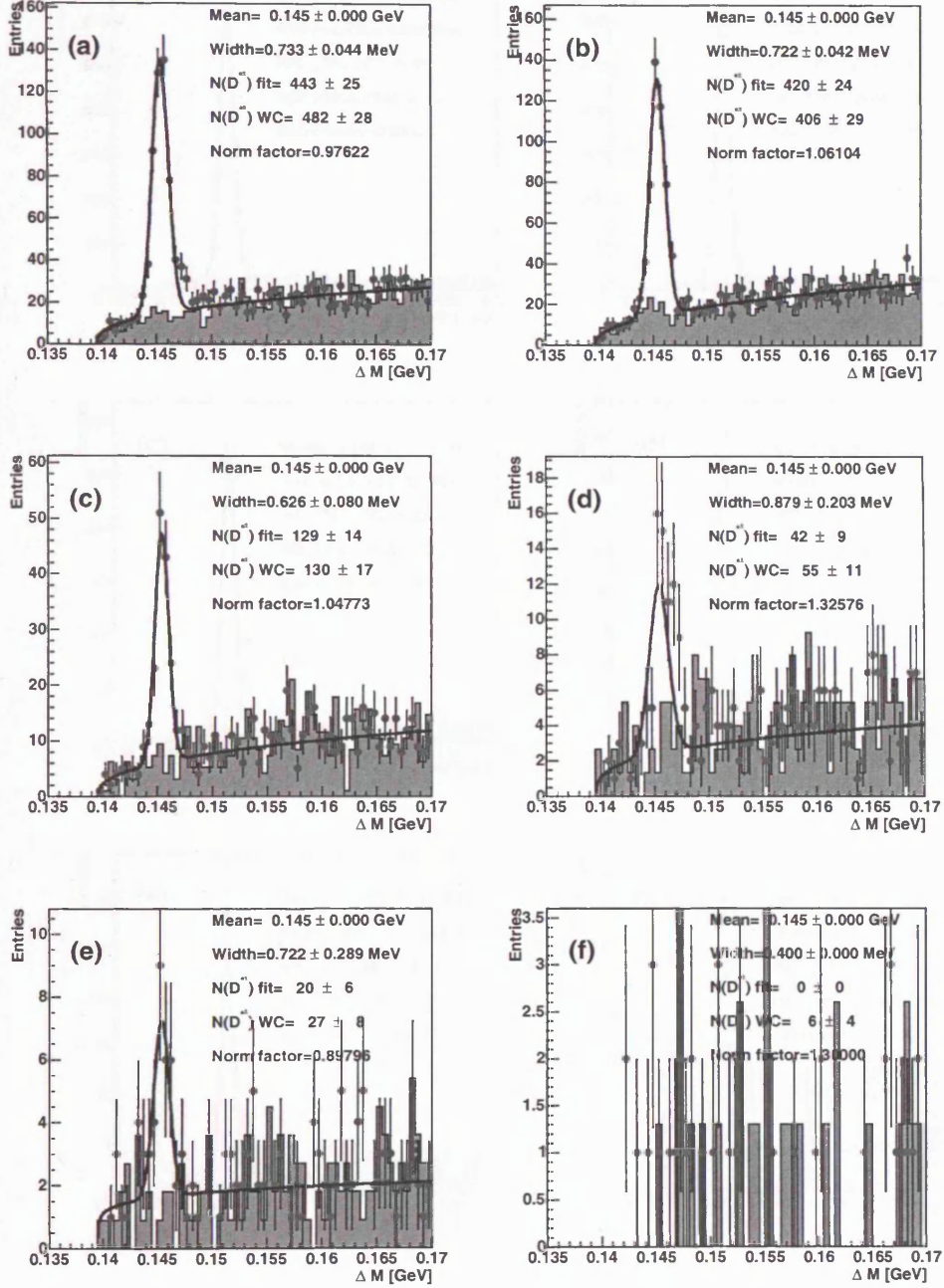


14.8  $d\sigma/dm^{jj}$  mass peaks, direct-enriched  $x_\gamma^{\text{obs}} > 0.75$ 

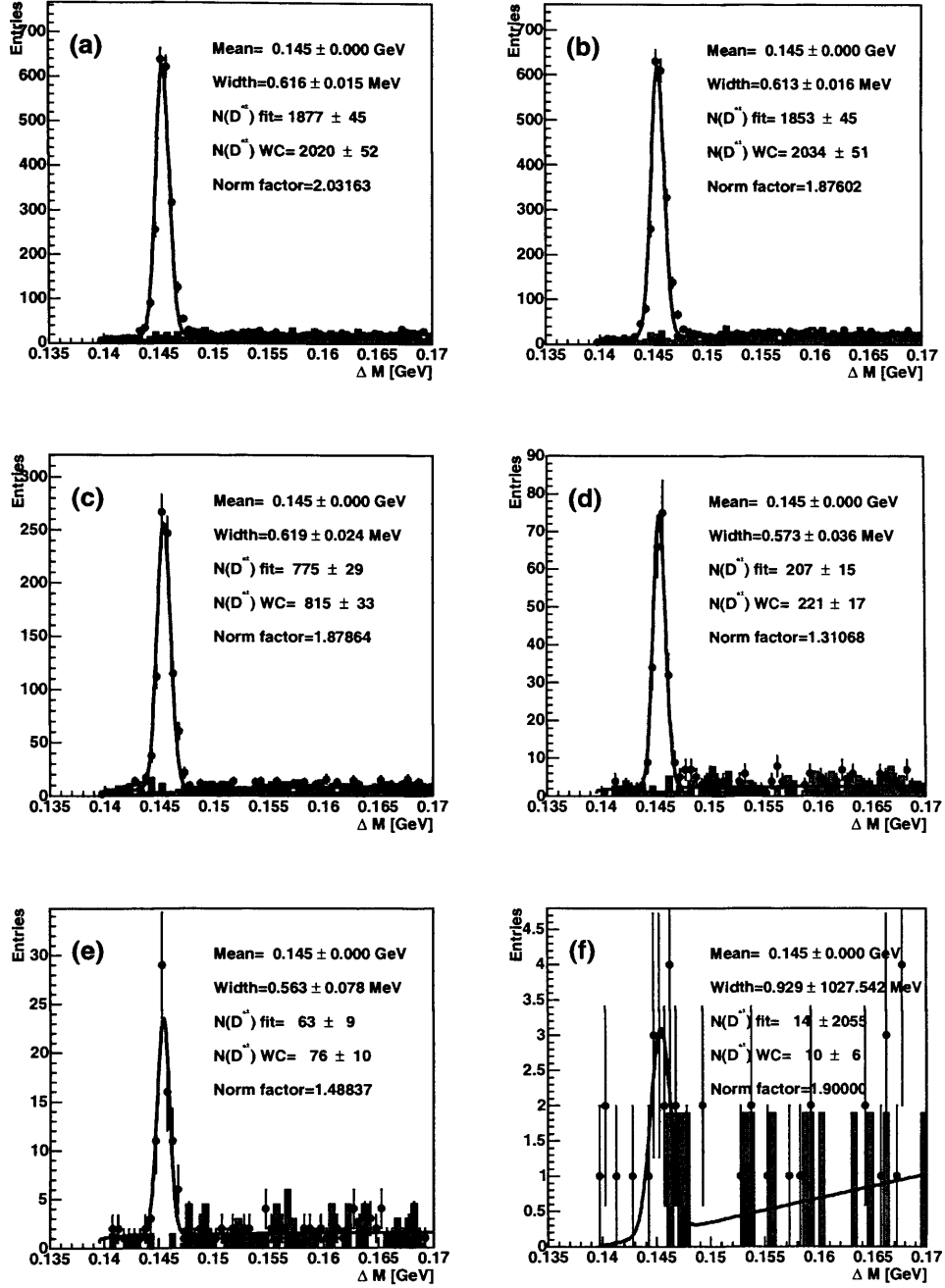
**Figure 14.15** Mass peaks for each bin of the dijet charm cross section  $d\sigma/dm^{jj}$  for 1998-2000 data  $78\text{pb}^{-1}$ , with  $x_\gamma^{\text{obs}} > 0.75$ . (a) goes from the lowest  $m^{jj}$  bin to (g) the highest.



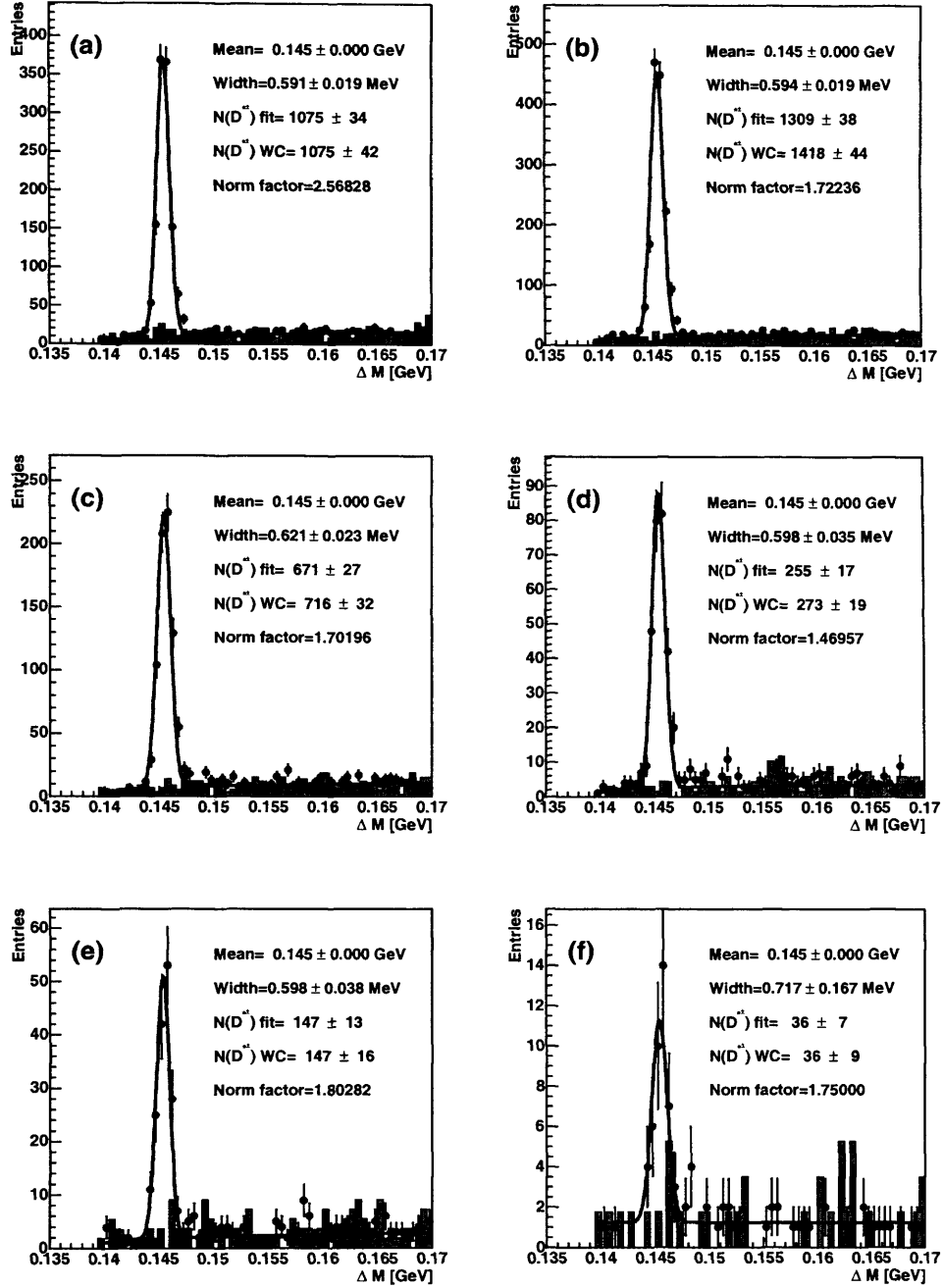
**Figure 14.16** Mass peaks for each bin of the dijet charm cross section  $d\sigma/dm^{jj}$  for  $886\text{pb}^{-1}$  of HERWIG MC, with  $x_{\gamma}^{\text{obs}} > 0.75$ . (a) goes from the lowest  $m^{jj}$  bin to (g) the highest.

14.9  $d\sigma/dp_T^{2jj}$  mass peaks, direct-enriched  $x_\gamma^{\text{obs}} > 0.75$ 


**Figure 14.17** Mass peaks for each bin of the dijet charm cross section  $d\sigma/dp_T^{2jj}$  for 1998-2000 data  $78\text{pb}^{-1}$ , with  $x_\gamma^{\text{obs}} > 0.75$ . (a) goes from the lowest  $p_T^{2jj}$  bin to (g) the highest.

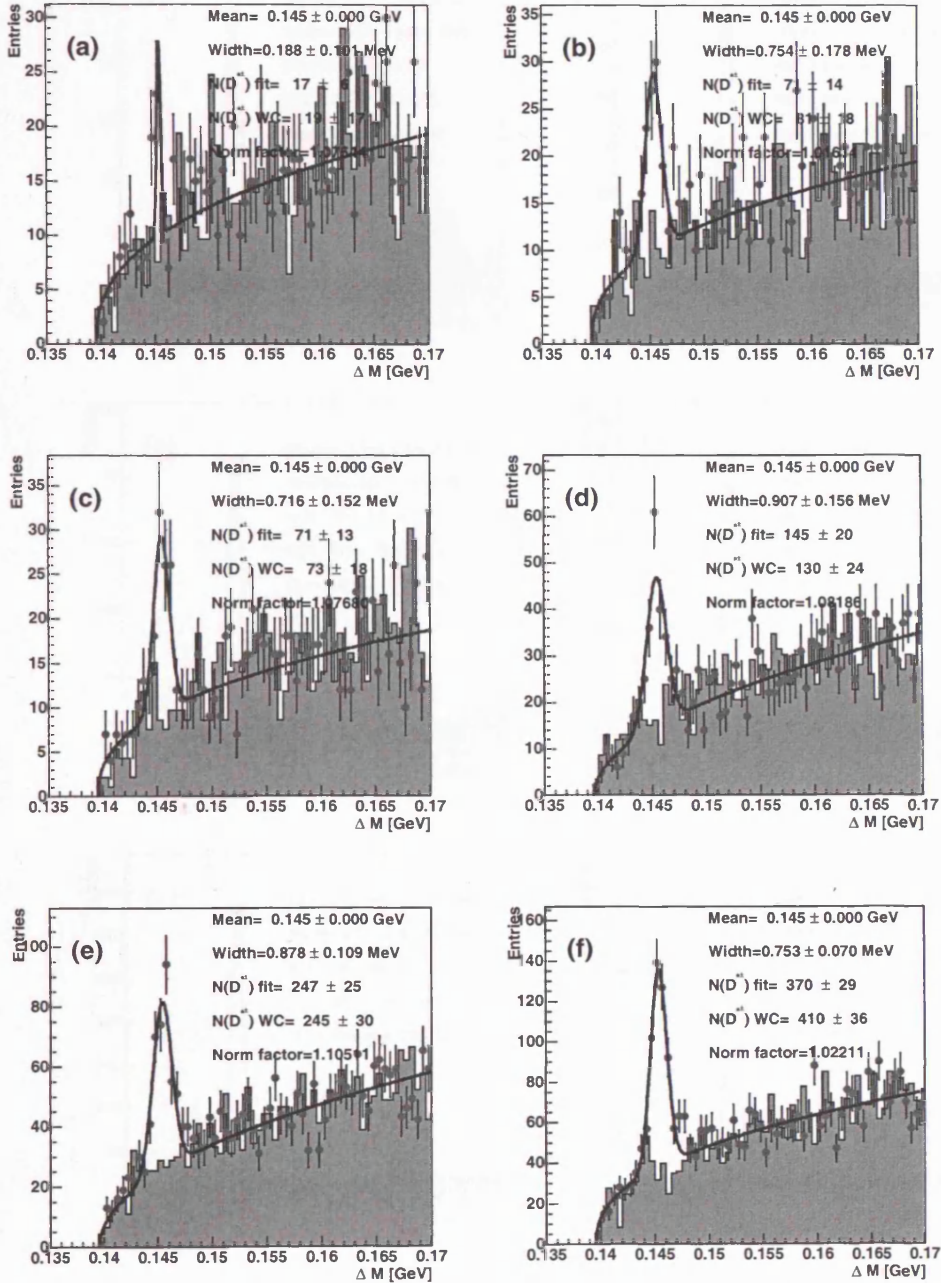


**Figure 14.18** Mass peaks for each bin of the dijet charm cross section  $d\sigma/dp_T^{2jj}$  for  $886pb^{-1}$  of HERWIG MC, with  $x_\gamma^{obs} > 0.75$ . (a) goes from the lowest  $p_T^{2jj}$  bin to (g) the highest.

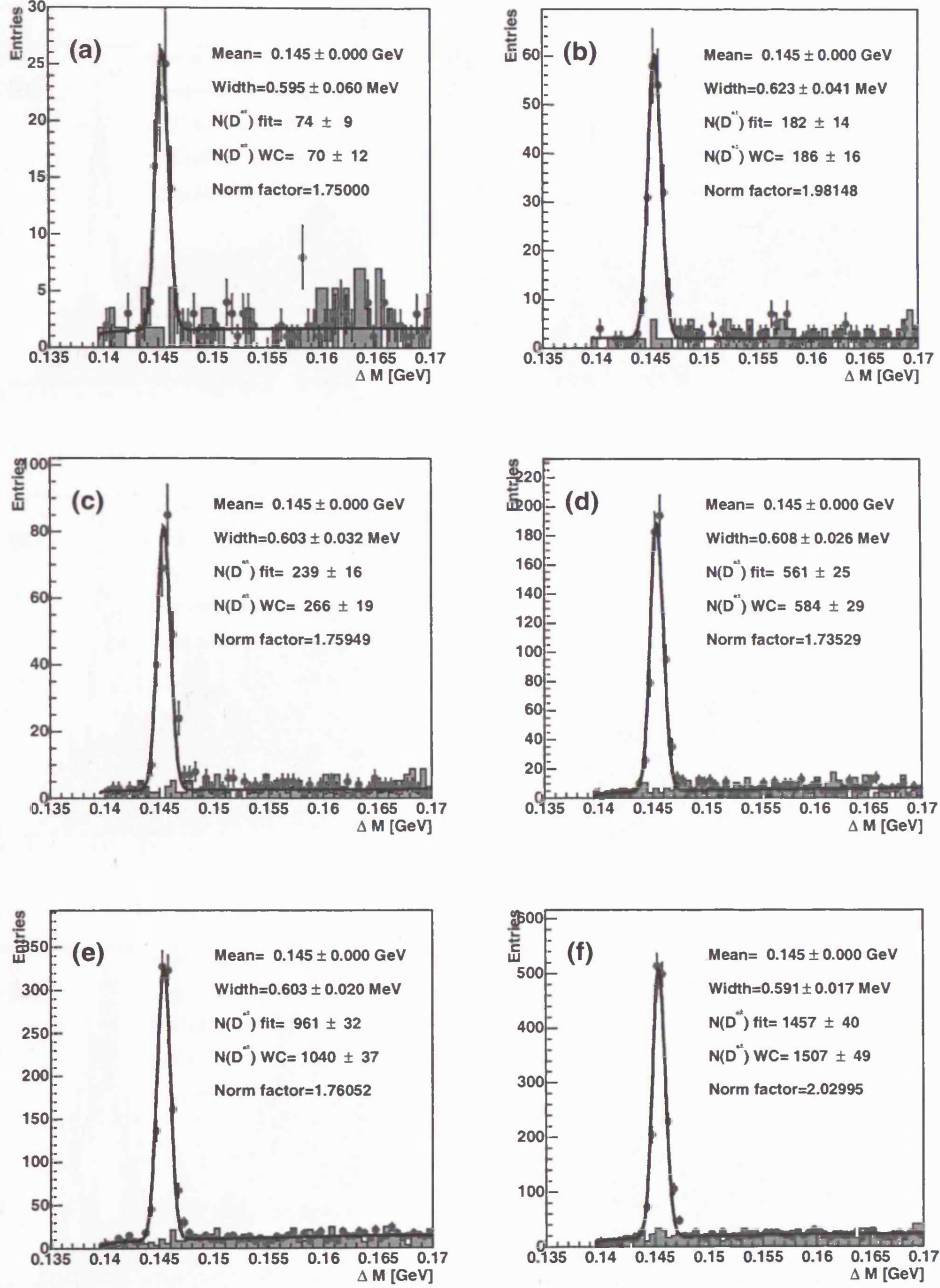


**Figure 14.20** Mass peaks for each bin of the dijet charm cross section  $d\sigma/dp_T^{jj}$  for  $886 pb^{-1}$  of HERWIG MC, with  $x_\gamma^{obs} < 0.75$ . (a) goes from the lowest  $p_T^{jj}$  bin to (g) the highest.

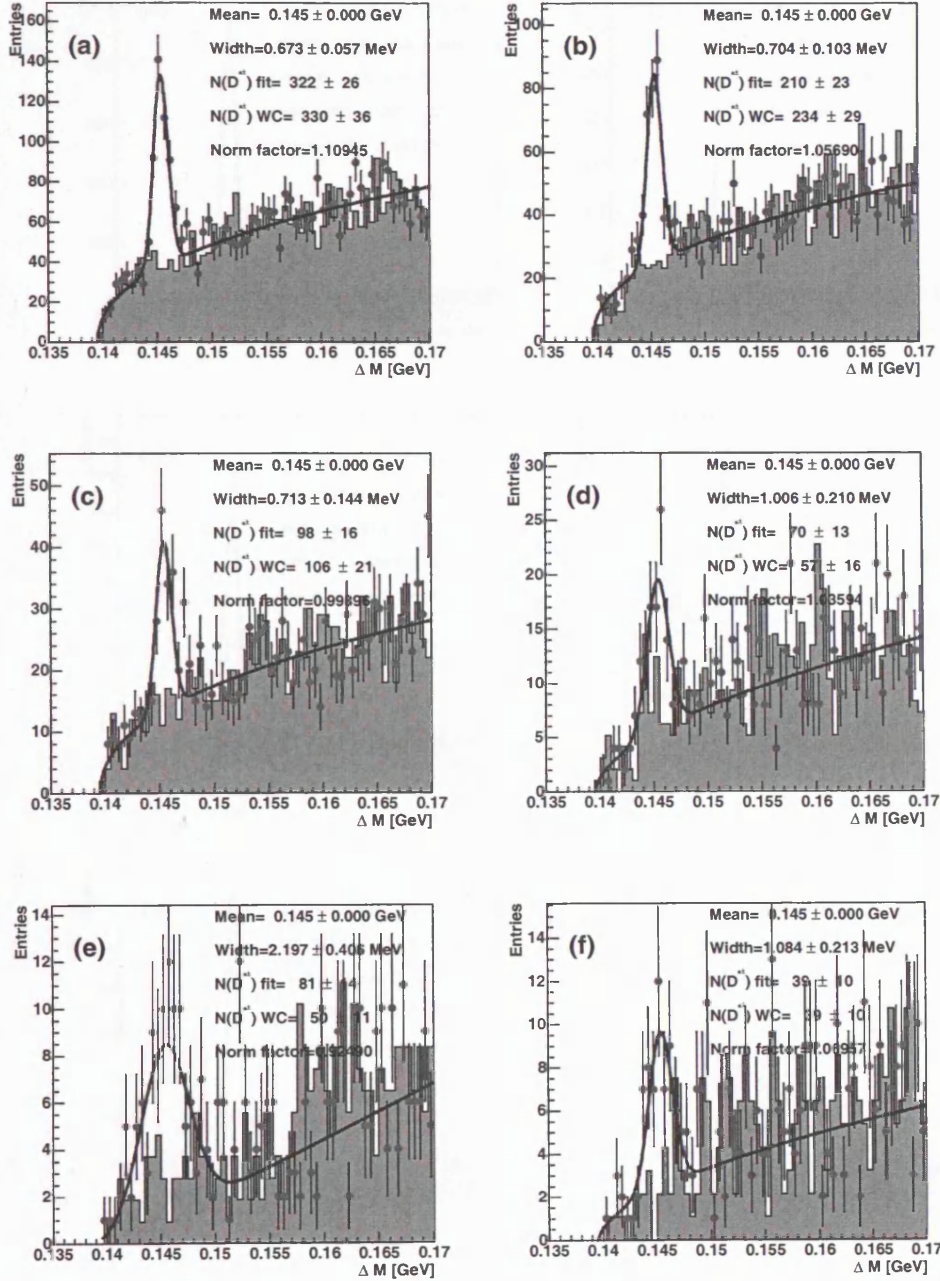


14.11  $d\sigma/d\Delta\phi^{jj}$  mass peaks, resolved-enriched  $x_\gamma^{\text{obs}} < 0.75$ 

**Figure 14.21** Mass peaks for each bin of the dijet charm cross section  $d\sigma/d\Delta\phi^{jj}$  for 1998-2000 data  $78\text{pb}^{-1}$ , with  $x_\gamma^{\text{obs}} < 0.75$ . (a) goes from the lowest  $\Delta\phi^{jj}$  bin to (g) the highest.

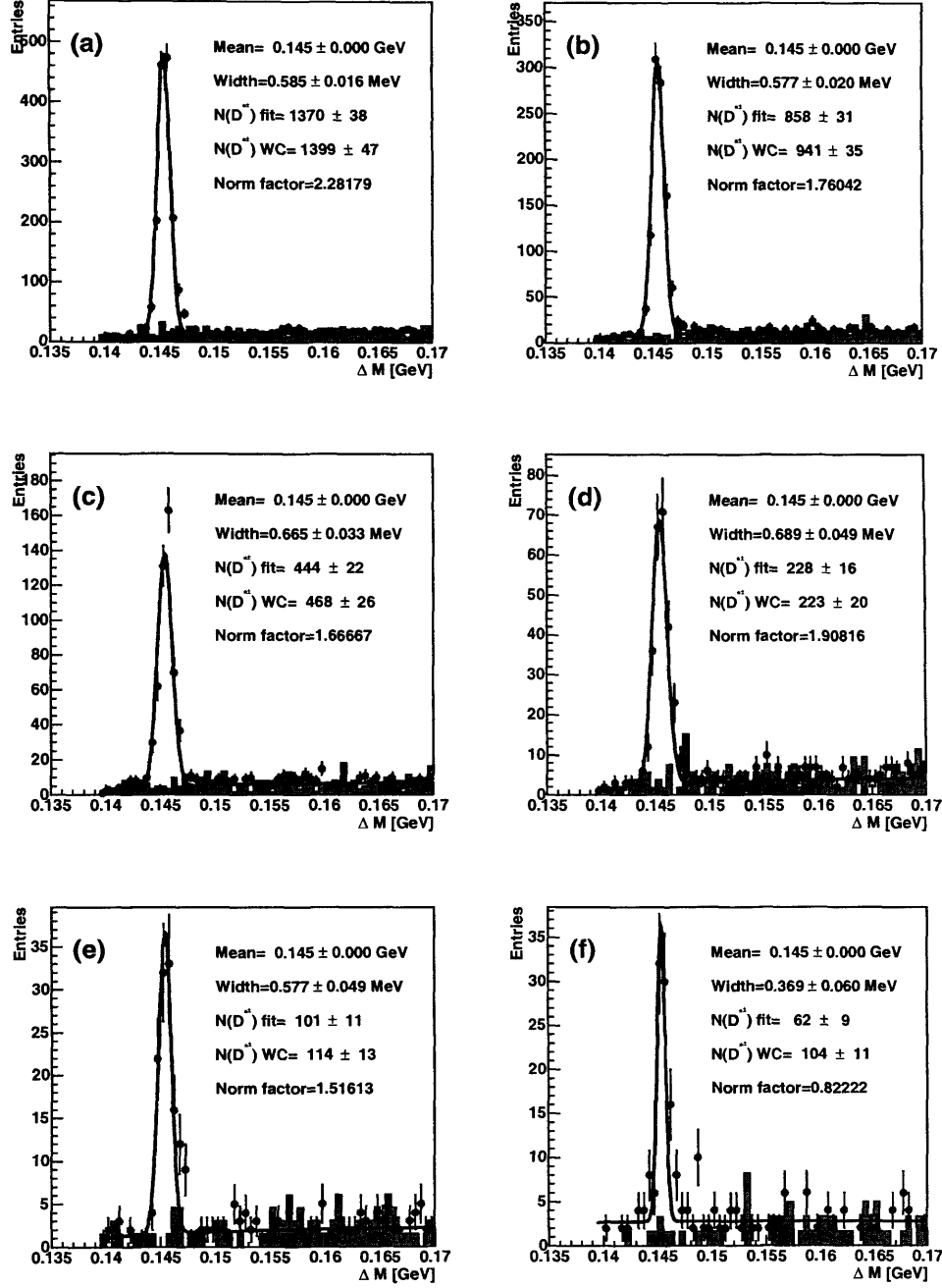


**Figure 14.22** Mass peaks for each bin of the dijet charm cross section  $d\sigma/d\Delta\phi^{jj}$  for  $886\text{pb}^{-1}$  of HERWIG MC, with  $x_\gamma^{\text{obs}} < 0.75$ . (a) goes from the lowest  $\Delta\phi^{jj}$  bin to (g) the highest.

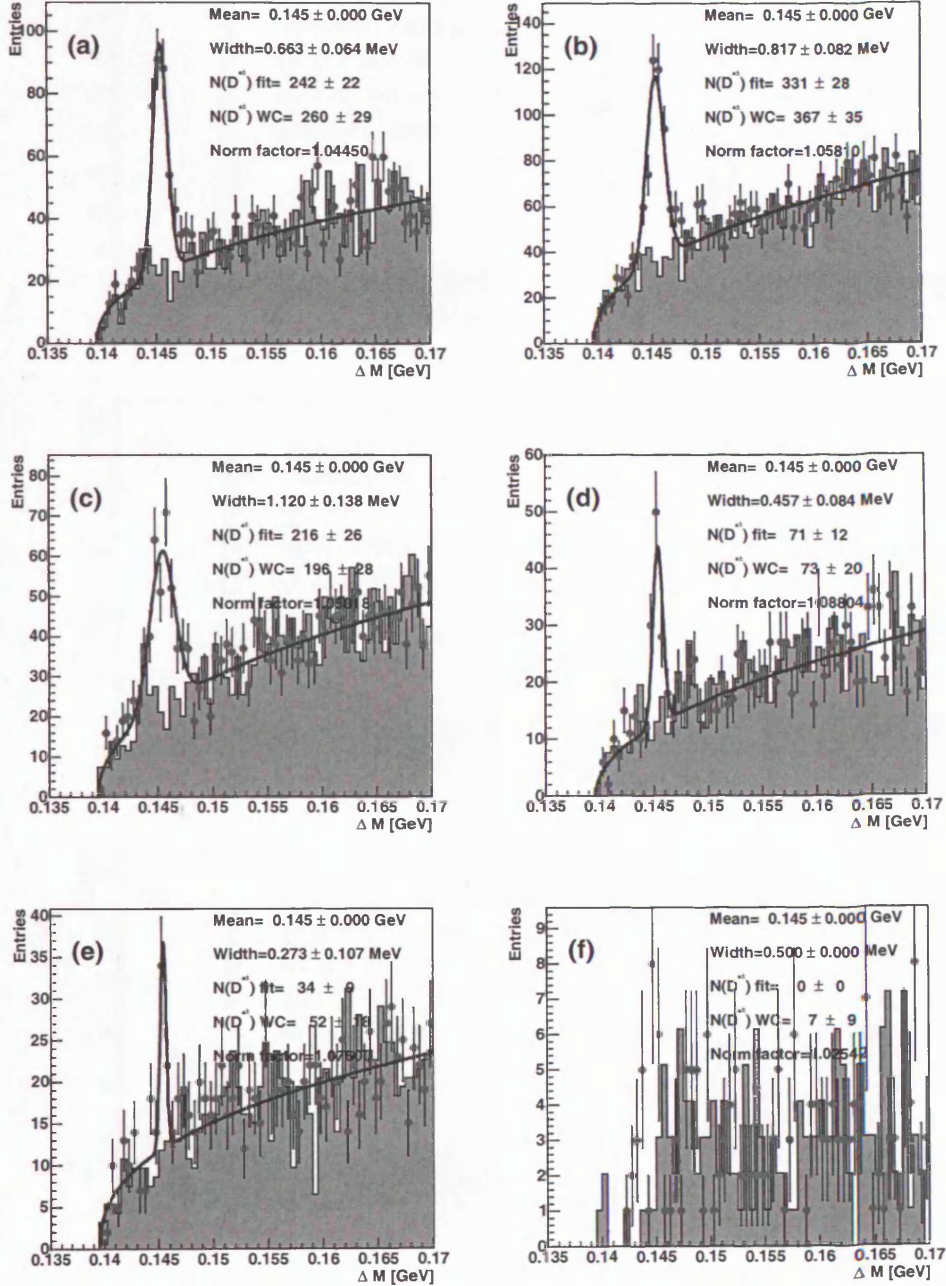
14.12  $d\sigma/dm^{jj}$  mass peaks, resolved-enriched  $x_\gamma^{\text{obs}} < 0.75$ 

**Figure 14.23** Mass peaks for each bin of the dijet charm cross section  $d\sigma/dm^{jj}$  for 1998-2000 data  $78\text{pb}^{-1}$ , with  $x_\gamma^{\text{obs}} < 0.75$ . (a) goes from the lowest  $m^{jj}$  bin to (g) the highest.

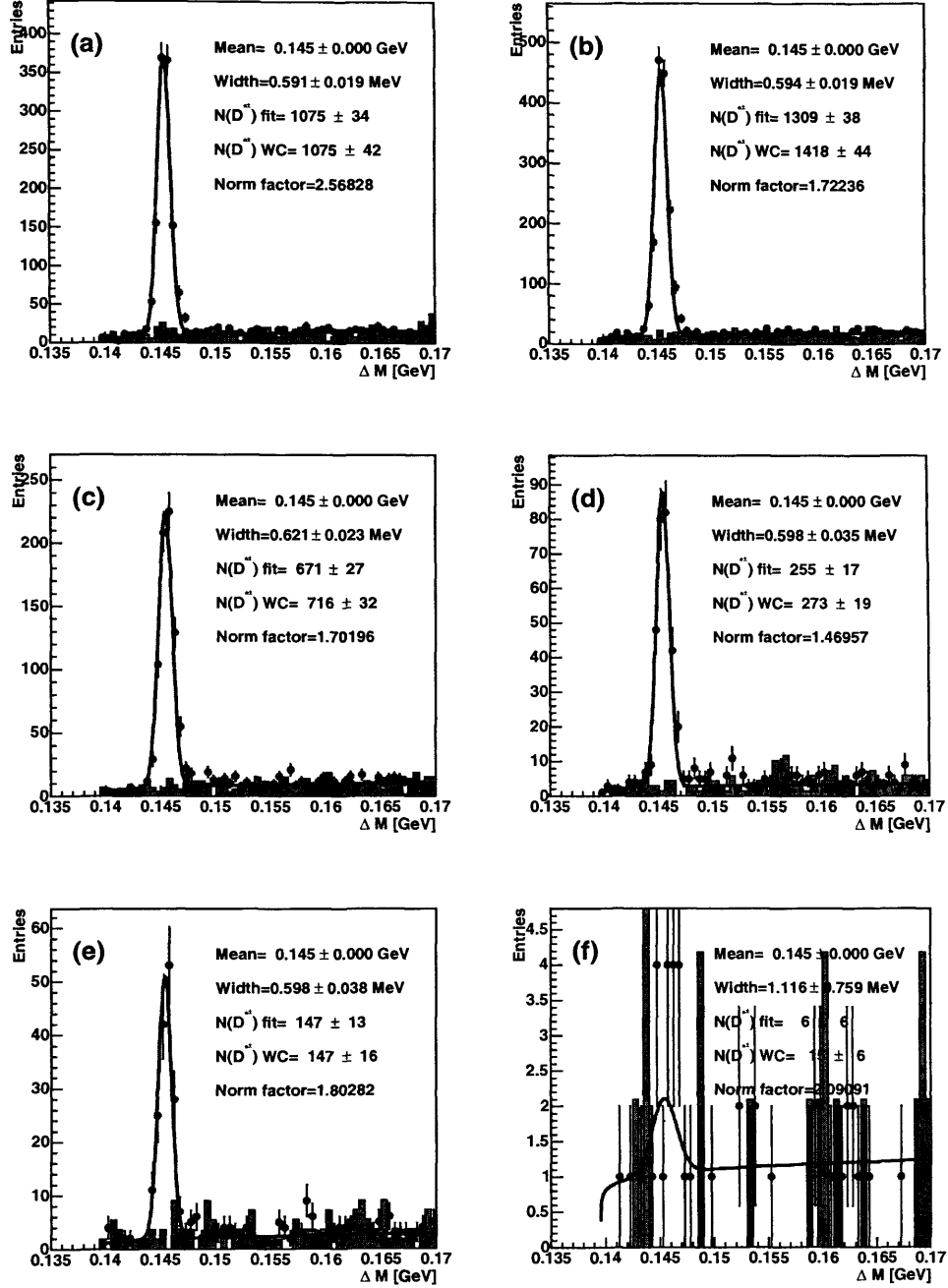




**Figure 14.24** Mass peaks for each bin of the dijet charm cross section  $d\sigma/dm^{jj}$  for  $886pb^{-1}$  of HERWIG MC, with  $x_{\gamma}^{obs} < 0.75$ . (a) goes from the lowest  $m^{jj}$  bin to (g) the highest.

14.13  $d\sigma/dp_T^{2jj}$  mass peaks, resolved-enriched  $x_\gamma^{\text{obs}} < 0.75$ 

**Figure 14.25** Mass peaks for each bin of the dijet charm cross section  $d\sigma/dp_T^{2jj}$  for 1998-2000 data  $78\text{pb}^{-1}$ , with  $x_\gamma^{\text{obs}} < 0.75$ . (a) goes from the lowest  $p_T^{2jj}$  bin to (g) the highest.



**Figure 14.26** Mass peaks for each bin of the dijet charm cross section  $d\sigma/dp_T^{2jj}$  for  $886pb^{-1}$  of HERWIG MC, with  $x_\gamma^{obs} < 0.75$ . (a) goes from the lowest  $p_T^{2jj}$  bin to (g) the highest.

---

## 15 Appendix C : Inclusive Jet

### Purity/Efficiency/Acceptance/Hadronisation Corrections

---

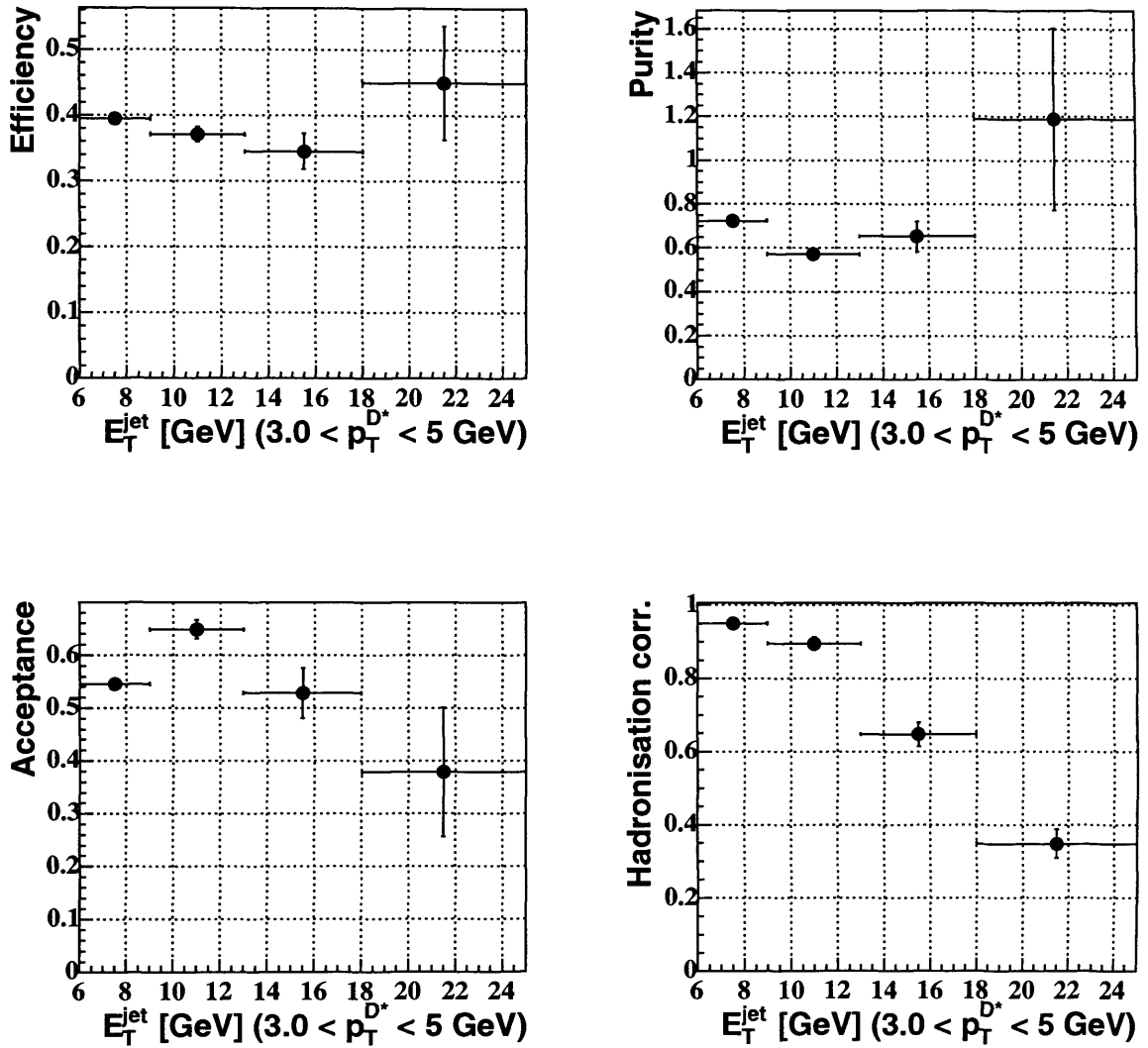
In this chapter the purity, efficiency, acceptance and hadronisation corrections are show for the inclusive jet distributions  $d\sigma/dE_T^{jet}$  for:

3.0 <  $P_T^{D^*}$  < 5.0 GeV Fig. 15.1,  
5.0 <  $P_T^{D^*}$  < 8.0 GeV Fig. 15.3 and for  
8.0 <  $P_T^{D^*}$  < 20.0 GeV Fig. 15.5.

Also for  $d\sigma/d\eta^{jet}$  in ranges of:

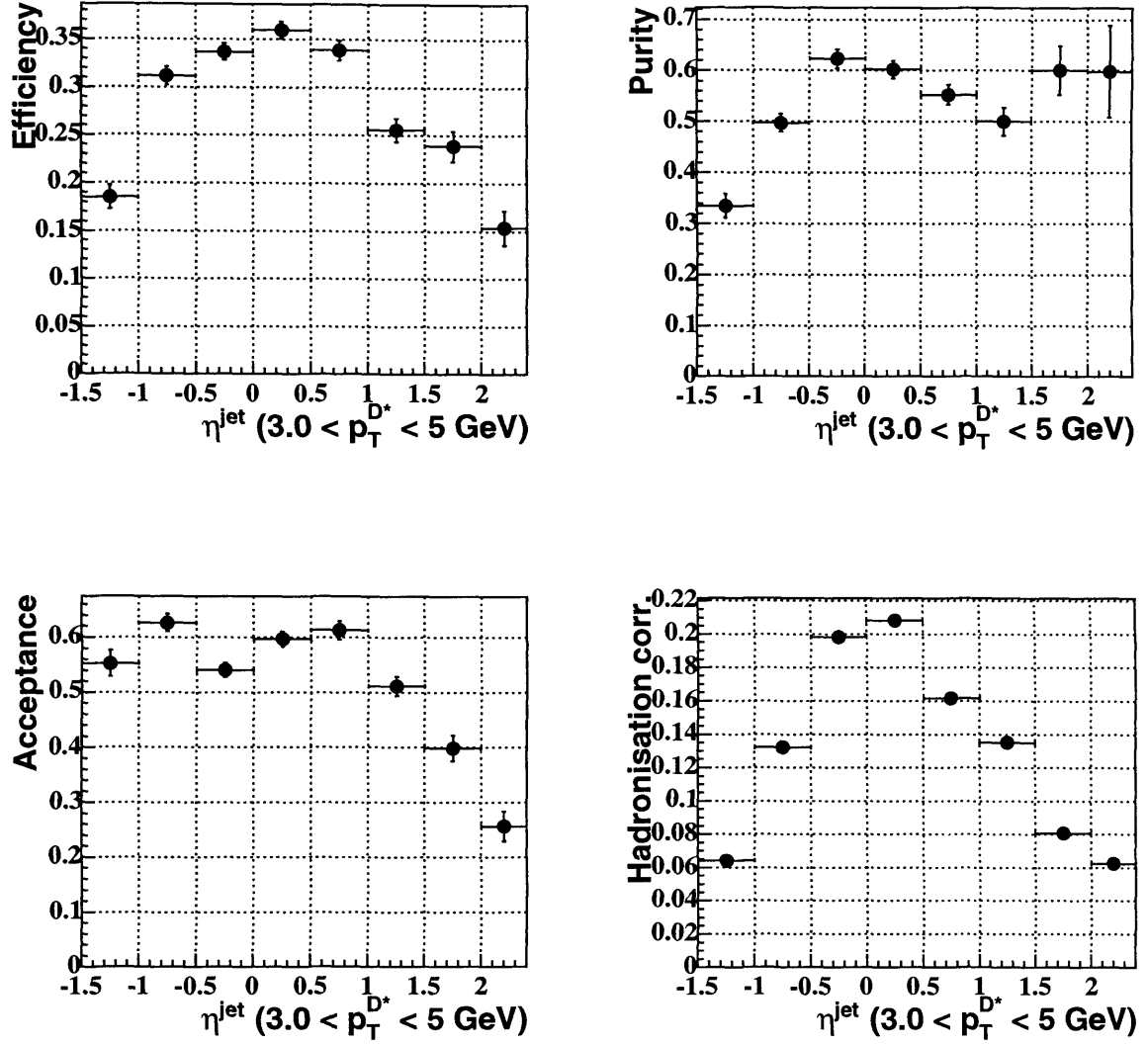
3.0 <  $P_T^{D^*}$  < 5.0 GeV Fig. 15.2,  
5.0 <  $P_T^{D^*}$  < 8.0 GeV Fig. 15.4 and for  
8.0 <  $P_T^{D^*}$  < 20.0 GeV Fig. 15.6.

### 15.1 Purity/efficiency/acceptance/hadronisation corrections for $d\sigma/dE_T^{jet}$ & $d\sigma/d\eta^{jet}$ for $3.0 < P_T^{D^*} < 5.0$ GeV



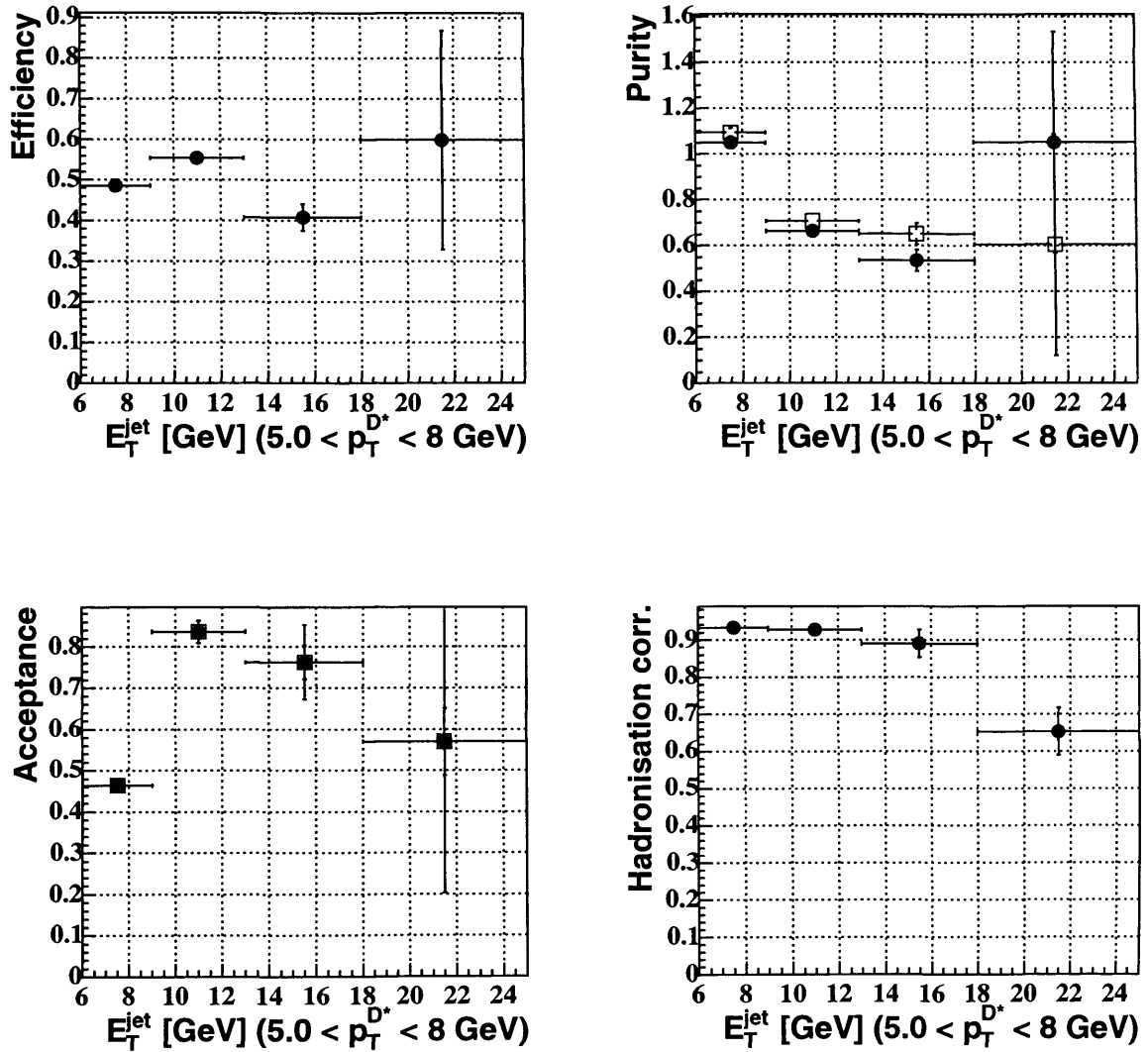
**Figure 15.1** Purity/efficiency/acceptance and hadronisation corrections for each bin of the inclusive charm jet cross section  $d\sigma/dE_T^{jet}$  in the range  $3.0 < P_T^{D^*} < 5.0$  GeV.

15.1 Purity/efficiency/acceptance/hadronisation corrections for  $d\sigma/dE_T^{jet}$  &  $d\sigma/d\eta^{jet}$  for  
 $3.0 < P_T^{D^*} < 5.0 \text{ GeV}$



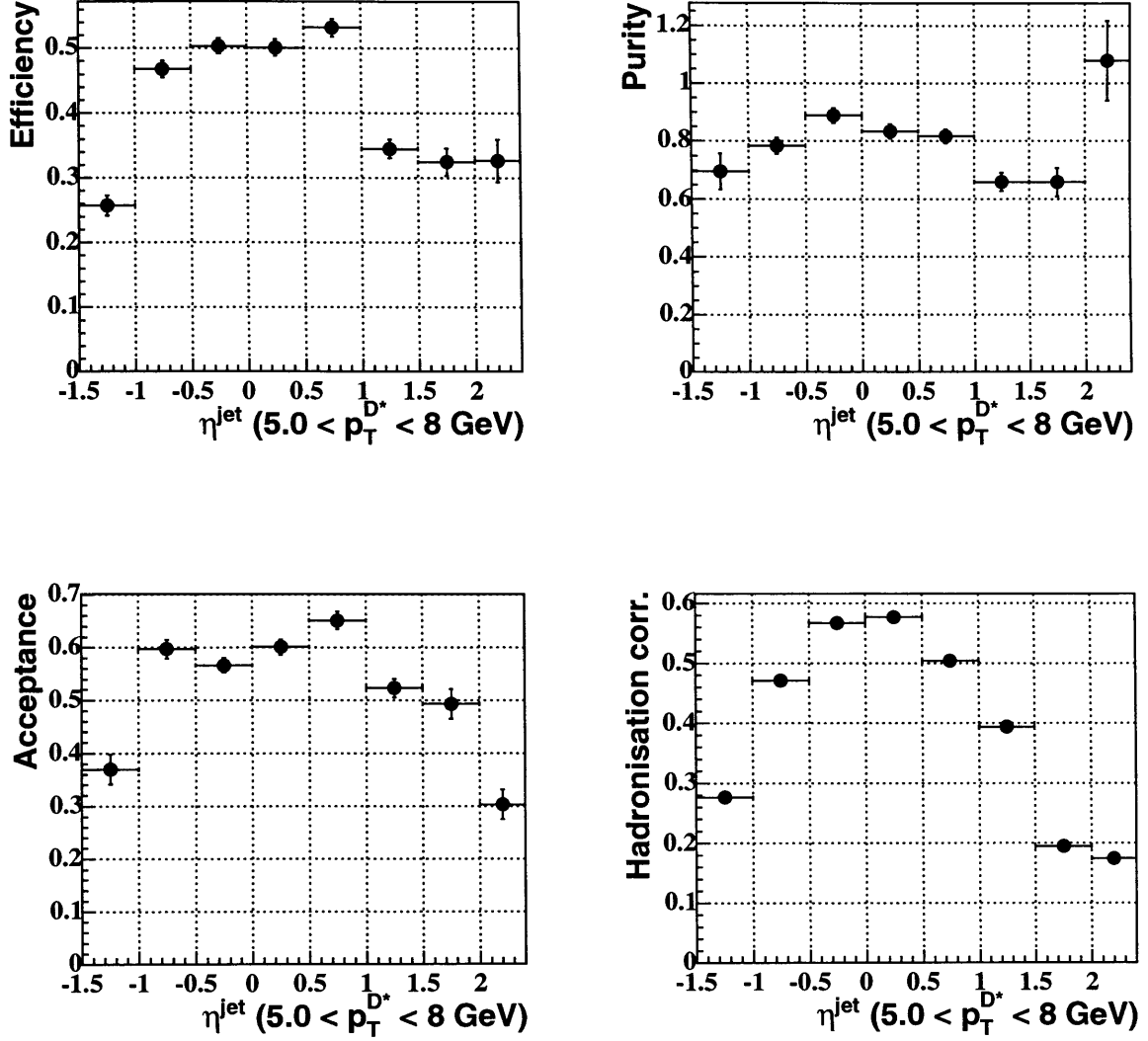
**Figure 15.2** Purity/efficiency/acceptance and hadronisation corrections for each bin of the inclusive charm jet cross section  $d\sigma/d\eta^{jet}$  in the range  $3.0 < P_T^{D^*} < 5.0 \text{ GeV}$ .

## 15.2 Purity/efficiency/acceptance/hadronisation corrections for $d\sigma/dE_T^{jet}$ and $d\sigma/d\eta^{jet}$ for $5.0 < p_T^{D^*} < 8.0$ GeV



**Figure 15.3** Purity/efficiency/acceptance and hadronisation corrections for each bin of the inclusive charm jet cross section  $d\sigma/dE_T^{jet}$  in the range  $5.0 < p_T^{D^*} < 8.0$  GeV.

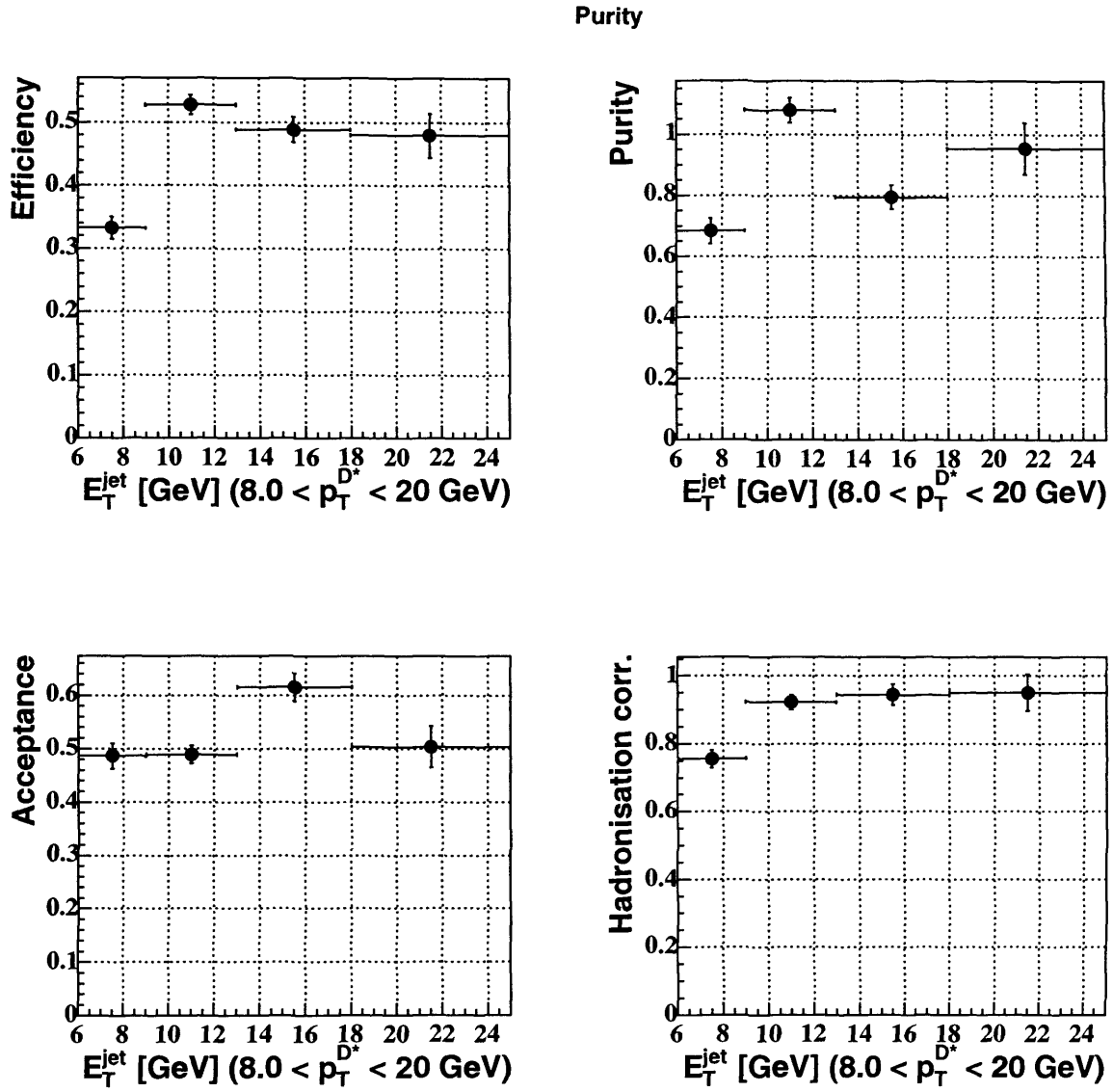
15.2 Purity/efficiency/acceptance/hadronisation corrections for  $d\sigma/dE_T^{jet}$  and  $d\sigma/d\eta^{jet}$  for  
 $5.0 < p_T^{D^*} < 8.0$  GeV



**Figure 15.4** Purity/efficiency/acceptance and hadronisation corrections for each bin of the inclusive charm jet cross section  $d\sigma/d\eta^{jet}$  in the range  $5.0 < P_T^{D^*} < 8.0$  GeV.

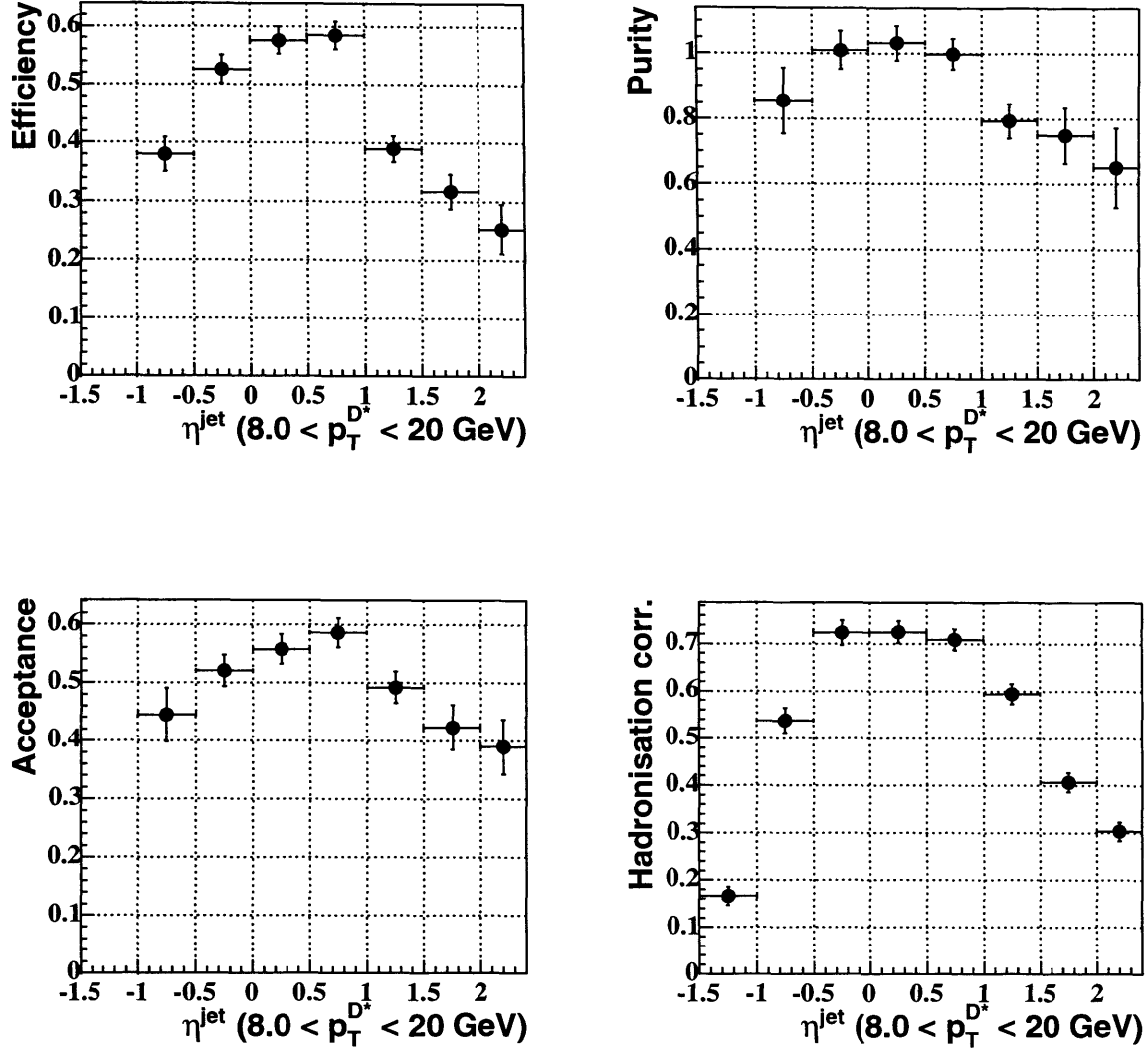


### 15.3 Purity/efficiency/acceptance/hadronisation corrections for $d\sigma/dE_T^{jet}$ and $d\sigma/d\eta^{jet}$ for $8.0 < p_T^{D^*} < 20.0$ GeV



**Figure 15.5** Purity/efficiency/acceptance and hadronisation corrections for each bin of the inclusive charm jet cross section  $d\sigma/dE_T^{jet}$  in the range  $8.0 < p_T^{D^*} < 20.0$  GeV.

15.3 Purity/efficiency/acceptance/hadronisation corrections for  $d\sigma/dE_T^{jet}$  and  $d\sigma/d\eta^{jet}$  for  
 $8.0 < p_T^{D^*} < 20.0$  GeV



**Figure 15.6** Purity/efficiency/acceptance and hadronisation corrections for each bin of the inclusive charm jet cross section  $d\sigma/d\eta^{jet}$  in the range  $8.0 < P_T^{D^*} < 20.0$  GeV.

---

## 16 Appendix D : Dijet purity/efficiency/acceptance/hadronisation corrections

---

In this chapter the purity, efficiency, acceptance and hadronisation corrections are show for the dijet distributions:

$d\sigma/dx_{\gamma}^{\text{obs}}$  Fig. 16.1,

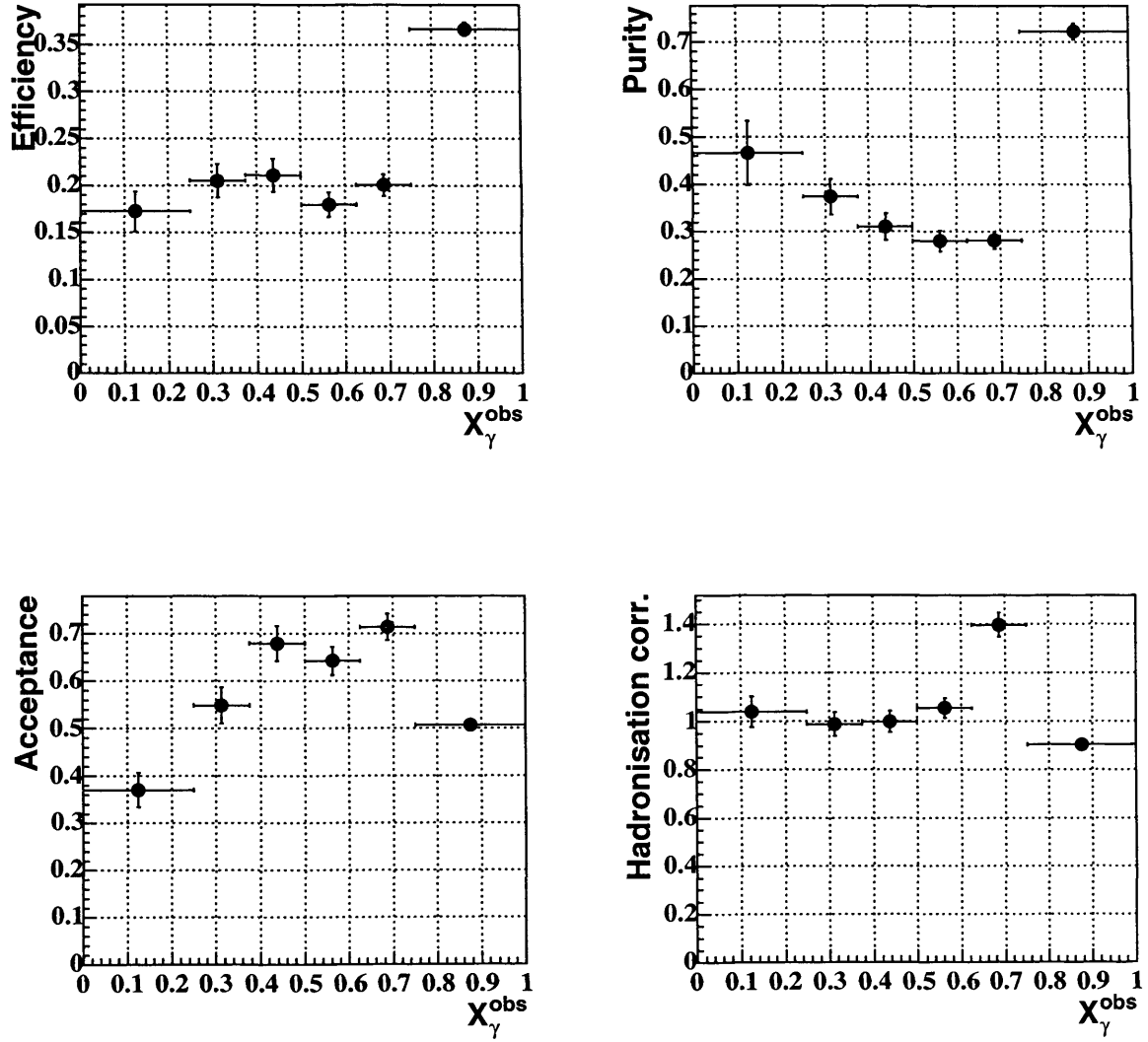
$d\sigma/m^{jj}$  16.2, direct-enriched Fig. 16.3, resolved-enriched Fig. 16.4,

$d\sigma/p_T^{jj}$  Fig. 16.5, direct-enriched Fig. 16.7, resolved-enriched Fig. 16.6,

$d\sigma/\Delta\phi^{jj}$  Fig. 16.8, direct-enriched Fig. 16.9, resolved-enriched Fig. 16.10,

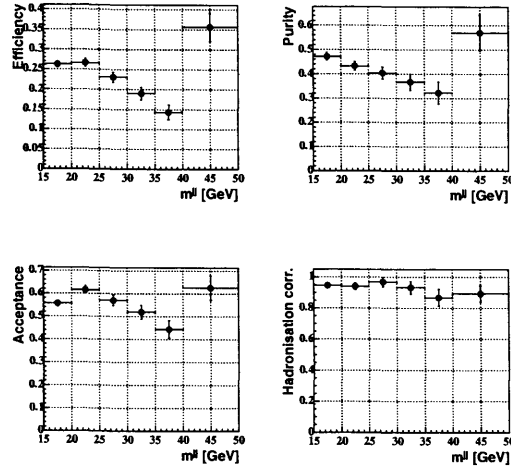
$d\sigma/p_T^{2jj}$  Fig. 16.11, direct-enriched Fig. 16.12, resolved-enriched Fig. 16.13.

## 16.1 $d\sigma/dx_\gamma^{\text{obs}}$ , purity/efficiency/acceptance/hadronisation corrections

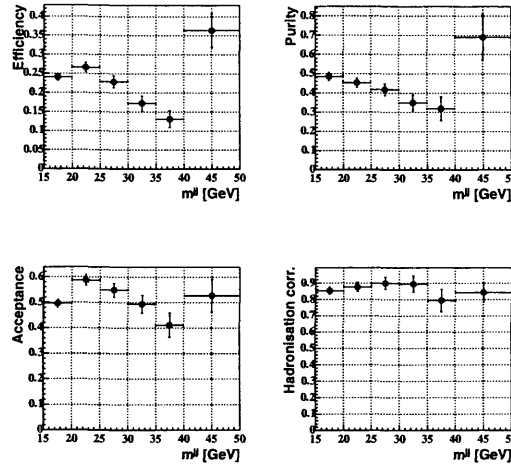


**Figure 16.1** Purity/efficiency/acceptance and hadronisation corrections for each bin of the dijet charm cross section  $d\sigma/dx_\gamma$  for HERWIG 886  $\text{pb}^{-1}$ .

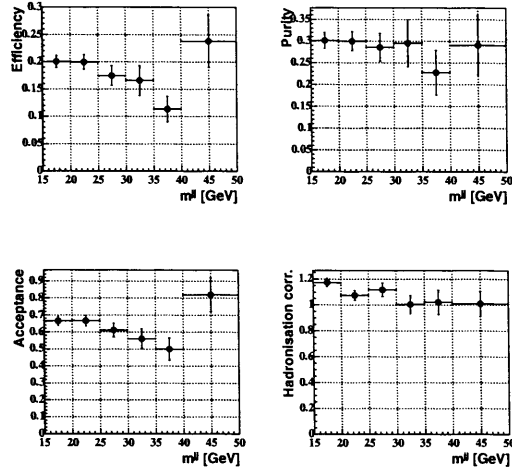
## 16.2 $d\sigma/dm^{jj}$ , purity/efficiency/acceptance/hadronisation corrections



**Figure 16.2** Purity/efficiency/acceptance and hadronisation corrections for each bin of the inclusive charm jet cross section  $d\sigma/dm^{jj}$  for HERWIG 886 pb<sup>-1</sup>.

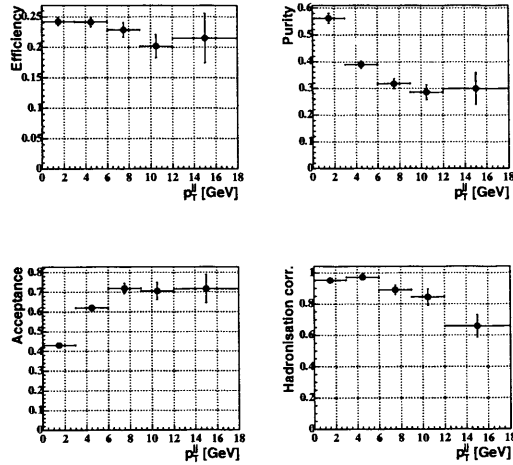


**Figure 16.3** Purity/efficiency/acceptance and hadronisation corrections for each bin of the inclusive charm jet cross section  $d\sigma/dm^{jj}$ , direct-enriched  $x_{\gamma}^{\text{obs}} > 0.75$  for HERWIG 886 pb<sup>-1</sup>.

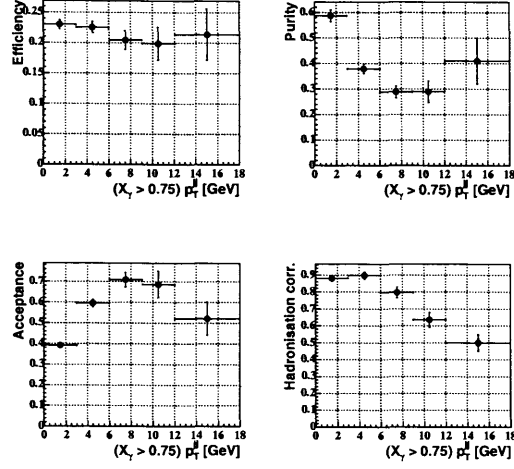


**Figure 16.4** Purity/efficiency/acceptance and hadronisation corrections for each bin of the inclusive charm jet cross section  $d\sigma/dm^{jj}$ , resolved-enriched  $x_\gamma^{\text{obs}} < 0.75$  for HERWIG 886  $\text{pb}^{-1}$ .

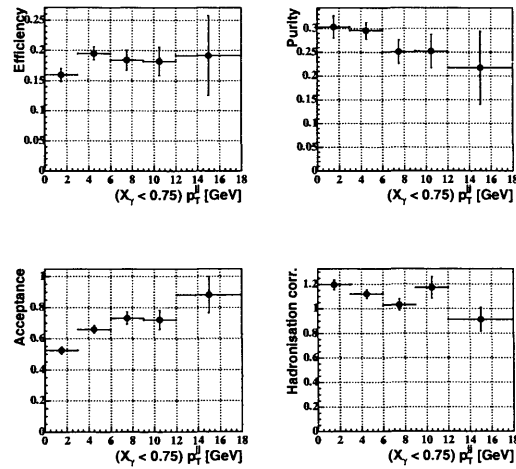
### 16.3 $d\sigma/dp_T^{jj}$ , purity/efficiency/acceptance/hadronisation corrections



**Figure 16.5** Purity/efficiency/acceptance and hadronisation corrections for each bin of the inclusive charm jet cross section  $d\sigma/dp_T^{jj}$  for HERWIG 886  $\text{pb}^{-1}$ .

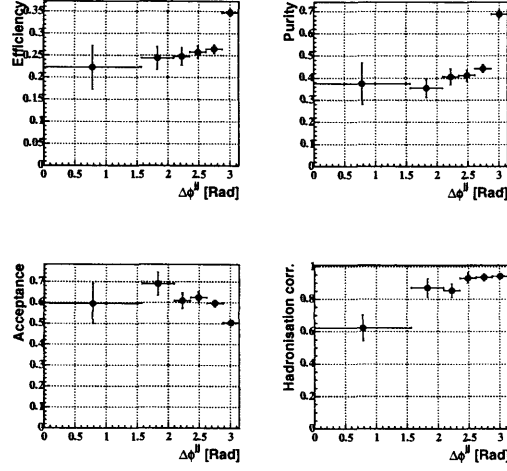


**Figure 16.6** Purity/efficiency/acceptance and hadronisation corrections for each bin of the inclusive charm jet cross section  $d\sigma/dp_T^{jj}$ , direct-enriched  $x_\gamma^{\text{obs}} > 0.75$  for HERWIG 886  $\text{pb}^{-1}$ .

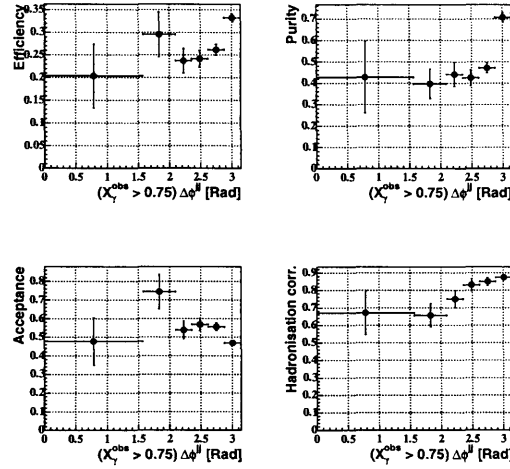


**Figure 16.7** Purity/efficiency/acceptance and hadronisation corrections for each bin of the inclusive charm jet cross section  $d\sigma/dp_T^{jj}$ , resolved-enriched  $x_\gamma^{\text{obs}} < 0.75$  for HERWIG 886  $\text{pb}^{-1}$ .

## 16.4 $d\sigma/d\Delta\phi^{jj}$ , purity/efficiency/acceptance/hadronisation corrections

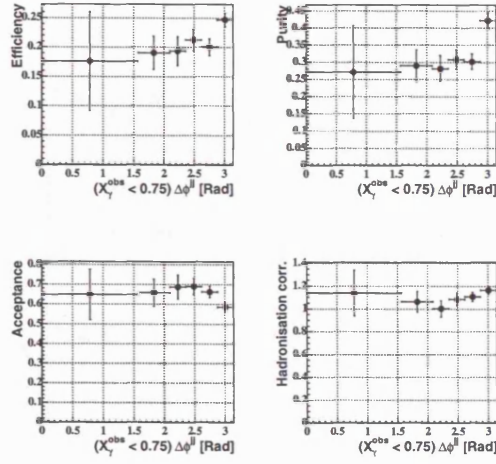


**Figure 16.8** Purity/efficiency/acceptance and hadronisation corrections for each bin of the inclusive charm jet cross section  $d\sigma/d\Delta\phi^{jj}$ , for HERWIG 886  $\text{pb}^{-1}$ .



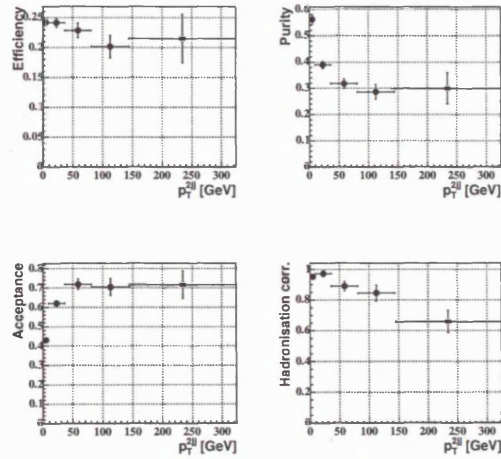
**Figure 16.9** Purity/efficiency/acceptance and hadronisation corrections for each bin of the inclusive charm jet cross section  $d\sigma/d\Delta\phi^{jj}$ , direct-enriched  $x_{\gamma}^{\text{obs}} > 0.75$  for HERWIG 886  $\text{pb}^{-1}$ .



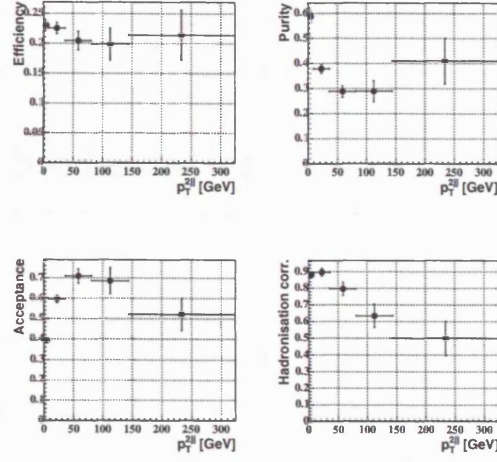


**Figure 16.10** Purity/efficiency/acceptance and hadronisation corrections for each bin of the inclusive charm jet cross section  $d\sigma/d\Delta\phi^{jj}$ , resolved-enriched  $x_\gamma^{\text{obs}} < 0.75$  for HERWIG 886  $\text{pb}^{-1}$ .

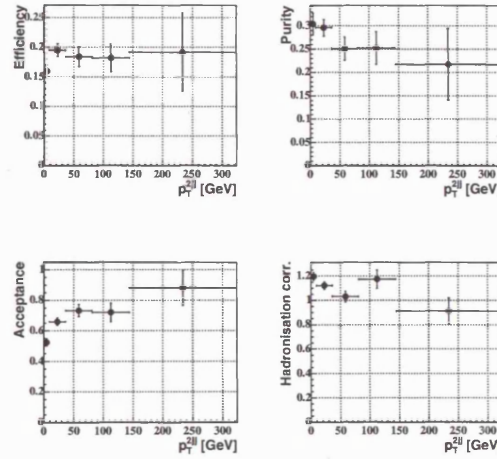
## 16.5 $d\sigma/dp_T^{2jj}$ , purity/efficiency/acceptance/hadronisation corrections



**Figure 16.11** Purity/efficiency/acceptance and hadronisation corrections for each bin of the inclusive charm jet cross section  $d\sigma/dp_T^{2jj}$ , for HERWIG 886  $\text{pb}^{-1}$ .



**Figure 16.12** Purity/efficiency/acceptance and hadronisation corrections for each bin of the inclusive charm jet cross section  $d\sigma/dp_T^{2jj}$ , direct-enriched  $x_\gamma^{\text{obs}} > 0.75$  for HERWIG 886 pb<sup>-1</sup>.



**Figure 16.13** Purity/efficiency/acceptance and hadronisation corrections for each bin of the inclusive charm jet cross section  $d\sigma/dp_T^{2jj}$ , resolved-enriched  $x_\gamma^{\text{obs}} < 0.75$  for HERWIG 886 pb<sup>-1</sup>.

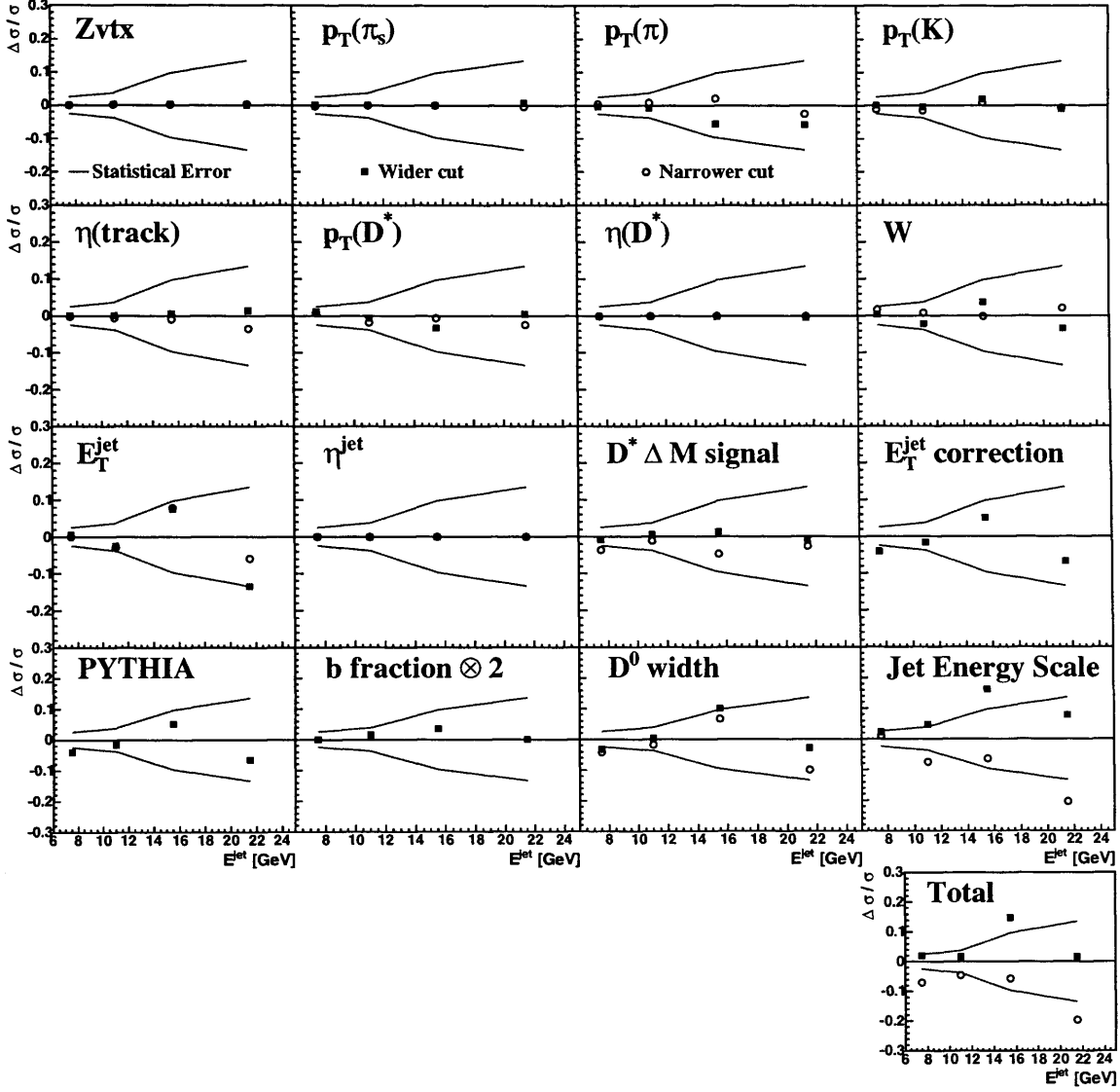
---

## 17 Appendix E :Systematics

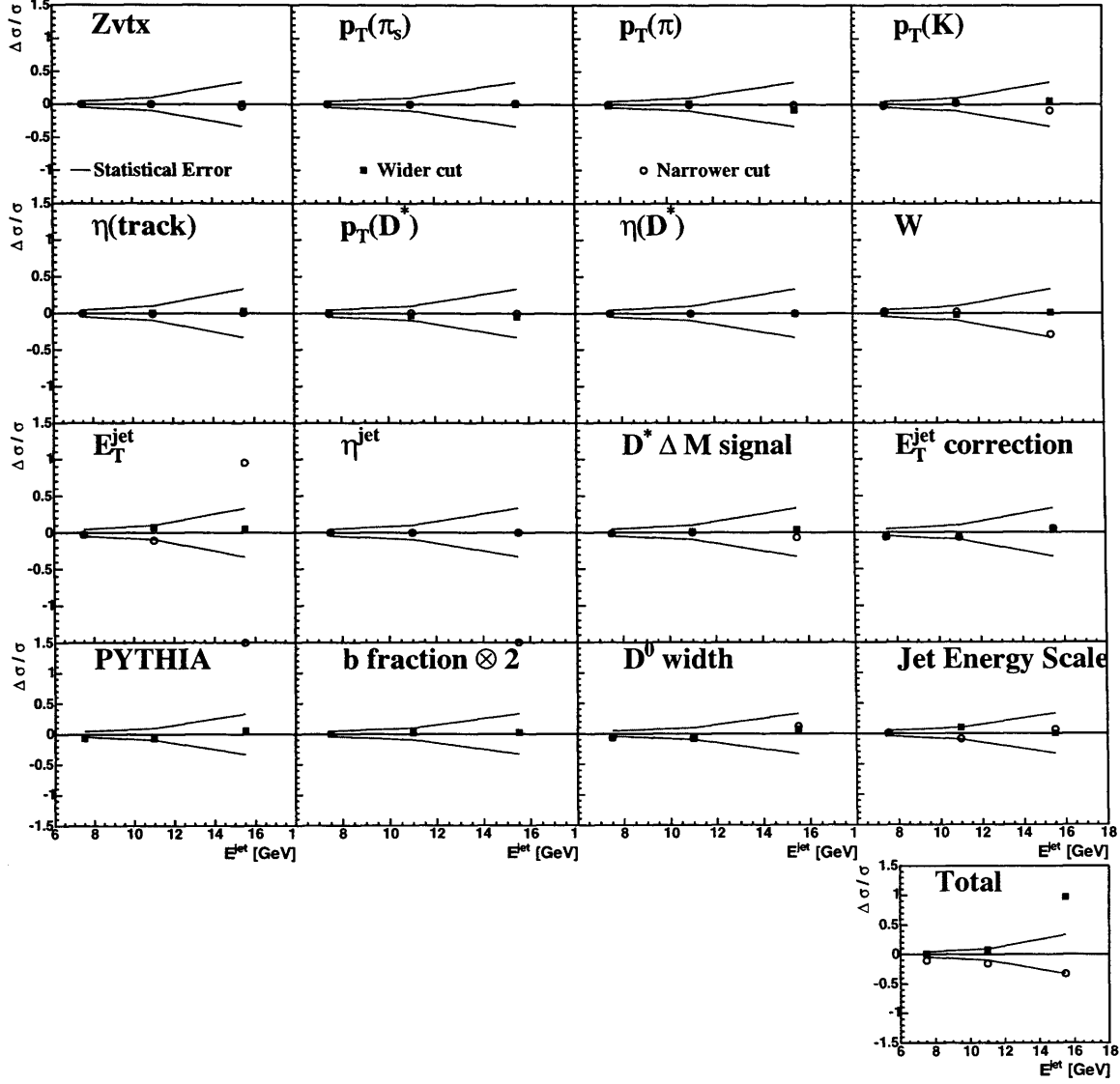
---

In this appendix the systematics are shown for the inclusive cross sections  $d\sigma/dE_T^{jet}$ ,  $d\sigma/d\eta^{jet}$  for both tagged and untagged  $D^*$  jets. Dijet systematics are also shown for  $x_\gamma^{obs}$ ,  $\Delta\Phi^{JJ}$ ,  $P_T^{JJ}$  and  $M^{JJ}$  in both  $x_\gamma^{obs} > 0.75$  (direct-enriched) and  $x_\gamma^{obs} < 0.75$  (resolved-enriched).

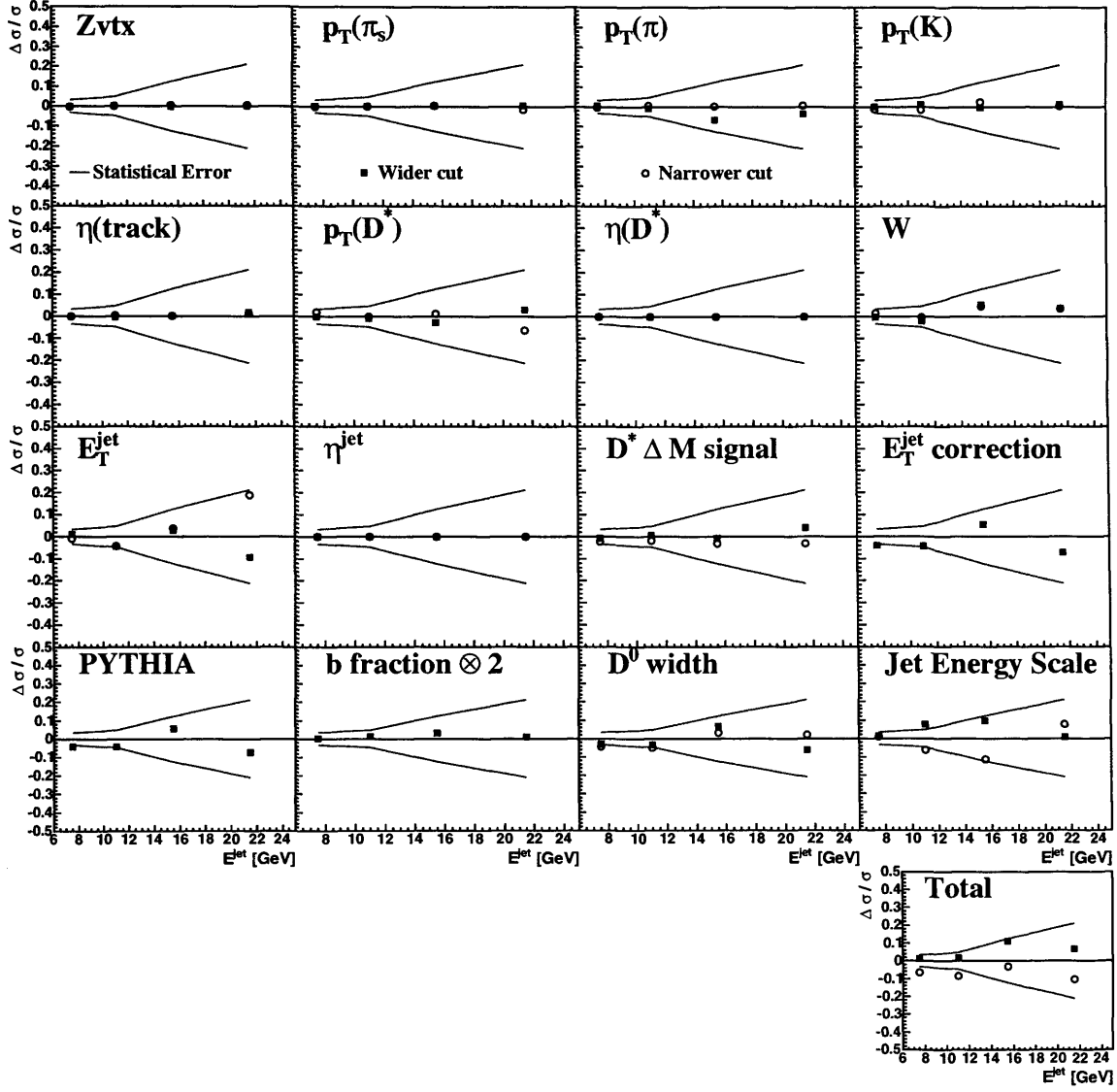
### 17.0.1 $d\sigma/dE_T^{jet}$ Systematics, $-1.5 < \eta^{jet} < 2.4$



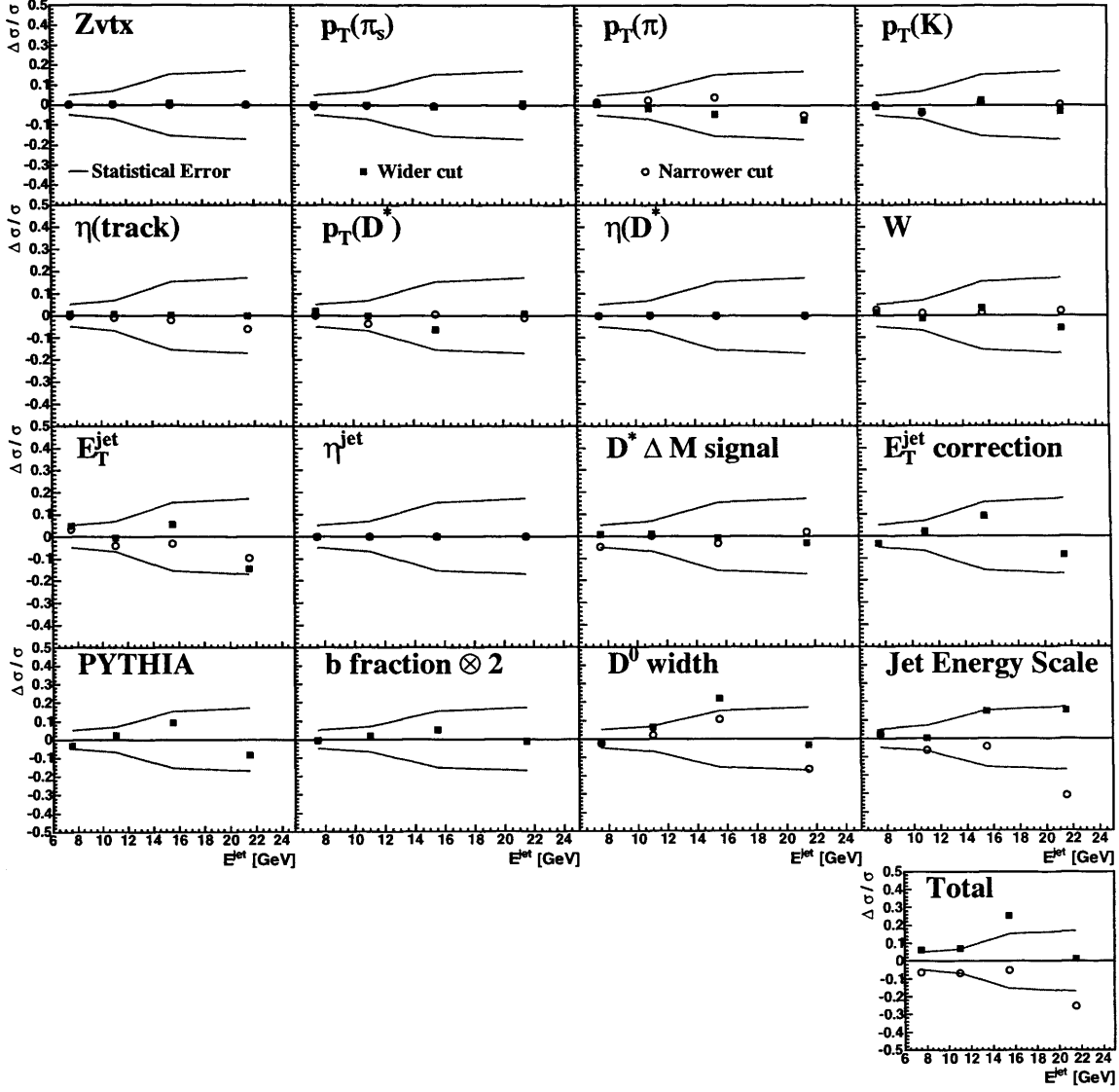
**Figure 17.1** Systematics for each bin of the inclusive charm jet cross section  $d\sigma/dE_T^{jet}$  in the range  $-1.5 < \eta^{jet} < 2.4$  for 1998-2000 data  $78pb^{-1}$ .

17.0.2  $d\sigma/dE_T^{jet}$  systematics,  $-1.5 < \eta^{jet} < -0.5$ 

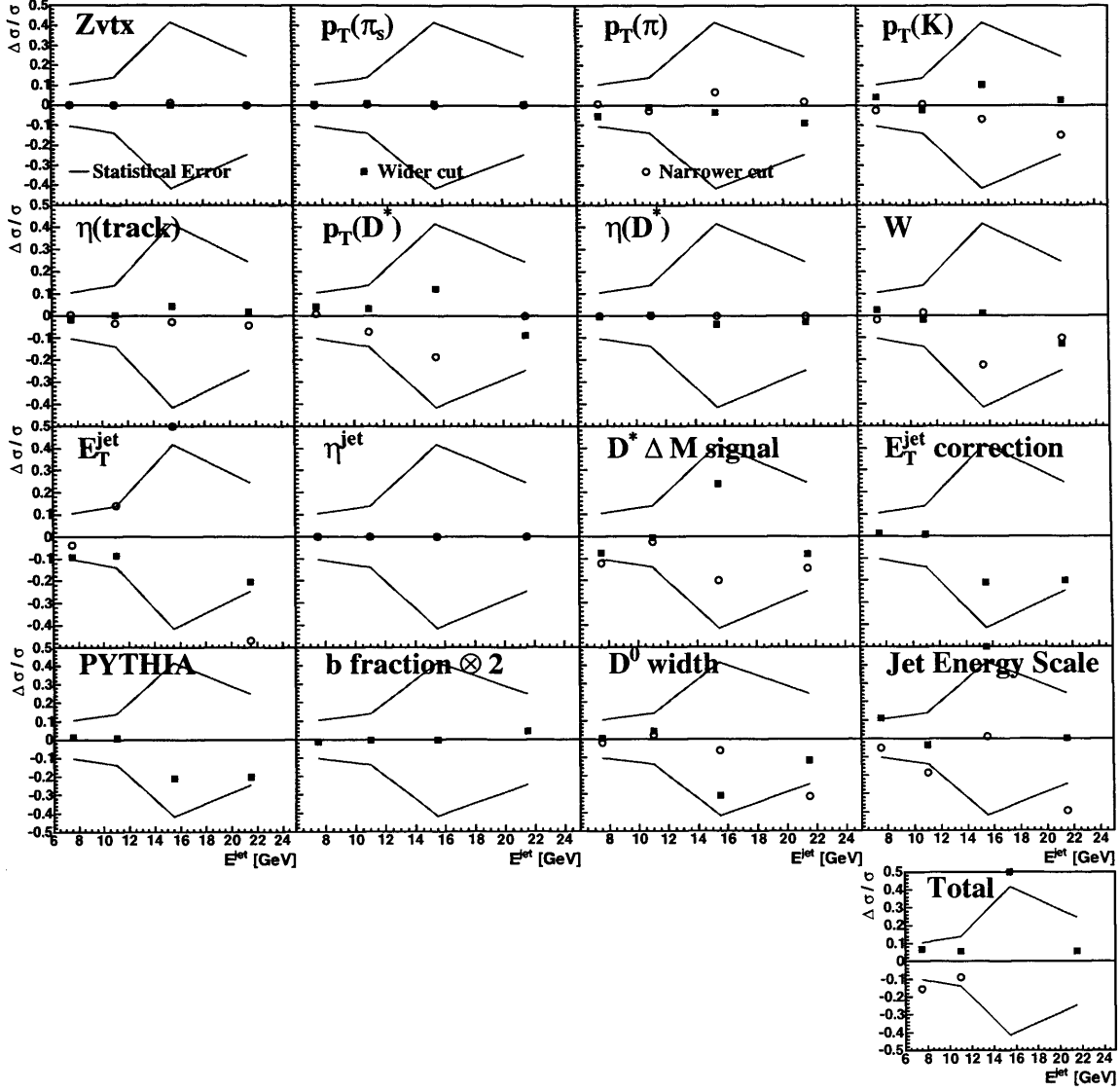
**Figure 17.2** Systematics for each bin of the inclusive charm jet cross section  $d\sigma/dE_T^{jet}$  in the range  $-1.5 < \eta^{jet} < -0.5$  for 1998-2000 data  $78pb^{-1}$ .

17.0.3  $d\sigma/dE_T^{jet}$  systematics,  $-0.5 < \eta^{jet} < 0.5$ 

**Figure 17.3** Systematics for each bin of the inclusive charm jet cross section  $d\sigma/dE_T^{jet}$  in the range  $-0.5 < \eta^{jet} < 0.5$  for 1998-2000 data  $78pb^{-1}$ .

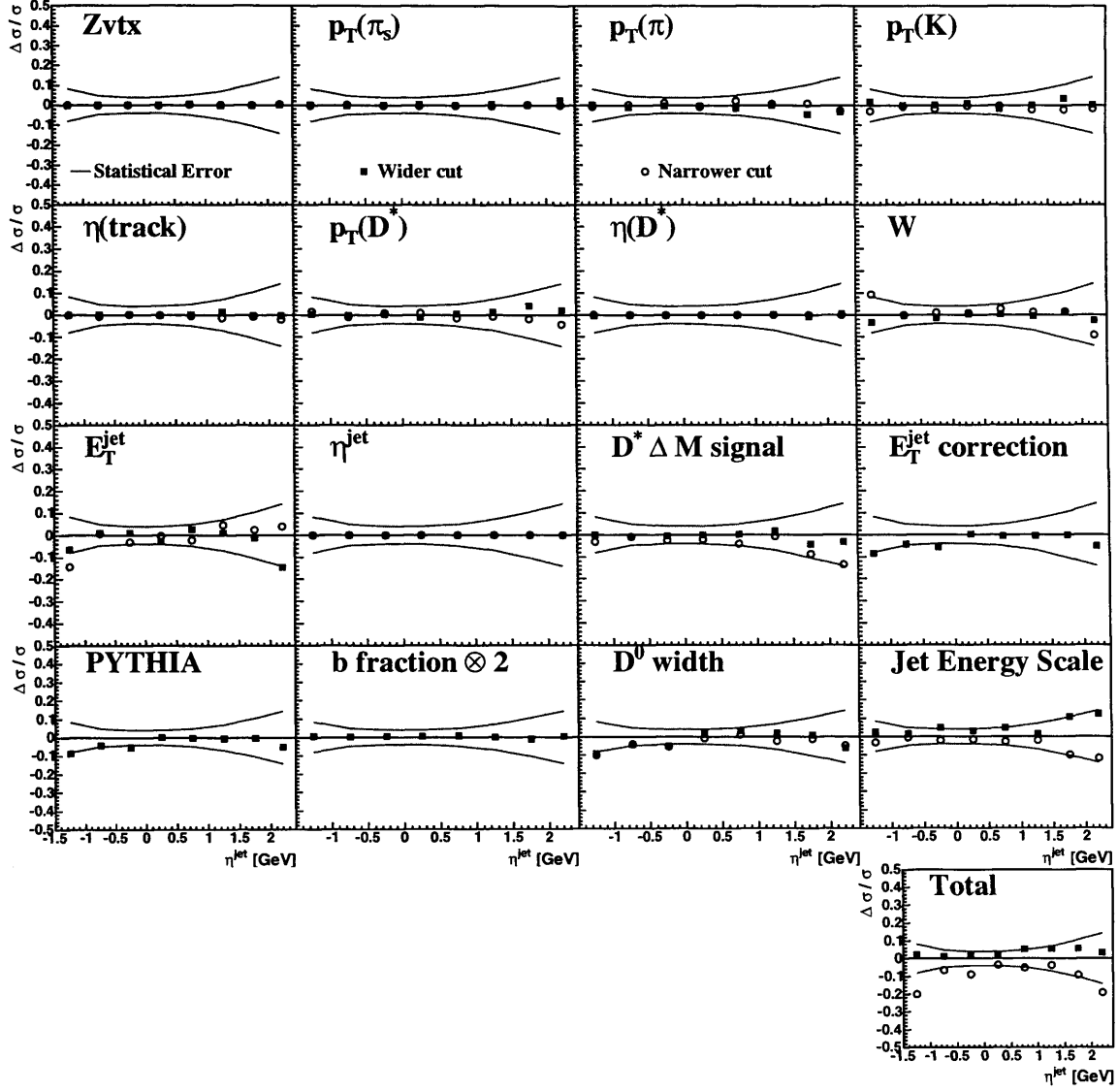
17.0.4  $d\sigma/dE_T^{jet}$  systematics,  $0.5 < \eta^{jet} < 1.5$ 

**Figure 17.4** Systematics for each bin of the inclusive charm jet cross section  $d\sigma/dE_T^{jet}$  in the range  $0.5 < \eta^{jet} < 1.5$  for 1998-2000 data  $78pb^{-1}$ .

17.0.5  $d\sigma/dE_T^{jet}$  systematics,  $1.5 < \eta^{jet} < 2.4$ 

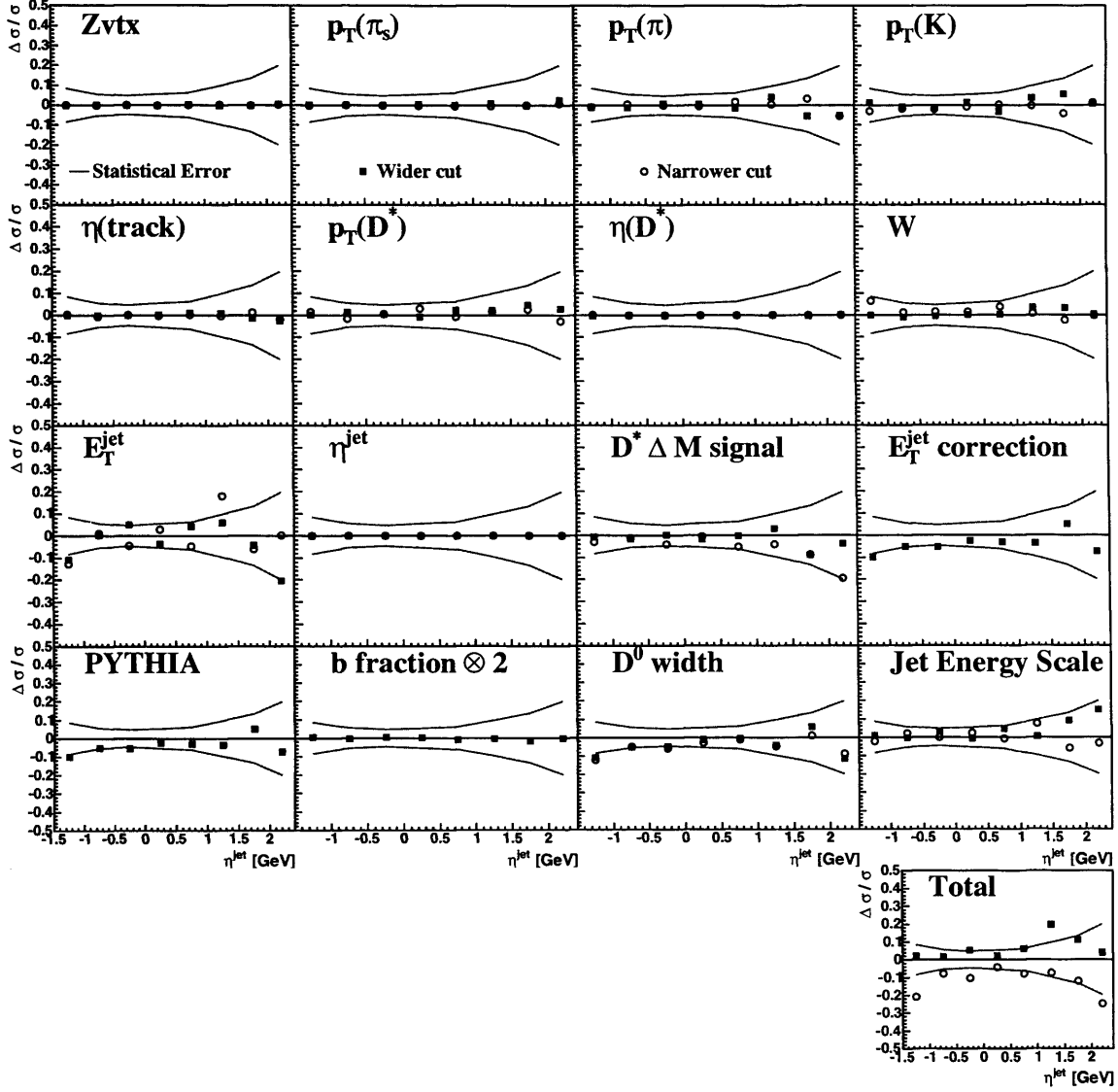
**Figure 17.5** Systematics for each bin of the inclusive charm jet cross section  $d\sigma/dE_T^{jet}$  in the range  $1.5 < \eta^{jet} < 2.4$  for 1998-2000 data  $78pb^{-1}$ .



17.0.6  $d\sigma/d\eta^{jet}$  systematics,  $E_T^{jet} > 6$  GeV

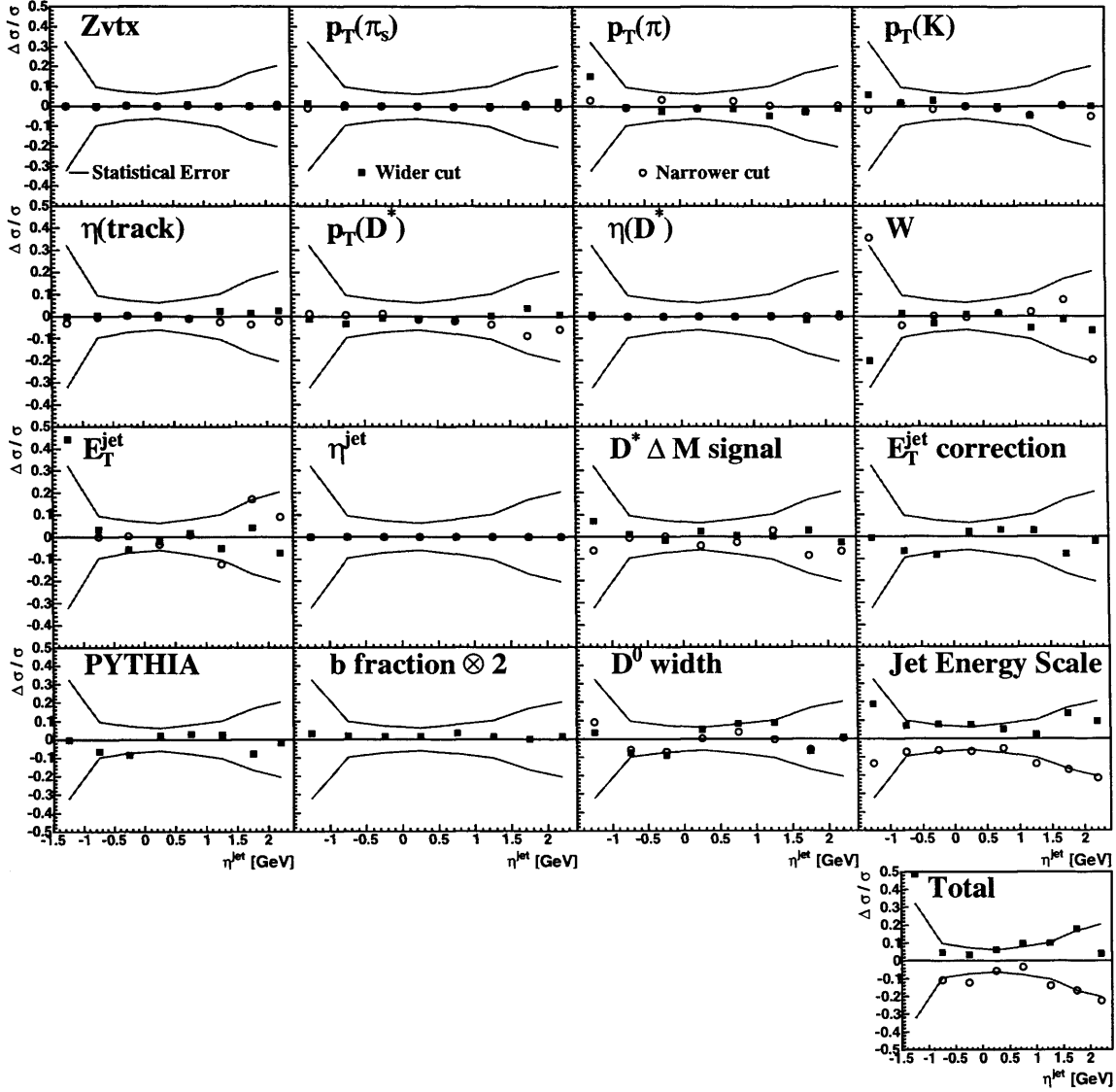
**Figure 17.6** Systematics for each bin of the inclusive charm jet cross section  $d\sigma/d\eta^{jet}$  in the range  $E_T^{jet} > 6$  GeV for 1998-2000 data  $78pb^{-1}$ .

### 17.0.7 $d\sigma/d\eta^{jet}$ systematics, $6 < E_T^{jet} < 9$ GeV



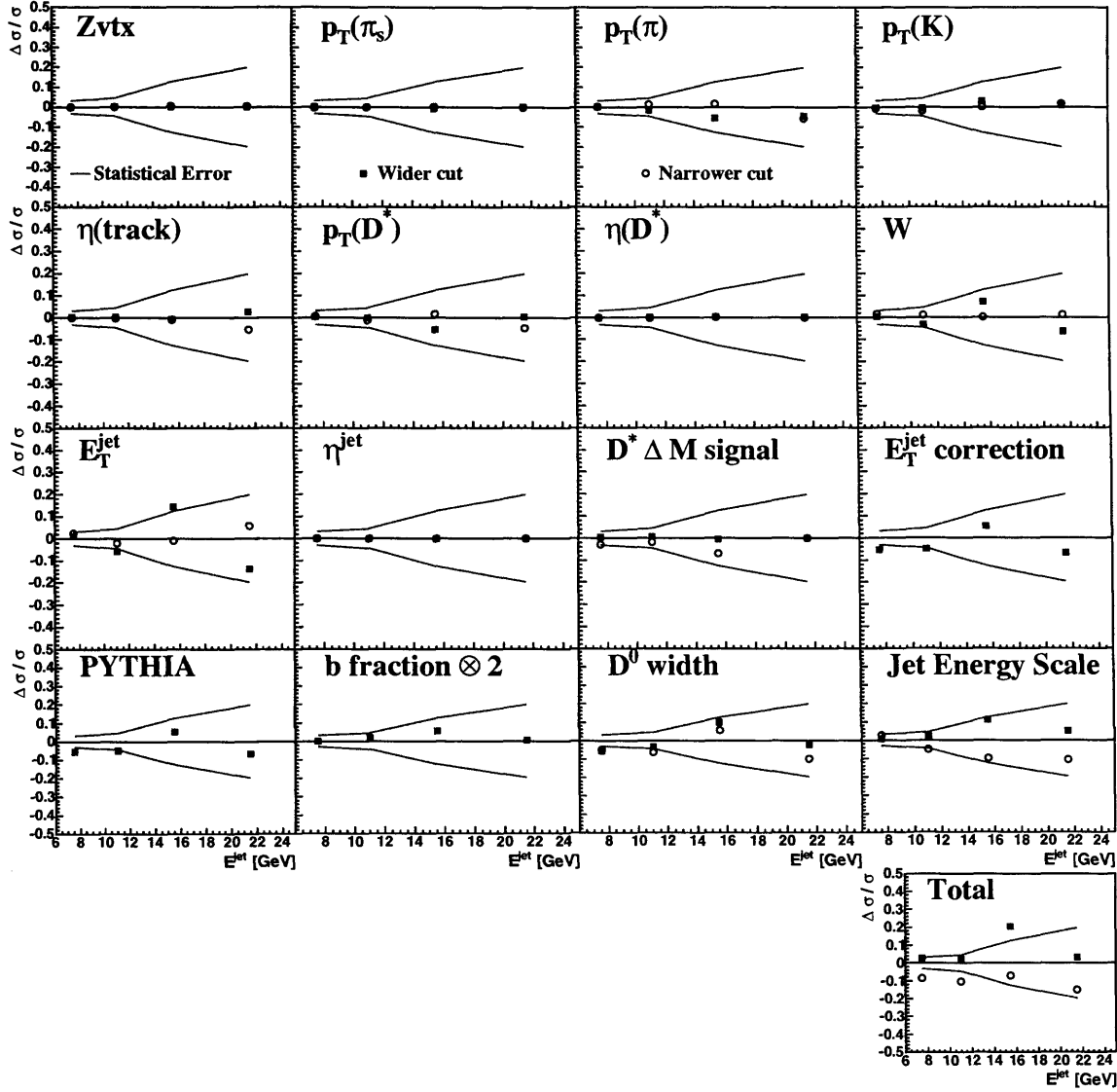
**Figure 17.7** Systematics for each bin of the inclusive charm jet cross section  $d\sigma/d\eta^{jet}$  in the range  $6 < E_T^{jet} < 9$  GeV for 1998-2000 data  $78\text{pb}^{-1}$ .

### 17.0.8 $d\sigma/d\eta^{jet}$ systematics, $E_T^{jet} > 9$ GeV

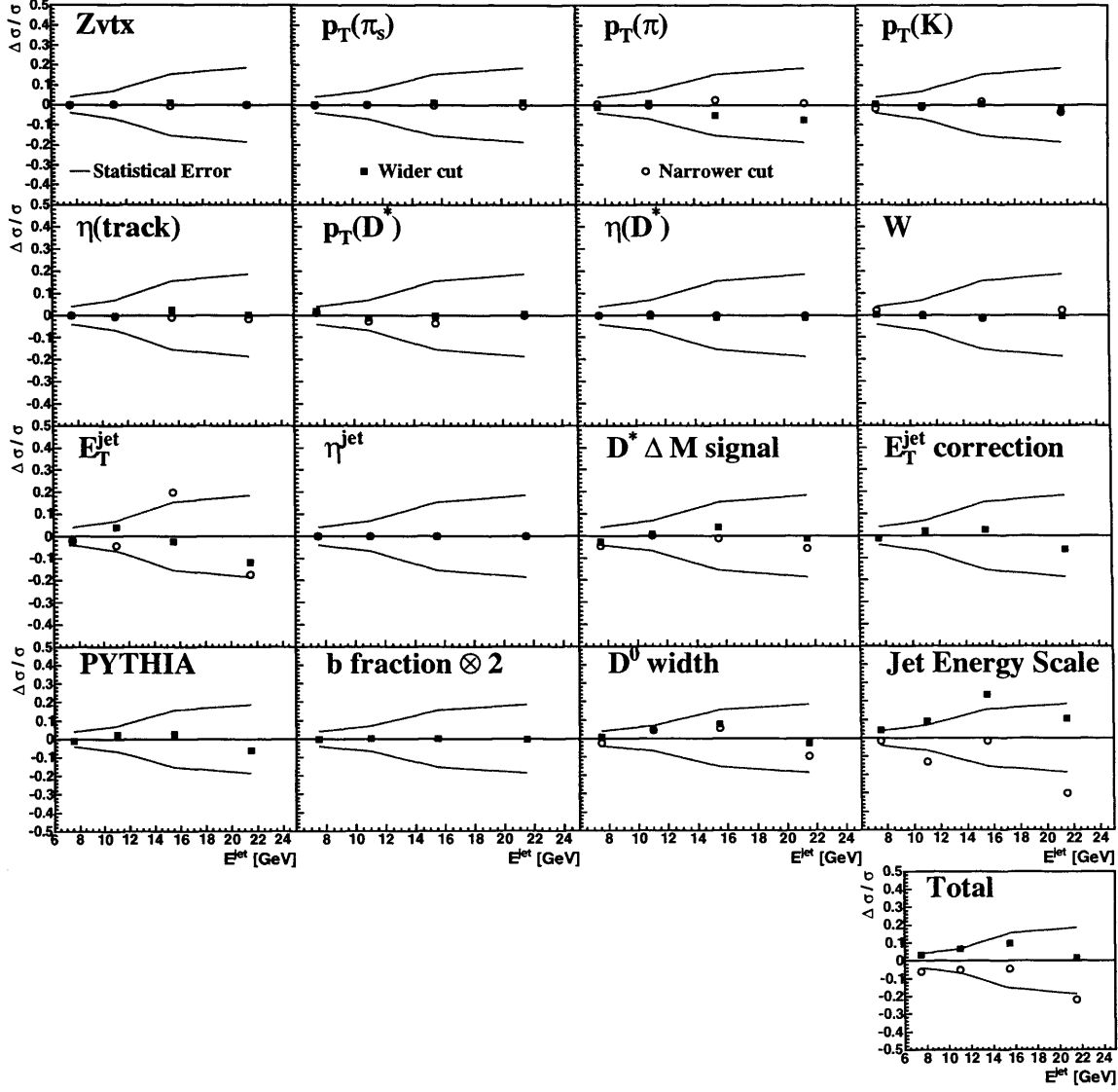


**Figure 17.8** Systematics for each bin of the inclusive charm jet cross section  $d\sigma/d\eta^{jet}$  in the range  $E_T^{jet} > 9$  GeV for 1998-2000 data  $78pb^{-1}$ .

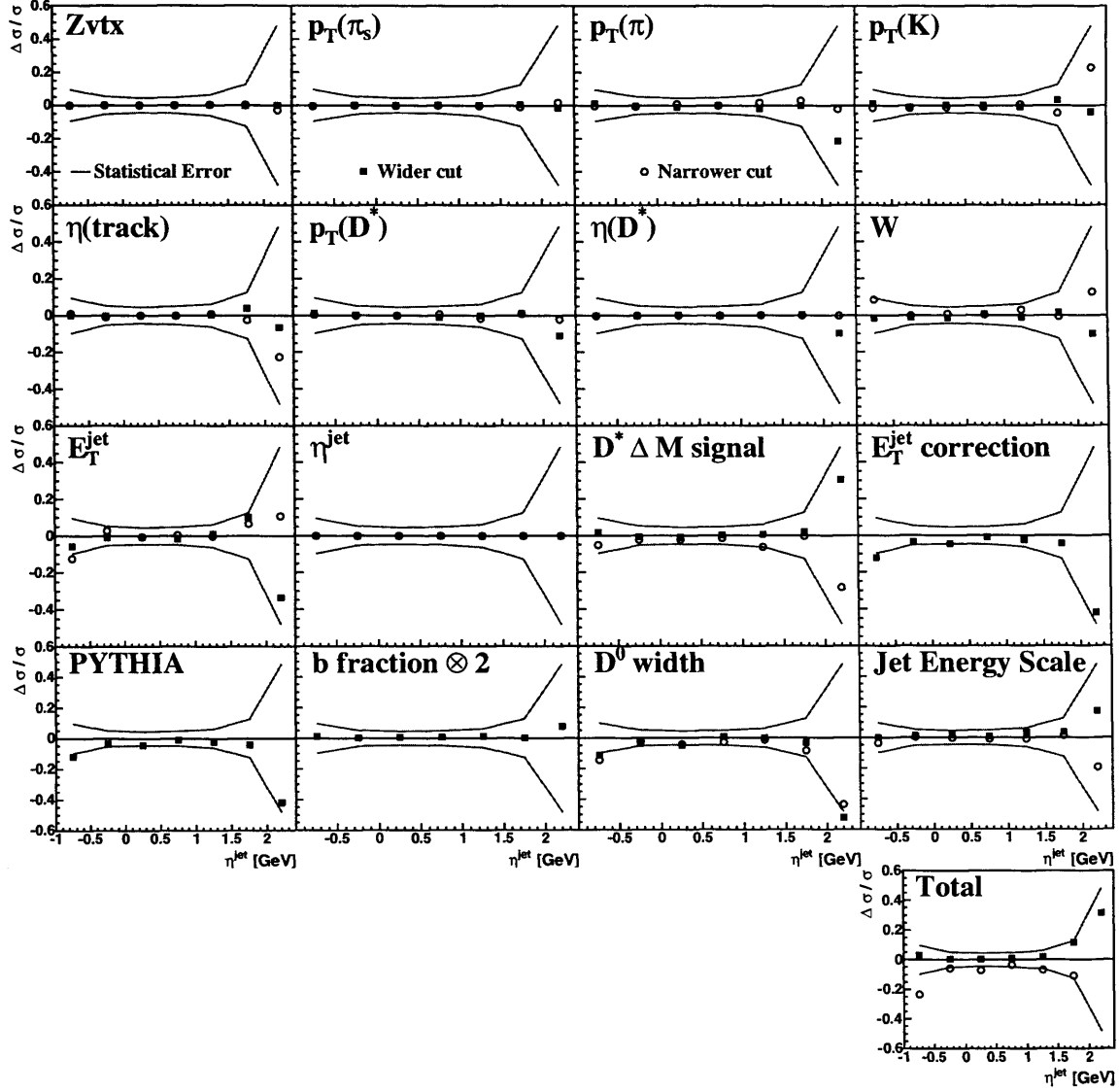
### 17.0.9 $d\sigma/dE_T^{jet}$ systematics, $-1.5 < \eta^{jet} < 2.4$ tagged $D^*$ jets



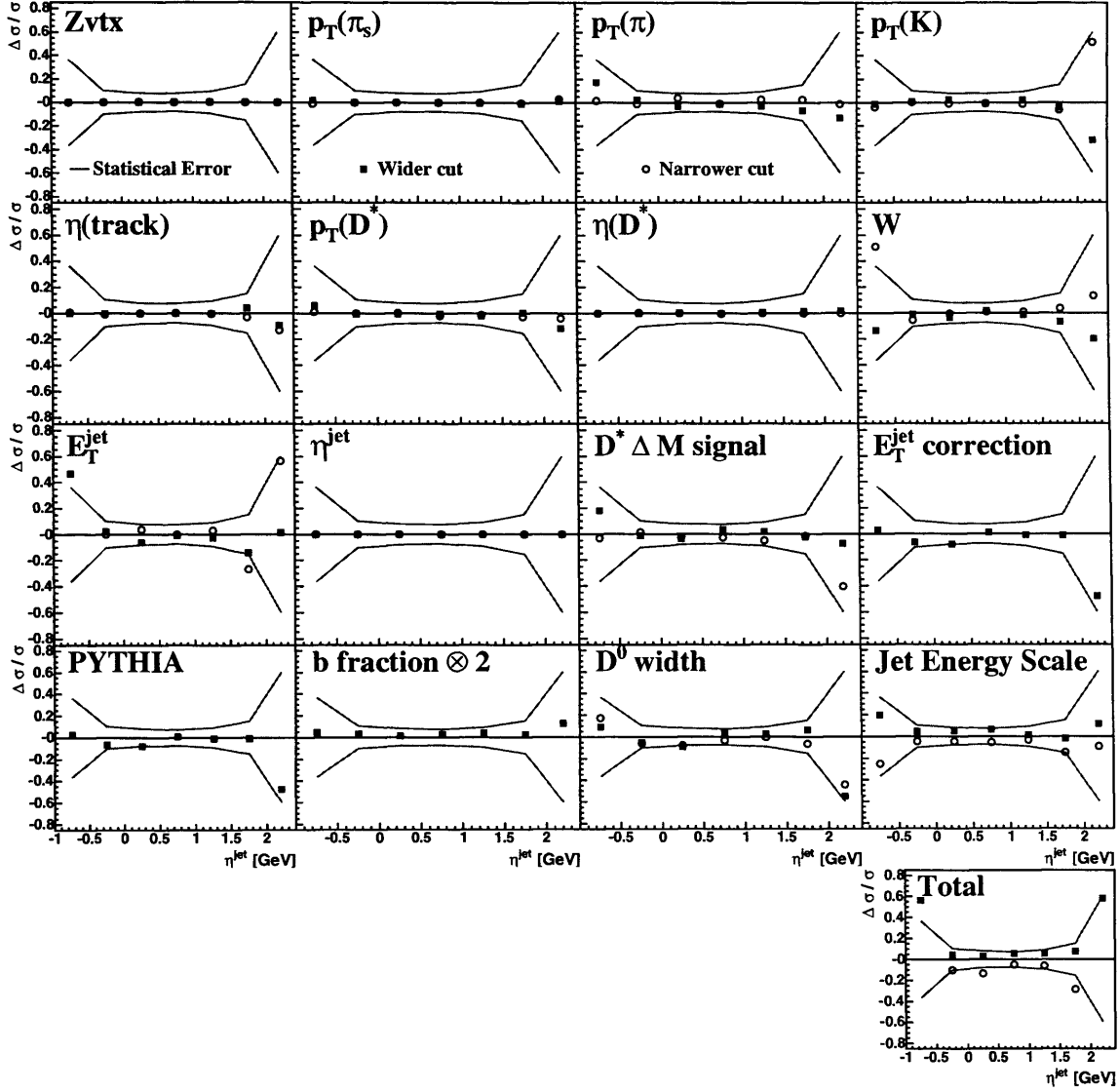
**Figure 17.9** Systematics for each bin of the tagged  $D^*$  jet cross section  $d\sigma/dE_T^{jet}$  in the range  $-1.5 < \eta^{jet} < 2.4$  for 1998-2000 data  $78pb^{-1}$ .

**17.0.10  $d\sigma/d\eta^{jet}$  systematics,  $E_T^{jet} > 6$  GeV untagged  $D^*$  jets**


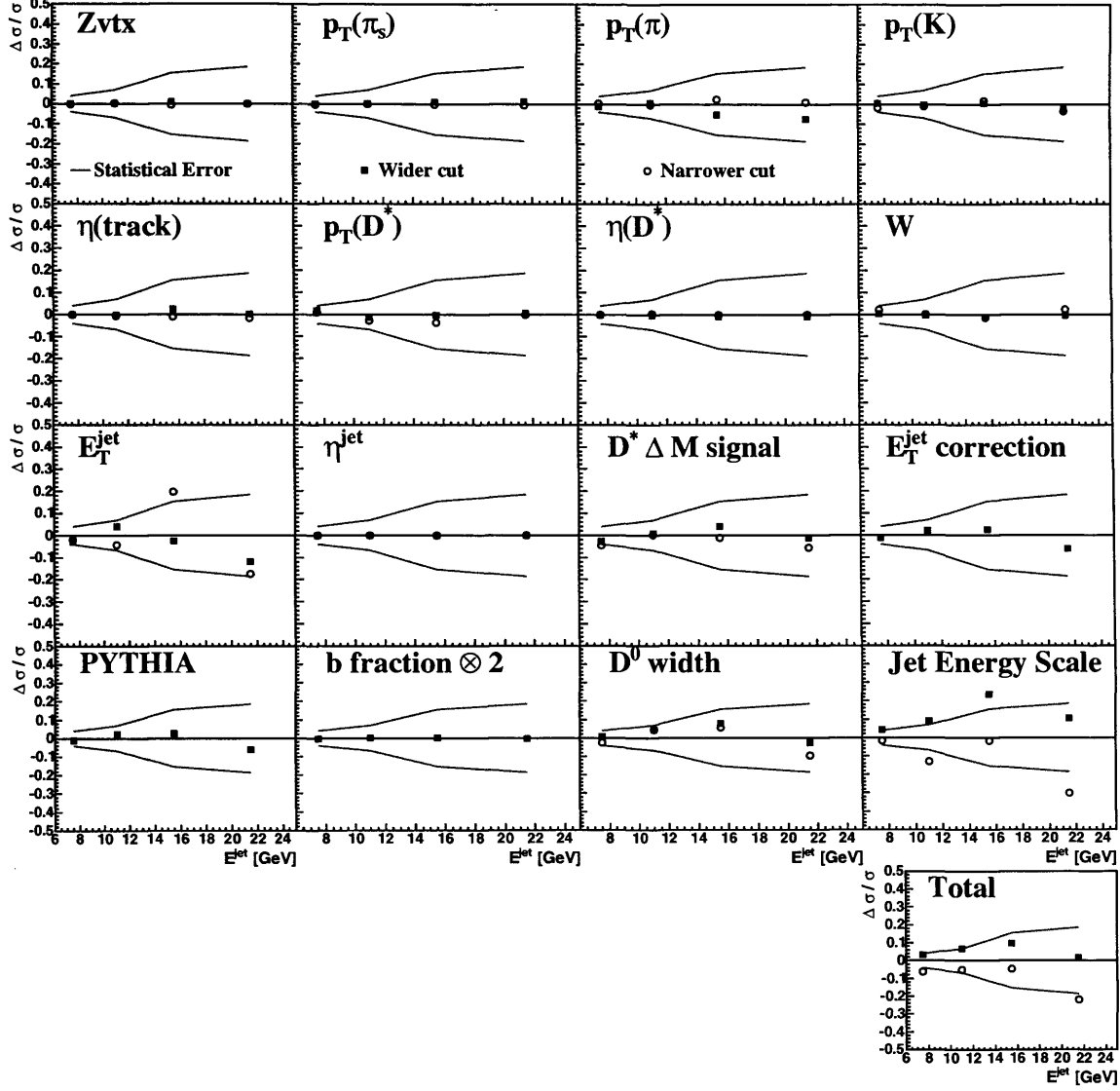
**Figure 17.10** Systematics for each bin of the untagged  $D^*$  jet cross section  $d\sigma/d\eta^{jet}$  in the range  $E_T^{jet} > 6$  GeV for 1998-2000 data  $78pb^{-1}$ .

**17.0.11  $d\sigma/d\eta^{jet}$  systematics,  $6 < E_T^{jet} < 9$  GeV tagged  $D^*$  jets**


**Figure 17.11** Systematics for each bin of the untagged  $D^*$  jet cross section  $d\sigma/d\eta^{jet}$  in the range  $6 < E_T^{jet} < 9$  GeV for 1998-2000 data  $78pb^{-1}$ .

17.0.12  $d\sigma/d\eta^{jet}$  systematics,  $E_T^{jet} > 9$  GeV tagged  $D^*$  jets

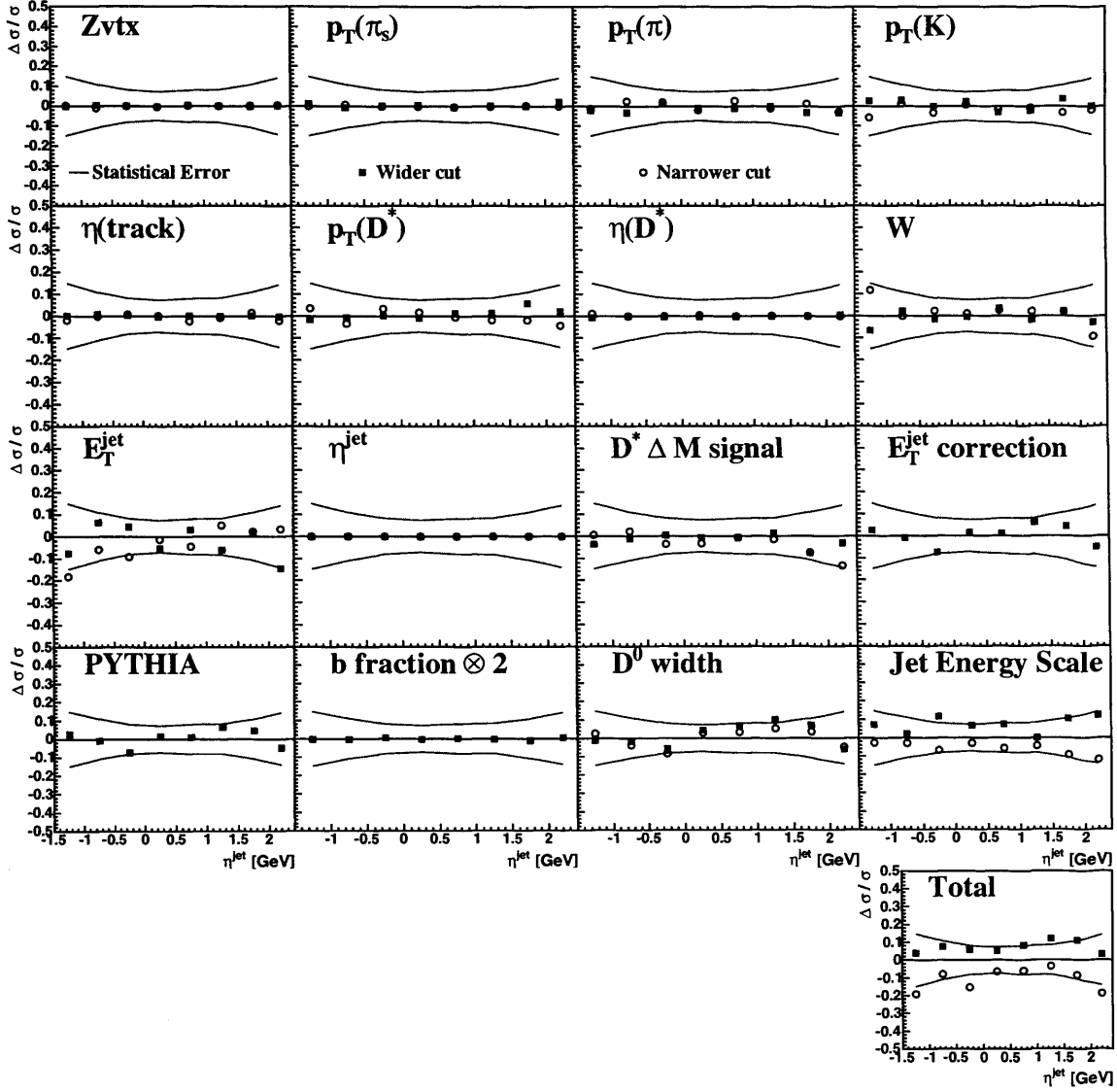
**Figure 17.12** Systematics for each bin of the untagged  $D^*$  jet cross section  $d\sigma/d\eta^{jet}$  in the range  $E_T^{jet} > 9$  GeV for 1998-2000 data  $78pb^{-1}$ .

**17.0.13  $d\sigma/dE_T^{jet}$  systematics,  $-1.5 < \eta^{jet} < 2.4$  untagged  $D^*$  jets**


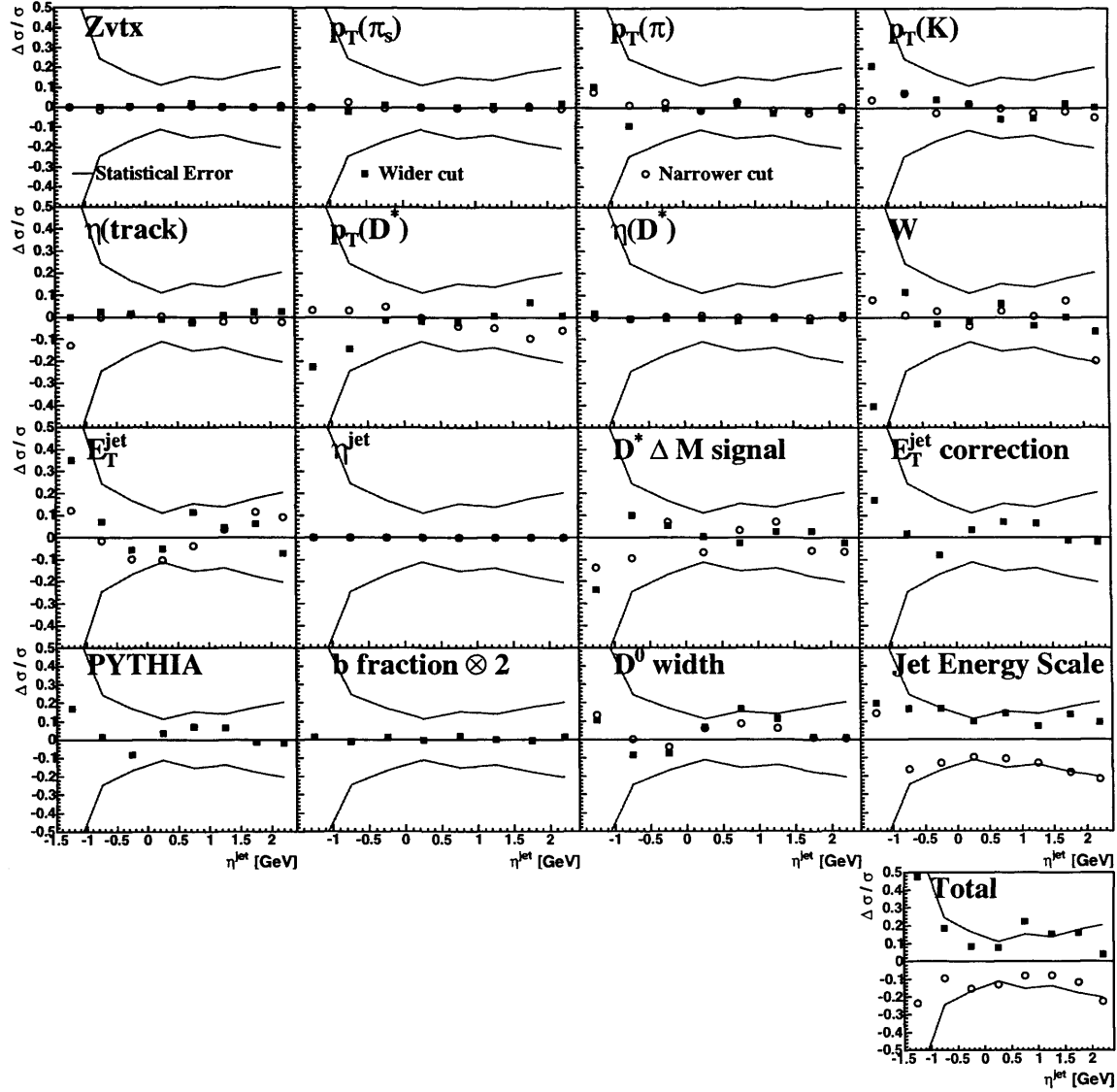
**Figure 17.13** Systematics for each bin of the untagged  $D^*$  jet cross section  $d\sigma/dE_T^{jet}$  in the range  $-1.5 < \eta^{jet} < 2.4$  for 1998-2000 data  $78pb^{-1}$ .



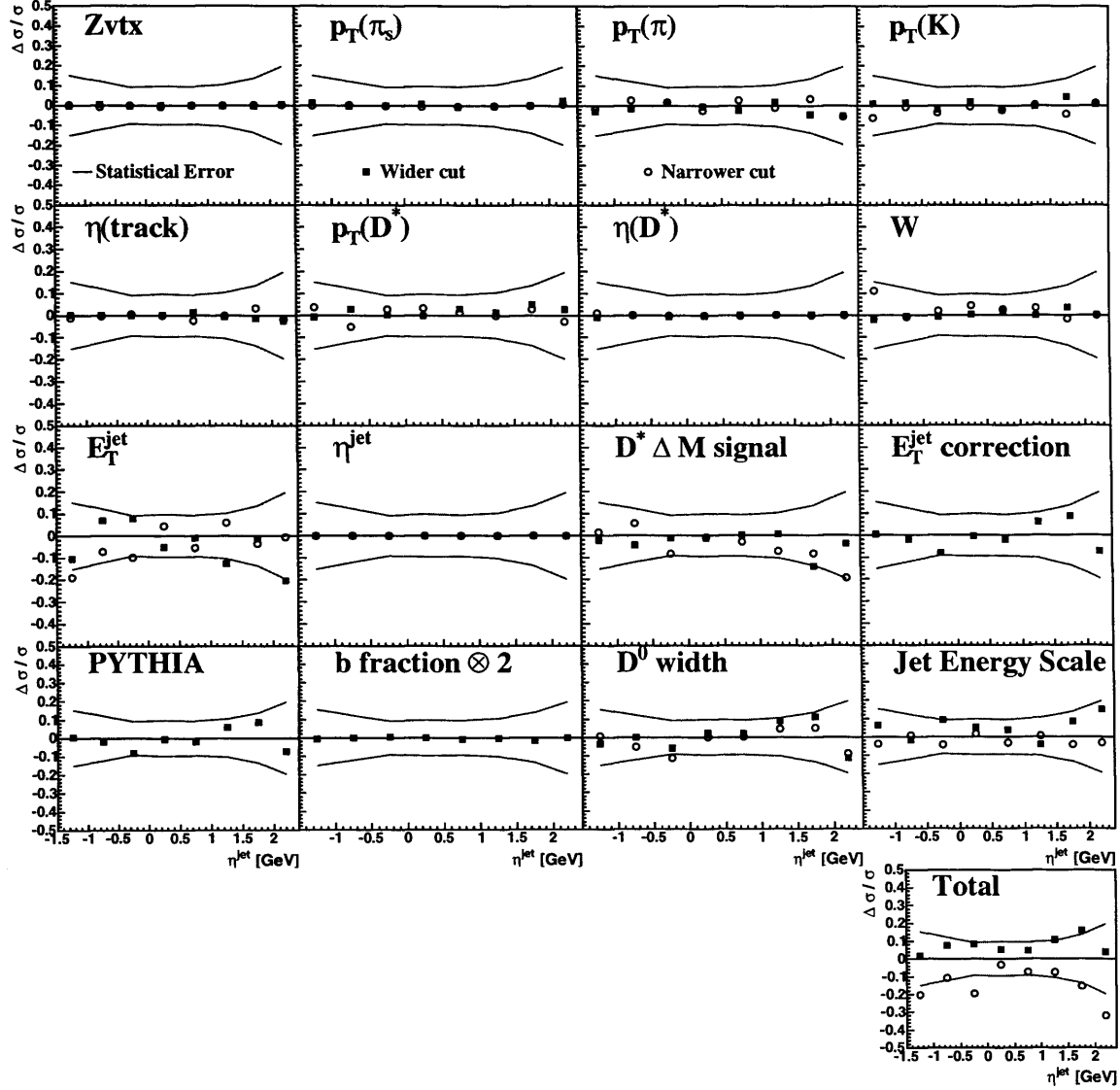
### 17.0.14 $d\sigma/d\eta^{jet}$ systematics, $E_T^{jet} > 6$ GeV untagged $D^*$ jets



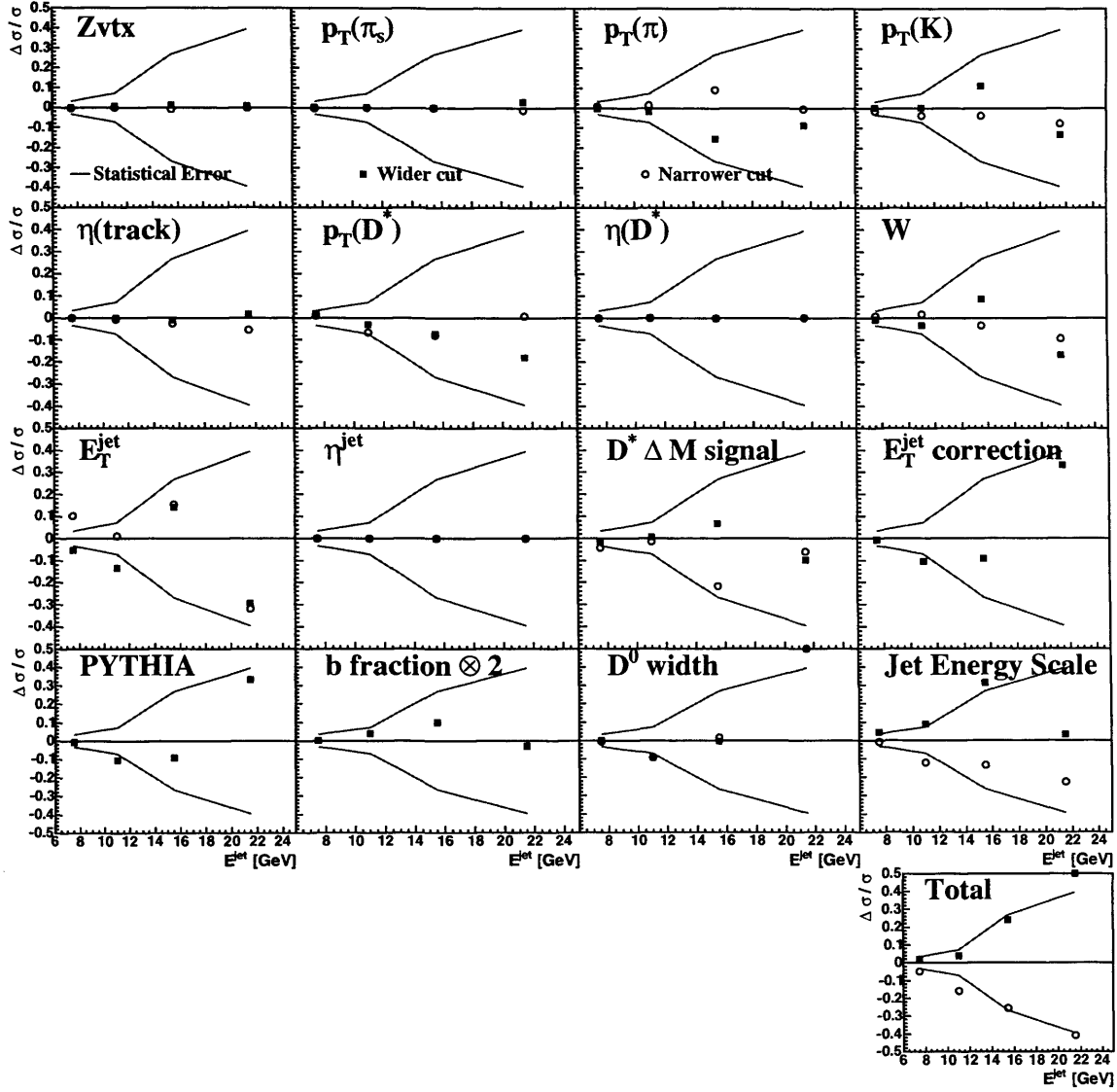
**Figure 17.14** Systematics for each bin of the untagged  $D^*$  jet cross section  $d\sigma/d\eta^{jet}$  in the range  $E_T^{jet} > 6$  GeV for 1998-2000 data  $78pb^{-1}$ .

17.0.15  $d\sigma/d\eta^{jet}$  systematics,  $6 < E_T^{jet} < 9$  GeV untagged  $D^*$  jets


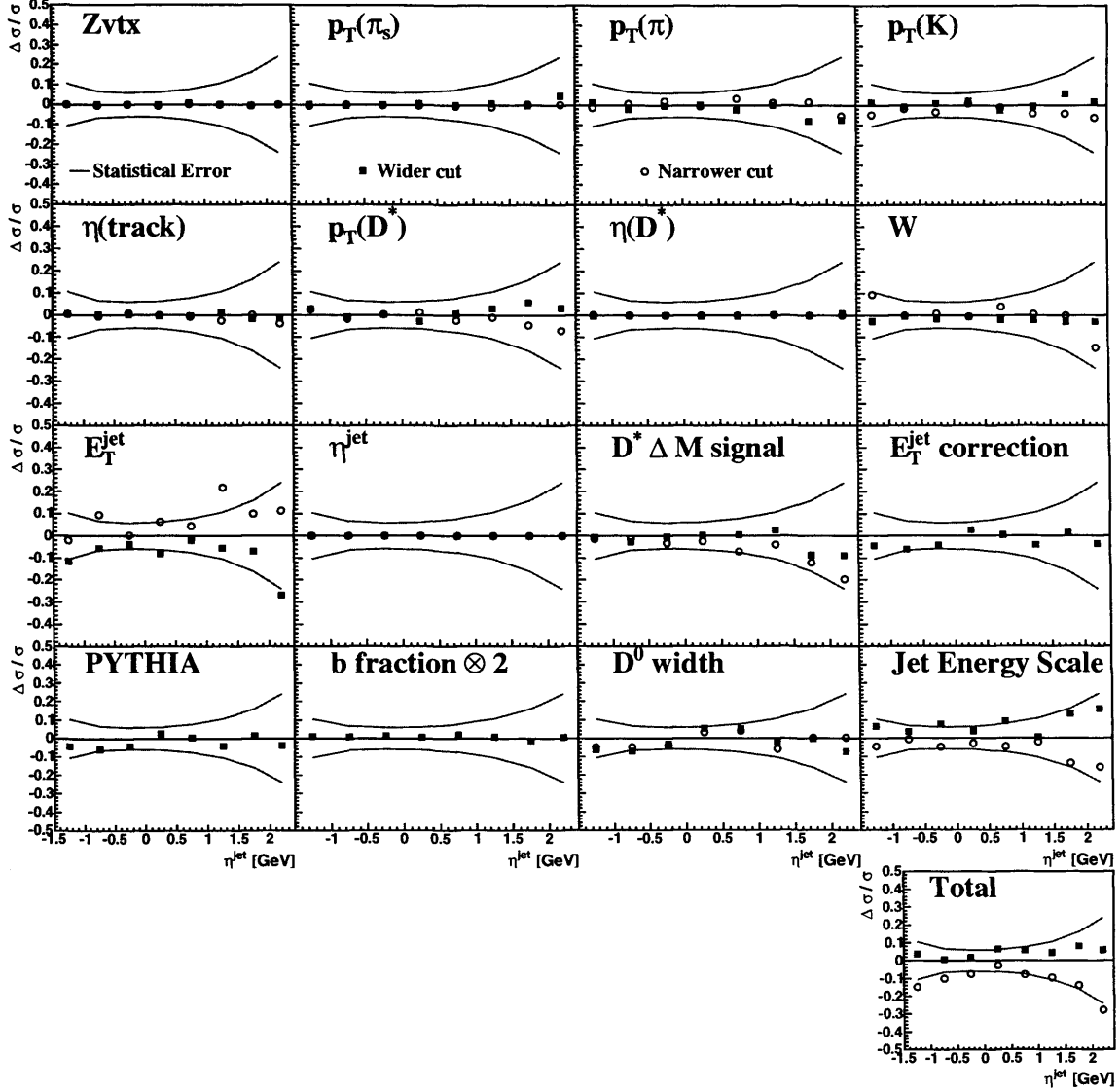
**Figure 17.15** Systematics for each bin of the untagged  $D^*$  jet cross section  $d\sigma/d\eta^{jet}$  in the range  $6 < E_T^{jet} < 9$  GeV for 1998-2000 data  $78pb^{-1}$ .

17.0.16  $d\sigma/d\eta^{jet}$  systematics,  $E_T^{jet} > 9$  GeV untagged  $D^*$  jets


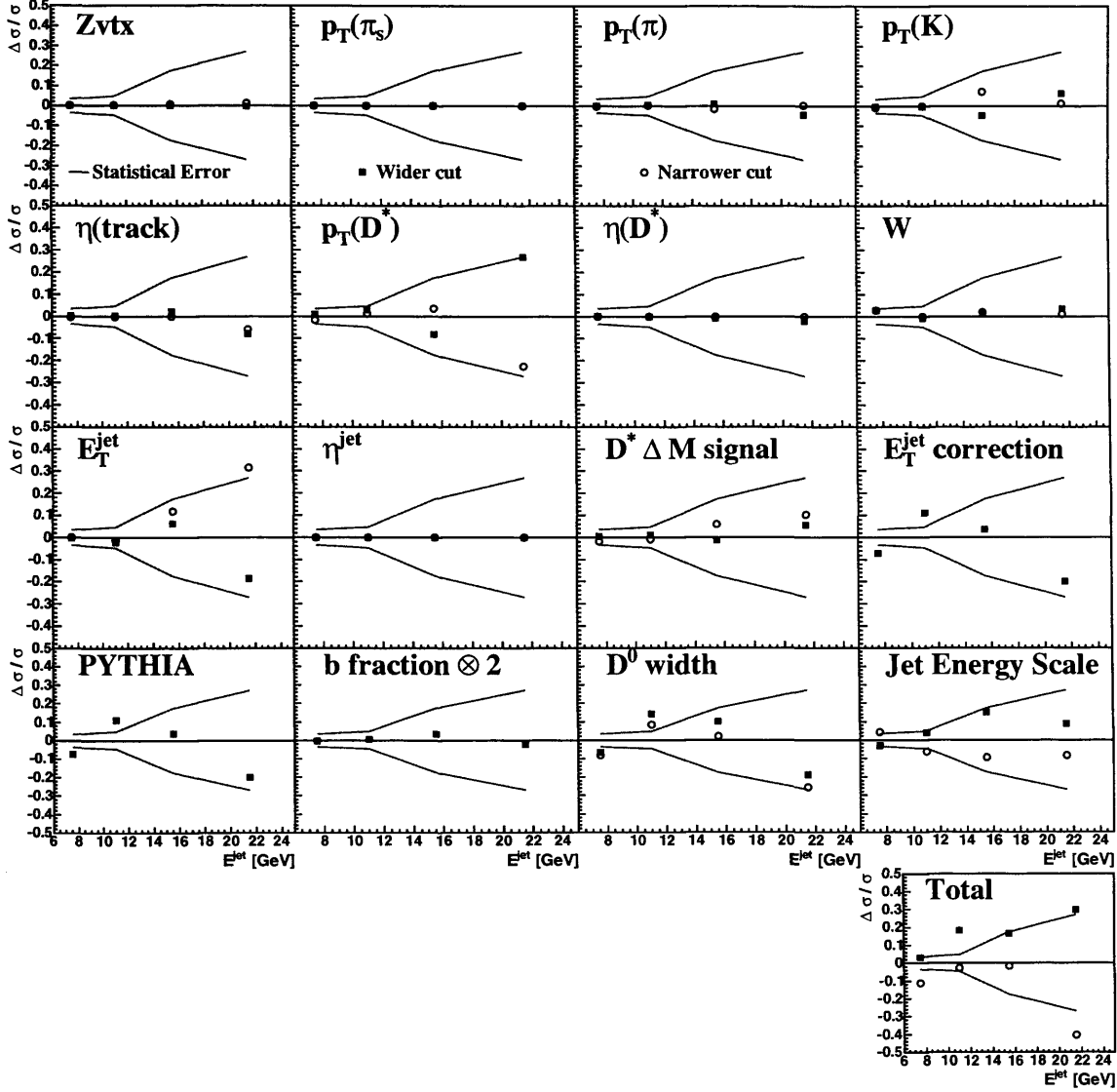
**Figure 17.16** Systematics for each bin of the tagged  $D^*$  jet cross section  $d\sigma/d\eta^{jet}$  in the range  $E_T^{jet} > 9$  GeV for 1998-2000 data  $78\text{pb}^{-1}$ .

17.0.17  $d\sigma/dE_T^{jet}$  systematics,  $3.0 < p_T^{D^*} < 5.0$  GeV


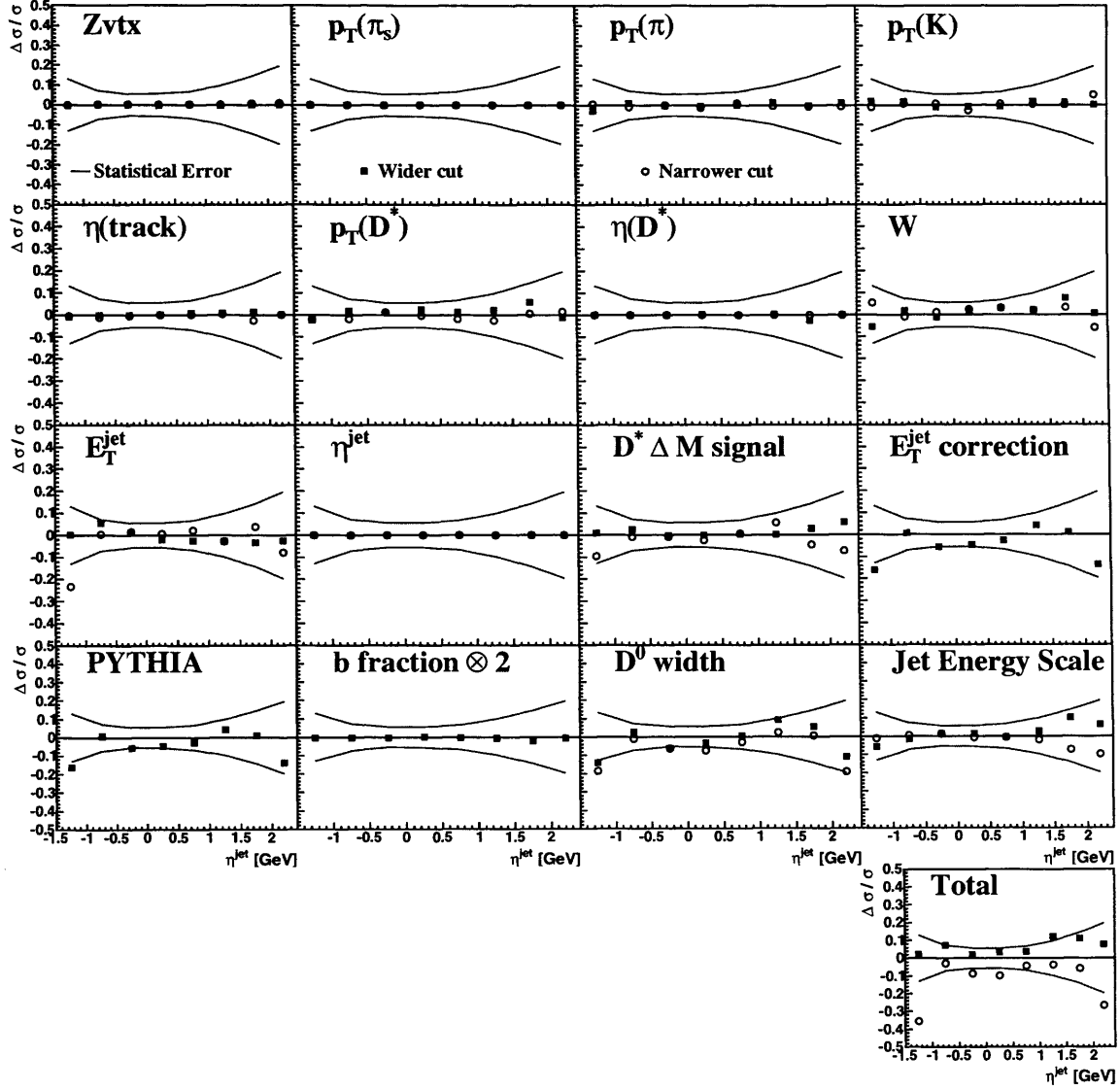
**Figure 17.17** Systematics for each bin of the inclusive charm jet cross section  $d\sigma/dE_T^{jet}$  in the range  $3.0 < p_T^{D^*} < 5.0$  GeV for 1998-2000 data  $78pb^{-1}$ .

17.0.18  $d\sigma/d\eta^{jet}$  systematics,  $3.0 < p_T^{D^*} < 5.0$  GeV


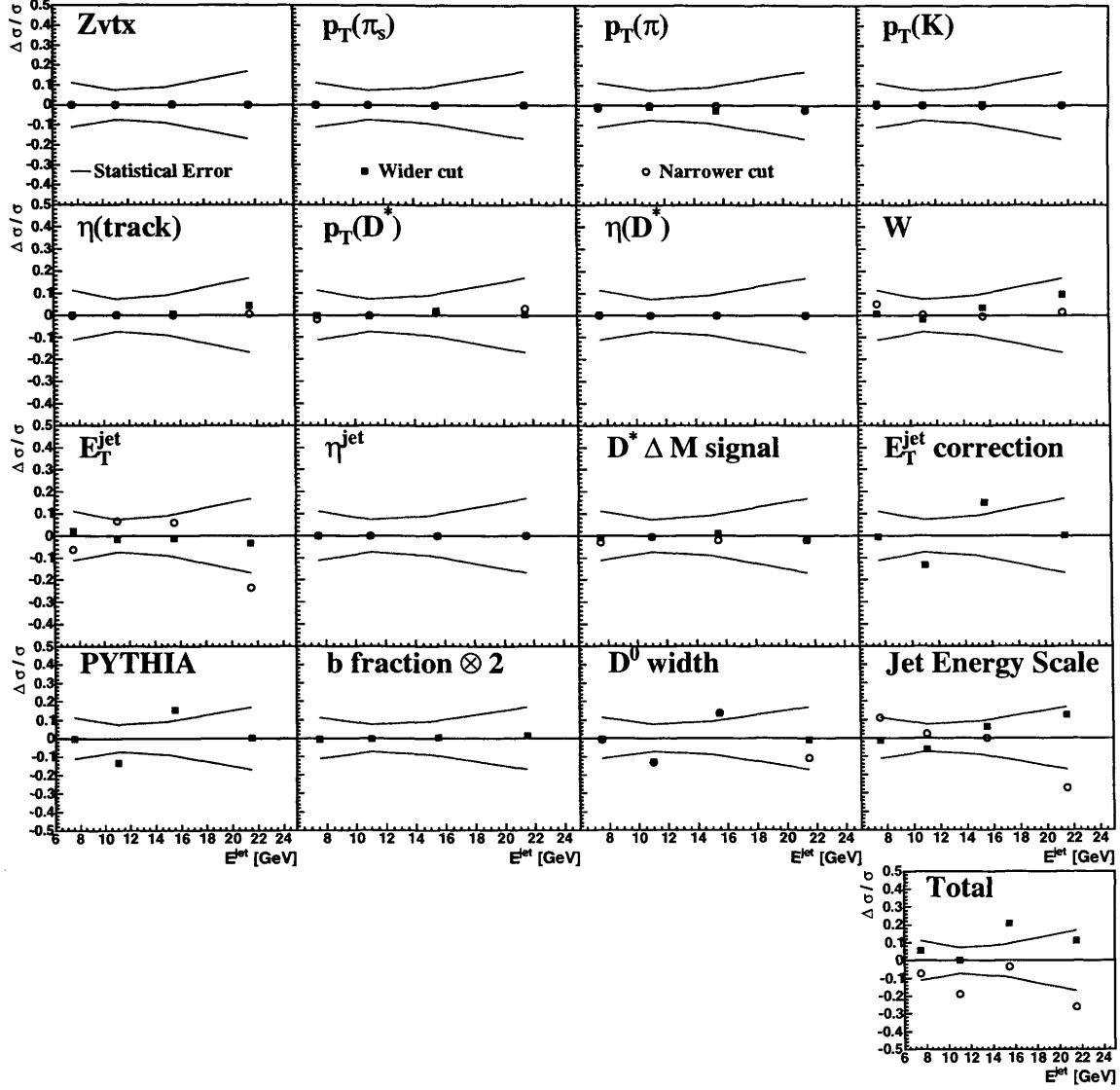
**Figure 17.18** Systematics for each bin of the inclusive charm jet cross section  $d\sigma/d\eta^{jet}$  in the range  $3.0 < p_T^{D^*} < 5.0$  GeV for 1998-2000 data  $78pb^{-1}$ .

**17.0.19  $d\sigma/dE_T^{jet}$  systematics,  $5.0 < p_T^{D^*} < 8.0$  GeV**


**Figure 17.19** Systematics for each bin of the inclusive charm jet cross section  $d\sigma/dE_T^{jet}$  in the range  $5.0 < p_T^{D^*} < 8.0$  GeV for 1998-2000 data  $78pb^{-1}$ .

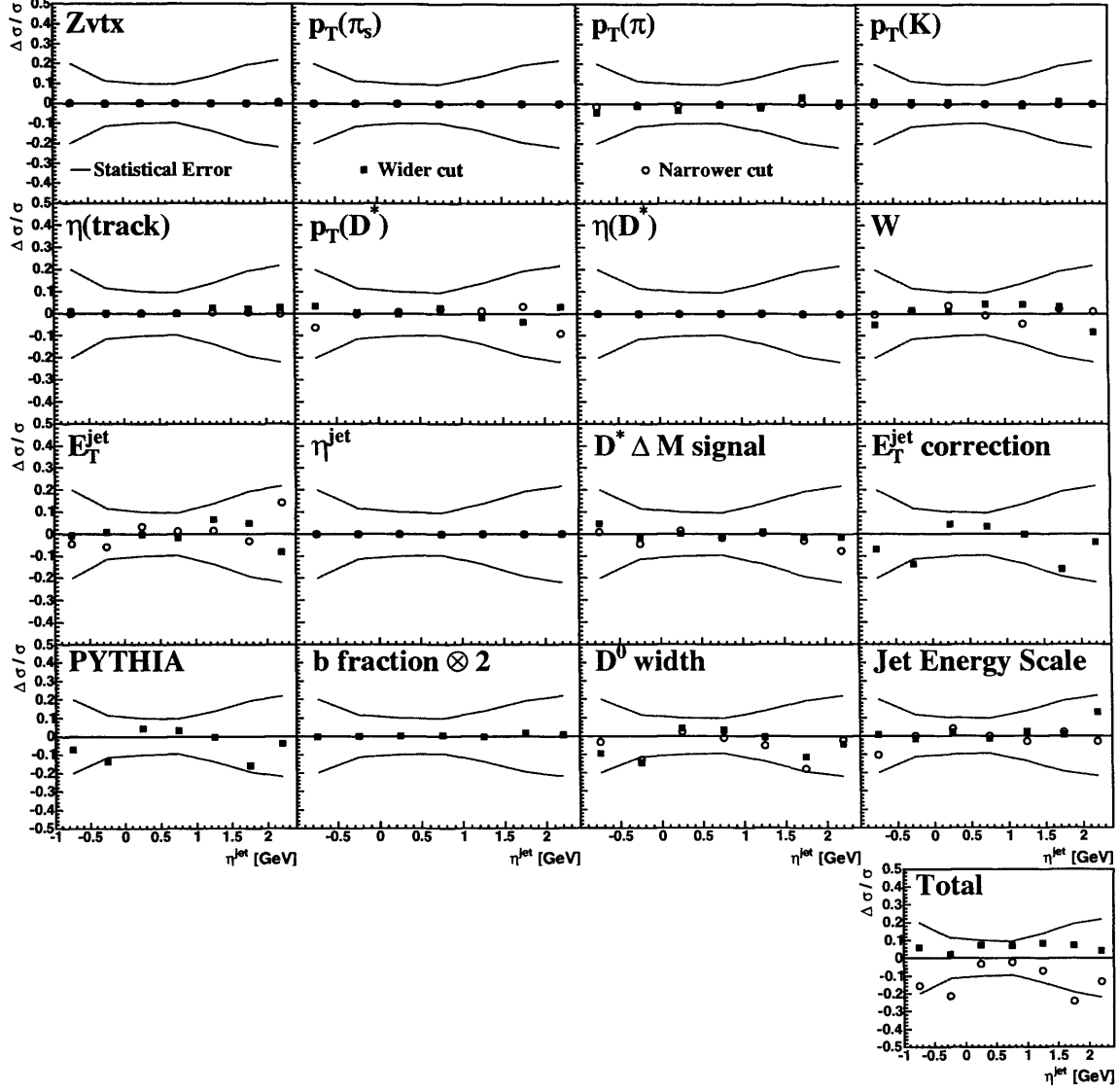
**17.0.20  $d\sigma/d\eta^{jet}$  systematics,  $5.0 < p_T^{D^*} < 8.0$  GeV**


**Figure 17.20** Systematics for each bin of the inclusive charm jet cross section  $d\sigma/d\eta^{jet}$  in the range  $5.0 < P_T^{D^*} < 8.0$  GeV for 1998-2000 data  $78pb^{-1}$ .

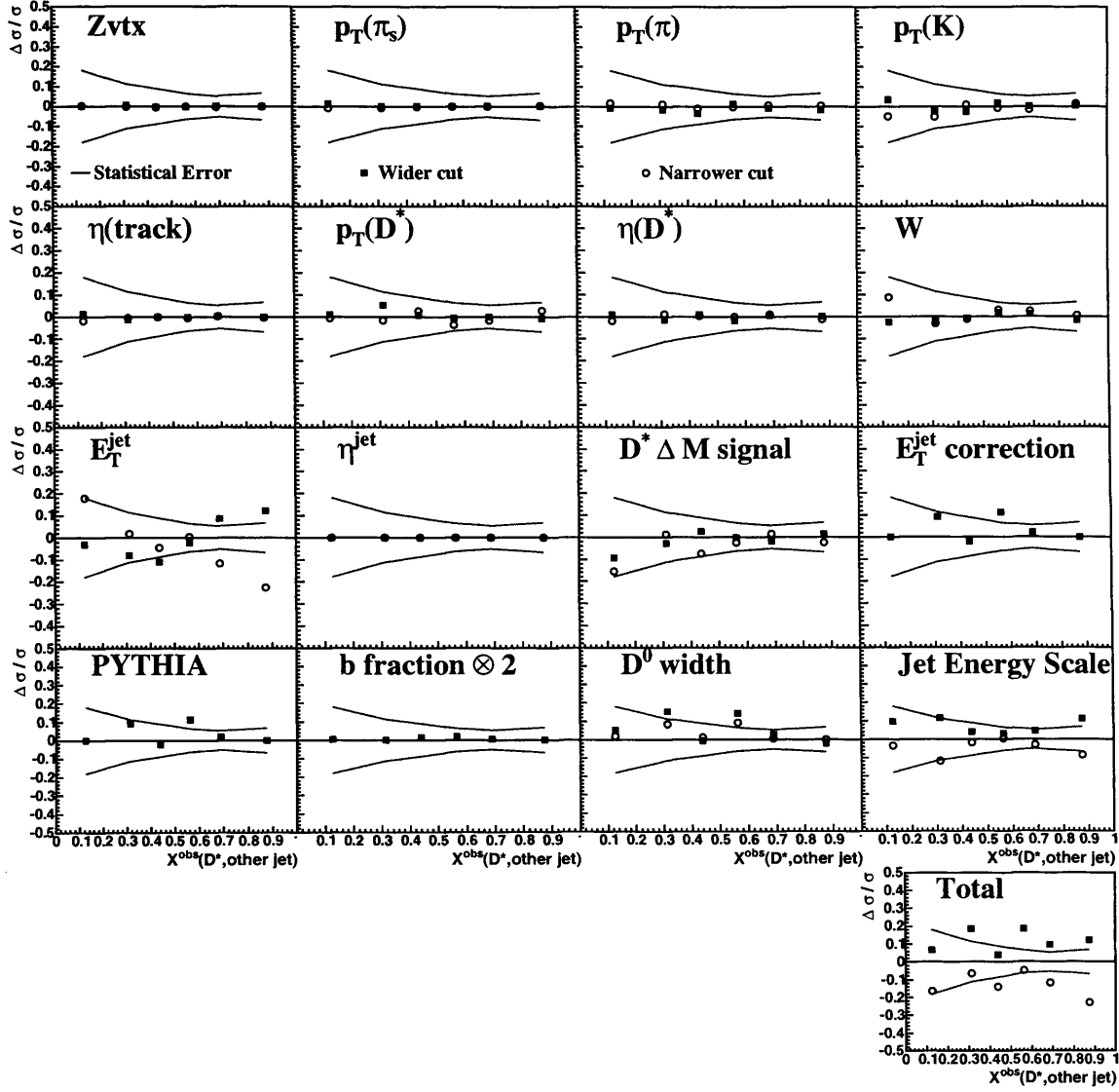
**17.0.21  $d\sigma/dE_T^{jet}$  systematics,  $8.0 < p_T^{D^*} < 20.0$  GeV**


**Figure 17.21** Systematics for each bin of the inclusive charm jet cross section  $d\sigma/dE_T^{jet}$  in the range  $8.0 < p_T^{D^*} < 20.0$  GeV for 1998-2000 data  $78pb^{-1}$ .

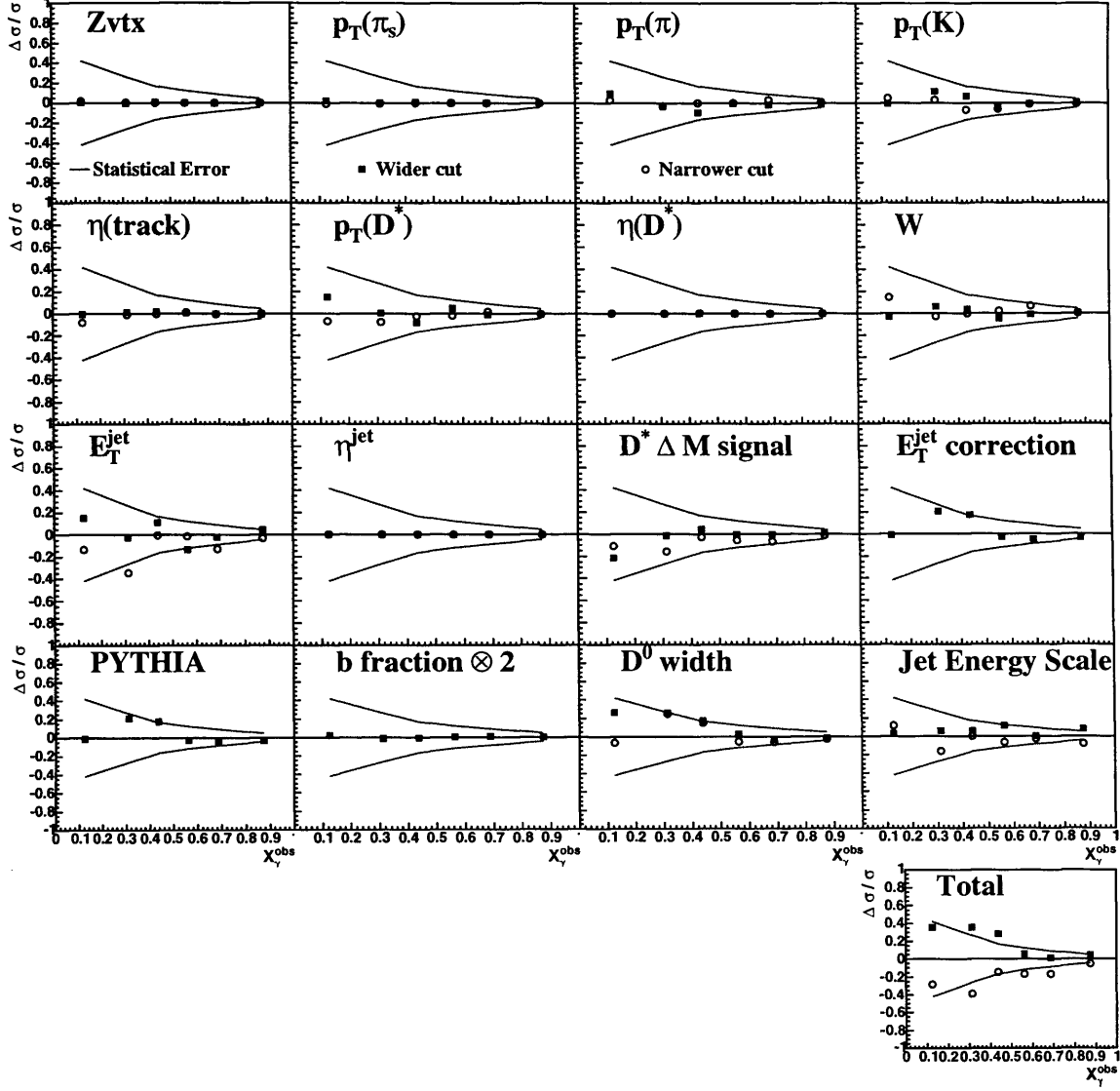


17.0.22  $d\sigma/d\eta^{jet}$  systematics,  $8.0 < p_T^{D^*} < 20.0$  GeV

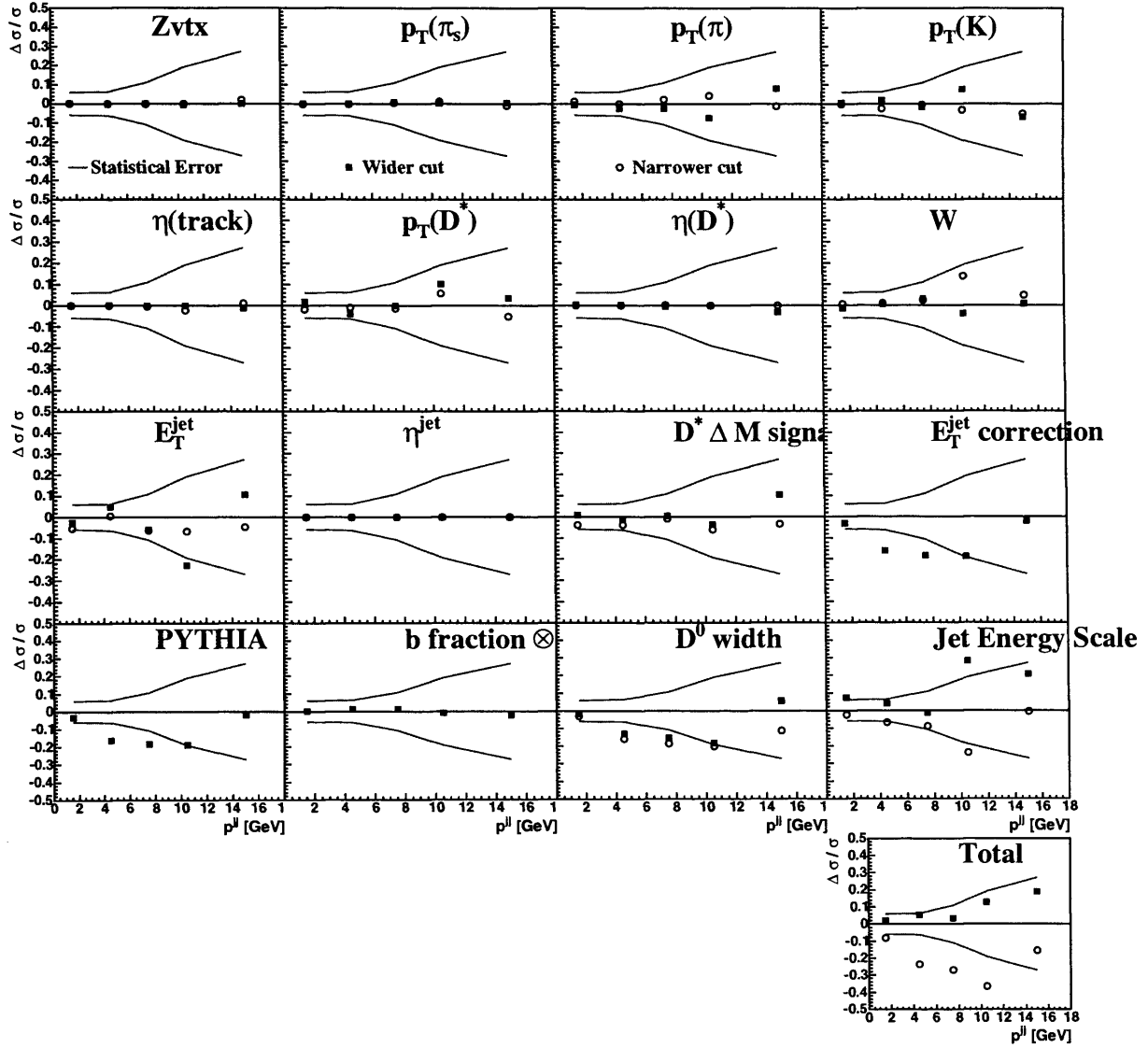
**Figure 17.22** Systematics for each bin of the inclusive charm jet cross section  $d\sigma/d\eta^{jet}$  in the range  $8.0 < P_T^{D^*} < 20.0$  GeV for 1998-2000 data  $78pb^{-1}$ .

17.0.23  $d\sigma/dx_\gamma^{\text{obs}}(D^*, \text{other jet})$  systematics

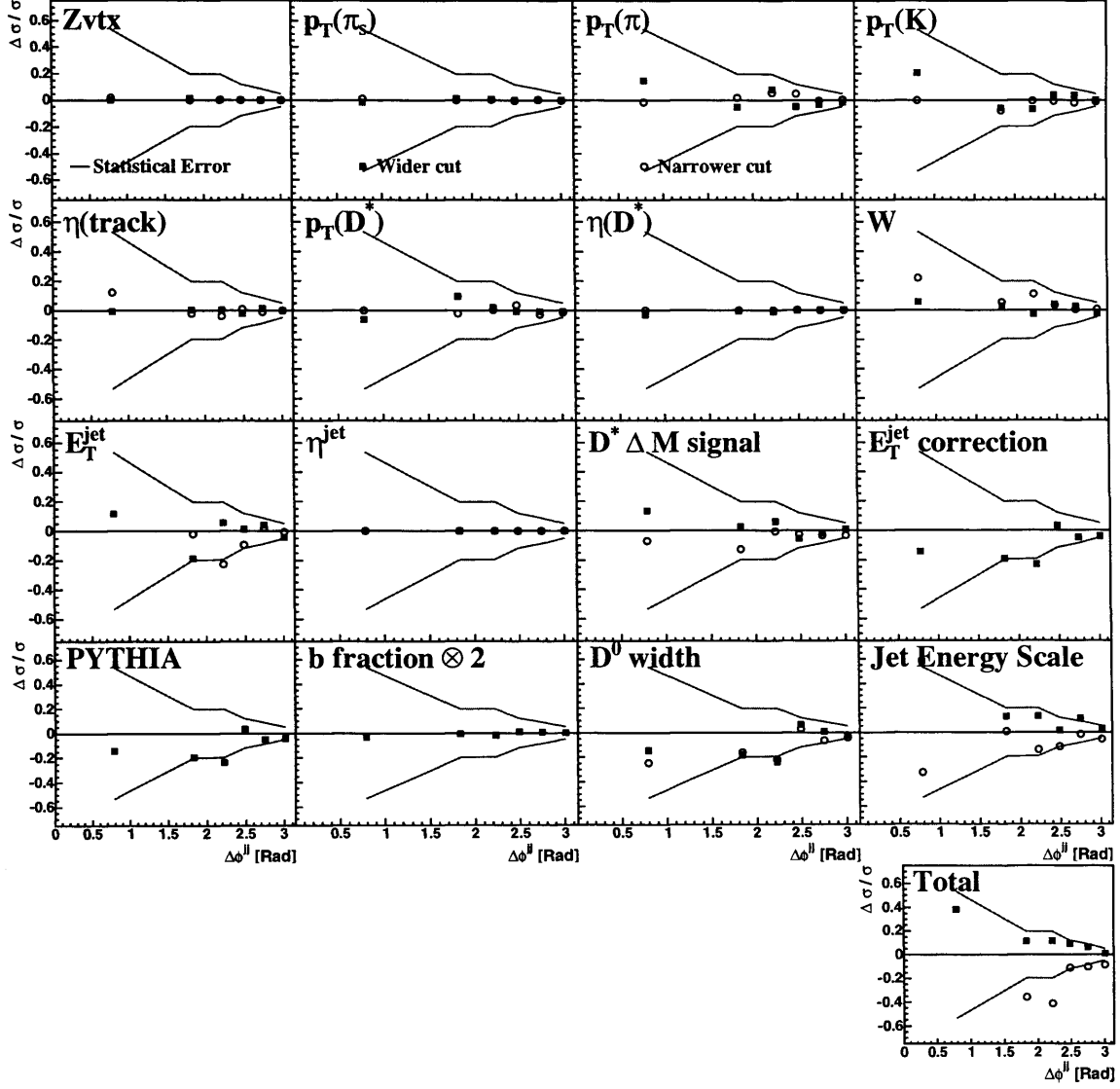
**Figure 17.23** Systematics for each bin of the inclusive charm jet cross section  $d\sigma/dx_\gamma^{\text{obs}}(D^*, \text{other jet})$  for 1998-2000 data  $78\text{pb}^{-1}$ .

17.0.24  $d\sigma/dx_\gamma^{\text{obs}}$  systematics

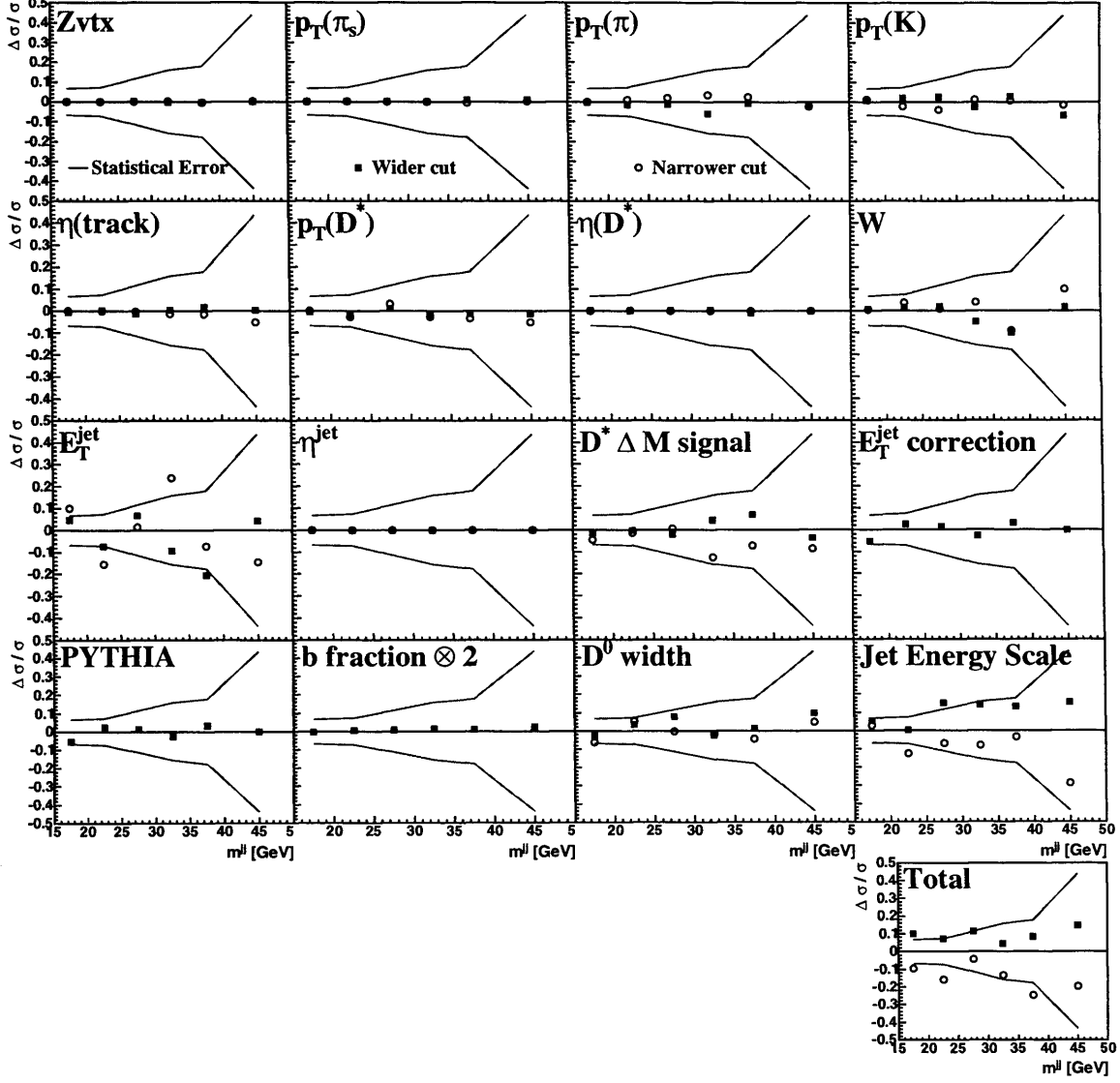
**Figure 17.24** Systematics for each bin of the dijet charm cross section  $d\sigma/dx_\gamma^{\text{obs}}$  for 1998-2000 data  $78\text{pb}^{-1}$ .

17.0.25  $d\sigma/dp_T^{jj}$  systematics

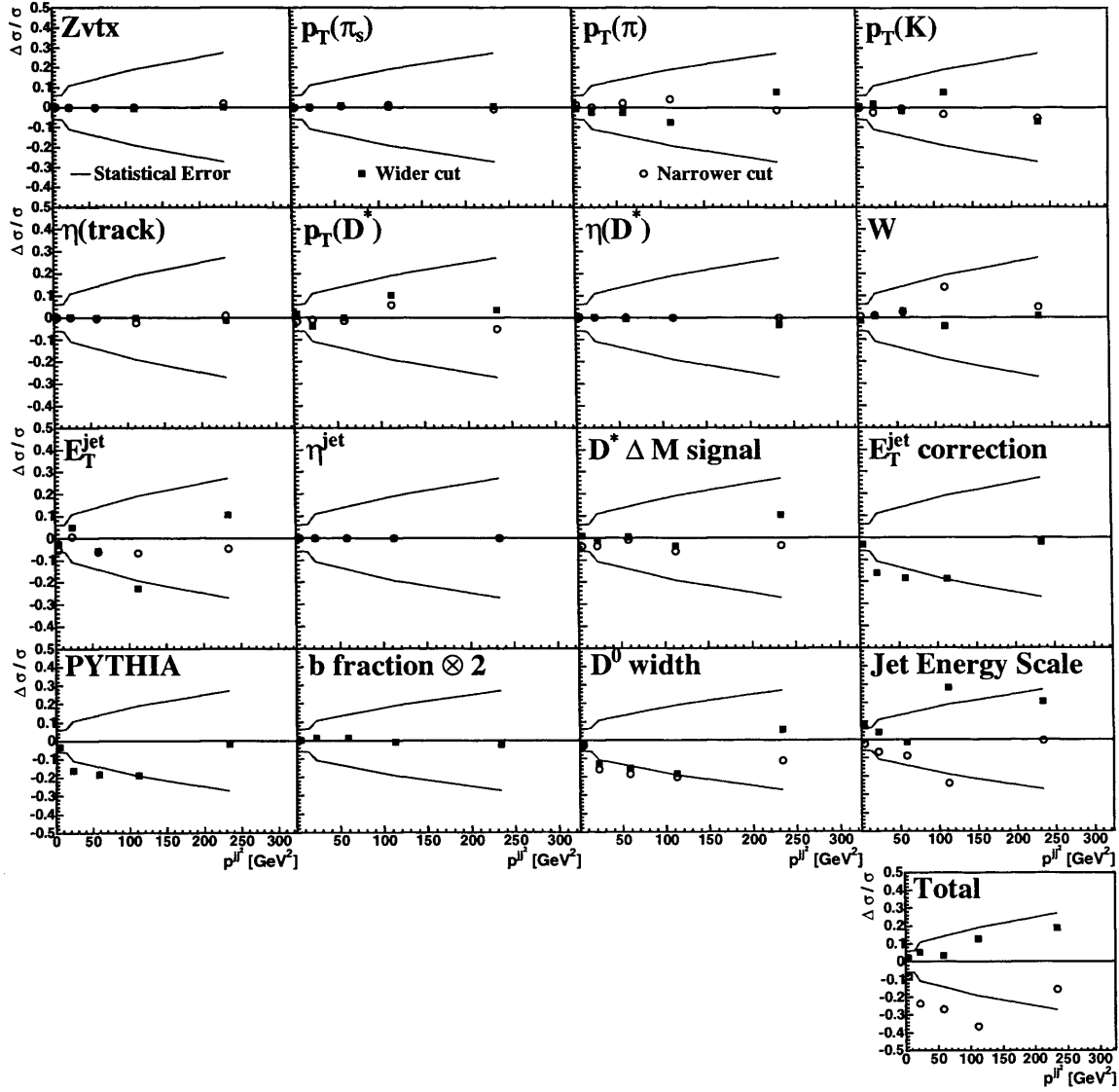
**Figure 17.25** Systematics for each bin of the dijet charm cross section  $d\sigma/dp_T^{jj}$  for 1998-2000 data  $78pb^{-1}$ .

17.0.26  $d\sigma/d\Delta\phi^{jj}$  systematics

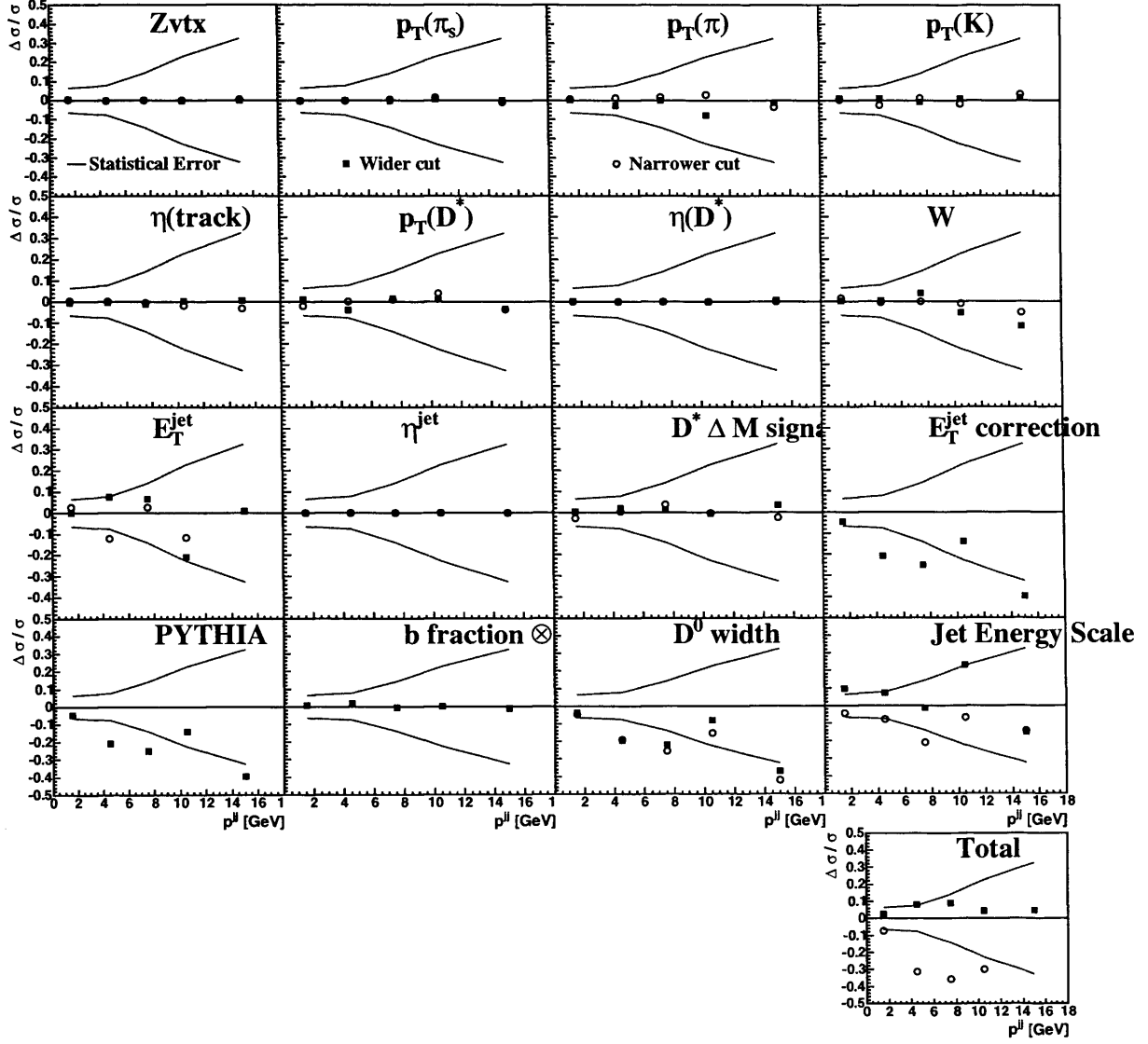
**Figure 17.26** Systematics for each bin of the dijet charm cross section  $d\sigma/d\Delta\phi^{jj}$  for 1998-2000 data  $78\text{pb}^{-1}$ .

17.0.27  $d\sigma/dm^{jj}$  systematics

**Figure 17.27** Systematics for each bin of the dijet charm cross section  $d\sigma/dm^{jj}$  for 1998-2000 data  $78\text{pb}^{-1}$ .

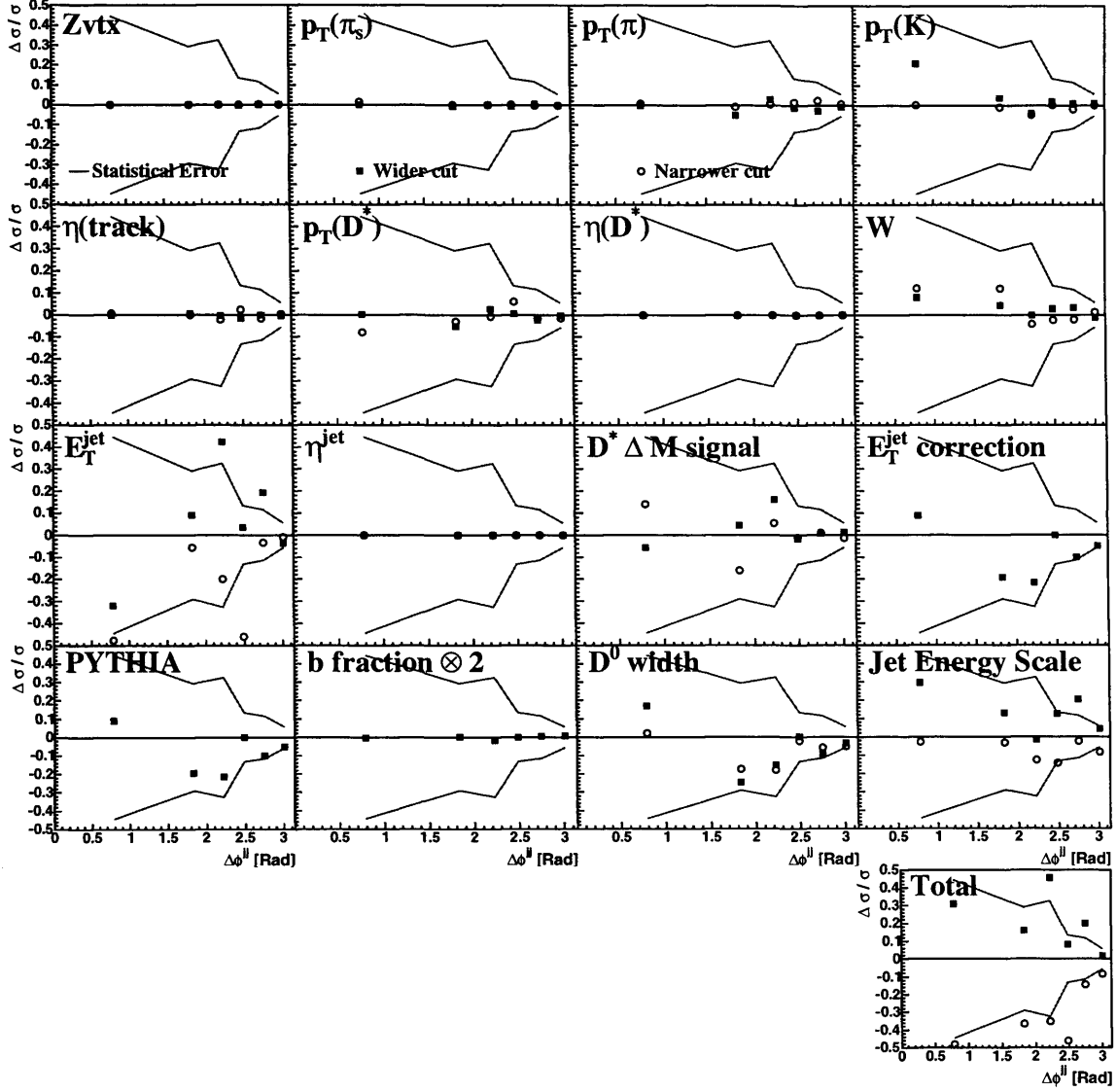
17.0.28  $d\sigma/dp_T^{2jj}$  systematics

**Figure 17.28** Systematics for each bin of the dijet charm cross section  $d\sigma/dp_T^{2jj}$  for 1998-2000 data  $78\text{pb}^{-1}$ .

17.0.29  $d\sigma/dp_T^{jj}$  systematics, direct-enriched  $x_\gamma^{\text{obs}} > 0.75$ 


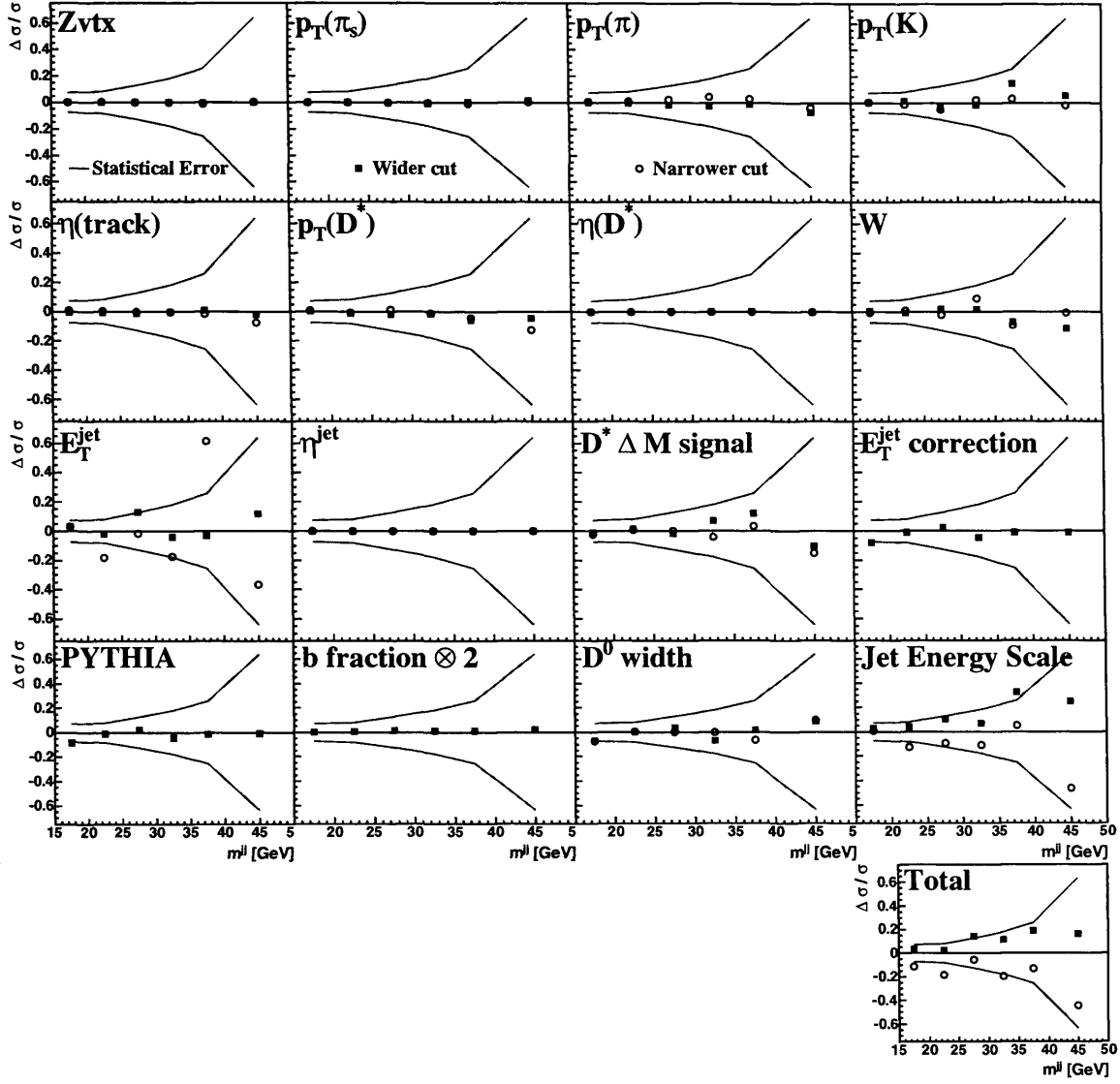
**Figure 17.29** Systematics for each bin of the dijet charm cross section  $d\sigma/dp_T^{jj}$  for 1998-2000 data  $78\text{pb}^{-1}$ , with  $x_\gamma^{\text{obs}} > 0.75$ .



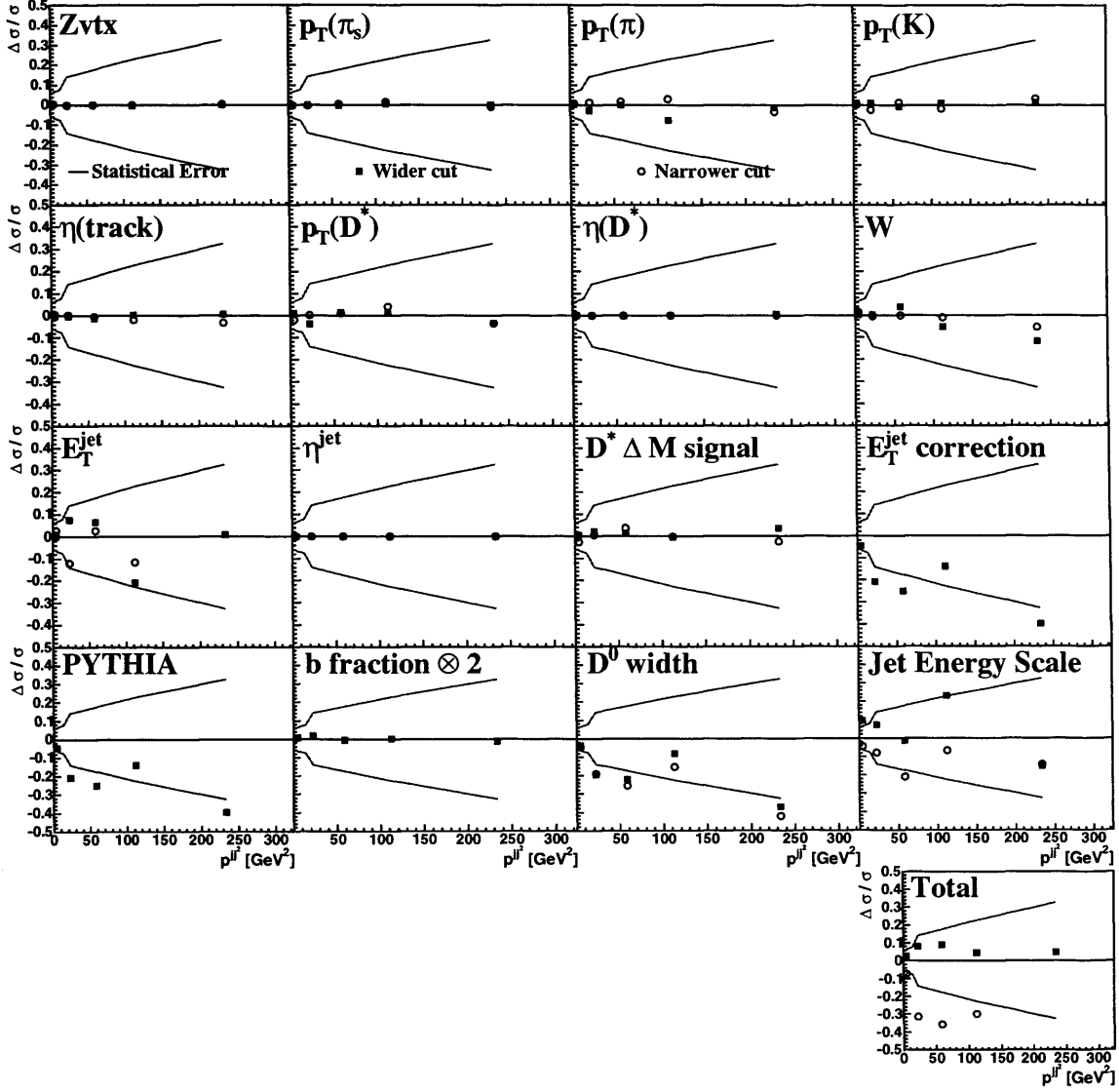
17.0.30  $d\sigma/d\Delta\phi^{jj}$  systematics, direct-enriched  $x_\gamma^{\text{obs}} > 0.75$ 


**Figure 17.30** Systematics for each bin of the dijet charm cross section  $d\sigma/d\Delta\phi^{jj}$  for 1998-2000 data  $78\text{pb}^{-1}$ , with  $x_\gamma^{\text{obs}} > 0.75$ .

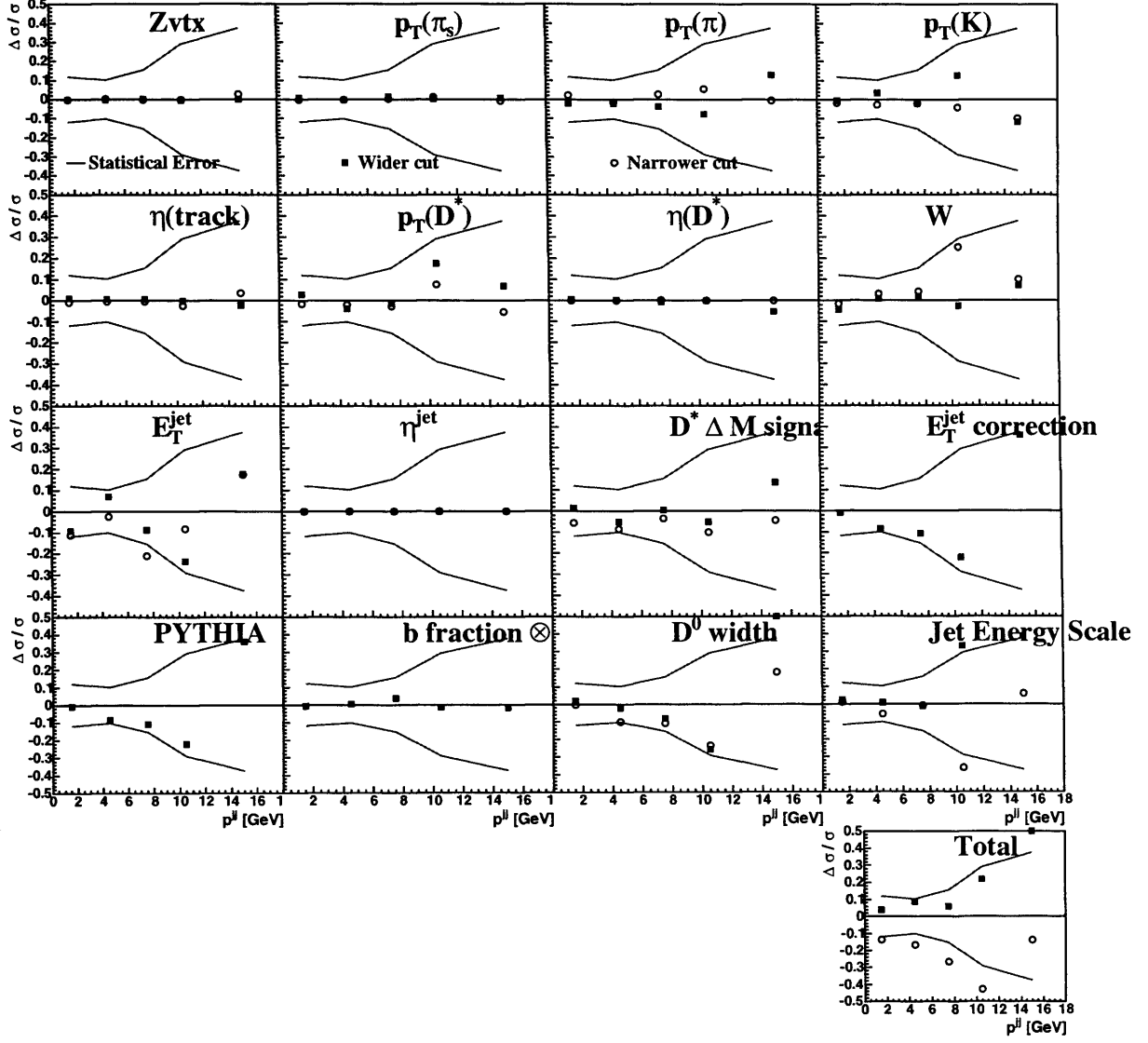
### 17.0.31 $d\sigma/dm^{jj}$ systematics, direct-enriched $x_\gamma^{\text{obs}} > 0.75$



**Figure 17.31** Systematics for each bin of the dijet charm cross section  $d\sigma/dm^{jj}$  for 1998-2000 data  $78pb^{-1}$ , with  $x_\gamma^{\text{obs}} > 0.75$ .

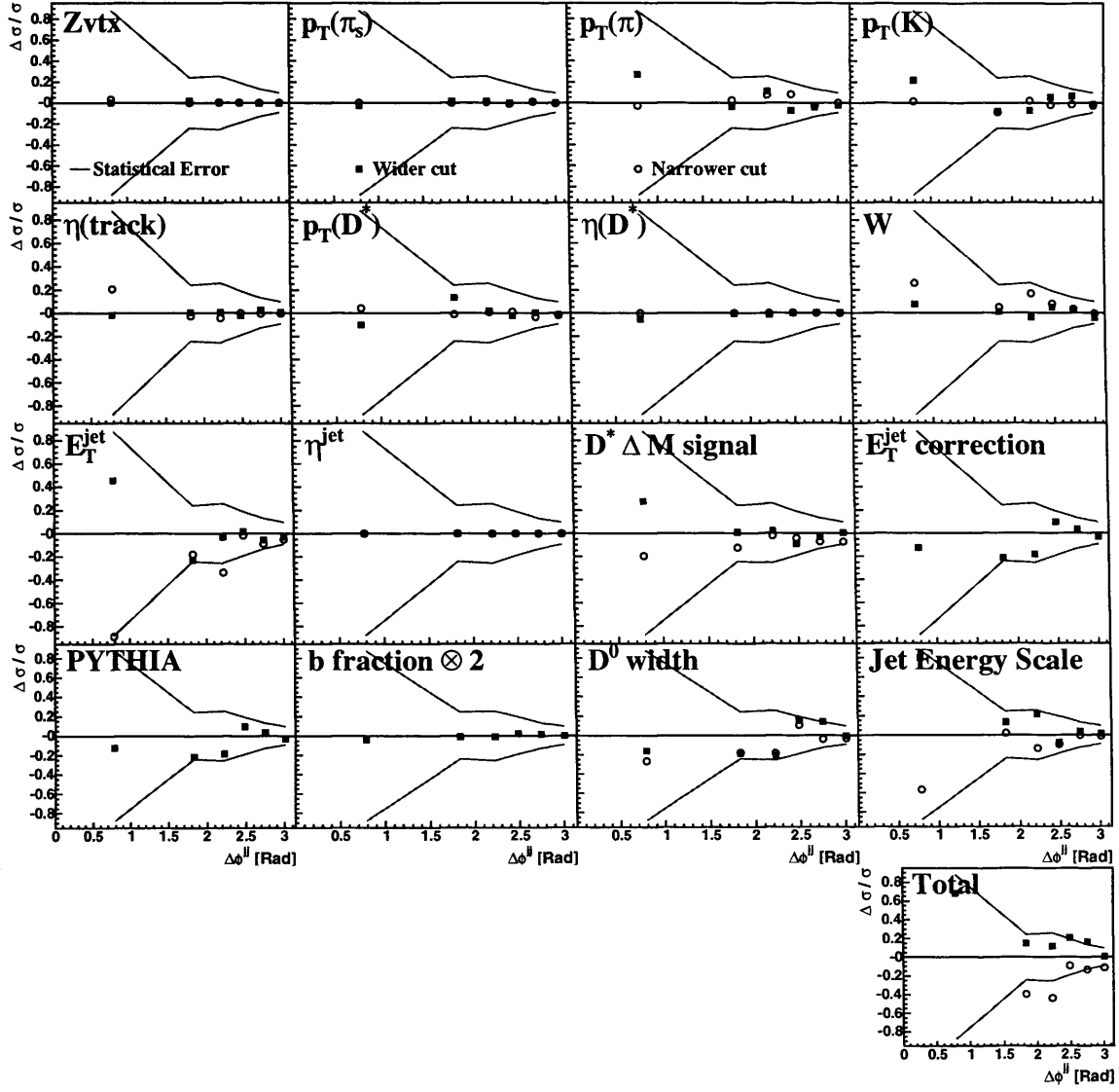
17.0.32  $d\sigma/dp_T^{2jj}$  systematics, direct-enriched  $x_\gamma^{\text{obs}} > 0.75$ 

**Figure 17.32** Systematics for each bin of the dijet charm cross section  $d\sigma/dp_T^{2jj}$  for 1998-2000 data  $78\text{pb}^{-1}$ , with  $x_\gamma^{\text{obs}} > 0.75$ .

17.0.33  $d\sigma/dp_T^{jj}$  systematics, resolved-enriched  $x_\gamma^{\text{obs}} < 0.75$ 

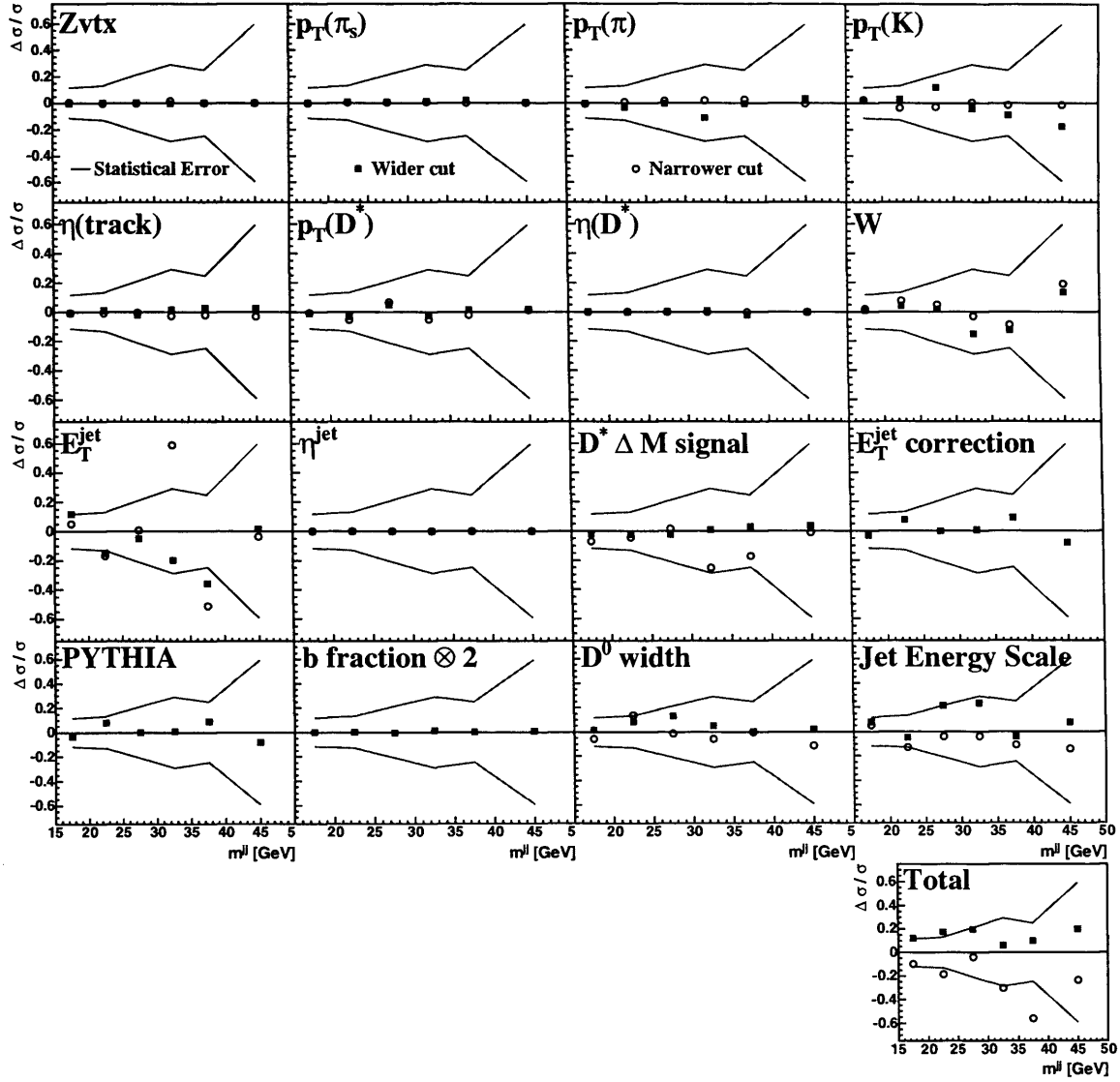
**Figure 17.33** Systematics for each bin of the dijet charm cross section  $d\sigma/dp_T^{jj}$  for 1998-2000 data  $78\text{pb}^{-1}$ , with  $x_\gamma^{\text{obs}} < 0.75$ .

### 17.0.34 $d\sigma/d\Delta\phi^{jj}$ systematics, resolved-enriched $x_\gamma^{\text{obs}} < 0.75$

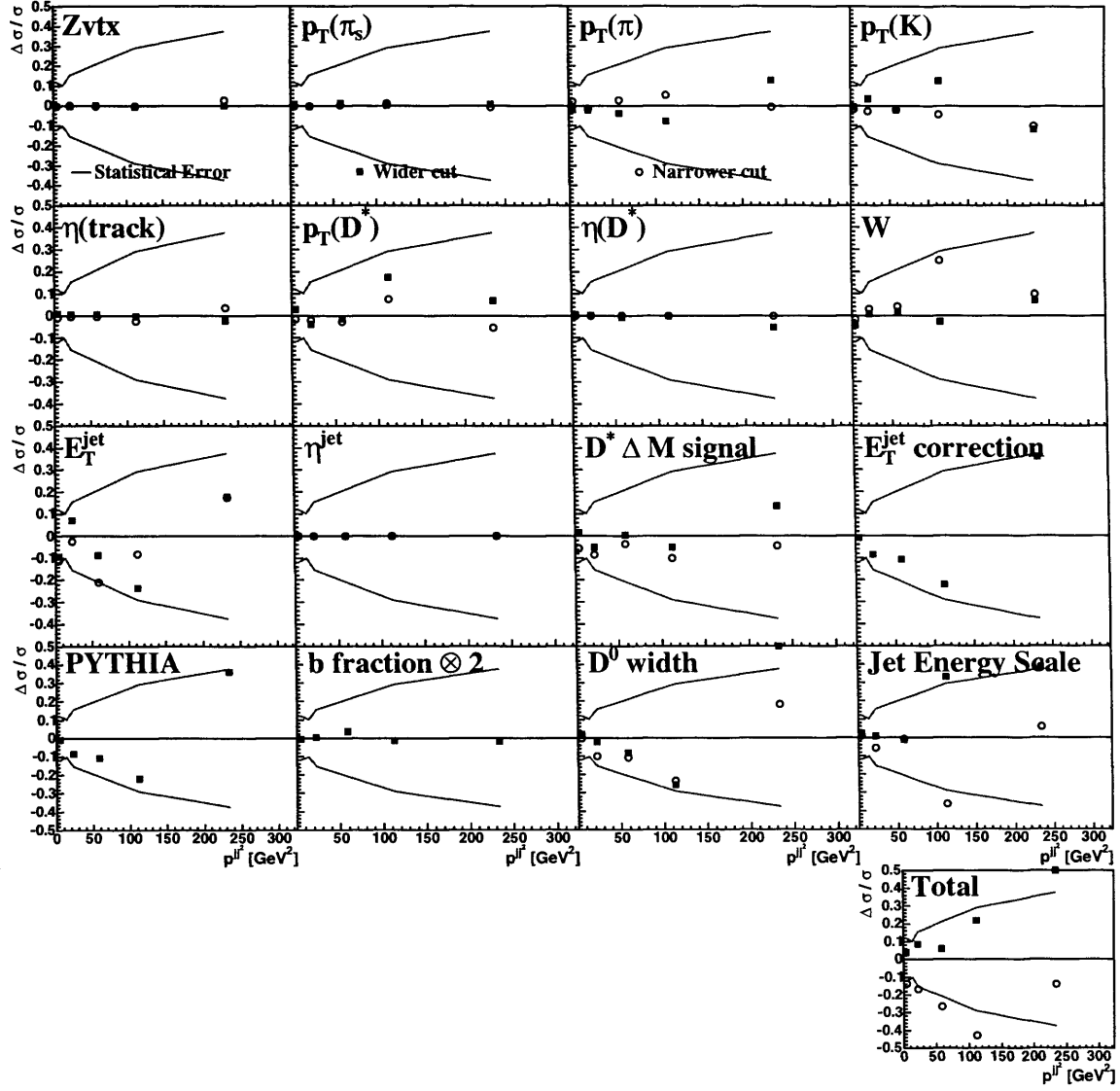


**Figure 17.34** Systematics for each bin of the dijet charm cross section  $d\sigma/d\Delta\phi^{jj}$  for 1998-2000 data  $78\text{pb}^{-1}$ , with  $x_\gamma^{\text{obs}} < 0.75$ .

### 17.0.35 $d\sigma/dm^{jj}$ systematics, resolved-enriched $x_\gamma^{\text{obs}} < 0.75$



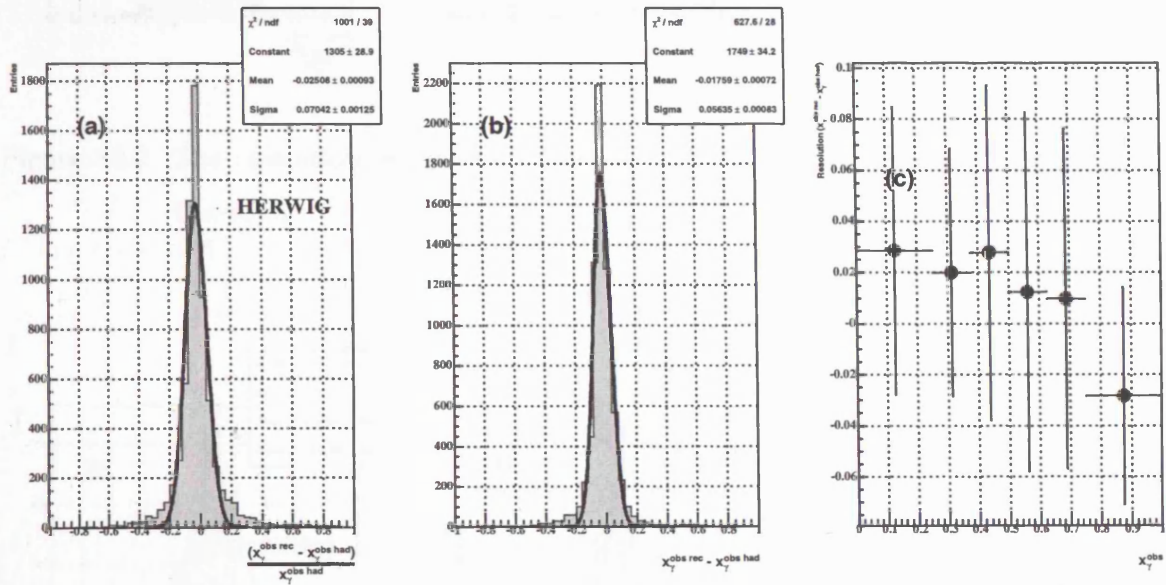
**Figure 17.35** Systematics for each bin of the dijet charm cross section  $d\sigma/dm^{jj}$  for 1998-2000 data  $78\text{pb}^{-1}$ , with  $x_\gamma^{\text{obs}} < 0.75$ .

17.0.36  $d\sigma/dp_T^{2jj}$  systematics, resolved-enriched  $x_\gamma^{\text{obs}} < 0.75$ 


**Figure 17.36** Systematics for each bin of the dijet charm cross section  $d\sigma/dp_T^{2jj}$  for 1998-2000 data  $78\text{pb}^{-1}$ , with  $x_\gamma^{\text{obs}} < 0.75$ .

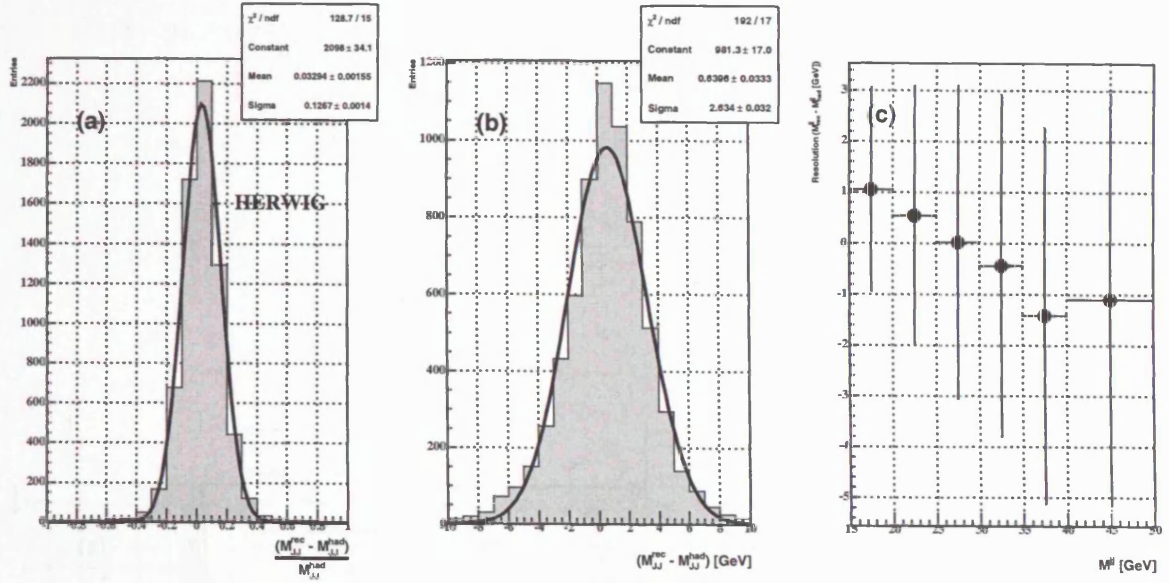
## 18 Appendix F : Resolutions

In this appendix the resolutions are shown for  $x_\gamma^{\text{obs}}$ ,  $m^{jj}$ ,  $p_T^{jj}$ , and  $\Delta\phi^{jj}$  in figures 18.1, 18.2, 18.3 and 18.4 respectively.

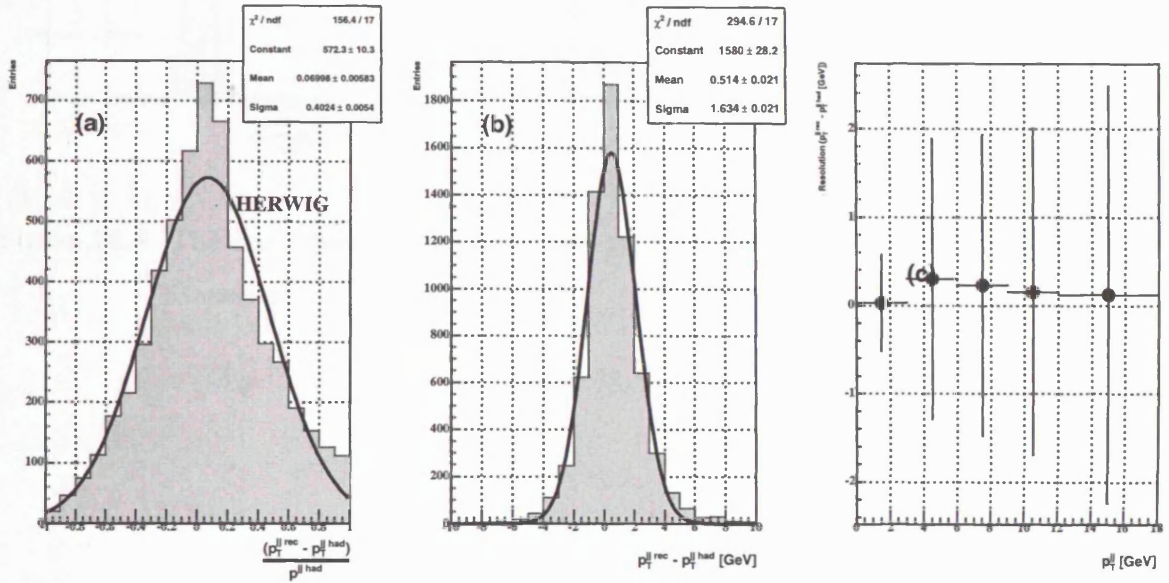


**Figure 18.1** The resolution of  $x_\gamma^{\text{obs}}$  using 886 pb<sup>-1</sup> of HERWIG Monte Carlo. The fits are Gaussian.

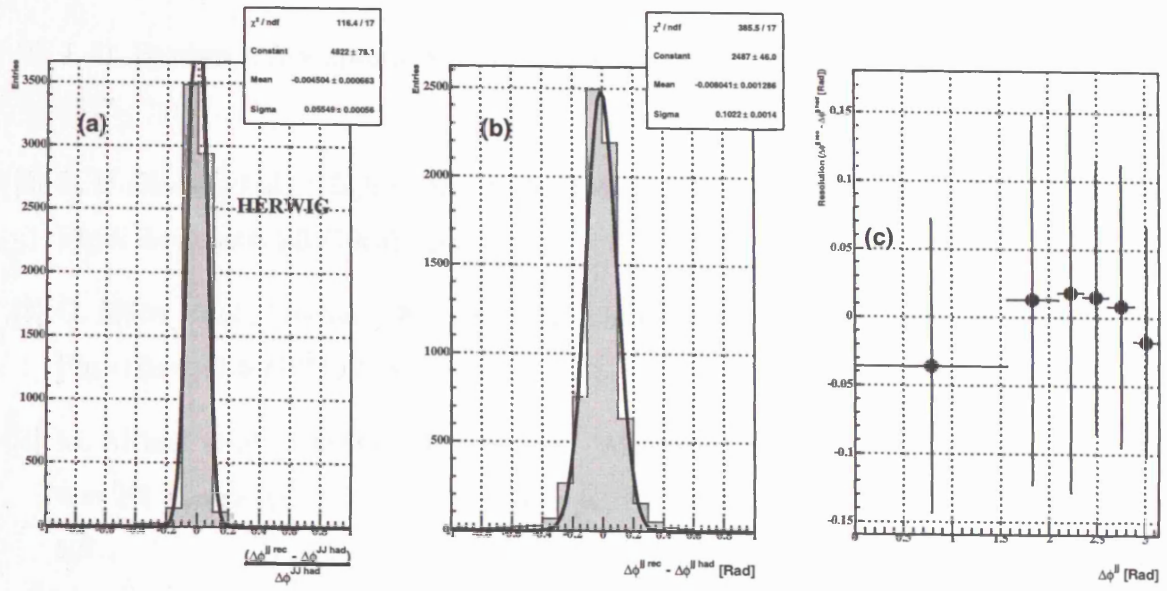




**Figure 18.2** The resolution of  $m^{\text{jj}}$  using  $886 \text{ pb}^{-1}$  of HERWIG Monte Carlo. The fits are Gaussian.



**Figure 18.3** The resolution of  $p_T^{\text{jj}}$  using  $886 \text{ pb}^{-1}$  of HERWIG Monte Carlo. The fits are Gaussian.



**Figure 18.4** The resolution of  $\Delta\phi^{jj}$  using 886 pb<sup>-1</sup> of HERWIG Monte Carlo. The fits are Gaussian.

---

## Bibliography

---

- [1] J. D. Bjorken, "Asymptotic Sum Rules At Infinite Momentum," Phys. Rev. **179** (1969) 1547.
- [2] E. D. Bloom *et al.*, "High-Energy Inelastic E P Scattering At 6-Degrees And 10-Degrees," Phys. Rev. Lett. **23** (1969) 930.
- [3] G. Miller *et al.*, "Inelastic Electron - Proton Scattering At Large Momentum Transfers," Phys. Rev. D **5** (1972) 528.
- [4] M. Althoff *et al.* [TASSO Collaboration], "Measurement Of The Photon Structure Function  $F_2(\gamma)$  At  $Q^2$  From 7-GeV/ $c^2$  To 70-GeV/ $c^2$ ," Z. Phys. C **31** (1986) 527.
- [5] R. Brandelik *et al.* [TASSO Collaboration], "Evidence For Planar Events In  $E^+ E^-$  Annihilation At High-Energies," Phys. Lett. B **86** (1979) 243.
- [6] Y. I. Azimov, Y. L. Dokshitzer, V. A. Khoze and S. I. Troian, "The String Effect And QCD Coherence," Phys. Lett. B **165** (1985) 147.
- [7] S. D. Ellis and D. E. Soper, "Successive combination jet algorithm for hadron collisions," Phys. Rev. D **48** (1993) 3160 [arXiv:hep-ph/9305266].
- [8] S. Frixione, M. L. Mangano, P. Nason and G. Ridolfi, "Total cross-sections for heavy flavor production at HERA," Phys. Lett. B **348** (1995) 633 [arXiv:hep-ph/9412348].
- [9] S. Frixione, P. Nason and G. Ridolfi, "Differential distributions for heavy flavor production at HERA," Nucl. Phys. B **454** (1995) 3 [arXiv:hep-ph/9506226].

- [10] Gudrun Heinrich and Bernd A. Kniehl. Next-to-leading-order predictions for  $D^{*\pm}$  plus jet photoproduction at desy hera. *Phys. Rev.*, D70:094035, 2004.
- [11] M. Cacciari, S. Frixione and P. Nason, “The p(T) spectrum in heavy-flavor photoproduction,” *JHEP* **0103** (2001) 006 [arXiv:hep-ph/0102134].
- [12] S. Frixione and P. Nason, “Phenomenological study of charm photoproduction at HERA,” *JHEP* **0203** (2002) 053 [arXiv:hep-ph/0201281].
- [13] G. Kramer and H. Spiesberger, “Inclusive photoproduction of  $D^*$  mesons with massive charm quarks,” *Eur. Phys. J. C* **38** (2004) 309 [arXiv:hep-ph/0311062].
- [14] H. Jung, “Hard diffractive scattering in high-energy e p collisions and the Monte Carlo generation RAPGAP,” *Comput. Phys. Commun.* **86** (1995) 147.
- [15] G. Ingelman, J. Rathsman and G. A. Schuler, “AROMA 2.2 - A Monte Carlo Generator for Heavy Flavour Events in  $ep$  Collisions,” *Comput. Phys. Commun.* **101** (1997) 135 [arXiv:hep-ph/9605285].
- [16] H. Jung, “The CCFM Monte Carlo generator CASCADE,” *Comput. Phys. Commun.* **143** (2002) 100 [arXiv:hep-ph/0109102].
- [17] V. M. Abazov *et al.* [D0 Collaboration], “Measurement of dijet azimuthal decorrelations at central rapidities in p anti-p collisions at  $s^{1/2} = 1.96\text{-TeV}$ ,” *Phys. Rev. Lett.* **94** (2005) 221801 [arXiv:hep-ex/0409040].
- [18] C. Peterson, D. Schlatter, I. Schmitt and P. M. Zerwas, “Scaling Violations In Inclusive  $E^+ E^-$  Annihilation Spectra,” *Phys. Rev. D* **27** (1983) 105.
- [19] P. Nason and C. Oleari, “A phenomenological study of heavy-quark fragmentation functions in  $e^+ e^-$  annihilation,” *Nucl. Phys. B* **565** (2000) 245 [arXiv:hep-ph/9903541].
- [20] G. Corcella *et al.*, “HERWIG 6.1 release note,” arXiv:hep-ph/9912396.
- [21] G. Corcella *et al.*, “HERWIG 6.3 release note,” arXiv:hep-ph/0107071.
- [22] Y. L. Dokshitzer, “Calculation Of The Structure Functions For Deep Inelastic Scattering And  $E^+ E^-$  Annihilation By Perturbation Theory In Quantum Chromodynamics. (In Russian),” *Sov. Phys. JETP* **46** (1977) 641 [*Zh. Eksp. Teor. Fiz.* **73** (1977) 1216].

- [23] G. Altarelli and G. Parisi, “Asymptotic Freedom In Parton Language,” Nucl. Phys. B **126** (1977) 298.
- [24] V. N. Gribov and L. N. Lipatov, “Deep Inelastic E P Scattering In Perturbation Theory,” Sov. J. Nucl. Phys. **15** (1972) 438 [Yad. Fiz. **15** (1972) 781].
- [25] T. Sjostrand, P. Eden, C. Friberg, L. Lonnblad, G. Miu, S. Mrenna and E. Norrbin, “High-energy-physics event generation with PYTHIA 6.1,” Comput. Phys. Commun. **135** (2001) 238 [arXiv:hep-ph/0010017].
- [26] J. Breitweg *et al.* [ZEUS Collaboration], “Measurement of inclusive  $D^{*+}$ - and associated dijet cross sections in photoproduction at HERA,” Eur. Phys. J. C **6** (1999) 67 [arXiv:hep-ex/9807008].
- [27] [H1 Collaboration], “ $D^*$  mesons and associated jet production in deep inelastic scattering” High energy physics. Proceedings, 32nd International Conference, ICHEP 2004, Beijing, China, August 16-22, 2004. Vol. 1 + 2, *Prepared for 32nd International Conference on High-Energy Physics (ICHEP 04), Beijing, China, 16-22 Aug 2004*
- [28] S. Chekanov *et al.* [ZEUS Collaboration], “Measurement of charm fragmentation ratios and fractions in photoproduction at HERA,” arXiv:hep-ex/0508019.
- [29] S. Chekanov [ZEUS Collaboration], “Measurement of  $D^*$  photoproduction at HERA” *Prepared for 31st International Conference on High Energy Physics (ICHEP 2002), Amsterdam, The Netherlands, 24-31 Jul 2002*
- [30] D. Acosta *et al.* [CDF Collaboration], “Measurement of prompt charm meson production cross sections in p anti-p collisions at  $s^{*}(1/2) = 1.96\text{-TeV}$ ,” Phys. Rev. Lett. **91** (2003) 241804 [arXiv:hep-ex/0307080].
- [31] M. Cacciari and P. Nason, “Charm cross sections for the Tevatron Run II,” JHEP **0309** (2003) 006 [arXiv:hep-ph/0306212].
- [32] B. A. Kniehl, G. Kramer and B. Potter, “Testing the universality of fragmentation functions,” Nucl. Phys. B **597** (2001) 337 [arXiv:hep-ph/0011155].

- [33] B. J. West [ZEUS Collaboration], "Charm and the virtual photon at HERA," *Prepared for International Conference on the Structure and Interactions of the Photon and 14th International Workshop on Photon-Photon Collisions (Photon 2001), Ascona, Switzerland, 2-7 Sep 2001*
- [34] B.J.West. Charm and the virtual photon at hera and a global tracking trigger for zeus. *Thesis, University College London (2001)*. (Unpublished)
- [35] M. Derrick *et al.* [ZEUS Collaboration], "Dijet cross-sections in photoproduction at HERA," *Phys. Lett. B* **348** (1995) 665 [arXiv:hep-ex/9502008].
- [36] G. A. Schuler and T. Sjostrand, "Parton Distributions of the Virtual Photon," *Phys. Lett. B* **376** (1996) 193 [arXiv:hep-ph/9601282].
- [37] The ZEUS detector. Status Report (unpublished), DESY, 1993.
- [38] J. Andruszkow *et al.* [ZEUS Luminosity Group Collaboration], "Luminosity measurement in the ZEUS experiment," *Acta Phys. Polon. B* **32** (2001) 2025.
- [39] N. Harnew *et al.*, "Vertex Triggering Using Time Difference Measurements In The Zeus Central Tracking Detector," *Nucl. Instrum. Meth. A* **279** (1989) 290.
- [40] B. Foster *et al.* [ZEUS Collaboration], "The Design and construction of the ZEUS central tracking detector," *Nucl. Instrum. Meth. A* **338** (1994) 254.
- [41] B. Foster *et al.*, "The Performance of the ZEUS central tracking detector z-by-timing electronics in a transputer based data acquisition system," *Nucl. Phys. Proc. Suppl.* **32** (1993) 181.
- [42] M. Derrick *et al.*, "Design and construction of the ZEUS barrel calorimeter," *Nucl. Instrum. Meth. A* **309** (1991) 77.
- [43] A. Andresen *et al.* [ZEUS Calorimeter Group Collaboration], "Construction and beam test of the ZEUS forward and rear calorimeter," *Nucl. Instrum. Meth. A* **309** (1991) 101.
- [44] A. Caldwell *et al.*, "Design and implementation of a high precision readout system for the ZEUS calorimeter," *Nucl. Instrum. Meth. A* **321** (1992) 356.

- [45] A. Bernstein *et al.* [ZEUS Barrel Calorimeter Group Collaboration], “Beam tests of the ZEUS barrel calorimeter,” Nucl. Instrum. Meth. A **336** (1993) 23.
- [46] J. Andruszkow *et al.* [ZEUS Luminosity Monitor Group Collaboration], “First measurement of HERA luminosity by ZEUS lumi monitor,” DESY-92-066
- [47] M. Derrick *et al.* [ZEUS Collaboration], “Measurement of total and partial photon proton cross-sections at 180-GeV center-of-mass energy,” Z. Phys. C **63** (1994) 391.
- [48] W. H. Smith, K. Tokushuku and L. W. Wiggers, “The ZEUS trigger system,” DESY-92-150B *Contributed to 10th International Conference on Computing in High Energy Physics (CHEP 92), Annecy, France, 21-25 Sept 1992*
- [49] F. Jacquet and A. Blondel. Detection of the charged current event – Method II. In U. Amaldi, editor, *Proceedings of the Study for an ep Facility for Europe*, page 391, Hamburg, Germany, 1979.
- [50] R. Sinkus and T. Voss, “Particle identification with neural networks using a rotational invariant moment representation,” Nucl. Instrum. Meth. A **389** (1997) 160.
- [51] H. Abramowicz, A. Caldwell and R. Sinkus, “Neural network based electron identification in the ZEUS calorimeter,” Nucl. Instrum. Meth. A **365** (1995) 508 [arXiv:hep-ex/9505004].
- [52] G. M. Briskin, “Diffractive dissociation in ep deep inelastic scattering,” DESY-THESIS-1998-036
- [53] W.. Buchmuller and G. Ingelman, “Physics at HERA. Proceedings, Workshop, Hamburg, Germany, October 29-30, 1991. Vol. 1,”
- [54] G.M Briskin and A. Caldwell ZEUS-95-035 1995, internal ZEUS-note.  
G.M. Briskin, Ph.D. Thesis, Tel Aviv University (1998). (Unpublished)
- [55] J. M. Butterworth, J. P. Couchman, B. E. Cox and B. M. Waugh, “KtJet: A C++ implementation of the K(T) clustering algorithm,” Comput. Phys. Commun. **153** (2003) 85 [arXiv:hep-ph/0210022].
- [56] Particle Data Group, S. Eidelman *et al.*, Phys. Lett. **B 592**, 1 (2004)

- [57] L. Gladilin, “Charm hadron production fractions,” arXiv:hep-ex/9912064.
- [58] S. Chekanov *et al.* [ZEUS Collaboration], “Inclusive charm jet cross sections in photo-production” High energy physics. Proceedings, 32nd International Conference, ICHEP 2004, Beijing, China, August 16-22, 2004. Vol. 1 + 2, *Prepared for 32nd International Conference on High-Energy Physics (ICHEP 04), Beijing, China, 16-22 Aug 2004*
- [59] J.H. Loizides, “Charm production at HERA I & heavy flavours at HERA II” High energy physics. Proceedings, 32nd International Conference, ICHEP 2004, Beijing, China, August 16-22, 2004. Vol. 1 + 2, *Prepared for 32nd International Conference on High-Energy Physics (ICHEP 04), Beijing, China, 16-22 Aug 2004*
- [60] T. Kohno, “Measurement of jet cross sections in  $D^{*+}$ - photoproduction at HERA,” KEK-REPORT-2004-3
- [61] T. Kohno [ZEUS Collaboration], “Jet cross sections in  $D^*$  photoproduction,” *Prepared for 12th International Workshop on Deep Inelastic Scattering (DIS 2004), Strbske Pleso, Slovakia, 14-18 Apr 2004*
- [62] H. L. Lai *et al.* [CTEQ Collaboration], “Global QCD analysis of parton structure of the nucleon: CTEQ5 parton distributions,” Eur. Phys. J. C **12** (2000) 375 [arXiv:hep-ph/9903282].
- [63] M. Gluck, E. Reya and A. Vogt, “Parton structure of the photon beyond the leading order,” Phys. Rev. D **45** (1992) 3986.
- [64] G. Corcella and A. Mitov, “Bottom Quark fragmentation in top quark decay,” Nucl.Phys **B623** (2002) 247-270 [hep-ph/0110319].
- [65] R. Brun, F. Bruyant, M. Maire, A. C. McPherson and P. Zancarini, “Geant3,” CERN-DD/EE/84-1
- [66] S. Nussinov, “Colored Quark Version Of Some Hadronic Puzzles,” Phys. Rev. Lett. **34** (1975) 1286.
- [67] K. Hagiwara *et al.* [Particle Data Group Collaboration], “Review of particle physics,” Phys. Rev. D **66** (2002) 010001.



- [68] S. Frixione and B. R. Webber, “Matching NLO QCD computations and parton shower simulations,” *JHEP* **0206** (2002) 029 [arXiv:hep-ph/0204244].
- [69] S. Frixione, P. Nason and B. R. Webber, “Matching NLO QCD and parton showers in heavy flavour production,” *JHEP* **0308** (2003) 007 [arXiv:hep-ph/0305252].
- [70] S. Chekanov *et al.* [ZEUS Collaboration], “Dijet angular distributions in photoproduction of charm at HERA,” *Phys. Lett. B* **565** (2003) 87 [arXiv:hep-ex/0302025].
- [71] D. Bailey and R. Hall-Wilton, “Experience with the ZEUS central tracking detector,” *Nucl. Instrum. Meth. A* **515** (2003) 37.
- [72] ZEUS Background Working Group. Study of beam-induced backgrounds in the zeus detector from 2002 hera running.
- [73] E.Maddox. “Study of heavy quark production at hera using the zeus microvertex detector”, *NIKHEF, PhD.Thesis* (2004).
- [74] S. Dhawan, “The architecture of the ZEUS second level Global Track Trigger”, 13<sup>th</sup> IEEE Real time conference. Proceedings, Montreal, Canada, May 18-23 (2003)
- [75] M. Sutton, “The ZEUS CTD-MVD Global Tracking Trigger Algorithm”, 13<sup>th</sup> IEEE Real time conference. Proceedings, Montreal, Canada, May 18-23 (2003)
- [76] C. Youngman, “The ZEUS silicon microvertex detector DAQ and slow control systems”, 13<sup>th</sup> IEEE Real time conference. Proceedings, Montreal, Canada, May 18-23 (2003)
- [77] A. Polini, “The Architecture of the Micro Vertex Detector DAQ and the Second Level Global Track Trigger” *Prepared for CHEP’03: Computing in High-Energy Physics and Nuclear, California, USA, 24-28 March 2003*
- [78] S. Chekanov *et al.* [ZEUS Collaboration], “Measurement of the neutral current cross section and F2 structure function for deep inelastic e+ p scattering at HERA,” *Eur. Phys. J. C* **21** (2001) 443 [arXiv:hep-ex/0105090].

–